Modeling of Multiphase Systems
in Pharmaceutical Applications

Dissertation

to obtain the academic degree of 'Doktor der technischen Wissenschaften' at the

Graz University of Technology

by Dipl.-Ing. Stefan Radl

Graz, June 2010

Institute for Process and Particle Engineering

Graz University of Technology

Graz, Austria

Stefan Radl

Modeling of Multiphase Systems
in Pharmaceutical Applications

Dissertation

First assessor

Univ.-Prof. Dipl.-Ing. Dr.techn. Johannes G. Khinast

Institute for Process and Particle Engineering

and

Research Center Pharmaceutical Engineering GmbH

Graz University of Technology

Second assessor

Prof. Dr.-Ing. Matthias Kraume

Department of Process Engineering

Technische Universität Berlin

STATUTORY DECLARATION

I declare that I have authored this thesis independently, that I have not used other than the declared sources / resources, and that I have explicitly marked all material which has been quoted either literally or by content from the used sources.

(Ich erkläre an Eides statt, dass ich die vorliegende Arbeit selbstständig verfasst, andere als die angegebenen Quellen/Hilfsmittel nicht benutzt, und die den benutzten Quellen wörtlich und inhaltlich entnommene Stellen als solche kenntlich gemacht habe.)

June, 2010 …………………………………………..

Dipl.-Ing. Stefan Radl

Für meine Großeltern

Preface

The first ideas for this work were born in a small pub near the Graz University of Technology in the Stremayrgasse. It was in December 2005 when I joined Harald Raupenstrauch to battle against the "Khinast Group" in table soccer. This was the time when I met Johannes Khinast and we directely started to talk about the direct numerical simulation of bubble swarms. I was impressed by his explanations and thought: "Wow, people doing this simulations must be very brave." So I joined his group to write my diploma thesis on this topic in April 2006.

I clearly remember the first day at the "Institute for Ressource Efficient and Sustainable Systems", in the office I used to call "The Jungle" - there were little bamboo trees everywhere. At that time, the group was made up of Heidi Woelfler and Georg "Schorsch" Schitter, two PhD students doing some organic chemistry in a tiny corner in a small lab. However, they were so enthusiastic about their job, that they could even convince me to go through thousands of lines of FORTRAN code day by day. Seven month later, I had written two manuscripts for papers and had manufactured a book made up of 140 pages that became my diploma thesis. At this moment it became crystal clear that I also want to start my PhD in this group, despite I knew this would not be an easy job.

I started working on this thesis in January 2007, and there seemed to be endless time to complete it. Still busy with the FORTRAN code of Johannes, I was quickly involved in practical engineering problems dealing with clean room decontamination and hot melt extrusion of pharmaceuticals. I realized quickly that there was plenty of space for research to be done in these two areas, and projects were wrapped around them. Starting with no clue in both areas, I met with peoply teaching me how a clean room and GMP documentation looks like. Despite this was definietely a work-intensive time, people were continously joining our group and the Research Center Pharmaceutical Engineering GmbH was slowly forming out of Johannes' ideas.

Now, more than four years after joining Johannes' group, my thoughts have also formed computer programs, metal, plexiglass and scientific publications. Also, I had the chance to introduce some students on how to write a diploma thesis, and I hope I did it well. I learned about parallel computing, C++, OpenFOAM, granular flows, mixing and chemical reactions, as well as other things in life. Most of my experiences during these years are reflected in this thesis lying in

front of you, and some are not. I'm sure, however, that I did my best to make it as complete as possible. I hope you find it useful, at least for some of your work, and enjoy reading it the same as I enjoyed writing it.

Kurzfassung

Die Modellierung von vielen Prozessen der pharmazeutischen Industrie hinkt der in anderen Industriebereichen (z.B. in der Automobilindustrie) hinterher. Zusätzlich ist gerade die Modellierung von Mehrphasensystemen in der pharmazeutischen Industrie besonders anspruchsvoll. Die derzeitigen Richtlinien der Behörden (z.B. der Food and Drug Administration und der European Medicines Agency) fordern ein tieferes Prozessverständnis, und auch die Hersteller von Pharmazeutika drängen nach einem tieferen Einblick in ihre Prozesse. Um diese Ziele zu erreichen, sind geeignete Modelle für die Produktionsprozesse von Wirkstoffen und Arzneimittelprodukten notwendig. Mit mechanistischen Modellen kann die höchste Stufe der Modellierung eines derartigen Prozesses erreicht werden, da diese auf einem detaillierten Verständnis der Sub-Schritte des Produktionsprozesses beruhen.

Die vorliegende Arbeit behandelt mechanistische Modelle für die Beschreibung von Mehrphasensystemen in der pharmazeutischen Industrie. Der Fokus liegt dabei auf der Beschreibung von Blasenströmungen und granularen Strömungen. Das Ziel der Arbeit ist eine detaillierte Beschreibung des derzeitigen Entwicklungsstandes, sowie die Durchführung verschiedener numerischer und experimenteller Untersuchungen dieser beiden Systeme. In einem ersten Schritt wurden relevante Mehrphasensysteme analysiert und geeignete Modellierungsstrategien ausgewählt. Reaktive Blasenströmungen wurden mit Direkten Numerischen Simulationen (DNS) und mit Large Eddy Simulationen (LES) berechnet. Granulare Strömungen wurden mit der Diskrete Elemente Methode (DEM) simuliert. Die granulare Strömung in einem gerührten Mischer, sowie über eine Einzelschaufel eines Mischers wurde mittels der granularen Particle Image Velocimetry (gPIV) experimentell untersucht.

Die DNS von Hydrierungsreaktionen zeigte, dass verschiedene Strömungsstrukturen im Nachlauf der Blase zu unterschiedlichen Umsätzen und Selektivitäten des Reaktionsnetzwerkes führen. Der Vergleich mit einer Vorhersage auf Basis des Filmmodells zeigt, dass dieser Effekt durch die Verwendung eines effektiven (anstatt des molekularen) Diffusionskoeffizienten für ein Zwischenprodukt modelliert werden kann. Um die Resultate der DNS mit den LES mit reaktivem Stoffaustausch zu kombinieren, muss ein Modell für die

Bildungsrate der skalaren Varianz berücksichtigt werden. Ein Zusammenhang für diesen Quellterm wurde vorgeschlagen. Die Ergebnisse der LES für die Blasenströmung zeigten eine hervorragende Übereinstimmung mit Literaturdaten. Weiters wurde auch ein Modell für die reaktive Vermischung im Flüssigkeits-Bulk validiert. Die DEM-Simulationen der granularen Strömung in einem Mischer zeigten hingegen nur eine qualitative Übereinstimmung mit den experimentellen Daten. Besonders problematisch ist der Fall einer feuchten Schüttung, wo die in der Simulation verwendete Partikelgröße einen entscheidenden Einfluss auf das berechnete Strömungsfeld hatte. Es wurde jedoch beschleunigtes Mischen im Fall einer feuchten Schüttung mit der Simulation prognostiziert, was auch experimentell nachgewiesen wurde.

Abstract

Currently, the level of modeling of various processes in the pharmaceutical industry lags behind that in other industries (e.g., the automotive industry). In addition, the modeling of multiphase systems encountered in the pharmaceutical industry is especially challenging. The current guidelines of regulatory authorities (i.e., the Food and Drug Administration or the European Medicines Agency) ask for a deeper process understanding and also manufacturers have realized the importance of process insight. To reach these goals, appropriate models of the production process for drug substances and drug products are required. Mechanistic models provide the most sophisticated level of modeling, since they are based on a detailed understanding of the sub-steps that influence the overall production process.

This work focuses on mechanistic models for the description of multiphase flow systems in the pharmaceutical industry. The focus is on bubbly flows, as well as on granular flows. The ultimate goal is to provide a thorough description of the current state of the art, as well as to perform various in-depth numerical and experimental analyses of these two flow systems. In a first step, relevant multiphase flow systems have been reviewed and appropriate modeling approaches have been selected. Reactive bubbly flows have been simulated using Direct Numerical Simulations (DNS), as well as Large Eddy Simulations (LES). Granular flows have been simulated using the Discrete Element Method (DEM). The granular flow in a bladed mixer, as well as over a single blade, has been experimentally investigated using granular Particle Image Velocimetry (gPIV).

The DNS of hydrogenation reactions revealed that different bubble wake types will result in different rates of yield and selectivity of the reaction network. The comparison with a solution obtained from film theory showed that this effect can be modeled by using an effective diffusion coefficient instead of the molecular one for the intermediate reactant. To link the results of the DNS with the LES, a model for the scalar variance generation due to mass transfer is required. A scaling for this source term has been proposed. The results of the LES of bubbly flow showed an excellent agreement with literature data. Also, a reactive mixing model for the liquid bulk was validated. The DEM simulations of granular flow in the mixer were only in qualitative agreement with experimental data. Especially in the case of wet

granular matter, the particle size used in the simulation had a significant impact on the calculated flow field. However, improved mixing was predicted in case of wet granular matter and confirmed also by our experimental results.

Contents

Acknowledgement 290

Appendices

1

Multiphase Systems
in the Pharmaceutical Industry

The pharmaceutical industry has grown to one of the most important branches of our economy. Besides the need of energy for our rapidly growing population, the supply of affordable pharmaceuticals is essential for our daily life. This supply is directly coupled to their efficient production, which is frequently performed in gas-liquid-solid, gas-solid, liquid-liquid or gas-liquid multiphase flow systems.

This chapter provides an introduction and motivation for the study of multiphase systems encountered within the pharmaceutical industry. The systems are classified following their position in the overall manufacturing process of a drug product. The focus of this classification is on solid dosage forms produced via a synthetic route. Also, some aspects of decontamination technology are reviewed in order to reflect current challenges in the engineering of multiphase systems in the pharmaceutical industry.

1.1 A Definition of Multiphase Systems

Multiphase systems are systems in which two or more fluid phases, as well as fluid and solid phases, are simultaneously present.[1] This includes a wide spectrum of systems, i.e., essentially all systems encountered in nature and industry. More difficult is the definition of multiphase flow systems and even the recent book of Prosperetti and Tryggvason[2] does not give an exact definition. A possible argument for the classification as a multiphase flow system is that its behavior is dominated by the interaction of two or more phases. This interaction can be of physical (e.g., momentum or mass transfer, changing physical properties, phase changes…), as well as chemical (e.g., reactions occurring at the interfaces) nature and requires special attention in these systems. For example, the particle flow in a clean room, which involves solid particles, as well as a gas phase, may not be treated as a multiphase flow system. This is because the particle loading is so low that the flow is not dominated by the phase interaction. However, if the particle loading in a gas-solid flow is substantially increased (e.g., to mass loadings in the order of 1 kg dispersed phase per kg continuous phase as it is the case for cyclone separators), there is no doubt on the definition as a multiphase flow system.

This interaction of phases typically leads to a complex system behavior, which in addition is hard to quantify from an experimental point of view. This has led to a situation, where the design of multiphase systems is purely based on trial-and-error methodologies instead of a rational approach. With "rational approach" we refer to simple models, either based on sound theory or on empiricism that enable us to predict the behavior of the system to a certain degree of accuracy. Currently, such models do not exist, or do not provide a prediction with an acceptable degree of accuracy, for all multiphase systems. In the following, some important multiphase (flow) systems encountered in the pharmaceutical industry are detailed.

1.2 Bulk Manufacturing

Bulk manufacturing refers to processes for the production of the active pharmaceutical ingredient (API) and excipients. APIs are typically complex organic molecules and their synthesis is often performed in the liquid phase, e.g., in a slurry bubble column. Due to their large size, pure API molecules are solids at standard temperature and pressure, having an amorphous or crystalline structure (see Figure 1.1). Often, multiple crystalline structures are observed showing different physical properties. This polymorphism can constitute a serious issue, since the exact crystal structure depends on the nuclei (e.g., impurities or homogeneous

seeds) present in the supersaturated solvent, and the crystallization conditions. In the following chapters, the most common types of equipment used for API synthesis and crystallization are reviewed.
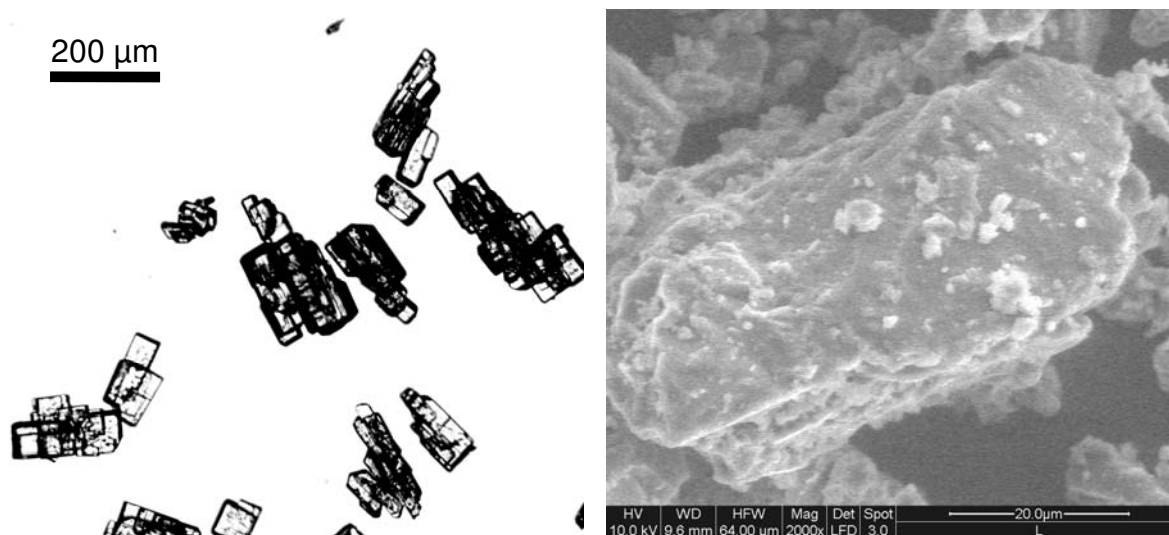
Figure 1.1: A typical crystalline API (left: acetylsalicylic acid obtained from a continuous crystallization process,[3] the image was taken using a conventional light microscope) and an excipient (right: lactose monohydrate,[a] the image was taken using a FEI Quanta 200 ESEM by Dr. Julian Wagner, FELMI, Graz University of Technology).

1.2.1 Synthetic Route

For the synthetic route of API production, the yield and selectivity of the reaction network is of main interest. Examples for the production of APIs and excipients or their precursors via a fully synthetic route are:

- The hydrogenation of dinitriles

This reaction is performed in a three-phase system involving a liquid phase, gas bubbles and a solid (i.e., a Raney-type Nickel catalyst[4]). It was shown that the adsorption of the dissolved educts is key for the overall kinetics, as well as the selectivity of the reaction network.

- The asymmetric hydrogenation of ethyl pyruvate

This hydrogenation is performed in an organic solvent (i.e., 1-propanol), using Pt/Al_2O_3 catalyst particles. Pure hydrogen is typically used and dispersed by an impeller. It was

---

[a] Lactose monohydrate has been donated by Dr. F. Reiter, G.L. Pharma GmbH, Lannach, Austria.

shown by Sun et al.,[5] that in this multiphase reaction system the enantioselectivity changes by a factor of three when mixing in the reactor is enhanced.

- The hydrogenation of o-nitroanisole

In this liquid-phase hydrogenation, methanol is used as a solvent and palladium on a carbon support as the catalyst. Hydrogen is brought into contact with the liquid via perforated walls in a microreactor. McGovern et al.[6] showed that in this reactive multiphase system the conversion strongly depends on the gas and liquid fluxes through the reactor.

- The hydrogenation of nitroarenes

This reaction occurs in methanol, where pure hydrogen is sparged into the system and the catalyst (typically supported copper, cobalt, platinum, palladium or nickel) is suspended as fine particles. The selectivity towards the final product can be controlled by catalyst design, gas hold-up, as well as the micro-mixing in the system.[7]

- Reactive extractions for chiral separations

An attractive process for the production of pure enantiomers of amines and amino-alcohols (i.e., key intermediates in the pharmaceutical industry) was studied in the paper of Steensma et al.[8] In this liquid-liquid process, the complexation of the enantiomers of phenylethylamine and phenylglycinol, as well as ligand-exchange reactions involving the enantiomers of leucine were analyzed. By using the film model for mass transfer as well as taking into account the reversible reaction network, the experimental results for the extraction rate could be reasonably-well predicted.

These examples show that the interaction of fluid flow, homogeneous, as well as heterogeneous reactions (i.e., reactions taking place on surfaces) can significantly change the behavior of the system. For fast reactions, i.e., reactions with a high Damköhler number, the exact distribution of the reactants dictates the selectivity of the reaction network. In multiphase systems where one or more reactants are transferred across an interface, these fast reactions typically occur near the interface. Thus, mixing on the scale of the concentration boundary layer may be of interest and will have a certain effect on the outcome of a reaction network. Since the work of Danckwerts in the late 1950's,[9] a huge amount of literature has accumulated on the prediction of these mixing effects in chemical reactors (see, e.g., the book of Baldyga and Bourne[10] or of Fox[11]). Various modeling approaches for interface reactions are

known in literature. Typically, the film model is used as a simple and still realistic model to study the influence of mass transfer characteristics on the reaction. More details on the modeling strategies are provided in Chapter 3.

1.2.2 Semisynthetic Route

Semisynthetic routes refer to a pharmaceutical production where a natural raw substance is chemically treated to obtain the final product. Examples include:

- The hydrogenation of sugars

These reactions are performed in a three-phase system (i.e., a carbon-supported Ruthenium catalyst, an aqueous solution of the sugar and hydrogen as the gas phase) to manufacture, e.g., sorbitol, an industrially extremely important intermediate.[12] The data by Crezee et al.[12] suggested that the reaction on the catalyst surface is the rate-limiting step. Using various adsorption models for hydrogen and the sugar, the experimental data could be predicted quantitatively correct.

- Semi-synthetic antibiotics

Cephalosporins are, in addition to penicillins, the most important antibiotics. They are produced via a semi-synthetic production route in which the final product is derived from the natural antibiotic cephalosporin C (CPC) or penicillin.[13] The production of these cephalosporins is a combination of enzymatic conversions and conventional aqueous-or organic-phase chemistry. The latter can be done using heterocyclic thiols in organic solvents and BF_3 gas.

1.2.3 Biopharmaceutics Production

During biopharmaceutics production typically plant, bacteria, fungi, algae or animal cells are used to manufacture the API. The shear stress experienced by these cells, as well as the volumetric mass transfer coefficient, play a key role in these reactors. Both factors are significantly influenced by the rheology of the suspension in these reactors, and have been intensively studied.[14-17] It is remarkable, that in typical aerobic fermentations the characteristic oxygen consumption time scale (defined by the ratio of the saturation concentration of oxygen and the specific oxygen consumption rate at the saturation concentration) can be in the order of 1 s.[18] This means that macro mixing within the reactor definitely plays a role (macro mixing is typically in the order of 10 to 100 s depending on the stirrer speed). For highly viscous

liquids, even the time scale for micro mixing might be larger than the characteristic time scale for oxygen uptake. Consequently, care has to be taken to avoid local oxygen depletion in these reactors.

Also, reactive multiphase systems are encountered in down stream processes of the biopharmaceutical industry. An example is the extraction of Penicillin G from the reaction broth.[19]

1.2.4 Chromatographic Systems

Preparative chromatography is the predominant final separation step in biopharmaceutics production. While the conventional co-current elution chromatography is primarily used in industrial practice, there are significant efforts for the development of a continuous chromatography system.[20] In a conventional chromatography system, the mobile phase is flowing through the chromatographic bed continuously. The mixture to be separated is injected into the mobile phase discontinuously. Depending on the interactions between the molecules to be separated and the stationary phase (i.e., the chromatography bed), the individual components are restrained differently and consequently separated. Different interaction mechanisms are known in literature (i.e., hydrophobic interaction, "reversed" phase, ion exchange, gel filtration, etc.).

Applications of chromatography in the pharmaceutical industry range from simple standard non-chiral separations to recent research focusing on chiral separations. The latter are of great interest for the industry, as asymmetric crystallizations or enantioselective synthesis are still not fully developed, hence expensive and time consuming. Examples for chromatography in the pharmaceutical industry are:

- the separation of racemic mixtures of tramadol,[21] ibuprofen,[20] as well as other enantiomers,[22]

- the separation of enzymes,[23]

- the separation of cis/trans-isomers of phytol,[24] as well as

- the purification of tocopherols.[20]

1.2.5 Crystallizers

Crystallization is an effective unit operation for[25]

- purification processes,

- polymorphism control,

- crystal design (i.e., particle size and shape control), or

- the stabilization of products.

Crystallization can be used for both organic and inorganic substances. For the former, crystallization is especially interesting in the context of purification processes. The control of crystallization processes is critical and has gained much interest within the years. Recent examples of crystallization reactors are based on microreactors[26] or continuous processes.[3]

1.3 Dosage Form Manufacturing

In order to provide a safe and convenient delivery of the API, the drug itself has to be formulated to yield the final drug product, i.e., the dosage form. Dosage forms include:

- tablets (i.e., compacted powder aggregates, the most frequently used dosage form),

- solutions, syrups and elixirs (i.e., a homogenous mixture of solutes in a solvent),

- capsules (i.e., a shell containing the drug substance and the excipients),

- emulsions (i.e., a mixture of at least two immiscible liquid phases),

- suspensions (i.e., finely dispersed particles in a liquid phase),

- aerosols (i.e., fine particles or droplets), and

- transdermal patches (i.e., patches that deliver the drug through the skin into the blood stream).

Nearly all of these dosage forms consist of a multiphase system or involve a multiphase system during their production (see the examples presented in Chapters 1.3.1 and 1.3.2). When focusing on the manufacturing of tablets, the powder mixture to be compacted has to have appropriate flow properties, and has to be homogenous. Due to the typically small particle size, the interaction of the particles with each other, as well as with the surrounding gas is of major importance. Consequently, the powder mixture consisting of the API and one

or more excipients is often granulated. Typically, this yields a granulate with a particle size between 0.05 and 2 mm (see Figure 1.2) that can be compressed in tablet presses. Exceptions are direct compression processes or processes in which the API is added to a granulate directly before compression.[27] In any case, glidants (such as, e.g., silica nanoparticles) and lubricants (such as, e.g., magnesium stearate) are often added to the mixture in order to control its flow, compaction or aerosolization[b] properties.
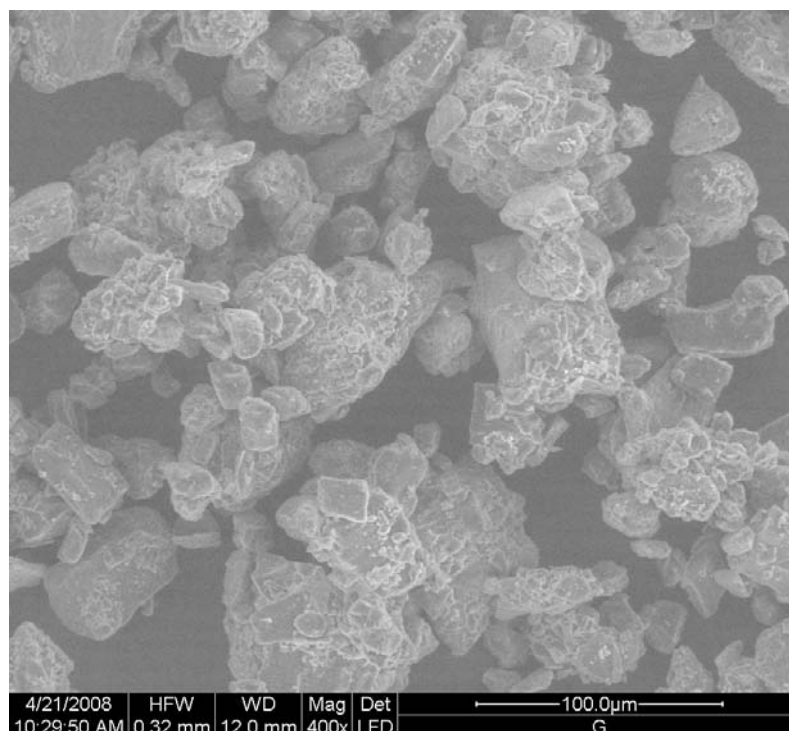
Figure 1.2: Product of a wet granulation process (API: Diltiacem HCl, excipient: lactose monohydrate, binder: Eudragit NE 30 D,[c] the image was taken using a FEI Quanta 200 ESEM by Dr. Julian Wagner, FELMI, Graz University of Technology).

Granulation is performed via a dry or wet granulation step. Less frequently, sinter granulation, melt granulation or other specialized granulation processes (e.g., granulation via spray drying, or single-pot technologies for highly potent drug formulations) are used. An overview over granulation processes in the pharmaceutical industry is provided by Ritschel and Bauer-Brandl.[27] While dry granulation gives a final tablet with a high hardness, the disadvantages of this granulation process are the higher disaggregation time and the excessive fines production

---

[b] Aerosolization refers to the ability of a powder to be dispersed into a gas stream and is important, e.g., for the design of powder inhalers. This ability is similar to the ability of a powder to be fluidized and strongly depends on the permeability of the powder, i.e., its particle size and shape distribution, as well as on cohesive forces.

[c] Diltiacem HCl, lactose monohydrate, and Eudragit have been donated by Dr. F. Reiter, G.L. Pharma GmbH, Lannach, Austria.

during manufacturing. Although wet granulation is time consuming and expensive, it is the most frequently used granulation technique. This is due to the fact that dust formation is suppressed, the API distribution can be controlled, binders with additional effects on drug release (e.g., retard formulations) can be used, as well as excellent flow properties and a high bulk density of the granulate can be achieved.[27]

1.3.1 Wet Granulation

During wet granulation, a three-phase system is formed consisting of solid particles (i.e., the API and the excipients), the ambient gas (e.g., air) and the binder solution. Wet granulation has the purpose to initially bind particles together with the aid of liquid bridge forces. These liquid bridges can exist between two or more particles, and even at low saturation levels their distribution is complex.[28] In the final drying step, binding is caused by solid bridges (caused by solidification of dissolved API or excipients), van der Waals forces or mechanical interlocks.

Wet granulation is typically performed in fluidized beds or high-shear granulators. In fluidized bed granulators the particles are agitated by a permanent gas flow. This causes inter-particle collision with a low characteristic impact velocity, which in turn yields relatively loose agglomerates. Also, fluidized bed granulation processes are determined by a wide range of process parameters that need to be optimized in order to achieve the desired product quality. Hence, these processes are only economic for a mass production of a drug product.

In contrast, high-shear granulators are much more simple, flexible, and robust. In these granulators the main impeller keeps the powder bed in motion (the tip speed is in the order of 10 m/s, which gives rotation speeds between 60 and 800 rpm depending on the scale of the equipment). A chopper (often located off center) spinning between 500 and 3,500 rpm is used to control the maximum granulate size. High-shear granulators are typically used in batch mode with a nominal volume between 10 and 1,200 liters. An excellent review of wet granulators is given in the book of Litster et al.[29]

1.3.2 Coating

The main purpose of a coating process is to cover the final dosage form, e.g., a tablet, with a well-defined film to control different properties of the formulation. These properties can be:

- the taste,

- the appearance (color, surface properties, printability),

- the shelf life-time,

- the application of an additional API in the coating,

- the location of disintegration in the human body, or

- the release properties, e.g., the rate of API release in the human body.

As these properties are central for the effect of the dosage form, the coating, as well as the coating process itself, is extremely important for the pharmaceutical industry.

During a typical coating process (i.e., film coating) a thin film (10 - 100 μm) of macromolecular substances is formed on the surface of tablets or capsules.[27] These solid dosage forms are coated in whether fluidized bed or rotating drum (also referred to as pan or perforated pan) coaters. Rotating drum coaters are very versatile and consequently frequently used.
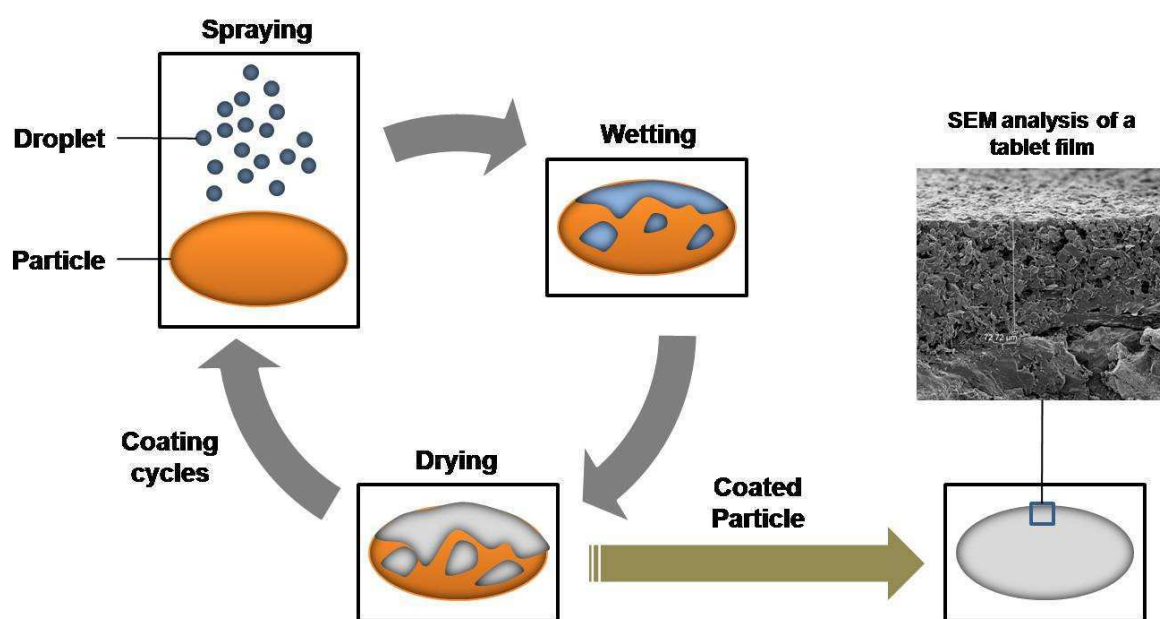
Figure 1.3: Principal sketch of a coating process.[30]

In rotating drum coaters, the particle circulate by cascading down the top surface of a granular bed and pass through the spray zone, which is formed by one or more nozzles at the upper section of the bed. In the spray zone, a so-called coating solution (often an aqueous dispersion of polymers) is sprayed onto the solid dosage form. The coating solution then spreads over the surface of the dosage form. Finally, the particles move out of the spray zone into a region where heating and evaporation of the coating solution are promoted. Here, the liquid

components evaporate into a warm gas stream (see Figure 1.3). This process may be facilitated, e.g., with microwaves or other forms of energy transfer to the coated particles.

Also, hot melt and powder coating processes are known, where the coating liquid consists of a molten substance, and cold air is blown over the coated particles to solidify the coating.[31]

The science behind coating processes is extremely complex as this process involves aspects of granular flow, multiphase flow, wetting, as well as spreading of a liquid film on a porous surface. Also, heat and mass transfer are important factors that are inherently coupled with the spreading of the film. More background on coating can be found in Ritschel and Bauer-Brandl.[27]

1.4 Decontamination Systems

The typical clean-in-place (CIP) and sterilize-in-place (SIP) procedures are practiced for a long time in the pharmaceutical industry. This decontamination practice typically involves steam and the use of thermocouples at multiple locations to guarantee sterilization conditions. The main challenge nowadays is to streamline these processes in order to reduce the overburden associated with validation procedures.[32] When it comes to the decontamination of surfaces in containers that cannot be pressurized or heated up, other strategies are needed. For example, in the (bio-)pharmaceutical industry the efficient decontamination of surfaces in lock lines, rooms and laboratories is of central importance. The main challenge in these applications is that all surfaces to be sterilized have to be reliably treated with the decontamination medium. Therefore, sterilization approaches based on gas-phase decontamination are drawing significant interest. An elegant method due to its simplicity and the environmentally friendly decontamination products is the use of gaseous hydrogen peroxide as decontamination medium, which has been used since the late 1980s.[33,34] In this method the degradation products are only water vapor and oxygen gas.

In the past decade decontamination by hydrogen peroxide (DHP) has been used frequently for sterilization purposes in a wide range of applications.[35-40] In these processes an aqueous hydrogen peroxide solution (typically 35 w% H_2O_2) is evaporated, brought into contact with a hot gas stream and fed into the containment to be sterilized. This process is often called "gassing". Afterwards, the chamber is purged with air until the hydrogen peroxide level is below the OSHA-safety level of 1 ppm(v). This is referred to as "aeration". There has been much interest in the theoretical analysis of the evaporation and condensation of aqueous

hydrogen peroxide solutions due to its relevance for DHP systems.[41-44] Recently, a few practical guidelines for the proper design and development of hydrogen peroxide decontamination systems have been published (see, e.g., the diagram shown in Figure 1.4).[45] Still there are significant challenges associated with DHP and

- the prediction of multicomponent mass transfer effects during the condensation of moist, hydrogen peroxide-laden air,[46]

- the quantification of adsorption and absorption effects of hydrogen peroxide to polymers and their subsequent release, and

- the assessment of the use of hydrogen peroxide mist for clean room sterilization.
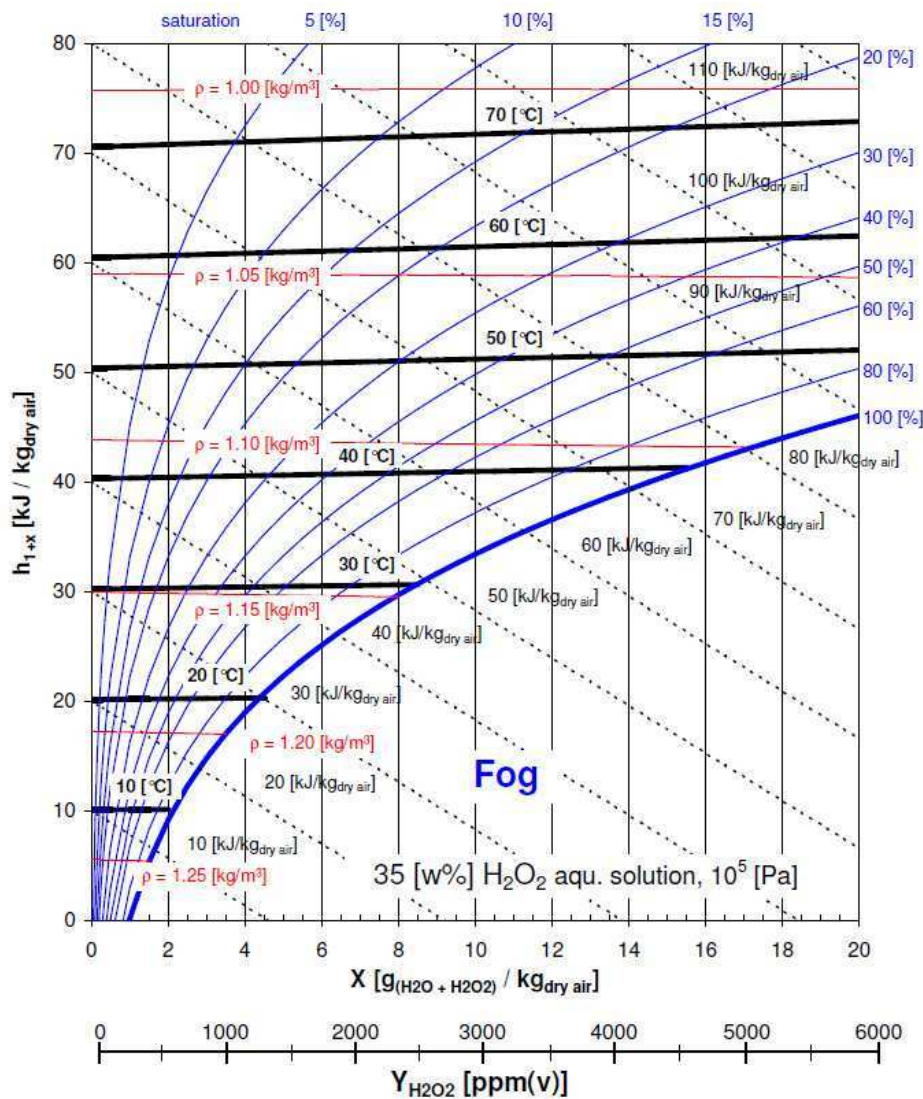
Figure 1.4: h-x Diagram for moist, hydrogen peroxide-laden air ($1 \cdot 10^5$ Pa, 35 w% H_2O_2 in the injected aqueous solution).[45]

1.5 Conclusions

Multiphase systems play a central role in pharmaceutical production, since the intermediate or the final product itself is a multiphase system. Also, sterilization processes (i.e., ancillary processes in almost every pharmaceutical production) are often based on evaporation and condensation processes, which are examples of multiphase systems involving a phase change.

The examples shown in this chapter reflect only a small fraction of multiphase systems found in the pharmaceutical industry. Due to their complex nature, this work can only focus on some of these examples for a more profound in-depth analysis.

1.6 Abbreviations

API   Active Pharmaceutical Ingredient

CIP   Clean In Place

CPC   Cephalosporin C

DHP   Decontamination by Hydrogen Peroxide

ESEM   Environmental Scanning Electron Microscope

FELMI   Institute for Electron Microscopy and Fine Structure Research (TU Graz)

OSHA   Occupational Safety and Health Administration

SIP   Steam (or Sterilize) In Place

1.7 References

(1)   Prosperetti A, Tryggvason G. Introduction: A computational approach to multiphase flow. In: Prosperetti A, Tryggvason G. Computational Methods for Multiphase Flow. Cambridge, UK: Cambridge University Press, 2007.

(2)   Prosperetti A, Tryggvason G. Computational Methods for Multiphase Flow. Cambridge, UK: Cambridge University Press, 2007.

(3)   Eder RJP, Radl S, Schmitt E, Innerhofer S, Maier M, Gruber-Woelfler H et al. Continuously Seeded, Continuously Operated Tubular Crystallizer for the Production of Active Pharmaceutical Ingredients. Crystal Growth & Design. 2010; 10:2247-2257.

(4)   Hoffer BW, Moulijn JA. Hydrogenation of dinitriles on Raney-type Ni catalysts: kinetic and mechanistic aspects. Applied Catalysis A-General. 2009; 352:193-201.

(5)   Sun YK, Wang J, LeBlond C, Landau RN, Blackmond DG. Asymmetric hydrogenation
       of ethyl pyruvate: Diffusion effects on enantioselectivity. Journal of Catalysis. 1996;
       161:759-765.

(6)   McGovern S, Harish G, Pai CS, Mansfield W, Taylor JA, Pau S et al. Investigation of
       multiphase hydrogenation in a catalyst-trap microreactor. Journal of Chemical
       Technology and Biotechnology. 2009; 84:382-390.

(7)   Radl S, Koynov A, Tryggvason G, Khinast JG. DNS-based Prediction of the Selectivity
       of Fast Multiphase Reactions: Hydrogenation of Nitroarenes. Chem Eng Sci. 2008;
       63:3279-3291.

(8)   Steensma M, Kuipers NJM, de Haan AB, Kwant G. Modelling and experimental
       evaluation of reaction kinetics in reactive extraction for chiral separation of amines,
       amino acids and amino-alcohols. Chem Eng Sci. 2007; 62:1395-1407.

(9)   Danckwerts PV. The Effect of Incomplete Mixing on Homogeneous Reactions. Chem
       Eng Sci. 1958; 8:93-102.

(10)   Baldyga J, Bourne JR. Turbulent mixing and chemical reactions. New York, US: Wiley,
       1999.

(11)   Fox RO. Computational Models for Turbulent Reacting Flows. Cambridge, UK:
       Cambridge University Press, 2003.

(12)   Crezee E, Hoffer BW, Berger RJ, Makkee M, Kapteijn F, Moulijn JA. Three-phase
       hydrogenation of D-glucose over a carbon supported ruthenium catalyst-mass transfer
       and kinetics. Applied Catalysis A-General. 2003; 251:1-17.

(13)   Barber MS, Giesecke U, Reichert A, Minas W. Industrial enzymatic production of
       cephalosporin-based beta-lactams. Molecular Biotechnology of Fungal Beta-Lactam
       Antibiotics and Related Peptide Synthetases. 2004; 88:179-215.

(14)   Radl S, Khinast JG. Prediction of mass transfer coefficients in non-Newtonian
       fermentation media using first-principles methods. Biotechnol Bioeng. 2007; 97:1329-
       1334.

(15)   Radl S, Tryggvason G, Khinast JG. Flow and mass transfer of fully resolved bubbles in
       non-Newtonian fluids. AIChE J. 2007; 53:1861-1878.

(16)   Kawase Y, Halard B, Mooyoung M. Liquid-Phase Mass-Transfer Coefficients in
       Bioreactors. Biotechnol Bioeng. 1992; 39:1133-1140.

(17)   Moilanen P, Laakkonen M, Aittamaa J. Modeling aerated fermenters with computational
       fluid dynamics. Industrial & Engineering Chemistry Research. 2006; 45:8656-8663.

(18)   Sweere APJ, Luyben KCAM, Kossen NWF. Regime Analysis and Scale-Down - Tools
       to Investigate the Performance of Bioreactors. Enzyme and Microbial Technology.
       1987; 9:386-398.

(19) Lee SC. Physical and reactive extraction equilibria of penicillin G in a hydrogen-bond acceptor solvent system. Biotechnology Progress. 2006; 22:731-736.

(20) Johannsen M. Modeling of Simulated Moving-Bed Chromatography. In: Keil FJ. Modeling of Process Intensification. Weinheim, D: Wiley-VCH, 2007:279-322.

(21) Cavoy E, Deltent MF, Lehoucq S, Miggiano D. Laboratory-developed simulated moving bed for chiral drug separations - Design of the system and separation of tramadol enantiomers. Journal of Chromatography A. 1997; 769:49-57.

(22) Rajendran A, Paredes G, Mazzotti M. Simulated moving bed chromatography for the separation of enantiomers. Journal of Chromatography A. 2009; 1216:709-738.

(23) Gottschlich N, Weidgen S, Kasche V. Continuous biospecific affinity purification of enzymes by simulated moving-bed chromatography - Theoretical description and experimental results. Journal of Chromatography A. 1996; 719:267-274.

(24) Johannsen M, Peper S, Depta A. Simulated moving bed chromatography with supercritical fluids for the resolution of bi-naphthol enantiomers and phytol isomers. Journal of Biochemical and Biophysical Methods. 2002; 54:85-102.

(25) Myerson AS. Handbook of Industrial Crystallization. 2nd ed. Boston, US: Butterworth-Heinemann, 2002.

(26) Gerdts CJ, Tereshko V, Yadav MK, Dementieva I, Collart F, Joachimiak A et al. Time-controlled microfluidic seeding in nL-volume droplets to separate nucleation and growth stages of protein crystallization. Angewandte Chemie-International Edition. 2006; 45:8156-8160.

(27) Ritschel WA, Bauer-Brandl A. Die Tablette. 2nd ed. Aulendorf, D: Editio Cantor Verlag, 2002.

(28) Scheel M, Seemann R, Brinkmann M, Di Michiel M, Sheppard A, Breidenbach B et al. Morphological clues to wet granular pile stability. Nature Materials. 2008; 7:189-193.

(29) Litster JD, Ennis BJ, Liu LX. The Science and Engineering of Granulation Processes. Dordrecht, NL: Kluwer Academic Publishers, 2004.

(30) Suzzi D, Radl S, Khinast JG. Local Analysis of the Tablet Coating Process: Impact of Operation Conditions on Film Quality. Chem Eng Sci. 2010; (submitted).

(31) Porter SC. Scale-Up of Film Coating. In: Levin M. Pharmaceutical Process Scale-Up. New York: Taylor & Francis, 2006:435-485.

(32) Junker B. Technical evaluation of the potential for streamlining of equipment validation for fermentation applications. Biotechnology and Bioengineering. 2001; 74:49-61.

(33) Klapes NA, Vesley D. Vapor-Phase Hydrogen-Peroxide As A Surface Decontaminant and Sterilant. Appl Environ Microbiol. 1990; 56:503-506.

(34)   Wang J, Toledo RT. Sporicidal Properties of Mixtures of Hydrogen-Peroxide Vapor and Hot Air. Food Technol. 1986; 40:62-67.

(35)   McAnoy, A. M., Sait, M., and Pantelidis, S. Establishment of a Vaporous Hydrogen Peroxide Bio-Decontamination Capability. Human Protection Performance Division DSTO. 2007.

(36)   Johnston MD, Lawson S, Otter JA. Evaluation of hydrogen peroxide vapour as a method for the decontamination of surfaces contaminated with Clostridium botulinum spores. J Microbiol Methods. 2005; 60:403-411.

(37)   Rohtagi, N., Schuber, W., Koukol, R., Foster, T. L., and Stabekis, P. D. Certification of Vapor Phase Hydrogen Peroxide Sterilization Process for Spacecraft Application. Society of Automotive Engineers, Inc. 2001.

(38)   Heckert RA, Best M, Jordan LT, Dulac GC, Eddington DL, Sterritt WG. Efficacy of vaporized hydrogen peroxide against exotic animal viruses. Appl Environ Microbiol. 1997; 63:3916-3918.

(39)   Hall L, Otter JA, Chewins J, Wengenack NL. Use of hydrogen peroxide vapor for deactivation of Mycobacterium tuberculosis in a biological safety cabinet and a room. J Clin Microbiol. 2007; 45:810-815.

(40)   Fischer J, Caputo RA. Barrier Isolator Decontamination Systems. Pharm Technol. 2004; Nov 2004:68-82.

(41)   Hultman C, Hill A, McDonnel G. The Physical Chemistry of Decontamination with Gaseous Hydrogen Peroxide. Pharm Eng. 2007; 27:22-32.

(42)   Watling D, Parks M. The Relationship between Saturated Hydrogen Peroxide, Water Vapour and Temperature. Pharm Technol Eur. 2004; 01-03-2004.

(43)   Unger-Bimczok B, Kottke V, Hertel C, Rauschnabel J. The Influence of Humidity, Hydrogen Peroxide Concentration, and Condensation on the Inactivation of Geobacillus stearothermophilus Spores with Hydrogen Peroxide Vapor. J Pharm Innov. 2008; 3:123-133.

(44)   Watling D. Theory and Practice of Hydrogen Peroxide Vapour. Pharmaceutical International.Copybook Solutions LTD, editor. http://www.pharmaceutical-int.com/categories/biodecontamination-using-hydrogen-peroxide-vapour/theory-and-practice-of-hydrogen-peroxide-vapour.asp. 2007.

(45)   Radl S, Ortner S, Sungkorn R, Khinast JG. The engineering of hydrogen peroxide decontamination systems. J Pharm Innov. 2009; 4:51-62.

(46)   Sungkorn R, Radl S, Khinast JG. Numerical Analysis of Multicomponent Flow and Condensation In a DHP Chamber. Philadelphia, PA: AIChE Annual Meeting 2008, 2008.

"The most important thing about having goals is having one."

(Geoffrey F. Albert)

2

Goals and Content

2.1 Goals

The outcome of this work should be a thorough description of the current state of the art in the modeling of multiphase flows with a focus on

- reactive mass transfer in bubble swarms, as well as

- flow and mixing of dry and wet bulk solids.

In the area of bubbly flows, the main goal is to significantly extend the current simulation approach that has been already used by the group of Khinast.[1,2] Specifically, different modeling approaches ranging from first-principles methods to more coarse grained modeling approaches such as Large Eddy Simulations (LES) should be used. The research should aim on (i) applying the current direct numerical simulation (DNS) code to an industrially relevant reaction system, (ii) to derive interface-near models for the reactive mass transfer with a focus on the phenomena in the wake of the bubble (i.e., micro mixing), as well as (iii) to adapt a coarse-grained simulation code to model mixing on a meso, i.e., a bubble-swarms, scale. To test the performance of the chosen modeling strategy, validation of the simulation results should be provided at each stage. In this part, the focus is on processes encountered during bulk manufacturing. These processes involve fast (bio)reactive systems where fluid motion, and consequently mixing, and induced shear stress on suspended particles, is essential for product quality.

In the area of granular flows, simulations based on the Discrete Element Method (DEM) should be used to investigate these flows on a particle level. The DEM is based on a direct modeling of the motion of individual particles facilitated with physically-sound particle-particle and particle-wall interaction models. The aim of this part is to explore the virtues, merits, as well as limitations of DEM-based simulations for wet granular matter. To asses the quality of this modeling approach, simulations should be validated with small-scale granular flow experiments. These experiments should focus on the measurement of instantaneous granular flow fields by means of high-speed imaging. The research on wet granular flow should lead to a better understanding of mixing and granulation by separating different mechanisms encountered in these unit operations.

2.2 Thesis Content

Chapter one provides some examples of multiphase systems encountered in the pharmaceutical industry and hence constitues the motivation of this work.

In chapter three, the modeling approaches for gas-liquid, as well as dry and wet granular flows are critically reviewed. The main purpose of this chapter is to make the reader familiar with the approaches used in the following chapters. Chapter three constitutes the main outcome from a modeling perspective.

2.2.1 Bubbly Flows

Chapter four details on the application of direct numerical simulations for the hydrogenation of nitroarenes. It also provides some perspectives for the modeling of interface-near reactions and the effect of the wake. The major advance over the current state of the art is the use of an improved convection scheme for reactive bubble swarms, which has been already used in previous work dealing with mass transfer in non-Newtonian liquids.[2,3] Also, the effect of the gas hold-up on liquid-phase mixing and hence on the selectivity of the hydrogenation reaction network has been analyzed for the first time. These simulations were limited to two-dimensional model systems for a qualitative prediction of the effect of process parameters on the outcome of reaction networks.

In chapter five, the analysis concentrates on three-dimensional single bubbles for the prediction of mass transfer and mixing effects. The central result of this chapter is the analysis of filtered concentration fields in the wake of the bubble. This has been done in order to provide closure information for the Large Eddy Simulations performed in chapter six. Conclusions were drawn on the generation of the scalar variance associated with mass transfer with the ultimate goal to extract a universal model for this quantity in bubbly flows.

Chapter six adopts the well-known Euler-Lagrange (EL) approach for the prediction of multiphase flow, mixing, as well as reactions in a dilute bubbly flow. Dilute means that bubble-bubble interactions, i.e., collisions, as well as coalescence and breakage, were neglected. The resulting numerical model is a relatively simple model for bubbly flows. However, an intense study of mixing in these multiphase systems was performed, which could not be found in literature. Specifically, a sub-grid-scale (SGS) reactive mixing model was implemented in the EL approach to account for fast reactions in the liquid phase. Due to the lack of experimental data in multiphase systems, the SGS model was validated with data from microreactors.

2.2.2 Granular Flows

Chapter seven details on the investigation of wet granular flows via discrete particle simulations. The focus is on the characterization of mixing in these systems by the analysis of mean and fluctuating velocity fields, as well as the analysis of the variance in the system. Also, some validation of the results with experimental results from granular particle image velocimetry (gPIV) is provided.

Chapter eight is dedicated to a more profound experimental investigation of granular flows. Again, gPIV has been used as the primarily measurement technique. Experiments have been performed in a bladed mixer, as well as in a two-dimensional, single-blade setup. The particles used for the experiments (i.e., glass beads of different sizes and colors) have been rigorously characterized using a pin-on-disc friction tester, high-speed recordings of particle bouncing, as well as a powder rheometer.

Chapter nine provides general conclusions on the art of modeling multiphase systems in pharmaceutical applications. It also gives an outlook to future activities that should be undertaken in order to refine the current modeling technology.

2.3 Abbreviations

DEM   Discrete Element Method

DNS   Direct Numerical Simulation

EL   Euler-Lagrange (method)

gPIV   Granular Particle Image Velocimetry

LES   Large Eddy Simulation

SGS   Sub Grid Scale

2.4 References

(1) Koynov A, Tryggvason G, Schlueter M, Khinast JG. Mass transfer and chemical reactions in reactive deformable bubble swarms. Applied Physics Letters. 2006; 88:134102.

(2) Radl S, Tryggvason G, Khinast JG. Flow and mass transfer of fully resolved bubbles in non-Newtonian fluids. AIChE J. 2007; 53:1861-1878.

(3) Radl S, Khinast JG. Prediction of mass transfer coefficients in non-Newtonian fermentation media using first-principles methods. Biotechnol Bioeng. 2007; 97:1329-1334.

"It can scarcely be denied that the supreme goal of all theory is to make the irreducible basic elements as simple and as few as possible without having to surrender the adequate representation of a single datum of experience."

(Albert Einstein, 1933)

3

Modeling Approaches

The modeling of multiphase systems is a highly specialized topic and various theoretical models exist for a certain system under consideration. Especially in the area of bubbly flows there is a wide span of approaches ranging from a direct resolution of the interface, over particle tracking approaches to simple integral models, e.g., for the prediction of circulation patterns in reactors. A review of the currently available models for gas-liquid systems with an emphasis on the description of reactive mass transfer and mixing is provided.

In the area of granular flows, particle-based modeling approaches, as well as continuum models are reviewed. Interface resolved model strategies for wet granular matter are also mentioned.

3.1 Bubbly Flows

Bubbly flows are multiphase flow systems constituted by deformable gas bubbles and a liquid continuous phase. The modeling of dilute bubbly flows is relatively easy, and can be done, e.g., by tracking of non-interacting fluid particles. For the modeling of dense bubbly flows, however, coalescence and breakup are essential mechanisms that influence the bubble size distribution, and hence, the flow behavior.

During the last decades, different modeling strategies have accumulated and are summarized in Table 3.1. For each phase, the principal approach for solving the governing equations is indicated. Furthermore, the characteristic domain size for which the modeling approach is applicable is indicated in the last column. With increasing scale, also the level of modeling needed to supply closure information from non-resolved phenomena increases.

	Approach	*Gas Phase*	*Liquid Phase*	*Scale*
1	Interface Resolved	Eulerian or none	Eulerian	Bubbles and bubble swarms (1 - 10 mm)
2	Point-Particle	Lagrangian	Eulerian	Bubble swarms (0.01 - 1 m)
3	Two-Fluid Models	Eulerian	Eulerian	Equipment scale (1 - 10 m)
4	Integral Models	Mixture (Eulerian)		Equipment scale (1 - 10 m)

Table 3.1: An overview of modeling approaches for bubbly flows.

The modeling approaches are illustrated in Figure 3.1. In this figure typical results for the modeling approaches 1 - 3 are shown, as well as a typical model structure for a simple integral model of a bubble column (i.e., approach 4). Approach 1 includes simulations that aim at directly modeling the underlying physics of the multiphase flow system. Thus, the changing physical properties in the system are modeled directly via a step function at the gas-liquid interface. Then, the conservation equations for mass and momentum can be solved without any interface closure models. Therefore, different numerical strategies can be followed, which are detailed in chapter 3.1.1. Within approach 2 already significant model assumptions are made, e.g., for the bubble shape and the resulting forces on the bubbles. However, this

approach is still based on a physical representation of bubbles as individual particles. More details of this approach are provided in chapter 3.1.2. Approach 3 does not represent bubbles as individual moving particles, but as a continuous "bubble phase" characterized by a local gas hold-up. This has severe implications for the accuracy of this approach and the handling of bubble swarms with a wide size distribution. The approach, as well as some of these implications, are detailed in chapter 3.1.3. Approach 4 is based on a relatively simple system of compartments, e.g., in a bubble column reactor and does not rely on a detailed representation of the bubbly flow anymore. Typically, these compartments are treated as spatially homogenous, which reduces the governing equations for mass and momentum conservation into a system of ordinary differential or, in the case of the steady-state assumption, algebraic equations. Some examples of these application-near models are detailed in chapter 3.1.4.
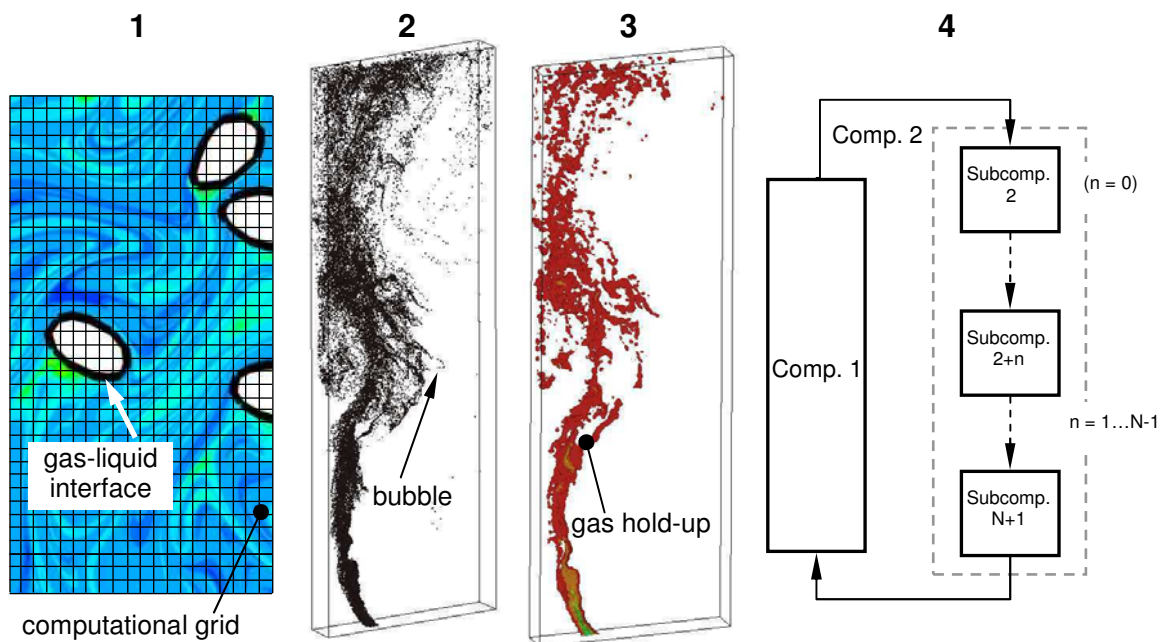
Figure 3.1: Schematic representation of the different modeling approaches for bubbly flows as per Table 3.1.[a]

3.1.1 Interface Resolved Approach

In this modeling approach the goal is to fully resolve all details of the multiphase flow, i.e., the exact location of the interface, as well as typically also the turbulent motion present within each phase. On top of these fluid flow predictions, mass transfer, as well as the concentration

---

[a] The compartment model has been adapted from the construction project of Mr. Andreas Eitzlmayr, Graz University of Technology, 2010.

field is of central interest. This is, however, connected to additional difficulties and hence simulations involving species transfer and transport have to be clearly separated from "pure" fluid flow calculations.

i)   Multiphase Flow

The simplest approach to study the flow in a multiphase system is to fix the position of the interface. For the two phases in contact, then fixed computational grids can be used. In the case appropriate boundary conditions can be set at the interface, it is even possible to use only one grid for the phase of interest. Such simulations are typically performed when complex physics are taken into account, and the shape of the phase boundary is well known. Such studies have been conducted, e.g., by Wegener et al.[1] to study interfacial instabilities.

To take into account also the deformation of the interface, more elaborate techniques are necessary. The book of Shyy et al.[2] gives an excellent overview over numerical methods involving deformable boundaries. Basically, (i) front tracking methods where a Lagrangian tracking of the phase boundary is performed (i.e., so-called "Lagrangian" methods), (ii) volume tracking methods in which a fixed Eulerian grid is used (i.e., so-called "Eulerian" methods), as well as (iii) Lattice Boltzmann methods can be distinguished. The front tracking approach has the main advantage that the motion of the interface is directly calculated and hence its (discretized) position is exactly known. However, the computational mesh has to be deformed for that purpose. Volume-tracking methods have the advantage that no mesh deformation has to be done. Combinations of Eulerian and Lagrangian methods are also know, resulting in algorithms with a broader applicability. Lattice Boltzmann methods solve an evolution equation for a particle probability distribution mimicking a two-component mixture, and hence, they are substantially different to conventional fluid dynamics schemes based on a continuum approach.

"Volume Of Fluid" (VOF) simulations are a popular simulation approach and are based on the Eulerian method. They are implemented in many commercial software codes, e.g., Ansys "FLUENT". Despite the difficulties associated with the accurate description of the interface - somewhat alleviated by the use of level-set methods[3] - these methods are widely used.[4-7] For example, VOF simulations of bubble formation and bubble rise in turbulent flows have been performed by Akhtar et al.[8] and also by the group of Harasek.[9] These simulations have the ambition to fully resolve bubble formation at the sparger, as well as the motion of multiple bubbles in a lab-scale bubble column. However, in both references, models for the unresolved

turbulent motion have been used (i.e., the k-ε turbulence model in the work of Akhtar et al.,[8] as well as a Large Eddy Simulation approach in Harasek et al.[9]). Thus, the interface motion was not fully resolved and hence these simulations cannot provide the basis for further studies on, e.g., mass transfer across interfaces. Also, it is speculated that such simulations heavily depend on the used grid size due to possibly unresolved thin filaments occurring during breakup and coalescence processes. Recent developments of the VOF method have been done by Kim and Lee,[10] as well as Boger et al.[11] The latter work significantly improved the VOF method to minimize parasitic currents generated near the interface. This is of great importance for bubbly flows at low Reynolds numbers, as well as for the subsequent prediction of species transfer across the interface.
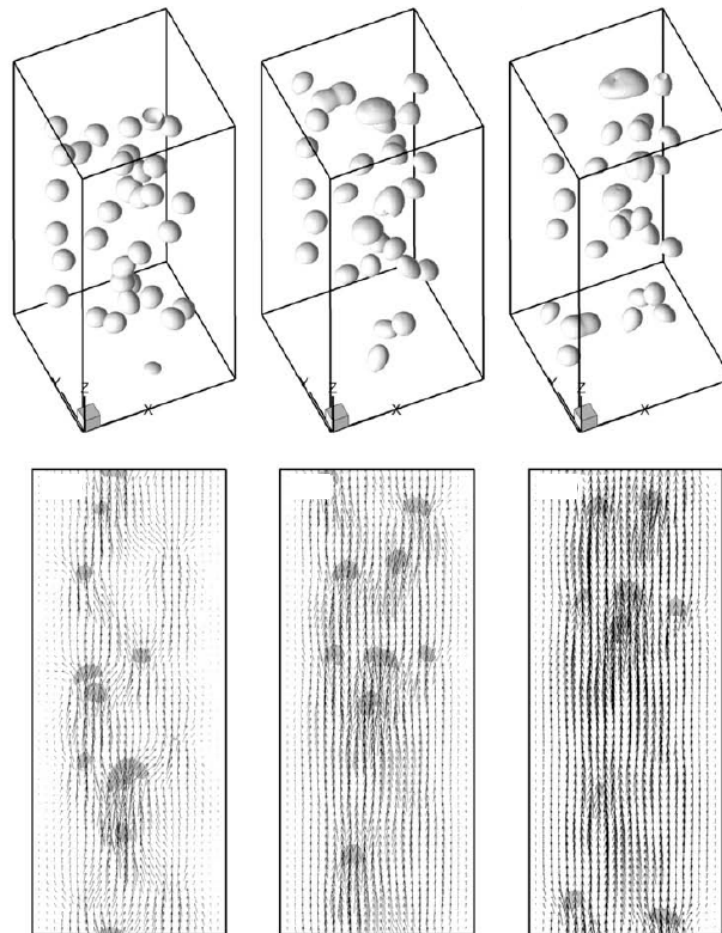
Figure 3.2: Bubble shape (top) and velocity vectors in a cross section for three time instances in a bubble swarm (simulation based on the Lattice Boltzmann method, Cheng et al.[12]).

Lagrangian methods in which the grid follows the fluid, have provided useful insight into the mechanisms of the deformation of bubbles, but are usually limited to single bubbles.[13-17]

In front tracking methods, a separate, deformable grid is used to track the interface.[18] Significant advances have been also achieved by the combination of front and volume tracking in the code initially proposed by Tryggvason et al.[19] Numerous research groups, e.g., the groups of Sommerfeld,[20-22] Kuipers,[23] as well as Khinast,[24-27] based their work on this methodology due to its high accuracy near the interface. This enabled a prediction, e.g., of turbulence statistics and concentration fields in three-dimensional, fully resolved bubbly flows. Currently, this methodology was further improved to include models for e.g., the extremely thin films in droplets when they are sliding down a sloping wall.[28]

Finally, Lattice Boltzmann (LB) methods have been used by Kemiha et al.,[29] Frank and Li,[30] as well as recently by Cheng et al.[12] for fully deformable bubble swarms (see Figure 3.2). Despite these recent advances, some drawbacks of LB methods remain, e.g., the phases are weakly compressible, and limitations in the maximum attainable Mach number exist. The comparison of Sankaranarayanan et al.[31] has shown, however, that LB methods yield reliable results for fully resolved bubbly flow and stability issues of the numerical schemes used in these simulations have been solved.

ii)   Multiphase Flow and Reactive Mixing

The mixing of inert and reactive scalars in multiphase systems has drawn little attention over the past decades. This is most likely connected to the fact, that even the description of single-phase mixing at low to intermediate Reynolds numbers is non-trivial. While the Reynolds number at the equipment scale can clearly indicate turbulent flow characteristics, the small-scale flow near individual bubbles is often characterized by a Reynolds number much lower than 1,000. Clearly, when mixing is of interest, the generation of fine striations patterns in these flows needs to be resolved. The reorientation of fluid elements creates an exponential growth of these striations. To resolve these fine structures would require significant computational resources. This limits the calculation of striation pattern especially in liquids, since the smallest size of concentration striations is proportional to $Sc^{-0.5}$ (Sc is the Schmidt number which is typically $O(10^3)$ in liquids). Thus, striation patterns in chaotic laminar mixing have been analyzed only recently by, e.g., Vikhansky and co-workers.[32-37] A deeper insight into the topic of laminar mixing is provided in Szalai et al.[38]

Due to this challenge, only a few researchers have attempted the simulate mixing in multiphase systems. For example, in the recent work of Derksen[39,40] the mixing induced by moving particles has been directly calculated. Specialized convection schemes are necessary to

suppress numerical diffusion in these simulations (for some snapshots of typical results see Figure 3.3). Research in this field is relatively rare and there has been, for example, no study that analyzed the isolated effect of bubble motion on liquid phase mixing. Clearly, more research is necessary in this area, using sophisticated numerical and experimental tools.
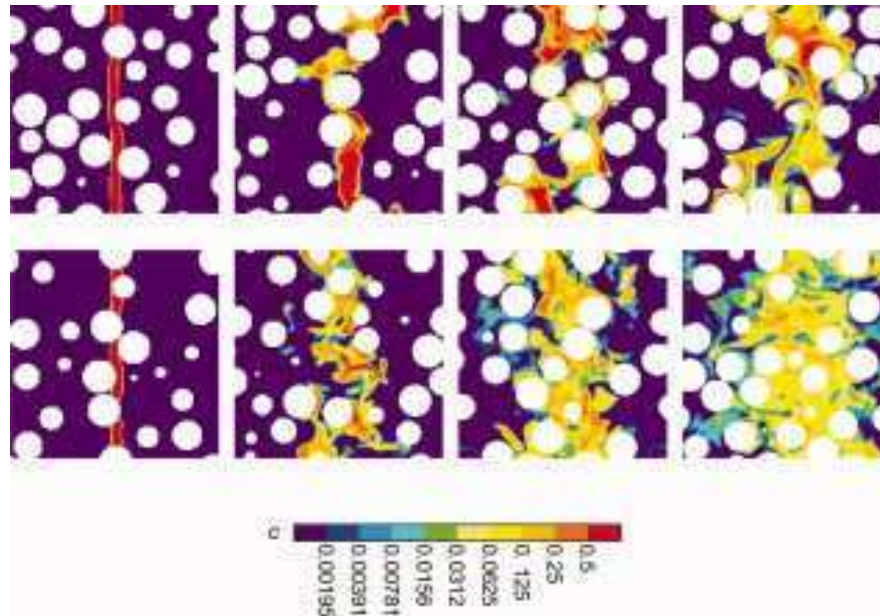
Figure 3.3: Cross section through a three-dimensional simulation of particle-induced mixing (the white disks represent cross sections of spherical particles, the contour plot indicates the log-scaled concentration field in the limit of an infinite Schmidt number, from Derksen[39]).

The next section is dedicated to the analysis of the combined effect of mass transfer and mixing on the concentration field in bubbly flows.

iii) Multiphase Flow and Mass Transfer

The direct prediction and modeling of mass transfer in bubbly flows has gained significant interest since the early work of Ponoth and McLaughlin.[41] This work already recognized the high-Schmidt number problem, i.e., the formation of an extremely thin concentration boundary layer at the interface. Almost at the same time, Khinast[42] published the first work on reactive mass transfer in a two-dimensional, single-bubble setup. Later, Darmana[23,43] extended this work to three-dimensional bubble swarms at low Schmidt numbers. Similar studies have been done by Onea et al.,[44] as well as Bothe et al.[45,46] based on the VOF approach. An interface-refined grid was used in the simulations of Jung and Sato[47] to study also mass transfer characterized by a high Schmidt number. This recent success was limited, however, to three-dimensional deformable single bubbles and was based on interface-fitted grids (i.e., a Lagrangian formulation). Further advances were the inclusion of the energy conservation

equation to study highly exothermic reactions,[48] or the extension to three-phase systems to analyze heterogeneously catalyzed reactions[49] or the shear damage of suspended cells.[50] More physics were introduced in simulations by the group of Kraume,[1,51] which focused on the effect of Marangoni convection on mass transfer, as well as in Radl et al.,[27,52] who focused on fluids with a complex rheology. Also, the surfactant transport at the gas-liquid interface of bubbles has been studied.[53] Micro-mixing effects, e.g., for chemical reactions, have been analyzed, which again demonstrated the power of direct numerical simulations for practical applications.[54-56] Typically, these simulations were based on a two-dimensional description of the multiphase system (see Figure 3.4 for a qualitative comparison with experimental results and three-dimensional simulations). This is because three-dimensional simulations are prohibitively expensive at high Schmidt numbers, as $O(10^9)$ grid cells are typically required.
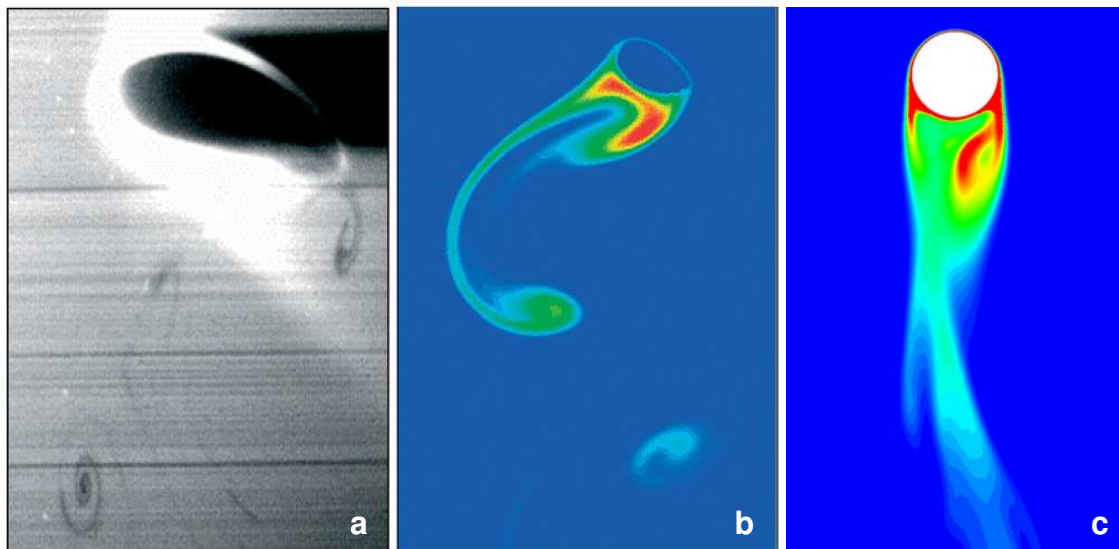
Figure 3.4: Qualitative features of concentration fields around single bubbles (a: experiments by Prof. Schlueter performed at the University of Bremen; b: two-dimensional simulations by Koynov and Khinast;[26] c: cross section through a three-dimensional simulation[57])

Recent developments are undertaken within the DFG priority program SPP 1506 "Transport Processes at Fluidic Interfaces". The outcome is a simplified interface-near model to account for the steep concentration gradient.[58] Finally, also the detailed experimental analysis of mass transfer from ascending bubbles performed by Kuck et al.[59] should be mentioned in this context.

3.1.2 The Point-Particle Approach

The point-particle approach refers to a methodology where each bubble, or a small cloud of bubbles, is tracked through the computational domain. Thus, Newton's equation of motion is

solved for each bubble and the bubble positions are obtained at each time instant. This approach is very similar to the methodology that is frequently used for granular flows (see chapter 3.2.1). In the point-particle approach different levels of fidelity in the modeling of the continuous phase (e.g., direct numerical simulations, large eddy simulations, etc.) and the particle phase can be used. The method used for the particle phase can be differentiated by the level of physics taken into account during bubble-bubble collisions and the number of bubbles represented by each point to be tracked. Phase interaction can be "one-way" (i.e., only the effect of the continuous phase on the disperse phase is taken into account), "two-way" (i.e., also the back coupling from the disperse phase to the continuous phase is accounted for), "three-way" (i.e., also local effects of suspended particles on other particles are taken into account), or even "four-way" (i.e., also bubble-bubble collisions are taken into account).[60]

i) Simple Models

The simplest models do not take into account particle-particle interactions and each individual bubble is tracked in the flow field. The prerequisite is that the gas hold-up is small enough, such that the effect of collisions is negligible (typically, the integral hold-up should be lower than 1% and the local lower than 10%). Also, the displacement of the liquid phase by the bubbles is typically neglected, such that the continuous phase governing equations are the Navier-Stokes equations[b] with (in case of two-way coupling) or without (in case of one-way coupling) external forces. Such simulations have been performed, e.g., by Mazzitelli et al.,[61-63] Lain et al.[64] and more recently by Nierhaus et al.,[65] as well as Hu and Celik.[66] The exclusion of bubble-bubble collisions also excludes the ability to model coalescence.

ii) Advanced Models with Coalescence and Breakup

Within the last ten years, there has been a significant interest in the prediction of coalescence effects in dense bubbly flows. In these flows, the displacement of the liquid phase is typically non-negligible and has been incorporated in the continuous phase governing equations. To model coalescence, the collisions between individual bubbles must be calculated. In the work of Delnoij et al.,[67] Deen et al.,[68] as well as in the publications of Darmana,[43,69-71] bubble-bubble collisions are calculated directly using the hard-sphere approach (for details refer to Chapter 3.2.1ii). A simple test case using this approach and showing the effect of coalescence is shown

---

[b] A filtered or Reynolds-averaged form of the Navier-Stokes equations may be used to overcome the limitations imposed by the resolution of turbulent eddies.

in Figure 3.5. This is a computationally expensive way to account for coalescence effects, since each collision must be detected and processed. Therefore, Sommerfeld et al.[72] used a statistical collision model that uses virtual collision "partner bubbles". To limit the growth of bubbles, bubble breakup also needs to be accounted for and can be implemented using several strategies (e.g., by limiting the maximum bubble size as done in Darmana,[43] see Figure 3.5-b1 to b3).
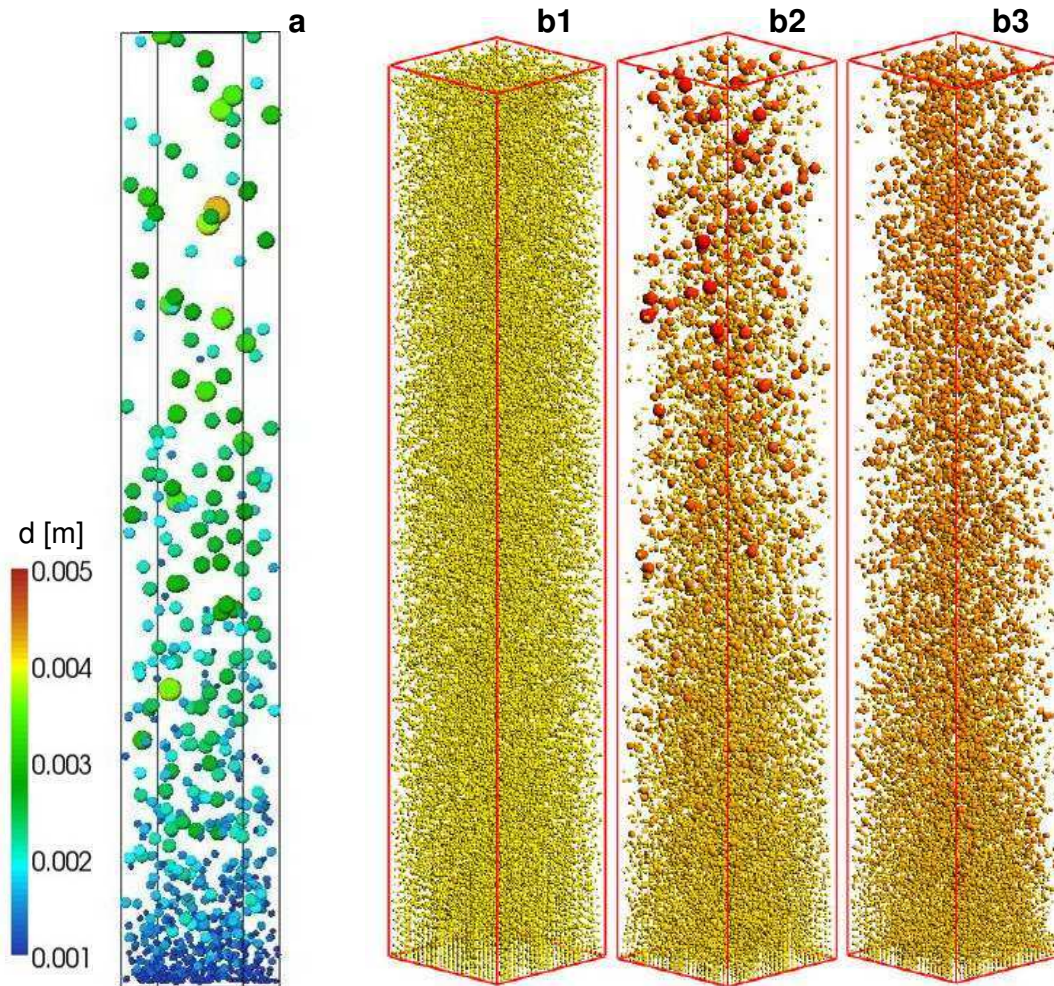
Figure 3.5: **Results of point-particle simulations of a bubble column taking into account coalescence (a: a simple test case for the air-water system, d denotes the bubble size in meters; b: simulations by Darmana[43] for a pilot-scale bubble column with a size of 0.2 x 0.2 x 1.2 m, b1: no coalescence, b2: coalescence, b3: coalescence with a limiter in the bubble size to mimic bubble break-up)**

3.1.3 Two-Fluid Models

Two-fluid models treat the bubbles as a continuous phase that penetrates the surrounding fluid. This approach is also called Euler-Euler approach, since the governing equations for both phases are solved on an Eulerian grid. The treatment of discrete bubbles as a continuum

has severe consequences: an averaging over the bubbles present in a computational grid cell has to be performed, which requires the modeling of phase-interaction and dispersed-phase details (i.e., bubble fluctuation velocities, bubble collision and breakup rates, etc.). The latter often leads to quite rigorous modeling approaches when the bubble size distribution is taken into account. While there is the principal possibility to connect the local turbulence properties to the bubble size, it is often necessary to solve additional transport equations for the bubble population. In such cases, the population balance equation is solved, either in a class-wise fashion (i.e., the bubble population is split into a fixed number of classes) or using the method of moments.[73] The review of Jakobsen et al.[74] describes current challenges associated with the modeling of bubble column reactors with a focus on the population balance equation. Clearly, the inclusion of the population balance equation for a more realistic representation of the bubble size distribution is a topic on its own. It has and will attract researchers from many fields, due to the complexity connected to its numerical solution.

The major advantage of the two-fluid approach is that the number of bubbles in the system does not influence the computational cost of the simulation. Consequently, simulations based on the two-fluid approach are predominantly used for industrial-scale systems.

3.1.4 Integral Models

This model type has recently been summarized by Zehner.[75] The basic assumption behind this modeling strategy is that the flow situation can be approximated by a system of compartments. For each of these compartments, integral mass and energy balances can be established and solved. Typically, this is done for a steady-state flow situation, such that a system of algebraic equations is obtained. For example, in the case of an aerated bubble column, the total power introduced by the gas bubbles ($P_{gassing}$) must be balanced by the energy dissipation due to bubble rise (P_{bubble}) and fluid circulation (P_{circ}):

$$P_{gassing} = P_{bubble} + P_{circ} \qquad\qquad\qquad\qquad\qquad\qquad (\,3.1\,)$$

The gassing power input can be easily calculated from the product of the static pressure drop and the volumetric gas flow rate.[c] The dissipation due to the bubble rise can be calculated from the static pressure drop, the gas hold-up, as well as the gas-liquid slip velocity. For the

---

[c] In case of large changes of the volumetric gas flow rate, e.g., due to temperature or pressure changes, or due to ab-/desorption of gases, a correction has to be taken into account.

loss due to fluid circulation, traditional concepts based on a friction coefficient can be adopted. In order to close the system of equations, this friction coefficient, as well as the slip velocity must be known (e.g., via correlations based on experimental data). Similar models can be derived for gassed stirred tanks, where a clear focus of the recent literature is the prediction of flooding. For example, the prediction of flooding in multi-impeller systems is extremely important for various large-scale applications of bubbly flows. Recent work in this area has been done by Bombac and Zun,[76] as well as Bombac et al.[77] Another example for the application of integral models is the work presented by Degaleesan et al.[78] In this work a bubble column was split up in multiple compartments and mixing was modeled using appropriate dispersion models.

Integral models have the advantage to provide quick answers for systems that have been already characterized, i.e., standard applications of bubbly flows. They provide reasonably good predictions of the flow situation, which is often sufficient to predict reactor performance. This is true for a wide range of industrial-scale applications of bubbly flows.

3.1.5 Conclusions for Bubbly Flows

The wide range of scales present in bubbly flows is reflected by the different modeling approaches for these systems. The modeling of fully deformable bubbles, i.e., a resolution of the gas-liquid interface, yields very accurate results for single bubbles and small bubble swarms. However, even this modeling strategy is limited to two-dimensional simulations (axisymmetric or based on Cartesian coordinates) which in the context of reactive mass transfer often allow only a qualitative investigation of bubble swarm effects. The current challenges with respect to the modeling of bubbly flows are:

- the coupling of many different physical and chemical effects on a wide range of scales needs to be taken into account,

- to take into account coalescence, breakup and the resulting polydispersity of the bubble population in a reactor,

- the direct study of chemical reaction networks in turbulent multiphase flow, as well as

- the validation of the models for the simulation of dense reactive bubbly flows.

Clearly, systematic studies are required to investigate the effects of bubble deformation, oscillation, adsorption of surfactants, internal circulation, and mixing in the liquid phase. In

addition, there are currently significant limitations imposed by the numerical solution of these models. Specifically, there is need for:

- the improvement of algorithms for the solution of large partial differential equations on computer clusters,

- the establishment of reliable and efficient bubble tracking, as well as collision algorithms on computer clusters,

- the improvement of multiphase flow solvers for interface-resolved simulations of dense bubble swarms, as well as

- an user-friendly and flexible software platform for easy application and extension to the system of interest.

The use of graphic processing units (GPU) might be a possible solution to minimize the time needed for the numerical calculations at relatively low cost. However, the use of GPUs is still challenging and memory is a serious problem. It can be expected, that computations on GPUs will significantly speed-up simulations compared to the use of conventional CPUs. For simulations based on Lagrangian particle tracking a speed-up by a factor of 20 to 100 is realistic, while for conventional continuum-based solvers the speed-up will be in the order of 2-10.

3.2 Granular Flows

The characterization of granular flow is of major importance for the pharmaceutical industry. Granular flows have a direct impact on both processes and products, and consequently, influence product quality.

The aim of this chapter is to provide a basis for the analysis of granular flows and to summarize the state of the art in the modeling of these flows. Special emphasis is put on mechanistic models for cohesive systems. Fully empirical models, i.e., so-called "black box models", are not reviewed since they often lack physical background. Also, the extensive work that has been done on modeling granulation processes using the population balance equation (PBE) is not discussed here in detail. This is because granular flows cannot be predicted with these models and are often even not considered in the PBE. The excellent review of Cameron et al.[79] provides further reading on the PBE approach. Also, there was no focus on the modeling of wet granulation processes in this chapter. The review of Iveson et al.,[80] as well as the book of Litster et al.,[81] provide an introduction to the underlying phenomena in this area.

While a recent review on dense gas-solid flow models has been presented by van der Hoef,[82] the focus of this work is the modeling of the particle phase. In chapter 3.2.1 and 3.2.2 the two basic models are detailed that can be used to describe the particle phase. In chapter 3.2.3 a rather unconventional simulation approach for highly saturated granular matter is presented.

3.2.1   Discrete Particle Models

In discrete particle models each individual particle in the bulk solid is tracked by solving Newton's equation of motion. Hence, these models provide the most natural way for modeling granular flows. They have the major advantage to be useful for essentially all granular flow regimes, from a very dilute particle assembly to densely-packed systems. Due to the nature of most granular flows, a large number of particles (often in the order of $O(10^6)$ particles) has to be tracked in order to mimic the behavior of a real system (made up from an incredibly large number of particles). However, with the advent of inexpensive computer power, the number of scientific publications using discrete particle models has increased rapidly.[83,84] An extensive review of discrete particle simulations is provided by Zhu et al.,[84] and the theoretical background has been summarized by Zhu et al.[83]

The major challenge connected to discrete particle models is the account of particle-particle interaction forces. Clearly, these forces are only relevant in moderately-dense to dense granular

flows which, however, are essential for the pharmaceutical, as well as many other industries. The different approaches for calculating particle-particle interaction forces are detailed in the following. Particle-wall collisions are significantly less problematic and only the consideration of the wall roughness is challenging. Wall roughness can be taken into account, e.g., by using a statistical approach.[85]

i)   The Soft Sphere Approach for Interparticle Collisions

The most sophisticated approach to calculate the forces occurring during particle-particle collisions is by calculating the particle deformation at the contact point. With the ultimate goal to track thousands to millions of individual particles, these deformations cannot be calculated directly, i.e., from the "real" behavior of the particles. Instead, simplified models have to be used. Cundall and Strack[86] were the first that used such a simple model based on a parallel combination of a spring (see Figure 3.6, characterized by a stiffness k) and a dashpot (characterized by a damping coefficient c). Here the subscripts n and t denote the normal and tangential direction, respectively. This simplified model can be adopted for both the normal, as well as the tangential direction, mimicking particle deformation due to the compression and shearing of the particle, respectively. Because particles can also slide against each other, a frictional slider has to be used in series with the tangential deformation model (the element denoted with μ in Figure 3.6).
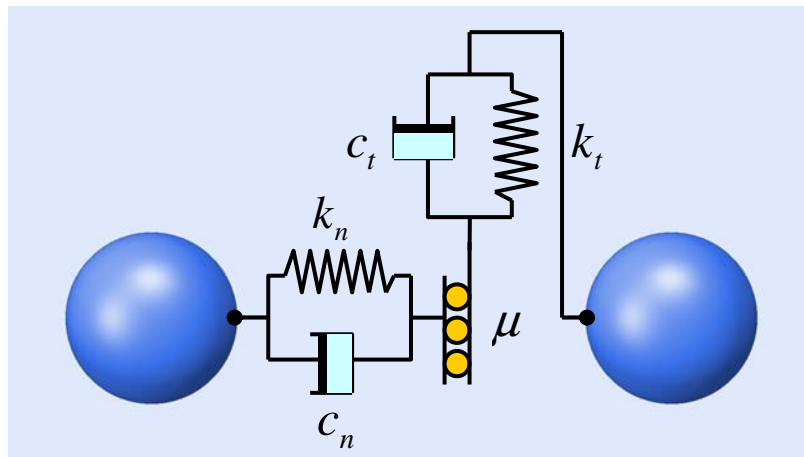
Figure 3.6: Typical spring-dashpot model used in the soft sphere approach.[87]

Discrete particles models based on the soft sphere approach are typically called Discrete (or Distinct) Element Methods (DEM). The major advantage of DEM is that multiple contacts can occur at the same time among particles. This requires, however, a time-resolved calculation of the (simplified) deformation process at each contact point. This results in

relatively small time steps in the order of 10^{-6} s that have to be used in the numerical solution procedure. Hence, DEM is the most expensive tool for studying granular flows from a computational point of view. However, recent advances enable the efficient study of large granular beds (i.e., $O(10^7)$ particles[88]) or non-spherical particles. The latter has been realized by using super-quadric particles in systems with a size of $O(10^5)$ particles.[89] Also, non-spherical particles in fluidized beds have been studied recently.[90]
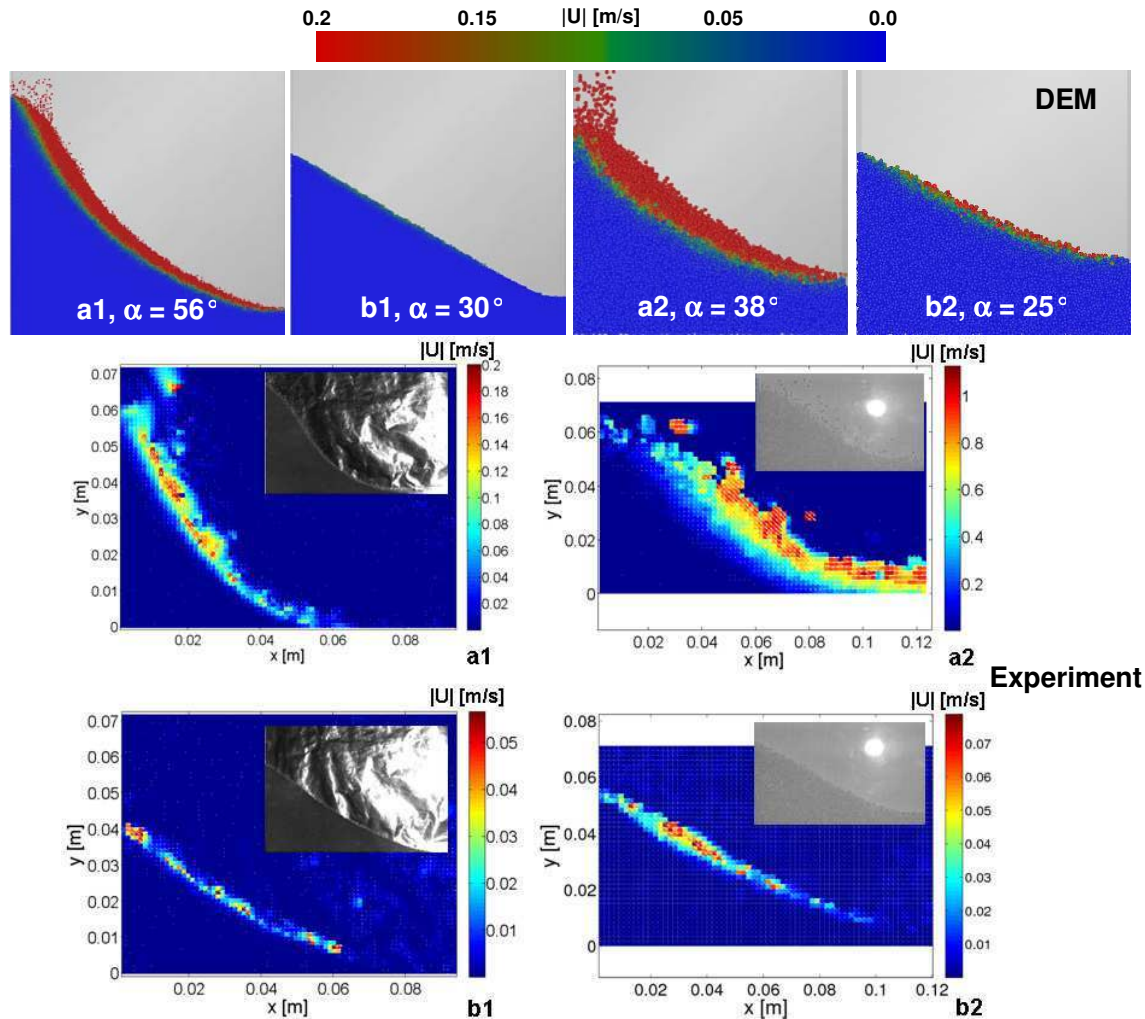
Figure 3.7: Comparison between DEM simulation results (top row) and measured velocity fields (bottom images) in a Hele-Shaw cell (spherical glass beads with 0.5 or 1.4 mm diameter, the inserts in the bottom images are the raw images used for the measurements via particle image velocimetry) a1: 0.5 mm-Phase 2, a2: 1.4 mm-Phase 2, b1: 0.5 mm-Phase 3. b2: 1.4 mm-Phase 3. Phase 2: Images were taken at the moment the last glass bead hit the pile. Phase 3: Images were taken when there was no longer a significant change of the angle of repose.[91]

Often, cohesive forces due to electro-static charge and wetting dominate flow behavior. In these cases DEM can be successfully used, as inter-particle forces can be taken into account directly. Hence, a direct consideration of micro-scale forces on the macro-scale flow can be

achieved with DEM. A comparison of simulation results obtained with the commercial DEM-code "EDEM 2.0" and experimental data is shown in Figure 3.7.

The DEM, as a cutting-edge simulation technique, has the highest potential to become the dominating powder flow simulation tool, at least in some areas. This is especially true when

- the system under consideration has densely-packed, as well as dilute regions,

- the number of particles in the system under consideration is relatively small,

- the particles have a wide size and shape distribution, and when

- mixing and segregation of individual particles is of interest.

Pharmaceutically-relevant systems having above features are encountered in:

- drum coating processes (i.e., relatively large tablets are moving in a rotating cylinder),

- die filling processes (i.e., when granulate particles are filled into the die before the tablet is compressed),

- transport and storage processes, as well as

- blending and granulation processes.

This situation is also reflected in the recent review by Ketterhagen et al.,[92] which details on the applications of the DEM in the pharmaceutical industry.

ii)   The Hard Sphere Approach for Interparticle Collisions

The hard sphere approach is typically used for rapid granular flows, e.g., for the simulation of fluidized bed, in which particles are in contact only for a short period of time. Hence, it can be assumed that only binary collisions occur in the granular flow. For these collisions, the post-collisional velocities can be calculated explicitly, without a detailed knowledge of the particle interaction forces. The properties of the particles are taken into account by using integral parameters, such as the coefficient of normal restitution or the friction coefficient. Typically, this results in an event-driven solution algorithm, where the time gap to the next particle collision in the system is calculated. The particles are then moved to this next collision event, the velocities of the colliding particles are updated and the algorithm starts searching for the next collision. If the granular flow is becoming dense, the time between individual particle collisions is approaching zero and more than two particles may be in contact. At this point,

the hard sphere approach cannot be used anymore. In addition, a spherical particle shape has to be typically assumed.

An often cited application of the hard sphere approach is the work of Hoomans et al.,[93] which studied bubble formation in a fluidized bed. The hard-sphere approach is in frequent use for certain applications (refer to the review of Deen et al.[94]) and has been recently extended to also include cohesive forces between a particle and a wall.[95] However, there is still no uniform methodology on how to include cohesive forces in particle-particle, as well as particle-wall collisions.

iii)   Statistical Approaches for Interparticle Collisions

Since collision detection imposes a severe computational overhead to the simulation, there has been a strong focus on accounting for interparticle collisions by statistical methods. This can be done essentially in two ways: (i) to calculate a representative collisions force from the local solid-phase hold-up, as well as (ii) to generate virtual collision partners.

The first approach has been taken by Andrews and O'Rourke[96] with the ultimate goal to model industrial-scale fluidized beds. In their method the inter-particle forces are calculated from an Eulerian particle model. Hence, this method can be seen as a hybrid between a particle-based and an Euler-based method. In their so-called Multiphase Particle-In-Cell Methodology (MP-PIC), particles are furthermore aggregated to so-called parcels (i.e., a cloud of particles) to minimize the number of Lagrangian particles to be tracked. Forces due to particle-particle interactions are taken into account via a gradient in the interparticle stress. The interparticle stress is calculated from the local solid-phase hold-up, as well as from the local granular temperature.[97] Recently, also a model to account for contact friction between particles was included.[98] This method has been applied to a relatively wide range of granular flows within the last decade.[96-99] The second approach, i.e., the generation of a virtual collision partner, has been developed by the group of Sommerfeld.[85,100,101] Such a stochastic collision model relies on the calculation of the collision probability based on the framework of the kinetic theory of granular flow. Consequently, no information on surrounding particles is necessary, which is critical for the numerical evaluation of the particle trajectories. However, the size, as well as the instantaneous velocity, of the virtual collision partner has to be estimated. This estimation is typically done by interpolating the local particle, as well as velocity distribution, followed by a stochastic sampling from these distributions. The key variable in this approach is the calculation of the fluctuating velocity of the virtual particle,

since this fluctuation is correlated to some extent with the velocity fluctuations of the continuous phase. Currently, there is still active research ongoing[100] to establish functions for this correlation.

3.2.2 Continuum Models

The flow of granular materials can be described using continuum flow models, i.e., the so-called Eulerian-Eulerian approach is used.[102] Such a description can then be used in conjunction with a fluid model to take into account the presence of, e.g., the air surrounding the particles under consideration. CFD software (e.g., the package "FLUENT", see, for example, the work of van Wachem and Sasic[103]) is commercially available for this type of models. For this technique constitutive relationships to describe the solid-phase stresses have to be incorporated. They can be based on concepts borrowed from fluid mechanics (e.g., the modeling of stresses via a granular viscosity based on the kinetic theory of gases[103,104] and solution of a generalized form of the Navier-Stokes equations) or elasto-plasticity (see the following paragraph). These constitutive relationships are a major source of uncertainty in these simulations. The basic difficulty within the Euler-based approach is to model the inhomogeneities on the particle scale level that, for example, may strongly effect the drag forces acting on individual particles. Active research is still ongoing to model these (unresolved) stress terms in the particulate phase.[105-107] Additional difficulties within the Euler-Euler models are the modeling of wall effects (e.g., wall roughness), the effect of particle rotation, as well as differences in particle properties (e.g., particle density or diameter). The latter may be overcome by sophisticated theoretical models, as shown by Zaichik et al.[108] This leads, however, to a tremendous increase in computational cost.

In the area of powder compaction (e.g., relevant for tabletting processes) researches started to use phenomenological elasto-plasticity relationships for powder modeling (see, e.g., Kremer and Hancock[102]). Recent developments in this field include the work of Kamrin,[109] which proposed a general three-dimensional continuum model. In this elasto-plastic model the stresses due to elastic deformation (i.e., a stress proportional to some function of the strain tensor) and plastic flow (i.e., a stress proportional to the deformation rate tensor) are accounted for. Within elasto-plasticity models the correct simulation of particle-die wall friction, as well as the experimental validation, is still a challenging task (see for example the compression simulations by Michrafy,[110] or the recent research by Cunningham et al.,[111] as well as Sinka et al.[112]). Research in this area is still ongoing and advanced elasto-plasticity models

have been published by Frenning,[113] as well as under the name of the so-called "Micro-Directional Model" (MDM) approach by Nicot.[114-117] The application to wet granular matter has been demonstrated by Scholtés et al.,[118] and good agreement with simulations using the discrete element method has been achieved.

Elasto-plastic models are only applicable to dense granular flow, and in general, fail in case of strong inelastic dilatations of the particle bed (the elastic dilatation of individual particles can be accounted for). Some relief is promised in the code "CoRheoGrain", that combines elasto-plasticity models with a kinetic modeling approach for fast granular flows.[119]

3.2.3 Interface Resolved Models for Highly Saturated Granular Matter

Although sophisticated particle-based models (e.g., the ones that use the soft-sphere approach and are detailed in Chapter 3.2.1) can predict the details of granular flow, these models cannot resolve liquid bridges present between two or more particles. Consequently, these models are not suitable for a realistic representation of the three-phase structure, e.g., of wet agglomerates. However, exactly this granule microstructure is an important factor that can have a significant effect, e.g., on the release rate of an API from a granule. The computational methods for calculating the dynamic or equilibrium liquid distribution on irregular shaped objects is a topic of current research. Basically, two approaches can be distinguished for finding the gas-liquid interface:[120] (i) a fluid dynamic approach, in which the Navier-Stokes equations are solved for a sufficiently long time with appropriate boundary conditions, as well as (ii) a shape transformation approach in which the equilibrium conditions are directly imposed, and an algorithm for adjusting the gas-liquid interface is designed to meet these conditions upon convergence. In the latter approach, the velocity field cannot be resolved and consequently dynamic effects, i.e., forces stemming from the fluid's inertia or viscosity, cannot be taken into account. In cases where these effects dominate the three-phase system (i.e., when the Weber and/or the capillary number is high), the fluid mechanics approach must be used.

Some authors have used the fluid mechanics approach to find the liquid distribution on irregularly-shaped objects.[121,122] However, this approach is computationally expensive. Therefore, Stepanek and Ansari,[123] as well as Stepanek and Rajniak,[120] have used the VOF method to generate granule microstructures based on the shape-transformation approach. Thus, certain rules were applied to the function describing the interface and the equilibrium shape of the gas-liquid interface on the particle was obtained. The particles were modeled as

irregular shaped objects with the ultimate goal to predict the formation of a granule by sequential deposition of particles and liquid droplets (see Figure 3.8).
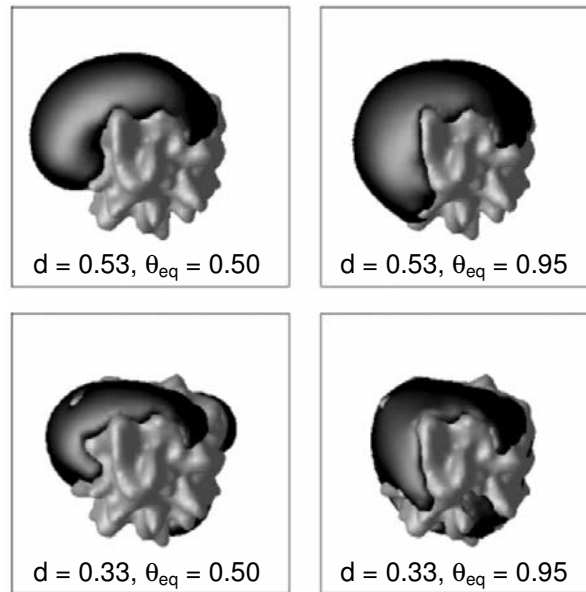
Figure 3.8: Equilibrium distribution of a liquid droplet on an arbitrary shaped particle for two different droplet sizes (d is the relative droplet diameter to the particle's mean gyration radius) and equilibrium contact angles θ_{eq}.[120]

Recent articles published by the group around Stepanek[124-126] include a novel computational scheme to calculate the gas-liquid interface in two-dimensional systems involving $O(10^2)$ arbitrary shaped particles.

3.2.4 Conclusions for Granular Flows

In addition to the possibility of resolving the interface of individual particles or even that of a gas-liquid-solid system, the Discrete Element Method constitutes the most detailed model for granular flows. It is now in use for over thirty years and is the only model that can predict particle flow in any flow regime (i.e., dilute or dense, quasi-static or fast). Virtually any particle size and shape distribution, as well as arbitrary interaction forces, can be taken into account. The remaining challenge is to further decrease the enormous simulation time required for "large" systems, i.e., systems involving more than 1 Mio. particles. Graphic processing units (GPUs) are already in use to alleviate this problem and have the potential to reduce simulation time by a factor of $O(10^2)$.

The other extreme, i.e., continuum models, can handle any size of the system, but require models for the stresses in the bulk solid. While there are efforts ongoing to include particle-

particle interaction forces in these stress models, the consideration of particle shape, as well as dilatation effects will remain a significant limitation.

The synthesis of continuum and discrete particle models, i.e., a hybrid model, is a logical consequence in order to use the advantages of both approaches. Research is ongoing for approximately ten years, and specialized computer programs have already evolved from this work (e.g., the code "Barracuda" developed by Snider,[98] or the work of Pirker et al.[127]). Hybrid models would require an extreme level of complexity in order to be suitable for all kinds of granular flows. However, they are a powerful tool for a certain spectrum of applications.

With respect to wet granular matter, the currently predominant modeling approach is the population balance equation (PBE). The use of the PBE requires kernels for the underlying processes (i.e., nucleation, growth, consolidation, attrition, breakage, and agglomeration). Information on these processes are typically obtained from experimental observations and used in the form of correlations or regime maps (e.g., see the book of Litster et al.[81]). However, this is often not enough and inaccurate for systems that have not been experimentally characterized. For example, the understanding of the strength of wet granular assemblies is critical for granule deformation and coalescence.[128] Such an understanding could be gained, for example, by numerical investigations (e.g., using the Discrete Element Method at the level of individual particles) to understand phenomena observed experimentally.[129,130] Clearly, the challenge on this scale is to predict the effect of liquid bridges between particle assemblies. This is extremely demanding for a highly saturated state, because simple models on the basis of pendular liquid bridges cannot be used any more. Also, on the equipment scale first attempts for using more sophisticated flow models for the prediction of wet granulation processes have been made.[131,132] Here, the challenge is to understand the motion of material within granulators and the interaction of granulation tools with the wet particle bed. Despite the predominant use of experimental methods in the area of wet granular matter, it is anticipated that more elaborate mathematical models will evolve in the future. These advances will primarily rely on the evolution in the area of interface-resolved simulation of gas-liquid-solid systems for the highly saturated wet granular matter.

3.3 Abbreviations

API   Active Pharmaceutical Ingredient

CFD   Computational Fluid Dynamics

CPU   Central Processing Unit

DEM   Discrete Element Method

DFG   Deutsche Forschungsgemeinschaft (German Research Institution)

GPU   Graphic Processing Units

MDM   Micro-Directional Model

MP-PIC   Multiphase Particle-In-Cell Methodology

LB   Lattice Boltzmann

PBE   Population Balance Equation

VOF   Volume Of Fluid

3.4 Nomenclature

P_{bubble} dissipation rate due to bubble rise [W]

P_{circ} dissipation rate due to fluid circulation [W]

$P_{gassing}$ power input due to gassing [W]

3.5 References

(1)   Wegener M, Eppinger T, Baumler K, Kraume M, Paschedag AR, Bansch E. Transient rise velocity and mass transfer of a single drop with interfacial instabilities-Numerical investigations. Chem Eng Sci. 2009; 64:4835-4845.

(2)   Shyy W, Udaykumar HS, Rao MM, Smith RW. Computational Fluid Dynamics with Moving Boundaries. Mineola, New York, U.S.: Dover Publications, 1996.

(3)   Osher S, Fedkiw RP. Level set methods: An overview and some recent results. Journal of Computational Physics. 2001; 169:463-502.

(4)   Brackbill JU, Kothe DB, Zemach C. A Continuum Method for Modeling Surface-Tension. Journal of Computational Physics. 1992; 100:335-354.

(5)   Lakehal D, Meier M, Fulgosi M. Interface tracking towards the direct simulation of heat and mass transfer in multiphase flows. International Journal of Heat and Fluid Flow. 2002; 23:242-257.

(6)   Scardovelli R, Zaleski S. Direct numerical simulation of free-surface and interfacial flow. Annual Review of Fluid Mechanics. 1999; 31:567-603.

(7)   van Wachem BGM, Schouten JC. Experimental validation of 3-D Lagrangian VOF model: Bubble shape and rise velocity. AIChE Journal. 2002; 48:2744-2753.

(8)   Akhtar A, Pareek V, Tade M. CFD Simulations for Continuous Flow of Bubbles through Gas-Liquid Columns: Application of VOF Method. Chemical Product and Process Modeling. 2007; 2:1-19.

(9)   Harasek M, Horvath A, Jordan C, Kuttner C, Lukasser M. CFD-Simulation einer Blasensäule mit dem VOF-Modell - Fluent vs. OpenFOAM vs. Experiment. Chemie Ingenieur Technik. 2008; 80:1291.

(10)   Kim MS, Lee WI. A new VOF-based numerical scheme for the simulation of fluid flow with free surface. Part I: New free surface-tracking algorithm and its verification. International Journal for Numerical Methods in Fluids. 2003; 42:765-790.

(11)   Boger M, Schlottke J, Munz C-D, Weigand B. Reduction of Parasitic Currents in the DNS VOF code FS3D. 12th Workshop on Two-Phase Flow Prdictions. Halle, Germany: 2010.

(12)   Cheng M, Hua JS, Lou J. Simulation of bubble-bubble interaction using a lattice Boltzmann method. Computers & Fluids. 2010; 39:260-270.

(13)   Shopov PJ, Minev PD, Bazhlekov IB, Zapryanov ZD. Interaction of A Deformable Bubble with A Rigid Wall at Moderate Reynolds-Numbers. Journal of Fluid Mechanics. 1990; 219:241-271.

(14)   Noh DS, Kang IS, Leal LG. Numerical-Solutions for the Deformation of A Bubble Rising in Dilute Polymeric Fluids. Physics of Fluids A-Fluid Dynamics. 1993; 5:1315-1332.

(15)   Ryskin G, Leal LG. Numerical-Solution of Free-Boundary Problems in Fluid-Mechanics .2. Buoyancy-Driven Motion of A Gas Bubble Through A Quiescent Liquid. Journal of Fluid Mechanics. 1984; 148:19-35.

(16)   Ryskin G, Leal LG. Numerical-Solution of Free-Boundary Problems in Fluid-Mechanics .1. the Finite-Difference Technique. Journal of Fluid Mechanics. 1984; 148:1-17.

(17)   Ryskin G, Leal LG. Numerical-Solution of Free-Boundary Problems in Fluid-Mechanics .3. Bubble Deformation in An Axisymmetric Straining Flow. Journal of Fluid Mechanics. 1984; 148:37-43.

(18)   Glimm J, Grove JW, Li XL, Oh W, Sharp DH. A critical analysis of Rayleigh-Taylor growth rates. Journal of Computational Physics. 2001; 169:652-677.

(19) Tryggvason G, Bunner B, Esmaeeli A, Juric D, Al-Rawahi N, Tauber W et al. A front-tracking method for the computations of multiphase flow. J Comput Phys. 2001; 169:708-759.

(20) Göz M, Bunner B, Sommerfeld M, Tryggvason G. Direct Numerical Simulation of Bidisperse Bubble Swarms. International Conference on Multiphase Flow. New Orleans, US: 2001.

(21) Göz M, Bunner B, Sommerfeld M, Tryggvason G. Direct Numerical Simulation of Bubble Swarms with a Parallel Front-Tracking Method. International FORTWIHR Conference on HPSEC. Erlangen, D: 2001.

(22) Göz M, Bunner B, Sommerfeld M, Tryggvason G. Simulation of bubbly gas-liquid flows by a parallel finite-difference/front tracking method. In: Krause E, Jäger W. High Performance Computing in Science and Engineering. Berlin, D: Springer, 2002:326-337.

(23) Darmana D, Deen NG, Kuipers JAM. Detailed 3D modeling of mass transfer processes in two-phase flows with dynamic interfaces. Chemical Engineering & Technology. 2006; 29:1027-1033.

(24) Koynov A, Khinast JG, Tryggvason G. Mass transfer and chemical reactions in bubble swarms with dynamic interfaces. AIChE J. 2005; 51:2786-2800.

(25) Koynov A, Tryggvason G, Schlueter M, Khinast JG. Mass transfer and chemical reactions in reactive deformable bubble swarms. Applied Physics Letters. 2006; 88:134102.

(26) Koynov AA, Khinast JG. Micromixing in reactive, deformable bubble, and droplet swarms. Chemical Engineering & Technology. 2006; 29:13-23.

(27) Radl S, Tryggvason G, Khinast JG. Flow and mass transfer of fully resolved bubbles in non-Newtonian fluids. AIChE J. 2007; 53:1861-1878.

(28) Tryggvason G, Thomas S, Lu J, Aboulhasanzadeh B. Multiscale Issues in Dns of Multiphase Flows. Acta Mathematica Scientia. 2010; 30:551-562.

(29) Kemiha M, Frank X, Poncin S, Li HZ. Origin of the negative wake behind a bubble rising in non-Newtonian fluids. Chem Eng Sci. 2006; 61:4041-4047.

(30) Frank X, Li HZ. Negative wake behind a sphere rising in viscoelastic fluids: A lattice Boltzmann investigation. Physical Review e. 2006; 74.

(31) Sankaranarayanan K, Kevrekidis IG, Sundaresan S, Lu J, Tryggvason G. A comparative study of lattice Boltzmann and front-tracking finite-difference methods for bubble simulations. International Journal of Multiphase Flow. 2003; 29:109-116.

(32) Vikhansky A. Enhancement of laminar mixing by optimal control methods. Chem Eng Sci. 2002; 57:2719-2725.

(33) Vikhansky A. Simulation of topological chaos in laminar flows. Chaos. 2004; 14:14-22.

(34) Vikhansky A. Quantification of reactive mixing in laminar microflows. Physics of Fluids. 2004; 16:4738-4741.

(35) Vikhansky A. Coarse-grained simulation of chaotic mixing in laminar flows. Physical Review e. 2006; 73.

(36) Vikhansky A, Cox SM. Reduced models of chemical reaction in chaotic flows. Physics of Fluids. 2006; 18.

(37) Vikhansky A, Cox SM. Conditional moment closure for chemical reactions in laminar chaotic flows. AIChE J. 2007; 53:19-27.

(38) Szalai ES, Alvarez MM, Muzzio FJ. Laminar Mixing: A Dynamical Systems Approach. In: Paul EL, Atiemo-Obeng VA, Kresta SM. Handbook of Industrial Mixing - Science and Practice. Hoboken, U.S.: John Wiley & Sons, Inc., 2010:89-143.

(39) Derksen JJ. Scalar mixing by granular particles. AIChE J. 2008; 54:1741-1747.

(40) Derksen JJ. Mixing by solid particles. Chemical Engineering Research & Design. 2008; 86:1363-1368.

(41) Ponoth SS, McLaughlin JB. Numerical simulation of mass transfer for bubbles in water. Chem Eng Sci. 2000; 55:1237-1255.

(42) Khinast JG. Impact of 2-D bubble dynamics on the selectivity of fast gas-liquid reactions. AIChE J. 2001; 47:2304-2319.

(43) Darmana D. On the multiscale modelling of hydrodynamics, mass transfer and chemical reactions in bubble columns. Twente, Netherlands: University of Twente, 2006.

(44) Onea A, Worner M, Cacuci DG. A qualitative computational study of mass transfer in upward bubble train flow through square and rectangular mini-channels. Chem Eng Sci. 2009; 64:1416-1435.

(45) Bothe D, Koebe M, Warnecke HJ. VOF-Simulation of the Rise Behavior of Single Air Bubbles with Oxygen Transfer to the Ambient Liquid. Conference on Transport Phenomena with Moving Boundaries. Berlin, Germany: 2005.

(46) Bothe D, Kroger M, Alke A, Warnecke HJ. VOF-based simulation of reactive mass transfer across deformable interfaces. Progress in Computational Fluid Dynamics. 2009; 9:325-331.

(47) Jung RT, Sato T. Numerical simulation of high Schmidt number flow over a droplet by using moving unstructured mesh. J Comput Phys. 2005; 203:221-249.

(48) Wang J, Bindal A, Leib TM, Khinast JG. Analysis of the complex nonlinear behavior of reacting bubble flows: steady-state multiplicity. Chem Eng Sci. 2004; 59:5575-5585.

(49) Raffensberger JA, Glasser BJ, Khinast JG. Analysis of heterogeneously catalyzed reactions close to bubbles. AIChE J. 2005; 51:1482-1496.

(50) Koynov A, Tryggvason G, Khinast JG. Characterization of the localized hydrodynamic shear forces and dissolved oxygen distribution in sparged bioreactors. Biotechnol Bioeng. 2007; 97:317-331.

(51) Wegener M, Paschedag AR, Kraume M. Experimental examinations as well as 2D-and 3D simulations of mass transport in single drops with Marangoni convection. Chemie Ingenieur Technik. 2007; 79:73-81.

(52) Radl S, Khinast JG. Prediction of mass transfer coefficients in non-Newtonian fermentation media using first-principles methods. Biotechnol Bioeng. 2007; 97:1329-1334.

(53) Tukovic Z, Jasak H. Simulation of Free-Rising Bubble with Soluble Surfactant using Moving Mesh Finite Volume/Area Methdo. Trondheim, Norway: 6th International Conference on CFD in Oil & Gas, Metallurgical and Process Industries, 2008.

(54) Radl S, Koynov A, Tryggvason G, Khinast JG. DNS-based Prediction of the Selectivity of Fast Multiphase Reactions: Hydrogenation of Nitroarenes. Chem Eng Sci. 2008; 63:3279-3291.

(55) Radl S, Suzzi D, Khinast JG. Assessment of Micro- and Mesomixing in Bubble Swarms via Simulations. 9th International Conference on Chemical and Process Engineering. Rome, Italy: AIDIC, 2009.

(56) Raffensberger JA, Glasser BJ, Khinast JG. Effect of Droplet-Wake Phenomena on Mixing-Sensitive Pharmaceutical Reactions. Pharmaceutical Technology. 2006; 30:66-80.

(57) Radl S, Gruber MC, Khinast JG. Scalar Variance and Fast Chemical Reactions in Bubble Column Reactors. Halle, Germany: 12th Workshop on Two-Phase Flow Predictions, 2010.

(58) Bothe D, Kröger M. Direct Numerical Simulation of high Schmidt Number Mass Transfer from Rising Air Bubbles using the Volume-of-Fluid-Method. 12th Workshop on Two-Phase Flow Prdictions. Halle, Germany: 2010.

(59) Kuck UD, Schlueter M, Rabiger N. Analysis of the bounded-material transport in freely climbing up gas bubbles. Chemie Ingenieur Technik. 2009; 81:1599-1606.

(60) Crowe C, Sommerfeld M, Tsuji Y. Multiphase Flows with Droplets and Particles. Boca Raton, US: CRC Press, 1998.

(61) Mazzitelli IM, Lohse D, Toschi F. On the relevance of the lift force in bubbly turbulence. Journal of Fluid Mechanics. 2003; 488:283-313.

(62) Mazzitelli IM, Lohse D, Toschi F. The effect of microbubbles on developed turbulence. Physics of Fluids. 2003; 15:L5-L8.

(63) Mazzitelli IM, Lohse D. Lagrangian statistics for fluid particles and bubbles in turbulence. New Journal of Physics. 2004; 6.

(64) Lain S, Broder D, Sommerfeld M, Goz MF. Modelling hydrodynamics and turbulence in a bubble column using the Euler-Lagrange procedure. International Journal of Multiphase Flow. 2002; 28:1381-1407.

(65) Nierhaus T, Abeele DV, Deconinck H. Direct numerical simulation of bubbly flow in the turbulent boundary layer of a horizontal parallel plate electrochemical reactor. International Journal of Heat and Fluid Flow. 2007; 28:542-551.

(66) Hu GS, Celik I. Eulerian-Lagrangian based large-eddy simulation of a partially aerated flat bubble column. Chem Eng Sci. 2008; 63:253-271.

(67) Delnoij E, Lammers FA, Kuipers JAM, vanSwaaij WPM. Dynamic simulation of dispersed gas-liquid two-phase flow using a discrete bubble model. Chem Eng Sci. 1997; 52:1429-1458.

(68) Deen NG, Sint Annaland A, Kuipers JAM. Multi-scale modeling of dispersed gas-liquid two-phase flow. Chem Eng Sci. 2004; 59:1853-1861.

(69) Darmana D, Deen NG, Kuipers JAM. Detailed modeling of hydrodynamics, mass transfer and chemical reactions in a bubble column using a discrete bubble model. Chem Eng Sci. 2005; 60:3383-3404.

(70) Darmana D, Deen NG, Kuipers JAM. Parallelization of an Euler-Lagrange model using mixed domain decomposition and a mirror domain technique: Application to dispersed gas-liquid two-phase flow. J Comput Phys. 2006; 220:216-248.

(71) Darmana D, Henket RLB, Deen NG, Kuipers JAM. Detailed modelling of hydrodynamics, mass transfer and chemical reactions in a bubble column using a discrete bubble model: Chemisorption of CO2 into NaOH solution, numerical and experimental study. Chem Eng Sci. 2007; 62:2556-2575.

(72) Sommerfeld M, Bourloutski E, Broder D. Euler/Lagrange calculations of bubbly flows with consideration of bubble coalescence. Canadian Journal of Chemical Engineering. 2003; 81:508-518.

(73) Hjertager BH. Introduction to Turbulent Multi-Fluid Models. Computational Models for Turbulent Multiphase Reacting Flows. Udine: CISM, 2006.

(74) Jakobsen HA, Lindborg H, Dorao CA. Modeling of bubble column reactors: Progress and limitations. Industrial & Engineering Chemistry Research. 2005; 44:5107-5151.

(75) Zehner P. Begasen im Rührbehälter. In: Kraume M. Mischen und Rühren - Grundlagen und moderne Verfahren. Weinheim, Germany: Wiley-VCH, 2003:241-271.

(76) Bombac A, Zun I. Individual impeller flooding in aerated vessel stirred by multiple-Rushton impellers. Chemical Engineering Journal. 2006; 116:85-95.

(77) Bombac A, Zumer M, Zun I. Power consumption in mixing and aerating of shear thinning fluid in a stirred vessel. Chemical and Biochemical Engineering Quarterly. 2007; 21:131-138.

(78) Degaleesan S, Roy S, Kumar SB, Dudukovic MP. Liquid mixing based on convection and turbulent dispersion in bubble columns. Chem Eng Sci. 1996; 51:1967-1976.

(79) Cameron IT, Wang FY, Immanuel CD, Stepanek F. Process systems modelling and applications in granulation: A review. Chem Eng Sci. 2005; 60:3723-3750.

(80) Iveson SM, Litster JD, Hapgood K, Ennis BJ. Nucleation, growth and breakage phenomena in agitated wet granulation processes: a review. Powder Technology. 2001; 117:3-39.

(81) Litster JD, Ennis BJ, Liu LX. The Science and Engineering of Granulation Processes. Dordrecht, NL: Kluwer Academic Publishers, 2004.

(82) van der Hoef MA, Annaland MV, Deen NG, Kuipers JAM. Numerical simulation of dense gas-solid fluidized beds: A multiscale modeling strategy. Annual Review of Fluid Mechanics. 2008; 40:47-70.

(83) Zhu HP, Zhou ZY, Yang RY, Yu AB. Discrete particle simulation of particulate systems: Theoretical developments. Chem Eng Sci. 2007; 62:3378-3396.

(84) Zhu HP, Zhou ZY, Yang RY, Yu AB. Discrete particle simulation of particulate systems: A review of major applications and findings. Chem Eng Sci. 2008; 63:5728-5770.

(85) Lain S, Sommerfeld M. Euler/Lagrange computations of pneumatic conveying in a horizontal channel with different wall roughness. Powder Technology. 2008; 184:76-88.

(86) Cundall PA, Strack ODL. Discrete Numerical-Model for Granular Assemblies. Geotechnique. 1979; 29:47-65.

(87) Kalvoda E. Simulation of Granular Mixing Processes via DEM. Graz University of Technology, Graz, 2008.

(88) Radeke C, Radl S, Khinast JG. Granular Flows - Showing Size Effects by Using High-Performance Simulations on GPUs. Multi-Scale Modelling Symposium. Melbourne, Australia: CSIRO Australia, 2009.

(89) Cleary PW. Industrial particle flow modelling using discrete element method. Engineering Computations. 2009; 26:698-743.

(90) Hilton JE, Mason LR, Cleary PW. Dynamics of gas-solid fluidised beds with non-spherical particle geometry. Chem Eng Sci. 2010; 65:1584-1596.

(91) Radl S, Brandl D, Heimburg H, Khinast JG. Granular Flows - How Size Matters. 5th Minisymposium Verfahrenstechnik. Vienna, Austria: TU Wien, 2009.

(92) Ketterhagen WR, Am Ende MT, Hancock BC. Process Modeling in the Pharmaceutical Industry using the Discrete Element Method. Journal of Pharmaceutical Sciences. 2009; 98:442-470.

(93) Hoomans BPB, Kuipers JAM, Briels WJ, vanSwaaij WPM. Discrete particle simulation of bubble and slug formation in a two-dimensional gas-fluidised bed: A hard-sphere approach. Chem Eng Sci. 1996; 51:99-118.

(94) Deen NG, Annaland MV, Van der Hoef MA, Kuipers JAM. Review of discrete particle modeling of fluidized beds. Chem Eng Sci. 2007; 62:28-44.

(95) Kosinski P, Hoffmann AC. Extension of the hard-sphere particle-wall collision model to account for particle deposition. Physical Review e. 2009; 79.

(96) Andrews MJ, ORourke PJ. The multiphase particle-in-cell (MP-PIC) method for dense particulate flows. International Journal of Multiphase Flow. 1996; 22:379-402.

(97) Snider DM. An incompressible three-dimensional multiphase particle-in-cell model for dense particle flows. Journal of Computational Physics. 2001; 170:523-549.

(98) Snider DM. Three fundamental granular flow experiments and CPFD predictions. Powder Technology. 2007; 176:36-46.

(99) Snider DM, O'Rourke PJ, Andrews MJ. Sediment flow in inclined vessels calculated using a multiphase particle-in-cell model for dense particle flows. International Journal of Multiphase Flow. 1998; 24:1359-1382.

(100) Lain S, Ernst M, Sommerfeld M. Colliding Particle-Pair Velocity Correlation Function in Turbulent Flows. Tampa, U.S.: 7th International Conference on Multiphase Flow, 2010.

(101) Sommerfeld M. Validation of a stochastic Lagrangian modelling approach for inter-particle collisions in homogeneous isotropic turbulence. International Journal of Multiphase Flow. 2001; 27:1829-1858.

(102) Kremer DM, Hancock BC. Process simulation in the pharmaceutical industry: A review of some basic physical models. Journal of Pharmaceutical Sciences. 2006; 95:517-529.

(103) van Wachem B, Sasic S. Derivation, simulation and validation of a cohesive particle flow CFD model. AIChE Journal. 2008; 54:9-19.

(104) Ding J, Gidaspow D. A Bubbling Fluidization Model Using Kinetic-Theory of Granular Flow. AIChE Journal. 1990; 36:523-538.

(105) Wang JW. A Review of Eulerian Simulation of Geldart A Particles in Gas-Fluidized Beds. Industrial & Engineering Chemistry Research. 2009; 48:5567-5577.

(106) Wang JW, Liu YN. EMMS-based Eulerian simulation on the hydrodynamics of a bubbling fluidized bed with FCC particles. Powder Technology. 2010; 197:241-246.

(107) Igci Y, Andrews AT, Sundaresan S, Pannala S, O'Brien T. Filtered two-fluid models for fluidized gas-particle suspensions. AIChE Journal. 2008; 54:1431-1448.

(108) Zaichik LI, Fede P, Simonin O, Alipchenkov VM. Statistical models for predicting the effect of bidisperse particle collisions on particle velocities and stresses in homogeneous anisotropic turbulent flows. International Journal of Multiphase Flow. 2009; 35:868-878.

(109) Kamrin K. Nonlinear elasto-plastic model for dense granular flow. International Journal of Plasticity. 2010; 26:167-188.

(110) Mikami T, Kamiya H, Horio M. Numerical simulation of cohesive powder behavior in a fluidized bed. Chem Eng Sci. 1998; 53:1927-1940.

(111) Cunningham JC, Sinka IC, Zavaliangos A. Analysis of tablet compaction. I. Characterization of mechanical behavior of powder and powder/tooling friction. Journal of Pharmaceutical Sciences. 2004; 93:2022-2039.

(112) Sinka IC, Cunningham JC, Zavaliangos A. The effect of wall friction in the compaction of pharmaceutical tablets with curved faces: a validation study of the Drucker-Prager Cap model. Powder Technology. 2003; 133:33-43.

(113) Frenning G. Analysis of pharmaceutical powder compaction using multiplicative hyperelasto-plastic theory. Powder Technology. 2007; 172:103-112.

(114) Nicot F. Constitutive modelling of a snow cover with a change in scale. European Journal of Mechanics A-Solids. 2003; 22:325-340.

(115) Nicot F. Constitutive modelling of snow as a cohesive-granular material. Granular Matter. 2004; 6:47-60.

(116) Nicot F. From constitutive modelling of a snow cover to the design of flexible protective structures Part II - Some numerical aspects. International Journal of Solids and Structures. 2004; 41:3339-3352.

(117) Nicot F. From constitutive modelling of a snow cover to the design of flexible protective structures Part I - Mechanical modelling. International Journal of Solids and Structures. 2004; 41:3317-3337.

(118) Scholtes L, Chareyre B, Nicot F, Darve F. Micromechanics of Granular Materials with Capillary Effects. International Journal of Engineering Science. 2008; In Press.

(119) Latz A. A new Simulation Ansatz for industrial granular flows from the dilute into the solidified regime. ACHEMA 09, Frankfurt/Main, Germany: 2009.

(120) Stepanek F, Rajniak P. Droplet morphologies on particles with macroscopic surface roughness. Langmuir. 2006; 22:917-923.

(121) Alam P, Toivakka M, Backfolk K, Sirvio P. Impact spreading and absorption of Newtonian droplets on topographically irregular porous materials. Chem Eng Sci. 2007; 62:3142-3158.

(122) Alleborn N, Raszillier H. Spreading and sorption of a droplet on a porous substrate. Chem Eng Sci. 2004; 59:2071-2088.

(123) Stepanek F, Ansari MA. Computer simulation of granule microstructure formation. Chem Eng Sci. 2005; 60:4019-4029.

(124) Ansari MA, Stepanek F. Design of granule structure: Computational methods and experimental realization. AIChE Journal. 2006; 52:3762-3774.

(125) Grof Z, Lawrence CJ, Stepanek F. Computer simulation of evolving capillary bridges in granular media. Granular Matter. 2008; 10:93-103.

(126) Grof Z, Lawrence CJ, Stepanek F. The strength of liquid bridges in random granular materials. Journal of Colloid and Interface Science. 2008; 319:182-192.

(127) Pirker S, Kahrimanovic D, Aichinger G. Modeling mass loading effects in industrial cyclones by a combined Eulerian-Lagrangian approach. Acta Mechanica. 2009; 204:203-216.

(128) Knight P. Challenges in granulation technology. Powder Technology. 2004; 140:156-162.

(129) Reynolds GK, Fu JS, Cheong YS, Hounslow M, Salman AD. Breakage in granulation: A review. Chem Eng Sci. 2005; 60:3969-3992.

(130) Fu J, Adams MJ, Reynolds GK, Salman AD, Hounslow MJ. Impact deformation and rebound of wet granules. Powder Technology. 2004; 140:248-257.

(131) Gantt JA, Gatzke EP. High-shear granulation modeling using a discrete element simulation approach. Powder Technology. 2005; 156:195-212.

(132) Gantt JA, Cameron IT, Litster JD, Gatzke EP. Determination of coalescence kernels for high-shear granulation using DEM simulations. Powder Technology. 2006; 170:53-63.

"Computation has made theory more relevant."

(Andrea Prosperetti and Gretar Tryggvason, 2007)

4

Direct Numerical Simulation of Reactive Mass Transfer - Catalytic Hydrogenations[*]

Catalytic hydrogenations of, e.g., nitroarenes are reactions of significant importance for the pharmaceutical, agro-chemical and dye-manufacturing industries. In the hydrogenation of nitroarenes, the reaction proceeds through a hydroxylamine intermediate, which is toxic, carcinogenic and thermally unstable. While many studies have been conducted, attempting to alter the catalyst to minimize the accumulation of hydroxylamine, the influence of the hydrodynamics on the product and intermediate formation has so far not been investigated. Due to the fast rate of reaction most of the hydrogen dissolved from the bubbles will be consumed in close proximity of the bubble surface. In such cases local mixing in the bubble wake impacts the reaction network far surpassing that of the reactor scale transport.

For the purposes of studying the local hydrodynamics in bubbly flows, direct numerical simulations (DNS) were performed of freely deformable gas bubbles rising in a liquid phase. It was found that the different bubble wake types observed at different conditions will result in different rates of hydroxylamine formation and selectivity. These differences will persist even in the case of clusters consisting of multiple bubbles. Also, simulation results have been compared with a solution obtained from film theory.

4.1 Introduction

The catalytic hydrogenation of nitroarenes, having long displaced the classic Bechamp reduction method, is a process of great importance for many branches of the chemical industry. Being the main mechanism for the production of arylamines, such as aniline, diphenylamine and phenylene-diamines, it is integral for the dye-manufacturing and agrochemical industries. In addition, it is an important step in the synthesis of key pharmaceutical intermediates.[1] Due to the ease of hydrogenation of the nitro group, different catalysts can be used, such as supported copper, cobalt, platinum, palladium and nickel, and often the choice of catalyst can be made to satisfy mechanical/economical considerations relating to particular applications.
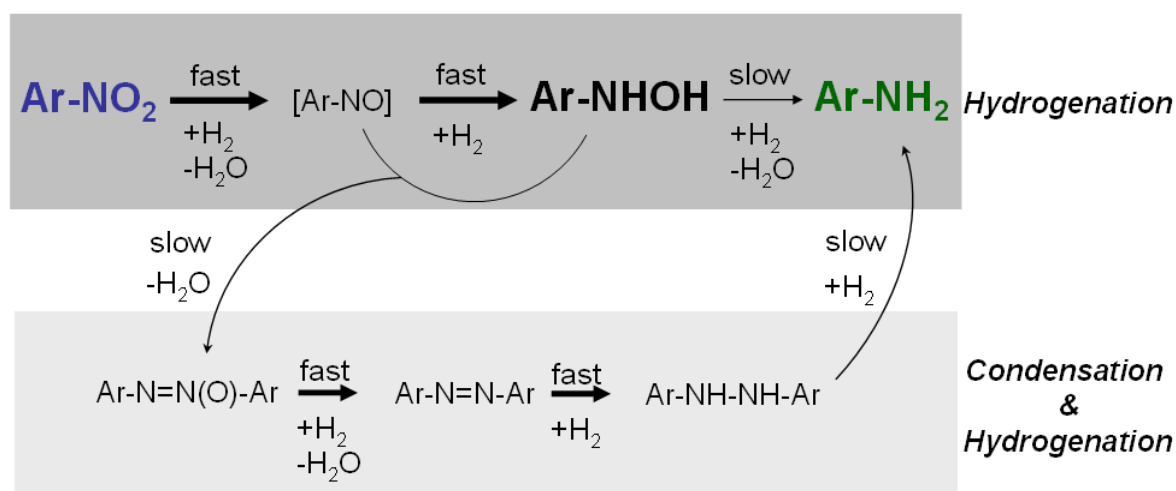
Scheme 4.1: Reaction network of nitroarene hydrogenation.

Scheme 4.1 shows a typical hydrogenation of a nitroarene, as it is carried out in industry. The reaction follows predominantly the monomeric pathway, in which the nitro group is hydrogenated to a nitroso group. The aryl nitroso compound is then further hydrogenated to a hydroxylamine (Ar-NHOH) and finally to an arylamine (Ar-NH$_2$). The rate at which the first two reactions proceed is so high that the nitroso intermediate is usually undetectable. In comparison, the final hydrogenation to the arylamine is relatively slow and, depending on the operating conditions, the accumulation of hydroxylamine can vary considerably. Such accumulation is usually undesirable for several reasons. Hydroxylamines are thermally unstable and can disproportionate exothermally, causing explosions that have repeatedly led to loss of life in the past.[2,3] They are also known to be carcinogenic and as such present a health hazard in high concentrations. Additionally, the accumulation of hydroxylamines could be detrimental

to product purity due to condensation with the nitroso compounds, producing azo and azoxy byproducts (shown in the bottom part of Scheme 1). These are usually yellow in color, which makes them particularly undesirable in pharmaceutical products and in the dye industry where arylamines are used for the production of whiteners.

Different techniques are implemented to reduce the concentration of hydroxylamines in industrial applications, from changing the pH of the medium to the promotion of the catalysts with metal ions (co-catalysts) to speed-up the aryl hydroxylamine disproportionation to the nitroso and amine products (top part of Scheme 1).[4-6] Another way of controlling the concentration of an intermediate, such as hydroxylamine, in a consecutive reaction would be to regulate the extent of mixing in the system.[7] It is well known that high mixing rates will promote the accumulation of intermediates in consecutive reactions, which is why stirred reactors are often considered undesirable for catalytic hydrogenations. Bubble columns and packed bubble columns are often utilized as being closest in mixing properties to the ideal case of the plug-flow reactor.

While the reactor-scale mixing characteristics in bubble columns are very important, for fast reactions (such as some catalyzed hydrogenations) a large portion of the dissolved hydrogen will react in the close vicinity of the individual bubbles. In such cases, the concentration profiles in the boundary layer and the local mixing in the bubble's wake will influence the outcome of the reaction network. Depending on the operating conditions, bubble properties (as defined by several dimensionless numbers) can change significantly along with the dynamics of the flow in their wakes. Since minimizing the overall accumulation of intermediates, such as hydroxylamine, is critical, knowledge of the hydrodynamics in the vicinity of bubbles can prove an invaluable tool. In this work we have provided a comparison of predictions made by film theory and numerical simulations of the motion of freely deformable bubbles and bubble swarms in a liquid medium. The mass transfer of hydrogen and its consumption by a liquid-phase hydrogenation reaction is also included in the simulations. The results from the different cases considered show that the accumulation of intermediates can be controlled to an extent by changing the hydrodynamics of the system.

4.2 Goals

Bubble column reactors are often chosen for carrying out catalytic hydrogenations, due to their beneficial mixing characteristics and ease of operation.[7] Since control of the mixing in

the chemical reactor can minimize the production of intermediates in consecutive reactions, knowledge of the transport on all scales pertinent to the process can prove invaluable. The reactor-scale hydrodynamics and their influence on the mass transport and chemical reactions have been studied extensively.[8-13] Furthermore, pioneering work on mass transfer with and without chemical reactions has been conducted in the 1970's using film and penetration/surface renewal theory.[14-18] The aim of these studies was to provide a mathematical model for the mass transfer enhancement observed in absorption and extraction processes. In parallel, there were efforts to predict the outcome of a chemical reaction network based on these theories.[19-21]

In contrast to the extensive research on reactive mass transfer and the macro-scale hydrodynamics in reactors, the local mixing in the wake of individual bubbles and in bubble swarms is not as well understood. This is due to the complex interaction of mass transfer and chemical reactions occurring in the boundary layer and in the wake of bubbles. While for slow reactions the reactor hydrodynamics determine the reaction outcome, for very fast reactions the effects in the boundary layer are critical. However, for the intermediate case, the mixing in the bubble wake determines the relative reaction rates, a phenomenon much less investigated.

In the case of our hydrogenation network, the reactions are in a regime where localized bubble mixing is highly important, as a significant portion of the dissolved hydrogen will be consumed close to the bubble surface, i.e., in the boundary layer and in the wake. Since these reaction steps occur in the vicinity of the bubble, each individual bubble (or a bubble cluster) can be thought of as a separate micro-reactor, consisting of the boundary layer and the wake, where the bubble acts as a reservoir to supply fresh gaseous reactant. In order to gauge the influence of continuous-phase transport on the product distribution, the velocity and concentration fields around the bubbles and especially in the bubble wake need to be resolved. This can be done either by using a simplification of the fluid dynamics and the reactive transport in the bubble's proximity (e.g., by applying film or penetration theory) or by performing exact fluid dynamical calculations of the flow, mass transfer and reaction. While the first approach allows a time-efficient prediction of reaction rates, the second method requires significant computational resources and know-how. As pointed out above, theories based on the film or penetration theory can predict only effects in the boundary layer. If the mixing in the wake is of importance (for which macro-scale models are too coarse), only detailed computations of individual reacting bubbles or bubble clusters can provide solutions

with sufficient accuracy. In this work we will compare results for both cases and show, how these results can be used to control the reactions for this complex reaction network. The goal is enable engineers to predict the impact of the flow hydrodynamics on the product distribution of the reaction for relatively fast reaction networks.

4.3 Background

Attempts to experimentally investigate the (reactive) flows around individual bubbles are usually based on Particle Image Velocimetry (PIV) or Laser Doppler Anemometry (LDA) techniques.[22-24] Recently, Bork and coworkers[25,26] successfully applied image analysis and fluorescence methods to study the flow dynamics and mass transfer from single bubbles. Despite these recent successes, the main limitation of optical methods still applies - they cannot be applied in opaque media such as catalytic slurries. Additionally, in high gas hold-up systems, the dynamics of the multiphase flow involving numerous bubbles rising in clusters and swarms differ dramatically from those observed in single-bubble cases. In such systems, the optical interference from the large number of bubbles renders optical techniques largely inapplicable.

4.3.1 Numerical Approach

Numerical simulations remain as the only viable alternative for the study of the multiphase hydrodynamics in bubbly flows, with several different techniques being applied, with varying degrees of success. The main challenge in simulating reactive bubbly flows is the proper resolution and tracking of the gas-liquid interface and the mass transfer through the interface. "Marker And Cell" (MAC) and "Volume Of Fluid" (VOF) methods perform this task by identifying the two phases directly on a uniform computational grid by using marker variables. Despite the difficulties associated with the accurate description of the interface - somewhat alleviated by the use of level-set methods[27] - these methods are widely used.[28-31] Lagrangian methods in which the grid follows the fluid, have provided useful insight into the mechanisms of the deformation of bubbles, but are usually limited to single bubbles.[32] In front tracking methods, a separate, deformable grid is used to track the interface.[33,34] In this work, a hybrid front-tracking/front-capturing method developed by Tryggvason et al.[35] is used to study the hydrodynamics of bubbly flows.

The influence of the hydrodynamics on the gas-liquid mass transfer has also been the subject of considerable scientific interest. Aris[36] studied the gas-liquid mass transfer during the steady

ascending motion of small spherical bubbles. Legendre and Magnaudet[37] investigated the mass and heat transfer from a spherical bubble in accelerated flows. These studies were extended by the group of Khinast[38,39] to bubble clusters including chemical reactions. Recently, Bothe et al.[40] performed three-dimensional VOF-based numerical simulations of the mass transfer from deformable bubbles and bubble chains. Koynov et al.[41] successfully used a front-tracking approach to examine the mass transfer from multiple simultaneously rising bubbles. Radl et al.[42] extended this approach to non-Newtonian fluids. An extension to fully 3D simulations has also been done by Darmana.[43] However, due to the current limitations in grid size and computation time, these 3D simulations have been conducted at a very low Schmidt number (Sc = 1), which is not encountered in liquids.

Furthermore, extensive literature is available based on film and penetration/surface renewal theory including chemical reactions.[14-18,44-47] The main limitation of these studies are the assumption of a perfectly mixed bulk phase and a homogenous boundary layer. Inhomogeneities outside the boundary layer are neglected, i.e., the mixing characteristics in the bubble's wake and bubble-bubble interactions in bubble clusters cannot be accounted for. This mixing in the wake is still relatively poorly understood and, as a consequence, rarely considered in the design and operation of industrial processes. In this work, numerical simulations have been performed of the liquid-phase catalytic hydrogenation of a nitroarene with freely moving, deformable bubbles as the source of hydrogen. These computations have been compared to film-theory predictions of the selectivity and the reaction rate.

4.3.2 Characterization of the Reaction Network

The reaction rates of the reactions are assumed to be

$$A(l) + 2H_2(l) = R(l) \qquad r_1 = k_1 \cdot c_{H_2} \tag{4.1}$$

$$R(l) + H_2(l) = S(l) \qquad r_2 = k_2 \cdot c_{H_2} \cdot c_R, \tag{4.2}$$

where A denotes the nitroarene, R the hydroxylamine, $H_2(l)$ the dissolved hydrogen, S the desired product aniline and k_1 and k_2 are the rate coefficients. Since the nitroso intermediate in the monomeric hydrogenation pathway is virtually undetectable in most cases, we have not considered this step and instead model the hydrogenation of the nitroarene to the corresponding hydroxylamine as a single reaction with an effective reaction rate. The high reaction rates of these reactions and the complexity of the processes associated with heterogeneous catalysis make the determination of the reaction kinetics very difficult. For the

hydroxylamine forming step, both first and zero-order apparent kinetics have been observed. These are determined by the chemistry on the catalyst surface rather than the transport processes and will, therefore not be influenced by the continuous phase transport, which is the focus of our study. In our model, the reaction has been treated as zero-order with respect to the starting material (this is a reasonable approximation, especially in systems, in which the amount of liquid-phase reactant is large). The second reaction step, in which the hydroxylamine is further hydrogenated to aniline, is treated as first-order with respect to the intermediate. The relative rate of the two reactions is

$$\frac{r_2}{r_1} = \frac{k_2}{k_1} c_R .$$ (4.3)

Thus, the desired consecutive reaction is favored in regions of high concentration of the intermediate.

The reaction rates have been chosen such that the ratio of $Da_1 / Da_2 = k_1 /(k_2 \cdot c_{A,0})$ is 40, i.e., the second reaction is slow compared to the first hydrogenation step. Here $c_{A,0}$ is the initial concentration of liquid phase reactant. Da_1 and Da_2 are the Damköhler numbers of the first and second reaction that will be introduced in the next chapter.

To characterize the outcome of the reaction network, we define a differential selectivity σ' towards the final product aniline

$$\sigma' = \frac{r_2}{r_1} .$$ (4.4)

The domain-averaged differential selectivity σ'_{av} was calculated directly by evaluating the integral change of species R and S in the domain.

Beside the chemical reaction parameters, appropriate boundary conditions for the mass transfer calculation have to be assumed. For that purpose the ratio between the concentration of nitroarene and the saturation concentration of hydrogen was chosen as 4:1. This is representative for an industrial applications operating at 20 bar and 160 mol/m³ of nitroarene in methanol (the solubility of hydrogen in methanol is approximately 2 mol/m³·bar following Radhakrishnan et al.[48]). Furthermore, mass transfer of liquid-phase components into the gas bubbles has been set to zero. Thus, a zero gradient boundary condition at the gas-liquid interface has been imposed for these components.

4.3.3 Dimensionless Numbers

In the present work we indented to present all results in the framework of dimensionless quantities. This has the benefit that the results are not only applicable to the hydrogenation of nitroarenes, but also to similar reaction networks. Therefore, dimensionless parameters relevant for the hydrodynamics, as well as parameters related to the chemical reaction have been defined.

The well established Morton number $Mo = g \cdot \mu_l^4 / (\rho_l \cdot \sigma^3)$ and the Eötvös number $Eo = g \cdot \rho_l \cdot d_b^2 / \sigma$ characterize the shape of the bubble, as well as flow properties.[49] They are the only hydrodynamic input parameter for the simulation. The Reynolds number $Re = \rho_l \cdot d_b \cdot U_t / \mu_l$ is a result of our simulation. Here U_t is the terminal rise velocity of the bubble and d_b is the diameter of the bubble.

For the chemical species we have used the initial concentration of liquid phase reactant $c_{A,0}$ as the reference concentration. The term

$$r_{ref} = \frac{U_t}{d_b} \cdot c_{A,0}$$
(4.5)

has been used to make the reaction rates dimensionless. Applied to the reaction network we obtain the following expressions for the dimensionless reaction rates

$$\bar{r}_1 = Da_1 \cdot \bar{c}_{H_2}$$
(4.6)

$$\bar{r}_2 = Da_2 \cdot \bar{c}_{H_2} \cdot \bar{c}_R ,$$
(4.7)

where

$$Da_1 = \frac{d_b k_1}{U_t} \text{ and } Da_2 = \frac{d_b k_2 c_{A,0}}{U_t}$$
(4.8)

are the Damköhler numbers. The overbars in above equations denote dimensionless quantities. Another dimensionless quantity used in this work is the Hatta number

$$Ha = \sqrt{k_1 \cdot D} / k_L .$$
(4.9)

where D is the diffusion coefficient and k_L is the mass transfer coefficient without chemical reaction. The Hatta number is a measure for the relative magnitude of reaction and mass transfer. High Hatta numbers signify mass-transfer limited reactions. Finally we have used the

Schmidt number $Sc = \mu_l / (\rho_l \cdot D)$ to characterize the relative rates of mass and momentum transfer in the liquid phase. By multiplying the Reynolds and Schmidt number the Pèclet number Pe can be obtained.

4.4 Film Theory for a Parallel Consecutive Reaction Network

The film-theory species conservation equations are a set of ordinary differential equations (ODEs). For an arbitrary parallel consecutive reaction network with general stoichiometric and kinetic order these ODEs can be written as

$$0 = D_i \cdot \frac{\partial^2 c_i}{\partial x^2} + \sum_j \nu_{ij} r_j .$$ (4.10)

This equation can be made dimensionless by using δ (the film thickness) as reference length and Eqn. 4.5 as a reference for the chemical reaction. This yields

$$0 = \frac{\partial^2 \overline{c}_i}{\partial \overline{x}^2} + \frac{Ha^2}{Da_1} \sum_j \nu_{ij} \overline{r}_j ,$$ (4.11)

which is equal to

$$0 = \frac{\partial^2 \overline{c}_i}{\partial \overline{x}^2} + Ha^2 \sum_j \left[\frac{Da_j}{Da_1} \cdot \nu_{ij} \cdot \prod_k \left(\overline{c}_k^{n_k} \right) \right] .$$ (4.12)

Here i is the index for the chemical species A, H_2, R and S, and j is the reaction index corresponding to the reaction network in Eqs. 4.1 and 4.2. n_k is the order of the reaction with respect to reactant k. The boundary conditions at the gas-liquid interface ($\overline{x} = 0$ is the interface) are

$$\overline{c}_{H_2} \big|_{\overline{x}=0} = \overline{c}_{H_2,i}$$ (4.13)

$$\frac{\partial \overline{c}_A}{\partial \overline{x}} \bigg|_{\overline{x}=0} = \frac{\partial \overline{c}_R}{\partial \overline{x}} \bigg|_{\overline{x}=0} = \frac{\partial \overline{c}_S}{\partial \overline{x}} \bigg|_{\overline{x}=0} = 0 .$$ (4.14)

The boundary conditions at the film-bulk interface are:

$$\overline{c}_{H_2} \big|_{\overline{x}=1} = \overline{c}_{H_2,0}$$ (4.15)

$$\overline{c}_A \big|_{\overline{x}=1} = 1$$ (4.16)

$$\left.\overline{c}_R\right|_{\overline{x}=1} = \overline{c}_{R,0} \tag{4.17}$$

$$\left.\overline{c}_S\right|_{\overline{x}=1} = 0 \tag{4.18}$$

All equations have been made dimensionless with the initial concentration of the liquid phase reactant $c_{A,0}$. Equal diffusivities for all species have been assumed. The set of boundary value problems needs to be solved numerically to obtain the concentration profiles and the differential selectivity. From Eqn. 4.12 it is clear that the only parameters that affect the concentration profiles (and hence the selectivity) are the Hatta number, the ratio between the Damköhler numbers and the stoichiometry, as well as the dimensionless concentrations at the interface and in the bulk. The Reynolds and Schmidt number affect the solution via a change in the Hatta number of the system.

4.5 Deformable Bubble Model and Numerical Method

A hybrid front-tracking/front-capturing method[35] coupled with chemical species conservation equations was used to simulate the hydrodynamics and species transport of the flows in the vicinity of freely deformable bubbles and bubble swarms in a liquid medium. For different values of these numbers, bubbles can have various shapes, as well as exhibit different types of wake flows. From the computational results, the bubble Reynolds number $\mathrm{Re} = d_b U_t \rho_l / \mu_l$ was estimated. As the simulations have been performed in 2D, the hold-up was calculated from the cross sectional area of the N bubbles having the diameter d_b and the total reactor area A_{tot}, i.e.,

$$\varepsilon = \frac{N \cdot d_b^2 \cdot \pi}{4 \cdot A_{tot}} . \tag{4.19}$$

For a detailed description of the method refer to Koynov et al.[50] and Radl et al.[42] In this method, the Navier-Stokes is integrated on a regular, fixed, two-dimensional grid. It is a single-fluid method, i.e., a single set of conservation equations is solved for both phases. An immersed boundary type formulation is used to provide the smoothing of the delta functions describing the jump in variable gradients at the bubble interface onto the computational grid. The actual interface is tracked using a separate, one-dimensional moving deformable grid. The model equations, describing the system, can be written as:

$$\frac{\partial \rho \mathbf{u}}{\partial t} + \nabla \cdot \rho \mathbf{u}\mathbf{u} = -\nabla P + \rho \mathbf{f} + \nabla \cdot \mu \left(\nabla \mathbf{u} + \nabla^T \mathbf{u}\right) + \oint \sigma \kappa' \mathbf{n}' \delta^2 (\mathbf{x} - \mathbf{x}') ds' \tag{4.20}$$

and

$$\frac{\partial c_i}{\partial t} = -\mathbf{u} \cdot \nabla c_i + D_i \Delta c_i + \sum_j \nu_{ij} r_j \,. \tag{4.21}$$

The equations are satisfied for the entire computational domain, regardless of discontinuities in material properties. In Eqn. 4.20, f is a body force, σ is the surface tension, κ' is the curvature of the interface, and δ^2 is a two-dimensional delta-function, equal to the product of δ(x-x') and δ(y-y'). In the species-balance equation (Eqn. 4.21) c_i is the concentration of species i dissolved in the liquid phase, D_i is the diffusion coefficient, r_j is the reaction rate of reaction j and ν_{ij} are stoichiometric coefficients. For dissolved hydrogen ($c_i = c_{H2}$),

$$c_{H_2}(x,y,t) = c_{l,H_2} H(x,y,t) + c_{g,H_2}[1 - H(x,y,t)], \tag{4.22}$$

where $c_{l,H2}$ is the concentration in the liquid phase, and $c_{g,H2}$ is its concentration in the gas phase. In Eqn. 4.22, H is a Heaviside step function, describing the discontinuities in variable values, which occur at the bubble surface. Inside the bubble H=0, and H equals 1 everywhere else. The concentration of hydrogen in the bubble, i.e., $c_{g,H2}$, is uniformly constant and is equal to the hydrogen saturation concentration for the liquid phase. This is a reasonable assumption for the cases, where the characteristic residence time of the bubble is short compared to the mass-transfer time scale.

The computational domain used in our simulations has a rectangular shape and dimensions of $6 \cdot d_b \times 18 \cdot d_b$ (for single bubble calculations) and $12 \cdot d_b \times 36 \cdot d_b$ (for bubble cluster calculations), d_b being the average bubble diameter. The hydrodynamic computations were carried out on a 200×600 grid, whereas the mass transport calculation grid was chosen to accurately resolve the boundary layer (up to 2,000×6,000 grid points). Simulations were performed on a 46-node dual-core cluster. The code was run in parallel using on average 4 CPUs per job. Computation time was between 30 (low-Reynolds number, single-bubble simulation) and 450 hours (high Reynolds number, bubble swarm simulation) for each simulation case.

Viscous terms have been considered implicitly, whereas buoyancy, surface tension and inertia have been added explicitly to the momentum equation.[42] The fluid velocities were interpolated onto the fine grid using a high-order, continuity-preserving scheme.[51] A semi-Lagrangian advection scheme together with an ADI algorithm was used to solve the reactive species conservation equation.[42] At the gas-liquid interphase a Dirichlet boundary condition for the

gas-phase reactant was imposed, whereas for the liquid-phase reactant and the products a Neumann boundary condition was used. Thus, no mass transfer of liquid-phase reactants into the bubble was considered.

Periodic boundary conditions were implemented at the top, bottom and both walls of the domain, ensuring that a fluid particle exiting the domain from one side will reenter from the other with the same velocity. The top and bottom periodic boundary conditions serve to approximate a batch system, in which bubbles are continuously sparged through the liquid phase. Additionally, these boundary conditions lead to a situation, in which bubbles move in their own wake flows - which mimics closely real gas-liquid flows where bubbles' motion is always influenced by the wakes of the bubbles rising above them. The range of the dimensionless numbers used in the simulation is given in Table 4.1.

Dimensionless number	*Value*
Re_b	5 – 58
Sc_i	10 - 100
Pe	50 - 3500
Mo	$7.2 \cdot 10^{-6}$-$2.3 \cdot 10^{-3}$
Eo	0.3-2.81
Ha	0.408 – 1.73
Da_1	0.03-0.08
Da_2	0.00075-0.002

Table 4.1: Range of simulation input parameters.

4.6 Results and Discussion

4.6.1 Film Theory Predictions

The diffusion-reaction problem defined by Eqs. 4.12 to 4.18 can be solved numerically with MATLAB®[52] to obtain the concentration profiles in the hypothetical liquid film. A verification of the numerical algorithm used is provided in Appendix A.

Figure 4.1 shows a typical concentration distribution of the gaseous reactant and the products computed numerically from film theory. For illustrative purposes we have chosen the kinetic parameters such that the ratio of the Damköhler numbers is unity in Figure 4.1. The film layer

thickness has been chosen to obtain a Hatta number of 5, i.e., comparably fast rates of reaction and mass transfer.
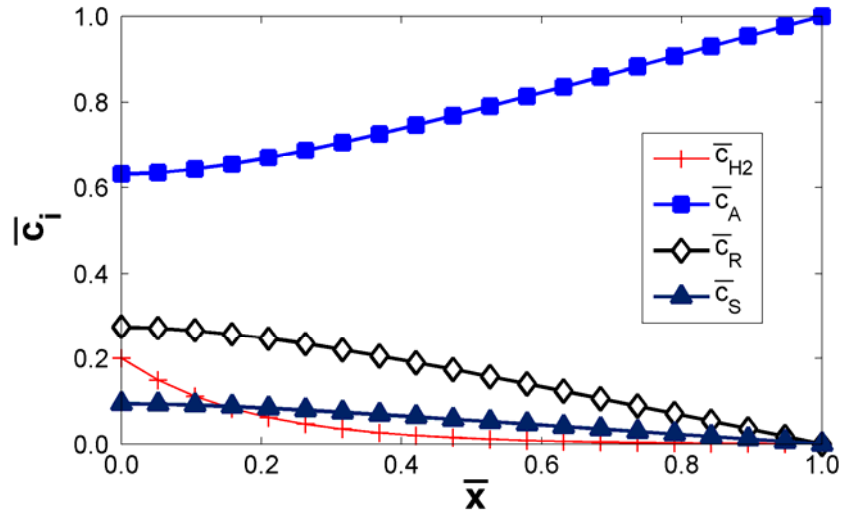
Figure 4.1: Dimensionless concentration profiles (Film theory numerical solution, Ha = 5, Da$_1$ / Da$_2$ = 1, $\bar{c}_{H2,i}$ = 0.2, $\bar{c}_{H2,0}$ = $\bar{c}_{R,0}$ = $\bar{c}_{S,0}$ = 0).
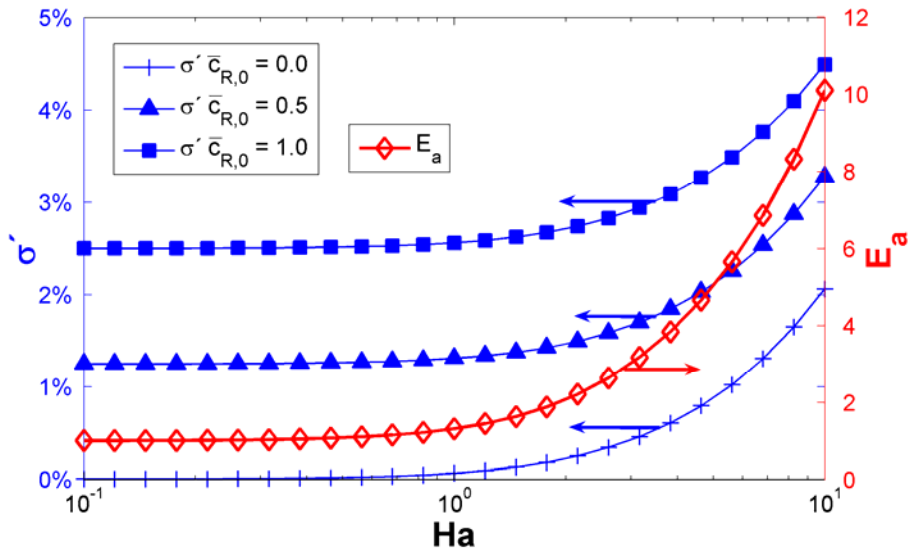
Figure 4.2: Enhancement factors and differential selectivities (numerical solution, Da$_1$/Da$_2$ = 40, $\bar{c}_{H2,i}$ = 0.2, $\bar{c}_{H2,0}$ = $\bar{c}_{S,0}$ = 0).

Figure 4.2 illustrates the resulting enhancement factors E$_a$ and the differential selectivity as a function of the Hatta number for the given reaction network. The influence of the bulk phase has been characterized by three different concentrations of the intermediate product R (lines with squares, triangles and crosses). The enhancement factor is defined as

$$E_a = \frac{\dot{N}_{H_2}}{k_L \cdot c_{H_2,i}} = \frac{-D_{H_2} \cdot \left.\dfrac{\partial c_{H_2}}{\partial x}\right|_{x=0}}{k_L \cdot c_{H_2,i}} = \frac{\left.\dfrac{\partial \overline{c}_{H_2}}{\partial \overline{x}}\right|_{\overline{x}=0}}{\overline{c}_{H_2,i}} \quad , \tag{4.23}$$

whereas the selectivity has been calculated using Eqn. 4.4.

In Eqn. 4.23 $\dot{N}_{H_2}$ denotes the molar flux of hydrogen into the reaction zone. It can be seen from Figure 4.2 that the selectivity towards the final product aniline increases with the Hatta number. In this case the first reaction is fast and more intermediate is accumulated in the film. This leads to an enhanced second reaction and an increasing selectivity. The same is true, if the bulk concentration of the intermediate is increased, as can be seen from the results.

In contrast to the selectivity, the enhancement factor only depends on the Hatta number, since for the reaction network chosen, the second reaction, and hence $\overline{c}_{R,0}$, has only a negligible effect on the mass transfer.

In order to compare predictions based on film theory with fully resolved numerical computations of the reactive flow around bubbles, several different cases were considered. First single bubbles were considered, followed by results for bubble clusters of up to 50 bubbles.

4.6.2 Single Bubbles

For single bubble studies parameters were chosen, which result in flows representative of the several different types of wake behavior observed in bubble reactors. The most commonly observed wakes are captured in Figure 4.3, which shows the hydroxylamine concentration in the vicinity of single bubbles. The time has been made dimensionless with the reference bubble rise time calculated from the terminal rise velocity and the bubble diameter. In the case of a low Reynolds number (Re = 5), the wake of the bubble is steady and closed. Due to the low liquid-phase velocities immediately behind the bubble, the transport of dissolved hydrogen is relatively slow, leading to its accumulation in the wake. This hydrogen will quickly react with the nitroarene to form hydroxylamine. This case is shown in Figure 4.3a. The rising bubble is captured at a time when it has already passed the domain once and has reentered it again.

At higher Reynolds numbers (e.g., larger bubbles), as the relative velocity of the liquid flowing past the bubble increases, the wake develops two symmetric recirculation cells attached to the

bottom of the bubble. Since the boundaries of these recirculation cells are closed streamlines, their interior is separated from the bulk of the liquid with respect to convective transport. The only mechanism available for transport from the recirculation cells is molecular diffusion. Thus, accumulation of dissolved hydrogen and hydroxylamine will occur in these zones, as shown in Figure 4.3b.
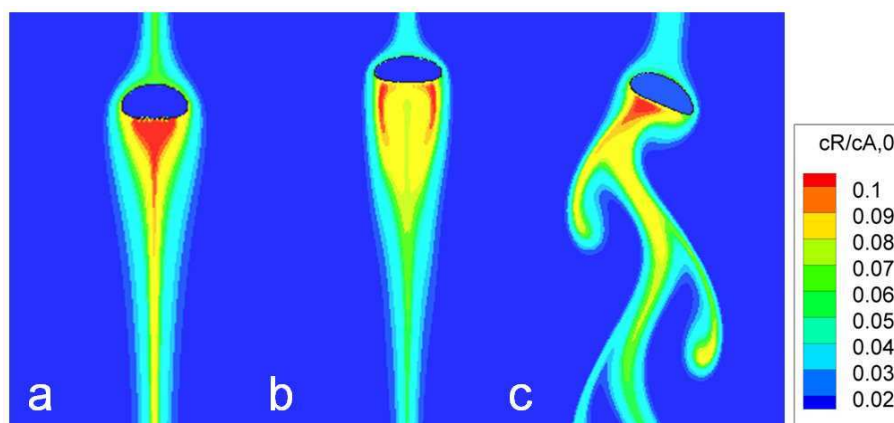
Figure 4.3: Dimensionless concentration of hydroxylamine around three different bubbles. a) Re=5, t*=50; b) Re=18, t*=50; c) Re=52, t*=50.

Further increases of the Reynolds number leads to flow instabilities that will cause one of the cells to grow faster than the other, breaking the symmetry of the wake. The growing zone will eventually pinch and separate in two parts – a smaller recirculation cell, still attached to the bubble and a free vortex, which will be advected downstream. At this point the other recirculation cell, now larger than the newly formed one, will start to grow and will, in turn, repeat the same process, leading to the shedding of another free vortex on the other side of the bubble wake. This periodic shedding of vortices on alternating sides of the bubble centerline will continue, leading to the formation of a von Karman "vortex street" behind the bubble as shown in Figure 4.3c for Re = 52. If the bubble were to rise in an infinite quiescent liquid, it would maintain a regular wavy trajectory. However, since, similarly to the bubbles discussed before, it reenters its own wake the bubble will invariably come into contact with the vortical structures that it contains. Interaction with these structures will cause the bubble to deviate from its regular trajectory, leading to meandering path with its wake expanding to cover the entire width of the computational domain.

In order to understand the influence of these different wakes, one must consider the effects of mixing. In the case of our reaction, the first step leading to the formation of hydroxylamine is faster than the subsequent hydrogenation to an amine. Thus, it will consume available

hydrogen preferentially. Figure 4.4 shows the stream-traces associated with the liquid-phase velocity fields around single rising bubbles. In the low Reynolds number case, the stream-traces are parallel to each other resulting in very little mixing and low mass transfer rates. In such a system, any dissolved hydrogen and hydroxylamine will tend to stay confined in the bubble wake. This will lead to a higher selectivity (compare to Eqn. 4.3).
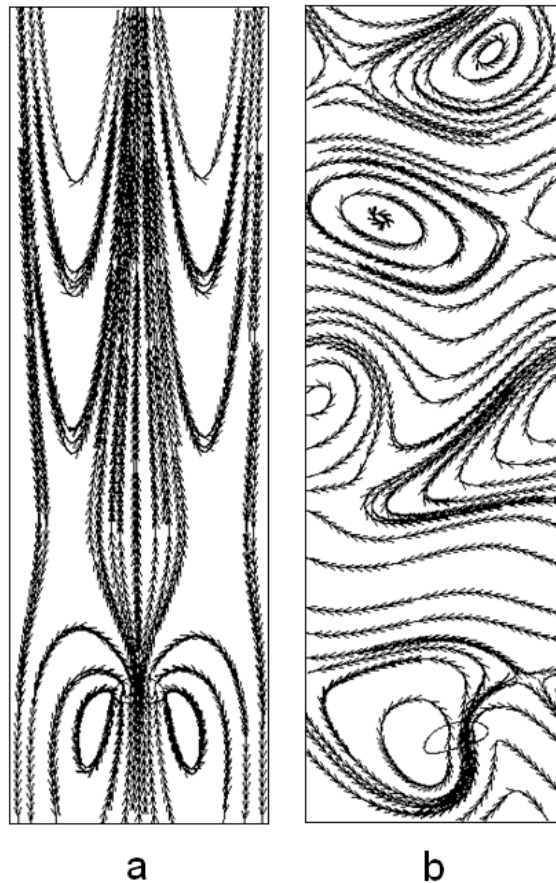
Figure 4.4: Stream-traces associated with the flow fields around rising bubbles. a) Re=5, t*=75; b) Re=52, t*=75.

Conversely, in the high-Reynolds-number case, the complex flow fields, characterized by large vortical structures will quickly disperse the dissolved hydrogen throughout the entire domain. This leads to a more homogenous distribution of all involved species and to a lower concentration of hydroxylamine next to the gas-liquid interface. Hence the second reaction step is suppressed (see Eqn. 4.2), preventing a consumption of hydroxylamine intermediate.

Clearly, the amount of mass transfer varies, as shown in Figure 4.5, which quantifies the influence of the Reynolds number on the accumulation of hydroxylamine intermediate. In this figure the Morton, the Schmidt number, the specific surface area *a*, and the kinetic parameters

have been kept constant, whereas the Eötvös number was varied. This is equal to a change in bubble size. The resulting Hatta number was between 0.483 (Re = 5) and 0.417 (Re = 38.9). The plot shows the average concentration of hydroxylamine in the domain for the case of three different Reynolds numbers. The Reynolds number is based on the computed rise velocity of the bubble. It can be seen that the overall accumulation of hydroxylamine increases with the Reynolds due to the higher mass transfer rate and the improved mixing. However, in contrast to the intuitive conclusion that the instantaneous selectivity should be higher with increasing Reynolds number according to Eqn. 4.3, the opposite is true as demonstrated in the next paragraph.
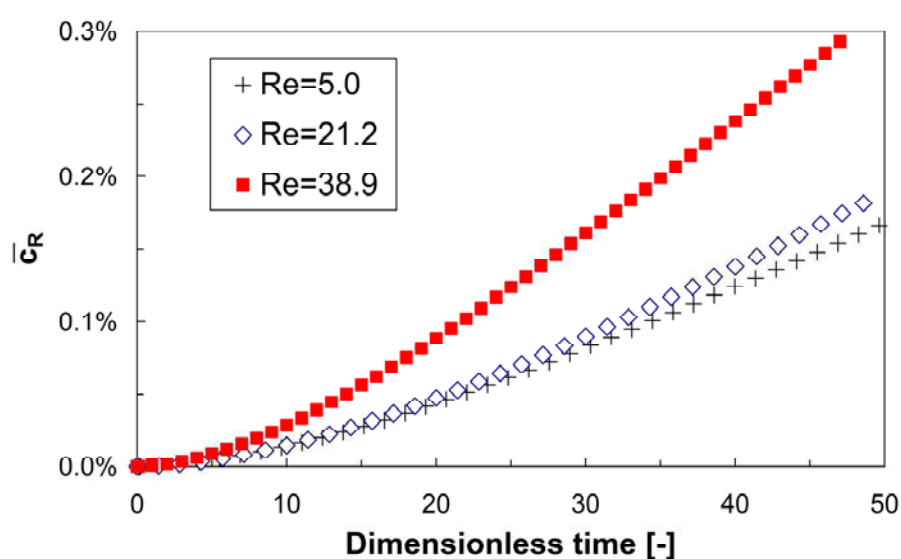
Figure 4.5: Dimensionless concentration of the hydroxylamine intermediate as a function of dimensionless time. For Sc = 50, Mo = 7.2·10^{-6}, Da$_1$/Da$_2$ = 40, Ha = 0.483 - 0.417, a = const).

The effect of reduced selectivity with increasing Reynolds number is illustrated in Figure 4.6. Here we show the locally averaged differential selectivity σ'_{av} as a function of the dimensionless time. The simulations showed that the Hatta numbers are around 0.5 (e.g., weak mass transfer enhancement, see Fig. 4.2). The Eötvös number, the Schmidt number, as well as the specific bubble surface area have been kept constant. Only the Morton number has been varied to mimic a changing liquid viscosity. Clearly, the selectivity increases with decreasing Reynolds number. The reason is that the concentration of R in the close vicinity of the bubble (where the reaction occurs) is significantly higher for smaller Reynolds numbers, leading to increased selectivity. Thus, the selectivity is higher for small Re, although the domain-averaged concentration of R is higher in the case of large Re. Thus, these computations illustrate nicely the need for a detailed understanding and analysis of micro-effects close to the bubble surface.

The stepwise increase in the selectivity for Re = 5.9 in Figure 4.6 is caused by the bubble encountering its own wake, where the hydroxylamine intermediate concentration is high, thus promoting the second reaction.
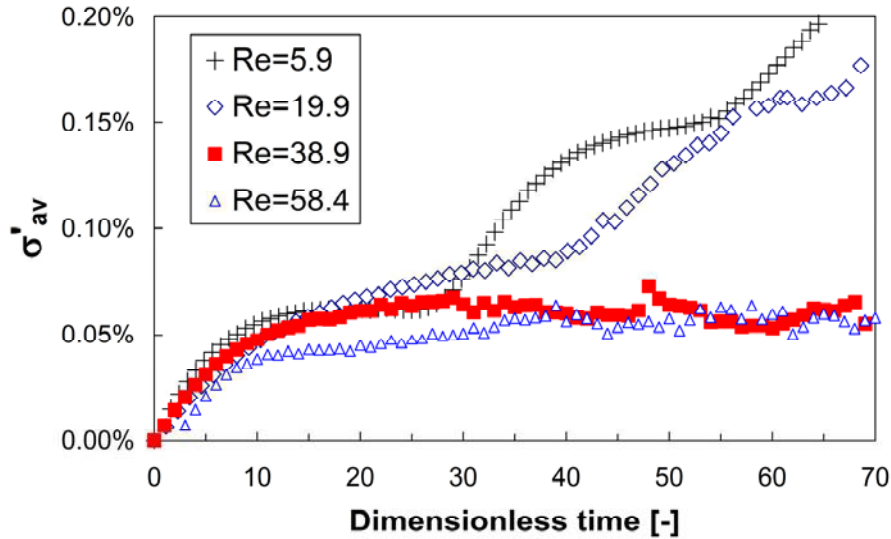
Figure 4.6: Selectivity towards aniline as a function of dimensionless time (Sc = 50, Eo = 2.81, Da_1/Da_2 = 40, Ha = 0.463 - 0.626, a = const).
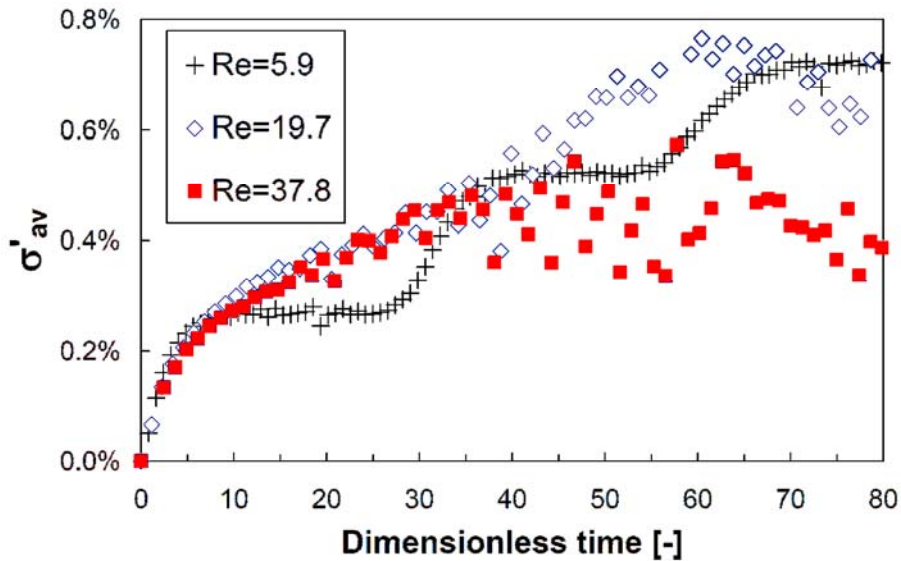
Figure 4.7: Selectivity towards aniline as a function of dimensionless time for a fast chemical reaction (Sc = 50, Eo = 2.81, Da_1/Da_2 = 40, Ha = 1.34 - 1.73, a = const).

From these simulations we conclude that in the range of the Hatta numbers investigated the concentration profiles both in the boundary layer and in the bulk have an effect on the selectivity of the reaction. At this intermediate Hatta number, reactants and products can leave the boundary layer. Local (micro-)mixing significantly changes the behavior of the reaction

network. Thus, the mixing in the proximity of the bubble is significant and small perturbations may change the accumulation of hydroxylamine intermediate and consequently selectivity.

Higher Hatta numbers imply a fast reaction compared to the mass transfer rate. To test if the Hatta number has an influence on the mixing sensitivity of the hydroxylamine formation, additional simulations were conducted with higher Hatta numbers of about 1.5, where a significant enhancement is already noticeable. At the same time, the ratio of the Damköhler numbers of both reactions was kept the same. The result, i.e., the averaged differential selectivity σ'_{av}, is shown in Figure 4.7. As can be seen, the selectivity is significantly higher in all wake regimes, and the dependence on the wake mixing is less pronounced. Due to the fast reactions, wake effects have less impact since the reaction is completed near the interface. The reason for the generally higher selectivity is that for faster reactions, more hydroxylamine intermediate is formed in the boundary layer, which has to diffuse from the gas-liquid interface to the liquid bulk. This in turn leads to a higher concentration of hydroxylamine near the bubble, where the second reaction is promoted and hydroxylamine is consumed ($\sigma'_{av} \sim$ c_R). The strong scatter of the data in the case of the higher Reynolds number is explained by the fact that here instantaneous selectivities are reported, which change rapidly due to the non-steady flow (vortex shedding).
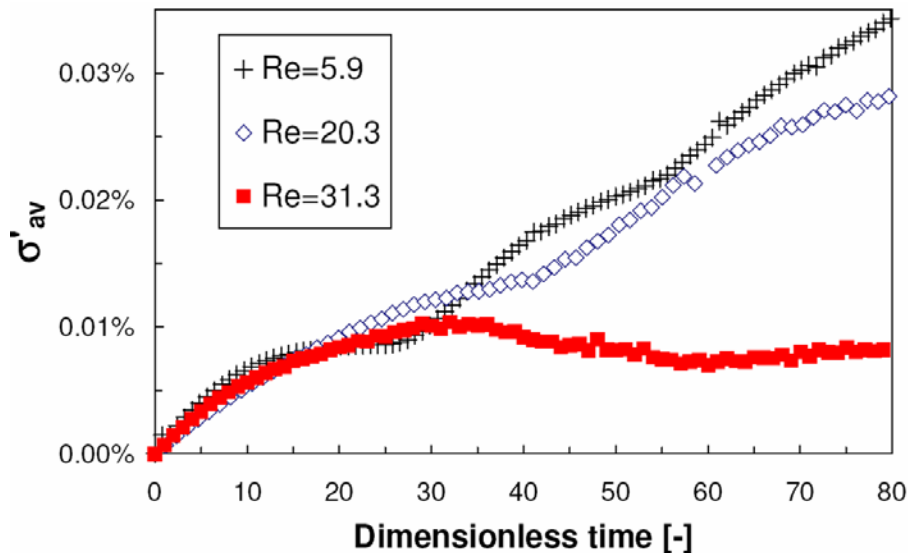
Figure 4.8: Selectivity towards aniline as a function of dimensionless time for a slow chemical reaction ($Sc = 50$, $Eo = 2.81$, $Da_1/Da_2 = 40$, $Ha = 0.145 - 0.198$, $a = const$).

In contrast, in the case of low Hatta numbers mixing strongly impacts the selectivity of the reaction network. The results for such a case ($Ha = 0.145$) are shown in Figure 4.8. Clearly,

the selectivity in general is very poor due to the slow reaction and consequently low concentrations of intermediate near the bubble.

4.6.3 Bubble Swarms

Realistic gas hold-ups in industrial reactors are typically significant, such that bubbles interact strongly. In such systems, bubble-bubble interactions are dominating the flow and steady straight trajectories are no longer observed. Although the reaction itself (in the case of fast reactions) may still be confined to the vicinity of a bubble, the hydrodynamic interactions are significant, leading to changing wake mixing characteristics. It is, therefore, important to verify, if the differences in mixing affect the chemical reaction network. For this purpose, simulations were carried out for multiple bubbles rising simultaneously at different Reynolds numbers.
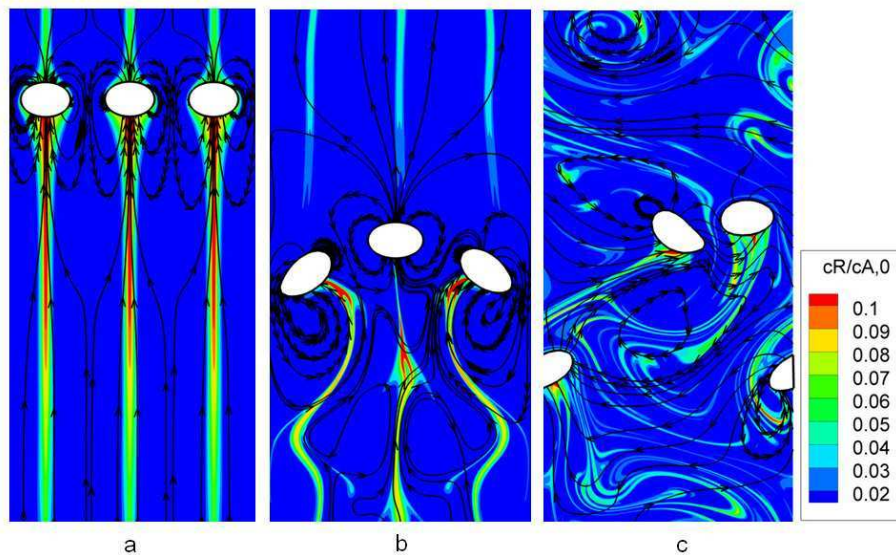
Figure 4.9: Dimensionless concentration of hydroxylamine around three simultaneously rising bubbles (a: Re = 19.7; b, c: Re = 37.8; Sc = 50, Da_1/Da_2 = 40, Ha = 0.463 - 0.626).

In a first step, the interaction of three bubbles was investigated. Figure 4.9 captures snapshots of the concentration field of the hydroxylamine intermediate around three bubbles rising simultaneously. The black lines in Figure 4.9 are streamlines and the white spots represent the bubbles. The bubbles have been characterized by their single-bubble Reynolds number. This allows a direct comparison between single- and multi-bubble selectivities. All other parameters have been kept constant from the single-bubble case. As can be seen from Figure 4.9a, in the case of three bubbles with Re = 19.7, the bubbles stay aligned and enter their own wakes without dispersing hydroxylamine to the bulk. These bubbles do not show wake-shedding

behavior (as observed for a single bubble at this Re number) since the effective Reynolds number is lower due to the bubble interactions, i.e., the down flow induced by one bubble is slowing other bubbles. As a consequence of this flow features we observe a long trail of concentrated hydroxylamine behind the bubbles.

If the Reynolds number is increased, we observe a chaotic oscillating bubble motion and good liquid-phase mixing (Figure 4.9b-c). This is underlined by a qualitative change of the shape of the stream traces (black lines) in Figure 4.9. At low Reynolds numbers (Re = 19.7) they are parallel to the trajectory of the bubbles whereas at higher Reynolds numbers (Re = 37.8) vortical structures are formed. These vortical structures lead to a chaotic stretching and folding of liquid elements. This results in very fine structures in the concentration field as can be seen in Figure 4.9c. These fine structures are smeared out quickly by molecular diffusion. This leads to better mixing in flows characterized by high Reynolds numbers.
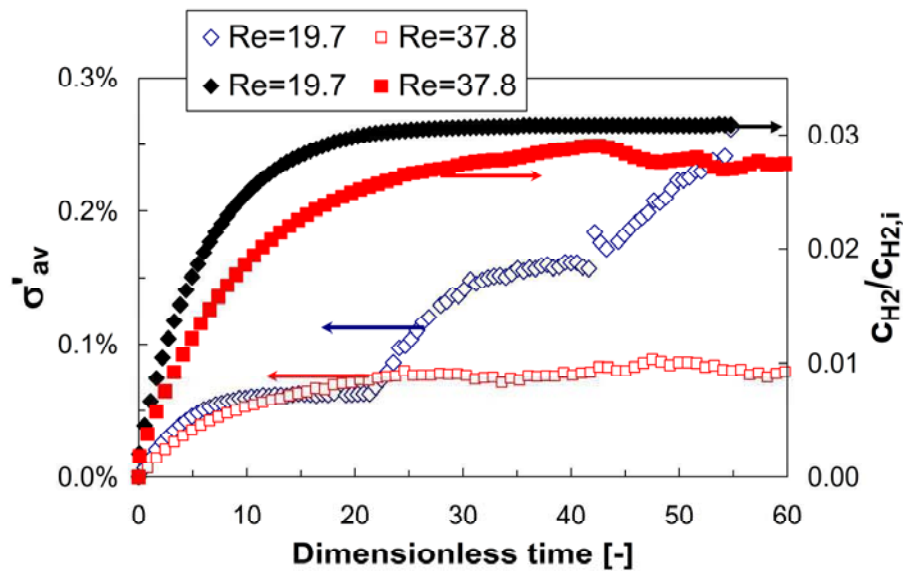
Figure 4.10: Selectivity towards aniline and average dimensionless hydrogen concentration as a function of dimensionless time for three bubbles and Sc = 50, Da_1/Da_2 = 40, Ha = 0.463 - 0.626.

The locally averaged differential selectivity σ'_{av} and the dimensionless hydrogen concentration averaged over the liquid phase are plotted in Figure 4.10. To make the hydrogen concentration dimensionless we have used the hydrogen interface concentration this time. The results for the selectivity and averaged concentration correspond to the case of three initially horizontally aligned bubbles discussed in the last paragraph. The expected trends, i.e., higher selectivity and a constantly increasing selectivity with time in the case of a lower Reynolds

number, are confirmed by the simulations. Thus, the qualitative behavior is similar to the single bubble case.

Furthermore we see, that the dimensionless concentration of hydrogen in the case Re = 37.8 is always lower than that in the case of Re = 19.7. As we have kept the Eötvös and Schmidt number constant in the current simulations, i.e., mimicking equally sized bubbles in different fluids, the mass transfer rate for Re = 37.8 is slightly smaller compared to the case of Re = 19.7. This is because the Sherwood number does not increase linearly with the Reynolds number. Hence, we have a lower mass transfer coefficient for a higher Reynolds number when holding the Schmidt number constant (D ~ µ).
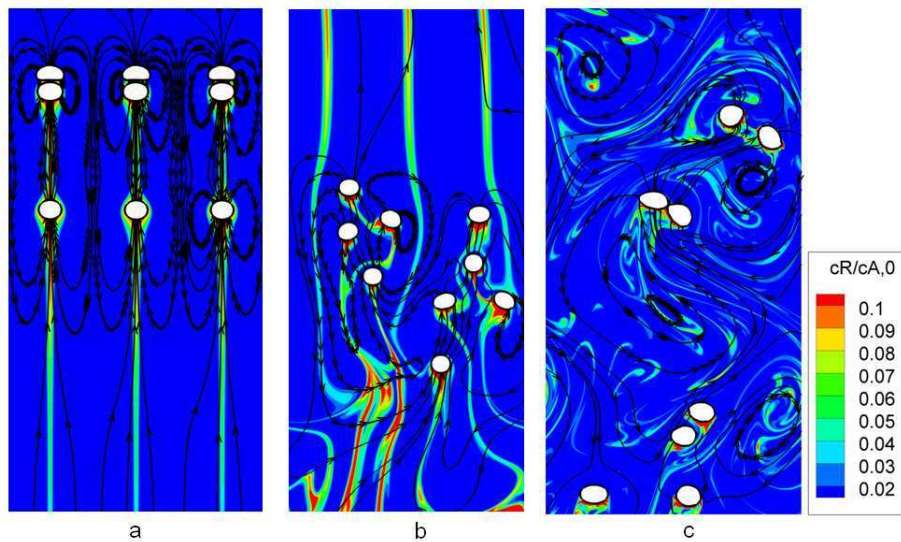
Figure 4.11: Dimensionless concentration of hydroxylamine around nine simultaneously rising bubbles (a, b: Re = 5.9; c: Re = 37.8, Sc = 50, Da_1/Da_2 = 40, Ha = 0.463 - 0.626).

Figure 4.11 depicts snapshots of the simultaneous motion of nine bubbles at different Reynolds numbers. Again, we have plotted the dimensionless concentration of hydroxylamine and the stream traces for visualizing the flow pattern. The bubbles are characterized by their single-bubble Reynolds number as before. It can be seen that in the low-Reynolds-number case (Re = 5.9, Figure 4.11a) the nine bubbles start to rise, where bubbles in the middle row are being accelerated due to interactions with the wakes of the preceding bubbles (which are deformed). Shortly thereafter, the flow becomes irregular (Figure 4.11b) indicated by a qualitative change in streamline pattern. In a system with a higher Reynolds number (Re = 37.8, Figure 4.11c) the flow becomes irregular immediately and liquid phase mixing is significantly enhanced. Due to the eddies formed behind the rising bubbles, stretching and folding of liquid elements is enhanced and very fine structures of dissolved hydrogen and

hydroxylamine can be observed (Figure 4.11c). Better mixing in high Re-number cases can also be identified by a more uniform distribution of hydroxylamine by inspection of Figure 4.11b and 4.11c.
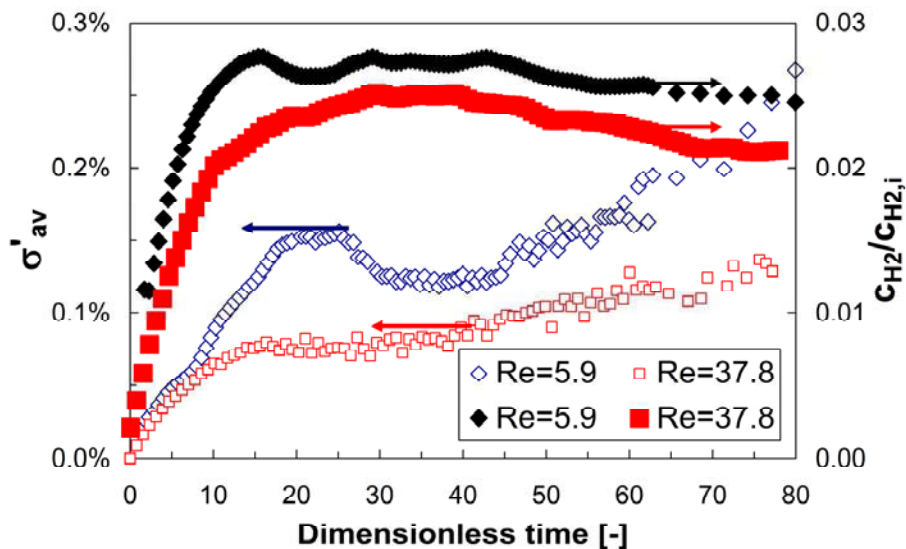
Figure 4.12: Selectivity towards aniline and average dimensionless hydrogen concentration as a function of dimensionless time for a nine bubble cluster and Sc = 50, $Da_1/Da_2 = 40$, Ha = 0.463 - 0.626).

It is interesting to observe the effect of the Reynolds number on the selectivity in the case of a nine-bubbles cluster, as shown in Figure 4.12. The simulations are the same as discussed in Figure 4.11. Again, we have added the time profile of the averaged dimensionless hydrogen concentration to this selectivity plot. The results in Figure 4.12 show that the increase in selectivity is more pronounced for the low-Reynolds number bubbles. Thus, we argue that the observations made in the single bubble case also predict the reactive effects in bubble swarm motion. The behavior of the averaged dimensionless hydrogen concentration is analogous to the three bubble case.

Figure 4.13 shows snapshots of hydrogen and hydroxylamine concentration profiles around large bubble clusters at two different Hatta numbers. The gas hold up in this case was 4.91 %, i.e., in the range of industrial applications. In the case of a low Hatta number (Figure 4.13a), there is a significant amount of unreacted hydrogen present in the bulk phase, i.e., far away from the gas-liquid interface. If the Hatta number is increased (Ha = 0.491, Figure 4.13b), the dissolved hydrogen gas is consumed by the reactions and the bulk concentration of hydrogen is nearly zero. Furthermore, the relative concentrations of intermediate product differ significantly from each other (compare Figure 4.13c and 4.13d), due to the low reaction rate in the case of a lower Hatta number.
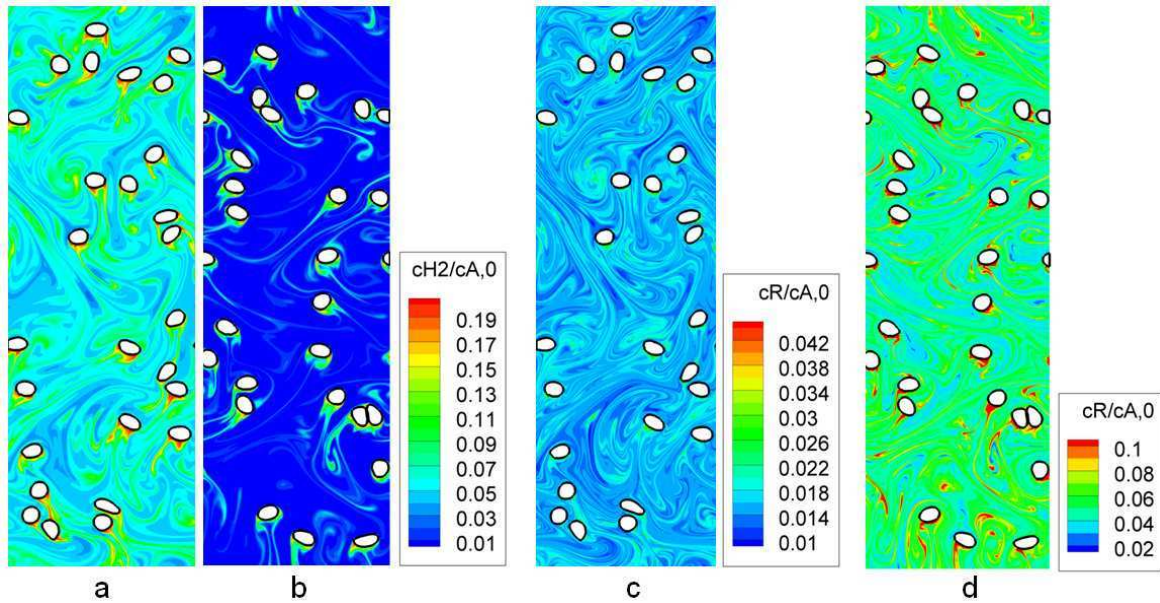
Figure 4.13: Dimensionless concentration of hydrogen (a, b) and hydroxylamine (c, d) around a large bubble cluster (Re = 38, Sc = 50, Da_1/Da_2 = 40; a, c: Ha = 0.164, t^* = 81; b, d: Ha = 0.491, t^* = 88).

4.6.4 Comparison between a Well-Mixed Two-Phase CSTR and Exact Simulations

In Figure 4.14 we compare the time course of the selectivity for different gas hold-ups. The flow was characterized by a single Reynolds number of 38, the ratio of the Damköhler numbers was identical to the previous simulations. The top figure represents the case of a high Hatta number, i.e., a fast reaction (Ha = 0.49), whereas in the bottom figure the Hatta number is lower and equal to Ha = 0.15. Clearly, for increased gas hold-ups, the selectivity of the reaction increases. The steady increase in selectivity is due to the accumulation of intermediate product in the bulk phase. This trend is similar for both Hatta numbers.

To separate the effects of mixing and accumulation of the intermediate product hydroxylamine, we compared our results with an idealized case of a perfectly mixed bulk phase. The results of this analysis for two different gas hold ups (0.73 % and 8.73 %) are shown in Figure 4.15. Here the squares indicate the simulated selectivity and the triangles indicate the idealized case of a perfectly mixed bulk phase. Assuming a well-mixed bulk phase, the differential selectivity is equal to the product of the average concentration of intermediate product and the ratio of the Damköhler numbers (combining Eqs. 4.4, 4.6 and 4.7).
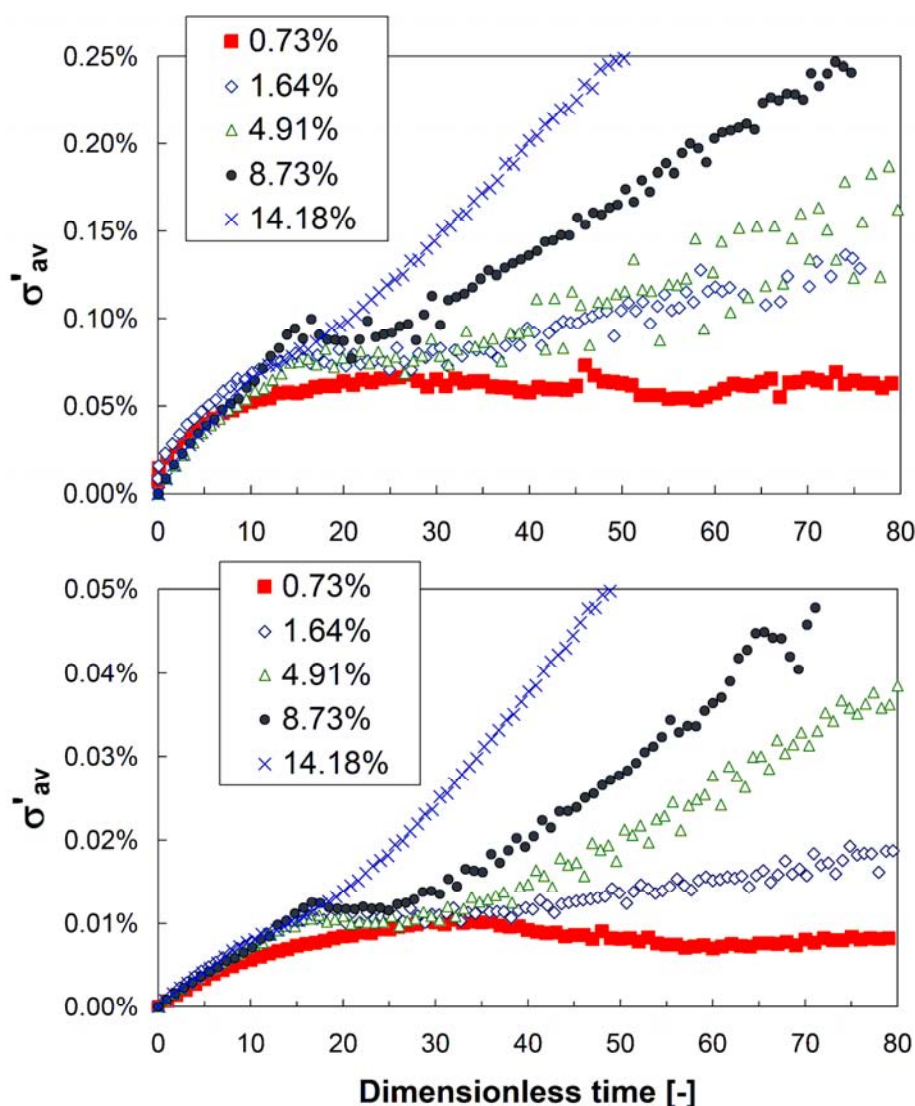
Figure 4.14: Selectivity for different gas hold-ups (Re = 38, Sc = 50; top: high Hatta number, bottom: low Hatta number).

As can be seen, there is a large deviation between results obtained by detailed calculations and by assuming a well-mixed system for higher Hatta numbers. In the case of a low gas hold up, mixing around the bubbles is poor and the differential selectivity is significantly higher than the one expected from the average concentration of intermediate product. In the case of a high gas hold-up and consequently good mixing the difference is smaller. However, the difference is still pronounced in the case of a high Hatta number (Figure 4.15, top). In the case of low Hatta numbers (Ha = 0.15), the selectivity calculated from the reaction rates and from the well-mixed model are in better agreement (Figure 4.15, bottom). In this case the reactants and the intermediate products are more homogenously distributed around the bubbles.
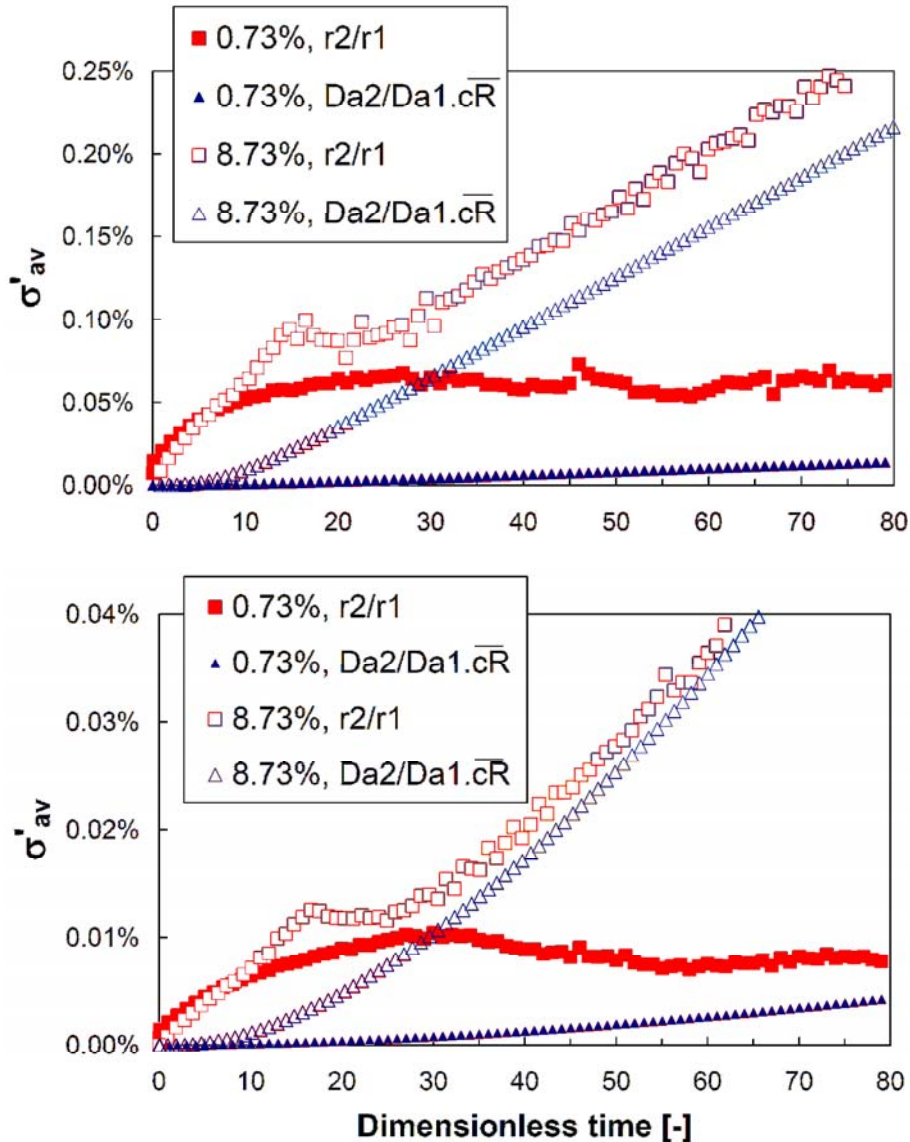
Figure 4.15: Comparison of simulated differential selectivities for different gas hold-ups (Re = 38, Sc = 50; top: high Hatta number, bottom: low Hatta number).

These comparisons illustrate the significant deviations between results obtained assuming a well-mixed two-phase CSTR and detailed simulation, with deviations of few hundred percent being possible. Thus, a detailed analysis of the reactions is necessary. In the next section the comparison between exact results and film theory is provided.

4.6.5 Comparison between Film Theory Predictions and Exact Simulations

A comparison of the exact simulation results (symbols) with the predictions of film theory (solid and dashed line) is presented in Figure 4.16. Characteristic values for the selectivity in the case of exact simulations were taken after the first local maximum was reached in the selectivity-time plot. In some cases the selectivity dropped significantly after the first local

maximum. These results are marked with "recirculation" as this was due to recirculation in the wake of the bubble.
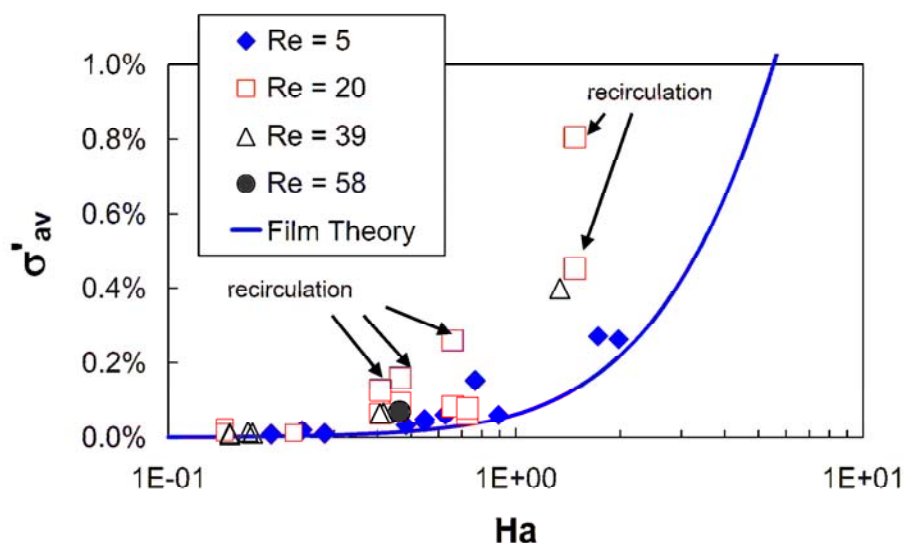
Figure 4.16: Comparison of simulation results with film theory for different Hatta- and Reynolds numbers (Sc = 10 - 50).

It can be seen from Figure 4.16 that the exact simulations follow the same trend as the film theory predicts, i.e., the selectivity increases with increasing Hatta number. However, film theory significantly underpredicts the selectivity for higher Reynolds numbers. The exact simulations show that in the case of very low Reynolds numbers the selectivity agrees quite well with film theory (solid line). This may be attributed to the fact that in case of low Reynolds numbers the wake is closed and the streamlines are almost parallel to the bubble interface. Film theory represents this situation reasonably well. Hence, the calculation of the selectivity in these situations can be based on a simple model. However, for higher Reynolds numbers exact numerical techniques should be used to give satisfactory predictions. As expected, the results in the case of recirculation wakes behind the bubbles lead to selectivities significantly higher than that expected by film theory. This is due to intermediate product accumulation in the wake of the bubbles and hence increased formation of final product. These effects are not considered within film theory as only reactions in the vicinity of the bubble are modeled.

4.7 Conclusions

Numerical simulations were performed for the liquid-phase hydrogenation of nitroarenes in bubbly flows with freely deformable interfaces. The reaction proceeds through the

hydroxylamine intermediate, which is carcinogenic, toxic and thermally unstable. It is therefore desirable to minimize the accumulation of hydroxylamine during the operation of industrial contactors.

Different scenarios were considered with the goal of investigating the impact of the local mixing in the vicinity of individual bubbles on the rate of formation of the intermediate. In the case of single bubbles, an increase in the Reynolds number leads to changes in the hydrodynamics of the bubble wakes, i.e., closed, recirculating or unsteady, vortex-shedding wakes. As expected, the improved mixing observed in higher Reynolds number wakes leads to an increase in the accumulation of hydroxylamine. Furthermore, the stability of the flow pattern, i.e., development of a vortex shedding regime plays a significant role in determining selectivities in complex reaction networks. We have compared our simulation results with film theory and find good agreement. However, a more refined model based on film or penetration theory that could account for accumulation effects has to be developed for the rapid prediction of selectivities.

In the cases of multiple bubbles rising simultaneously the differences in wake fluid flow were still sufficient to cause differences in local mixing and as a consequence in the rates of hydroxylamine accumulation. Furthermore, our simulations show that even in large bubble clusters of about 50 bubbles the selectivity is partly influenced by the reaction in the film. However, this is only the case for medium to high Hatta numbers ($Ha > 0.5$). For low Hatta numbers ($Ha < 0.5$) and high Re-numbers ($Re > 40$) the simulations show that bulk mixing should be sufficient to justify the assumption of a well mixed bulk phase.

These results can be potentially useful in the design and operation of bubble reactors, such as the ones used for the liquid-phase hydrogenation of nitroarenes.

4.8 Abbreviations

ADI   Alternating Direction Implicit (algorithm)

CPU   Central Processing Unit

CSTR   Continuously Stirred Tank Reactor

LDA   Laser Doppler Anemometry

MAC   Marker And Cell (method)

PIV   Particle Image Velocimetry

VOF   Volume Of Fluid (method)

4.9 Nomenclature

a_i specific interfacial area of the bubbles [m^2/m^3_{liquid}]

A_{tot} area of the computational domain [m^2]

$c_{i,0}$ initial concentration of reactant i in the liquid bulk [$kmol/m^3$]

c_i concentration of species i [$kmol/m^3$]

$c_{i,0}$ concentration of species i in the liquid bulk [$kmol/m^3$]

$c_{j,i}$ concentration of species j at the gas-liquid interface [$kmol/m^3$]

$c_{l,i}$ concentration of species i in the liquid phase [$kmol/m^3$]

$c_{g,i}$ concentration of species i in the gas phase [$kmol/m^3$]

D   diffusion coefficient [m^2/s]

D_i diffusion coefficient for species i [m^2/s]

Da_j Damköhler number of the j-th reaction, $Da_j = d_b \cdot k_j \cdot c_{A,In} / U_t$

ds'   differential element of the bubble contour [m]

d_b bubble diameter [m]

E_A mass transfer enhancement factor

Eo   Eötvös number, $Eo = g\rho_l d_b^2 / \sigma$

f   body forces [m/s^2]

g   gravitational acceleration [m/s^2]

H   Heaviside function

Ha   Hatta number, $Ha = \sqrt{k_1 \cdot D} / k_L$

k_j reaction rate constant of the j-th reaction [j=1: 1/s; j=2: $m^3/kmol/s$]

k_L liquid-side mass transfer coefficient [m/s]

m, n, p, q   exponents of the rate expression

Mo   Morton number, $Mo = g\mu_l^4 / (\rho_l \cdot \sigma^3)$

n_k order of the reaction with respect to species k

N   number of bubbles

$\dot{N}_i$ molar flux of species i across the interface [kmol/(m²·s)]

n´   vector normal to the bubble interface

P   pressure [Pa]

r_j reaction rate of the j-th reaction [kmol/m³·s]

Re   bubble Reynolds number, $Re = d_b U_t \rho_l / \mu_l$

Sc   Schmidt number, $Sc = \mu / (\rho \cdot D)$

t   time [s]

t*   dimensionless time t = t/t_{ref}

t_{ref} reference bubble rise time, $t_{ref} = d_b/U_t$ [s]

u   velocity vector [m/s]

U_t terminal rise velocity [m/s]

x   position vector [m]

x   x-coordinate [m]

y   y-coordinate [m]

Greek letters

δ   film thickness [m]

ε   gas hold up [m³$_{gas}$/m³$_{tot}$]

κ´   curvature

μ   dynamic viscosity [Pa.s]

μ_l dynamic liquid-phase viscosity [Pa.s]

ν_{ij} stoichiometric coefficient of species i in reaction j

ϱ   density [kg/m³]

ϱ_l liquid-phase density [kg/m³]

σ surface tension [N/m]

σ'   differential selectivity

4.10 References

(1)   Downing RS, Kunkeler PJ, vanBekkum H. Catalytic syntheses of aromatic amines. Catalysis Today. 1997; 37:121-136.

(2)   Stoessel F. Experimental-Study of Thermal Hazards During the Hydrogenation of Aromatic Nitro-Compounds. Journal of Loss Prevention in the Process Industries. 1993; 6:79-85.

(3)   Wei CY, Rogers WJ, Mannan MS. Application of runaway reaction mechanism generation to predict and control reactive hazards. Computers & Chemical Engineering. 2007; 31:121-126.

(4)   Baumeister P, Blaser HU, Studer M. Strong reduction of hydroxylamine accumulation in the catalytic hydrogenation of nitroarenes by vanadium promoters. Catalysis Letters. 1997; 49:219-222.

(5)   Iwata Y, Koseki H. Decomposition of hydroxylamine/water solution with added iron ion. Journal of Hazardous Materials. 2003; 104:39-49.

(6)   Studer M, Neto S, Blaser HU. Modulating the hydroxylamine accumulation in the hydrogenation of substituted nitroarenes using vanadium-promoted RNi catalysts. Topics in Catalysis. 2000; 13:205-212.

(7)   Westerterp KR, Molga EJ, van Gelder KB. Catalytic hydrogenation reactors for the fine chemicals industries. Their design and operation. Heterogeneous Catalysis and Fine Chemicals Iv. 1997; 108:47-57.

(8)   Darmana D, Deen NG, Kuipers JAM. Detailed modeling of hydrodynamics, mass transfer and chemical reactions in a bubble column using a discrete bubble model. Chemical Engineering Science. 2005; 60:3383-3404.

(9)   Lapin A, Maul C, Junghans K, Lubbert A. Industrial-scale bubble column reactors: gas-liquid flow and chemical reaction. Chemical Engineering Science. 2001; 56:239-246.

(10)   Larachi F, Desvigne D, Donnat L, Schweich D. Simulating the effects of liquid circulation in bubble columns with internals. Chemical Engineering Science. 2006; 61:4195-4206.

(11)   Monahan SM, Vitankar VS, Fox RO. CFD predictions for flow-regime transitions in bubble columns. AIChE Journal. 2005; 51:1897-1923.

(12)   Monahan SM, Fox RO. Effect of model formulation on flow-regime predictions for bubble columns. AIChE Journal. 2007; 53:9-18.

(13)   Pan Y, Dudukovic MP, Chang M. Dynamic simulation of bubbly flow in bubble columns. Chemical Engineering Science. 1999; 54:2481-2489.

(14)   Onda K, Sada E, Kobayash T, Fujine M. Gas Absorption Accompanied by Complex Chemical Reactions: 1. Reversible Chemical Reactions. Chem Eng Sci. 1970; 25:753-760.

(15)   Onda K, Sada E, Kobayash T, Fujine M. Gas Absorption Accompanied by Complex Chemical Reactions: 2. Consecutive Chemical Reactions. Chem Eng Sci. 1970; 25:761-768.

(16)   Onda K, Sada E, Kobayash T, Fujine M. Gas Absorption Accompanied by Complex Chemical Reactions: 3. Parallel Chemical Reactions. Chem Eng Sci. 1970; 25:1023-1100.

(17)   Onda K, Sada E, Fujine M, Kobayash T. Gas Absorption Accompanied by Complex Chemical Reactions: 4. Unsteady State. Chem Eng Sci. 1972; 27:247-255.

(18)   Westerterp KR, van Swaaij WPM, Beenackers AACM. Chemical Reactor Design and Operation (2nd edition). Norwich, GB: John Wiley & Sons, 1984.

(19)   Harriott P. Effect of Mass Transfer on Selectivity for Heterogeneous Reactions. Canadian Journal of Chemical Engineering. 1970; 48:109.

(20)   Darde T, Midoux N, Charpentier JC. Contribution to the Analysis of the Selectivity in Gas-Liquid Reaction .1. Literature and Theory. Chemical Engineering Communications. 1983; 22:221-241.

(21)   Bourne JR. Mixing and the selectivity of chemical reactions. Organic Process Research & Development. 2003; 7:471-508.

(22)   Choi HM, Kurihara T, Monji H, Matsui G. Measurement of particle/bubble motion and turbulence around it by hybrid PIV. Flow Measurement and Instrumentation. 2001; 12:421-428.

(23)   Raymond F, Rosant JM. A numerical and experimental study of the terminal velocity and shape of bubbles in viscous liquids. Chemical Engineering Science. 2000; 55:943-955.

(24)   Tokuhiro A, Maekawa M, Iizuka K, Hishida K, Maeda M. Turbulent flow past a bubble and an ellipsoid using shadow-image and PIV techniques. International Journal of Multiphase Flow. 1998; 24:1383-1406.

(25)   Bork O, Schlüter M, Scheid S, Räbiger N. New phenomena of mass transfer in gas/liquid flows. Proceedings of ASME HTD, Fluid-Physics and Heat Transfer for Macro- and Micro-Scale Gas-Liquid and Phase Change Flows. New York: 2001.

(26)   Bork O, Schlüter M, Scheid S, Räbiger N. Analysis of the effect of local hydrodynamics on mass transfer from bubbles using laser induced fluorescence. Proceedings of FEDSM'03. 1-7.: 2003.

(27)   Osher S, Fedkiw RP. Level set methods: An overview and some recent results. Journal of Computational Physics. 2001; 169:463-502.

(28) Brackbill JU, Kothe DB, Zemach C. A Continuum Method for Modeling Surface-Tension. Journal of Computational Physics. 1992; 100:335-354.

(29) Lakehal D, Meier M, Fulgosi M. Interface tracking towards the direct simulation of heat and mass transfer in multiphase flows. International Journal of Heat and Fluid Flow. 2002; 23:242-257.

(30) Scardovelli R, Zaleski S. Direct numerical simulation of free-surface and interfacial flow. Annual Review of Fluid Mechanics. 1999; 31:567-603.

(31) van Wachem BGM, Schouten JC. Experimental validation of 3-D Lagrangian VOF model: Bubble shape and rise velocity. AIChE Journal. 2002; 48:2744-2753.

(32) Shopov PJ, Minev PD, Bazhlekov IB, Zapryanov ZD. Interaction of A Deformable Bubble with A Rigid Wall at Moderate Reynolds-Numbers. Journal of Fluid Mechanics. 1990; 219:241-271.

(33) Glimm J, Grove JW, Li XL, Oh W, Sharp DH. A critical analysis of Rayleigh-Taylor growth rates. Journal of Computational Physics. 2001; 169:652-677.

(34) Sankaranarayanan K, Kevrekidis IG, Sundaresan S, Lu J, Tryggvason G. A comparative study of lattice Boltzmann and front-tracking finite-difference methods for bubble simulations. International Journal of Multiphase Flow. 2003; 29:109-116.

(35) Tryggvason G, Bunner B, Esmaeeli A, Juric D, Al-Rawahi N, Tauber W et al. A front-tracking method for the computations of multiphase flow. J Comput Phys. 2001; 169:708-759.

(36) Aris R. Mass transfer from small ascending bubbles. Chemical Engineering Science. 1997; 52:4439-4446.

(37) Legendre D, Magnaudet J. Effect of flow acceleration on mass or heat transfer at the surface of a spherical bubble. Comptes Rendus de l Academie des Sciences Serie Ii Fascicule B-Mecanique Physique Astronomie. 1999; 327:63-70.

(38) Khinast JG. Impact of 2-D bubble dynamics on the selectivity of fast gas-liquid reactions. AIChE Journal. 2001; 47:2304-2319.

(39) Koynov A, Khinast JG. Effects of hydrodynamics and Lagrangian transport on chemically reacting bubble flows. Chemical Engineering Science. 2004; 59:3907-3927.

(40) Bothe D, Koebe M, Warnecke HJ. VOF-Simulation of the Rise Behavior of Single Air Bubbles with Oxygen Transfer to the Ambient Liquid. Conference on Transport Phenomena with Moving Boundaries. Berlin, Germany: 2005.

(41) Koynov A, Khinast JG, Tryggvason G. Mass transfer and chemical reactions in bubble swarms with dynamic interfaces. AIChE Journal. 2005; 51:2786-2800.

(42) Radl S, Tryggvason G, Khinast JG. Flow and mass transfer of fully resolved bubbles in non-Newtonian fluids. AIChE J. 2007; 53:1861-1878.

(43) Darmana D. On the multiscale modelling of hydrodynamics, mass transfer and chemical reactions in bubble columns. Twente, Netherlands: University of Twente, 2006.

(44) Darde T, Midoux M, Charpentier JC. Selectivity in Gas-Liquid Contactors - Original Modeling and Confrontation Theory Experiments. Hungarian Journal of Industrial Chemistry. 1984; 12:83-89.

(45) Vicum L, Ottiger S, Mazzotti M, Makowski L, Baldyga J. Multi-scale modeling of a reactive mixing process in a semibatch stirred tank. Chem Eng Sci. 2004; 59:1767-1781.

(46) Körner UF. Verfahren zur Bestimmung eines makrokinetischen Modells für flüssig/flüssig-Reaktionen aus kalorimetrischen Messungen. Berlin: Technical University Berlin, 2004.

(47) Hoorn JAA, Versteeg GF. Modelling of mass transfer in combination with radical reactions. Chem Eng Sci. 2006; 61:5137-5148.

(48) Radhakrishnan K, Ramachandran PA, Brahme PH, Chaudhari RV. Solubility of Hydrogen in Methanol, Nitrobenzene, and Their Mixtures - Experimental-Data and Correlation. Journal of Chemical and Engineering Data. 1983; 28:1-4.

(49) Clift R, Grace JR, Weber ME. Bubbles, Drops, and Particles. Mineola, US: Dover Publications Inc., 2005.

(50) Koynov A, Tryggvason G, Schlueter M, Khinast JG. Mass transfer and chemical reactions in reactive deformable bubble swarms. Applied Physics Letters. 2006; 88:134102.

(51) Koynov A, Khinast JG, Tryggvason G. Mass transfer and chemical reactions in bubble swarms with dynamic interfaces. AIChE J. 2005; 51:2786-2800.

(52) Matlab 7.3.0 (R2006b). The Mathworks, Inc., 2006.

"When some external agency imposes on a fluid large-scale variations of some dynamically passive, conserved, scalar quantity θ like temperature or concentration of solute, turbulent motion of the fluid generates small-scale variations of θ."

(George K. Batchelor, 1959)

5

Analysis of Micro Mixing in the Wake of a Single Bubble[*]

Mixing and fast chemical reactions in sparged stirred tanks are of great importance in the chemical industry. If multiple reaction steps occur within one apparatus, a detailed understanding of local mixing is crucial to precisely control the reaction network. However, a single, rigorous framework describing the interaction between reactions, mass transfer and liquid phase mixing is currently not available in the literature. This chapter focuses on the local distribution of a gas dissolving from a gas bubble with the vision to predict the rate and selectivity of chemical reaction networks in multiphase systems. To quantify the source of scalar variance due to mass transfer around bubbles, we filtered results of direct numerical simulations (DNS). This information can be used subsequently in LES of bubbly flows.

5.1 Introduction

Bubble column reactors play an important role, e.g., in the fine chemical, biochemical or pharmaceutical industry due to their simple construction and their low operating costs. In these reactors, oxidations, hydrogenations or chlorinations are performed, for which typically high chemical reaction rates are observed. The ability to predict the yield and selectivity of these reaction networks is essential for an economic recovery of the desired product. However, this prediction is complicated due to the interaction of the multiphase flow, mixing, mass transfer and chemical reactions. Hence, there were significant efforts in the past to study the interaction of mass transfer, mixing and reactions based on first principles simulations.[1-10] Recent advances also include reactive systems, which has improved the understanding of micro-mixing effects close to bubbles.[5] Micro-mixing refers to mixing down to the molecular scale, such that reactions can occur. If fast reactions occur at a time scale of the same order or smaller than the time-scale of micro-mixing, mixing effects may delay the reaction. Clearly, micro-mixing can be the controlling step for the yield and selectivity of reaction networks.

In principal, reactive micro-mixing processes can be fully predicted by momentum and species transport equations using the intrinsic kinetics for the chemical reaction.[3,5,6] However, this approach requires extremely high spatial and temporal resolution for higher Schmidt numbers typical for liquid-phase systems. Thus, the outcome of reactions on the equipment scale cannot be predicted using a direct approach. Instead, one has to characterize the concentration distribution on a sub-grid-scale level by linking it with the known properties on the grid level. This can be done, e.g., using a probability density function (PDF) of the local concentration. For a PDF characterized by a mean and a variance, only one additional equation, i.e., that for the variance Y_V of the scalar quantity Y (e.g., the molar fraction of a dissolving component) has to be solved. The variance Y_V is defined as $Y_V = \overline{YY} - \overline{Y} \cdot \overline{Y}$ and its transport equation in the continuous phase (here the liquid is denoted with "L") of a multiphase system is:

$$\frac{\partial(\varepsilon_L \cdot Y_V)}{\partial t} + \nabla \cdot (\varepsilon_L \cdot \overline{\mathbf{u}} Y_V) = \nabla \cdot (\varepsilon_L \cdot D_{eff} \cdot \nabla Y_V)$$
$$+ 2 \cdot \varepsilon_L \cdot D_{eff} \cdot \nabla \overline{Y} \cdot \nabla \overline{Y} - 2 \cdot \varepsilon_L \cdot \frac{C_\Phi}{\tau_\Phi} \cdot Y_V + g_{Y_V}$$

$$(5.1)$$

It includes the accumulation, the convective and diffusive transport of the scalar variance (left-hand side, as well as the first term on the right-hand side of Eqn. 5.1), as well as the

generation and the dissipation of scalar variance in the liquid phase (term two and three on the right-hand side of Eqn. 5.1, respectively). In Eqn. 5.1 ε_L and $\overline{\mathbf{u}}$ are the liquid-phase hold up and the filtered velocity, respectively. D_{eff} is the effective diffusion coefficient, taking into account sub-grid-scale fluctuations. For the dissipation term the turbulence time scale is typically defined as:

$$\tau_\Phi = \frac{\Delta^2}{D_{eff}}.$$
(5.2)

C_Φ is a constant characterizing the ratio of the characteristic time for the decay of the velocity fluctuations and the decay of concentration fluctuations. See Chapter 6 for more details on this approach.

In order to model multiphase systems, we also need to account for the sources due to mass transfer (i.e., the term denoted with g_{Y_V} in the transport equation of the scalar variance). For this last term in Eqn. 5.1 no appropriate model exists for gas-liquid flows. Hence, the goal was to directly calculate the variance generated by the flow around a single bubble and to calculate its generation rate by a filtering operation. This is a first step ahead to reliably predict the scalar variance field in large bubbly swarms without fully resolving the concentration field.

5.2 Mathematical Model

In this work we have used a laminar flow solver together with a species transport solver to study mass transfer from a rigid bubble. Hence, we solved the Navier-Stokes equations for an incompressible fluid:

$$\frac{\partial \mathbf{u}}{\partial t} + \nabla \cdot (\mathbf{uu}) = -\nabla p' + \nu \cdot \nabla^2 \mathbf{u}$$
(5.3)

$$\nabla \cdot \mathbf{u} = 0$$
(5.4)

Here $\mathbf{u}$ denotes the fluid velocity, p' the kinematic pressure (i.e., the pressure divided by the fluid density), and ν is the kinematic viscosity of the fluid. The transport equation for an inert component Y is:

$$\frac{\partial Y}{\partial t} + \nabla \cdot (\mathbf{u}Y) = D \cdot \nabla^2 Y$$
(5.5)

Here D denotes the molecular diffusion coefficient of a certain component in the liquid phase. As we use high-order schemes and a sufficiently fine numerical grid, we claim to fully resolve all details of the fluid motion, as well as the thin concentration boundary layer near the bubble interface. We therefore refer to these simulations as direct numerical simulations. This methodology follows the ideas of our previous work for two-dimensional elliptical bubbles[3] and other literature available in that field (see, e.g., the work of Jung and Sato[11]). However, our focus here is to analyze mixing in greater detail, which has not been done before.

The geometrical setup for our simulations consists of a spherical bubble that was placed in a sufficiently large cylindrical fluid domain. Appropriate boundary conditions were applied and the set of equations was solved using OpenFOAM.[12]
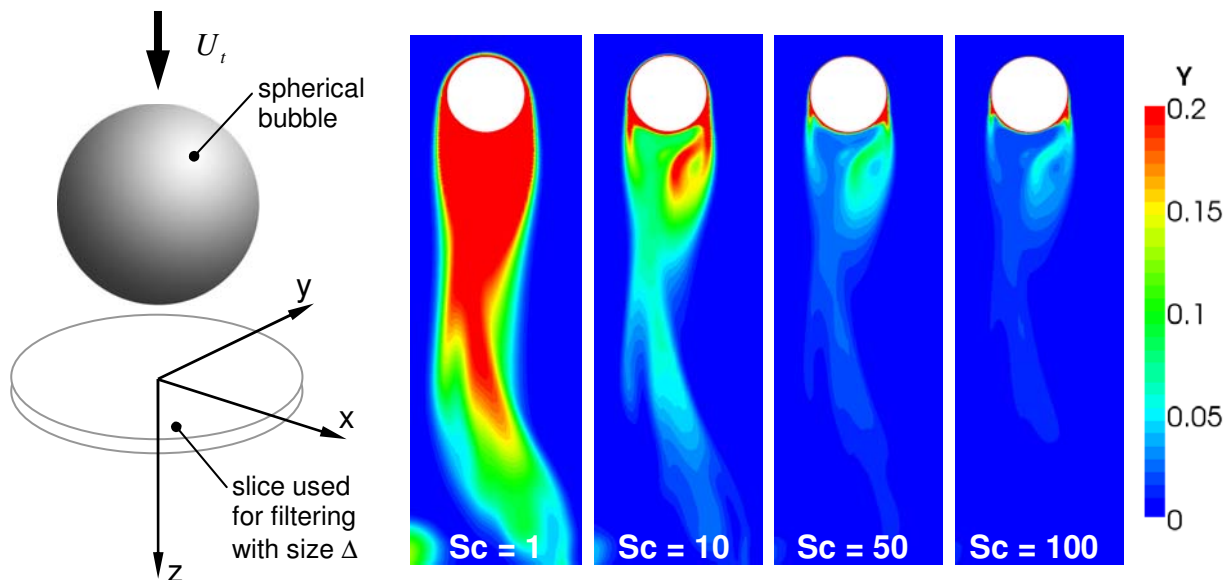
Figure 5.1: Principal sketch of the setup used for the direct numerical simulation of mass transfer around a single bubble (left), as well as results for the instantaneous concentration field for Re = 500 and different Schmidt numbers (right).

5.3 Results

5.3.1 Setup

Mass transfer of a dissolving gas from a single bubble was directly simulated for different Reynolds and Schmidt numbers. In Figure 5.1 we show the basic setup for the study of the variance generation near the bubble. The simulation setup consists of the flow around a rigid sphere with the diameter d_p. An inert component is allowed to dissolve in the liquid phase, with the interface concentration set to unity. Since the species transport Eqn. (i.e., Eqn. 5.5) is

linear in the concentration, the calculated concentration fields can be interpreted as dimensionless concentration fields that have been normalized with the interface concentration.

This setup, i.e., a spherical rigid bubble, mimics most applications involving small bubbles in a gas-liquid system. The flow domain consisted of a sufficiently large cylindrical domain with a diameter and length of $10 \cdot d_p$ and $15 \cdot d_p$, respectively. An almost full resolution of the concentration field up to a Schmidt number of Sc = 100 could be obtained by using an extremely fine grid (approx. 1.3 Mio. cells) near the sphere's surface. Furthermore, second order schemes were used for space and time discretization. The Schmidt number was varied between unity and 100 by changing the diffusion coefficient of the dissolving component.
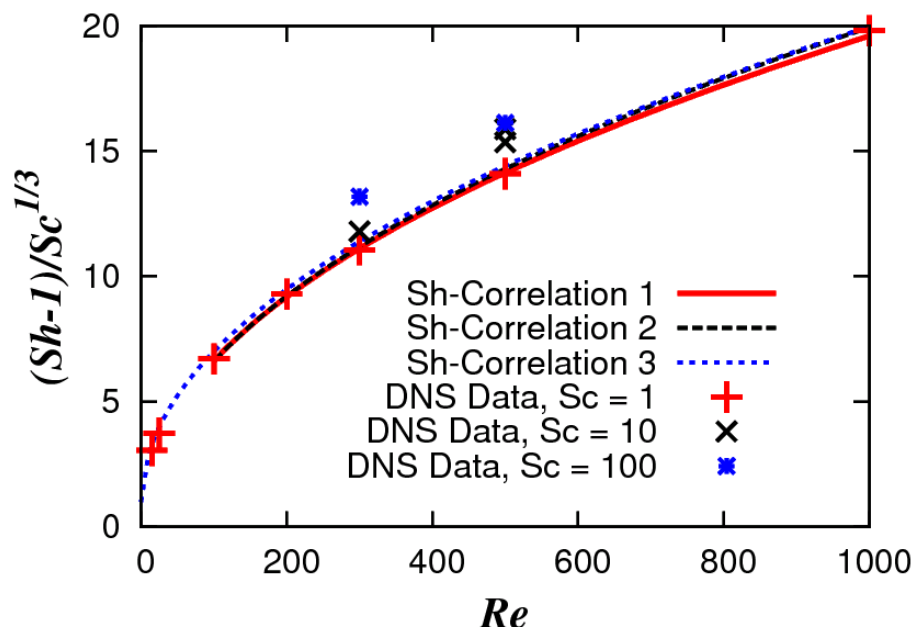
Figure 5.2: Comparison of simulated Sherwood numbers (symbols) with correlations from literature (correlation 1 from Clift et al.,[13] p. 123/Table 5.4/Eqn. (E); correlation 2 from Clift et al.,[13] p. 123/Table 5.4/Eqn. (C); correlation 3 from Ranz and Marshall[14])

The results have been validated by comparing the calculated Sherwood numbers with correlations found in the literature (see Figure 5.2). Clearly, at larger Schmidt numbers and in the wake-shedding region, the calculated Sherwood number is somewhat higher than calculated from the correlation. Grid dependency tests showed, however, only a small change when the resolution of the numerical grid was increased.

5.3.2 Scalar Variance Generation due to Mass Transfer

To analyze the generation of variance behind the bubble, we spatially filtered the results for the concentration field. Filtering was done using a box filter G^{Box} in thin slices perpendicular to the mean flow direction, i.e., parallel to the x-y-plane as shown in Figure 5.1:

$$G^{Box}(x, y) = \begin{cases} 1/\Delta^2 ...|x|,|y| \leq \Delta/2 \\ 0........|x|,|y| > \Delta/2 \end{cases}$$
(5.6)
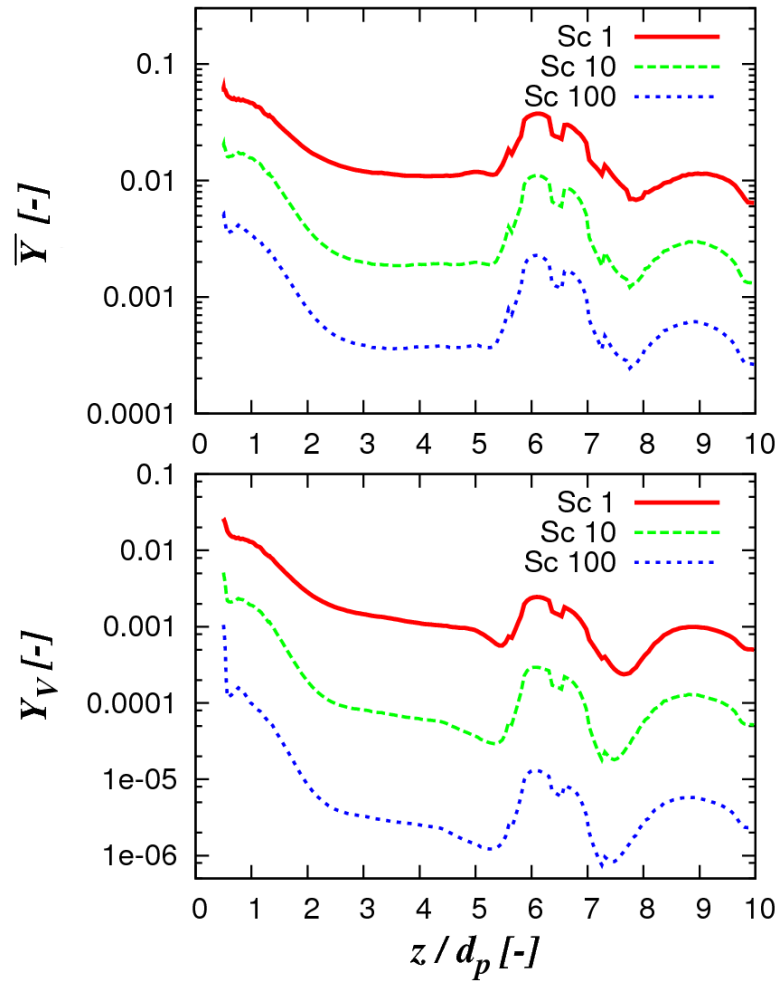
Figure 5.3: Instantaneous filtered concentration (top) and variance field (bottom) in the wake of a single bubble (Re = 500, Δ = 3·d$_p$).

This filtering was motivated by Meneveau and Katz.[15] The filter length Δ was chosen to be equal to three times the bubble diameter d_p. The results of this analysis are shown in Figure 5.3 for different distances z from the center of the sphere at z = 0. Clearly, the filtered concentration $\overline{Y}$, as well as the variance Y_V decreases with increasing distance from the interface

up to approx. $5 \cdot d_p$. However, after that distance, $\overline{Y}$ and Y_V start to fluctuate, which is due to the flow instability at the studied Reynolds number (the onset of this wake instability occurs already between Re = 130 and 400).
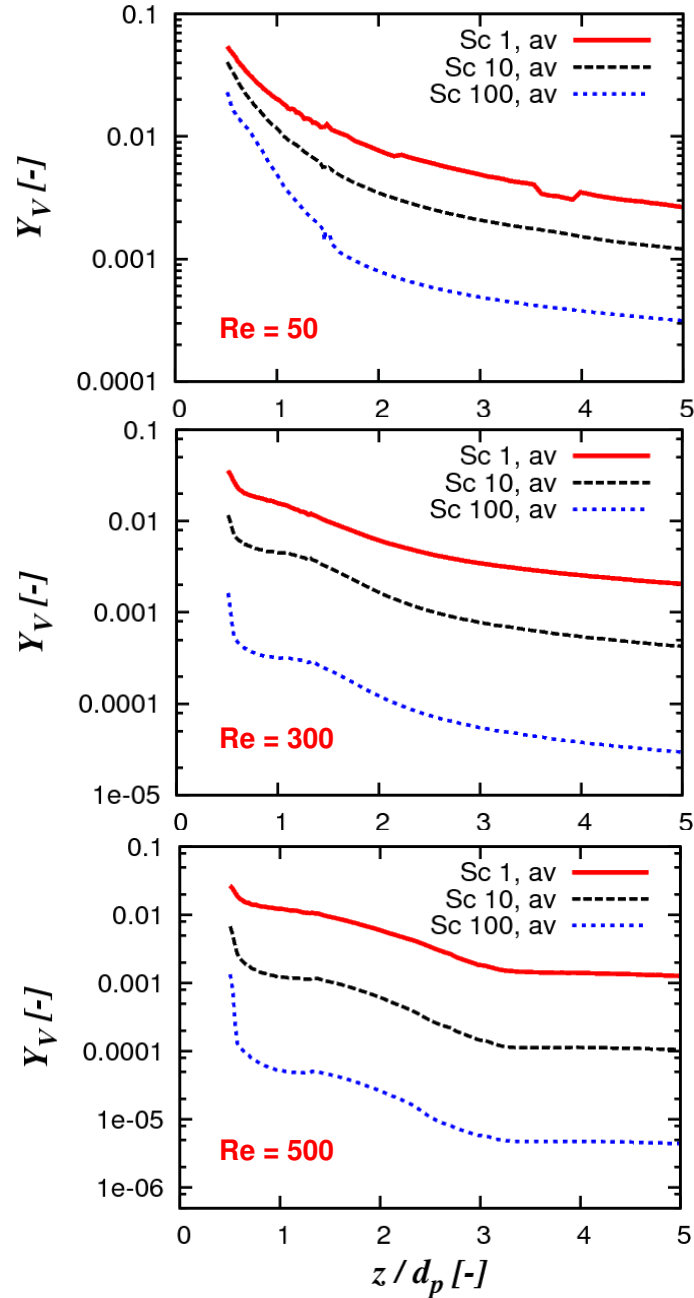
Figure 5.4: Time-averaged variance field in the wake of a single bubble for different Reynolds numbers ($\Delta = 3 \cdot d_p$).

Our results for $\overline{Y}$ suggest that there exists a high-concentration area near the rear stagnation point of the bubble, which has a length of approximately $2 \cdot d_p$. This region is also visible in Figure 5.1. The observed concentration of dissolved gas depends, however, strongly on the

Schmidt number used. Also, in this region the variance is highest, with a global maximum for Y_V directly at the surface of the sphere, i.e., at the gas-liquid interface. However, the variance decreases rapidly (by approximately two orders of magnitude!) until it starts to fluctuate in an erratic manner (i.e., in the region $z/d_p > 5$).

The trends with the Schmidt number in Figure 5.3 indicate, that with decreasing diffusion coefficient (i.e., increasing Schmidt number), the filtered concentration in the wake of the bubble (i.e., the total amount of transferred mass) decreases as expected. Also, the scalar variance gets smaller with increasing Sc, suggesting that the generation of scalar variance (i.e., the term g in Eqn. 5.1) is directly proportional to the transferred mass.

The time-averaged variances are shown in Figure 5.4. Also, in these graphs the near wake region characterized by a rapid decrease of scalar variance, as well as a plateau region further away from the interface is visible. This plateau is less pronounced in the low-Reynolds cases (i.e., Re = 50 and Re = 300). It is speculated that this is due to a higher amount of diffusion for the cases with a lower Reynolds number, i.e., a lower Peclet number.

5.3.3 Scaling of Scalar Variance Generation

In order to derive a model for scalar variance generation due to mass transfer, the scaling of the calculated variances far away from the gas-liquid interface (i.e., at a dimensionless distance from the center of the sphere of 5) has been investigated. At this distance the scalar variance is only weakly influenced by the distance to the sphere's center. In Figure 5.5, the logarithm of this variance versus the logarithm of the Schmidt number is plotted. The linear correlation between these two quantities suggests a scaling in the form of

$$Y_V = K \cdot Sc^{-n}.$$ (5.7)

Note, that Y_V in our simulations was dimensionless and scales with the interface concentration squared. Clearly, the simulation results indicate a value for n that is approximately 0.5 for the low-Reynolds-number case (i.e., Re = 50) and between 0.9 and 1.2 for the wake shedding regime (i.e., Re = 300 and Re = 500). Also, the value for K decreases for increasing Reynolds number (i.e., it decreases from $3.0 \cdot 10^{-3}$ to $1.4 \cdot 10^{-3}$ in the range of the studied Reynolds numbers). Thus, it can be assumed that K is some function of the Reynolds number to the power of a negative exponent. This finally leads to a suggested scaling of the variance in the form of:

$$Y_V = A \cdot Re^{-m} \cdot Sc^{-n}$$
(5.8)

Our simulations show that the value for m should be in the order of unity (this value can be easily obtained from a linear regression of ln(K) vs. ln(Re)) and A is a positive constant.
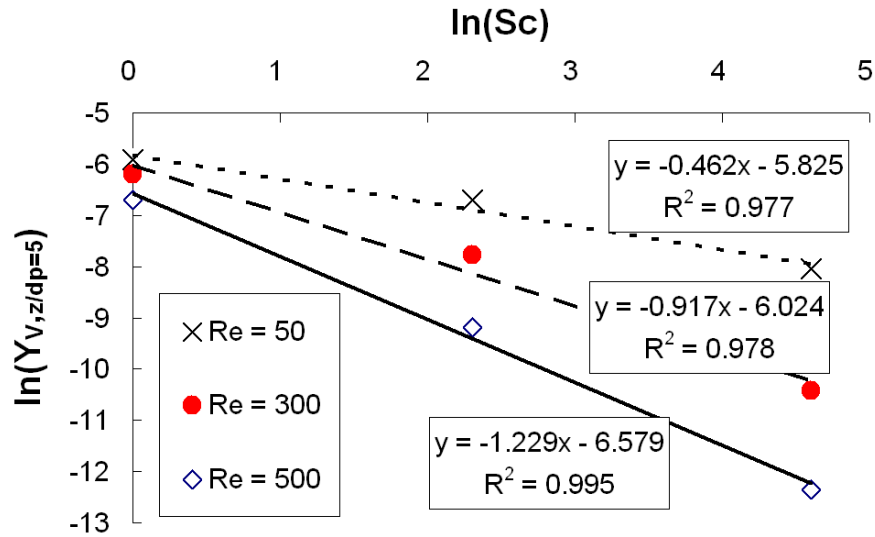
Figure 5.5: Scaling of the scalar variance at $z/d_p = 5$ for different Reynolds numbers vs. the Schmidt number ($\Delta = 3 \cdot d_p$).

The proposed scaling for the variance is similar to the scaling of the Sherwood number and the mean dimensionless concentration in the wake of the bubble. "Mean" hereby refers to a spatially filtered value of the concentration using the filter length Δ. The mean dimensionless concentration in the wake of the bubble can be calculated from

$$\overline{Y} = \frac{\beta \cdot d_p{}^2 \cdot \pi}{U_t \cdot \Delta^2} = Sh \cdot \pi \cdot \left(\frac{\Delta}{d_p} \right)^{-2} \cdot Re^{-1} \cdot Sc^{-1}$$
(5.9)

and depends on the filter width.[b] Here, β, U_t and Sh refer to the mass transfer coefficient, the terminal bubble rise velocity and the Sherwood number, respectively. The Sherwood number is typically expressed as a function of the form:[14]

$$Sh = B + C \cdot Re^{1/2} \cdot Sc^{1/3}.$$
(5.10)

---

[b] This follows from a simple mass balance, i.e., $\overline{Y}$ must be equal to the total mass transfer rate to the liquid phase divided by the total volumetric flow to which the mass is transferred to. The latter has been taken to be equal to the cross section of the box filter, i.e., Δ^2 and the bubble rise velocity U_t.

At high Reynolds numbers, the second part on the right hand side of Eqn. 5.10 is significantly larger than the constant B (typically assumed to be equal to two), and the following overall scaling of the mean concentration in the wake is obtained:

$$\overline{Y} \approx D\left(\frac{\Delta}{d_p}\right) \cdot Re^{-1/2} \cdot Sc^{-2/3} \qquad (5.11)$$

Here, D is a constant that depends on the filter length normalized with the bubble diameter. This expression for the mean dimensionless concentration in the wake is similar to Eqn. 5.8 (i.e., the scaling of the variance in the wake) except for the exponents for Re and Sc. It is therefore concluded, that the dimensionless variance in the wake of the bubble scales with

$$Y_V \approx E\left(\frac{\Delta}{d_p}\right) \cdot \overline{Y}^p, \qquad (5.12)$$

where p is an exponent in the order of two (compare Eqn. 5.8 and 5.11 and the exponents for m and n detailed in the text) and E is a constant that depends on the relative filter length. Hence, the scalar variance in the wake can be calculated with appropriate correlations of the Sherwood number and Eqn. 5.12. The (dimensionless) source term for the scalar variance due to mass transfer can then be calculated using

$$g_{Y_V} = \frac{U_t}{\Delta} \cdot Y_V. \qquad (5.13)$$

This equation is based on the use of a box filter and an identical filter length for the filtering of the concentration field around the single bubble and the coarse-grained simulation (e.g., a Large Eddy Simulation that uses Eqn. 5.1). To obtain Eqn. 5.13, the mean variance in the wake has been multiplied with the volumetric flow rate passing the bubble and divided by the volume of the filtered element (i.e., a box of size Δ). To calculate the dimensional source term for the variance, Eqn. 5.13 has to be multiplied with the squared interfacial concentration.

5.4 Conclusions

In this work our focus was the prediction of the scalar variance generation due to mass transfer in gas-liquid systems. Literature data for this quantity with respect to bubbly flows is scarce. Hence, direct numerical simulations of the flow and species transport around single bubbles were performed to quantify this term. The simulations showed that the variance is

highest directly at the surface of the gas bubble. The rapid decrease of the scalar variance in the wake of the bubble may lead to the conclusion that the scalar variance is small in the bulk of bubble swarms. However, this is only valid for the dissolving component. If liquid-phase reactants have to be mixed into the system, their scalar variance may be significant and the micro-mixing rate may become rate-limiting. Further studies are necessary to quantify this influence.

The behavior of the variance in the wake at low Reynolds numbers is hard to model, since the variance constantly decreases downstream of the bubble. This is because diffusion and the induced fluid motion in the wake leads to a significant dissipation of scalar variance. At higher Reynolds numbers, however, a plateau exists indicating that scalar variance is generated next to the bubble, which is essentially unchanged when the flow has exited the wake region. The theoretical considerations for the scaling of scalar variance far away from the interface show that the (dimensionless) variance decreases with increasing Reynolds and Schmidt number. This is similar to the (well established) scaling of the mean concentration in the wake. The exponents in the proposed scaling of the scalar variance are approximately twice that for the mean concentration. Thus, it is expected, that there is some correlation between the mean concentration and the scalar variance in the wake. However, the filter width impacts the absolute value of the mean and the variance of the concentration field in the wake. Future work is required to quantify this influence in order to reliably calculate the scalar variance generated by mass transfer around single bubbles. Also, the variance upstream of the bubble was always zero in the simulations. The influence of already existing concentration variances in the flow approaching a bubble needs further systematic investigation.

5.5 Abbreviations

DNS   Direct Numerical Simulation

LES   Large Eddy Simulation

PDF   Probability Density Function

5.6 Nomenclature

A, B, C, D, E   constants in correlations

d_p particle (i.e., bubble) diameter [m]

D   molecular diffusion coefficient [m²/s]

D_{eff} effective diffusion coefficient [m²/s]

C_Φ constant

g_{Y_V} source of variance due to mass transfer [1/s]

G^{Box} box filter function in two dimensions [1/m²]

K   constant

m, n, p   exponents in correlations

p'   kinematic pressure [m²/s²]

Re   bubble Reynolds number, $Re = d_p U_t / \nu$

Sc   Schmidt number, $Sc = \nu / D$

Sh   Sherwood number

t   time [s]

u   velocity vector [m/s]

$\bar{\mathbf{u}}$ filtered velocity vector [m/s]

U_t terminal rise velocity [m/s]

Y   molar fraction of a component in the liquid phase

$\bar{Y}$ filtered molar fraction of a component in the liquid phase

Y_V variance of a component in the liquid phase

z   downstream distance from the center of the bubble [m]

Greek letters

β   mass transfer coefficient [m/s]

Δ   filter length [m]

ε_L liquid-phase hold up [m³$_L$/m³$_{tot}$]

ν   kinematic viscosity [m²/s]

τ_Φ turbulence time scale [s]

5.7 References

(1) Bothe D, Kroger M, Alke A, Warnecke HJ. VOF-based simulation of reactive mass transfer across deformable interfaces. Progress in Computational Fluid Dynamics. 2009; 9:325-331.

(2) Darmana D, Deen NG, Kuipers JAM. Detailed 3D modeling of mass transfer processes in two-phase flows with dynamic interfaces. Chemical Engineering & Technology. 2006; 29:1027-1033.

(3) Khinast JG. Impact of 2-D bubble dynamics on the selectivity of fast gas-liquid reactions. AIChE J. 2001; 47:2304-2319.

(4) Onea A, Worner M, Cacuci DG. A qualitative computational study of mass transfer in upward bubble train flow through square and rectangular mini-channels. Chem Eng Sci. 2009; 64:1416-1435.

(5) Radl S, Koynov A, Tryggvason G, Khinast JG. DNS-based Prediction of the Selectivity of Fast Multiphase Reactions: Hydrogenation of Nitroarenes. Chem Eng Sci. 2008; 63:3279-3291.

(6) Radl S, Suzzi D, Khinast JG. Assessment of Micro- and Mesomixing in Bubble Swarms via Simulations. 9th International Conference on Chemical and Process Engineering. Rome, Italy: AIDIC, 2009.

(7) Radl S, Khinast JG. Prediction of mass transfer coefficients in non-Newtonian fermentation media using first-principles methods. Biotechnol Bioeng. 2007; 97:1329-1334.

(8) Radl S, Tryggvason G, Khinast JG. Flow and mass transfer of fully resolved bubbles in non-Newtonian fluids. AIChE J. 2007; 53:1861-1878.

(9) Wegener M, Paschedag AR, Kraume M. Experimental examinations as well as 2D-and 3D simulations of mass transport in single drops with Marangoni convection. Chemie Ingenieur Technik. 2007; 79:73-81.

(10) Wegener M, Eppinger T, Baumler K, Kraume M, Paschedag AR, Bansch E. Transient rise velocity and mass transfer of a single drop with interfacial instabilities-Numerical investigations. Chem Eng Sci. 2009; 64:4835-4845.

(11) Jung RT, Sato T. Numerical simulation of high Schmidt number flow over a droplet by using moving unstructured mesh. J Comput Phys. 2005; 203:221-249.

(12) OpenFoam 1.5 User Guide (www.opencfd.co.uk). OpenCFD Ltd, 2008.

(13) Clift R, Grace JR, Weber ME. Bubbles, Drops, and Particles. Mineola, US: Dover Publications Inc., 2005.

(14) Ranz WE, Marshall WR. Evaporation from Drops .1. Chemical Engineering Progress. 1952; 48:141-146.

(15)   Meneveau C, Katz J. Scale-invariance and turbulence models for large-eddy simulation. Annual Review of Fluid Mechanics. 2000; 32:1-32.

"At the moment there is no method whereby the history of the molecules flowing through an arbitrarily-chosen reactor can be determined and the results formulated in such a way that the output could be predicted for a reaction of known kinetics."

(Peter Victor Danckwerts, 1958)

6

Euler-Lagrange Simulations of Multiphase Flow and Reactive Mixing in Dilute Bubble Swarms[*]

High-fidelity three-dimensional simulations of multiphase flow and mixing in dilute bubble swarms using the Euler-Lagrange simulation approach have been performed. Species transport, as well as complex chemical reactions have been included in the simulations.

It was found that the algebraic SGS model satisfactory predicts experimental data for the mean flow field. The detailed description of multiphase flow developed in our work was used to simulate the time evolution of scalar and reactive mixing in a bubble column. An analysis involving the scale of segregation Φ, a metric that characterizes the mean driving force for mixing, is applied for the first time to multiphase flow. The study shows that Φ is inversely proportional to the bubble diameter at constant gas feed rate, but only a weak function of the gas feed rate. Also, we observe significant differences of mixing metrics in reactive and non-reactive systems.

6.1 Introduction

Reactive multiphase flows can be found in many applications in the chemical, pharmaceutical and biotechnology industries. Typical examples include the Fischer-Tropsch synthesis,[1] catalytic hydrogenations,[2] oxidations,[3] the production of benzoic acid[4] or the aeration of bioreactors, e.g., for the production of penicillin or EPO.[5] However, a detailed mathematical description of these flows is still challenging, since the interaction of mixing, mass transfer and the (bio-)chemical reactions dominates the yield, selectivity or productivity of the reactor, which complicates the design and optimization of such processes. For example, certain cell cultures are highly shear-sensitive and vigorous agitation, while improving mass transfer and mixing, maybe reduce productivity and product quality due to shear-related necrotic and apoptotic effects or due to damage of the target protein. Another well-known example for mixing-sensitive reaction systems of industrial interest are catalytic oxidations using pure oxygen.

In order to study reactive multi-phase flows in detail, experimental and numerical methods have been used in the past. State-of-the-art experimental tools include the use of laser optical methods (laser-Doppler-anemometry, LDA; as well as phase-Doppler-anemometry, PDA) for bubbles up to 1 mm in diameter, as well as tomographic methods and particle image velocimetry (PIV) for systems involving larger bubbles. Using the latter technique it is possible to determine the velocity fields of both phases and to measure the shape and size of individual bubbles using specialized illumination techniques.[6] Such methods are crucial for the model validation of bubbly flows and have encouraged many groups to perform highly detailed numerical simulations of these flows. Also, concentration fields around single bubbles have been measured using the laser-induced fluorescence technique (LIF).[7-10] In these methods, a laser sheet is used to record the instantaneous concentration fields of a dissolving, non-reacting species in the liquid phase. For example, Bork et al.[7] have combined LIF with PIV to develop a novel mass transfer correlation for bubbles with wake shedding. However, all of these studies concentrate on the dissolution of an inert scalar and a direct experimental quantification of chemical reactions in the vicinity of gas-liquid interfaces of bubbly flows has not been reported. The same is true for the direct quantification of scalar mixing within bubble swarms. Experimental studies in literature involve either very simple qualitative experiments using ink (see, e.g., Wiemann[11]) or more quantitative techniques, using radioactive particles (see, e.g., Yang et al.[12]), liquid phases with different temperatures (see, e.g., Lorenz et

al.[13]) or colored solutions together with photometers (see, e.g., Yang et al.[14]). When using these quantitative techniques it is not possible to measure the instantaneous concentration of a tracer substance in the whole flow field but only at distinct locations. Consequently, scalar mixing can be quantified only by integral parameters, e.g., by an axial dispersion coefficient. To the best of our knowledge, the details of (spatially resolved) scalar mixing in a bubble column have not been the focus of experimental studies so far. For the Becker case studied in this work, not even experimental data for scalar mixing in terms of integral parameters (such as a dispersion coefficients) exist.

6.1.1 Computational Analysis of Bubbly Flows

For the computational analysis of bubbly flows different methods have been developed, each of them having different advantages and drawbacks. An overview over the currently available approaches and future challenges can be found in Sundaresan[15], as well as in Koynov and Khinast.[16] Also, Sommerfeld and Decker[17] provide a detailed overview of the subject with a focus on stirred tanks. In analogy to single-phase simulations, a variety of methods can be used to describe turbulent flows in multiphase reactors, including (a) a full resolution of all scales with direct numerical simulations (DNS), (b) the use of a filtered set of the momentum equations via so-called Large Eddy Simulations (LES), and (c) the use of the ensemble-averaged Navier-Stokes equations, either steady or unsteady, often referred to as the Reynolds-Averaged-Navier-Stokes (RANS) approach.

Currently, the most detailed methods allow the analysis of the deformation of individual bubbles, which are here referred to as multiphase direct numerical simulations (MDNS), because they usually involve DNS of all the phases. These techniques include the volume of fluid method (e.g., see the recent work by Kim and Lee[18]), Lagrangian methods (where the grid follows the gas-liquid interface, e.g., Li et al.[19] and Hameed et al.[20]), as well as the front-tracking (FT) method introduced by Unverdi and Tryggvason.[21] The latter method has attracted numerous groups[22-29] to study also mixing effects including chemical reactions. For example Koynov, Khinast and Tryggvason[22] used the FT method for the first time to study reactive bubble swarms (~100 bubbles) with fully-resolved deformable and dynamic interfaces.[22] Earlier work by our group also included heterogeneously catalyzed reactions close to bubbles.[30]

Another approach is the Euler-Euler (EE) method, which treats the involved phases as interpenetrating continua. The advantage of this method is that the number of particles is not

limiting, as there are no particles or bubbles. Hence, the simulation of large-scale reactors becomes feasible. However, the interface between the phases is not resolved and consequently, sophisticated closure models that predict the local bubble size have to be used to correctly describe the interaction of the involved phases. Often, a population balance equation (PBE) needs to be solved in conjunction with mass, momentum and possibly the energy balance, which is computationally demanding. In addition it can cause instabilities in the solution procedure and is still a topic of active research, as breakage and coalescence kernels cannot be predicted from theory alone and remain somewhat of a fitting parameter.[31,32]

The last major approach is the Lagrangian Particle Tracking (LPT) method in which the disperse phase, e.g., the individual bubbles, are tracked in the flow field as point sources. The motion of the continuous phase is solved on an Eulerian frame of reference. Therefore, this approach is often referred to as Euler-Lagrange (EL) approach.[33] It has been first applied to gas-solid flows in the mid 90's.[34,35] For the EL approach direct numerical simulations of the continuous phase, i.e., a full resolution of all length scales (Nierhaus et al.[36]), as well as the filtered Navier-Stokes equations[37] have been reported. One of the first applications of the EL approach for bubbly flows was the work of Delnoij et al.[33] who solved the governing equations on a two-dimensional grid. In the same year Tomiyama et al.[38] reported a similar approach on a three-dimensional grid. The EL approach has been also extended to gassed stirred tanks. A recent example is the work of Arlov et al.[39] However, all of these studies are concerned with the multiphase flow only and do not focus on mixing or chemical reactions (see below) within the gas and/or liquid phase.

Since a full resolution of individual bubbles in a realistic system (there are approximately $1.5 \cdot 10^6$ bubbles/m³ assuming a bubble diameter of 5 mm and a gas hold-up of 10%) is still computationally infeasible, the EL approach has significant potential of becoming the standard method for the detailed analysis of multiphase flow and mixing. This is because the modeling effort is lower compared the EE technique. For example, the change in bubble size due to coalescence and breakage of bubbles can be easily captured directly using the EL approach. In contrast, in the EE approach a separate PBE has to be solved for that purpose.

Nevertheless, several issues need to be addressed in the EL method, including (a) the development of more reliable schemes to map Lagrangian properties onto the Eulerian frame of reference and vice versa,[40] (b) a detailed treatment of bubble-wall and bubble-bubble collisions, (c) sophisticated modeling of the sub-grid-scale velocity fluctuations,[41-43] as well as

(d) the inclusion of coalescence phenomena.[27] In a recent example, Hu and Celik[40] published a LPT study for relatively large individual bubbles. For the so-called "backward coupling" or Lagrange-to-Euler mapping (i.e., the mapping of forces exerted on the liquid phase by the bubbles), they used a novel approach called the "particle-source-in-ball" (PSI-ball) concept. Darmana[27] also used a special approach in which it is possible for bubbles to become larger than individual cells of the Eulerian grid. He considered also the local liquid-phase volume fraction in the momentum equation, i.e., the replacement of the continuous phase by dispersed bubbles. This more advanced treatment of the continuous phase dates back to the work of Delnoij et al.[33] When taking the continuous phase volume fraction into account, the EL approach can also be utilized to study dense bubble swarms, i.e., a high local gas hold-up. To cope with the large number of bubbles in such cases, it is possible to track bubble clusters instead of individual bubbles.[17] Also, coalescence and breakage can be accounted for in the EL approach as discussed in this work.

6.1.2 Mixing and Chemical Reactions

In multiphase reactor, the understanding of the impact of the multiphase flow on the chemical reactions is another import aspect. As chemical reactions usually take place only in the liquid phase or on the surface of a solid catalyst, the correct prediction of mixing in the liquid phase is of great importance.[44] Hence, a quantification of micro-mixing (i.e., mixing on the smallest scales), meso-mixing (i.e., mixing on intermediate scales) and macro-mixing (i.e., mixing on the reactor scale) is required to characterize and predict the performance of the reactor.

During the last years, several researchers have analyzed mixing and chemical reactions in multiphase systems. In the beginning, studies focused mostly on experimental techniques in single-phase systems, e.g., by the use of so-called Bourne reactions[45-48] or the reaction of iodine with tyrosine.[49] Frequently, competing reactions were used which yield different product distributions depending on the efficiency of micro-mixing.[50-52] Recent experimental methods in the field of multiphase mixing also include the tracking of radioactive particles.[53] Furthermore, conductance measurements in simple tracer experiments are still popular to study macro-mixing in bubble column reactors.[54-57] Other methods for the detection of tracers are summarized in the publication of Joshi.[58] However, these experiments provide only an integral picture of macro-mixing in these reactors. Micro- and mesomixing cannot be quantified.

In the area of micro-mixing in bubbly flows, the first computational studies on non-deformable two-dimensional bubbles were reported by Khinast[59] and later extended to fully deformable bubble swarms in complex fluids involving arbitrary chemical reactions.[24-26] Also, it became possible with the aid of massively parallelized computer software to study mass transfer around three-dimensional bubbles.[27] However, this work was limited to cases with unrealistically low Schmidt numbers (Sc = 1) in the continuous phase. In addition, it was shown that the results of these high-fidelity reactive micro-mixing simulations can be described to some extent by simplified models.[24] Also, recent studies of (micro-) mixing of a fluid with granular particles were reported,[60,61] encouraging future work in this area. However, a detailed analysis of mixing including mass transfer has not been reported[60,61] and is also missing in most of the literature dealing with multiphase mixing.

Macro-mixing in bubble column reactors was studied numerically by various researchers using virtual tracer experiments.[62,63] These simulations focus on the analysis of an inert tracer in the liquid phase and hence are not involving the effects of mass transfer and reaction. Also, they are incapable - same as real tracer experiments - to quantify the local distribution of mixing, as well as the temporal fluctuation. Hence, a detailed multiscale quantification of the local distribution of mixing rates cannot be found in literature as of yet.

In summary, there has been significant progress in describing flow and mixing in multiphase systems at the micro and macro scales. These studies focused mainly on an integral measure for mixing (e.g., an axial dispersion coefficient) or were concerned with micro-scale mixing. However, the quantification of mixing on the meso-scale, i.e., on the level of a bubble plume, has not been reported. Furthermore, nearly all of the experiments and simulations reported in literature were concerned with a tracer already dissolved in the liquid phase. Thus, conclusive results for the effect of mass transfer on the distribution of an inert scalar are scarce. An exception is the work of Darmana.[27] However, they did not investigate the effects of the process parameters on mixing and chemical reactions, nor did they model these effects. Consequently, the analysis of mixing involving mass transfer still requires a significant amount of research as systematic studies highlighting the interaction of mass transfer, mixing and chemical reactions in large bubble plumes are rare, especially for meso-scale effects. Even fundamental concepts describing these mesomixing effects and the interaction of mesomixing with the micro- and macro-scales are still absent. Thus, it is the aim of this study is to provide the basis for such a concept.

6.2 Objectives

The objective of this work is to analyze in detail the flow, mixing and the chemical reactions in a bubbly flow, which are encountered in many industrial applications including bubble column reactors and bioreactors. Specifically, it is our goal to:

-   perform validated, state-of-the-art simulations of large bubble swarms (up to 10^5 bubbles) including species transport and chemical reactions based on Large Eddy Simulations (LES),

-   study the numerical aspects of the simulation tool,

-   apply our simulation code to highlight the relative importance of several parameters on inert and reactive mixing in large bubble swarms, and

-   provide novel perspectives for a rigorous modeling of the mixing effects in bubble swarms.

For this purpose, we first present an advanced numerical method for analyzing in detail the multiphase flow and mixing in dilute bubble columns. Subsequently, we employ state-of-the-art tools for the analysis of mixing that we adopt from single-phase mixing studies. Thus, we can present for the first time a detailed picture of multiphase mixing in dilute bubble swarms by means of computer simulations. Also, we are the first that systematically analyze the effect of process parameters on inert and reactive mixing in large bubble swarms. To account for sub-grid-scale reactive mixing, we have incorporated a PDF (probability density function)-based approach. Finally, we focused on the distribution of the scale of segregation in multiphase systems with and without mass transfer. This is a completely new aspect on how to analyze mixing in these complex systems.

6.3 Problem Formulation

6.3.1 Multiphase Flow

In the present work we use an LES-based Euler-Lagrange method to study flow, mixing and reactions in an unstirred bubble column. The momentum balance equations for multiphase flow consist of the filtered incompressible Navier-Stokes equations for the liquid phase and Newton's equation of motion for the disperse phase. The boundary conditions for the filtered

Navier-Stokes equations include the typical conditions for the liquid phase at the wall (no-slip, as well as closures for the sub-grid-scale stress), as well as a perfect-slip condition at the top outlet of the bubble column (to mimic an inviscid gas-phase top layer). The interaction of the liquid phase with the disperse phase is incorporated via source terms in the momentum equation, i.e., we perform a two-way coupling of the involved phases. The initial conditions for the disperse phase, i.e., Newton's equation of motion, consist of specified positions and velocitys at the inlet. At the boundaries we perform an inelastic bounce back of the disperse phase with a coefficient of restitution of 0.9.

Following Darmana[27] the filtered continuity and momentum balance equation for the continuous phase can be written as:

$$\frac{\partial \varepsilon_L}{\partial t} + \nabla \cdot \left(\varepsilon_L \cdot \overline{u} \right) = 0 \tag{6.1}$$

$$\frac{\partial \overline{\varphi}_L}{\partial t} + \nabla \cdot \left(\overline{\varphi}_L \overline{u} \right) = -\varepsilon_L \cdot \nabla \overline{p} - \nabla \cdot \left(\varepsilon_L \cdot \overline{\tau}_L \right) + \varepsilon_L \cdot \rho_L \cdot g + \Phi \tag{6.2}$$

with:

$$\overline{\varphi}_L = \varepsilon_L \cdot \rho_L \cdot \overline{u} \tag{6.3}$$

Here ρ_L is the (constant) liquid density, ε_L is the liquid-phase volume fraction, and $\overline{u}$ is the filtered velocity vector of the liquid phase. Note, that we have neglected the mass transfer between the two phases in the continuity equation Eqn. 6.1 since its contribution is very small. This is due to the fact that we concentrate on dilute bubble swarms, and hence, mass transfer rates for reactive, as well as nonreactive systems are typically negligible compared to the total liquid mass in these systems. In the momentum equation (Eqn. 6.2), $\overline{\varphi}_L$ is the filtered liquid phase mass flux, $\overline{p}$ is the resolved pressure, $\overline{\tau}_L$ is the liquid-phase stress tensor, g is the gravitational acceleration vector and Φ is the volume-specific coupling force exerted by the dispersed phase (see the numerics section of this work).

The liquid stress tensor needs additional modeling. Here we use the eddy viscosity concept and calculate the total stress from an effective viscosity:

$$\overline{\tau}_L = -\mu_{eff,L} \cdot \left[\left(\nabla \overline{u} + \nabla \overline{u}^T \right) - \frac{2}{3} \cdot I \cdot \left(\nabla \cdot \overline{u} \right) \right] \tag{6.4}$$

The effective viscosity is the sum of the molecular and sub-grid-scale viscosity in the liquid phase $\mu_{SGS,L}$

$$\mu_{eff,L} = \mu_L + \mu_{SGS,L}$$ (6.5)

In most of our simulations the turbulent viscosity is calculated from a simple algebraic model, i.e., the standard Smagorinsky model:

$$\mu_{SGS,L} = \rho_L \cdot (C_s \cdot \Delta)^2 \cdot |\overline{S}|$$ (6.6)

Here, C_s is the Smagorinsky constant with a typical value of 0.1, (see Darmana[27]) Δ is the filter length and $|\overline{S}|$ is the magnitude of the filtered strain rate tensor. The filtered strain rate tensor is defined as:

$$\overline{S} = \frac{1}{2} \cdot \left(\nabla \overline{u} + \nabla \overline{u}^T \right)$$ (6.7)

The implementation in our code for the calculation of $\mu_{SGS,L}$ is slightly different from Eqn. 6.6, as we first calculate the sub-grid-scale kinetic energy k from Eqn. 6.8. This implementation enables a separate calculation of k and $\mu_{SGS,L}$ which can be useful for comparison purposes.

$$k = \frac{2 \cdot C_k}{C_e} \cdot \Delta^2 \cdot |\overline{S}|^2$$ (6.8)

In Eqn. 6.8, C_k and C_e are model constants.

Having calculated k, the sub-grid-scale viscosity is calculated from:

$$\mu_{SGS,L} = \rho_L \cdot C_k \cdot \sqrt{k} \cdot \Delta$$ (6.9)

After substituting Eqn. 6.8 in Eqn. 6.9, we recover Eqn. 6.6 with the relation

$$C_S = \left(\frac{2 \cdot C_k^{3}}{C_e} \right)^{1/4}$$ (6.10)

In addition to the algebraic model, we have used a more advanced differential sub-grid-scale model to account for non-resolved turbulent fluctuations. The one-equation model used in this work solves the following differential equation for the sub-grid-scale kinetic energy k:[64]

$$\frac{\partial k}{\partial t} + \nabla \cdot (k\overline{u}) = \nabla \cdot \left(\frac{\mu_{eff,L}}{\rho_L} \cdot \nabla k \right) - \varepsilon - \overline{\tau}_L : \overline{S}$$ (6.11)

Here ε is the sub-grid-scale energy dissipation given by:

$$\varepsilon = \frac{C_\varepsilon \cdot k^{3/2}}{\Delta}$$

(6.12)

The sub-grid-scale viscosity is then calculated according to Eqn. 6.9. When using these algebraic and differential sub-grid-scale models, we exclude the effect of bubble motion on the generation of the sub-grid-scale fluctuations, i.e., so-called bubble induced turbulence (BIT). The influence of BIT on the sub grid scale viscosity could be modeled by using (for example) the model of Sato and Sekoguchi.[65] However, the studies of Deen et al.,[37] as well as of Niceno et al.[66] indicate only marginal effects of BIT on the mean and fluctuating flow field in dilute bubble swarms. Hence, the exclusion of BIT from our simulations is justified and in line with previous work published in that field.[27,40] In our work we use wall functions for the computation of the sub-grid-scale viscosity near the no-slip boundaries. This treatment of the walls can be used for a wide range of dimensionless wall distances, as it incorporates the velocity profile from the laminar, to the buffer and the fully turbulent region.[64] Specifically, we use the following (implicitly-defined) dimensionless velocity profile near the wall, which was initially introduced by Spalding:[67]

$$y^+ = u^+ + \frac{1}{E} \cdot \left[\exp\left[\kappa \cdot u^+\right] - 1 - \kappa \cdot u^+ - \frac{1}{2} \cdot \left(\kappa \cdot u^+\right)^2 - \frac{1}{6} \cdot \left(\kappa \cdot u^+\right)^3 \right]$$

(6.13)

Here, $y^+ = y_0 \cdot u_\tau / \nu$ and $u^+ = \bar{u}_0 / u_\tau$ denote the dimensionless wall distance and the dimensionless velocity profile, respectively. y_0, u_τ, $\bar{u}_0$ and ν are the wall normal distance of the first computational cell near the wall, the friction velocity, the filtered wall parallel velocity in the first computational cell near the wall, and the kinematic velocity of the liquid phase, respectively. In our code we directly insert the definition of the non-dimensional variables y^+ and u^+ in Eqn. 6.13 to obtain a nonlinear equation for u_τ. Using an initial guess for u_τ, we then solve iteratively for the friction velocity using a Newton algorithm. The wall shear stress can then be calculated directly out of u_τ. Details of this procedure can be found in deVilliers.[64]

Newton's equation of motion for each individual bubble is (see Figure 6.1):

$$m_p \cdot \frac{dU}{dt} = F_G + F_p + F_D + F_L + F_A$$

(6.14)

Here m_p is the mass of the particle, i.e., the bubble, $\mathbf{U}$ is the velocity vector of the bubble, $\mathbf{F_G}$ is the gravity force, $\mathbf{F_p}$ is the force due to a pressure gradient, $\mathbf{F_D}$ is the drag force, $\mathbf{F_L}$ is the lift

and $\mathbf{F_A}$ is the added-mass force. The models for each of these forces are summarized in Table 6.1.

Force	Model Equation
$\mathbf{F_G}$	$m_p \cdot \boldsymbol{g}$
$\mathbf{F_P}$	$-V_p \cdot \nabla \overline{p}$
$\mathbf{F_D}$	$-C_D \cdot \dfrac{1}{2}\rho_L \cdot \left|\boldsymbol{U_{rel}}\right| \cdot \boldsymbol{U_{rel}} \cdot A_{cross},$ $\boldsymbol{U_{rel}} = \boldsymbol{U} - (\overline{\boldsymbol{u}} + \boldsymbol{u}_{fluct}),$ $C_D = \begin{cases} 24\big/Re_p \cdot \left(1 + 0.15 \cdot Re_p{}^{0.687}\right), Re_p \leq 800 \\ 0.44, Re_p > 800 \end{cases}$ $Re_p = \dfrac{\left|\boldsymbol{U_{rel}}\right| \cdot d_p \cdot \rho_L}{\mu_L}$
$\mathbf{F_L}$	$-C_L \cdot \rho_L \cdot V_p \cdot \boldsymbol{U_{rel}} \times \boldsymbol{\omega}, \ \boldsymbol{\omega} = \nabla \times \overline{\boldsymbol{u}}$
$\mathbf{F_A}$	$-C_A \cdot \rho_L \cdot V_p \cdot \dfrac{d}{dt}\boldsymbol{U_{rel}}$

Table 6.1: Force models used for the Lagrangian particle tracking.
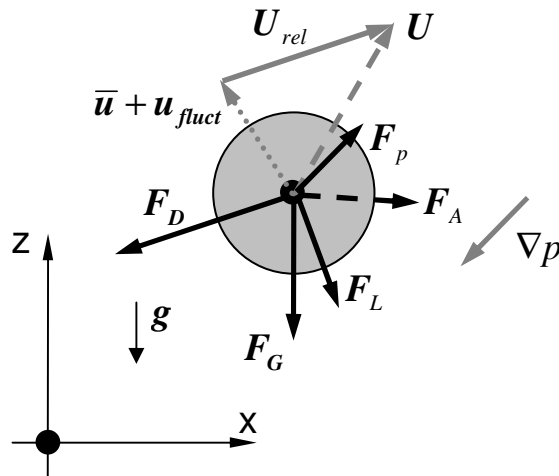
Figure 6.1: Forces acting on a particle.

Throughout our work we assume that the spin of the bubble is equal to the fluid spin surrounding the bubble. This is justified by the very low density of the gas inside the bubble

resulting in a negligibly small moment of inertia of the bubble. Thus, we do not need to solve the conservation equation for rotational momentum, hence saving computation time and memory. In our work we use the standard drag curve[68] for a rigid sphere to account for the drag forces the bubble experiences. This is thought to represent the conditions in experimental systems (e.g. that of Becker[69]) reported in literature best, since already small amounts of contaminations in the liquid phase cause bubbles to behave like rigid spheres.

The model used for the lift force dates back to the PhD thesis of Auton[70] and takes into account forces due to velocity gradients, i.e., vorticity, in the liquid phase. This model is valid for homogenous bubble flows, i.e., for cases where both bubble radius and liquid-phase vorticity are small.[33,71] It is well established for Euler-Lagrange modeling of gas-liquid flows (see for example Darmana[27]). Note that we neglect Magnus lift forces as we already assumed identical rotation rates of the bubbles and the surrounding liquid. The model for the added mass force was adapted from Hu and Celik[40] and is suitable for describing this type of forces in dilute bubble swarms. The lift and added mass coefficient were chosen as C_L=0.53 (based on Auton[70]) and C_A=0.5 (based on Hu and Celik[40]), respectively. In our work we have neglected the Basset history forces, since it has been shown by both simulations,[72] as well as experiments[73] that it is negligibly small in the flow of small bubbles around 1 mm. In Eqn. 6.14 "d/dt" refers to the substantial derivative along the particle trajectory. More details on the procedures of how to obtain the values of relevant variables at the bubble position are detailed in the numerics section (i.e., Chapter 6.4) of this work.

6.3.2 Species Transport

The species conservation equation for species i in the liquid phase is:

$$\frac{\partial\left(\varepsilon_L \cdot \overline{Y_i}\right)}{\partial t} + \nabla \cdot \left(\varepsilon_L \cdot \overline{\boldsymbol{u}}\,\overline{Y_i}\right) = \nabla \cdot \left(\varepsilon_L \cdot D_{eff,i} \cdot \nabla \overline{Y_i}\right) + \Phi_{\dot{N}_i} + \varepsilon_L \cdot \sum_j \nu_{i,j} \cdot r_j + \overline{Y_i} \cdot \frac{\partial\left(\varepsilon_{L,mean}\right)}{\partial t} \qquad (6.15)$$

$$D_{eff,i} = D_i + \frac{\mu_{eff,L}}{\rho_L \cdot Sc_{SGS}} \qquad (6.16)$$

Here $\overline{Y_i}$ is the filtered concentration of species i in the liquid phase, D_i is the molecular diffusion coefficient, and Sc_{SGS} is the sub-grid-scale Schmidt number. The last term in Eqn. 6.15 accounts for the artificial addition/removal of the liquid phase to ensure the overall conservation of the two-phase mixture in the computational domain (refer to the numerics section, i.e., Chapter 6.4, for more details). Furthermore, $\nu_{i,j}$ is the stoichiometric coefficient of

reactant i in the homogenous liquid-phase reaction j, and r_j is the reaction rate of reaction j. A value of $Sc_{SGS} = 0.7$ is used in most of the simulations performed in this work, as this value is frequently reported in numerous computational studies on scalar mixing. However, there is significant discussion regarding the value of the sub-grid-scale Schmidt number for LES depending on the flow situation. Unfortunately, LES studies investigating this parameter are scarce. For example, a value of $Sc_{SGS} = 0.5$ has been suggested by Tominaga and Stathopoulos[74]. Others used the molecular Schmidt number (Darmana,[27] as well as Feng et al.[75]) or suggested $Sc_{SGS} = 0.4$ (Fox[76]). Consequently, we have investigated the impact of Sc_{SGS} on our calculations for mixing (see the results section, Chapter 6.5).

The volumetric source term $\Phi_{\dot{N}_i}$ is related to the mass transfer rate from the bubble swarm according to

$$\Phi_{\dot{N}_i} = \frac{\partial \dot{N}_i}{\partial V}. \qquad (6.17)$$

Here ∂V is the differential volume on the Eulerian grid and $\partial \dot{N}_i$ is the differential mass transfer rate from the disperse phase to this differential volume. The differential mass transfer rate $\partial \dot{N}_i$ depends on the local properties of the surrounding liquid. It can be calculated by the sum over all particles in the differential volume ∂V:

$$\partial \dot{N}_i = \sum_z \partial A_{p,z} \cdot \beta_z \left(\text{Re}_{p,z}, Sc_i \right) \cdot \left(Y_{eq,i} - \overline{Y}_{amb,i,z} \right) \qquad (6.18)$$

Here z is the particle index of all particles in the volume ∂V, $\partial A_{p,z}$ is the interfacial area of particle z in the volume ∂V, β_z is the mass transfer coefficient of particle z, $\text{Re}_{p,z}$ is the particle Reynolds number of particle z, $Y_{eq,i}$ is the equilibrium concentration of species i at the gas-liquid interface and $\overline{Y}_{amb,i,z}$ is the ambient concentration of species i near particle z in the liquid phase.

For spherical particles (i.e., the assumption in our work), the mass transfer term simplifies to:

$$\partial A_{p,z} \cdot \beta_z \left(\text{Re}_{p,z}, Sc_i \right) \cdot \left(Y_{eq,i} - \overline{Y}_{amb,i,z} \right) = d_{p,z} \cdot \pi \cdot D_i \cdot Sh_{i,z} \left(\text{Re}_{p,z}, Sc_i \right) \cdot \left(Y_{eq,i} - \overline{Y}_{amb,i,z} \right) \qquad (6.19)$$

when assuming that the total interfacial area of particle z is in the volume ∂V, i.e., $\partial A_{p,z} = A_{p,z}$. The standard definition[77] of the Sherwood number $Sh_{i,z}$ has been used in this work.

6.3.3 Basic Reaction Model

We have implemented a reaction model involving j independent reactions. The reaction kinetics of each of these reactions are modeled as Michaelis-Menten kinetics, i.e.,

$$r_j = k_j \cdot \prod_k \frac{\overline{Y_k}^{e_{kj}}}{K_{kj} + \overline{Y_k}^{E_{kj}}} \qquad (6.20)$$

Here k_j is the rate constant of reaction j, k is the running index for all species, e_{kj} and E_{kj} are the reaction exponents of species k in reaction j and K_{kj} is a reaction constant for species k in reaction j. With this reaction model we are able to study complex reaction networks with arbitrary order of reaction, which are typical for biochemical reactions. As we use only filtered concentrations without a closure for small scale mixing in Eqn. 6.20, we do not take micro-mixing effects stemming from the non-linearity of the reactions into account.[78,79] This assumption is justified, as long as the characteristic reaction time is larger than the micro mixing time, i.e., the time it takes for concentration variances on the sub grid scale to vanish. For faster reactions, the more advanced methodologies presented in Chapter 6.3.4 have to be adopted.

6.3.4 The Effect of Fast Reactions

The focus will be on a film model for fast reactions near the gas-liquid interface, as well as on the micro-mixing effects for liquid-phase reactions. A validation of our approach to account for micro-mixing effects is presented based on already published experimental data, as well as simulation results from literature.[78,80]

i)   Film Model

A detailed analysis of fast chemical reactions near a dynamic gas-liquid interface is challenging due to the interaction of mass transfer, multiphase flow and reactions. Furthermore, steep concentration gradients develop near the interface due to the typically high Schmidt numbers of the dissolving species in the liquid phase. Hence, a simplified model for the reaction-convection-diffusion problem near the gas-liquid interface has to be used. For example, the film or penetration theory can be used for this purpose. In our work we use a approach similar to the one by Kenig und Gorak[81]. Although the approach of Kenig and Gorak is in use for several years, it has not been combined with detailed simulations of the continuous phase. However, this approach is well suited to overcome the scale-gap between the reactions near the gas liquid interphase and the mixing on the equipment scale. A principal sketch of how a

film model can be used to couple different scales is provided in Figure 6.2. In this sketch a bubble column is considered, which is discretized using a 3D finite-volume (FV) approach.
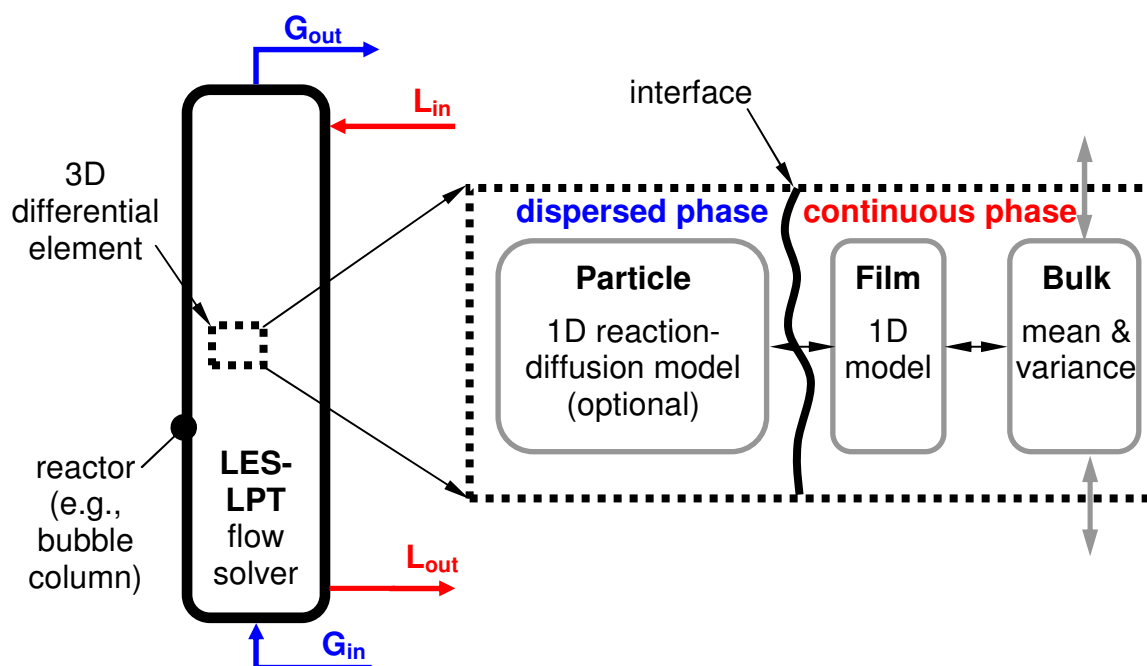
Figure 6.2: Interface model for dispersed-flow multiphase reactors (red: continuous phase, blue: dispersed phase).

The transport equations in the reactor can be solved, e.g., using the LES method together with Lagrangian particle tracking (LPT) for the dispersed phase. A species transport solver can be coupled with the LES to obtain the local distribution of mean and sub-grid-scale properties in the bulk of the continuous phase. Sub-grid-scale properties may be the sub-grid-scale viscosity or the variance of the concentration in the bulk, as described below. Next to the interface, see Figure 6.2 right, a one-dimensional film model is proposed to model reactions. This is necessary, as it would be extremely demanding to resolve the concentration boundary layer in the vicinity of each particle. Furthermore, species transport inside the tracked particle may be accounted for. In the current work, we have not taken into account intra-particle species transport and consequently have assumed a constant concentration of the dispersed phase. This assumption may be justified in the case of pure gases and if exchange rates are low. In all other cases, depletion (or accumulation) of the transferring species in the dispersed phase has to be accounted for.

In our previous work on the hydrogenation of nitroarenes (see Chapter 4) it has already been shown that the selectivity of a two-step reaction can be qualitatively predicted using the film theory.[24] However, for a quantitative prediction DNS has to be used, because the complex

flow around bubbles, such as recirculation and vortex shedding, significantly changes the concentration distribution in the wake of the bubbles. Therefore, a calibration of the film theory results via DNS results is proposed here. To model the accumulation of reactants near the gas-liquid interface, an additional parameter has to be introduced. This can be done, for example by replacing the diffusion coefficient of certain reactants with an effective diffusion constant D_{eff}. This effective diffusion is smaller than the molecular diffusion coefficient if an accumulation of the reactant near the gas-liquid interface occurs. It is larger if the reactant is preferentially removed from the gas-liquid interface. Thus, the species transport in the small-scale flow behind the bubble is modeled with a reduced or accelerated diffusive transport in the film. The advantage of such an approach is that the influence of micro-mixing, introduced, e.g., by vortex shedding, near the gas-liquid interface can be taken into account in more coarse grained simulations. The selection of the reactant to be used for fitting the DNS data will depend on the reaction network to be studied. Thus, calibration has to be done individually for each reaction network. It is speculated, however, that the effective diffusion coefficients for certain small-scale flow situations, e.g., recirculation behind the bubble, will be similar for different reaction networks. This needs, however, proof in future work dealing with a wide range of different reaction networks.
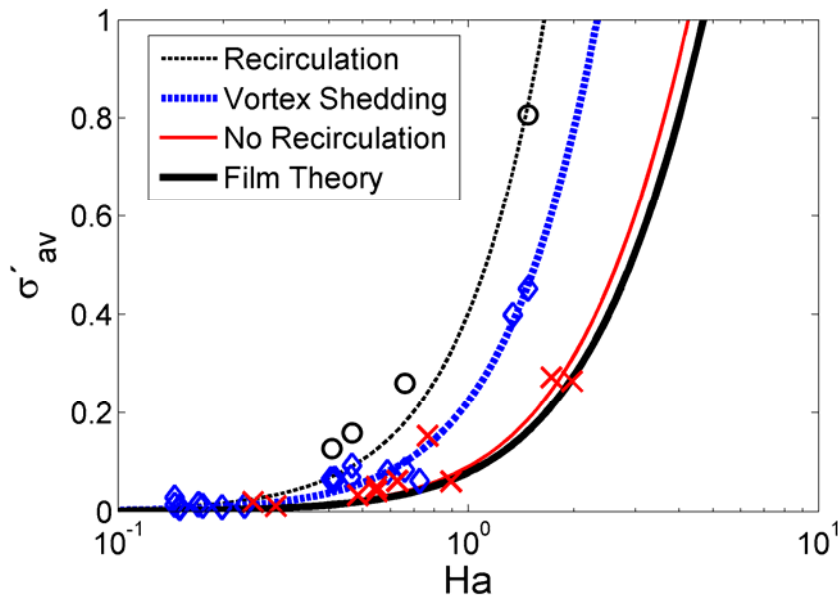
Figure 6.3: Differential interface selectivity [%] vs. Hatta number for various Reynolds numbers resulting in different flow regimes behind the bubble (symbols represent results of DNS, lines are results obtained via film theory. The data is valid for a Schmidt number between 10 and 50. Details of the chemical reaction network are discussed in Chapter 4).

In Figure 6.3, results from DNS[24] are compared with such a calibrated film theory. Specifically, the hydrogenation of nitroarenes was investigated in depth, which basically is a two-step consecutive reaction. In this reaction hydrogen can react with a liquid-phase reactant (species A, the nitroarene) to form an intermediate product R (i.e., hydroxylamine). In a second reaction, hydroxylamine can react with hydrogen to form the final product S (i.e., an arylamine). Details on the reaction mechanism and the physical properties can be found in Chapter 4. In order to fit the DNS data, we have adjusted the effective diffusion constant D_{eff} of the intermediate product (i.e., a hydroxylamine) for the various bubble flow regimes. The film model (i.e., assuming steady-state diffusion in a stagnant layer near the interface) has the basic form:

$$0 = D_i \cdot \frac{\partial^2 c_i}{\partial x^2} + \sum_j \nu_{ij} r_j \qquad (6.21)$$

with the appropriate boundary conditions at the gas-liquid interface, as well as at the film-bulk interface. Here, D_i is the diffusion coefficient of species i, c_i is the concentration of species i, x is the film coordinate, ν_{ij} is the stoichiometric coefficient of species i in reaction j, and r_j is the reaction rate of reaction j. The film model is evaluated with non-equal diffusion coefficients and the effective diffusion constant for the intermediate product R is adjusted to fit our DNS result. The selection of the intermediate product R as the reactant with a fitted effective diffusion coefficient is motivated by the fact, that its accumulation near the gas-liquid interface has a strong influence on the selectivity of the reaction. Thus, a high concentration of R near the interface directly causes an acceleration of the second reaction and consequently a shift in the selectivity of the reaction network.

Consequently, in the case of (i) no recirculation, an effective diffusion constant of $0.87\,D$ is obtained, (ii) for the vortex shedding regime the coefficient is $0.35\,D$, and (iii) for the case of a closed recirculation zone $D_{eff} = 0.20\,D$. Here, D is the molecular diffusion coefficient, which has been taken as constant and is identical for all involved species. Evaluation of the film equations can be easily done using a numerical boundary-value solver, as well as a simple least-square algorithm in MATLAB®.[82] In Figure 6.3 the differential selectivity σ' [%] towards the final product of a hydrogenation reaction is plotted as a function of the Hatta number Ha. These quantities are defined as:

$$\sigma' = \frac{r_2}{r_1} \cdot 100\%$$

(6.22)

$$Ha = \sqrt{k_1 \cdot D} \, / \, k_L$$

(6.23)

Here, r_1 and r_2 are the net reaction rates of reaction 1 and 2 in the film, respectively. These two quantities must be equal to the net product fluxes out of the film, since the formation of the products must be balanced with their transport out of the film. The latter is given by Fick's law of diffusion, and hence, it is proportional to the gradient of the concentration field and the diffusion coefficient. Thus, the net reaction rates can be calculated easily after the film model equations have been solved. k_1 and k_L are the reaction rate constant, and the liquid-phase mass transfer coefficient without chemical reaction, respectively. The latter coefficient determines the thickness δ of the film via the fundamental assumption of the film model, i.e., $k_L = D / \delta$. Clearly, Figure 6.3 shows that the film model with a fitted effective diffusion coefficient predicts the DNS results reasonably well. This indicates that even when a single fitting-parameter for the film model is used, correct quantitative prediction of the selectivity of fast reactions near the gas-liquid interphase can be achieved. In addition, mass transfer enhancement factors can be obtained from such a model, which is well documented in the literature.[83]
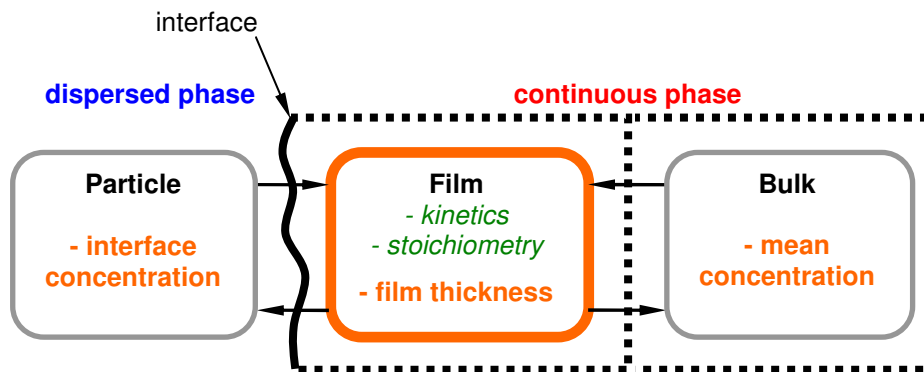
Figure 6.4: Input and output of the film model (green text: constants, orange text: input variables of the film model).

By using the proposed film model, a database of the outcome of a fast reaction near the gas-liquid interphase can be created. This database needs to reflect the influence of various process parameters on the outcome of the reactions in the film, e.g., the gradient of each individual species at the film-bulk interface. The general structure of the database, as well as the input variables affecting the reactions in the film has been illustrated in Figure 6.4. Clearly,

the interface concentration $c_{Int,i}$, as well as the concentration in the bulk phase $c_{Bulk,i}$, will influence the reaction in the film. Also, the actual flow around each individual particle has to be taken into account as it affects the film model via the film thickness that has to be calculated for each particle as well. This can be done using well-known Sherwood correlations (e.g., Bird et al.[77]) to calculate the actual liquid-side mass transfer coefficient k_L. In addition, reaction rate constants and the stoichiometry of the reaction influence the effective reaction rate. The most important results of the film model are the gradients of each species at the film-bulk interface. These gradients determine the species transfer into the bulk, and take into account the reactions in the film. In summary, there are (2·N+1) input variables to the film model, i.e., $c_{Int,i}$, $c_{Bulk,i}$ and k_L, as well as N output variables, i.e., the N fluxes. Here N denotes the total number of species in the reaction system.
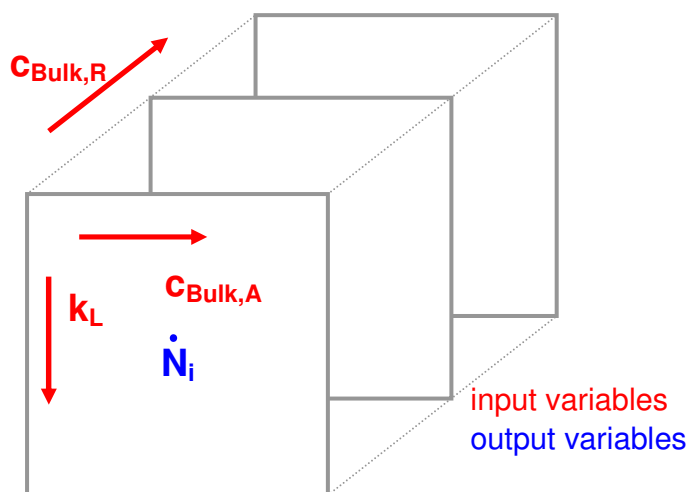
Figure 6.5: Data arrangement in the film model data base for the hydrogenation of nitroarenes.

In order to illustrate such a film-model database, the hydrogenation of nitroarenes is again used as a model case. In this special case, only the interface concentration of hydrogen, the bulk concentrations of the liquid-phase reactant A and that of the intermediate product R, as well as the mass transfer rate k_L influence the reactions in the film. In addition, the interface concentration of hydrogen $c_{Int,H2}$ can be assumed to be constant, since hydrogenation reactors are typically operated using pure hydrogen. Thus, the interface concentration of hydrogen can be seen as a known parameter for a certain simulation case and the film-model database can be built based on $c_{Int,H2} =$ const. Consequently, the input parameters reduce to a set of three variables as shown in Figure 6.5. The output consists of four variables $\dot{N}_i$, which are the fluxes of hydrogen, the bulk-phase reactant A and the two products R and S at the film-bulk

interface. Therefore, the film model database consists of four three-dimensional matrices, one matrix for each output. The species transfer into the bulk phase can be evaluated easily during the simulation, e.g., by trilinear interpolation from these matrices. In Figure 6.6, the gradient of species R (i.e., the intermediate product) is plotted as a function of the mass transfer rate and the interface concentration of hydrogen. In this plot the bulk concentrations of species A (the liquid-phase reactant), as well as species R, are fixed. As can be seen from Figure 6.6, the gradient of R, and hence its transfer rate into the bulk, depends almost linearly on the interface concentration of H_2. This is expected, since R is formed from the reaction of A with H_2. However, with increasing mass transfer rate k_L, the formation of R decreases. This is because the relative time scales of reaction and mass transfer (i.e., the Hatta number) becomes smaller, causing more unreacted H_2 to reach the bulk phase.
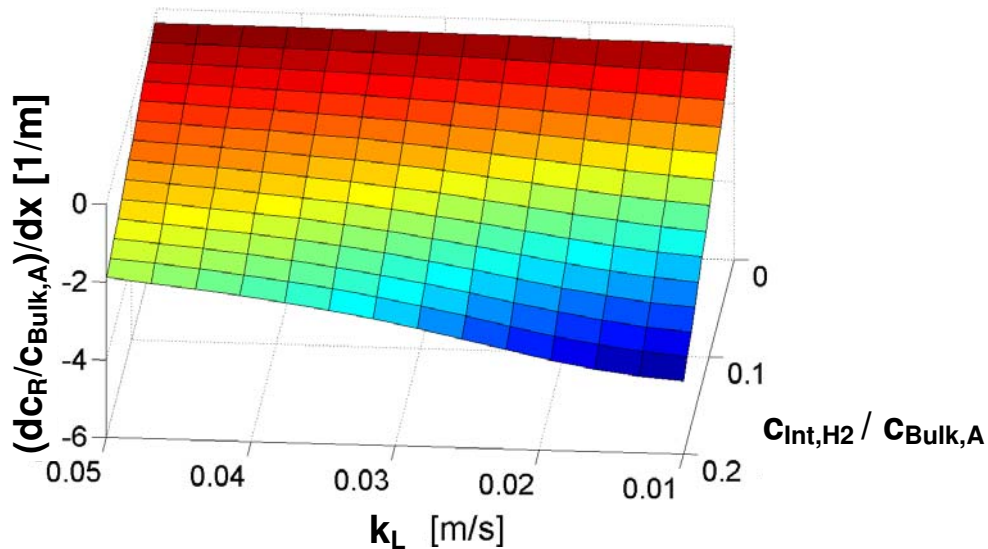
Figure 6.6: Gradient of species R (intermediate product) at the film-bulk interface as a function of the mass transfer coefficient k_L and the interface concentration of hydrogen (the dimensionless bulk concentration of species A and R are 1 and 0, respectively. Also, the concentration of hydrogen is made dimensionless using the bulk concentration of species A).

The film model discussed in this work may be used in a next step to predict the outcome of fast reactions near the interface in a large system, e.g., a whole reactor. Such a prediction can then be based on coarse-grained multiphase flow simulations, such as Large Eddy Simulations (LES) or simulations based on the Reynolds-Averaged-Navier Stokes (RANS) equations. In a next step, validation of such predictions can be made using experimental data. The validation of the (calibrated) film model with experimental data is, however, extremely difficult, since the net reaction rate in the film around a single bubble would have to be measured. Such a sophisticated experimental study was not part of this work. In order to continue our analysis

of fast reactions in multiphase systems, we decided to separate the analysis of the film model from the analysis of fast reactions in the liquid bulk phase. In the next paragraph, we focus on the description of the latter and the aspects of its implementation. The analysis of liquid-phase reactive mixing, a different reaction network was selected, because relevant data for the hydrogenation of nitroarenes are not available. However, the micro-mixing methodology presented in the next chapter can be applied also to industrially-relevant hydrogenation reactions.

ii)   Micro-mixing in the Liquid Phase

Micro-mixing refers to mixing down to the molecular scale, such that reactions can occur. If fast reactions occur at a time scale of the same order or smaller than the time-scale of micro-mixing, mixing effects may delay the reaction. Often, reactions are slow compared to the micro-mixing rate, such that the description of the latter is not necessary. However, micro-mixing can be the controlling step for the yield and selectivity of reactions.

In principal, micro-mixing processes can be fully predicted by momentum and species transport equations using the intrinsic kinetics for the chemical reaction. Examples of such an approach include the studies conducted by us for reactions near gas-liquid interfaces.[24,59,84] However, this approach requires extremely high spatial and temporal resolution for higher Schmidt numbers typical of liquid-phase systems. Thus, the outcome of reactions on the equipment scale cannot be predicted using a direct approach. Instead, one has to characterize the concentration distribution on a sub-grid-scale level by linking it with the known properties on the grid level. This can be done, e.g., using a probability density function (PDF) of the local concentration. As will be clear later, the PDF of an inert tracer is often sufficient to predict mixing effects in reactive systems.

To analyze inert sub-grid-scale mixing in our simulations, additional transport equations need to be solved. For a PDF characterized with a mean and a variance, only one additional equation, i.e., that for the variance $Y_{V,i}$ of the scalar Y_i, has to be solved. Here "mean" refers to the explicitly know quantity (i.e., the filtered value) on the computational grid. The transport equation of the filtered concentration $\overline{Y_i}$ has been already mentioned (see Eqn. 6.15).

The variance $Y_{V,i}$ is defined as $Y_{V,i} = \overline{Y_i Y_i} - \overline{Y_i} \cdot \overline{Y_i}$ and its transport equation for the liquid phase in a multiphase system is shown in Eqn. 6.24. This equation is similar to the one presented by Jaberi et al.,[85] as well as that of Colucci et al.[86] It includes the accumulation, the convective and

diffusive transport of scalar variance (left-hand side, as well as first term on the right-hand side of 6.26), as well as generation and dissipation of scalar variance in the liquid phase (term two and three on the right-hand side of Eqn. 6.24). We have used the IEM (interaction by exchange with the mean) closure as suggested by Colucci et al.[86] For the dissipation term the turbulent time scale has been defined as $\tau_\Phi = \Delta^2 / D_{eff,i}$. C_Φ is a constant characterizing the ratio of the characteristic time for the decay of velocity fluctuations to that for the decay of concentration fluctuations. The most frequently used choice for LES is $C_\Phi = 2$ (Raman et al.,[87]) and was also used in this work. Note, that the choice of C_Φ is critical for LES and future studies are required to investigate the effects on the predictability of our model. In order to model multiphase systems, we accounted for the liquid-phase hold-up ε_L, as well as for sources due to mass transfer (i.e., the last term on the RHS of Eqn. 6.24) in the transport equation of the scalar variance. The source of variance due to the transferred mass can be modeled using a simple model involving an adjustable parameter α, which is motivated by Pera et al.[88] Another model for this source term has been proposed in Chapter 5.

$$
\frac{\partial(\varepsilon_L \cdot Y_{V,i})}{\partial t} + \nabla \cdot (\varepsilon_L \cdot \overline{\mathbf{u}} Y_{V,i}) = \nabla \cdot (\varepsilon_L \cdot D_{eff,i} \cdot \nabla Y_{V,i})
$$
$$
+ 2 \cdot \varepsilon_L \cdot D_{eff,i} \cdot \nabla \overline{Y}_i \cdot \nabla \overline{Y}_i - 2 \cdot \varepsilon_L \cdot \frac{C_\Phi}{\tau_\Phi} \cdot Y_{V,i} + 2 \cdot \alpha \cdot Y_{V,i} \cdot \frac{\Phi_{\dot{N}_i}}{\overline{Y}_i}
$$

$$
\tag{6.24}
$$

$$
\tau_\Phi = \frac{\Delta^2}{D_{eff,i}} \tag{6.25}
$$

More sophisticated approaches exist in literature to describe the production and decay of the sub-grid-scale variance. For example, Baldyga and Orchiuch[89] split the variance into three parts, i.e., the variance caused by the (i) inertial-convective, (ii) viscous-convective and (iii) viscous-diffusive subrange of the turbulence spectrum. This approach has been used for the RANS-based simulations in Lindenberg et al.[79] The transfer of this sophisticated approach to LES will need significant adaptations, since LES only resolves some part of the turbulence spectrum. Such an adaptation has been excluded from the current study.

iii) Coupling Fast Reactions and Micro Mixing

In order to account for fast reactions in the liquid phase, a presumed PDF method is used for the LES. Marchisio[78] showed that a presumed PDF method can be used in principle for a parallel-competitive reaction network with one instantaneous reaction in LES. Marchisio used

in total 5 additional equations to characterize the PDF of the sub-grid-scale variables based on the DQMOM (direct quadrature method of moments)-IEM method. This is a computationally expensive approach. Also, the inclusion of source terms in the scalar variance equation, e.g., due to mass transfer, are not straight forward in this method. Hence, we do not follow his computational strategy, but rather rely on the classical approach that has been demonstrated by Lindenberg et al.[79] However, in contrast to the latter work, a pre-calculated look-up table is used in order to calculate the local reaction rates. This should enhance the simulation speed significantly compared to the approach used by Lindenberg et al.,[79] where a complex integral has to be solved during the simulation. Thus, the approach presented here is suitable for large-scale LES with a highly detailed resolution of the flow dynamics. In summary, the outcome of fast chemical reactions is computed by solving the transport equations for the filtered mixture fraction $\overline{\xi}$, the mixture fraction variance ξ_V and a reactive scalar D. The source term for the reactive scalar is, as mentioned before, explicitly calculated from a look-up table.

The model reaction system is the parallel-competitive reaction between acid-base neutralization (denoted as species A and B, respectively) and the hydrolysis of 2-2-di-methoxy-propane (DMP, denoted here as species D):

$$A + B \xrightarrow{k_1} S \tag{6.26}$$

$$A + D \xrightarrow{k_2} A + P_1 + 2 \cdot P_2 \tag{6.27}$$

Here, S, P_1 and P_2 are water, acetone and methanol, respectively. This reaction is typically carried out in an aqueous solution with 25w% ethanol as solvent. S, P_1 and P_2 do not affect the reactions, since both reactions are assumed to be irreversible. The first reaction is assumed to be instantaneous, i.e., $k_1 \rightarrow \infty$. This has consequences for the mathematical treatment of this reaction, which is discussed further below. For the second reaction we assume first order with respect to both reactants:

$$r_2 = k_2 \cdot Y_A \cdot Y_D \tag{6.28}$$

with a reaction rate constant for a temperature range between 298 and 313 K, a base concentration between 100 and 1,200 mol/m³, as well as an acid and DMP concentration between 25 and 1,333 mol/m³ of:[90]

$$k_2 = 7.32 \cdot 10^7 \cdot \exp[-5556/T] \cdot 10^{0.05434 + 7.07 \cdot 10^{-5} \cdot Y_A} \tag{6.29}$$

The second reaction is still fast with a characteristic reaction time scale in the order of 10 ms, depending on the acid and DMP concentration. In order to close the reaction term properly, Eqn. 6.28 can be rewritten using filtered quantities:

$$\bar{r}_2 = k_2 \cdot \overline{Y_A \cdot Y_D} = k_2 \cdot \left(\overline{Y_A} \cdot \overline{Y_D} + \overline{Y_A' Y_D'} \right) \qquad (6.30)$$

The closure requires an expression for the last term in Eqn. 6.30, i.e., for the mean covariances between species A and D. One approach could be solving the transport equations for the scalar covariances itself. This, however, leads to a closure problem for the chemical source term in the scalar-covariance transport equation. Simpler closure models attempt to relate the covariances of the reactive scalars to the variance of the mixture fraction ξ_V (see, e.g., Fox[76]). This approach is taken in our work.

As already discussed, the first reaction is assumed to be instantaneous, i.e., species A and B cannot coexist at a certain location. This information can be used to replace these two species concentrations with a single, dimensionless variable Y_I, as shown by Lindenberg et al.[79] Here, the difference between species A and B is chosen, as this will yield a variable that behaves like a non-reacting tracer, because A and B are consumed at exactly the same rate (note that there is no net consumption of A in the reaction with DMP) and an identical transport diffusion coefficient is assumed. If this difference is normalized by the inlet concentration of species A, i.e., $Y_{A,0}$, the following dimensionless scalar Y_I is obtained:

$$Y_I = \frac{Y_A - Y_B}{Y_{A,0}} \qquad (6.31)$$

As already noted, Y_I can be represented by a non-reacting, thus inert, tracer, which is called the mixture fraction ξ.[76] The transport equation of the filtered mixture fraction in a multiphase system is:

$$\frac{\partial \left(\varepsilon_L \cdot \bar{\xi} \right)}{\partial t} + \nabla \cdot \left(\varepsilon_L \cdot \bar{\mathbf{u}} \bar{\xi} \right) = \nabla \cdot \left(\varepsilon_L \cdot D_{eff,i} \cdot \nabla \bar{\xi} \right) + \bar{\xi} \cdot \frac{\partial \left(\varepsilon_{L,mean} \right)}{\partial t} \qquad (6.32)$$

in analogy to that of an inert species. Similar to Lindenberg et al.,[79] the variable Y_I is expressed by the mixture fraction ξ using a linear relationship:

$$Y_I = \xi \cdot (1 + \beta) - \beta, \qquad (6.33)$$

with the constant:

$$\beta = \frac{Y_{B,0}}{Y_{A,0}} \qquad (6.34)$$

Now, the fact that species A and B cannot coexist is used once again. Thus, in case we have an excess of acid (i.e., Y_I is positive, see Eqn. 6.31), the concentration of base is zero and that of the acid is equal to the difference between the amount of acid and base (see Eqn. 6.35). In case of an excess of base (i.e., Y_I is negative), the concentration of species A is zero and species B can be calculated from Eqn. 6.36.

$$Y_A = \frac{|Y_I| + Y_I}{2} \cdot Y_{A,0} \qquad (6.35)$$

$$Y_B = \frac{|Y_I| - Y_I}{2} \cdot Y_{A,0} \qquad (6.36)$$

For example, at the acid inlet (i.e., the inlet where $Y_A = Y_{A,0}$),

$$Y_I = \frac{Y_A - Y_B}{Y_{A,0}} = \frac{Y_{A,0} - 0}{Y_{A,0}} = 1 \qquad (6.37)$$

Thus, this correctly describes the boundary conditions $Y_A = Y_{A,0}$ and $Y_B = 0$. At the base inlet Y_I becomes:

$$Y_I = \frac{Y_A - Y_B}{Y_{A,0}} = \frac{0 - Y_{B,0}}{Y_{A,0}} = -\frac{Y_{B,0}}{Y_{A,0}} \qquad (6.38)$$

Thus, the terms $Y_A = 0$ and $Y_B = (Y_{B,0}/Y_{A,0}) \cdot Y_{A,0} = Y_{B,0}$ are correctly evaluated as well.

In summary, the concentration of A and B is known when Y_I is known. However, Y_I is a linear function of the mixture fraction ξ (see Eqn. 6.33). The local mixture fraction ξ follows a certain distribution, because all details of the concentration field cannot be resolved. This distribution is described using a PDF denoted as ϕ in this work. The shape of this PDF is typically assumed to follow a Beta-function,[76] with the mean value and the width as a function of the mean (i.e., filtered), as well as the variance of the mixture fraction:

$$\phi(\xi) = \frac{\xi^{v-1} \cdot (1-\xi)^{w-1}}{\int_0^1 u_\xi^{v-1} \cdot (1-u_\xi)^{w-1} du_\xi} \qquad (6.39)$$

Here, v and w are defined as functions of $\overline{\xi}$ and I_S:[91]

$$v = \bar{\xi} \cdot \frac{1 - I_S}{I_S}$$

(6.40)

$$w = \left(1 - \bar{\xi}\right) \cdot \frac{1 - I_S}{I_S}$$

(6.41)

where I_S is the intensity of segregation defined by:[91]

$$I_S = \frac{\xi_V}{\bar{\xi} \cdot \left(1 - \bar{\xi}\right)} .$$

(6.42)

In order to calculate the rate of the second reaction, an expression for the local concentration of species D (i.e., DMP) is needed. This is again done by using a dimensionless variable that characterizes the relative amount of species D compared to the inlet concentration $Y_{D,0}$:

$$D = \frac{Y_D}{Y_{D,0}} .$$

(6.43)
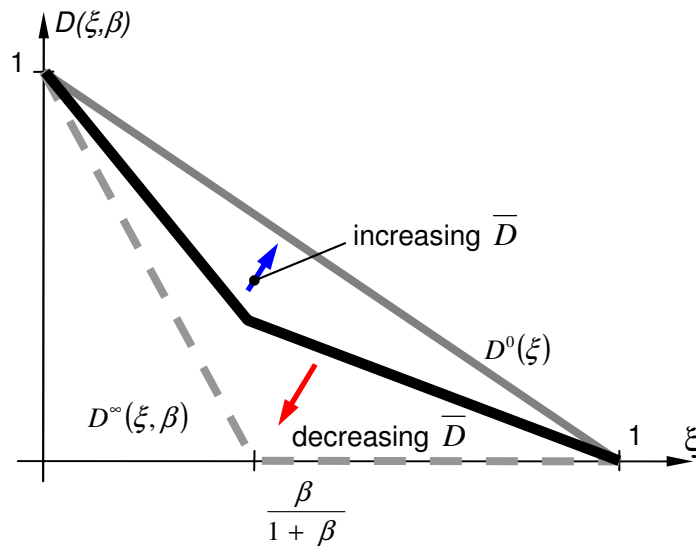
Figure 6.7: Dependency of the local concentration of species D on the mixture fraction.

The dimensionless concentration D (and its PDF) is now approximated using the method that has been documented in Baldyga and Bourne.[92] The approach has been applied to the neutralization/hydrolysis-reaction system studied in this work by Lindenberg et al.[79] Basically, the PDF of D is assumed to be a function of the mixture fraction, the ratio of the acid and the base, as well as its mean value. The approach relies on a linear interpolation between two extremes:

(i) there is an infinitely fast (second) reaction that consumes all excessive DMP in the mixture instantaneously. This situation leads to the following dependency of D on the mixture fraction:[79]

$$D^\infty(\xi,\beta) = \begin{cases} 1 - \xi \cdot \dfrac{1+\beta}{\beta}, \xi \le \dfrac{\beta}{1+\beta} \\ 0, \xi \ge \dfrac{\beta}{1+\beta} \end{cases} \qquad (6.44)$$

(ii) there is no hydrolysis reaction. Hence, the distribution of D is directly proportional to the mixture fraction as no DMP has reacted, i.e., $D^0(\xi) = 1-\xi$.

The interpolation between the two extremes is performed via (see Figure 6.7):

$$D(\xi,\bar{\xi},\xi_v,\overline{D},\beta) = D^\infty(\xi,\beta) + \frac{\overline{D} - \overline{D^\infty}}{(1-\bar{\xi}) - \overline{D^\infty}} \cdot [(1-\xi) - D^\infty(\xi,\beta)] \qquad (6.45)$$

with

$$\overline{D^\infty}(\bar{\xi},\xi_v,\beta) = \int_0^{\frac{\beta}{1+\beta}} D^\infty(\xi,\beta) \cdot \phi(\xi,\bar{\xi},\xi_v) d\xi \qquad (6.46)$$

While the two extreme cases are exact, this linear interpolation is somewhat arbitrary. It is, however, mechanistic in a way that larger values of $\overline{D}$ will lead to larger values of D. The resulting distribution of D is, however, not a Beta-function as can be seen in Figure 6.8. The distribution $\phi(D)$ can be easily evaluated from Eqns. 6.39 and 6.45, as well as a subsequent normalization. The discontinuity in the graph for $\phi(D)$ (see Figure 6.8) is caused by the discontinuity in the function $D^\infty(\xi,\beta)$. One may question if the model shown in Baldyga and Bourne[92] is also applicable to LES. This model is an *a priori* assumption on the local PDF of DMP and essentially does not depend on any assumption on the underlying turbulence spectrum. Hence, it is just a sub-model for the relationship between the local D and the local mixture fraction. Assuming a Beta-PDF for the mixture fraction distribution is, however, well accepted for LES (see Fox[76]).

Note, that $\overline{D^\infty}$ always has to be smaller than unity, since the integral from zero to unity of the Beta-function has to be smaller than unity (also, D^∞ is always smaller than unity). Also, D has to be smaller than unity, since Y_D cannot become larger than the inlet concentration.
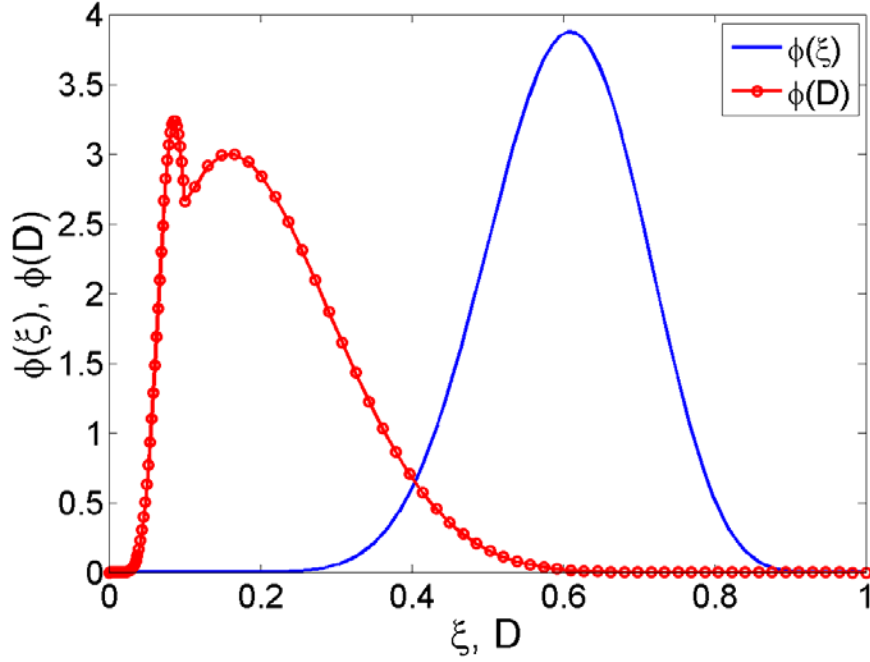
Figure 6.8: Probability density function of species D and the mixture fraction ($\bar{\xi}$ =0.6, ξ_v=0.01, $\overline{D}$ = 0.1, β = 1.05).

Having both the concentration of species A and D expressed as a function of the local mixture fraction, the reaction rate of the second reaction can be calculated. The only additional information needed is the distribution of the local mixture fraction ξ. This quantity, however, has already been assumed to be a Beta-PDF. Also, the mean and the variance for ξ can be calculated solving the respective transport equations as already discussed (note that the transport equation for the variance of the mixture fraction is given by Eqn. 6.24). Thus, the following relationship needs to be solved:

$$\bar{r}_2\left(\bar{\xi},\xi_v,\overline{D},\beta\right)= k_2 \cdot Y_{A,0} \cdot Y_{D,0} \cdot \int_0^1 \frac{\left|Y_I(\xi,\beta)\right|+Y_I(\xi,\beta)}{2} \cdot D\left(\xi,\bar{\xi},\xi_v,\overline{D},\beta\right)\cdot \phi\left(\xi,\bar{\xi},\xi_v\right)d\xi \quad (6.47)$$

This integral cannot be solved analytically, and depends on the three main variables $\overline{D}$ (via the term D), $\bar{\xi}$ and ξ_v. Note, that the dependency on β is "static", since this variable depends only on the inlet concentrations of A and B. Also, the integration boundaries can be relaxed, since the first term in the integration, i.e.,

$$\frac{\left|Y_I(\xi,\beta)\right|+Y_I(\xi,\beta)}{2} \quad (6.48)$$

is non-zero only if $Y_I > 0$. This is the case when

$$\xi \geq \frac{\beta}{(1+\beta)}.$$

(6.49)

Physically, this means that species A must be present to start the second reaction. This is only the case when the mixture fraction is above a certain threshold. This simplifies the integral to:

$$\bar{r}_2 = k_2 \cdot Y_{A,0} \cdot Y_{D,0} \cdot \int_{\frac{\beta}{(1+\beta)}}^{1} Y_I(\xi,\beta) \cdot D(\xi,\bar{\xi},\xi_v,\bar{D},\beta) \cdot \phi(\xi,\bar{\xi},\xi_v) d\xi$$

(6.50)

.

6.4 Numerics

We use the open-Source CFD Package 'OpenFOAM'[93] which is designed for parallel computing and hence is a good basis for future extension to very large systems containing a significant amount of individual bubbles. OpenFOAM uses a finite volume discretization and offers a large number of numerical schemes for discretizing partial differential equations.[94] In the next few paragraphs we discuss our advanced mapping procedures and our new strategy to solve the multiphase flow equations. Also, we shortly comment on some details of the species transport and the bubble tracking algorithm.

6.4.1 Mapping Procedures

i)   Lagrangian-to-Euler Mapping

To recover the liquid phase fraction ε_L in each computational cell, the volume fraction of each individual bubble in this cell has to be known. For arbitrary shapes of the bubble and the cell this is computationally very expensive. Hence, an idealized shape of the bubble has to be assumed. For example, Darmana[27] used a cubic approximation of each bubble, as this shape allows a computationally efficient calculation and seems to represent the bubble shape reasonably well. However, it is difficult to account for non-cubic cells of an arbitrary grid, restricting the method to simple rectangular Cartesian grids.

Another approach has been reported by Hu and Celik[40] for the mapping of Lagrangian sources terms onto an Eulerian grid. In their particle-in-cell-ball (PSI-ball) method they use the distances between the centers of surrounding cells within a defined influence radius and the particle center as basis for their distribution. In this method the inverse of these distances corresponds to the weight of the Lagrangian source terms in each individual cell.

In our work we use a more sophisticated approach to recover the Lagrangian quantities on the Eulerian grid. These quantities are (i) the local liquid phase volume fraction, (ii) the momentum source term $\boldsymbol{\Phi}$, (iii) as well as the species source term $\boldsymbol{\Phi}_{\dot{N}_i}$. While parts of our method have been in use for some years, our numerical implementation results in a better accuracy and reduced computational time. Our approach consists of three steps, i.e., (a) the determination of the cells that are in the range of the bubble, (b) the calculation of a (virtual) overlapping volume of the bubble with each individual surrounding cell, and (c) the distribution of the Lagrangian properties among the surrounding cells. For the first step we scan all surrounding cells and check if the distance x_{dist} between the cell center and the particle center is smaller than:

$$x_{dist} < \frac{d_p}{2} + x_{cell,max} \qquad (6.51)$$

This is essential to save computational time as the calculation of the virtual overlapping volume (see below) is time consuming. An additional feature of our implementation is that the surrounding cells are determined before the calculation starts. This information is then saved and loaded at each time step. Hence, we avoid searching for all surrounding cells, which may become limiting for large grids. In Eqn. 6.51 the variable $x_{cell,max}$ is the maximum distance from the cell center to a cell's boundary point. It has to be calculated and saved for each individual cell. As we have used uniform rectangular grids in our work, $x_{cell,max}$ corresponds to $\sqrt{3/4}$ of the cell length. For step (b), i.e., the overlap calculation, we use a fourth-order template function similar to Deen et al.[95] The half length for this calculation was set to 1.5 bubble diameters. Hence, the computed overlap is not a physically correct overlap of the bubble with the surrounding cell, but a virtual overlap that characterizes the influence of the bubble on this cell. Finally, we distribute the Lagrangian properties among the surrounding cells according to their relative virtual overlapping volumes with the particle. This guarantees that Lagrangian properties are conserved during the mapping. Also, our methodology yields a sufficiently smooth distribution of the Lagrangian properties on the Eulerian grid. However, care must be taken during the distribution of the particle volume. We had to impose a lower bound on the liquid-phase void fraction ε_L, as otherwise the filtered Navier-Stokes equation cannot be solved efficiently. We set the lower bound of ε_L equal to 0.05 as proposed by Darmana.[27]

ii)   Euler-to-Lagrangian Mapping

The Euler-to-Lagrangian mapping is the interpolation of the solution on the Eulerian grid at discrete particle locations. Previous studies[27,33,38] frequently employed a simple linear interpolation at the center position of the particle. This is problematic, as the particles have a physical size, and therefore, the value at the particle center may not appropriately represent their environment. Furthermore, problems with this approach have been shown by Darmana[27] in the form of spurious oscillations in the rise velocity of a single bubble. Our analysis shows that these oscillations originate from the fact that a relatively coarse Eulerian mesh is used in EL simulations onto which the interface terms are imposed. This results in a poor resolution of the effect of these forces on the Eulerian grid. For example, it has significant impact on the velocity field whether the particle is completely in one cell or it is crossing a cell boundary. In the latter case the force is distributed among two or more cells. Thus, the peak velocity is significantly smaller than in the former case, and a slightly oscillating velocity field is obtained. Consequently, even the best interpolation algorithm leads to oscillations of the bubble's rise velocity. Although this effect can be somewhat alleviated by the Lagrangian-to-Euler mapping, these oscillations are directly transferred during the mapping procedure using conventional linear interpolation at the particle center position. In the present work we again use the virtual overlapping volumes from the Lagrangian-to-Euler mapping procedure to map Eulerian quantities at the particle position. The value at the particle position was obtained by summation of the product of the relative overlapping volume and the cell center value over all surrounding cells. This strategy turned out to give only insignificant bubble rise velocity oscillations and was computationally efficient, as the relative overlapping volumes were already computed during the Lagrangian-to-Euler mapping.

6.4.2 Multiphase Flow Solver

The numerical solution procedures for solving the multiphase flow equations have been adopted from existing literature on the EE[96] and the EL approach.

In the EE approach usually the Pressure-Implicit-Split-Operator (PISO) algorithm[97] is adopted to solve for the pressure-velocity coupling. Also, the momentum equation is frequently divided by the phase fraction to obtain a "phase-intensive" momentum equation.[96] This is beneficial for the numerical solution procedure, as numerical noise is suppressed at low phase fractions. Thus, the momentum equation can be transformed into (refer to Crowe et al.[34])

$$\varepsilon_L \cdot \rho_L \cdot \frac{\partial(\overline{\boldsymbol{u}})}{\partial t} + \varepsilon_L \cdot \rho_L \cdot \nabla \cdot (\overline{\boldsymbol{u}}\overline{\boldsymbol{u}}) + \rho_L \cdot \overline{\boldsymbol{u}} \frac{\partial(\varepsilon_L)}{\partial t} + \rho_L \cdot \overline{\boldsymbol{u}} \cdot \nabla \cdot (\varepsilon_L \overline{\boldsymbol{u}}) =$$
$$-\varepsilon_L \cdot \nabla \overline{p} - \nabla \cdot (\varepsilon_L \cdot \overline{\boldsymbol{\tau}}_L) + \varepsilon_L \cdot \rho_L \cdot \boldsymbol{g} + \boldsymbol{\Phi}$$
(6.52)

.

Taking into account the continuity equation, the third and fourth term on the left-hand side vanish. After division by ε_L and ρ_L, we obtain the phase-intensive momentum equation for the liquid phase:

$$\frac{\partial \overline{\boldsymbol{u}}}{\partial t} + \nabla \cdot (\overline{\boldsymbol{u}}\overline{\boldsymbol{u}}) =$$
$$-\nabla \frac{\overline{p}}{\rho_L} + \frac{1}{\varepsilon_L} \cdot \nabla \cdot \left[\varepsilon_L \cdot \nu_{eff,L} \cdot \left(\nabla \overline{\boldsymbol{u}} + \nabla \overline{\boldsymbol{u}}^T - \frac{2}{3} \cdot \boldsymbol{I} \cdot (\nabla \cdot \overline{\boldsymbol{u}}) \right) \right] + \boldsymbol{g} + \frac{\boldsymbol{\Phi}}{\varepsilon_L \cdot \rho_L}$$
(6.53)

.

Note that $\nabla \cdot \overline{\boldsymbol{u}}$ is not equal to zero in our case and that $\boldsymbol{I}$ represents the identity matrix. This equation can be solved directly imposing appropriate boundary conditions. Since the hydrostatic pressure gradient may be significant, we exclude this contribution from the momentum equation by defining a modified pressure gradient according to:

$$\nabla \overline{p}^* = \nabla \overline{p} - \rho_L \cdot \boldsymbol{g}$$
(6.54)

The boundary condition for $\overline{p}^*$ can then be approximated by a zero gradient for static, impermeable walls. In our work, the final momentum equation for the liquid phase that is solved together with the continuity equation Eqn. 6.1 is:

$$\frac{\partial \overline{\boldsymbol{u}}}{\partial t} + \nabla \cdot (\overline{\boldsymbol{u}}\overline{\boldsymbol{u}}) =$$
$$-\nabla \overline{p}' + \frac{1}{\varepsilon_L} \cdot \nabla \cdot \left[\varepsilon_L \cdot \nu_{eff,L} \cdot \left(\nabla \overline{\boldsymbol{u}} + \nabla \overline{\boldsymbol{u}}^T - \frac{2}{3} \cdot \boldsymbol{I} \cdot (\nabla \cdot \overline{\boldsymbol{u}}) \right) \right] + \frac{\boldsymbol{\Phi}}{\varepsilon_L \cdot \rho_L}$$
(6.55)

Here we have abbreviated the pressure gradient term by the definition:

$$\nabla \frac{\overline{p}^*}{\rho_L} = \nabla \overline{p}'$$
(6.56)

During the simultaneous solution of Eqn. 6.1 and Eqn. 6.55, the liquid-phase volume fraction on the Eulerian grid is known as this information is obtained after the Lagrangian-to-Euler mapping. Thus, the first term on the left-hand side of Eqn. 6.1, i.e., the time derivative of the liquid-phase volume fraction is known explicitly. Hence, most of the numerical algorithms that are used for incompressible flows may be used. In this work the PISO algorithm is adopted. Details of this algorithm for single-phase flows can be found in the original work of Issa,[97] as well in the publications of Nilsson[98] and Kaerrholm[99]. Here we focus on the handling

of the velocity-pressure coupling only, i.e., the heart of the solution algorithm. The discretized momentum equation, i.e., Eqn. 6.55, has the general shape:

$$a_P^u \cdot \overline{\boldsymbol{u}}^P + \sum_N a_N^u \, \overline{\boldsymbol{u}}^N = \boldsymbol{r} - \nabla \overline{p}' \qquad (6.57)$$

Here a_P^u and a_N^u are the diagonal and off-diagonal coefficients in the system of algebraic equations, respectively. These vectors are obtained during the discretization of the momentum equation. The vectors $\overline{\boldsymbol{u}}^P$ and $\overline{\boldsymbol{u}}^N$ are the velocity vectors at the cell center P and at the neighboring cells, respectively. The vector $\boldsymbol{r}$ incorporates the known part of the system, i.e., the force from the dispersed phase $\boldsymbol{\Phi}$, as well as the viscous part (i.e., the second term on the right-hand side of Eqn. 6.55). Next, we define an operator $\mathbf{H}(\overline{\mathbf{u}})$ as follows:

$$\boldsymbol{H}(\overline{\boldsymbol{u}}) = \boldsymbol{r} - \sum_N a_N^u \, \overline{\boldsymbol{u}}^N \qquad (6.58)$$

Hence, the velocity at the cell center point P can be calculated from:

$$\overline{\boldsymbol{u}}^P = \left(a_P^u\right)^{-1} \left[\boldsymbol{H}(\overline{\boldsymbol{u}}) - \nabla \overline{p}' \right] \qquad (6.59)$$

By multiplication with ε_L and applying the continuity equation Eqn. 6.1, we obtain the following expression for the pressure:

$$\nabla \cdot \left[\varepsilon_L \cdot \left(a_P^u\right)^{-1} \nabla \overline{p}' \right] = \nabla \cdot \left[\varepsilon_L \cdot \left(a_P^u\right)^{-1} \boldsymbol{H}(\overline{\boldsymbol{u}}_L) \right] + \frac{\partial \varepsilon_L}{\partial t} \qquad (6.60)$$

In this equation the right-hand side is known from the previous calculation steps of the PISO algorithm, and the resulting equation can be solved for the unknown pressure $\overline{p}'$. For this purpose we use fast geometric-algebraic multi-grid (GAMG) solvers with preconditioning.[93] Finally, the velocity $\overline{\boldsymbol{u}}^P$ at each point P can be calculated using Eqn. 6.59.

The above mentioned algorithm together with no-slip and perfect-slip boundary conditions works for the special case where the mean liquid-phase void fraction is constant over time, i.e., the amount of liquid phase in the computational domain does not change. However, in the current work bubbles are continuously entering and leaving the bubble column and consequently the total gas-phase volume and the mean liquid-phase void fraction fluctuate over time, leading to a variable fill level of the two-phase mixture in the bubble column. Therefore, in conventional Euler-Euler simulations a top layer of the disperse phase, e.g., the gas phase, together with appropriate boundary conditions is used to capture the fluctuations

of the fill level. However, in the current work we do not use a top layer of the gas phase as we reconstruct the distribution of ε_L directly from the particle (bubble) positions. As we use a fixed grid, we solve all equations for a fixed amount of the two-phase mixture. Hence, we have to account for in- and outflow of the liquid phase as a consequence of net out- and inflow of the gas phase. In the previous work of Darmana,[27] for example, this problem was solved by using "pressure cell slits" on top of the computational domain. Due to these prescribed pressure cells, hydrodynamic instabilities at the surface have been reported. These instabilities were suppressed using a certain geometrical configuration of the pressure cell slits.[27] In the current work we follow a more advanced approach, in which we subtract the net change of the void fraction in the column from the continuity equation of the liquid phase. To the best of our knowledge, this approach is new and has not been documented in literature before. Thus, we subtract or add liquid volume uniformly over the whole computational domain whether the mean liquid-phase void fraction decreases or increases, respectively. By doing so, we fully preserve the local effects of the changing void fraction on the one hand and deal in an elegant way with the displacement of liquid-phase volume on the other hand. The reformulated continuity equation is:

$$\frac{\partial \varepsilon_L}{\partial t} + \nabla \cdot \left(\varepsilon_L \cdot \overline{\boldsymbol{u}} \right) = \frac{\partial \varepsilon_{L,Mean}}{\partial t} \qquad\qquad (6.61)$$

Hence, the pressure equation that we solve for is:

$$\nabla \cdot \left[\varepsilon_L \cdot \left(a_P^u \right)^{-1} \nabla \overline{p}' \right] = \nabla \cdot \left[\varepsilon_L \cdot \left(a_P^u \right)^{-1} \boldsymbol{H}\left(\overline{\boldsymbol{u}}_L \right) \right] + \frac{\partial \varepsilon_L}{\partial t} - \frac{\partial \varepsilon_{L,Mean}}{\partial t} \qquad (6.62)$$

The term $\partial \varepsilon_{L,Mean} / \partial t$ can be evaluated explicitly from the known local distribution of ε_L by volume averaging. This method has the advantage that we avoid discrete locations where liquid flows out of the domain. Consequently, we do not observe any instability. However, this artificial addition and removal of the liquid phase has to be taken into account when solving the species transport equation.

The schemes for discretizing the convection terms were second-order accurate. We have used the implicit Euler time integration scheme with a time step giving a maximum Courant number of approximately 0.3.

6.4.3 Bubble Tracking

Newton's equation of motion was solved after manipulation and introducing the density ratio $\gamma_\rho = \rho_p / \rho_L$ in the following form:

$$
\begin{aligned}
\frac{dU}{dt} = {} & \frac{\gamma_\rho}{\gamma_\rho + C_A} \cdot \boldsymbol{g} - \frac{1}{\gamma_\rho + C_A} \cdot \frac{\nabla \overline{p}}{\rho_L} - \frac{3}{4} \frac{C_D}{d_p} \cdot \frac{1}{\gamma_\rho + C_A} \cdot \left| \boldsymbol{U}_{rel} \right| \cdot \boldsymbol{U}_{rel} \\
& - C_L \cdot \frac{1}{\gamma_\rho + C_A} \boldsymbol{U}_{rel} \times \boldsymbol{\omega} + C_A \cdot \frac{1}{\gamma_\rho + C_A} \cdot \frac{d}{dt} (\overline{\boldsymbol{u}} + \boldsymbol{u}_{fluct})
\end{aligned}
\tag{6.63}
$$

The sub-grid-scale fluctuating velocities $\mathbf{u}_{flcut}$ were set to zero, as it can assumed (based on previous work[40,95]) that this will not have a substantial effect on the solution.

The details of the particle tracking routine are described in the PhD thesis of Kaerrholm[99]. In this face-to-face technique each individual bubble "knows" when it is crossing a cell face, and hence, the source terms for each computational cell can be treated accurately. Using this approach, the particle cannot cross a cell boundary without exchanging momentum and mass with it. A more detailed description of the numerical details can be found in MacPherson et al.[100]

The following discretization of Eqn. 6.63 was used:

- $\frac{dU}{dt} \approx \frac{U^{n+1} - U^n}{\Delta t}$ (i.e., explicit Euler integration)

- $\nabla \overline{p}$ is calculated using a selectable gradient scheme

- $\boldsymbol{\omega}$ is calculated using a selectable gradient scheme

The time step for the bubble tracking routine is user-selectable and was chosen as $1/10^{th}$ of the time step used for integrating the filtered Navier-Stokes equations.

The total force acting from the bubble on the surrounding liquid is the opposite from the sum of the drag, lift, and added mass force that is exerted onto the bubble. Hence, the volumetric source term $\boldsymbol{\Phi}$ is the sum over all particles i in the pertaining cell j:

$$
\Phi_j = \frac{\sum\limits_i -(\boldsymbol{F}_{D,i} + \boldsymbol{F}_{L,i} + \boldsymbol{F}_{A,i})}{\Delta V_{cell,j}}
\tag{6.64}
$$

Verification of the particle tracking algorithm is provided in Appendix B.

6.4.4 Species Transport

The volumetric source terms $\Phi_{\dot{N}_i}$, as well as the chemical source term in the species transport equation Eqn. 6.15 were treated explicitly. All other terms were discretized implicitly. For the convective term a second-order accurate scheme was used. The boundary conditions were set to zero gradient for all walls and the top surface.

6.4.5 Fast Reactions

The integral in Eqn. 6.50 has to be evaluated during the simulation in each computational cell. Since this integration has no analytical solution, it has to be solved numerically. In order to reduce the computational effort, it is suggested solving it off-line, tabulating the results and then interpolating the values of the integral during the simulation run. Specifically, this means that the integral

$$I_{\overline{r_2}}\left(\overline{\xi},\xi_v,\overline{D}\right)= \int_{\frac{\beta}{(1+\beta)}}^{1} Y_I(\xi,\beta)\cdot D\left(\xi,\overline{\xi},\xi_v,\overline{D},\beta\right)\cdot \phi\left(\xi,\overline{\xi},\xi_v\right)d\xi \qquad (6.65)$$

needs to be evaluated before the simulation for a fixed value of β to create a look-up table of the form $I_{\overline{r_2}}\left(\overline{\xi}_i,\xi_{v,j},\overline{D}_k\right)$. Here i, j and k are indices for the three vectors containing nodes of the mean mixture fraction, its variance and the mean concentration of species D, i.e., DMP. During the simulation, the value for the reaction term can then be approximated using (for example) a linear interpolation between the nodes.

Also, there are some simplifications for calculating the function D. Since the value for D^{∞} is zero for $\xi \geq \dfrac{\beta}{1+\beta}$, it will always be zero when evaluating the integral.

The structure of the look-up table is particularly important. Since there are strong gradients near $\xi_V=0$, the spacing for this variable near the origin should be significantly smaller. This is realized by spacing in this direction using a geometric series:

$$\Delta\xi_{V,i} = \Delta\xi_{V,0}\cdot q^i \qquad (6.66)$$

with, e.g., q = 1.10. This value for q gives an appropriate spacing of the look-up table.

A validation of the proposed numerical strategy for fast reactions in a micro reactor is documented in Appendix C.

6.5 Results

6.5.1 Multiphase Flow

i)   Setup

In this study we have selected the "Becker" case[40] as a reference for our computations. The setup consists of a quasi-2D unstirred bubble column, where gas enters a water-filled rectangular box through an excentric sparger (sparger diameter d_s=0.04 m, distance from the left wall x_s=0.15 m). The geometrical setup is illustrated in Figure 6.9 and the system parameters are listed in Table 6.2.
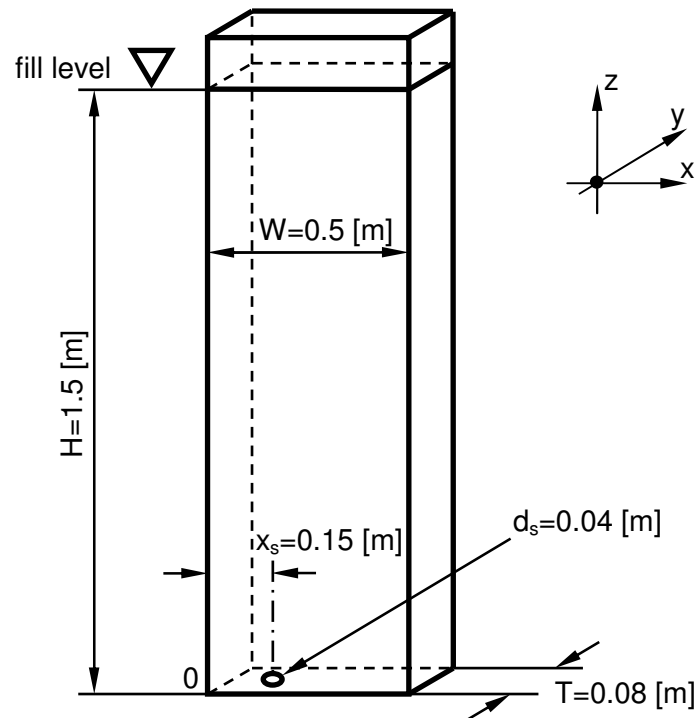
Figure 6.9: Geometrical setup of the "Becker" case.

It is noted here, that in the paper of Becker[69] a bubble size distribution has not been documented. Furthermore, in the Euler-Euler simulations of Sokolichin and Eigenberger[101] only a constant slip velocity (assumed to be 0.2 m/s) has been used to model bubbles with a mean diameter between 1 and 10 mm. Hence, a mean bubble diameter had to be selected in our work, due to the lack of further information. Our choice of mono-disperse bubbles with a size of 1.6 mm is in accordance with the work of Hu and Celik.[40], which yields a terminal rise velocity of 0.172 m/s and is the range specified by Sokolichin and Eigenberger.[101] Also, it has been shown by Diaz et al.[102] that for low superficial gas velocities (i.e., below approximately 1

cm/s) the use of mono-disperse bubbles is sufficient to reproduce experimental results for gas hold up and the plume oscillation period. The selection of the gas feed rate, as well as of viscosity and diffusion coefficient, is in accordance with previous experimental[69] and theoretical[101] work in this field.

Parameter	Abbreviation	Value
Particle size	d_p	1.6 mm
Gas feed rate	V_G	1.6 L/min
Liquid-phase viscosity	ν_L	$1 \cdot 10^{-6}$ m²/s
Diffusion coefficient	D_i	$2 \cdot 10^{-9}$ m²/s

Table 6.2: Process parameters for the EL simulations (base case).
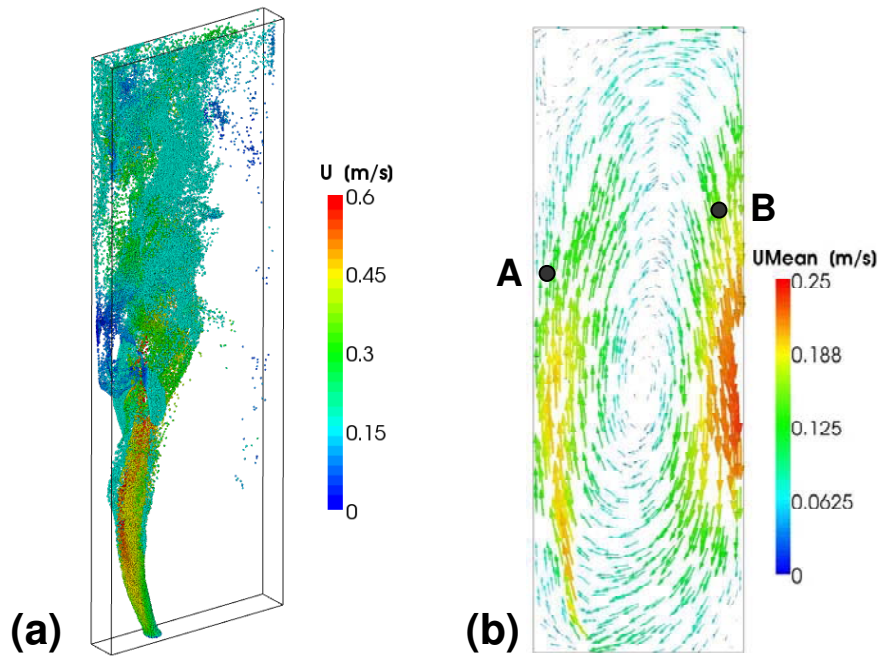
Figure 6.10: Principal flow fields in the bubble column: (a) snapshot of the instantaneous bubble distribution (bubbles are colored according to their velocity), (b) time-averaged liquid-phase velocity distribution in the bubble column (the points A and B indicate the probing locations for Figure 6.11).

The box has a width of W=0.5 m, a depth of 0.08 m and is filled with liquid phase (water) up to a level of 1.5 m. Due to the excentric sparger, a non-homogenous distribution of the gas bubbles is observed and an unsteady circulation loop develops in the bubble column. The time-averaged liquid-phase flow field obtained with our simulation is shown in Figure 6.10

(right). Also, we have illustrated the principal shape of the rising bubble swarm in Figure 6.10 (left). In this snapshot we have colored the bubbles according to their absolute velocity in the bubble column.

The gassing rate is such that the total gas hold-up is in the range of 0.25 to 0.35 %, i.e., very low. To obtain time-averaged data, we have averaged the simulation output over a sufficiently long time (>100 s) to ensure that transient effects are excluded.

ii)   Unsteady Fluid Motion in the Bubble Column

It is well known, that even in the relatively simple setup considered in this work, i.e., the Becker case, the multiphase flow is unsteady and shows rich dynamic features. The correct prediction of the unsteady motion of the gas bubbles and the liquid phase is essential for a correct prediction of mixing.
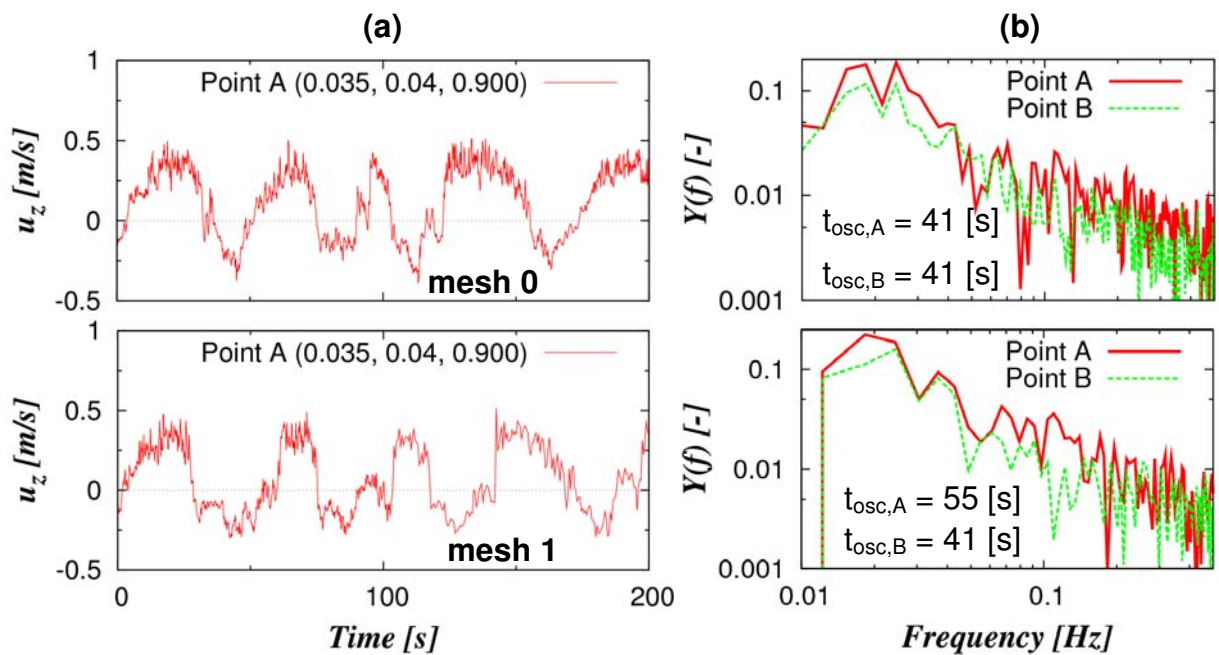
Figure 6.11: Time profiles at probing location A (a) and power spectrum of the time profile at probing location A and B (b) (Probing locations acc. to Figure 6.10; top: LES with coarse mesh "mesh 0", bottom: LES with fine mesh "mesh 1").

In order to verify our approach, we have focused on the time profile of the vertical component (i.e., along the z-direction) of the liquid-phase velocity at two distinct points in the bubble column. These two points are located in the upflow region, where a relatively high gas hold up exists (Point A in Figure 6.10b), as well as in the down flow region which is essentially free of bubbles (Point B in Figure 6.10b). The time signals for point A, as well as the power

spectrum (obtained by frequency analysis using the fast Fourier transformation, FFT) of the u_z-velocity in point A and B are shown in Figure 6.11 for two different meshes (mesh 0: 64 x 10 x192 = 122,880 cells; mesh 1: 83 x 13 x 250 = 269,750 cells). Clearly, the time profiles (Figure 6.11a) for both meshes indicate similar features, i.e., a low frequency oscillating motion as well superimposed high frequency fluctuations. In our work the minimum (filtered) velocities at point A was calculated as -0.39 and -0.30 m/s for the coarse and fine mesh, respectively. Whereas the peak velocity at point A are both 0.51 m/s for the coarse and fine grid. These features agree very well with the LDA measurements of Sokolichin and Eigenberger[101] (their minimum and maximum velocities were -0.4 and 0.8 m/s, respectively), as well as the simulations of Hu and Celik[40] (their minimum and maximum velocities were -0.3 and 0.5 m/s, respectively). A quantitative comparison of the oscillating motion is possible when looking at the results of the frequency analysis shown in Figure 6.11b. In point A the dominating oscillation period (indicated by the highest peak in the power spectrum) is equal to 41 s and 55 s for the coarse and the fine mesh respectively. The oscillation period t_{osc} in point B is identical for both grids and equal to 41 s. Both values agree exceptionally well with literature data (Hu and Celik,[40] as well as Becker et al.[69] reported an oscillation period of 41 s).

iii)   Grid Refinement Study

Simulation Case	*Mean Squared Velocity Difference*
mesh 0	$4.9 \cdot 10^{-4}$ m²/s²
mesh 1	$2.3 \cdot 10^{-4}$ m²/s²
mesh 2	$6.9 \cdot 10^{-4}$ m²/s²
mesh 0, no SGS Model	$16.4 \cdot 10^{-4}$ m²/s²
mesh 0, $C_s = 0.16$	$52.9 \cdot 10^{-4}$ m²/s²
mesh 0, One-Eqn. SGS Model	$39.0 \cdot 10^{-4}$ m²/s²

Table 6.3: Mean squared velocity differences for the grid sensitivity study, as well as for the sensitivity to the subgrid-scale model.

In order to validate the results of our LES/Euler-Lagrange simulations, we performed a grid sensitivity study and compared the results to experimental data (from Sokolichin and Eigenberger[101]). We quantitatively compared the mean vertical velocity profiles at a relative

height of z/h=0.35 for three different mesh configurations (mesh 0: 64 x 10 x192 = 122,880 cells; mesh 1: 83 x 13 x 250 = 269,750 cells; mesh 2: 120 x 19 x 360 = 820,800 cells). All meshes are uniform, i.e., locally unrefined, and consisted of hexaeders. As can be seen from Figure 6.12, all grids gave excellent agreement with the experimental data. The mean squared velocity differences (i.e., $1/N\Sigma(u_{mean,z,sim} - u_{mean,z,exp})^2$, where N is the total number of points used for comparison and $u_{mean,z,sim}$ and $u_{mean,z,exp}$ are the simulated and experimentally measured z-velocity at the same location, respectively) obtained with the different meshes are summarized in Table 6.3. Mesh 1 was more accurate, whereas mesh 2 gave significant over-prediction of in the region on the left side of the column. It is speculated that this over-prediction is due to the insufficient time averaging performed for mesh 2, which was due to restriction in computational time. Thus, we conclude that even with the coarsest grid the unsteady motion of big turbulent eddies is captured accurately enough. Hence, we have chosen the coarsest grid, i.e., mesh 0 for all subsequent simulations.
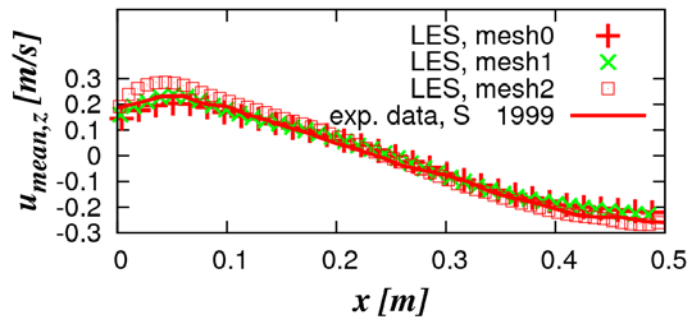
Figure 6.12: Comparison of the mean vertical velocity profiles at z/H=0.35 for three different grids. The data shown for mesh 0 and mesh 1 has been averaged over more than 100 s, data for Mesh 2 over 61.4 s.

iv) Sensitivity to the Sub-Grid-Scale Model

Furthermore, we studied the influence of the subgrid-scale model on the results for the mean flow field and the subgrid-scale viscosity in the bubble column. The simulation included cases with (a) no subgrid-scale model, (b) the Smagorinsky model with C_s=0.032 as suggested by Hu and Celik,[40] (c) the standard Smagorinsky model with C_s=0.16, as well as (d) a differential one-equation model with standard coefficients (C_k=0.07 and C_ε=1.05). The reason for selecting the latter model is the suggestion of deVilliers[64]. He stated that more sophisticated dynamic models (which are not used in this work) become quite inaccurate in cases with poorly resolved wall regions. In contrast, the differential one-equation model is a good compromise between accuracy and computational resources needed.

The results for these four sub-grid-scale models are depicted in Figure 6.13 and the results for the quantitative comparison are summarized in Table 6.3. Clearly, the Smagorinsky model with a low constant of $C_s=0.032$ gives by far the best prediction of the mean flow field. The dynamic model (Figure 6.13d) has no significant advantages over the Smagorinsky model (Figure 6.13c), although it is computationally more expensive.

Both models with standard coefficients strongly over-predict the sub-grid-scale viscosity (compare the scales for the SGS viscosities in Figure 6.13). As expected, the simulation with the subgrid-scale model switched off (Figure 6.13a) over predicts the mean flow field due to the absence of subgrid-scale energy dissipation. However, the overprediction is much weaker than the significant underprediction resulting from the standard SGS models.
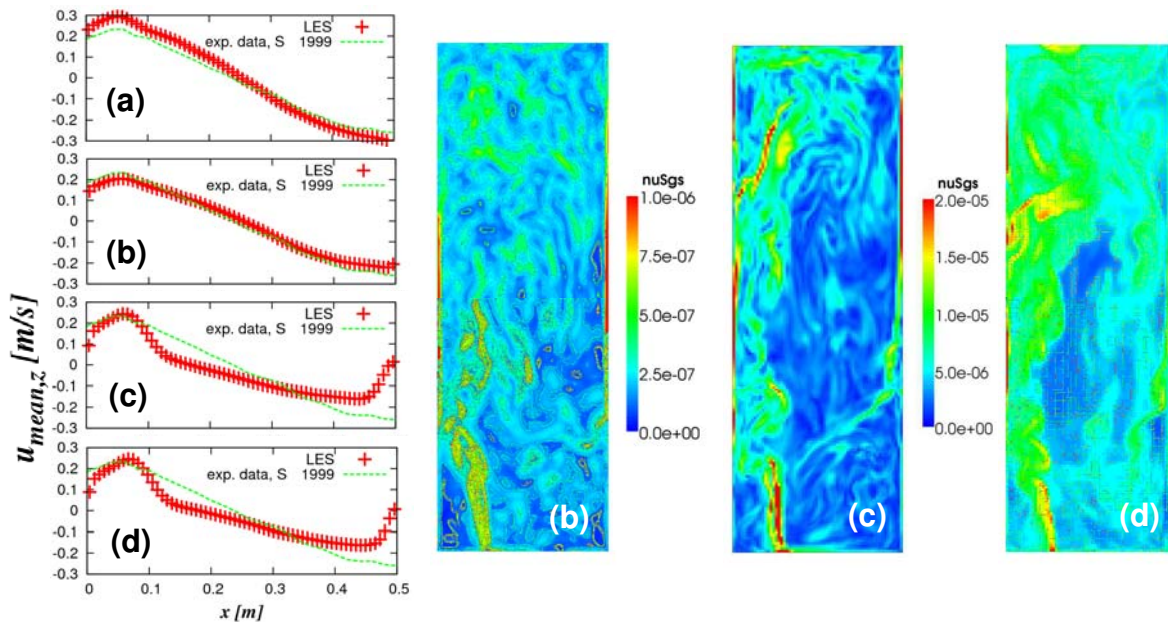
Figure 6.13: Comparison of the mean vertical velocity profiles at z/H=0.35 (left) and snapshots of the sub-grid-scale viscosity for three different sub-grid-scale models (right; a: no SGS model, b: Smagorinsky model with $C_s=0.032$ acc. to Hu and Celik, c: standard Smagorinsky model with $C_s=0.16$, d: differential SGS model; c and d share the same colorbar for the subgrid-scale viscosity given in m²/s).

When looking at the predicted subgrid-scale viscosity values (Figure 6.13 right), the best model (i.e., the Smagorinsky model with $C_s=0.032$) shows SGS viscosity values in the order of the molecular viscosity. This substantiates once more that the effect of the SGS velocity fluctuations on the mean flow field are rather small. However, the absence of the SGS model led to a too high oscillation period (i.e., approx. 70 s for the SGS model switched off, vs. 41 s when the Smagorinsky model is activated) compared with experimental data. Hence, it is clear that for the multiphase simulations performed in this work (i) the Smagorinsky model together with the wall function approach of deVillier[64] is best suited for describing the sub-grid-scale

fluctuations and (ii) the standard value of C_s typically used for single-phase simulations is too high for multiphase flow simulations. Consequently, we have performed all following studies using the Smagorinsky model with C_s=0.032. The underlying physical explanation for this very small Smagorinsky constant is most likely connected to the dissipation of turbulent kinetic energy by the gas bubbles. Thus, we assume that velocity fluctuations in the liquid phase are dampened out by the deforming gas-liquid interphase. This leads to a reduced amount of small-scale velocity fluctuations, which is not accounted for in the computer model used in our work. Similar speculations can be found in the PhD thesis of Hu.[103] Clearly, a more detailed analysis of these effects require future work in this area.

v)   Sensitivity to the Mapping Scheme
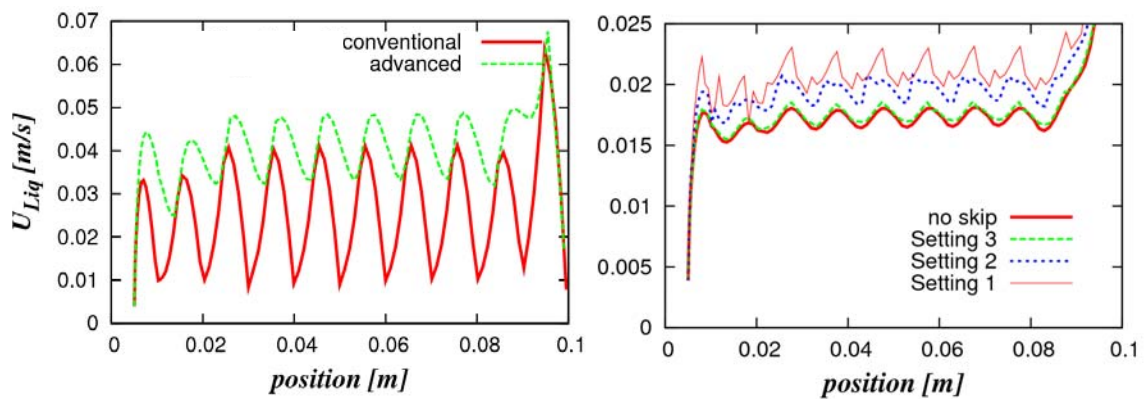
Figure 6.14: Comparison of different mapping schemes for the liquid-phase velocity at the bubble's center position (left: comparison of the Euler-to-Lagrangian mapping, right: comparison of different settings for the calculation of the virtual overlapping volume).

In order to test the effect of the implemented mapping scheme, we have analyzed the oscillations that occur in the liquid-phase velocity field when performing the full two-way coupling between gas and liquid phase. These oscillations have been reported also by other researchers.[27] As a test case, an air bubble (d_p=0.010 m) is tracked in an initially quiescent liquid (water). During the simulation the liquid-phase velocity at the bubble's position was recorded and subsequently plotted versus the vertical bubble position. The grid consisted of a rectangular box with the dimension $5 \cdot d_p$ x $5 \cdot d_p$ x $10 \cdot d_p$ and had a grid spacing of $1 \cdot d_p$. The results of this analysis are shown in Figure 6.14. As can be seen, the oscillations have a wave length equal to the grid spacing. To investigate this effect in more detail, we have analyzed the Euler-to-Lagrangian mapping scheme which performs the interpolation of Eulerian quantities at discrete locations (Figure 6.14 left). When this mapping is performed with the advanced method presented above, i.e., calculation via the virtual overlapping volumes (green dashed

line in Figure 6.14 left), the oscillations of the liquid-phase velocity can be reduced significantly. Furthermore, we have analyzed how different settings of the Lagrangian-to-Euler mapping influence the oscillations (Figure 6.14 right). We present here some results connected to the overlap calculation scheme described above. The red continuous line (Figure 6.14 right, labeled "no skip") corresponds to a setting where all cells in the vicinity of the bubble's position for the overlap calculation are considered. This is computationally very expensive. The other curves correspond to settings for which cells are skipped that are out of the range of the bubble. This check was performed for three different values of $x_{cell,max}$ in Eqn. 6.51. The value for $x_{cell,max}$ was increased linearly from setting 1 to setting 3. Clearly, when a too low value of $x_{cell,max}$ was selected, the total liquid velocity was (i) higher and (ii) the liquid-phase velocity fluctuations were significantly larger. Therefore, we used setting 3 in all following simulations. This setting required about 20% of the simulation time compared to the case in which the virtual overlapping volumes were calculated for all cells in the vicinity of the bubble's position (setting "no skip").

6.5.2 Mixing and Slow Reactions

Mixing in the liquid phase of a bubble column was studied by analyzing the filtered concentration distribution $\overline{Y}_i$ of an inert or reactive scalar. The filtered concentration distribution was obtained from the species transport equation (Eqn. 6.15) after the flow field in the bubble column had already reached a quasi-steady state. This was the case after approximately 100 s. To analyze mixing, we either (i) set an initial distribution of a scalar quantity in the liquid phase, i.e., mixing without mass transfer, or (ii) switched on mass transfer from the bubbles, i.e., mixing with simultaneous mass transfer.

i)   Definition of Mixing Metrics

In order to quantify mixing, we define two metrics that characterize the intensity, as well as the scale of segregation. The intensity of segregation is:

$$\sigma^2 = \frac{1}{\varepsilon_{L,mean} \cdot V_{tot}} \cdot \int_{V_{tot}} \left(\overline{Y}_i - \overline{Y}_{i,mean} \right)^2 \cdot \varepsilon_L dV \qquad (6.67)$$

To characterize the scale of segregation (initially introduced by Bothe et al.[104]) we define the quantity:

$$\Phi = \frac{1}{\varepsilon_{L,mean} \cdot V_{tot}} \cdot \int_{V_{tot}} \left| \nabla \overline{Y_i} \right| \cdot \varepsilon_L dV \tag{6.68}$$

Φ is a metric for the mean driving force for mixing in the liquid phase and has been previously used to investigate mixing in microreactors.[104-106] In Eqn. 6.67 and 6.68, $\overline{Y}_{i,mean}$ is the mean concentration of species i in the bubble column and V_{tot} is the total volume of the bubble column. ε_L is the local liquid-phase volume fraction. We have also analyzed the local distribution of these metrics by plotting the quantities $m_{\sigma^2} = \left(\overline{Y}_i - \overline{Y}_{i,mean} \right)^2$, as well as $m_{\Phi} = \nabla \overline{Y}_i$.
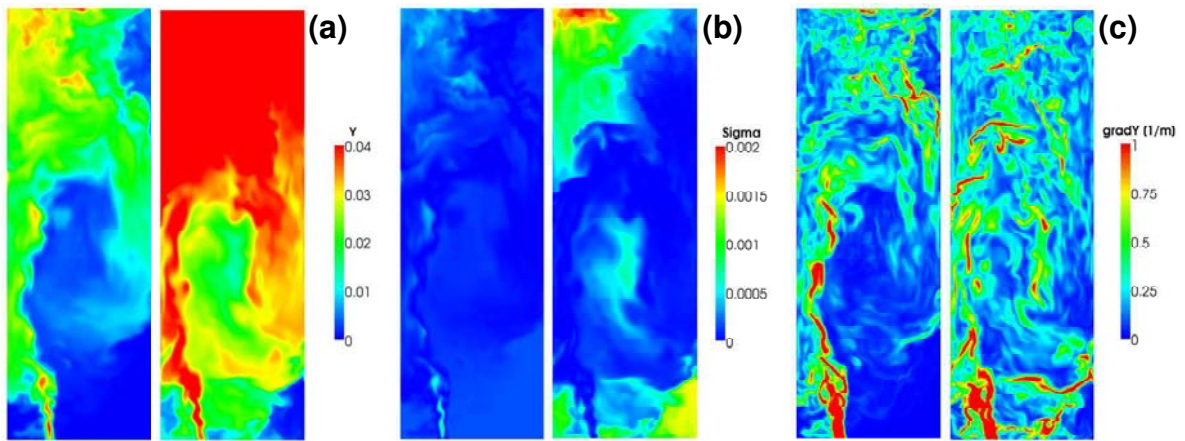
Figure 6.15: Contour plots of (a) concentration field Y, (b) local distribution of the intensity of segregation σ², and (c) scale of segregation Φ (left: t=5s, right: t=15s).

Typical snapshots of these quantities are shown in Figure 6.15 (shown is the base case as detailed in Table 6.2 using "mesh 0"). In Figure 6.15a the concentration has been made dimensionless using the equilibrium concentration at the gas-liquid interface. As can be seen from Figure 6.15a mass transfer from the gas to the liquid phase is slow and after 15s the maximum concentration level is only about 4%. Furthermore, due to the inhomogeneous distribution of the gas bubbles in the bubble column, there exist regions that are void of dissolving gas. From Figure 6.15b it can be seen, that the intensity of segregation is initially small (Figure 6.15b, left) and increases at locations with high mass transfer rates and poor agitation by bubbles, e.g., at the top where the bubble plume becomes more widespread. Furthermore, the local distribution of σ² (Figure 6.15b) indicates high values at the lower right corner. In this area the transport of dissolved species is slowest. This is due to the large-scale circulation pattern in the bubble column. Figure 6.15c is a plot of Φ, i.e., it shows where local

mixing occurs and how this areas change over time. Clearly, there is a strong driving force for mixing in the vicinity of the bubble swarm. However, as can be seen from Figure 6.15c (right), significant gradients in the concentration field are also present away from the bubble plume (bottom right corner).

To complete our understanding of mixing, we have also analyzed the volume distribution of m_{σ^2} and m_Φ. Thus, we have calculated the cumulative volume distributions $Q_3(m_{\sigma^2})$ and $Q_3(m_\Phi)$, as well as the corresponding volumetric frequency distributions $q_3(m_{\sigma^2})$ and $q_3(m_\Phi)$. This analysis was performed class-wise, i.e., we have defined 30 classes (defined by an upper and lower limit) ranging from zero to the maximum values of m_{σ^2}, as well as m_Φ. For the distribution functions of the intensity of segregation this can be formally written as:

$$Q_3\left(m_{\sigma_u^2,i}\right) = \frac{1}{\varepsilon_{L,mean} \cdot V_{tot}} \cdot \sum_{V_{tot}} H\left(m_{\sigma_u^2,i} - m_{\sigma^2,j}\right) \cdot \varepsilon_L \cdot \Delta V_j \tag{6.69}$$

$$q_3\left(m_{\sigma_m^2,i}\right) = \frac{\Delta Q_3\left(m_{\sigma_m^2,i}\right)}{\Delta m_{\sigma_m^2,i}} = \frac{Q_3\left(m_{\sigma_u^2,i}\right) - Q_3\left(m_{\sigma_u^2,i-1}\right)}{m_{\sigma_u^2,i} - m_{\sigma_u^2,i-1}} \tag{6.70}$$

Here, H() is the Heaviside step function. The indices i and j indicate the class index and the volume element index, respectively. The upper limit of the class i is denoted by $m_{\sigma_u^2,i}$ and the mean of class i by $m_{\sigma_m^2,i}$.

For the distribution of m_Φ similar expressions can be derived. By analyzing these two distributions it is possible to characterize the homogeneity of mixing in the reactor. To facilitate such an analysis, we have fitted the frequency distribution of m_Φ with a logarithmic normal distribution of the form:

$$q_{3,LN}(x) = \frac{1}{\sqrt{2\pi} \cdot \sigma \cdot x} \cdot \exp\left[-\frac{\left\{\ln\left(\frac{x}{\mu}\right)\right\}^2}{2 \cdot \sigma^2}\right] \tag{6.71}$$

Here, σ is the standard deviation and μ is the mean of the distribution.

ii)   Scalar Mixing without Mass Transfer

In order to analyze the liquid-phase mixing of an inert scalar in the bubble column without mass transfer we simply switched off mass transfer. In addition, these simulations were used to check the accuracy of the developed method with respect to the conservation of scalars, i.e., we monitored the total mass of the scalar during the simulation. This conservation check showed that the used numerical schemes and the settings of the solver led to a conservation of the total mass of the inert scalar within ± 0.2 % for a total simulation time of 100 s.
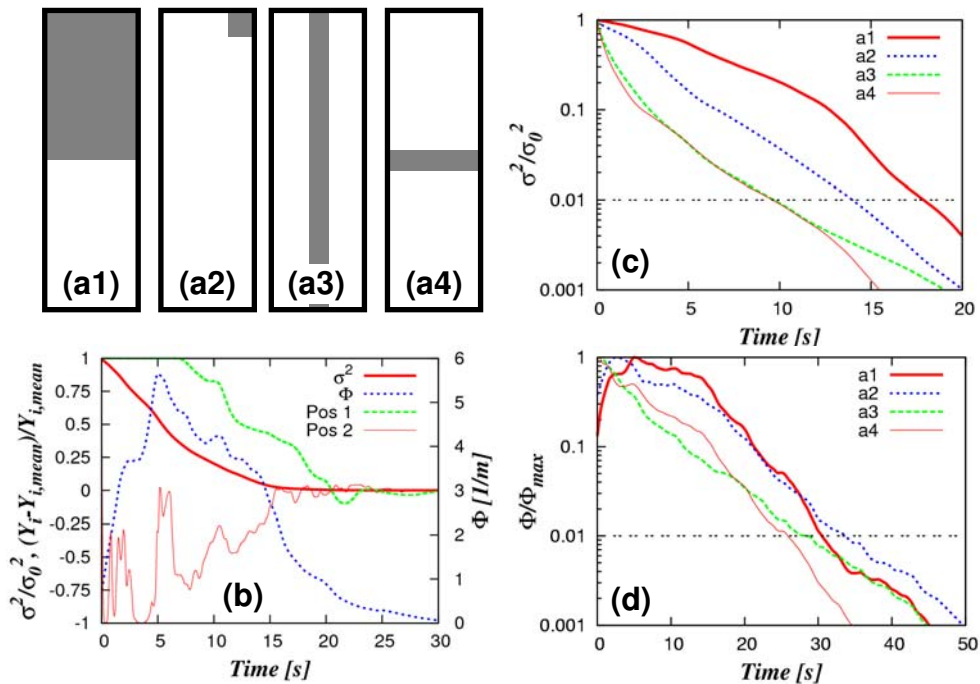
Figure 6.16: Analysis of mixing metrics for different initial distributions of an inert scalar without mass transfer (a1: 'half-half' distribution; a2: 'corner' distribution; a3: 'vertical' distribution; a4: 'horizontal' distribution; b: mixing metrics for the half-half initial distribution, Pos 1: x=0.001 y=0.001 z=0.001, Pos 2: x=0.250 y=0.040 z=0.750; c: normalized intensity of segregation vs. time; d: normalized scale of segregation vs. time)

The initial distributions of the inert scalar are shown in Figure 6.16a1 to Figure 6.16a4. First, we analyzed which mixing metric is the most suitable one to be used for our studies. Therefore, the scale and intensity of segregation are plotted together with the normalized concentrations at two different positions (see Figure 6.16b, Pos 1 refers to a position in the corner of the bubble column whereas Pos 2 is located in the center of the bubble column). For this study the 'half-half' initial distribution was used (Figure 6.16a1). As can be seen clearly from Figure 6.16b, the time profiles of the normalized concentration distributions give a highly noisy signal. The plots indicate that complete mixing is obtained after approx. 18 and 25 s for Pos. 2 and Pos. 1, respectively. In contrast, the time profiles in Figure 6.16b for the

normalized intensity and scale of segregation show a smooth profile. This is because they represent an integral measure for mixing, and hence, better represent the total state of the bubble column. In addition, these curves show characteristic points, i.e., the scale of segregation has a pronounced peak after approx. 5 s and then shows a steady decrease. This peak can be interpreted as the time when the maximum driving force is present in the system, i.e., where mixing is fastest. In conclusion, the mixing metrics σ^2 and Φ seem to be better suited to define mixing time scales than concentration profiles, as the latter are sensitive to local velocity fluctuations and the position in the reactor.

Second, we analyzed the effect of the initial distribution of the inert scalar on the mixing metrics of interest (Figure 6.16c and d). As can be seen from these graphs, the normalized intensity of segregation (the initial value of σ^2 was used as the reference) shows large differences in the time profiles for different initial distributions and predicts characteristic mixing times between 9 and 17 s (deviation of ± 31 %, we have taken $\sigma^2/\sigma_0^2 = 0.01$ as 'perfectly mixed'). In contrast, the normalized scale of segregation is much less sensitive to the initial distribution of the scalar and gives significantly higher mixing times between ca. 27 and 34 s (deviation of ± 11 %, we have taken $\Phi/\Phi_{max} = 0.01$ as 'perfectly mixed'). In conclusion, the scale of segregation, representing the driving force for mixing, seems to be the most appropriate metric for investigating mixing times.
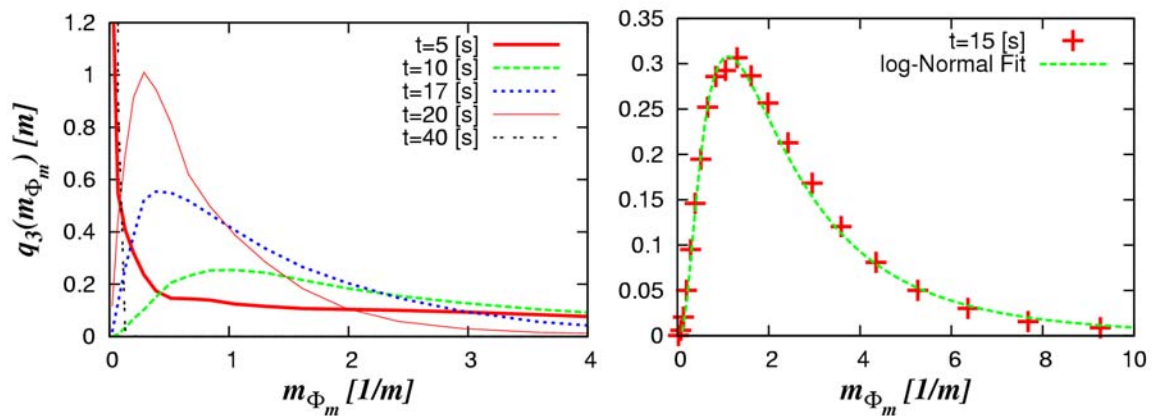
Figure 6.17: Distribution of the scale of segregation for an inert scalar without mass transfer (initial distribution according to Figure 6.16a1; left: comparison of distributions for different times, right: log-normal fit of the distribution after a time of 15 s).

In Figure 6.17 we have analyzed the frequency distribution of the scale of segregation for the case of the 'half-half' distribution of the inert scalar. For time zero, the distribution of the scale of segregation has two peaks: (i) at zero (corresponding to the zone where the

concentration is uniform) and at (ii) infinity (corresponding to the interface between the region with and without inert scalar) Clearly, for the shortest time (see Figure 6.17 left) the peak near zero is still present, whereas for higher values of the scale of segregation the curve is monotonically decreasing. After approximately 10s, zones of uniform concentration have completely vanished. This is indicated by the fact that the distribution now has a value of zero at the origin. As mixing goes on, the distribution becomes narrower and the peak is moving to a smaller value of m_{Φ_m}. Thus, the concentration field becomes more uniform and the driving force for mixing is decreasing. Interestingly, also the driving force becomes more uniformly distributed as indicated by the narrower distribution at later times.

In Figure 6.17 right, we show the fit of the distribution of the scale of segregation after 15s. Clearly, the correspondence between simulation results and the fitting function (Eqn. 6.71) is nearly perfect indicated by a root-mean-square value of residuals for this fit of 0.00942. A detailed analysis of this surprising finding was not performed in our work. However, it strongly suggests that the distribution of concentration gradients in bubble columns is possibly caused by a simple mechanism, e.g., stretching and folding of fluid elements similar to single phase flow.

iii) Scalar Mixing with Mass Transfer – Distribution of the Scale of Segregation
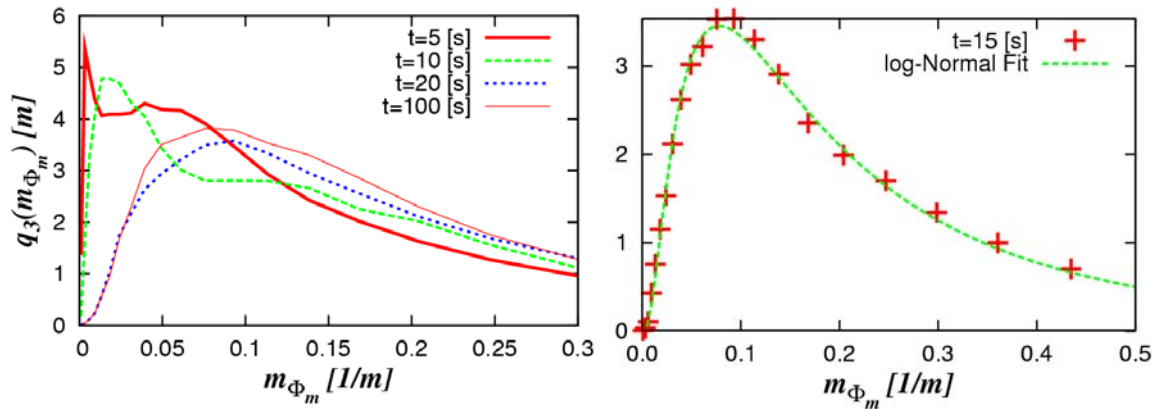
Figure 6.18: Distribution of the scale of segregation for the base case with mass transfer (d_P=1.6 mm, V_G=1.6 L/min, mesh 0) (left: comparison of distributions for different times, right: log-normal fit of the distribution after a time of 15 s).

In Figure 6.18 we illustrate the distribution of the scale of segregation for the base case with mass transfer (d_p=1.6 mm, V_G=1.6 L/min). Similar to the case without mass transfer the distribution becomes almost perfectly log-normal after a certain time (see Figure 6.18 right). However, in contrast to the case without mass transfer, initially no peak at $m_{\Phi_m} = \infty$ is

present. Furthermore, the slow mass transfer from the gas- to the liquid phase leads to areas having a small scale of segregation (see Figure 6.18 left, peak in the curve for t = 10s).

iv) Mixing with Mass Transfer – Basic Observations and Impact of Sc_{SGS} on the Mixing Metrics

Before analyzing the mixing in the system including mass transfer, the effect of different values of the sub-grid-scale Schmidt number Sc_{SGS} on the mixing metrics was quantified. Figure 6.19 shows the dependency of the two mixing metrics σ^2 and Φ vs. time for two different values of Sc_{SGS}. For this analysis we set the equilibrium concentration at the gas-liquid interface equal to one, i.e., the following results are also applicable to concentration fields normalized with the equilibrium concentration.
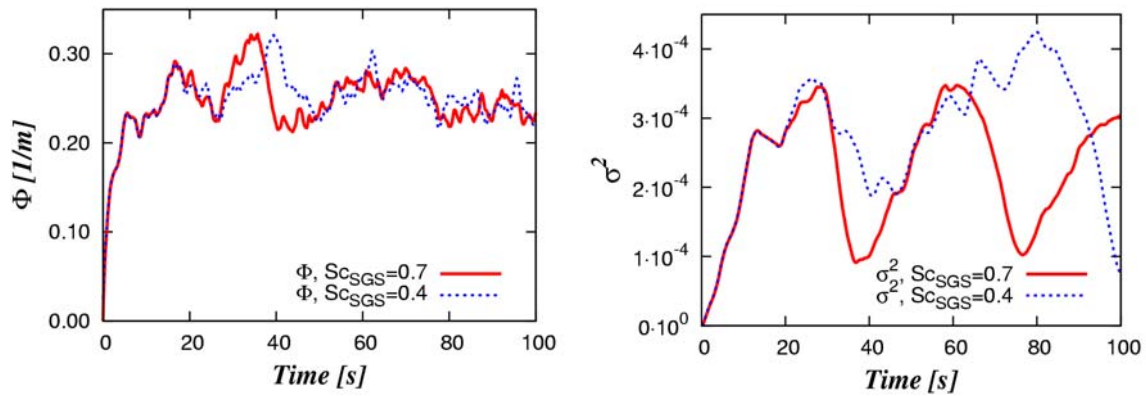
Figure 6.19: Mixing metrics for different sub-grid-scale Schmidt numbers Sc_{SGS} (left: scale of segregation, right: intensity of segregation).

As can be seen in Figure 6.19, the characteristics of the time profiles of both mixing metrics are substantially different from the case without mass transfer (Figure 6.16c-d). First, the scale of segregation seems to reach a plateau value after an initial increase. This means that a slightly fluctuating driving force for mixing is established rapidly in the bubble column. Second, the intensity of segregation fluctuates significantly stronger and the fluctuations show a characteristic frequency of approximately 40s. This characteristic frequency corresponds to the fluctuation of the gas hold-up (see Figure 6.23c, curve for d_p=1.6 mm). Thus, when the gas hold-up decreases, also the intensity of segregation decreases. This effect is caused by two phenomena: first, due to the decreased rate of mass transfer at a lower gas hold-up, the local concentration fluctuations in the bubble column also become smaller. Second, the instantaneous mixing rate is only weakly influenced by the gas hold-up. This is due to the slowly decaying liquid-phase turbulent motion in the liquid phase. Both phenomena lead to a

strong increase in the intensity of segregation as the quadratic deviations from the mean concentration are used for the calculation of σ^2 (see Eqn. 6.67). To illustrate this effect, dimensionless concentration contour plots for different times between t=30s and t=38s are shown in Figure 6.20. Clearly, at t=30s a cloud of high concentration has formed at the top section of the bubble column. At this moment, due to fluctuations in the liquid-phase velocity field, the gas hold-up starts to decrease (see Figure 6.23c). Subsequently, the cloud is transported downwards by the main recirculation loop and mixed with the liquid in the lower right corner of the bubble column (see Figure 6.20, images for t=32s to t=38s).
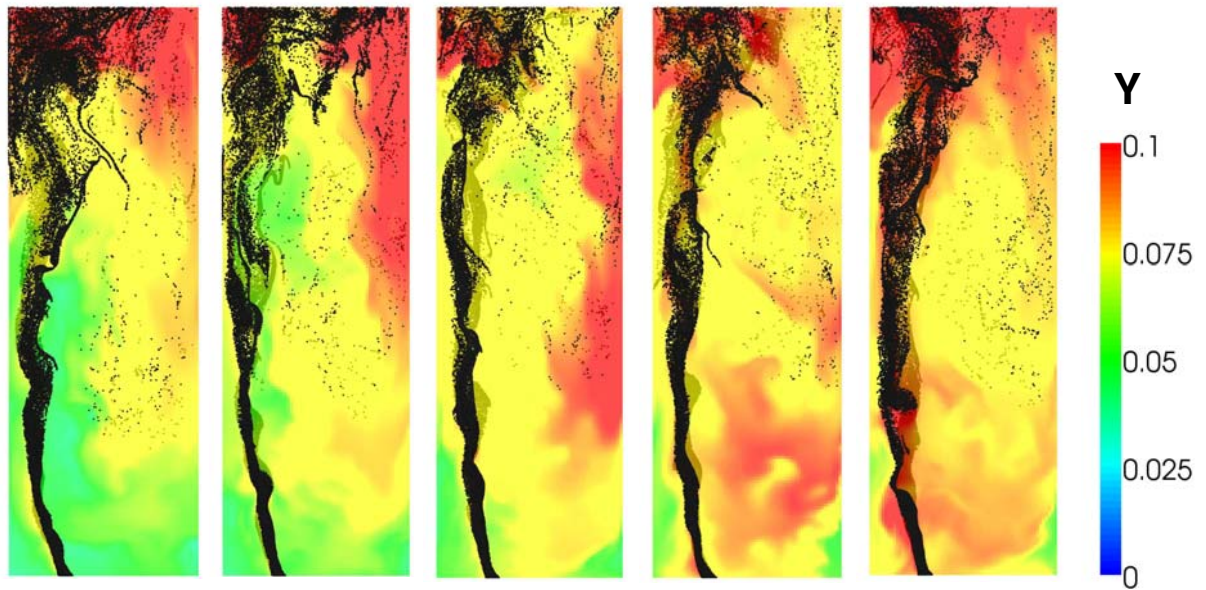
Figure 6.20: Concentration contour plot and bubble positions for Sc_{SGS}=0.7 (images correspond to snapshots at t=30s, t=32s, t=34s, t=36s and t=38s from left to right, the concentration field has been made dimensionless using the equilibrium concentration at the gas-liquid interface).

When comparing this behavior for different Sc_{SGS} (see Figure 6.19), we observe that the magnitudes of both mixing metrics are very similar in both cases. Therefore, we conclude that the sub-grid-scale Schmidt number does not have a significant impact on mixing. Hence, we used the value of Sc_{SGS}=0.7 for all following computations in our work.

v)   Impact of Grid Size on the Mixing Metrics

Same as for the liquid-phase flow, we have performed a grid-sensitivity analysis of the results for the mixing metrics. Again, we have set the equilibrium concentration at the gas-liquid interface equal to 1.

As can be seen from Figure 6.21, with the medium and fine grid more details of the concentration field can be resolved and hence a larger scale of segregation Φ is obtained. In

addition, it is clear that numerical diffusion decreases with increasing mesh resolution resulting in a higher accuracy with respect to the resolution of the concentration field. However, as we have used identical numerical schemes throughout this work, the effect of numerical diffusion is identical for all simulation cases.
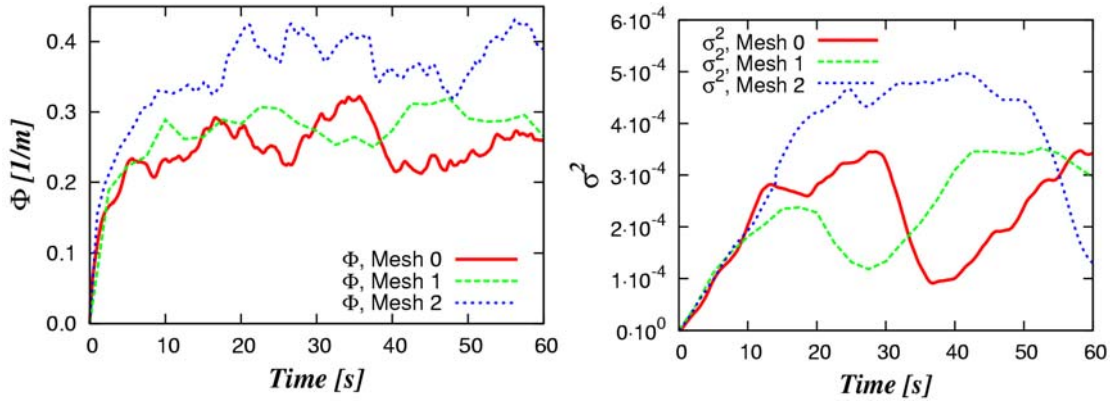
Figure 6.21: Grid sensitivity study of mixing metrics (left: scale of segregation, right: intensity of segregation).

Parameter	Mesh 0	Mesh 1	Mesh 2
$\varepsilon_{G,mean,0\text{-}100s}$	0.187	0.181	0.202
$\Phi_{av,0\text{-}100s}$ [1/m]	0.247	0.253	0.378
$\sigma^2_{av,0\text{-}100s}$	$2.24 \cdot 10^{-4}$	$2.02 \cdot 10^{-4}$	$4.04 \cdot 10^{-4}$
$\mu_{m_\Phi,60s}$ [1/m]	0.192	0.185	0.271
$\sigma_{m_\Phi,60s}$	1.02	0.911	0.864
Δx [mm]	7.81	6.00	4.17

Table 6.4: Grid dependency of gas hold-up and mixing metrics, d_p = 1.6 mm, V_G = 1.6 L/min (time-averaging was performed for 60 s only for the case involving mesh 2).

For the intensity of segregation (refer to the trend of $\sigma^2_{av,0\text{-}100s}$ in Table 6.4) a similar trend is observed. However, the strong fluctuation in this mixing metric prohibits a direct comparison of the curves for different grids. This effect is due to the sensitivity of σ^2 to the local flow field, i.e., the grid resolution affects the flow field and consequently the gas hold-up, as well as the local concentration distribution. In conclusion, also the coarsest grid gives satisfactory resolution of the concentration field and it is supposed that trends for mixing are well captured with this grid.

In Table 6.4 we show the influence of a finer grid spacing on the time-averaged mean gas hold-up and different metrics for mixing. First, the differences in the calculated gas hold-ups averaged over 100s, i.e., $\varepsilon_{G,mean,0\text{-}100s}$, are small and are well below 10%. Thus, the grids give essentially the same results for multiphase flow. Second, the mixing metric Φ_{av}, i.e., the scale of segregation, increases with increasing mesh resolution. Thus, spatial gradients in the concentration field are resolved better with a smaller grid spacing. This gives a significantly higher value for Φ_{av} for the finest grid. This trend is also visible for the mean value $\mu_{m_\Phi,60s}$ of the distribution of m_Φ taken after 60s. Similar to the scale of segregation, the intensity of segregation is highest for the finest grid. This is due to the fact, that (i) the concentration field is better resolved with a finer grid, (ii) numerical diffusion is reduced when using smaller grid spacing and (iii) the intensity of segregation is a function of the sample volume which corresponded to the volume of a computational cell, i.e., was much smaller for the finer grid. Third, the standard deviation $\sigma_{m_\Phi,60s}$ of the distribution of the scale of segregation decreases with increasing grid resolution. This also reflects the higher spatial resolution of the concentration field, less numerical diffusion and hence a narrower distribution in case of a smaller grid spacing.

In summary, while the hydrodynamics seem to be unaffected by the grid size, the trends in the calculated mixing metrics show a certain grid dependency. This grid dependency stems from (i) the high Schmidt numbers in the liquid phase leading to extremely fine concentration patterns that cannot be resolved with the current LES and (ii) the principal inability of LES to yield grid independent results.[107] Since it is clear that it will be never possible to fully resolve all details of the concentration field by using LES, it is essential to show and recognize the trends due to different grid sizes. Clearly, the observed trends for the mixing metrics over the grid size are consistent. Hence, at a fixed grid size it should be possible to compare simulation results for different operating conditions. Thus, we conclude that the used grid size (i.e., mesh 0) is suitable to study the influence of bubble size, gas feed rate, domain size, as well as relatively slow chemical reactions (i.e., that are not influenced by subgrid scale fluctuations) on the mixing conditions in the bubble column.

vi)   Long-Term Behavior of the Mixing Metrics

For the medium grid used in our work (mesh 1), we studied the long-term behavior of the mixing metrics. With long-term behavior we refer to the influence of the accumulated species that is transferred from the gas to the liquid phase.

In Figure 6.22 we show the time profiles for σ^2 and Φ together with curves that are of the form:

$$y(t) = y_0 \cdot \exp\left[-\frac{t}{\tau}\right], \tag{6.72}$$

where y is one of the two mixing metrics used, i.e., Φ or σ^2, y_0 is the mixing metric at time zero and τ is the time constant for mass transfer, i.e., $1/(k_L a)$. Thus, Eqn. 6.72 predicts the time evolution of the concentration difference between the equilibrium concentration at the interface (set equal to one in our simulations) and the mean concentration in the liquid phase (Eqn. 6.72 can be derived from a simple mass balance of the dissolving species in the liquid phase). Note, that the average of $k_L a$ is known from the simulations and that y_0 has been calculated by fitting y(t) to the instantaneous values for σ^2 and Φ. As can be seen from Figure 6.22, the function given by Eqn. 6.72 is able to approximate the decrease of both mixing metrics in time reasonably well. Thus, both mixing metrics depend linearly on the concentration difference between the gas-liquid interface and the mean bulk concentration. This result reflects the simple fact that the mixing metrics only depend on concentration differences and not on absolute values for the concentration.
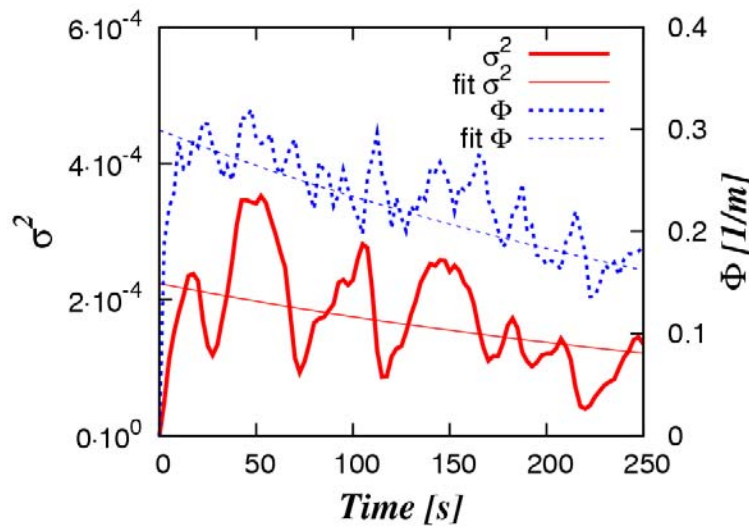
Figure 6.22: Time profiles for the mixing metrics σ^2 and Φ for long times (mesh 1).

vii) Effect of the Bubble Size on Mixing

In the following, we analyzed the effect of the bubble size on the mixing in the bubble column. For this analysis we have included mass transfer from the gas phase to the liquid phase (equilibrium concentration set equal to 1) and have assumed zero initial concentration in the liquid phase. Also, we have kept the gas feed rate constant, i.e., the total power input into the system is not increased (the total power input is the product of the gas feed rate and the pressure difference between gas inlet and outlet). However, we expect the total mass transfer rate to increase with decreasing bubble size and to get similar mixing rates in the system as the power input is identical. The driving force, i.e., the scale of segregation, should decrease with increasing bubble size because the total mass transferred into the liquid bulk becomes smaller.
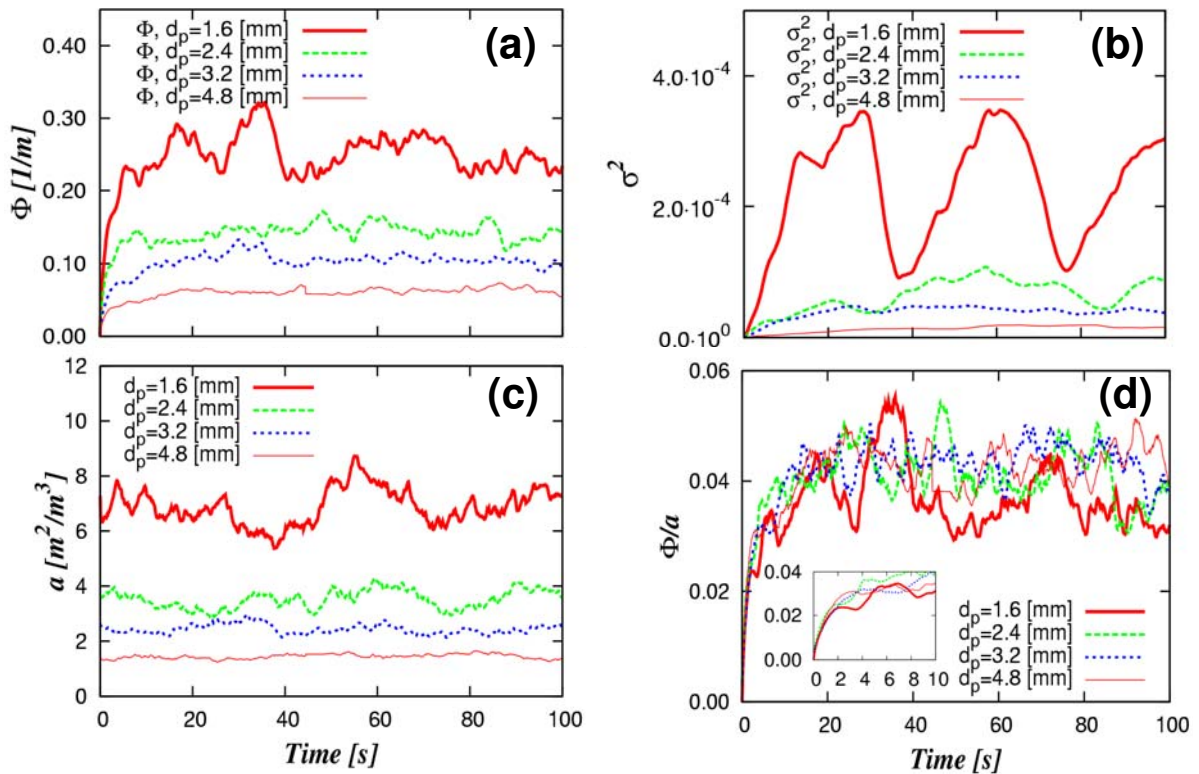
Figure 6.23: Time profiles of mixing metrics and interfacial area for different bubble sizes: (a) scale of segregation, (b) intensity of segregation, (c) interfacial area, (d) ratio of scale of segregation and interfacial l area.

The time profiles for these simulations are shown in Figure 6.23 and important results are summarized in Table 6.5. Clearly, the initial transient for Φ is similar, i.e., very fast, for all bubble diameters indicating similar mixing rates. However, the main difference is that, as expected, the scale of segregation (Figure 6.23a), as well as the intensity of segregation (Figure

6.23b) is smaller for the larger bubbles. In addition, the latter measure is fluctuating significantly more strongly for smaller bubbles. This is caused by the stronger fluctuations in the gas hold-up resulting in a fluctuation of the specific interfacial area a (Figure 6.23c). Note, that the interfacial area was calculated directly from the mean gas hold-up by $a=\varepsilon_G \cdot 6/d_p$. To quantify the effect of the specific interfacial area on Φ, we have calculated the dimensionless quantity Φ/a. As can be seen from Figure 6.23d, this quantity is similar for all cases studied. Thus, a important result of our work is that the scale of segregation is inversely proportional to the bubble diameter. Also, the intensity of segregation decreases with increasing bubble diameter, since the total amount of dissolved gas and consequently its mean concentration is lower due to the lower interfacial area of the larger bubbles. Again, as we see in the insert in Figure 6.23d (showing the first 10s of the Φ/a time profile), the initial transient in Φ/a is similarly fast indicating similar mixing rates.

Parameter	$d_p=1.6$ mm	$d_p=2.4$ mm	$d_p=3.2$ mm	$d_p=4.8$ mm	$V_G=0.4$ L/min	$V_G=0.8$ L/min	$V_G=3.2$ L/min
ε_G	0.187	0.141	0.129	0.116	0.0523	0.0923	0.357
a [m²/m³]	7.00	3.52	2.42	1.45	1.96	3.46	13.4
$\mu_{m_\Phi,60s}$ [1/m]	0.192	0.127	0.0661	0.0467	0.109	0.132	0.154
$\sigma_{m_\Phi,60s}$	1.02	0.988	0.992	1.138	1.05	0.891	0.968

Table 6.5: Influence of bubble size (at $V_G=1.6$ L/min) and gas flow rate (with $d_p=1.6$ mm) on gas hold-up, interfacial area and mixing metrics.

viii) Effect of the Gas Feed Rate on Mixing

As the power input is directly proportional to the gas feed rate, an increase in the feed rate should lead to an increase of the mixing rate. In other words, the meso-mixing time scale should become smaller. Also, the gas hold-up will increase with increasing gas feed rate, leading to a higher rate of mass transfer and consequently to an increase of the scale of segregation.

In Figure 6.24 the results are shown by plotting the two mixing metrics as a function of time. Important results for the effect of the gas feed rate on mixing are summarized in Table 6.5. As expected, in the case of $V_G=0.4$ L/min, we observe the slowest transient in σ^2 (Figure 6.24b).

Also, a small increase in the scale of segregation is visible from our simulation results. This increase is, however, significantly less pronounced compared to the effect of the bubble size. This is due to the fact, that the increased mass transfer rate (see Figure 6.24c where we have plotted the specific interfacial area *a*) is counterbalanced by increased mixing for the higher gas feed rate. Consequently, if we try to make Φ dimensionless by division by *a*, we do not get similar dimensionless values for Φ/a for different gas feed rates (see Figure 6.24d). In contrast, the case with the lowest gas feed rate, i.e., V_G=0.4 L/min gives the highest dimensionless value of Φ/a indicating the lowest mixing rate in the system.
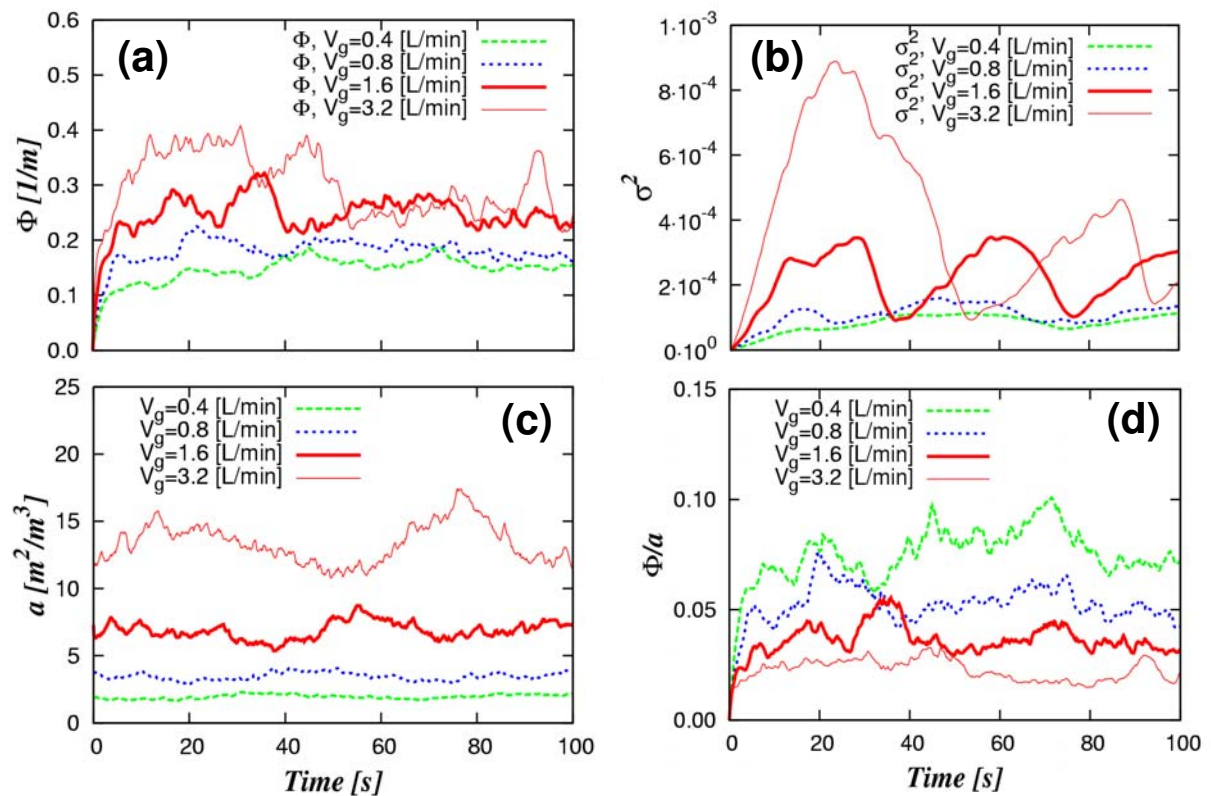
Figure 6.24: Time profiles of mixing metrics and interfacial area for different gas feed rates: (a) scale of segregation, (b) intensity of segregation, (c) interfacial area, (d) ratio of scale of segregation and interfacial area.

ix) Scale-Up: Effects of the Domain Size on Mixing

We also investigated the effect of the system size on the mixing properties and thus, performed two additional simulations with identical superficial gas velocity for different widths (dimension W in Figure 6.9) of the bubble column. The two simulations were performed with one-half and one-quarter of the width of the bubble column, i.e., with W=0.25 m and W=0.125 m, respectively. We used an identical grid spacing for all these

simulations in order not to influence the mixing metrics. This is especially important with respect to the calculation of the scale of segregation Φ. Also, bubble size, height to width-ratio and the depth of the bubble column where held constant. We have kept the depth of the column constant in order to minimize effects stemming from different cell counts in y-direction.

In the simulations of the smaller bubble columns the mean gas hold-up and consequently the interfacial area were essentially the same as for the base case detailed in Table 6.2 (see Figure 6.10, ε_G was 0.196 and 0.204 for the case with one-half and one-quarter of the size, respectively). Also, the mean liquid-phase velocity distribution in the bubble column agreed well with that of the base case (see Figure 6.25 and Figure 6.10b). However, the overall liquid-phase velocities were significantly smaller for the simulations with reduced size.
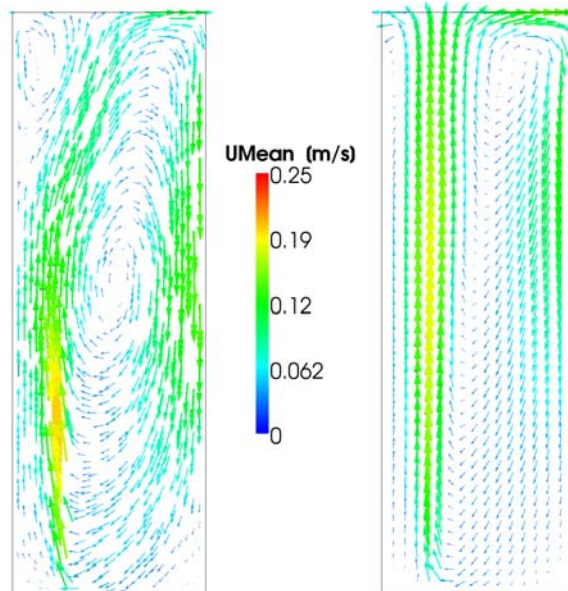
Figure 6.25: Time-averaged flow field for the bubble column with (left) one half and (right) one quarter of the size as the base case (both figures share the same color bar).

For the quarter-sized column (Figure 6.25 right), the recirculation zone near the top disappeared, and the main circulation loop was significantly shifted upwards. As expected, the intensity of segregation (see Figure 6.26 right) is the highest and the frequency of the oscillation is the lowest for the full scale bubble column. The significantly higher frequency in the oscillation of σ^2 for the smallest bubble column (Figure 6.26 right, ¼ size) is due to the fact that all bubbles rise almost vertically in this setup, i.e., there is no significant oscillation of the gas hold-up (results not shown). Hence, it seems that the intensity of segregation does not only depend on the superficial gas velocity or the specific power input (note that the latter is

also constant as the superficial gas velocity was held constant). Surprisingly, Φ is only weakly influenced by the scale (see Figure 6.26 left). This is an interesting finding, since it provides a basis for the scale-up of bubble columns with respect to mass transfer and mixing.
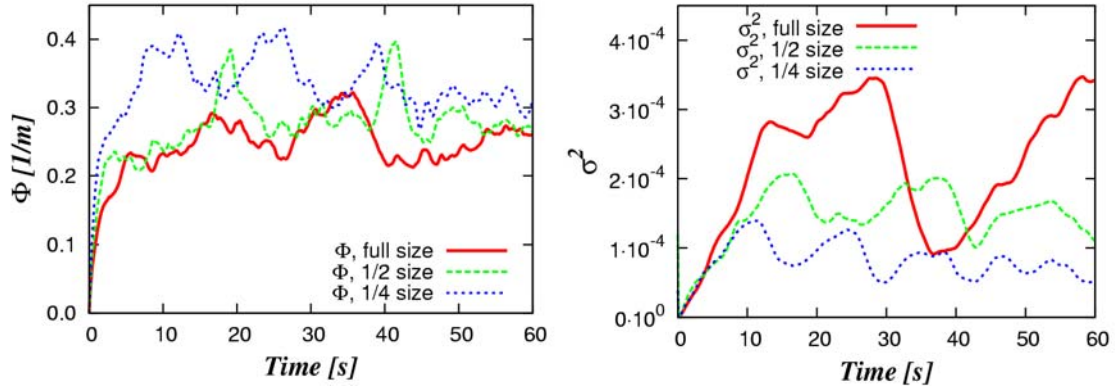
Figure 6.26: Effect of the size of the computational domain on the mixing metrics.

x)   Mixing and Chemical Reactions in Fermentation Reactors

The interaction of meso-scale mixing with a typical fermentation reaction was investigated. For this purpose we studied the oxygen uptake by microorganism suspended in the liquid phase of the bubble column. For typical conditions in an industrial fermenter, the oxygen saturation concentration $Y_{O2,sat}$ in the liquid phase should be between 5 and 8 mg/L. The oxygen consumption in such a fermentation can become significant, such that mixing and mass transfer become rate limiting. Furthermore, it is well known that under non-ideal conditions, the microorganisms excrete byproducts, e.g. ethanol and glycerol,[108] leading to a reduction of the yield. Hence, a strategy to estimate mixing and mass transfer in these reactors would give better tools for an optimized design.

The kinetic expression for oxygen uptake by microorganisms in fermentations can be described, e.g., by a Michaelis-Menten type rate equation:

$$r_{O_2} = k_{0,0} \cdot \frac{Y_{O_2}}{K_O + Y_{O_2}} \qquad\qquad (6.73)$$

Here r_{O2} is the oxygen uptake rate, $k_{0,0}$ is a reaction rate constant, Y_{O2} is the concentration of oxygen in the reactor and K_O is the Michaelis-Menten constant. K_O is typically small compared to the equilibrium concentration of oxygen in the liquid phase. Consequently, the oxygen uptake rate r_{O2} is nearly constant, i.e., we have an almost zero-order oxygen uptake in the fermenter. For the current analysis we have taken $K_O = 5 \cdot 10^{-5}\, kg/m^3$, which is typical for

fermentations (e.g., refer to the analysis of Sweere et al.[108] for baker's yeast). K_O is two orders of magnitude smaller compared to the oxygen saturation concentration $Y_{O_2,I} = Y_{O_2,sat} = 5 \cdot 10^{-3} \, kg/m^3$.

In our work we focus on relatively slow reaction kinetics and analyze the concentration distribution, as well as the interaction with mixing for characteristic reaction times τ_R ranging from 10 to 200 s. τ_R is defined as the ratio of the oxygen saturation concentration and the reaction rate constant, i.e., $\tau_R = Y_{O_2,I}/k_{0,0}$. Thus, compared to the mass transfer time constant in the bubble column (which can be calculated from the inverse of the average value for $k_L \cdot a$, yielding approximately 400 s), the oxygen uptake by the microorganisms is faster. Furthermore, the micro-mixing time τ_M can be estimated using the engulfment model Eqn. 6.74.[109]

$$\tau_M = 17 \cdot \left(\frac{\nu}{\varepsilon}\right)^{1/2} \tag{6.74}$$
,

A micro-mixing time of approximately 0.2 s is obtained when assuming that the energy dissipation rate ε is uniformly distributed in the bubble column. Thus, micro mixing is at least one order of magnitude faster than the oxygen uptake. Consequently, we do not need to take into account a sub-grid-scale model for the interaction of micro mixing and reactions and can calculate the reaction rate from the filtered concentration distribution.

In the following, our simulations are compared with results for a well-mixed bulk phase. A simple mass balance gives the differential equation for the well-mixed reactor:

$$\varepsilon_L \cdot V_{tot} \cdot \frac{dY_{O_2,mean}}{dt} = k_L \cdot A \cdot \left(Y_{O_2,I} - Y_{O_2,mean}\right) - \varepsilon_L \cdot V_{tot} \cdot r_{O_2} \tag{6.75}$$

Here A is the total gas-liquid interface and V_{tot} is the total volume of the multiphase mixture, i.e., the volume of the computational domain. After inserting the kinetic expression Eqn. 6.73, the above equation can be numerically integrated to give the time profile of $Y_{O2,mean}$. The comparison of the simulated mean concentration in the bubble column and the well-mixed reactor is shown in Figure 6.27a-c. In these plots we have normalized the resulting mean concentration fields by the interface concentration, i.e., $Y_{O_2,I}$. As can be seen, fundamental differences are caused by the oxygen uptake rate. Specifically, we observe that a fast reaction

with a small reaction time constant τ leads to a high frequency in the oscillations of the mean concentration. In addition to the high-frequency oscillation in Figure 6.27a, also a low-frequency oscillation can be observed. This slow change in the mean concentration is caused by the change of the gas hold-up and consequently of the interfacial area in the bubble column (refer to the discussion earlier in this work and the curve for d_p=1.6 mm in Figure 6.23c where we have quantified the oscillation of the interfacial area a). For slower reaction rates, this low frequency oscillation is even more pronounced and clearly visibly from Figure 6.27b and Figure 6.27c.
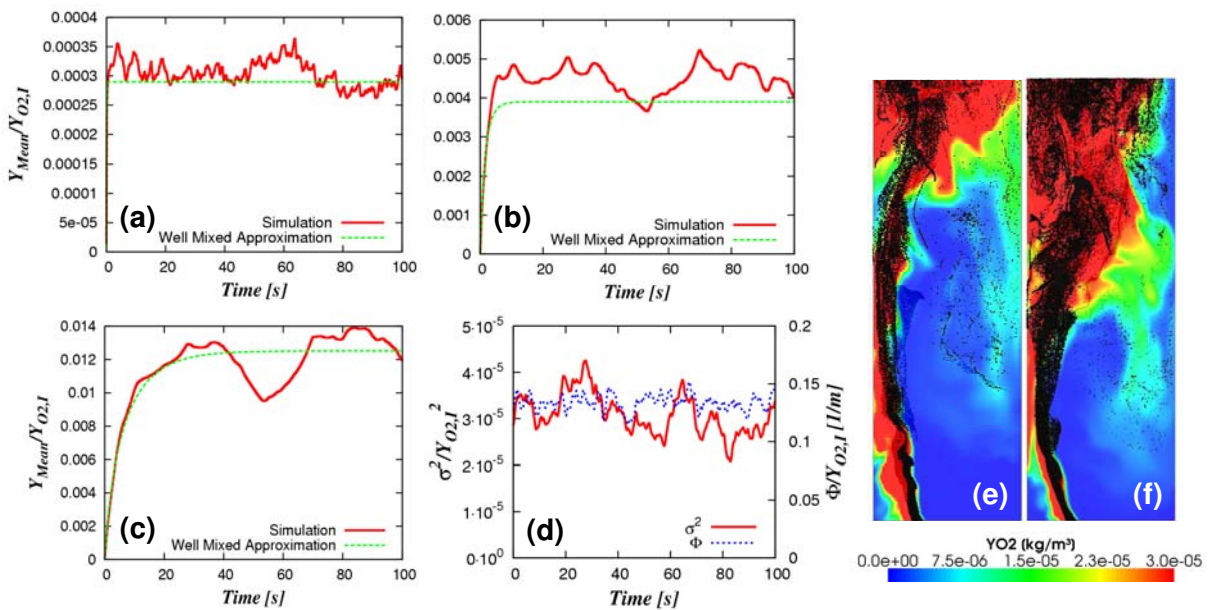
Figure 6.27: Dimensionless mean concentration profiles: (a) τ_R=10s, (b) τ_R=100 s, (c) τ_R=200 s; (d) mixing metrics for the case with τ_R=100 s; and snapshots of the concentration profile and bubbles for the case with τ_R=100 s: (e) t=52 s, (f) t=70 s).

We included two snapshots of the oxygen concentration distribution, as well as the position of individual bubbles in Figure 6.27e (at t=52 s, i.e., where the mean concentration in Figure 6.27b has a local minimum) and Figure 6.27f (at t=70 s, i.e., where the mean concentration in Figure 6.27b has a local maximum). Clearly, the concentration distribution is strongly inhomogeneous in both figures and zones with nearly no oxygen exist. Thus, for these system parameters mass transfer is limiting which leads to regions starving of oxygen.

To quantify mixing under these circumstances, we have plotted the time profiles of the mixing metrics σ^2 and Φ in Figure 6.27d. This mixing metrics correspond to the time profile of the mean concentration in Figure 6.27b. Also, we have made the mixing metrics dimensionless by

dividing Φ and σ^2 with $Y_{O_2,I}$ and $Y_{O_2,I}^{\;2}$, respectively. Clearly, both the normalized intensity of segregation σ^2, as well as the normalized scale of segregation Φ, are significantly smaller compared to the case of non-reactive mixing (see Figure 6.19). Also, the fluctuation of σ^2 is much smaller compared to the case of inert mixing. The scale of segregation Φ is essentially constant, indicating a constant mean driving force for mixing. Finally, we have analyzed the distribution of the normalized scale of segregation Φ for the case with a reaction time constant of τ_R=100 s in Figure 6.28 for different times. In contrast to the case without reactions, the distribution has a peak at m_Φ=0. This is due to the fact, that most of the liquid phase is depleted of dissolved oxygen, and hence, has zero driving force for mixing. Also, the distribution does not change significantly between the time steps that have been studied, indicating that mixing and the chemical reaction are balanced in this system within a very short time period.
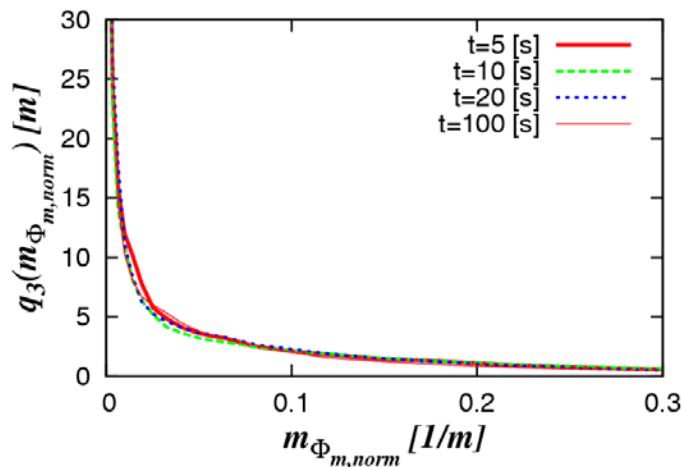
Figure 6.28: Normalized distribution of the scale of segregation for a reactive scalar (τ_R=100 s)

6.5.3 Analysis of Fast Reactions

By taking mass transfer into account, the concentration field of a dissolving (inert) species (e.g., oxygen) can be visualized in a bubble column. This has been done by plotting both the filtered concentration, as well as the scalar variance field in Figure 6.29 for two different time instances. For these simulations, the scalar variance source term due to mass transfer has been set to zero (i.e., the last term in Eqn. 6.24). This was done because no setting for the parameter α in Eqn. 6.24 yielded stable solutions for the scalar variance. Also, literature data on this parameter for gas-liquid flow were not available. The plots in Figure 6.29 have been made dimensionless with the saturation concentration and the squared saturation

concentration, respectively. As can be seen, both the filtered concentration field, as well as the variance field show similar features, i.e., extremely high values near the inlet and at the upper part of the column. The scalar variance is, however, approximately four orders of magnitude lower than the filtered dimensionless concentration. This is thought to be due to the relatively large mass-transfer time scale, which is in the order of 200 s. Thus, the mass transfer is so slow that the mixing induced by the bubble motion is much quicker, leading to a very low scalar variance.
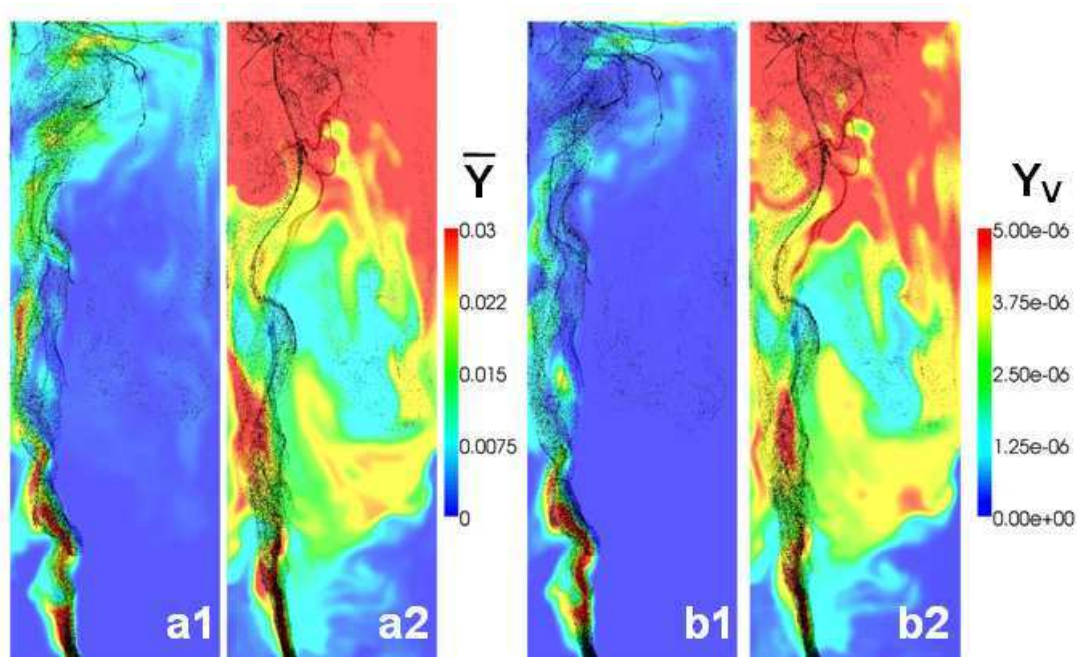
Figure 6.29: Dimensionless, filtered concentration (a1, a2) and scalar variance (b1, b2) contour plots after 2 s (left) and 10 s (right) for an inert scalar.

i)   Results for the Chemical Reaction Source Term

In order to analyze fast chemical reactions, we investigated the outcome of a parallel chemical reaction network,[48] i.e., the hydrolysis of DMP in the "Becker" case. This choice is motivated by the fact that the hydrolysis of DMP has been already studied, and experimental, as well as numerical results, can be found in literature.

The first task was to calculate the look-up table for a fixed set of process parameters summarized in Table 6.6. This setup resulted in a value for β of 1.05. The resulting look-up table has then been calculated using Eqns. 6.39-6.42, 6.44-6.46, as well as Eqn. 6.65. An example for the integral for a fixed of $\overline{D}$, as well as for a fixed ξ_V is shown in Figure 6.30. Due to the fact that DMP is consumed during the reaction, $\overline{D} \leq 1 - \overline{\xi}$ must hold. Following

this rule, we have marked accessible and inaccessible regions in Figure 6.30, indicating the regions of concentration combinations that will or will not be observed during a simulation. When focusing on the dependency of the second reaction on the filtered mixture fraction, as well as on its variance, two distinct regions are found in Figure 6.30a: one for relatively low ξ_V values (up to approx. 0.1) and one for high ξ_V. The reason for this behavior is the change in the principal shape of the beta-function: for low values, the distribution of ξ has a single maximum at $\overline{\xi}$ (see curve for $\xi_V = 0.025$ in Figure 6.31).

Parameter	Value
T	298 K
ρ	962.5 kg/m³
μ	0.001995 Pa·s
D	$2.0 \cdot 10^{-9}$ m²/s
$\phi_{A,0} = \phi_{C,0} = \phi_S$	202 mol/m³
$\phi_{B,0}$	212 mol/m³
k_2	0.6855 m³/mol/s
t_{ref}	$14.10 \cdot 10^{-3}$ s
Re	700; 1,900; 2,700

Table 6.6: Reaction conditions for the hydrolysis of DMP.
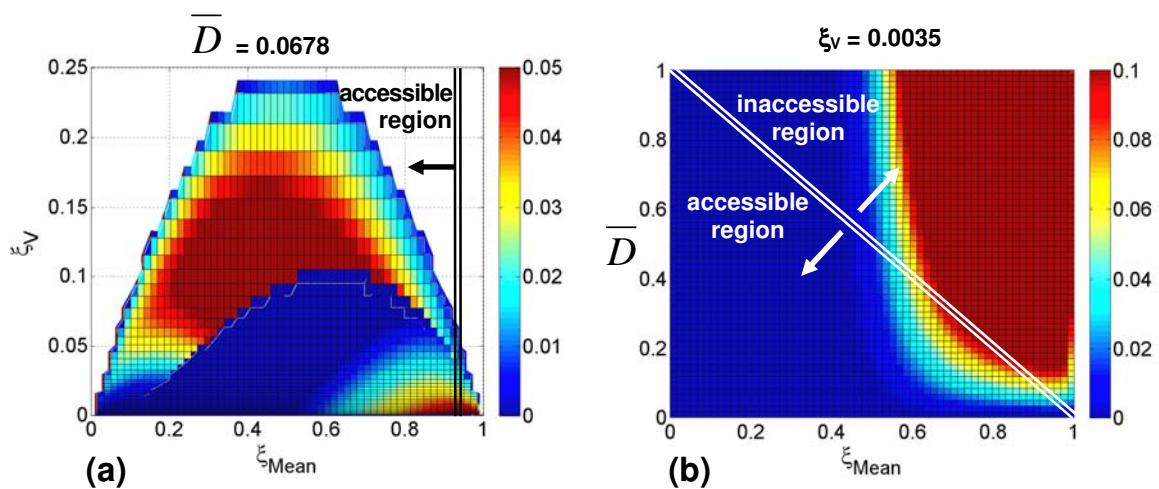
Figure 6.30: Integrals for (a) D = 0.0678 and (b) ξ_V = 0.0035.

At the extreme case, where $\xi_V = 0$, a perfectly mixed system is obtained. This would mean that the reaction rate can be calculated from the filtered species concentrations of acid and DMP. For this extreme situation the following relationship holds:

$$I_{\overline{r_2}}\left(\overline{\xi}, 0, \overline{D}\right) = \overline{D} \cdot \max\left(0, \overline{\xi} \cdot (1 + \beta) - \beta\right) \qquad (6.76)$$

Eqn. 6.76 can be derived from Eqns. 6.30, 6.33 and 6.43, because also the covariance is zero when the variance of the mixture fraction becomes zero. As ξ_V gets larger, the distribution becomes wider and singularities near $\xi = 0$ and 1 occur (see curve for, e.g., $\xi_V = 0.125$, in Figure 6.31). This shift in the distribution causes a sharp increase in the reaction rate due to the concentration of ξ-values near 1. This reflects a situation where, at a constant mean mixture fraction, the variance of ξ is high, i.e., we have an inhomogeneous distribution of acid at the sub-grid scale. Hence, regions of very high acid concentration are observed, causing a local depletion of the base. This leads to a rapid hydrolysis of DMP. A similar situation would occur when we hold ξ_V constant and decrease $\overline{\xi}$.
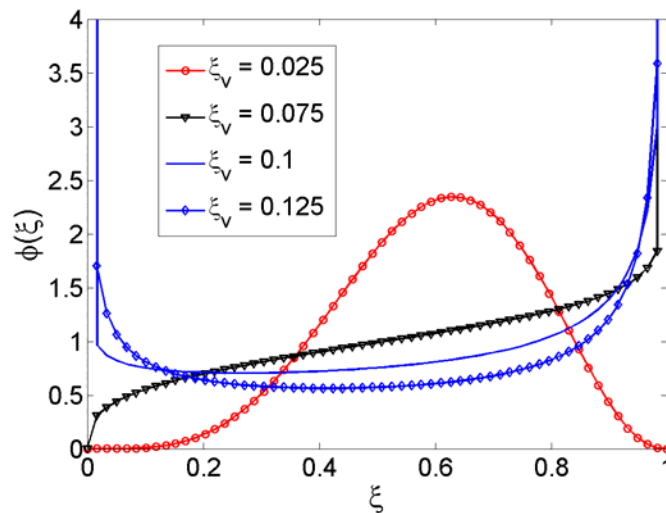
Figure 6.31: Beta-function for different variances ξ_V of the mixture fraction ($\overline{\xi}$ = 0.6, β = 1.05).

ii)   Application to Multiphase Systems

In order to apply this micro mixing model to our bubble column, the focus is on mixing in the liquid without mass transfer. The goal is to show how a micro-mixing model with reaction can be applied to a multiphase system. Therefore, first the micro-mixing time in the "Becker" bubble column is estimated (0.5 x 0.08 x 1.5 m in size, all other geometrical details can be found in Chapter 6.5.1) by using a simple approach. This time-scale is then used to set proper

system parameters in order to get a mixing-sensitive reaction. For this purpose, the micro-mixing time τ_M can be estimated using the engulfment model (see Eqn. 6.74).[109] A micro-mixing time of $\tau_M = 0.2$ s is obtained when assuming that the energy dissipation rate is uniformly distributed in the bubble column. Thus, the total power input (i.e., the volumetric flow rate times the hydrostatic pressure difference from the surface to the bottom of the bubble column) is divided by the total liquid volume to obtain an average energy dissipation rate.

Gavi et al.[80] defined the reference time for the DMP hydrolysis reaction as:

$$t_{ref} = \frac{\left(\phi_{A,0} + \phi_{D,0}\right)}{k_2 \cdot \left(\phi_{A,0} \cdot \phi_{D,0}\right)} \tag{6.77}$$

If identical concentrations of A and D are assumed, the initial concentration of acid can be estimated by taking the reference time for the reaction t_{ref} equal to the micro-mixing time t_M. This yields:

$$\phi_{A,0} = \frac{2}{k_2 \cdot \tau_M} \tag{6.78}$$

Char. Reaction Time [s]	*Concentration [mol/m³]*
0.5	5.86
0.2	14.6
0.1	29.3
0.05	58.6
0.01	292.9

Table 6.7: Concentrations of the acid and DMP corresponding to a certain characteristic reaction time (T = 298 K, k_2 assumed to be constant and equal to 0.6828 m³/mol/s).

Afterwards, simulations with different characteristic reaction times have been performed in order to estimate the real micro-mixing rate in the reactor. The desired characteristic reaction times where therefore translated into the concentrations of acid and DMP, as shown in Table 6.7. The bubble column is operated in a semi-batch mode, i.e., there is no continuous in and outflow of the liquid phase. Hence, an initial distribution of the acid, base and DMP had to be chosen. This was done by placing a blob of acid with a size of 0.1 x 0.08 x 0.1 m (i.e., 1.3% of the total volume) exactly at the sparger's position (0.15 from the wall, centered at the bottom

of the column). The rest of the column was filled with base and DMP in the concentration to yield the desired characteristic reaction time. This setup should mimic an instantaneous injection of acid into the system near the sparger.
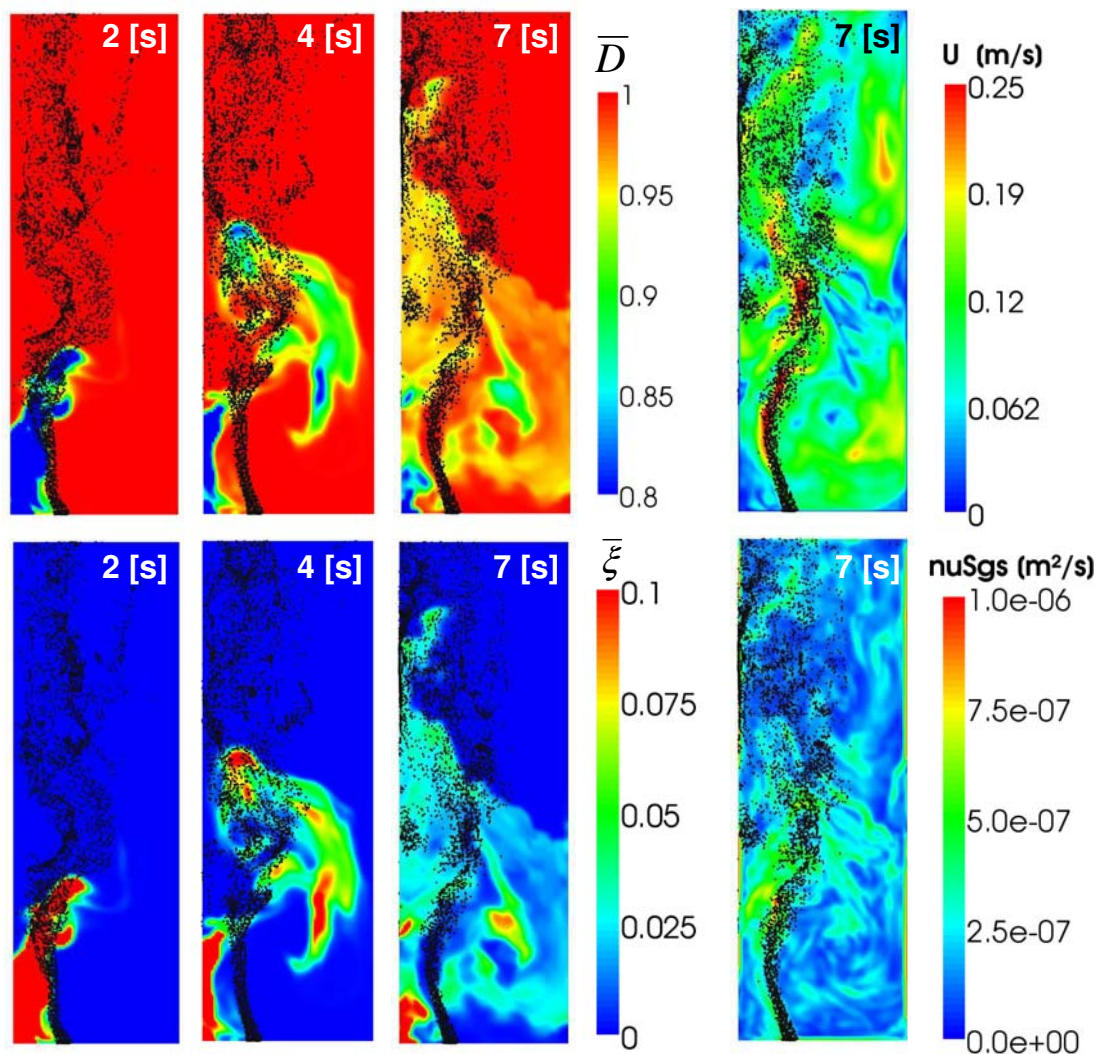
Figure 6.32: Instantaneous filtered concentration of DMP $\overline{D}$ (top left), filtered mixture fraction $\overline{\xi}$ (bottom left), filtered instantaneous velocity field $\overline{u}$ (top right, in m/s), as well as instantaneous sub-grid scale viscosity (bottom right, in m²/s) for a characteristic reaction time of 0.05 s (d_P = 3.2 mm, V_G = 1.6 l/min).

Results for the reaction with a characteristic reaction time of 0.05 s are displayed in Figure 6.32. For these simulations the standard settings, as illustrated previously,[110] were used to obtain the flow field. The liquid phase was water with typically transport properties at 25°C, and the gas-phase was air. No mass transfer was taken into account, and the same chemical reaction network as for the analysis of the microreactor was used. The computational grid consisted of approx. 123,000 hexaeders, and about 10^4 bubbles with a diameter of 3.2 mm

were in the system. The simulation time step used was 1 ms for the fastest reaction and 5 ms for all other reactions in Table 6.7. The same discretization schemes as that for the validation case (i.e., the microreactor discussed in Appendix C) were used in the analysis of the bubble column as well.

As can be seen, the maximum sub-grid-scale viscosity is in the order of $1 \cdot 10^{-6}$ m²/s, i.e., approximately the same as the molecular viscosity. This is in excellent agreement with the work of Hu et al.[40] Also, the flow field is unsteady, as expected. However, the grid is fine enough to resolve most of the turbulent kinetic energy in the system.

Focusing on the mixing-sensitive reaction, the left side of Figure 6.32 is relevant. As can be seen, the blob of acid (characterized by the mixture fraction) is quickly transported upwards, and then to the right. After approximately 7 s, the filtered mixture fraction in the system is below 0.1 in the system and it takes only 2 s to have a filtered mixture fraction in the system below 0.5 (data not shown). Thus, after a few seconds there are basic conditions everywhere in the reactor. This indicates that the hydrolysis reaction has already stopped in the reactor. This is confirmed by the fact that a conversion of approximately 0.8% of the total amount of DMP in the bubble column is obtained after 2.5 s, which is already stable at that time. Simulations with a characteristic reaction time of 0.5 s and 0.2 s indicate conversions of 0.20% and 0.49%, respectively. The trends in the calculated conversions indicate that the characteristic mixing time in the bubble column must be in the order of 1 s to mix the acidic blob. The overall low conversion in the system is, however, limited by the fact that only a small fraction (in our case 1.3Vol.%) of the reaction volume had initially acidic conditions. This can be overcome in experimental work, as well as in future simulations, by using higher molar concentrations of the acid, or the injection of larger amounts of acid.

6.6 Summary and Conclusion

6.6.1 Multiphase Flow and Mixing

In this work we have demonstrated that the EL approach together with a Large Eddy Simulation (LES) of the liquid phase is an accurate method to study flow and mixing in dilute bubble swarms. For the first time, we have analyzed in detail:

- the effect of different subgrid-scale models and grid resolution on flow and mixing in dilute bubble swarms,

- new concepts for the quantification of mixing in multiphase systems,

- the distribution of the scale of segregation in multiphase systems,

- the effect of bubble size and gas flow rate on mixing,

- the effect of scale-up on mixing in dilute bubble swarms, and finally

- the effect of biochemical reactions on different mixing metrics in multiphase systems.

We have shown that the Smagorinsky model with appropriate model constants is able to capture the mean flow field in the bubble column. More sophisticated differential models, such as the one-equation model used in this work, do not improve accuracy. Furthermore, we have shown that when sophisticated mapping schemes are used, the spurious oscillations, that inevitably occur when using the EL approach, can be suppressed to a large extent. In addition, when using a smart scheme for checking the distance between the particles and the cells, significant computational time can be saved. Also, we have used a novel technique to ensure the conservation of the liquid-phase volume on a fixed grid that does not introduce instabilities as previously reported by other researchers.

The investigations have shown that the scale of segregation Φ, the driving force for mixing, is an appropriate metric to interpret mixing involving mass transfer. For example, we have shown that the dimensionless quantity Φ/a, i.e., the scale of segregation normalized with the specific interfacial area, is constant for a certain gas feed. Using this dimensionless quantity, the principal mode of mixing, i.e., whether the driving force increases or decreases, can be quantified. We conclude that Φ is uniquely correlated with the bubble diameter and consequently with the specific interfacial area for a given power input, i.e., gas feed rate. Also, the dimensionless quantity Φ/a is largely unaffected by the scale of the system, i.e., Φ/a will be constant at scale up. The influence of the gas feed rate on Φ is small, such that Φ/a is a function of the gas feed rate and consequently the power input. Thus, Φ/a seems to be an appropriate measure to quantify the mixing rate in bubble columns. This effect has been demonstrated in this work for the first time. Clearly, when an appropriate correlation for the gas hold-up and the specific interfacial area is available, the scale of segregation can be calculated. This can be then done by knowing the correlation between the specific power input and the dimensionless quantity Φ/a.

Furthermore, our analysis shows that Φ is almost perfectly log-normal distributed. Thus, we anticipate that a simple mathematical model may be derived that allows a theoretical justification of this behavior. Also, this simple mathematical model may be subsequently useful for estimating the yield and selectivity of reaction networks. This may significantly impact the design of multiphase reactors, as one is not forced to perform high-fidelity simulations but can estimate yield and selectivity from a simple model.

Furthermore, we have shown that the time scale of meso mixing (ranging from 2-10 s) involving mass transfer is significantly smaller than the time scale for mixing of an inert scalar already dissolved in the liquid phase (approximately 30 s). This is due to the fact that the dissolving gas is already distributed to some extent due to the irregular motion of the individual bubbles. It is clear that the exact relation between these two mixing time scales depends on the geometrical setup of the bubble column. However, it is expected that mixing time scales involving mass transfer are always smaller than time scales without mass transfer for most industrial applications.

Lastly, we conclude that the method presented is also (in principle) capable of describing dense bubble swarms. This is due to the fact that we already take the gas hold-up into account when calculating the liquid-phase conservation equations. Sophisticated coalescence, breakage and bubble-bubble interaction models will be incorporated to study also dense bubble swarms in the near future using our method.

6.6.2 Reactions

Finally, we have investigated how mixing interacts with a liquid-phase chemical reaction, i.e., oxygen uptake by microorganisms. For dilute bubble swarms we could show that the assumption of a well-mixed bulk phase gives reasonable agreement with our detailed numerical predictions. The major part of the deviation between the detailed simulation and the assumed well-mixed bulk phase is due to the fluctuating gas hold-up in the simulation. Hence, we conclude that a detailed treatment of liquid-phase reactions requires information on the gas hold-up and its fluctuation. Furthermore, the levels of the normalized values for σ^2 and Φ are significantly smaller for a reactive scalar than for a non-reactive one. Also, the principal shape of the distribution of Φ changes from a log-normal (in case of an inert scalar) to a monotonically decreasing function. The predictions for the distribution of the mixing

quantities presented in this work may be useful for the construction of a simple mathematical model that is able to predict yield and selectivity in reactive multiphase systems.

Fast reactions in large, dilute bubble swarms require additional models to account for the unresolved concentration field. This is because it is impossible to perform direct numerical simulations for systems with significantly more than $O(10^2)$ bubbles. One is forced to use models that describe the steep concentration gradients near the gas-liquid interface, as well as the concentration distribution in the liquid phase. In a first step the challenges stemming from these two sources were isolated and a computational strategy was proposed to tackle both problems.

For mass transfer a film model was proposed, where a rigorous validation is still needed and will most likely require sophisticated experimental equipment. For the micro-mixing analysis of fast reactions, an approach was taken based on well established techniques for single-phase mixing analysis. The novelty of our approach is that a look-up table was used for the evaluation of the local reaction rate, which saves computational time. In addition, our approach requires the solution of only three additional transport equations, while for the DQMOM-IEM approach presented by Marchisio[78] five equations have to be solved. This is especially relevant for Large Eddy Simulations. LES already require substantial computational resources, and high mesh resolution is critical for these simulations. However, it has to be mentioned, that we assumed the PDF of the reacting scalar following the methodology of Baldyga and Orciuch.[89] The general validity of this methodology needs furher analysis. However, it worked well for our computations. Also, the differences in the computation time in comparison to the DQMOM-IEM approach need further assessment.

The extension of the neutralization-hydrolysis reaction network, well-known for single phase systems, to multiphase systems was investigated in the last part of this chapter. This analysis showed that the reaction time scale has to be lowered, in order to fit the lower micro-mixing time in the relatively large bubble column studied. This may be done by using smaller concentrations of acid, base and DMP to achieve characteristic reaction time scales in the order of 0.1 to 1 s. It is then possible to quantify the micro-mixing time in a bubble column by analyzing the total amount of the products of the DMP hydrolysis. By changing the injection position, it should then be possible to even investigate the spatial distribution of micro-mixing rates, and with some theory also the local energy dissipation. This might be very helpful when

one tries to optimize bubble column reactors, if micro-mixing is expected to be the rate limiting step.

Scalar variance generation due to mass transfer has been excluded from our analysis, as this is a topic on its own and was already analyzed in Chapter 5. Also, the validation of the film model and its connection to the micro-mixing model in the liquid phase needs certainly to be analyzed in greater detail in future work.

6.7 Abbreviations

BIT   Bubble Induced Turbulence

DMP   2,2-Di-Methoxy-Propane

DNS   Direct Numerical Simulations

EE   Euler-Euler (method)

EL   Euler-Lagrange (method)

EPO   Erythropoietin

FT   Front-Tracking

GAMG   Geometric-Algebraic Multi-Grid (solver)

LDA   Laser Doppler Anemometry

LES   Large Eddy Simulation

LIF   Laser-Induced Fluorescence

LPT   Lagrangian Particle Tracking

PBE   Population Balance Equation

PDA   Phase Doppler Anemometry

PDF   Probability Density Function

PIV   Particle Image Velocimetry

PSI-Ball   Particle-Source-In-Ball (concept)

RANS   Reynolds-Averaged-Navier-Stokes (equation)

6.8 Nomenclature

a_P^u, a_N^u	coefficients in the system of algebraic equations
A_{cross}	cross-sectional area of the particle [m²]
$A_{p,z}$	interfacial area of particle z [m²]
c_i	concentration of species i [kg/m³]
$c_{Bulk,i}$	concentration of species i in the liquid bulk [kg/m³]
$c_{Int,i}$	concentration of species i at the interface [kg/m³]
C_A	added mass coefficient
C_e	model constant for the Smagorinsky model
C_ε	model constant for the dynamic sub-grid-scale model
C_k	model constant for the Smagorinsky model
C_L	lift coefficient
C_s	Smagorinsky constant
d_s	sparger diameter [m]
D_i	molecular diffusion coefficient for species i [m²/s]
$D_{eff,i}$	effective diffusion coefficient for species i [m²/s]
d_p	particle diameter [m]
e_{kj}	enumerator reaction exponent of species k in reaction j
E_{kj}	denominator reaction exponent of species k in reaction j
$\mathbf{F}_A$	added-mass force [kg·m/s²]
$\mathbf{F}_D$	drag force [kg·m/s²]
$\mathbf{F}_G$	gravity force [kg·m/s²]
$\mathbf{F}_L$	lift force [kg·m/s²]
$\mathbf{F}_P$	force due to a pressure gradient [kg·m/s²]
$\mathbf{g}$	gravitational acceleration vector [m/s²]

H   height of the bubble column [m]

$H(\overline{u}_L)$ operator involving the known part in the system of algebraic equations

Ha   Hatta number

I_S intensity of segregation

I   identity matrix

k   sub-grid-scale kinetic energy [m²/s²]

k_j reaction rate constant reaction j (units depending on e_{kj} and E_{kj})

$k_L \cdot a$ volumetric mass transfer coefficient [1/s]

k_L liquid-phase mass transfer coefficient [m/s]

$k_{0,0}$ zero-order reaction rate [kg/m³/s]

K_{kj} reaction constant for species k in reaction j (units depending on E_{kj})

K_O Michaelis-Menten constant in [kg/m³]

m_P particle mass [kg]

m_Φ local distribution of the scale of segregation [1/m]

m_{σ^2} local distribution of the intensity of segregation

$\dot{N}_i$ mass transfer rate from the disperse phase [kg/s]

$\overline{p}$ resolved pressure [kg/m/s²]

$\overline{p}*$ modified pressure (excluding the hydrostatic pressure) [kg/m/s²]

$\overline{p}'$ modified kinematic pressure (excluding the hydrostatic pressure) [m²/s²]

Q_3 cumulative volume distribution of a quantity

q_3 volumetric frequency distribution of a quantity

r   known part in the system of algebraic equations

r_{O2} oxygen uptake rate [kg/m³/s]

r_j reaction rate of the j-th reaction [kg/m³/s]

Re_P particle Reynolds number

$\overline{\boldsymbol{S}}$	filtered strain rate tensor [1/s]
Sc_i	Schmidt number of species i in the liquid phase
Sc_{SGS}	sub-grid-scale Schmidt number
$Sh_{i,z}$	Sherwood number of species i and particle z
T	thickness of the bubble column [m]
$\overline{\boldsymbol{u}}$	filtered liquid-phase velocity [m/s]
$\mathbf{u}_{mean}$	time-averaged liquid-phase velocity [m/s]
$\mathbf{U}$	particle velocity [m/s]
$\mathbf{U}_{rel}$	particle relative velocity [m/s]
v, w	parameters of the beta-function
V	volume [m³]
V_G	gas flow rate [m³/s]
V_{tot}	total reactor volume [m³]
V_p	particle volume [m³]
W	width of the bubble column [m]
$x_{cell,max}$	maximum distance from the cell center to a cell's boundary point [m]
x_{dist}	distance between the cell center and particle [m]
x_s	distance of the sparger's center to the left wall of the bubble column [m]
$\overline{Y}_{amb,i,z}$	ambient concentration of species i near particle z [kg/m³]
$Y_{eq,I}$	equilibrium concentration of species i [kg/m³]
$\overline{Y}_i$	filtered concentration of species i [kg/m$_L$³]
Y_I	dimensionless scalar
Y_{O2}	concentration of oxygen in the reactor in [kg/m³]
$Y_{O2,I}$	interface concentration of oxygen in the reactor in [kg/m³]
$Y_{O2,sat}$	oxygen saturation concentration [kg/m³]

$Y_{V,i}$	variance of species i in the liquid phase [kg²/m⁶]

Greek letters

β	base-to-acid ratio
β_z	mass transfer coefficient of particle z [m/s]
Δ	filter length [m]
ε	sub-grid-scale energy dissipation rate [m²/s³]
ε_G	gas-phase volume fraction [m³$_G$/m³$_{tot}$]
ε_L	liquid-phase volume fraction [m³$_L$/m³$_{tot}$]
$\varepsilon_{L,mean}$	mean liquid-phase volume fraction [m³$_L$/m³$_{tot}$]
ϕ	distribution function
$\overline{\varphi_L}$	filtered liquid phase mass flux [kg/m²/s]
$\boldsymbol{\Phi}$	volume-specific coupling force [kg/m²/s²]
Φ	scale of segregation [1/m]
$\boldsymbol{\Phi}_{\dot{N}_i}$	volumetric source term for species i [kg/m³/s]
γ_ρ	density ratio
μ	mean value of a distribution
μ_L	dynamic liquid-phase viscosity [Pa·s]
$\mu_{eff,L}$	effective dynamic liquid-phase viscosity [Pa·s]
$\mu_{SGS,L}$	sub-grid-scale liquid-phase viscosity [Pa·s]
ν	kinematic liquid-phase viscosity [m²/s]
ν_{ij}	stoichiometric coefficient of species i in reaction j
$\nu_{eff,L}$	effective kinematic liquid-phase viscosity [m²/s]
ϱ_L	liquid-phase density [kg/m³]
σ^2	intensity of segregation [kg²/m⁶]

σ	standard deviation of a distribution
σ'_{av}	differential average selectivity in the film
$\bar{\tau}_L$	liquid-phase stress tensor [kg/m/s²]
τ_M	micro mixing time scale [s]
τ_R	reaction time constant [s]
ω	rotation vector of the liquid-phase velocity field [1/s]
ξ	mixture fraction
ξ_V	mixture fraction variance

6.9 References

(1)   Troshko AA, Zdravistch F. CFD modeling of slurry bubble column reactors for Fisher-Tropsch synthesis. Chem Eng Sci. 2009; 64:892-903.

(2)   Downing RS, Kunkeler PJ, vanBekkum H. Catalytic syntheses of aromatic amines. Catalysis Today. 1997; 37:121-136.

(3)   Mills PL, Chaudhari RV. Reaction engineering of emerging oxidation processes. Catalysis Today. 1999; 48:17-29.

(4)   Tang SW, Liang B. Kinetics of the liquid-phase oxidation of toluene by air. Industrial & Engineering Chemistry Research. 2007; 46:6442-6448.

(5)   Amanullah A, Buckland BC, Nienow AW. Mixing in the Fermentation and Cell Culture Industries. In: Paul EL, Atiemo-Obeng VA, Kresta SM. Handbook of Industrial Mixing - Science and Practice. Hoboken, US: John Wiley & Sons Inc., 2004.

(6)   Bröder D. Anwendung optischer Messtechniken zur Untersuchung disperser Gas-Flüssigkeits-Strömungen. Halle(Saale), Germany: Universität Halle-Wittenberg, 2003.

(7)   Bork O, Schlueter M, Raebiger N. The impact of local phenomena on mass transfer in gas-liquid systems. Canadian Journal of Chemical Engineering. 2005; 83:658-666.

(8)   Dani A, Guiraud P, Cockx A. Local measurement of oxygen transfer around a single bubble by planar laser-induced fluorescence. Chem Eng Sci. 2007; 62:7245-7252.

(9)   Roy S, Duke SR. Laser induced fluorescence measurements of dissolved oxygen concentration fields near air bubble surfaces. Review of Scientific Instruments. 2000; 71:3494-3501.

(10) Roy S, Duke SR. Visualization of oxygen concentration fields and measurement of concentration gradients at bubble surfaces in surfactant-contaminated water. Experiments in Fluids. 2004; 36:654-662.

(11) Wiemann D, Mewes D. Prediction of backmixing and mass transfer in bubble columns using a multifluid model. Industrial & Engineering Chemistry Research. 2005; 44:4959-4967.

(12) Yang YB, Devanathan N, Dudukovic MP. Liquid Backmixing in Bubble-Columns. Chem Eng Sci. 1992; 47:2859-2864.

(13) Lorenz O, Schumpe A, Ekambara K, Joshi JB. Liquid phase axial mixing in bubble columns operated at high pressures. Chem Eng Sci. 2005; 60:3573-3586.

(14) Yang NS, Chen BH, Mcmillan AF. Axial Mixing and Mass-Transfer in Gas-Liquid Karr Columns. Industrial & Engineering Chemistry Process Design and Development. 1986; 25:776-780.

(15) Sundaresan S. Modeling the hydrodynamics of multiphase flow reactors: Current status and challenges. AIChE J. 2000; 46:1102-1105.

(16) Koynov AA, Khinast JG. Micromixing in reactive, deformable bubble, and droplet swarms. Chemical Engineering & Technology. 2006; 29:13-23.

(17) Sommerfeld M, Decker S. State of the art and future trends in CFD simulation of stirred vessel hydrodynamics. Chemical Engineering & Technology. 2004; 27:215-224.

(18) Kim MS, Lee WI. A new VOF-based numerical scheme for the simulation of fluid flow with free surface. Part I: New free surface-tracking algorithm and its verification. International Journal for Numerical Methods in Fluids. 2003; 42:765-790.

(19) Li J, Hesse M, Ziegler J, Woods AW. An arbitrary Lagrangian Eulerian method for moving-boundary problems and its application to jumping over water. J Comput Phys. 2005; 208:289-314.

(20) Hameed M, Siegel M, Young YN, Li J, Booty MR, Papageorgiou DT. Influence of insoluble surfactant on the deformation and breakup of a bubble or thread in a viscous fluid. Journal of Fluid Mechanics. 2008; 594:307-340.

(21) Unverdi SO, Tryggvason G. A Front-Tracking Method for Viscous, Incompressible, Multi-Fluid Flows. J Comput Phys. 1992; 100:25-37.

(22) Koynov A, Khinast JG, Tryggvason G. Mass transfer and chemical reactions in bubble swarms with dynamic interfaces. AIChE J. 2005; 51:2786-2800.

(23) Koynov A, Tryggvason G, Schlueter M, Khinast JG. Mass transfer and chemical reactions in reactive deformable bubble swarms. Applied Physics Letters. 2006; 88:134102.

(24) Radl S, Koynov A, Tryggvason G, Khinast JG. DNS-based Prediction of the Selectivity of Fast Multiphase Reactions: Hydrogenation of Nitroarenes. Chem Eng Sci. 2008; 63:3279-3291.

(25) Radl S, Khinast JG. Prediction of mass transfer coefficients in non-Newtonian fermentation media using first-principles methods. Biotechnol Bioeng. 2007; 97:1329-1334.

(26) Radl S, Tryggvason G, Khinast JG. Flow and mass transfer of fully resolved bubbles in non-Newtonian fluids. AIChE J. 2007; 53:1861-1878.

(27) Darmana D. On the multiscale modelling of hydrodynamics, mass transfer and chemical reactions in bubble columns. Twente, Netherlands: University of Twente, 2006.

(28) Göz M, Bunner B, Sommerfeld M, Tryggvason G. Direct Numerical Simulation of Bidisperse Bubble Swarms. International Conference on Multiphase Flow. New Orleans, US: 2001.

(29) Göz M, Bunner B, Sommerfeld M, Tryggvason G. Direct Numerical Simulation of Bubble Swarms with a Parallel Front-Tracking Method. International FORTWIHR Conference on HPSEC. Erlangen, D: 2001.

(30) Raffensberger JA, Glasser BJ, Khinast JG. Analysis of heterogeneously catalyzed reactions close to bubbles. AIChE J. 2005; 51:1482-1496.

(31) Lehr F, Millies M, Mewes D. Bubble-size distributions and flow fields in bubble columns. AIChE J. 2002; 48:2426-2443.

(32) Troshko AA, Zdravistch F. CFD modeling of slurry bubble column reactors for Fisher-Tropsch synthesis. Chem Eng Sci. 2009; 64:892-903.

(33) Delnoij E, Lammers FA, Kuipers JAM, vanSwaaij WPM. Dynamic simulation of dispersed gas-liquid two-phase flow using a discrete bubble model. Chem Eng Sci. 1997; 52:1429-1458.

(34) Crowe C, Sommerfeld M, Tsuji Y. Multiphase Flows with Droplets and Particles. Boca Raton, US: CRC Press, 1998.

(35) Sommerfeld M. Modellierung und numerische Berechnung von partikelbeladenen turbulenten Strömungen mit Hilfe des Euler/Lagrange-Verfahrens. Aachen, D: Shaker Verlag, 1996.

(36) Nierhaus T, Abeele DV, Deconinck H. Direct numerical simulation of bubbly flow in the turbulent boundary layer of a horizontal parallel plate electrochemical reactor. International Journal of Heat and Fluid Flow. 2007; 28:542-551.

(37) Deen NG, Solberg T, Hjertager BH. Large eddy simulation of the gas-liquid flow in a square cross-sectioned bubble column. Chem Eng Sci. 2001; 56:6341-6349.

(38) Tomiyama A, Zun I, Higaki H, Makino Y. A three-dimensional particle tracking method for bubbly flow simulation. Nuclear Engineering and Design. 1997; 175:77-86.

(39)   Arlov D, Revstedt J, Fuchs L. Numerical Simulation of a gas-liquid Rushton stirred Reactor - LES and LPT. Computers & Fluids. 2008; 37:793-801.

(40)   Hu GS, Celik I. Eulerian-Lagrangian based large-eddy simulation of a partially aerated flat bubble column. Chem Eng Sci. 2008; 63:253-271.

(41)   Bini M, Jones WP. Particle acceleration in turbulent flows: A class of nonlinear stochastic models for intermittency. Physics of Fluids. 2007; 19:035104.

(42)   van Dijk GJ. The implementation of a Lagrangian Particle Dispersion Model in Large Eddy Simulations of the Atmospheric Boundary Layer. Delft University of Technology, The Netherlands, 2007.

(43)   Marchioli C, Salvetti MV, Soldati A. Some issues concerning large-eddy simulation of inertial particle dispersion in turbulent bounded flows. Physics of Fluids. 2008; 20:040603.

(44)   Martin M, Montes FJ, Galan MA. On the contribution of the scales of mixing to the oxygen transfer in stirred tanks. Chemical Engineering Journal. 2008; 145:232-241.

(45)   Baldyga J, Bourne JR, Walker B. Non-isothermal micromixing in turbulent liquids: Theory and experiment. Canadian Journal of Chemical Engineering. 1998; 76:641-649.

(46)   Bourne JR, Hilber CP. The Productivity of Micromixing-Controlled Reactions - Effect of Feed Distribution in Stirred Tanks. Chemical Engineering Research & Design. 1990; 68:51-56.

(47)   Bourne JR, Kut OM, Lenzner J. An Improved Reaction System to Investigate Micromixing in High-Intensity Mixers. Industrial & Engineering Chemistry Research. 1992; 31:949-958.

(48)   Bourne JR, Yu SY. Investigation of Micromixing in Stirred-Tank Reactors Using Parallel Reactions. Industrial & Engineering Chemistry Research. 1994; 33:41-55.

(49)   Paul EL, Treybal RE. Mixing and Product Distribution for A Liquid-Phase, Second-Order, Competitive-Consecutive Reaction. AIChE J. 1971; 17:718-&.

(50)   Lin WW, Lee DJ. Micromixing effects in aerated stirred tank. Chem Eng Sci. 1997; 52:3837-3842.

(51)   Fournier MC, Falk L, Villermaux J. A new parallel competing reaction system for assessing micromixing efficiency - Experimental approach. Chem Eng Sci. 1996; 51:5053-5064.

(52)   Fournier MC, Falk L, Villermaux J. A new parallel competing reaction system for assessing micromixing efficiency - Determination of micromixing time by a simple mixing model. Chem Eng Sci. 1996; 51:5187-5192.

(53)   Luo HP, Al-Dahhan MH. Macro-mixing in a draft-tube airlift bioreactor. Chem Eng Sci. 2008; 63:1572-1585.

(54) Al-Dahhan MH, Mills PL, Gupta P, Han L, Dudukovic MP, Leib TM et al. Liquid-phase tracer responses in a cold-flow counter-current trayed bubble column from conductivity probe measurements. Chemical Engineering and Processing. 2006; 45:945-953.

(55) Alvare J, Al-Dahhan MH. Liquid phase mixing in trayed bubble column reactors. Chem Eng Sci. 2006; 61:1819-1835.

(56) Moustiri S, Hebrard G, Thakre SS, Roustan M. A unified correlation for predicting liquid axial dispersion coefficient in bubble columns. Chem Eng Sci. 2001; 56:1041-1047.

(57) Vial C, Poncin S, Wild G, Midoux N. Experimental and theoretical analysis of axial dispersion in the liquid phase in external-loop airlift reactors. Chem Eng Sci. 2005; 60:5945-5954.

(58) Joshi JB. Computational flow modelling and design of bubble column reactors. Chem Eng Sci. 2001; 56:5893-5933.

(59) Khinast JG. Impact of 2-D bubble dynamics on the selectivity of fast gas-liquid reactions. AIChE J. 2001; 47:2304-2319.

(60) Derksen JJ. Scalar mixing by granular particles. AIChE J. 2008; 54:1741-1747.

(61) Derksen JJ. Mixing by solid particles. Chemical Engineering Research & Design. 2008; 86:1363-1368.

(62) Roy S, Joshi JB. Effect of liquid velocity on axial mixing in gas-liquid dispersions: A CFD simulation. Chemical Engineering & Technology. 2006; 29:1034-1041.

(63) Joshi JB. Computational flow modelling and design of bubble column reactors. Chem Eng Sci. 2001; 56:5893-5933.

(64) deVilliers E. The Potential of Large Eddy Simulation for the Modeling of Wall Bounded Flows. Imperial College of Science, Technology and Medicine, London, UK, 2006.

(65) Sato Y, Sekoguchi K. Liquid Velocity Distribution in 2-Phase Bubble Flow. Bulletin of the Jsme-Japan Society of Mechanical Engineers. 1976; 19:825.

(66) Niceno B, Dhotre MT, Deen NG. One-equation sub-grid scale (SGS) modelling for Euler-Euler large eddy simulation (EELES) of dispersed bubbly flow. Chem Eng Sci. 2008; 63:3923-3931.

(67) Spalding DB. A single formula for the law of the wall. Journal of Applied Mechanics. 1961; 28:455-458.

(68) Clift R, Grace JR, Weber ME. Bubbles, Drops, and Particles. Mineola, US: Dover Publications Inc., 2005.

(69) Becker S, Sokolichin A, Eigenberger G. Gas-liquid flow in bubble columns and loop reactors: Part II. Comparison of detailed experiments and flow simulations. Chem Eng Sci. 1994; 49:5747-5762.

(70)   Auton TR. The dynamics of bubbles, drops and particles in motion in liquids. University of Cambridge, Cambridge, U.K., 1983.

(71)   Loth E. Numerical approaches for motion of dispersed particles, droplets and bubbles. Progress in Energy and Combustion Science. 2000; 26:161-223.

(72)   Mei RW, Lawrence CJ, Adrian RJ. Unsteady Drag on A Sphere at Finite Reynolds-Number with Small Fluctuations in the Free-Stream Velocity. Journal of Fluid Mechanics. 1991; 233:613-631.

(73)   Sridhar G, Katz J. Drag and Lift Forces on Microscopic Bubbles Entrained by A Vortex. Physics of Fluids. 1995; 7:389-399.

(74)   Tominaga Y, Stathopoulos T. Turbulent Schmidt numbers for CFD analysis with various types of flowfield. Atmos Environ. 2007; 41:8091-8099.

(75)   Feng W, Wen JP, Liu CY, Yuan Q, Jia XQ, Sun Y. Modeling of local dynamic behavior of phenol degradation in an internal loop airlift bioreactor by yeast Candida tropicalis. Biotechnol Bioeng. 2007; 97:251-264.

(76)   Fox RO. Computational Models for Turbulent Reacting Flows. Cambridge, UK: Cambridge University Press, 2003.

(77)   Bird RB, Stewart WE, Lightfood EN. Transport Phenomena. New York: John Wiley & Sons, Inc., 2002.

(78)   Marchisio DL. Large Eddy Simulation of mixing and reaction in a Confined Impinging jets Reactor. Computers & Chemical Engineering. 2009; 33:408-420.

(79)   Lindenberg C, Scholl J, Vicum L, Mazzotti M, Brozio J. Experimental characterization and multi-scale modeling of mixing in static mixers. Chem Eng Sci. 2008; 63:4135-4149.

(80)   Gavi E, Marchisio DL, Barresi AA. CFD modelling and scale-up of Confined Impinging Jet Reactors. Chem Eng Sci. 2007; 62:2228-2241.

(81)   Kenig EY, Gorak A. Rigorous modeling of reactive absorption processes. Chemical Engineering & Technology. 2003; 26:631-646.

(82)   Matlab 7.3.0 (R2008a). The Mathworks, Inc., 2008.

(83)   Westerterp KR, van Swaaij WPM, Beenackers AACM. Chemical Reactor Design and Operation (2nd edition). Norwich, GB: John Wiley & Sons, 1984.

(84)   Radl S, Suzzi D, Khinast JG. Assessment of Micro- and Mesomixing in Bubble Swarms via Simulations. 9th International Conference on Chemical and Process Engineering. Rome, Italy: AIDIC, 2009.

(85)   Jaberi FA, Colucci PJ, James S, Givi P, Pope SB. Filtered mass density function for large-eddy simulation of turbulent reacting flows. Journal of Fluid Mechanics. 1999; 401:85-121.

(86)   Colucci PJ, Jaberi FA, Givi P, Pope SB. Filtered density function for large eddy simulation of turbulent reacting flows. Physics of Fluids. 1998; 10:499-515.

(87)   Raman V, Pitsch H, Fox RO. Hybrid large-eddy simulation/Lagrangian filtered-density-function approach for simulating turbulent combustion. Combustion and Flame. 2005; 143:56-78.

(88)   Pera C, Reveillon J, Vervisch L, Domingo P. Modeling subgrid scale mixture fraction variance in LES of evaporating spray. Combustion and Flame. 2006; 146:635-648.

(89)   Baldyga J, Orciuch W. Barium sulphate precipitation in a pipe - an experimental study and CFD modelling. Chem Eng Sci. 2001; 56:2435-2444.

(90)   Johnson BK, Prud'homme RK. Chemical processing and micromixing in confined impinging jets. AIChE J. 2003; 49:2264-2282.

(91)   Baldyga J, Henczka M. Closure Problem for Parallel Chemical-Reactions. Chemical Engineering Journal and the Biochemical Engineering Journal. 1995; 58:161-173.

(92)   Baldyga J, Bourne JR. Turbulent mixing and chemical reactions. New York, US: Wiley, 1999.

(93)   OpenFoam 1.5 User Guide (www.opencfd.co.uk). OpenCFD Ltd, 2008.

(94)   Jasak H. Error Analysis and Estimation for the Finite Volume Method with Applications to Fluid Flow. London, UK: Department of Mechanical Engineering, Imperial College of Science, Technology and Medicine, 1996.

(95)   Deen NG, Sint Annaland A, Kuipers JAM. Multi-scale modeling of dispersed gas-liquid two-phase flow. Chem Eng Sci. 2004; 59:1853-1861.

(96)   Rusche H. Computational Fluid Dynamics of Dispersed Two-Phase Flows at High Phase Fractions. London, UK: Imperial College of Science, Technology and Medicine, 2002.

(97)   Issa RI. Solution of the Implicitly Discretized Fluid-Flow Equations by Operator-Splitting. J Comput Phys. 1986; 62:40-65.

(98)   Nilsson H. PhD course in CFD with OpenSource Software. Chalmers University of Technology, Gothenburg, Sweden . 2008.

(99)   Kaerrholm FP. Numerical Modelling of Diesel Spray Injection, Turbulence Interaction and Combustion. Chalmers University of Technology, Gothenburg, Sweden, 2008.

(100) MacPherson GB, Nordin N, Weller HG. Particle Tracking in Unstructured, Aritrary Polyhedral Meshes for Use in CFD and Molecular Dynamics. Communications in Numerical Methods in Engineering. 2009; 25:263-273.

(101) Sokolichin A, Eigenberger G. Applicability of the standard k-epsilon turbulence model to the dynamic simulation of bubble columns: Part I. Detailed numerical simulations. Chem Eng Sci. 1999; 54:2273-2284.

(102) Diaz ME, Iranzo A, Cuadra D, Barbero R, Montes FJ, Galan MA. Numerical simulation of the gas-liquid flow in a laboratory scale bubble column Influence of bubble size distribution and non-drag forces. Chemical Engineering Journal. 2008; 139:363-379.

(103) Hu GS. Towards Large Eddy Simulation of Dispersed Gas-Liquid Two-Phase Turbulent Flows. West Virginia University, Morgantown, U.S., 2005.

(104) Bothe D, Sternich C, Warnecke HJ. Fluid mixing in a T-shaped micro-mixer. Chem Eng Sci. 2006; 61:2950-2958.

(105) Bothe D, Stemich C, Warnecke HJ. Theoretical and experimental studies on the mixing processes in T-shaped microreactors - Part 1: Numerical simulation and assessment of flow mixing. Chemie Ingenieur Technik. 2004; 76:1480-1484.

(106) Bothe D, Stemich C, Warnecke HJ. Computation of scales and quality of mixing in a T-shaped microreactor. Computers & Chemical Engineering. 2008; 32:108-114.

(107) Celik IB, Cehreli ZN, Yavuz I. Index of resolution quality for large eddy simulations. Journal of Fluids Engineering-Transactions of the ASME. 2005; 127:949-958.

(108) Sweere APJ, Luyben KCAM, Kossen NWF. Regime Analysis and Scale-Down - Tools to Investigate the Performance of Bioreactors. Enzyme and Microbial Technology. 1987; 9:386-398.

(109) Patterson GK, Paul EL, Kresta SM. Mixing and Chemical Reactions. In: Paul EL, Atiemo-Obeng VA, Kresta SM. Handbook of Industrial Mixing - Science and Practice. Hoboken, NJ (USA): John Wiley & Sons, Inc., 2004:755-868.

(110) Radl S, Khinast JG. Multiphase Flow and Mixing in Dilute Bubble Swarms. AIChE J. 2009; (in press).

"A body is liquid when it is divided into several smaller parts that move separately, and it is solid when all its parts are in contact."

(René Descartes, 1644)

7

Mixing Characteristics of
Wet Granular Matter in a Bladed Mixer[*]

We performed numerical simulations of dry and wet granular flow inside a four-bladed mixer using the discrete element method (DEM). A capillary force model was incorporated to mimic the complex effects of pendular liquid bridges on particle flow. The simulations are able to capture the main features of granular flow, which is substantiated by the comparison of our results with experimental data.

It was found that mean and fluctuating velocity fields for wet and dry particles differ significantly from each other. Our results indicate a strong increase in heap formation for wet particles and hence velocity fluctuations in the vertical direction become more pronounced. We observe that mixing in bladed mixers is strongly heterogeneous for wet granular matter due to the formation of different flow regimes within the mixer. The analysis of mixing quality shows that the spatial distribution of mixing intensity is influenced by the moisture content. This can lead to locally and even globally higher mixing rates for wet particles compared to dry granular matter.

7.1 Introduction

Mixing and drying of granular materials is an important processing step in such diverse areas such as pharmaceutical production, food technology, biotechnology, mineral processing, detergents and in the coal, steel and agrochemical industry. Industrial mixers and dryers include high-shear mixers, agitated filter beds, fluidized beds and rotating drums. In the pharmaceutical industry for instance, efficient mixing is of critical importance to achieve uniform concentration of the active ingredient, eliminating the chance of producing super- or sub-potent tablets. Often manufacturing protocols require mixing of a batch for a predefined amount of time. Process understanding, i.e., the ability to predict mixedness as function of revolutions or time, might dramatically reduce processing time in many operations. Uniform drying of a batch of particles is of equal importance to enable optimal processing conditions in subsequent steps or to avoid over-drying of solvate systems.

Instabilities in fluid flows have been the topic of research since the pioneering work of Reynolds in the 19th century. However, mixing mechanisms in dry and moist granular systems have been studied in detail only in the recent past. For example, chaotic mixing of particles was first described by Shinbrot et al.[1] Clearly, there is still significant work to be done in the description and mathematical modeling of granular flows.

Recent experimental studies focused on the visualization of granular flows in different mixer geometries using mainly two techniques: PEPT (positron emission particle tracking) and PIV (particle image velocimetry). In PEPT-measurements a single particle is radioactively marked and tracked.[2] PEPT-measurements are frequently used to validate computer simulations, as demonstrated by Kuo et al.[3] and Stewart et al.[4] PIV is a 2D method to visualize the granular flow using a video camera. Typical acquisition rates range from 15 frames per second (fps) for relatively slow flows[5] to 2,000 and more, e.g., for spouted[6] or vibrated granular beds.[7] The specific acquisition rate has to be selected such that errors in the subsequent image analysis procedure are minimized[6] and the transients in the velocity field are well captured. PIV has been applied to study segregation of a dry granular bed in a lab-scale four-bladed mixer by Conway et al.[8] Recently, PIV was used to examine wet granular flows by Lekhal et al.[9] and Darelius et al.[10]

Computer simulations have the advantage of providing more insight into the process than experimental methods, if carried out with confidence and precision. For example, all particles

can be located at every time and force and velocity fields are easily accessible. Drawbacks of computer simulations include the need to verify computational results and the limited number of particles and interaction forces that can be included in the simulation. In recent years discrete element methods (DEM) have become a powerful tool to simulate granular flows. For example, the flow in bladed mixers has been simulated and successfully validated experimentally by Stewart et al.[4]

A large number of researchers have studied granular flow and mixing in different blender geometries. Several mixing mechanisms and regimes, as well as segregation phenomena, have been described.[11,12] When studying granular flows, the surrounding gas-phase is usually neglected and only the particles and their interactions are considered. This is also true for most approaches dealing with wet granular flow, with some exceptions in recent literature that consider the detailed prediction of granule microstructure.[13-16] This simplifies the analysis to some extent, as forces stemming from the interaction of the gas with the granular material are excluded. Despite significant progress that has been made in recent years, the description of the flow of wet granular materials is still challenging. Recent interest in this topic shows, that a better understanding of flow and mixing of wet granular matter is necessary to enable rational scale-up and optimization of processes such as drying, granulation, spheronization and mixing of moist material. However, there have been only a few studies quantifying the flow in agitated mixers. These agitated or convective mixers consist of a stationary vessel and a rotating impeller. Convective mixers have been investigated both numerically and experimentally by Stewart et al.,[4] as well as Zhou et al.[17] Furthermore, the segregation in bladed mixers has been studied numerically by Zhou et al.[18] and experimentally by Conway et al.[8] A characterization of cohesionless granular flows in a bladed mixer has been performed recently by Remy et al.[19] However, mixing mechanisms of wet granular flows in bladed mixers have not yet been analyzed.

Thus, the present work investigates the effect of moisture content in agitated granular flows. Specifically we focus on the simulation of wet powder flows in a bladed mixer containing mono-disperse particles. The setup considered in our study, i.e., a bladed mixer, serves as a prototype for large-scale industrial processes, such as high-shear granulators, powder mixing equipment and agitated dryers. In this vessel, we investigate the mean and fluctuating velocity field and detail the qualitative differences between wet and dry powder beds. The simulation

results are then compared to experimental data, which were recorded by particle image velocimetry (PIV).[8,9]

Finally, we concentrate on the quantification of mixing mechanisms including convective, diffusive and shear mixing for both dry and wet powder beds. The results of this work will be useful for the development of a new generation of particle processing equipment as they provide a mechanistic view of many aspects of wet granular flow.

7.2 Computational Method

7.2.1 Background on the Discrete Element Method

i)   Introduction to the Discrete Element Method

In the Discrete Element Method the trajectory of each particle is computed to simulate the behavior of the whole granular assembly. At every time step the forces acting on each particle are updated, and Newton's equation of motion is solved to obtain the new positions and velocities of the particles. The forces acting on the particles include the body force $\vec{F}_{b,i}$, the contact forces between particles i and j, as well as additional cohesion forces $\vec{F}_{coh,ij}$ that also act between two particles but are not necessarily connected with a physical contact. Details on the basic principals of DEM simulations can be found in the recent review of Zhu et al.[20] DEM simulations have been widely used in academic and industrial research related to the pharmaceutical industry, e.g., by the group of Muzzio.[21-24] Relevant equipment that has been simulated using the DEM includes

-   bladed mixers (see, e.g., Bertrand et al.,[25] Remy et al.,[19,26]),

-   V- and bin-blenders (see, e.g., Lemieux et al.[27]),

-   Bohle Tote blenders (see, e.g., Arratia et al.[28]),

-   various types of granulators (see, e.g., Goldschmidt et al.[29]), as well as

-   pan coaters (see, e.g., Pandey et al.[30]).

ii)   Modeling Cohesive Forces by using the DEM

A theoretical analysis of the effect of cohesive forces for particle mixing and segregation has been conducted by Li and McCarthy[31]. They used the granular Bond number Bo to

characterize the cohesive forces and proposed a phase diagram to predict mixing and segregation. However, the details of granular flow have not been taken into account for this theoretical analysis. Simulations based on the DEM remain the most powerful tool to show the effect of cohesive forces on granular flow and mixing.

An excellent review on currently used interaction forces within the DEM has been given by Zhu,[20] as well as Di Renzo and Di Maio.[32] For wet powders Li et al.[33] have proposed a new method to study fully saturated wet granular matter. This new method combines the DEM and smoothed particle hydrodynamics. Recent work has also been done in the analysis of cohesive powders by the group of Muzzio.[22] They used a relatively simple approach in which the cohesive force was assumed to be proportional to the particle weight. McCarthy[34] used the model of Lian et al.[35] to calculate liquid-bridge forces. He was the first to show a higher mixing rate in case of an intermediate degree of cohesion using the DEM.

Also, simulations have been conducted by Rognon et al.[36] for two-dimensional shear flows using a simple cohesion force model. Soulie et al.[37] investigated the mechanical strength of polydisperse granular materials both experimentally and with simulations. They focused on the macroscopic mechanical behavior of the material and found only poor agreement between simulations and experimental data. This highlights the importance of the liquid distribution for the mechanical behavior of wet granular matter. Especially at a low water content this causes great deviations between simulations and experiments. This is explained by the effect of surface roughness in the experiments that could not be simulated directly. The prediction of liquid distribution is, however, extremely demanding and only recently it could be measured in static assemblies of wet particles (see Figure 7.1). Other groups that investigated the liquid distribution in wet granular matter include Kohonen et al.,[38] Fournier et al.,[39] as well as Herminghaus.[40] The investigation of Soulie et al.[37] also showed that the formation of liquid bridges can be modeled with relative simplicity, i.e., when the particle surface comes into contact, a liquid bridge forms. A recent computational study was performed by Schulz et al.[41] with the focus on relatively small systems (i.e., involving several hundred spheres) taking into account simplified liquid bridge forces under an inhomogeneous force field. They found, that when the force is above a certain threshold, wet granular matter exhibits fluid-like behavior. This was indicated by a sudden increase in the granular diffusion coefficient. Herminghaus[40] analyzed this increase with a simple microscopic picture and energy arguments: he compared the energy that is consumed by the shear field and the energy which must be afforded to break

the liquid bridges. The differences in these two energy budgets correspond to the kinetic energy of the material, which is directly proportional to the square of the diffusion coefficient.
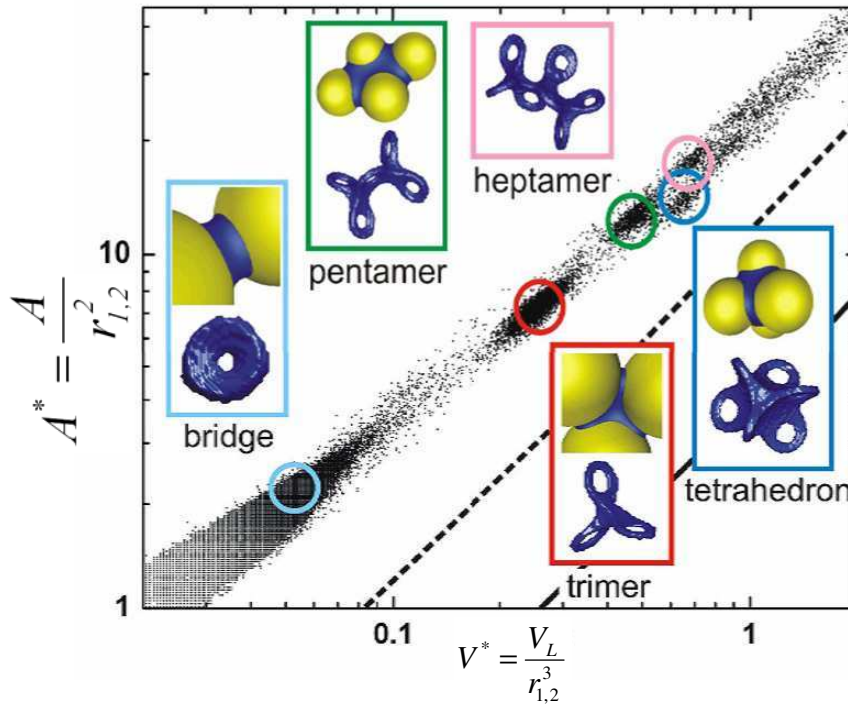
Figure 7.1: Distribution of liquid bridges in a bed of wet glass beads (each point represents a single capillary bridge characterized by its surface S and volume V, lines indicate the ratio S/V under the assumption of an idealized liquid distribution; W=0.035 (about 8% saturation, Scheel et al.[42])

Various authors (e.g., Mikami et al.[43], Yang and Hsiau,[44] as well as Yang et al.[45]) detailed on how to incorporate capillary forces into the DEM. The capillary force model used by Yang et al.[45] is based on an analytical solution for the shape of the liquid bridges when the toroidal meniscus approximation is used. More work on the forces between unequal spheres has been published by Willet et al.,[46] as well as Soulie et al.[47] Recently, Luding[48] presented a simple contact model, that is also able to mimic cohesive forces. His adhesive-elasto-plastic contact model is based on a linear hysteretic spring model. It can, however, not exactly model the forces associated with liquid bridges

In summary, modeling of cohesive forces in DEM simulations is relatively straight forward, and the major challenge is to account for the liquid distribution in case of liquid-bridge forces.

iii) DEM for the Modeling of Wet Granulation

There have been several attempts to model wet granulation processes using DEM. The main goal was to simulate the coalescence and breakage of agglomerates. For the representation of

agglomerates in DEM simulations two strategies exits: (i) the discrete elements can strictly present primary particles, as well as (ii) agglomerates are represented by discrete elements. The latter approach allows for the simulation of large systems. The disadvantage is, however, that assumptions have to be made, e.g., for porosity or shape of the formed granules. Furthermore, the possibility of agglomerate breakage is not implicit in the simulation. However, various researchers used this approach to investigate granulation processes via DEM. For example, Gantt and Gatzke[49] directly simulated the granulation process by determining the probabilities of aggregation and breakage via a hard-sphere discrete particle model. They used the coalescence model of Liu et al.[50] Periodic boundary conditions, as well as perfectly spherical granules have been assumed in the simulation of Gantt and Gatzke.[49] In a more recent paper, they used DEM simulations to determine coalescence kernels, as well as compaction rates in high-shear granulators.[51] In these simulations they used periodic boundary conditions and a unique boxing scheme to model particle flow in a high-shear mixer. The boxing scheme significantly reduced the computational expenses due to a simplified collision detection between the individual elements (in total 5,000 granules in a wedge-shaped $\pi/32$-section have been studied). A soft-sphere DEM code was used in this study. However, coalescence was excluded in their simulations, and only the relevant information on the collision was recorded to derive a coalescence kernel. Also, Gantt and Gatzke[52] investigated the suitability of the kinetic theory of granular flow (KTGF) for the modeling high-shear mixers using a similar simulation approach.

When adapting the first approach, i.e., the representation of primary particles in the simulation, the granulation process can be studied directly. Thus, no rigorous models for the mechanical properties of the granules are needed. For example, Goldschmidt et al.[29] performed such detailed DEM simulations of fluidized bed granulation processes based on the hard-sphere model. They also incorporated models for binder solidification. These simulations have been based on a two-dimensional geometry. A significantly lower number of particles as in the real application has been used. Other examples for the simulation of wet agglomerates are the studies of Talu et al.,[53] as well as of Khan and Tardos.[54] Recent advances in this area were achieved by Richefeu et al.[55] They analyzed the shear properties of wet granular materials included liquid bridges in the pendular state. Other saturation states have not been modeled by their group but might be of central importance in granulation. Subsequent studies of Richefeu et al.[56] also focused on the pendular state only.

In summary, there has been significant interest in DEM-based simulations of wet granulation processes, mainly focusing on agglomerate formation and breakage. The major challenge is the real-scale, primary-particle-based simulation of these processes. Also, the wet granular flow and the mixing of wet particles in these granulators have not been fully understood yet.

7.2.2 An Adapted Particle Model

i)   General Strategy

We use the so-called soft-sphere method or time-driven method (TDM). In this method, collisions are modeled as enduring contacts (over a few time steps) and the new particle positions and velocities are computed in fixed time-intervals. The particles are allowed to overlap to model the deformation of the particles and the contact forces are a function of these overlaps. This allows an accurate consideration of particle elasticity, as well as damping and sliding effects due to friction.[57] The influence of hydrodynamic forces stemming from the interaction of the granular flow with the surrounding air has been neglected. The total momentum $\vec{M}_{total,i}$ acting on the particle has to be taken into account, which is evaluated from the contribution of each individual force by multiplication with the normal distance with respect to the center of gravity for each individual particle.

In our work the Linear-Spring-Dashpot model is used,[58] because the parameters are readily determined, and analytic solutions are available for a straightforward verification of numerical schemes. The benefit of using more sophisticated non-linear interaction models is small in comparison to the additional computational effort. Therefore, this model is still widely used in the area of DEM simulations.[32]

The normal force for this model can be calculated as follows:

$$F_{c,n,ij} = k_n \delta_{n,ij} + c_n \dot{\delta}_{n,ij}$$

(7.1)

The first term is the elastic term modeled by a spring and the second term represents the dissipation modeled by a dashpot. k_n is the normal stiffness coefficient, c_n the normal damping coefficient and δ_n stands for the normal overlap between the particles. k_n can be evaluated from the material and geometrical properties of the particles in contact, as well as from a characteristic collision velocity.[59]

In the tangential direction we use a similar model based on a linear spring and dashpot model with a frictional slider:

$$F_{c,t,ij} = \begin{cases} k_t \delta_{t,ij} + c_t \dot{\delta}_{t,ij} & for \quad F_{c,t,ij} \leq \mu F_{c,n,ij} \\ \mu F_{c,n,ij} \dfrac{\delta_{t,ij}}{|\delta_{t,ij}|} & for \quad F_{c,t,ij} > \mu F_{c,n,ij} \end{cases} \qquad (7.2)$$

In analogy to the normal force model, the term $k_t \delta_{t,ij}$ represents the force of the spring in tangential direction, and $c_t \dot{\delta}_{t,ij}$ is the contribution of the damping element, i.e., the dashpot. The frictional slider is characterized by the friction coefficient μ between the two materials in contact.

In the current work we also account for rolling friction via Eqn. 7.3:

$$M_r = -\mu_r |F_{c,n,ij}| r_i \cdot \frac{\dot{\theta}_i}{|\dot{\theta}_i|} \,. \qquad (7.3)$$

Here $||$ denotes the norm of a vector.

ii)   Liquid Bridge Effects

When a liquid phase, i.e., the binder, is added to a dry granular material, the surface of the particles is wetted and the binder is distributed between the particles in contact. Depending on the ratio between binder and solid volume, different states of binder distribution can be observed: (i) at low moisture content, i.e., the pendular state, two particles are held together by lens-shaped rings of liquid; (ii) if liquid bridges form between more than two particles, the funicular state is reached, and finally (iii) when almost all the pores between the particles are filled with the liquid and the liquid pressure is still lower than the air pressure,[60] the capillary state is reached. The forces between the particles depend strongly on the exact shape of the liquid bridge. For the pendular state, the shape can be relatively easily calculated for spherical particles and the resulting forces agree well with experimental data.[46] This is done by solving the Young-Laplace equation describing the pressure difference between the gas and liquid phase due to capillary forces.

In the funicular state the situation is significantly more complex, because the randomly packed structure of the particles leads to a complex geometrical configuration of the liquid bridges.

The same is true for the capillary state. A detailed reconstruction of this situation by means of computer simulations has been attempted recently by several groups (for example Stepanek and Rajniak,[16] as well as Grof et al.[14,15]). However, it is extremely demanding and currently limited to a relatively small number of particles due to the high requirement for the spatial resolution of the liquid bridges. To circumvent this problem, a simplified model based on the treatment of the liquid phase as a continuum has been published.[33] However, this approach neglects the details of the flow in between particles, and consequently, capillary forces cannot be taken into account. In the current work we have restricted our analysis to the pendular state.

The recent review of Zhu et al.[20] shows that various approaches exist to calculate capillary forces for DEM simulations. Since in softsphere-DEM simulations the contact forces have to be calculated directly, it is necessary to provide an explicit function for the capillary force. Here basically two approaches can be distinguished: (i) an approximate solution of the Young-Laplace equation, or (ii) an appropriate fit of the results obtained from the solution of the Young-Laplace equation. The former approach was used by Lian et al.[35] to calculate liquid-bridge forces and successfully incorporated by McCarthy[34] into DEM simulations. The latter approach was employed by Willet et al.[46] over a wide range of relative liquid volumes and showed errors in the force estimate of less than 3 %. In our work we have used the results of Willet et al.[46] to calculate the liquid bridge forces between two particles. Willet et al.[46] showed that their approach together with the Derjaguin approximation gives relatively accurate results for powder beds consisting of spheres of both equal and unequal size. However, if the diameter ratio of the two spheres in contact is too large or too small, the capillary bridge model of Willet et al.[46] becomes inaccurate. Hence, to model forces between particles and walls, we use the results of Mikami et al.[43] that were fitted to the limiting case in which one of the two radii of the spheres becomes infinite. They are similar to the more recent results of Willet et al.[46] and have been obtained by fitting the numerical solution of the Young-Laplace equation. The results of Mikami et al.[43] are also applicable to particle-particle interactions, but are slightly less accurate compared to the work of Willet et al.[46] for this situation. Hence, we use the results of Willet et al.[46] for particle-particle interactions (Eqn. 7.4) and that of Mikami et al.[43] for particle-wall interactions (Eqn. 7.5).

$$ \mathrm{F}_{cap,pp} = 2 \cdot \pi \cdot r_{1,2} \cdot \gamma_s \cdot \exp\left\{ f_1 - f_2 \cdot \exp\left[f_3 \ln\left(\frac{S^*}{\sqrt{V^*}}\right) + f_4 \cdot \ln^2\left(\frac{S^*}{\sqrt{V^*}}\right) \right] \right\} \qquad (7.4) $$

$$F_{cap,pw} = \pi \cdot r_{1,2} \cdot \gamma_s \cdot \left(\exp\left[A \cdot S^* + B \right] + C \right) \tag{7.5}$$

The functions f_1, f_2, f_3, f_4, A, B and C are fit functions in the variables ϕ and V* and can be found in the work of Willet et al.[46] and Mikami et al.[43] γ_s is the surface tension and $r_{1,2}$ is the harmonic mean sphere radius:

$$\frac{1}{r_{1,2}} = \frac{1}{2} \cdot \left(\frac{1}{r_1} + \frac{1}{r_2} \right) \tag{7.6}$$

In our case, $r_{1,2}$ is equal to the particle radius, as we have mono-disperse particles. Furthermore, S* is the dimensionless half distance, i.e., the half distance between the two particle surfaces for particle-particle interactions and the distance between the wall and the particle surface for particle-wall interactions. The reference length is the harmonic mean sphere radius $r_{1,2}$. Then S* can be calculated from the dimensional distances S:

$$S^* = \frac{S}{r_{1,2}} \tag{7.7}$$

To make the liquid volume per capillary bridge, V_L dimensionless, we introduce V* as the dimensionless liquid volume per capillary bridge:

$$V^* = \frac{V_L}{r_{1,2}^3} \,. \tag{7.8}$$

Using this approach, we only account for static forces resulting from the liquid bridges. Dynamic forces due to lubrication effects are neglected. This is an appropriate assumption, since the Capillary number, i.e., the ratio of viscous forces in the liquid film and capillary forces, is sufficiently small in typical applications.

$$Ca = \frac{\eta \cdot U_c}{\gamma_s} \tag{7.9}$$

Here η is the dynamic viscosity of the liquid phase, U_c is a characteristic velocity and γ_s is the surface tension. For example, assuming a characteristic velocity of 1 m/s, for the case of bladed mixers, a dynamic viscosity of $\eta = 10^{-3}$ Pa·s and $\gamma_s = 7 \cdot 10^{-2}$ N/m (typical for water), one obtains Ca = 0.014. This, in analogy to the arguments by Mikami et al. [43], justifies the use of static liquid-bridge forces only.

The liquid-bridge force models require as input parameters the size of the particles, the contact angle, the separation distance of the surfaces, the surface tension and the volume of the liquid bridge. While all other parameters are known or can be easily calculated, the liquid volume between the surfaces cannot be computed directly and has to be based on assumptions of liquid distribution in the particle bed. In our work we assume the liquid is evenly distribution over the powder bed and consequently assign a fixed liquid volume to each capillary bridge. Follow-up studies will model non-uniform liquid distribution in addition to the granular flow.

Finally, a rupture distance has to be introduced in the simulation that marks the breakage of the liquid bridge and consequently the termination of the capillary force. In this work we adopt the result of Lian et al.,[35] reporting that the rupture half-distance S_{rup} is proportional to the cube root of the liquid volume V_L and the contact angle ϕ.

$$2 \cdot S_{rup} = \left(1 + \frac{\phi}{2} \right) \cdot \sqrt[3]{V_L} \qquad\qquad (7.10)$$

Note, for particle-wall collisions, $2 \cdot S_{rup}$ is the critical particle-wall distance for rupture. The implementation of the liquid bridge model has been tested and the results are shown in Appendix D.

7.2.3 Simulation Input Parameters

Glass beads with a size of 3 mm and 1 mm were considered with the physical properties detailed in Table 7.1. The particle density is 2,500 kg/m³ and the bladed mixer was filled with glass beads such that the upper edge of the blade was still fully covered with particles. Therefore, approximately 7,200 particles were placed in the mixer. The normal and tangential stiffness coefficients k_n and k_t respectively were set to $1.05 \cdot 10^5$ N/m to reduce computational time. This value resulted in maximal particle overlaps that were under 5%. Consequently the influence on the simulation results was minimal, which is also well documented in literature (see for example Stewart et al.[4]). The damping coefficients in normal and tangential direction were set such that a predefined coefficient of restitution (COR) was obtained. The simulations have been conducted in triplicate with COR values equal to 0.7, 0.8 and 0.98. The sliding and the rolling friction coefficients were taken as 0.5 and 0.01 respectively.

All simulations involving wet particles were conducted for a dimensionless liquid volume V* of 0.01 for each capillary bridge. For an average amount of 6 capillary bridges per particle

(supported by experiments by Fournier et al.[39]) this corresponds to a liquid content of 0.72 Vol% or 0.29 w%. Note, that this liquid content is only an approximate value, since we have kept the volume of liquid in each liquid bridge constant. As the number of contacts between particles and particles and the wall changes during the simulation, the total liquid will also change during the simulation.

The contact angle ϕ was taken to be zero. In order to mimic capillary forces between particles with a diameter of 0.5 mm (i.e., in agreement with the experiments of Lekhal et al.[9]), we adjusted the surface tension in the simulation. The scaling of the surface tension was based on a constant Bond number, i.e., constant ratio between body and surface tension forces,

$$Bo = \frac{\rho_P \cdot g \cdot d_P^2}{\gamma_s} \, . \tag{7.11}$$

Parameter	Symbol	Value
Particle density	ρ_P	2,500 kg/m³
Normal stiffness	k_n	$1.05 \cdot 10^5$ N/m
Tangential stiffness	k_t	$1.05 \cdot 10^5$ N/m
Coefficient of restitution	COR	0.98, 0.8, 0.7
Sliding friction coefficient	μ	0.5
Rolling friction coefficient	μ_r	0.01
Particle diameter	d	3 mm (1 mm)
Dimensionless liquid volume	V*	0.01
Contact angle	ϕ	0 °
Particle diameter for capillary forces	$d_{p,capill}$	0.5 mm
Surface tension	γ_s	0.073 N/m
Bond number[b]	Bo	0.084

Table 7.1: Simulation input parameters.

---

[b] Based on $d_{p,capill}$.

The resulting Bond number in our simulations is 0.084. Some authors (e.g., McCarthy[34]) use a so called "granular" Bond number Bo_g, that is proportional to the inverse of the Bond number used in this work:

$$Bo_g = \frac{3 \cdot \gamma_s}{2 \cdot (d_p/2)^2 \rho_P \cdot g} \cdot \qquad (7.12)$$

A $Bo_g > 10$ characterizes an already strongly cohesive wet granular matter with a static heap angle of $> 70°$.[61] Our simulations correspond to a granular Bond number of $Bo_g = 71$ indicating very strong cohesive forces between the particles in the simulation. The schematic representation of the bladed mixer geometry is shown in Figure 7.2 and the dimensions are listed in Table 7.2. The geometry is similar to that used in the experimental work of Lekhal et al.[9]
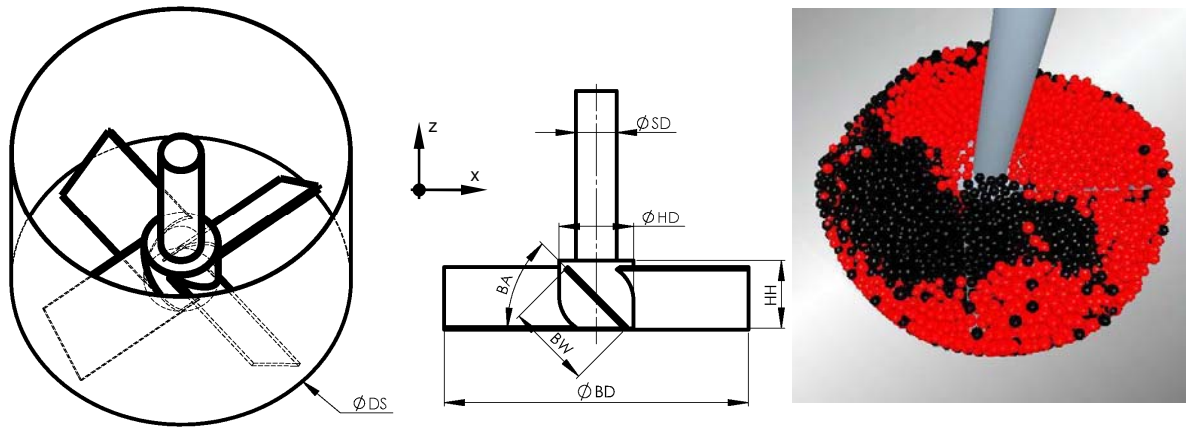
Figure 7.2: Schematic representation of the bladed mixer (left and middle) and mixer with particles (right, shown is the particle distribution after 1.25 impeller revolutions).

Parameter	Symbol	Value
Blade width	BW	25 mm
Blade diameter	BD	95 mm
Blade angle	BA	45 °
Hub diameter	HD	22 mm
Hub height	HH	20 mm
Shaft diameter	SD	12 mm
Stator diameter	DS	100 mm

Table 7.2: Geometric parameters of the bladed mixer.

7.3 Results

7.3.1 Granular Flow in a Bladed Mixer

i)   Results for Dry Particles

In this section we compare our simulation results with data obtained via particle image velocimetry (PIV) by Conway et al.[8] Similar experimental results have been presented by Lekhal et al.[9] and are in qualitative agreement with the experimental data of Conway et al.[8] Since their experimental data were obtained from 2D images of the powder surface, in our simulation we analyzed the velocity field only of the uppermost particles. Similar to Conway et al.,[8] we report the time evolution of the circumferential and radial velocity at a fixed point on the powder bed's surface. This point is located at a radial distance of 0.030 m from the stirrer axis, i.e., the half distance between rotor and wall. In the experiments of Conway et al.[8] the blade pitch was obtuse, i.e., same as in all our simulations.

The particles used by Conway et al.[8] were significantly smaller than in our simulations (approximately 400 μm in the experiment versus 3 mm particles in the simulation). However, with current computational capabilities it is too time consuming to simulate the approximately 4 million particles present in the experiment of Conway et al.[8] Furthermore, it was shown that particle size in cohesionless flows has little effect on the principal flow pattern in a bladed mixer.[19]

In Figure 7.3 we show the time evolution of the absolute instantaneous velocity at the top of the powder bed at a fixed point (half distance between rotor and wall). In Figure 7.3 V_{circ} and V_r are the velocities in circumferential and radial direction, respectively. The velocities have been normalized with the tip-speed of the impeller and the time has been multiplied with the impeller rotational speed to obtain dimensionless quantities. The sampling interval for probing the velocity was chosen identical to the characteristic time for the particle motion defined as $t_p = d_p/V_{tip}$. Here d_p is the particle diameter and V_{tip} is the tip speed of the impeller. In our simulations the highest tip speed was equal to 0.298 m/s and the particle diameter was 3 mm, i.e., we have chosen a sampling frequency of 0.01 s. Sampling at a 5-times higher frequency revealed additional high-frequency oscillations of the velocity field (refer to the insert in Figure 7.3). However, in general the main features of the flow are well represented with the lower sampling frequency of 0.01 s.
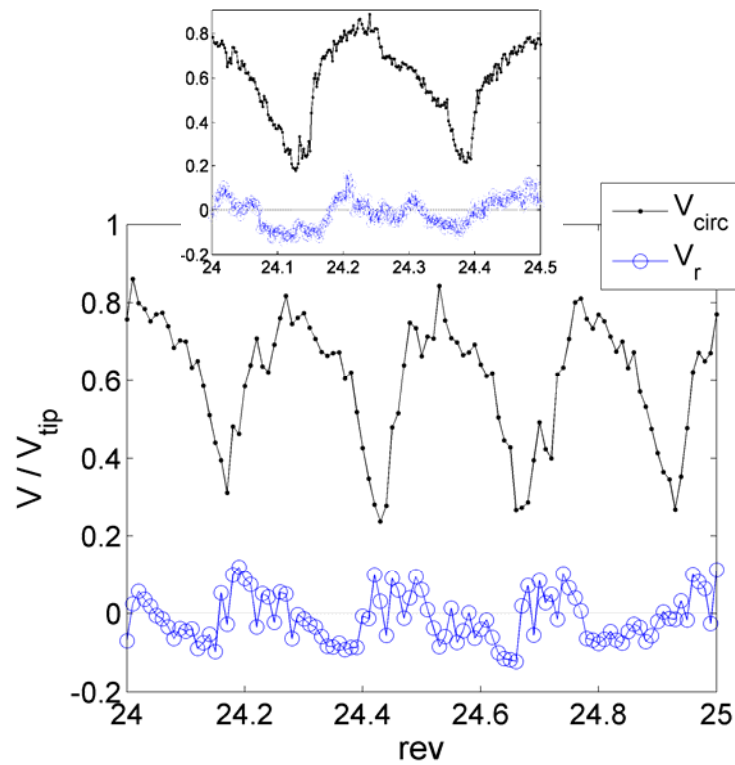
Figure 7.3: Simulated velocity profiles in time for dry particles (60 rpm, the insert was obtained using a 5-times higher sampling frequency).
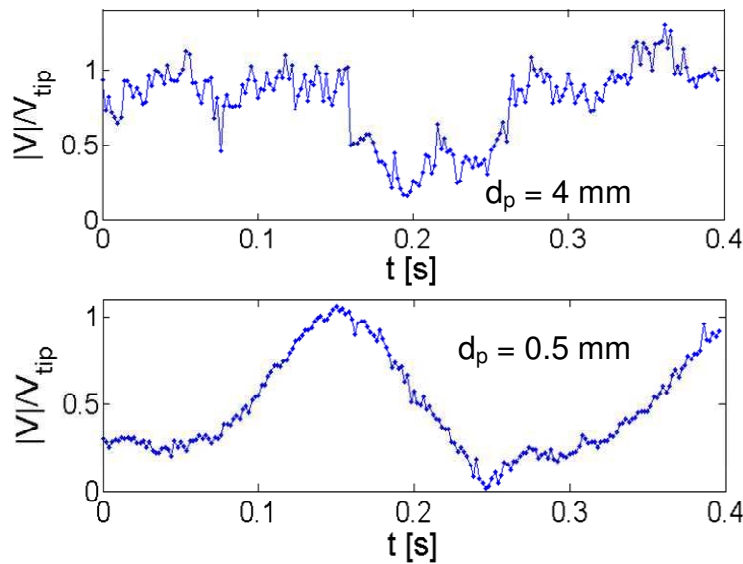
Figure 7.4: Experimental results for velocity profiles in time for dry particles (60 rpm, top: 4 mm glass spheres, bottom: 0.5 mm glass spheres).

The results presented in Figure 7.3 show the same qualitative features as the results of Conway et al.[8] First, a slow periodic oscillation of the circumferential velocity can be observed. This is due to the passage of the blade, and the frequency perfectly corresponds to the rotational

speed of the stirrer. Experimental results obtained by us also confirm this finding and are presented in Figure 7.4 for two different particle sizes. In order to resemble the situation in the simulation most accurately, we used glass beads for our experiments. Equipment and analysis method were similar to the one used by Conway et al.[8] While in the experiments also zero (and sometimes even negative) velocities are observed for the small particles, the simulations, as well as the experiments with larger particles do not reveal such features.

Also, fast oscillations of the circumferential and the radial velocity component with a lower amplitude have been observed by Conway et al.[8] This can be also seen in our experimental data for large particles (and to a lesser extent in the experiments with small particles). It is also predicted by our simulations. Our simulations indicate maximal particle velocities similar to the tip speed. This is in good agreement with our experimental data. A more detailed experimental investigation of the size effect on the flow in a bladed mixer is presented in Chapter 8.

ii)   Results for Wet Particles
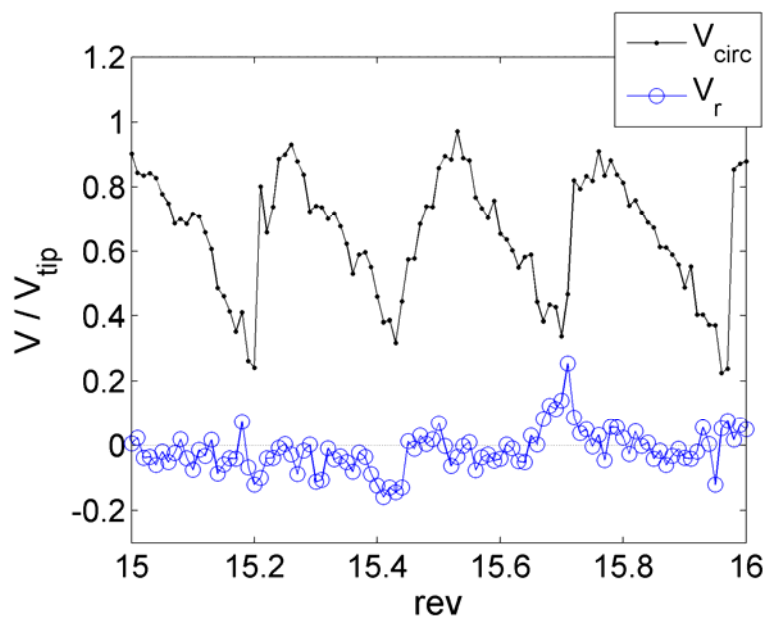
Figure 7.5: Simulated velocity profiles in time for wet particles.

For a wet powder bed we compare our simulations with the experimental results of Lekhal et al.[9] These experiments are similar to those for the dry particles and have been conducted at varying moisture contents between 0 w% and 4 w%. Our results for the circumferential and radial velocity profile at a fixed point on the powder surface is shown in Figure 7.5 for a moisture content of 0.29 w%. Again, simulations and the experiments by Lekhal et al.[9] show a

slow periodic oscillation of the circumferential velocity, as well as a high-frequency oscillation that is superimposed. In the radial direction the experiments show somewhat higher oscillation amplitudes compared to the flow with dry particles (refer to Figure 7.3) and also our simulations show this tendency. However, the simulation still shows some discrepancies due to the significantly smaller particles that were present in the experiment.

iii) Comparing Wet and Dry Granular Flow

Principal differences in wet and dry powder flows are highlighted in Figure 7.6 and Figure 7.7. In Figure 7.6 the blue dots mark the center of a particle and the red lines are cross sections of the blades.
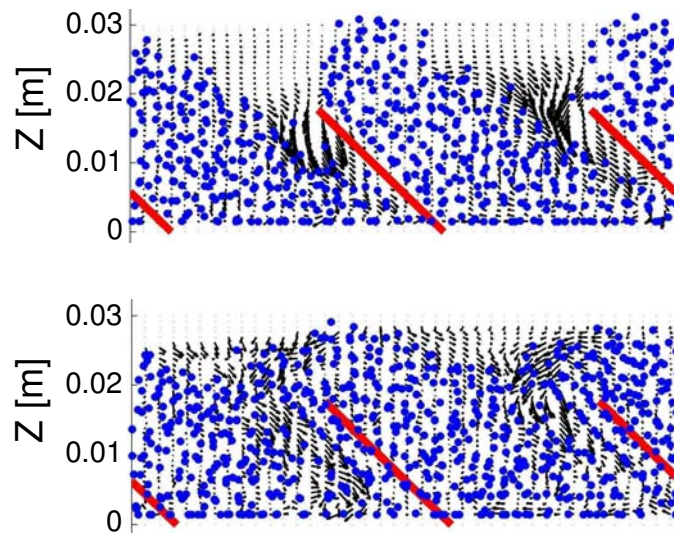
Figure 7.6: Distribution of particles and instantaneous velocity for wet (top) and dry (bottom) particles (r = 0.025 m).
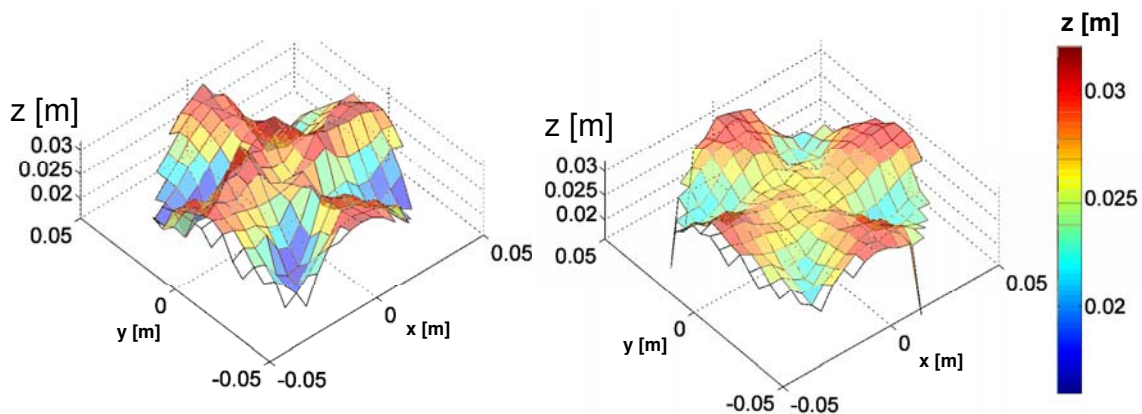
Figure 7.7: Surface contour for wet (left) and dry (right) particles.

The view shows a cylindrical cross section of the powder bed, where the horizontal axis depicts the circumferential direction and the vertical axis corresponds to the z-direction. As can be seen, the major feature of wet granular flow is that heaps form at the upper blade tip, which leads to a significant higher "roughness" of the powder bed surface. To illustrate the flow field, we have included the instantaneous velocity vectors relative to the impeller motion in Figure 7.6. Clearly, particles move over the tip, fall down and then move towards the blade such that they are finally located under the blade. This is the case for both wet and dry particles. However, this effect is much more pronounced in the wet case. To stress once more the difference between wet and dry powder flow, we show a three-dimensional representation of the powder surface in Figure 7.7. Clearly, the increased roughness is significant and has been also observed by Lekhal et al.[9] in their experiments.

7.3.2 Details of the Granular Flow and Velocity Fluctuations

Velocity fluctuations are an important quantity as diffusive particle mixing is related to the fluctuating velocity profile in the powder bed. Velocity fluctuations, as well as time- and locally-averaged velocities, have to be analyzed on an Eulerian grid. In order to get velocity information on an Eulerian grid (in contrast to the Lagrangian grid defined by individual particles), the locally-averaged velocity in an arbitrary grid cell has to be calculated. This is done by using the surrounding particle information and the function `griddata` in Matlab®. Thus, we fit the particle velocity information with a continuous function on the Eulerian grid, in order to ensure that a meaningful locally-averaged velocity $\vec{u}_{av,i,j}$ is calculated even when there are only a few (or even no) particles in the volume characterized by the indices i and j. A similar calculation is done for the blade-relative velocity $\vec{u}_{av,rel}$. Please note that for most of the analysis in this work, only blade-relative velocities in a blade-fixed coordinate system have been used. Details for the calculation of these velocities are provided in Appendix E.

The time-averaged velocity fluctuation $\overline{\vec{u}^2}$ is then computed from the locally-averaged (instantaneous) relative velocity $\vec{u}_{av,rel}$ and its time-averaged value $\overline{\vec{u}_{av,rel}}$ according to:

$$\overline{\vec{u}_{i,j}^2} = \frac{1}{N_t} \cdot \sum \left(\vec{u}_{av,rel,i,j} - \overline{\vec{u}_{av,rel,i,j}} \right)^2 . \tag{7.13}$$

Here, N_t denotes the total number of time steps analyzed. Clearly, the velocity fluctuation $\vec{u}^2$ is a three-dimensional vector that characterizes velocity fluctuations in each spatial coordinate. In order to obtain a scalar value that quantifies velocity fluctuations, we define a mean velocity fluctuation as:

$$U_{i,j}^2 = \frac{\left(\overline{u_{i,j}^2} + \overline{v_{i,j}^2} + \overline{w_{i,j}^2}\right)}{3}. \tag{7.14}$$

Here, the overbars indicate time-averaged quantities, and u, v and w refer to the components of the velocity fluctuations as per Eqn. 7.13 on a Cartesian grid. Time averaging has been performed over at least 200 time samples and was started after several full revolutions of the impeller to avoid transient effects influencing our results.

The mean velocity fluctuation U^2 can be seen as a metric for diffusive mixing from a mesoscopic perspective, as it is calculated from the locally-averaged velocity of an assembly of particles. This quantity cannot, however, reflect the (possibly uncoordinated) motion of individual particles from a microscopic, i.e., particle perspective (see below in the section on "Mean Squared Velocity Fluctuations vs. Granular Temperature").

To identify the main direction of the velocity fluctuations, we have also analyzed the individual radial, circumferential and axial velocity fluctuations u_{circ}, u_{rad} and u_z, respectively. This was done by a simple transformation of the coordinate system. In order to compare the fluctuation levels at different stirrer speeds, the calculated mean and fluctuating quantities have been normalized by the tip speed and the tip speed squared, respectively.

i)   Results for the Mean and Fluctuating Quantities

The most important features of the mean velocity field in wet and dry granular flows are presented in Figure 7.8. Here we show 2D cross sectional views normal to the mixer axis for two different heights (top: 1 mm, bottom: 15 mm). The velocity field again is relative to the impeller motion. As can be seen in Figure 7.8, the particles move in opposite direction to the impeller motion over the blades. The shape of the silhouette of the blade is indicated as a solid black line whereas the intersection of the blade and the 2D cross section is shown as dashed white line. Comparing the cross sections at an elevation of 1 mm, i.e., directly at the bottom of the mixer, we see that the mean velocity is significantly higher for the wet particles. We hypothesize that this is due to the increased normal forces stemming from the capillary forces

and consequently higher normal friction forces. However, the flow pattern is basically the same.
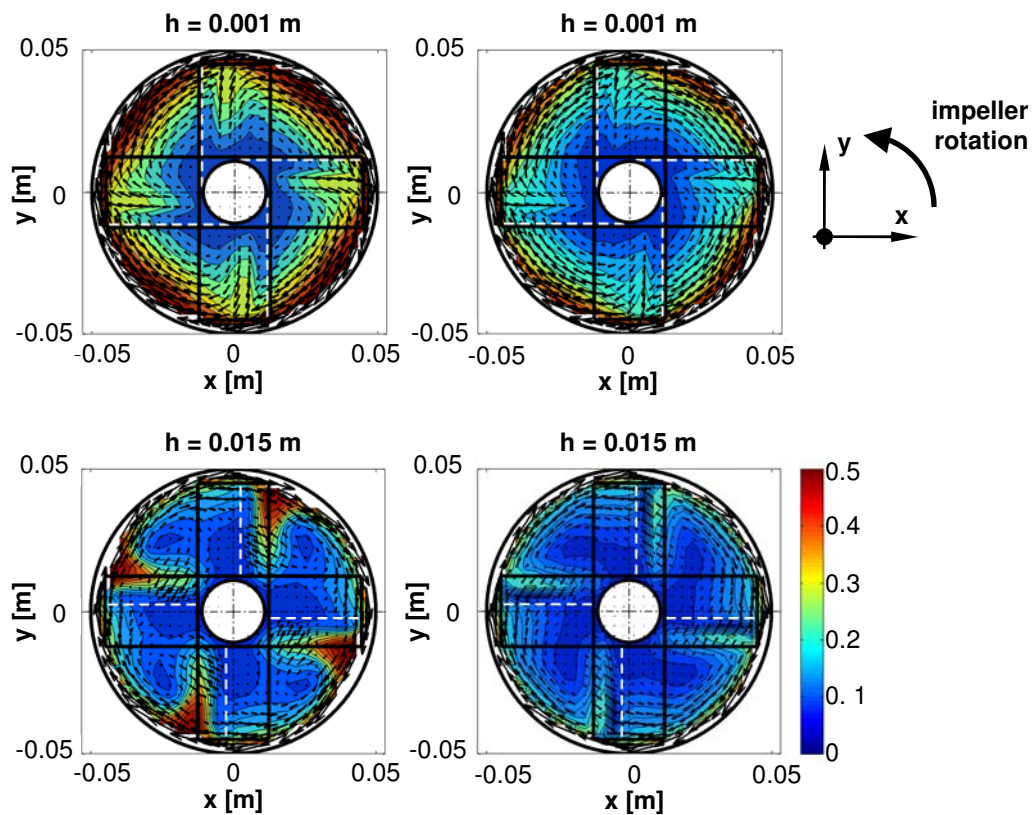
Figure 7.8: Instantaneous and mean velocity field for wet (left) and dry (right) granular matter (60 rpm, the velocity has been normalized with the tip speed).

The effect of the higher blade relative velocity is even more pronounced in the cross section at an elevation of 15 mm. Clearly, for wet particles the interaction forces between particles and stator lead to significantly higher blade relative velocities. This also leads to a significant change in flow pattern, such that the recirculation behind the blade is more pronounced for the wet particles compared to dry particles. From this, also an impact on the mixing might be expected, which is analyzed in detail in the following two sections.

In Figure 7.9 we analyze the mean velocity fluctuation U'^2 in 2D cross sections normal to the mixer axis for wet and dry powder beds at 60 rpm. The cross section at a height of 15 mm above the bottom of the mixer has been selected. The contours of the blades are indicated with solid black lines. The intersection of the blade with the 2D cross section is again marked with a dashed white line. Particle data considered to generate the velocity fields for these cross sections were picked in slices that were $1.2 d_{particle}$ thick. As can be seen from Figure 7.9, zones with a high fluctuation level are localized behind the blade and near the wall. As expected, the

contour plot of the mean velocity fluctuation is nearly symmetric with respect to the four blades. By comparing the mean velocity fluctuation for dry and wet particles (refer to Figure 7.9), we see that for the dry particle bed the mean velocity fluctuations are significantly smaller than for the wet particles. The higher mean velocity fluctuation calculated for wet particles reflects an increased large-scale fluctuation of the powder bed's (i.e., particle mean) velocity. Clearly, our simulations show that it is possible to enhance large-scale velocity fluctuations in bladed mixers by adding a defined amount of moisture. This behavior is similar to trends that have been theoretically predicted by Li and McCarthy,[31] i.e., improved mixing in wet powder beds. Note, that this does not automatically mean that velocity fluctuations on the particle level (i.e., the variance of particle velocities) are also increased by liquid bridges. One may even expect the contrary on the particle level, i.e., the inhibition of velocity differences on the small scale. This is illustrated in the following paragraphs.
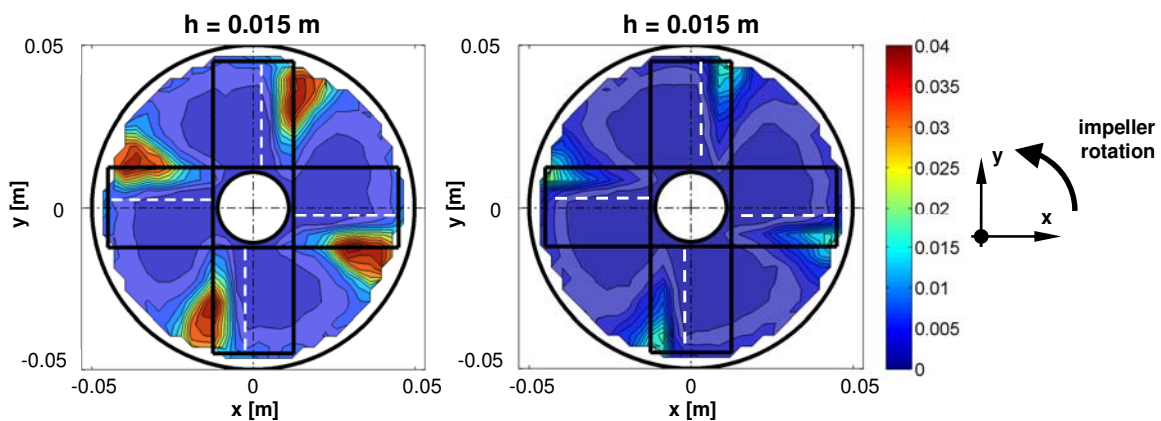
Figure 7.9: Comparison of the mean velocity fluctuations between wet (left) and dry (right) granular matter (60 rpm, velocity fluctuations have been normalized with the tip speed squared).

The analysis of the velocity fluctuation directions is shown in Figure 7.10. In this figure, we have calculated the mean squared velocity fluctuations in circumferential, radial and z-direction separately and normalized them with the squared tip speed. As before, the mean velocity fluctuation is significantly lower for the dry powder bed compared to the wet powder. Clearly, the major contribution to the mean velocity fluctuation stems from the fluctuations in the z-direction. This is due to the fact that particles are falling down behind the blade and then move in circumferential and radial direction in a chaotic manner. Since the falling distance for the wet powder bed is higher due to increased heap formation, also the mean kinetic energy of the particles is increased. Obviously this leads to higher velocity fluctuations. Clearly, the mean velocity fluctuations in the radial direction are weakest, as can be seen from a comparison of

Figure 7.11a-c. However, this might have been expected because the major direction of particle motion is in the circumferential (motion of the impeller) and axial direction (particles falling from the heaps).
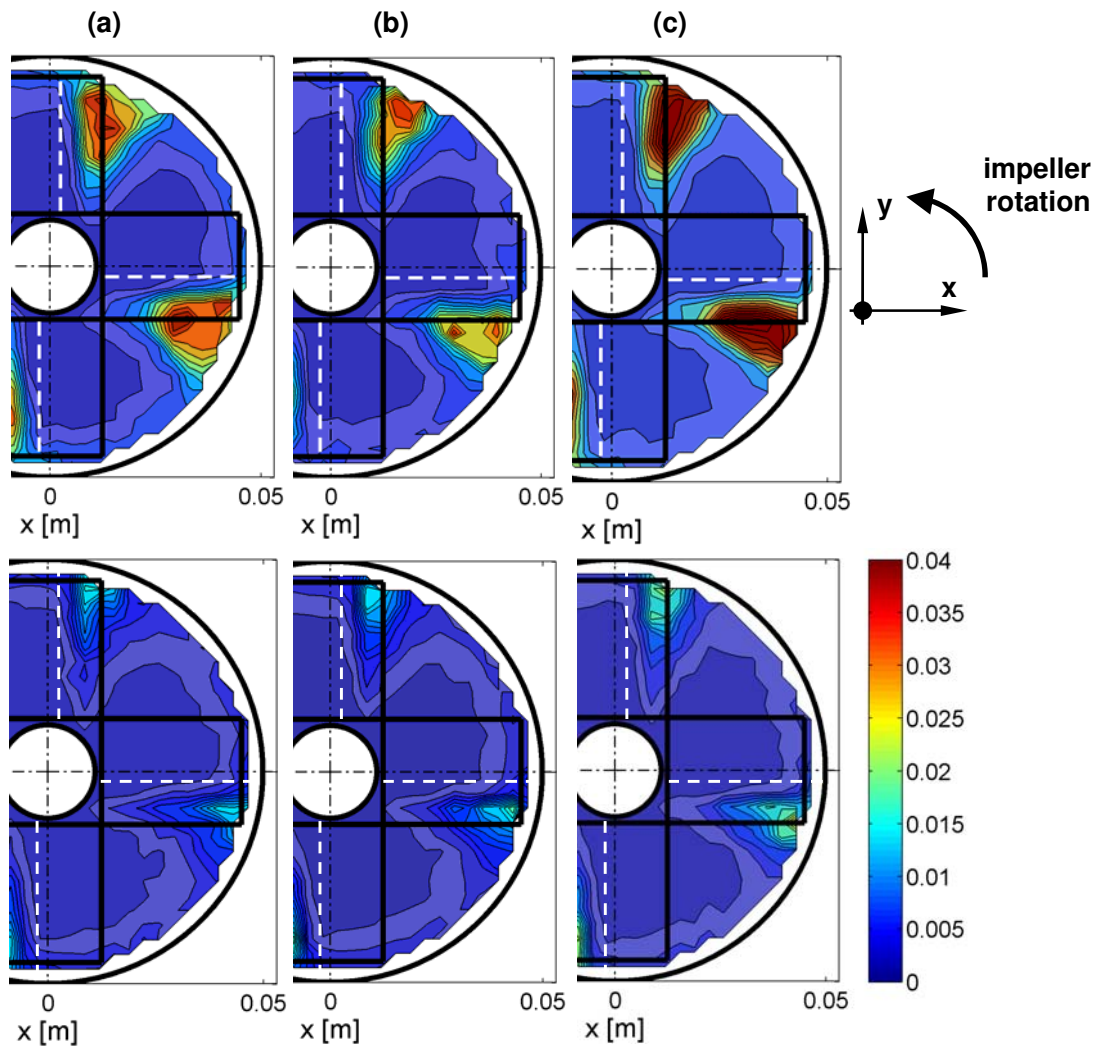
Figure 7.10: Comparison of velocity fluctuations in (a) circumferential, (b) radial and (c) axial direction for wet (top) and dry (bottom) granular matter (60 rpm, velocity fluctuations have been normalized with the tip speed squared).

To compare the mean velocity fluctuation for different powder bed properties and stirrer speeds, we calculated the average values over the circumferential direction and over the full bed height and plotted them as a function of the radial distance. The results of this plot for a dry and wet powder bed are shown in Figure 7.11 as a function of the radial distance. The velocity fluctuations have been normalized with the tip speed squared in this figure as before. We observe similarly high normalized velocity fluctuations in Figure 7.11 for different stirrer

speeds. Hence, we argue that our normalization with the square of the tip speed is correct to a first approximation.
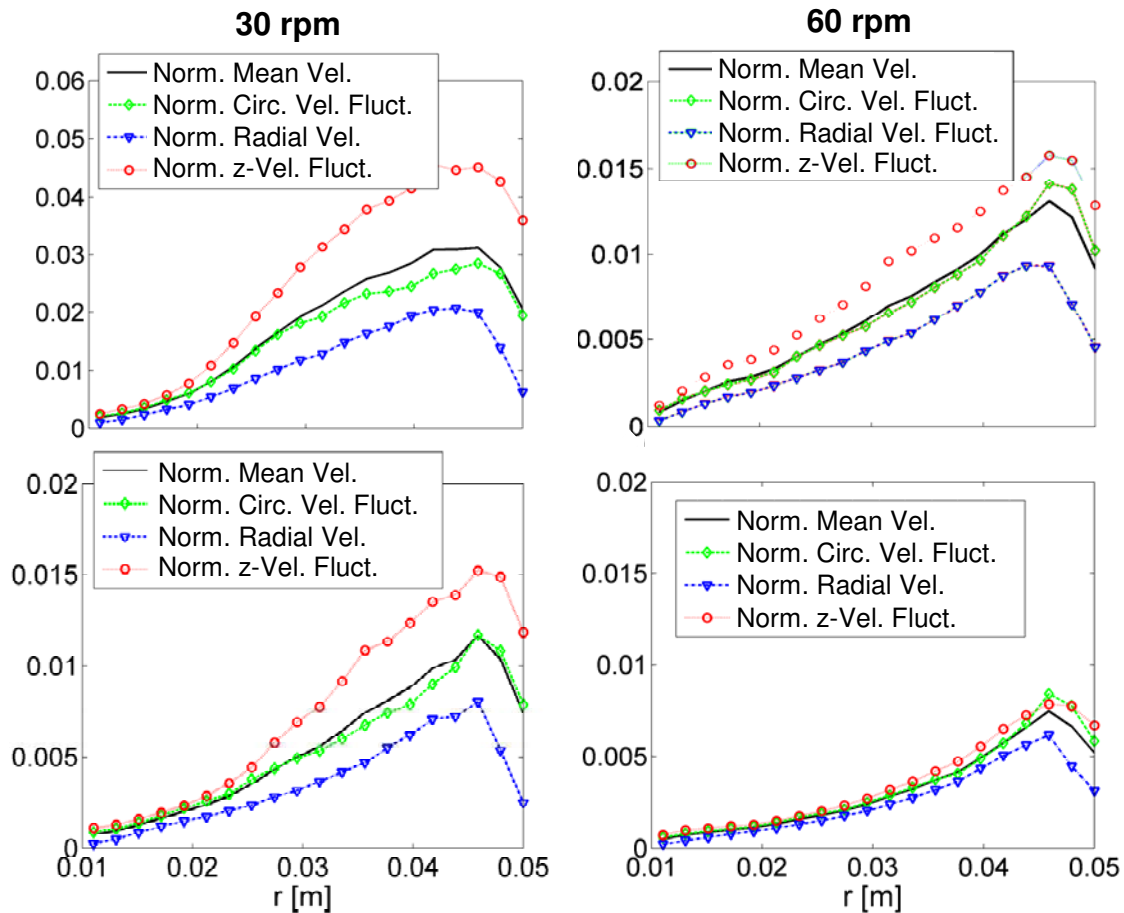
Figure 7.11: Comparison of averaged mean velocity fluctuations vs. radial distance for different stirrer speeds for wet (top) and dry (bottom) granular matter (averaging has been performed over the circumferential and axial direction, velocity fluctuations have been normalized with the tip speed squared).

As can be seen, the velocity fluctuations in different directions, as well as the mean velocity fluctuation are significantly higher for wet granular matter. This effect is more pronounced for lower stirrer speeds resulting in an approximately threefold higher normalized mean velocity fluctuation at 30 rpm for wet granular matter. Another interesting observation is that with decreasing stirrer speed the normalized mean velocity fluctuation, as well as the normalized squared velocity fluctuations increase. This effect is weak for dry granular matter, where the dimensional mean velocity fluctuation and squared velocity fluctuations roughly scale with the square of the tip speed. However, this is definitely not true for the wet particle bed, where the dimensional mean velocity fluctuation is only 29 % lower for 30 rpm compared to the case of 60 rpm (linear scaling with the square of the tip speed would mean a 75 % lower value). We

hypothesize that this effect is due to heap formation: in wet granular flow, the height of the heap does not depend on the stirrer speed and consequently the kinetic energy of the particles falling down from the heap is also invariant. Consequently, the velocity fluctuations are similar and identical velocity fluctuations in the z-direction are expected. This speculation is supported by the fact, that the dimensional z-velocity fluctuation for 30 rpm is only 14 % lower than the one for 60 rpm.

Furthermore, we observe anisotropic mean velocity fluctuations in all cases. However, this effect is most pronounced for the lower stirrer speed and wet granular matter. This may be explained by the fact that in a wet granular flow the mean velocity fluctuation is mainly driven by the kinetic energy of the falling particles. Thus, especially the mean velocity fluctuations in z-direction can be expected to be higher for wet particles compared to a dry granular matter. The mean velocity fluctuations in circumferential and radial direction are only moderately affected by liquid bridge forces. This is thought to cause an increased anisotropy of the mean velocity fluctuations in wet granular matter.

Looking at the shape of the curves in Figure 7.11, we observe a local maximum near the wall for all cases. An almost linear increase of all quantities except for the case of low stirrer speed and wet particles is noticed. In the latter case the nonlinearity in the radial direction seems most pronounced and a relatively shallow behavior near the local maximum is observed. This can be explained by the more complex behavior of wet granular masses, i.e., the fact that liquid-bridge forces break under a certain normal force and are sustained below a critical value. Hence, near the axis of the stirrer the particle bed rotates with the stirrer and velocity fluctuations are small because particles do not move over the blade. However, at a certain radial distance the force acting on the liquid bridges are overcome. As a consequence, particles do move over the blade resulting in a strong increase of velocity fluctuations.

Finally, we see that the velocity fluctuation in the circumferential direction resembles the mean velocity fluctuation, whereas the fluctuation in the z-direction is always higher and in the radial direction always lower. Hence, for these cases we conclude that a proper estimate of the mean velocity fluctuations can be gained by measurements of the squared velocity fluctuation in the circumferential direction, i.e., from 2D measurements at the top of the powder bed. However, such 2D measurements cannot predict velocity fluctuations inside the powder bed. The distribution of the mean velocity fluctuations over the bed height is shown in Figure 7.13 and discussed in the corresponding paragraph.
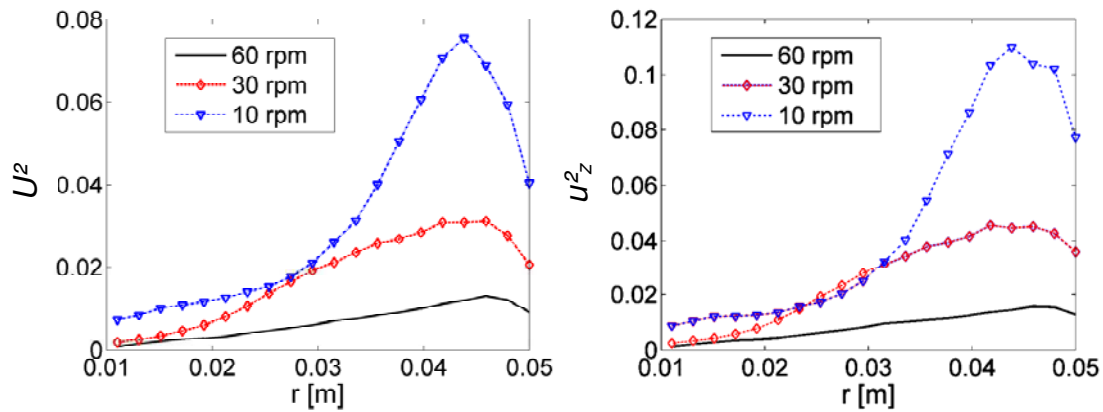
Figure 7.12: Comparison of averaged mean velocity fluctuations (left) and averaged z-velocity fluctuations (right) vs. radial distance for different stirrer speeds for wet particles (velocity fluctuations have been normalized with the tip speed squared).

To investigate the effect of the stirrer speed on the anisotropy of velocity fluctuations for wet granular flow in more detail, we conducted additional simulations at 10 rpm. In Figure 7.12 we compare the flow for three different stirrer speeds and illustrate the effect on the mean and on the z-velocity fluctuations. Clearly, the maximum of the mean velocity fluctuations becomes more pronounced for lower stirring speeds. One would expect that at lower stirrer speeds velocity fluctuations also decrease in the mixer. The normalized velocity fluctuations shown in Figure 7.12 would be similar for different stirrer speeds, if the fluctuations are only induced by the speed of the blades. The differences in the normalized velocity fluctuations found in our work are likely due to velocity fluctuations associated with particles falling from heaps.
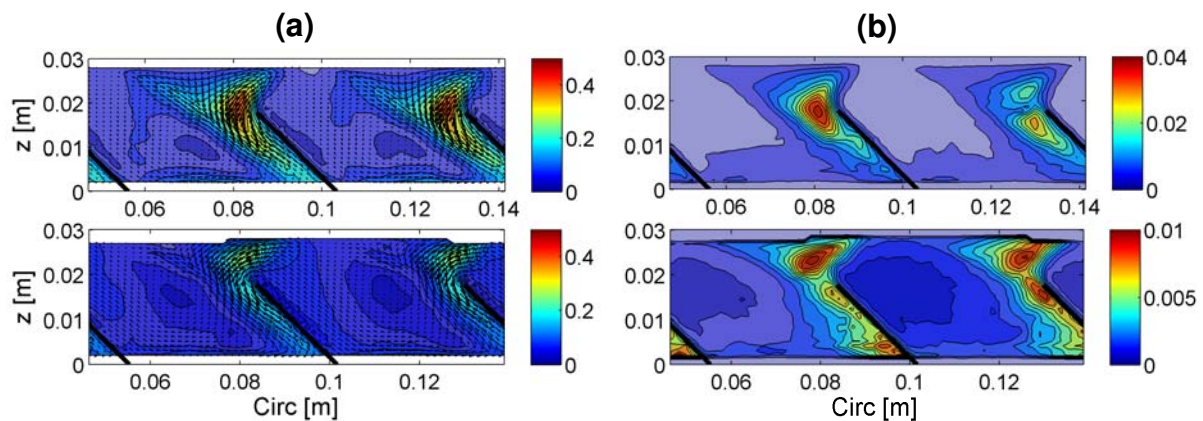
Figure 7.13: Mean velocity field (a) and mean velocity fluctuations (b) for wet (top) and dry (bottom) granular matter (60 rpm, r = 0.03 m, mean velocities and velocity fluctuations have been normalized with the tip speed and the tip speed squared, respectively).

To illustrate the flow pattern and mixing in the bladed mixer, the mean velocity distribution and the mean velocity fluctuations are plotted in a cylindrical cross section parallel to the

stirrer axis (Figure 7.13). The mean velocity relative to the stirrer is significantly higher for the wet material compared to the dry material. This may be again attributed to heap formation, i.e., due to the higher falling distance of the wet particles.

Also, the magnitude and spatial distribution of the mean velocity fluctuations (see Figure 7.13b) is different for wet and dry granular matter. Whereas for the wet material the mean velocity fluctuations are significantly higher and more localized (see Figure 7.13b top), for the dry particles we observe small and more homogenous mean velocity fluctuations over the height of the mixer. This again illustrates nicely the characteristics of wet granular flow, namely the generation of strong mean velocity fluctuations via falling of particles from the heap. At the same time the particle fluctuation is inhibited in radial and circumferential direction due to capillary forces leading to a strongly anisotropic distribution of velocity fluctuations. In contrast, for dry particles the mean velocity fluctuations are more isotropic due to lower interaction forces between particles. Obviously, this is caused by the effect illustrated in the previous section on the mean velocity fluctuations: due to the capillary forces the particles stick together near the stirrer axis and cannot be separated from each other as the dynamic forces acting on them are below a critical threshold.
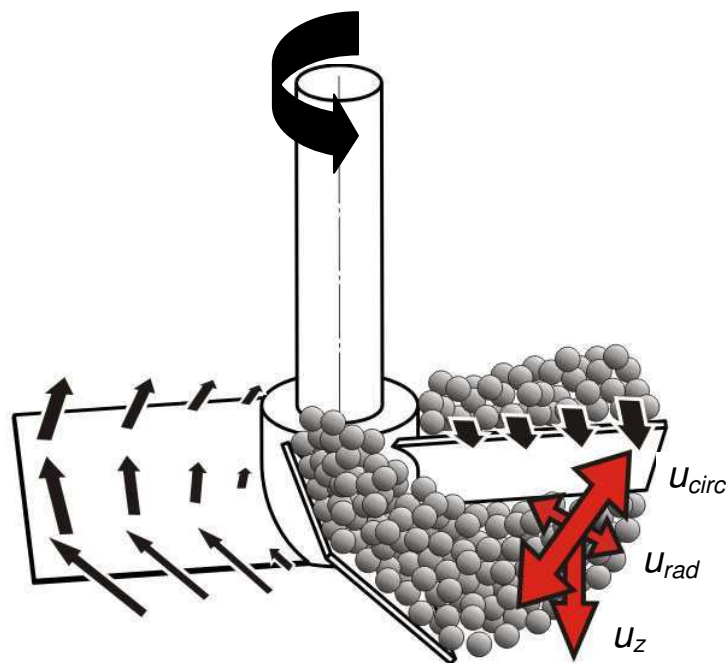
Figure 7.14: Schematic representation of mean velocity and fluctuating velocity field for wet granular flow.

To illustrate the details of wet granular flow in the bladed mixer, we have included a schematic representation of the mean velocity field and the mean fluctuating velocities in Figure 7.14. The relative flow direction of the particles over the blade is indicated on the left-hand-side blade of this figure. The flow direction at the lower blade edge (near the bottom of the mixer) is directed outside (see also Figure 7.8, top left). As the particles move over the blade, they change their velocity direction such that they move radially inward when they arrive at the top blade edge. Then, the particles drop down from the upper blade edge (right-hand-side blade of Figure 7.14). This results in a strong velocity fluctuation in the axial direction (u_z), weaker velocity fluctuations in circumferential direction (u_{circ}) and small velocity fluctuations in the radial direction (u_{rad}).

ii) Shear Rate Distribution

Next we concentrated on the shear rate distribution in wet and dry granular flow. Therefore, we have calculated the velocity gradient in the x- and y-direction from a horizontal cross section and evaluated the shear rate in this plane, which is defined as:

$$\dot{\gamma}^* = \sqrt{2\left(\frac{\partial U^*}{\partial x^*}\right)^2 + 2\left(\frac{\partial V^*}{\partial y^*}\right)^2 + \left(\frac{\partial U^*}{\partial y^*} + \frac{\partial V^*}{\partial x^*}\right)^2} \qquad (7.15)$$

In Eqn. 7.15 U* and V* refer to the mean velocities normalized with the tip speed, and x* and y* are the coordinates normalized with the mixer diameter.
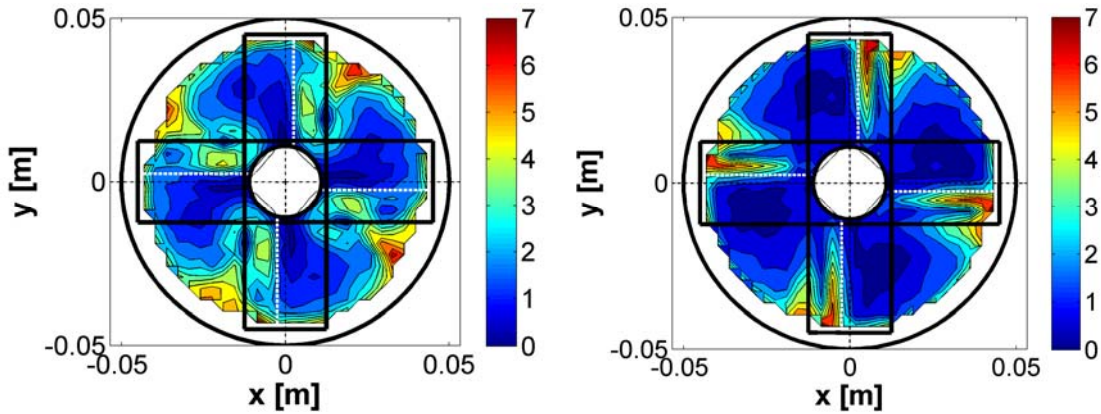
Figure 7.15: Normalized shear rate distribution in a wet (left) and dry (right) powder bed (60 rpm).

The calculated shear rate in Eqn. 7.15 is based on a continuum description of the granular bed. The shear rate is the second invariant (i.e., the "magnitude") of the symmetric part of the velocity gradient tensor[62] and reduces to Eqn. 7.15 in the case of a plane flow, i.e., the horizontal cross section we are interested in. The results of this analysis are shown in Figure

7.15, which shows that in wet granular flow (Figure 7.15, left), the shear rate is much more diffuse. It is again argued, that this is due to the capillary forces that affect the mean flow field (as can be seen from Figure 7.8, the mean blade-relative velocity is higher for wet particles) and consequently also the shear rate. Instead, in dry granular flow (Figure 7.15, right) the shear rate is localized - especially in front of the blade - and very small.

7.3.3 Mean Squared Velocity Fluctuations vs. Granular Temperature

In the sections above the mean velocity fluctuations have been used to analyze the diffusive mixing process in the system. However, we also want to introduce a metric used in many other studies, i.e., the granular temperature. In order to compute the granular temperature, first the variance $\vec{s^2}$ of the velocity in each spatial direction is taken as a metric for particle velocity fluctuations. It is calculated from the locally-averaged blade-relative velocity $\vec{u}_{av,rel}$ and the blade-relative particle velocity $\vec{v}_{P,\mathrm{Re}l}$ in the blade-fixed coordinate system (see Appendix E on how the blade-relative velocities in the blade-fixed coordinate system have been calculated):

$$\vec{s^2}_{i,j} = \frac{1}{N_{i,j}} \cdot \sum_{P \in p_{i,j}} \left(\vec{u}_{av,rel,i,j} - \vec{v}_{P,\mathrm{Re}l,i,j} \right)^2 \tag{7.16}$$

Here, $N_{i,j}$ and $p_{i,j}$ denote the total number of particles, as well as the list of particles in the grid cell, respectively. The variance $\vec{s^2}_{i,j}$ characterizes the degree of uncoordinated particle motion in a certain grid cell at a certain point in time. Similarly to the mean velocity fluctuation, we define a scalar quantity S^2 that quantifies the mean level of (time-averaged) particle velocity fluctuations:

$$S^2_{i,j} = \left(\overline{s^2_{x,i,j}} + \overline{s^2_{y,i,j}} + \overline{s^2_{z,i,j}} \right) / 3, \tag{7.17}$$

Note that $\overline{s^2_{x,i,j}}$, $\overline{s^2_{y,i,j}}$ and $\overline{s^2_{z,i,j}}$ denote the Cartesian components of the time-averaged particle velocity fluctuations as per Eqn. 7.16. The quantity defined in Eqn. 7.17 is often called "granular temperature" in literature[63] and can be used to quantify diffusive mixing.[64]

Figure 7.16a illustrates the local averaging process for obtaining locally averaged velocity information on the Eulerian grid. Figure 7.16b highlights the different metrics. The granular temperature S^2 is the time-average of the variance of the particle velocity. Thus, if particles

move coordinated, i.e., by formation of agglomerates, the local variance goes to zero, as well as the granular temperature, even if the velocity of the agglomerate is fluctuating. In our study "agglomerate" refers to a particle ensemble in which particles stick together and are weakly held together by capillary forces. In contrast, the mean velocity fluctuations are a time-average of velocity fluctuations with respect to the average velocity in a grid cell. Thus, the mean velocity fluctuation will not go to zero in case of a fluctuating agglomerate. Consequently, these two metrics can be used to analyze the effect of cohesion on the formation of agglomerates.
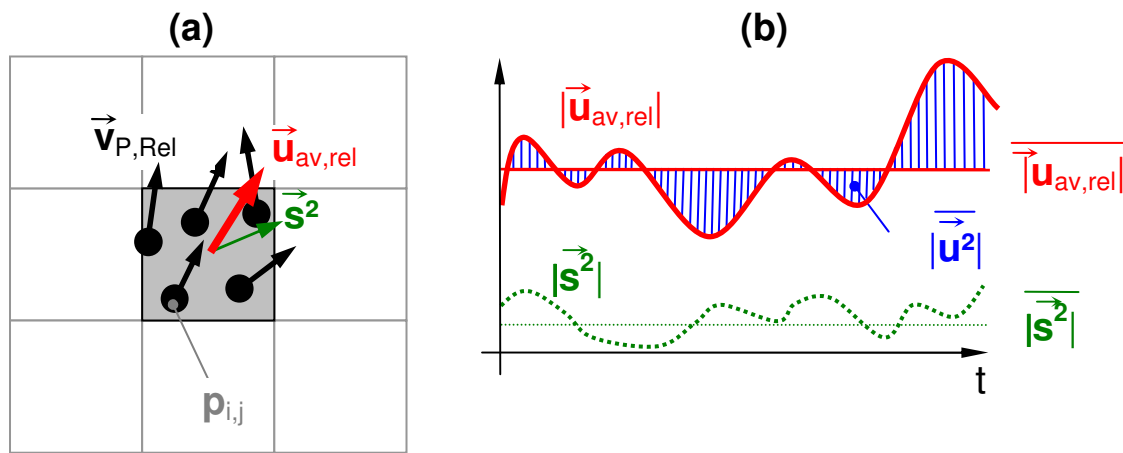
Figure 7.16: (a) Sketch of the averaging process and (b) time profiles of the locally-averaged and time-averaged quantities (vertical lines indicate the norm of a vector, horizontal lines indicate time-averaged quantities; the spatial indices i and j have been omitted for clarity).

In contrast to the mean velocity fluctuations, the granular temperature is strongly grid-size dependent (with "grid" we here refer to the Eulerian grid). This is because the granular temperature is calculated from the variance of particle velocities in a certain grid cell. When the grid cell gets smaller, also the number of particles in this cell decreases until we have a situation with only one particle left. Then, the granular temperature becomes zero, because the locally-averaged velocity $\vec{u}_{av,rel}$ is equal to the particle velocity $\vec{v}_{P,Rel}$. If we, however, increase the size of the grid cell (e.g., to cover the complete particle bed), the granular temperature would be at a maximum. This is because we would have a locally-averaged velocity very close to zero and the differences of the particle velocities to this small locally-averaged velocity would be at a maximum. In contrast, the mean velocity fluctuations do not depend strongly on the grid size, because we use locally-averaged particle velocities. Thus, if we decrease the size of the grid cells, we still obtain a good estimate of the locally-averaged particle velocity as we take into account surrounding particle information when using the ‚griddata' function in

Matlab®. If we increase the grid cells size, however, we reduce the spatial resolution of our analysis, i.e., we obtain a more smeared-out result. Hence, when performing an analysis of the mean velocity fluctuations, a fine grid with a size in the order of the diameter of the particles should be used. This yields grid-independent mean and fluctuating quantities as shown in the next paragraph.
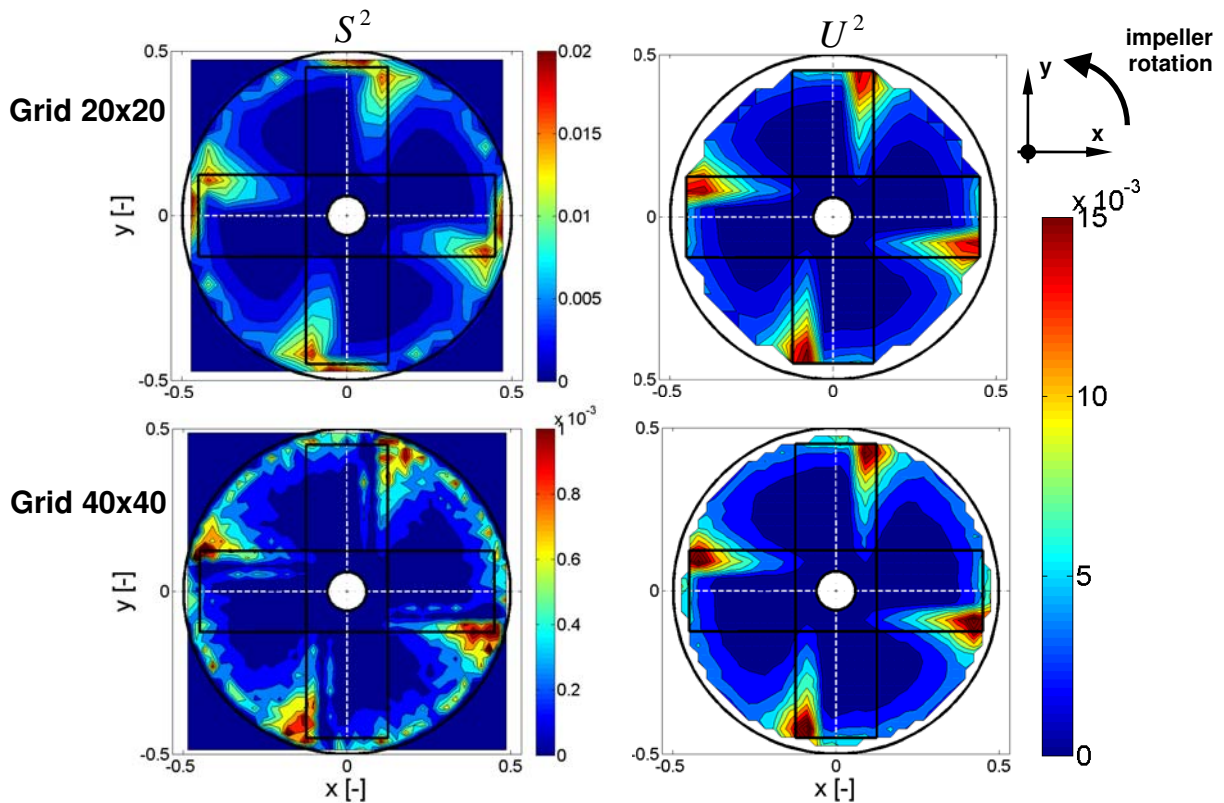
Figure 7.17: Comparison of the mean particle velocity fluctuation S² (left) and the mean velocity fluctuation U² (right) obtained with two different grids (dry particles, 60 rpm, velocity fluctuations have been normalized with the tip speed squared, d_P = 3 mm).

The differences between the mean particle velocity fluctuation S² and the mean velocity fluctuation U^2 are shown in Figure 7.17. For this analysis we have used the simulation results with 3 mm particles. To highlight the effect of the size of the grid cells, we have used two grids (20x20 grid elements for the coarse grid, as well as 40x40 grid elements for the fine grid). The 20x20 grid translates into a spacing of 5 mm, i.e., 1.67-times the particle diameter, whereas the 40x40 grid has a grid spacing of only 0.83-times the particle diameter. As can be seen, both grids give very similar results for the mean velocity fluctuation U^2 (see Figure 7.17 right). This is because when calculating U^2, we use already locally-averaged information, which is rather grid insensitive. However, differences in the mean particle velocity fluctuation S² are clearly visible between the two grid levels (see Figure 7.17 left). The differences are due to the

fact, that on the finer grid the particles are already bigger than the grid spacing. Hence, not every grid element holds a particle, and the calculation of the variance of the particle velocities in elements holding no particle is impossible. This leads to a drastically lower level of mean particle velocities (see Figure 7.17 left). Thus, care has to be taken when calculating the mean particle velocity fluctuation S², and the dependency of the results with respect to the grid size should be checked.

Interestingly, both quantities, i.e., U^2 and S², show similar quantitative features with respect to their spatial distribution. Thus, these quantities seem to be connected and one can expect a local maximum of S² in case U^2 is large in this area and vice versa, except for the formation of agglomerates, as shown in the next section.

7.3.4 Influence of the Particle Size
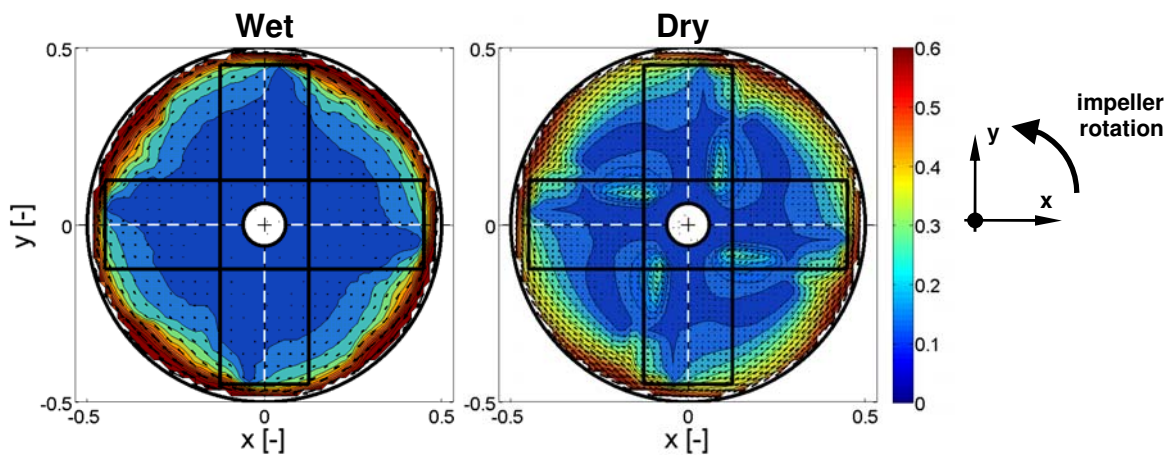
Figure 7.18: Influence of moisture content on the mean velocity for small particles (d_p=1 mm)

Particle size has an important impact on particle dynamics simulations for two reasons: (i) the particle size may impact the mean and especially the fluctuating flow pattern, and (ii) smaller particles strongly increase simulation time. In order to quantify the first effect, we have performed simulations with a particle diameter of 1 mm. For the wet simulations, we have scaled the surface tension in order to keep the Bond number constant.

The results for the time-averaged blade-relative flow field are shown in Figure 7.18 for a particle diameter of 1 mm for wet and dry particles. Most obviously, there are differences in the flow fields near the wall: due to capillary forces the small particles have a significantly higher blade-relative velocity in this region. Dry particles do not stick to the wall; hence, they

can move over the blade more easily, leading to lower blade-relative velocities. In contrast to the wall-near region, the wet particle's blade-relative velocity goes to zero away from the wall, while dry particles show a significant time-averaged motion. This is due to the association of the particles with the blades caused by increased sticking to the stirrer.

The most pronounced effect of particle size seems to exist for wet particles (see the results for d_p = 3 mm and d_p = 1 mm in Figure 7.18 right). We therefore conclude that selecting a small enough particle diameter for simulations involving cohesive particles is critical even for predicting time-averaged flow fields.
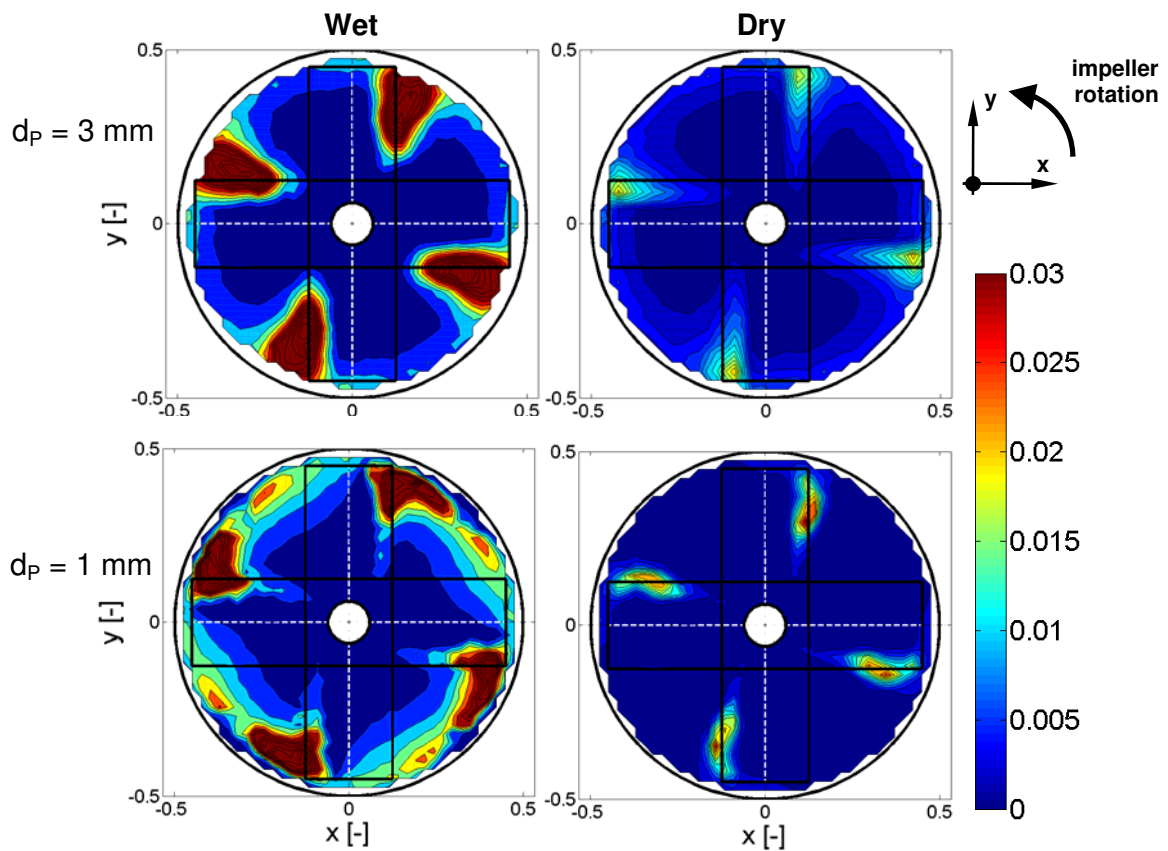
Figure 7.19: Influence of particle size on the mean velocity fluctuations U^2 for dry and wet granular matter (60 rpm, velocity fluctuations have been normalized with the tip speed squared).

Figure 7.19 and Figure 7.20 depict the impact of particle size on the mean velocity fluctuations (Figure 7.19) and the granular temperature (Figure 7.20). Clearly, mean velocity fluctuations U^2 (Figure 7.19) also depend on particle size to some extent. However, the mean velocity fluctuations increase with moisture content for both particle sizes. Hence, mean velocity fluctuation levels increase when particles are wet, no matter what size the particles are. Also, we observe that for the small wet particles the velocity fluctuations are less localized behind

the blade but are also present between the impeller blades. This also reflects the change in flow pattern that was already visible in the time-averaged velocity fields.
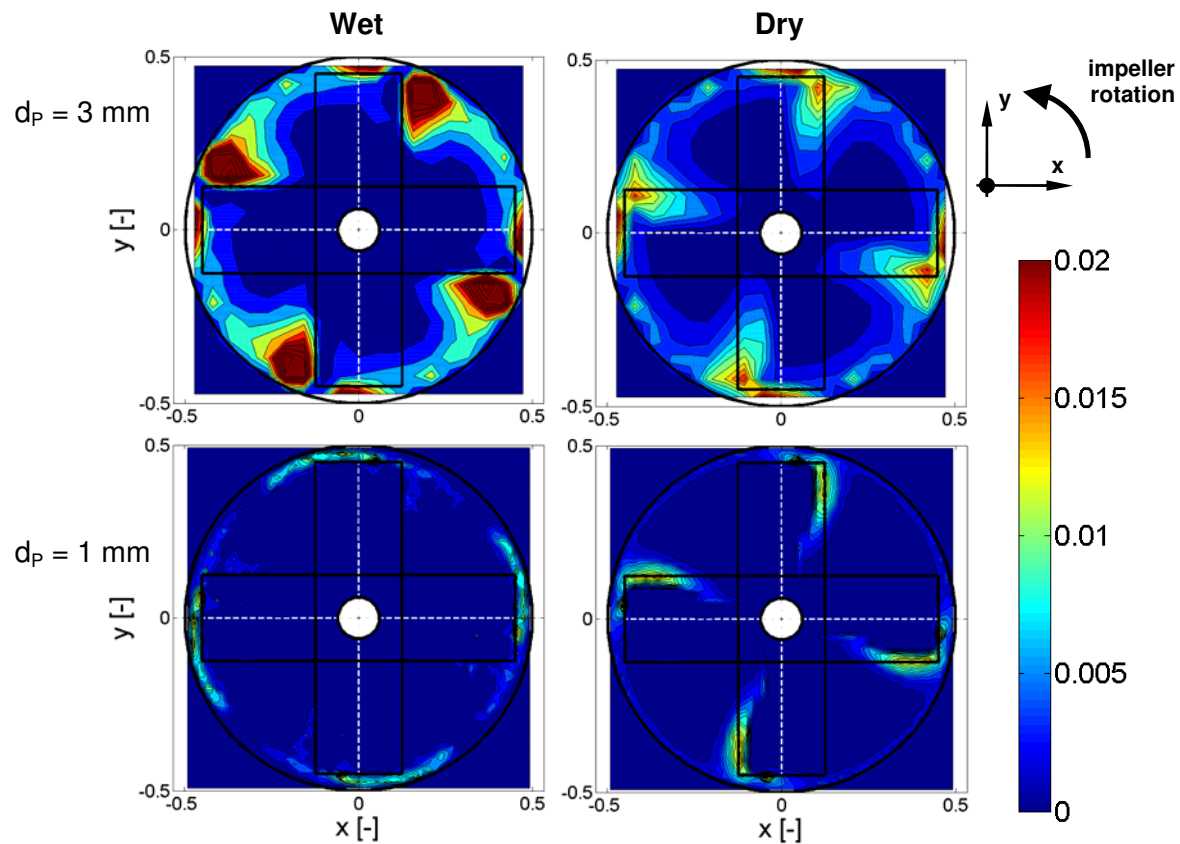
Figure 7.20: Influence of particle size on the granular temperature S² for dry and wet granular matter (60 rpm, coarse particles: grid 20x20, fine particles: grid 60x60, velocity fluctuations have been normalized with the tip speed squared).

The source of this higher fluctuation velocity is probably caused by the formation of agglomerates between the blades. For example, such agglomerates have been observed in bladed mixers by Lekhal et.[9] (refer to their Figure 6). Based on a visual inspection of the simulation results we assume that these agglomerates are pushed by the impeller. We hypothesize that these agglomerates break down from time-to-time, leading to relatively large velocity fluctuations. Further work focusing on the formation and breakage of agglomerates is needed to verify this. In summary, the trends of the mean velocity fluctuation with the moisture content are consistent for both particle sizes.

A similar increase in granular temperature S² is observed for the large particles in Figure 7.20, as fluctuations are increased by the presence of moisture. We speculate that in the case of these larger particles wall effects, and the formation of stronger force chains due to the capillary forces (similar to increasing friction coefficients), play a dominant role, leading to the

transfer of more energy into the granular flow. In this figure we have displayed the results for the large particles on the coarse grid, i.e., the 20x20 grid and for the fine particles on a 60x60 grid. This is to keep the ratio of grid spacing and particle size constant as the mean particle velocity fluctuations depend on this ratio.

The interesting finding is, that for the smaller particles with d_p = 1 mm, the fluctuation level decreases with increasing moisture content. This clearly indicates agglomerate formation in the case of smaller particles, i.e., particles moving with an identical velocity in the particle bed. Hence, agglomerate formation in wet granular matter is confirmed by this analysis. Only in the small gap between the rotor and the stator, particle velocity fluctuations slightly increase in the case of wet particles. This is because capillary bridges force particles to stick to the surface of the impeller and the cylindrical wall. This leads to higher differences in the velocity of individual particles in this region, i.e., a higher value for S^2.

In summary, we have shown that for smaller particles the two metrics, i.e., the mean velocity fluctuations and the granular temperature show opposing trends. This is due to the formation of agglomerates. Thus, a suitable metric has to be chosen for analyzing the effects of interest. However, more work is needed to fully elucidate the impact of stirrer and mixer geometry and other variables on these effects.

7.3.5 Influence of the Coefficient of Restitution

We have investigated the effect of the coefficient of normal restitution (COR_n) on the simulation results. Specifically, we compared the velocity profiles, as well as the radial distribution of the mean velocity fluctuation for COR_n = 0.98 and COR_n = 0.7. The results for a stirrer speed of 30 rpm and dry particles are shown in Figure 7.21. As can be seen, a smaller COR_n, i.e., more damping during the particle contacts, leads to lower velocity fluctuations (-13% of the peak mean velocity fluctuations). Similar observations have been made for higher stirrer speeds and wet particles, where the reduction in mean velocity fluctuations is slightly more significant (-24% and -19% respectively). However, the qualitative behavior for different COR_n is very similar and we hence have performed the subsequent analysis with the results for COR_n = 0.98 only.
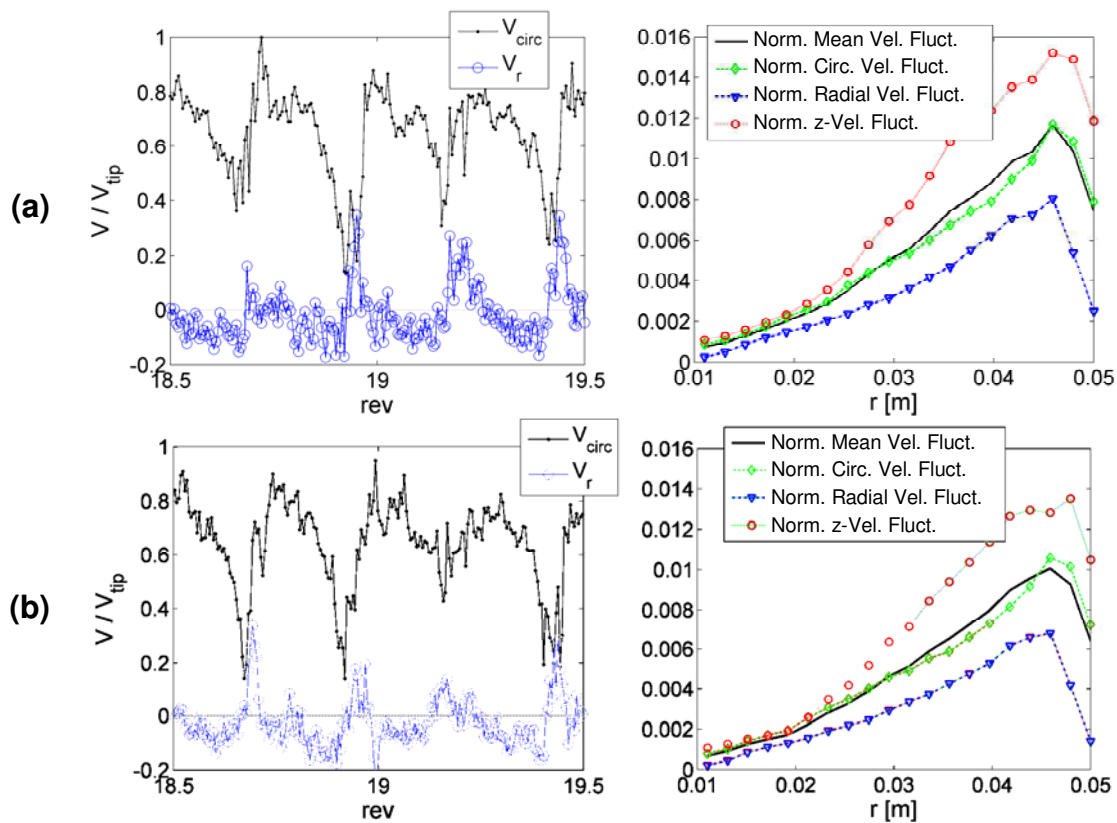
Figure 7.21: Influence of the coefficient of normal restitution on velocity profiles and distribution of the mean velocity fluctuations (30 rpm, dry particles, a: $COR_n = 0.98$, b: $COR_n = 0.7$, velocity fluctuations have been normalized with the tip speed squared).

7.3.6 Quantification of Mixing Mechanisms from Particle Distribution

Mechanisms of solids mixing were first introduced by Lacey.[11] He proposed three mixing regimes, similar to fluid mixing: Convective, diffusive and shear mixing. In the convective mixing regime, mixing occurs due to the transfer of large groups of particles. Diffusive mixing is governed by the small-scale random movement of individual particles. The third mechanism, shear mixing, is caused by the relative movement of a region of particles due to external shearing or convection. Mixing due to shear and convection cannot be distinguished in dense granular systems[12] and are referred to in this work as convective-shear mixing. Ottino and Khakhar[65] provided a comprehensive review on mixing and segregation of powders. Among different segregation mechanisms, size and density segregation has been addressed by most researchers (e.g., Kuo et al.[3] or Conway et al.[8]). Also, the influences of cohesion[9,22] and shape[66] have been investigated.

With respect to the mixing mechanisms, diffusive mixing occurs in analogy to molecular diffusion in fluids: it is caused by the random movements of individual particles, i.e., it occurs

at the micro scale. The major difference between fluids and granular systems is, that in the former diffusion happens spontaneously,[67] while in granular systems the particles must be energized, e.g., by means of agitation. In contrast, convective mixing is caused by the motion of larger particle groups on the macroscopic level.

To quantify the influence of the individual mixing mechanisms, two principal possibilities exist: (i) direct observation of the movement of the particles and (ii) analyzing the time evolution of the spatial distribution of one component in the mixture.

i)   Analysis of Particle Movement

In case data of the movement of particles are directly available, diffusive mixing can be quantified directly by analyzing velocity fluctuations or diffusive displacements. In the former method the concept of granular temperature is introduced in which the kinetic energy of the particles is interpreted as temperature $T_{gran} = \langle \vec{u}_{fluct} \cdot \vec{u}_{fluct} \rangle / 3$ (see for example Rosato et al.[64]). The brackets in this definition refer to the temporal average of the fluctuating velocity vector $\vec{u}_{fluct} \cdot \vec{u}_{fluct}$ can be calculated locally from the instantaneous particle velocities and the mean velocity. The square root of the granular temperature can then be taken as a proportionality factor for the granular self-diffusion coefficient (see Savage and Dai[68]), i.e., a metric for granular mixing.

A second method for quantifying the self-diffusion coefficient dates back to Albert Einstein and has been detailed in the paper of Hsiau and Yang.[69] In this method individual tracer particles have to be tracked and the bulk displacement due to the mean velocity of the powder bed has to be subtracted. The self-diffusive displacements are then computed as a function of time and the self-diffusion coefficient can be evaluated. We have already analyzed velocity fluctuations in the particle bed and hence focus only on the second approach, i.e., the analysis of the spatial distribution of one component in the mixture.

ii)   Analysis of the Spatial Distribution of One Component

To quantify global mixing, the Lacey Index M can be used to quantify the mixing state in the mixer[18]

$$M = \frac{\sigma_0^{\ 2} - \sigma^2}{\sigma_0^{\ 2} - \sigma_r^{\ 2}},$$

(7.18)

where σ_0^2 is the variance of an initial, typically fully segregated state, σ_r^2 is the variance of a perfectly mixed state and σ^2 is the actual variance obtained with the mixing.

σ_0^2 and σ_r^2 are given by[18]

$$\sigma_0^2 = p \cdot q \text{, and} \tag{7.19}$$

$$\sigma_r^2 = \frac{p \cdot q}{N} \text{,} \tag{7.20}$$

where p and q are the proportions of the two components in the mixture, and N is the total number of particles in the mixture.

The actual variance σ^2 has to be determined from different samples in the powder bed. It is important to keep the sample volume constant, i.e., the number or volume of particles, as it has a strong influence on the resulting variance. For example, it was demonstrated that the sample size has a significant influence on M, especially if the mixing mechanism is convective-shear mixing.[67] Hence, it is possible to obtain a qualitative picture of the relative importance of diffusive and convective-shear mixing by plotting the time evolution of the mixing index M versus the sample size.

Other techniques that can be found in the literature to quantify the mixing mechanisms include (a) correlation techniques in which auto-correlograms are generated for different correlation steps, (b) fractal analysis, i.e., by using Richardson plots, (c) phase space techniques where the mixture is analyzed using phase portraits, and (d) spectral density techniques, where Fast Fourier Transformation (FFT) is used to characterize the concentration variation in terms of a power spectrum. All these methods have as input information the time evolution of the distribution of one component in the mixture.

For the evaluation of the mixing intensity in a cylindrical control volume a sampling scheme has been developed. Sampling locations were organized in a pattern of concentric circles and are shown in Figure 7.22. Each sample location consists of a cylindrical volume with a diameter of 8 mm and ranges from the bottom of the mixer to the powder bed surface. Samples containing an identical number of randomly-selected particles (the total number of particles was chosen as $N_p = 18$) were taken from each sample location. Care was taken, that the sample locations did not overlap to avoid multiple counting of particles.
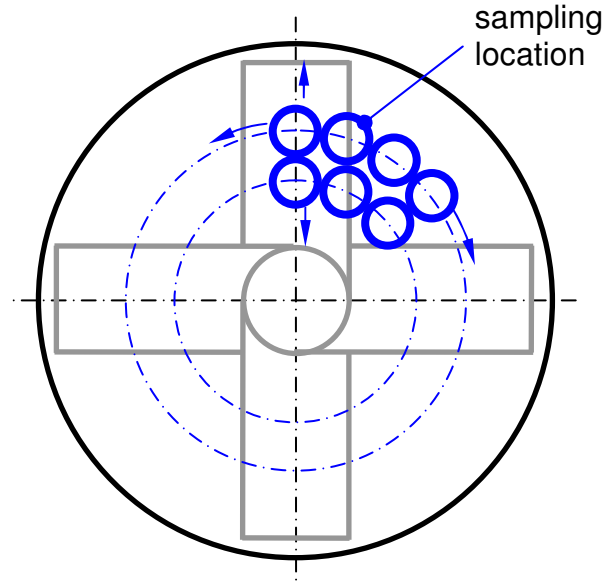
Figure 7.22: Sampling locations for the quantification of mixing.

Each sample has then been characterized by its content of marked particles x_{ij}, where the index i refers to the circumferential direction and j to the radial direction.

$$x_{ij} = \frac{N_{pm,ij}}{N_p} \, . \tag{7.21}$$

In Eqn. 7.21, $N_{pm,ij}$ is the number of marked particles in the sample in region ij. To enable a local characterization of mixing, the variance of x_{ij} was first analyzed using samples with constant index j, i.e., at the same radius,

$$\sigma_j^{\,2} = \frac{1}{N_{s,j}} \sum_i \left(x_{ij} - \bar{x}_j \right)^2 . \tag{7.22}$$

Here $N_{s,j}$ is the number of samples that were taken at the radius with index j. Thus, σ_j characterizes how good the powder bed is mixed in the circumferential direction. Furthermore, the total variation in the mixer was analyzed using Eqn. 7.23

$$\sigma^2 = \frac{1}{N_s} \sum_j \sum_i \left(x_{ij} - \bar{x} \right)^2 . \tag{7.23}$$

Here $\bar{x}$ is the mean content of marked particles in all samples and N_s is the number of all samples.

To get an impression of the time evolution of mixing, the local distribution of marked particles x_{ij} is shown in Figure 7.23. Initially, the marked particles are fully segregated, i.e., one

half of the particle bed in the mixer was marked. As can be seen from the upper left representation of x_{ij} in Figure 7.23, mixing occurs mainly near the outer diameter of the impeller. In contrast, near the axis of the impeller, mixing is very slow and even after 2 revolutions the region with a high and low content of marked particles are clearly visible.
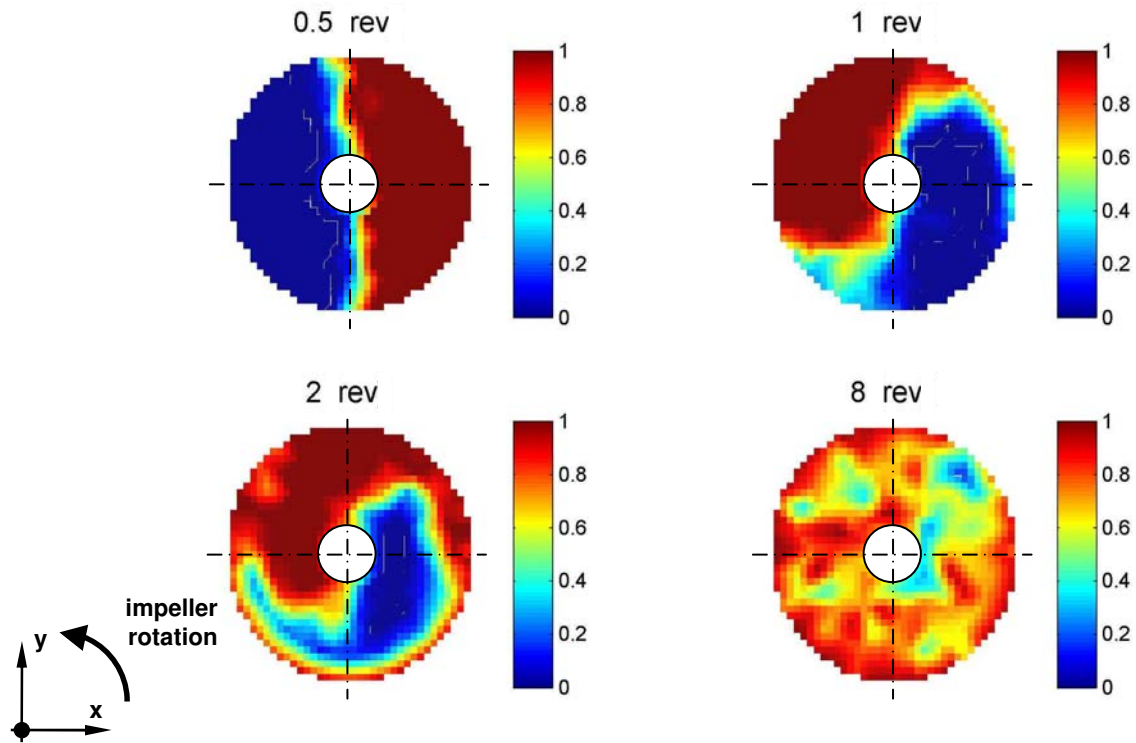
Figure 7.23: Evolution of the local marked particle content x_{ij} for dry particles after different revolutions of the impeller (60 rpm).

To get a more quantitative result for this mixing behavior, we plot the variance σ_j^2 in circumferential direction as a function of the radial distance in Figure 7.24. As can be seen, in all cases the variance is reduced first at the outer radius of the mixer, i.e., at r = 0.050 m. Comparing the simulation results involving wet and dry particles, we observe that the variance between r = 0.035 m and r = 0.050 m for the wet particle bed decreases rapidly. This is caused by the significantly stronger mean velocity for this type of granular matter. For the higher stirrer speed of 60 rpm this leads to a better mixing over the whole radial distance, whereas for the stirrer speed of 30 rpm the variance after 4 revolutions is lower for the dry particle bed than for the one with wet particles.

Finally we concentrate on the characterization of the overall mixing behavior in the bladed mixer. Therefore, we have plotted the mixing index M (see Figure 7.25) as a function of the

impeller revolutions. This mixing index characterizes global mixing in the system. Note, that this index cannot characterize mixing on a level below the sample size (in our work $N_p = 18$).
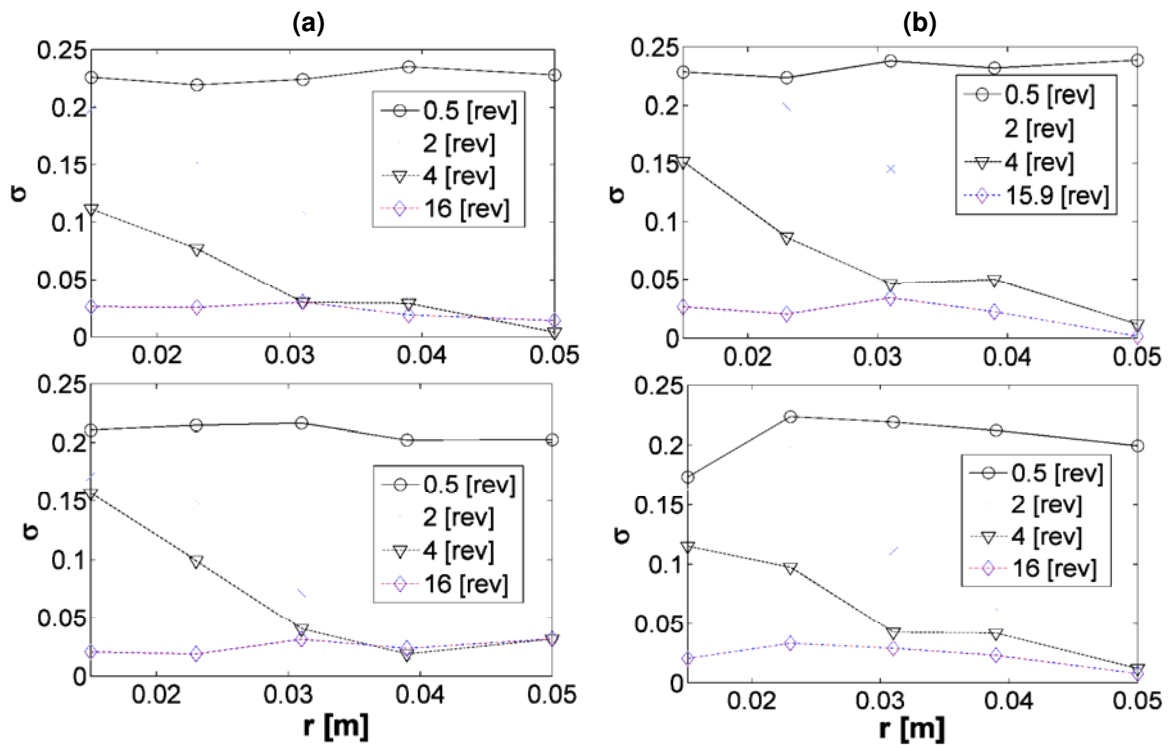
Figure 7.24: Variance σ_j in circumferential direction for (a) wet and (b) dry particles at different stirrer speeds (top: 60 rpm, bottom: 30 rpm).
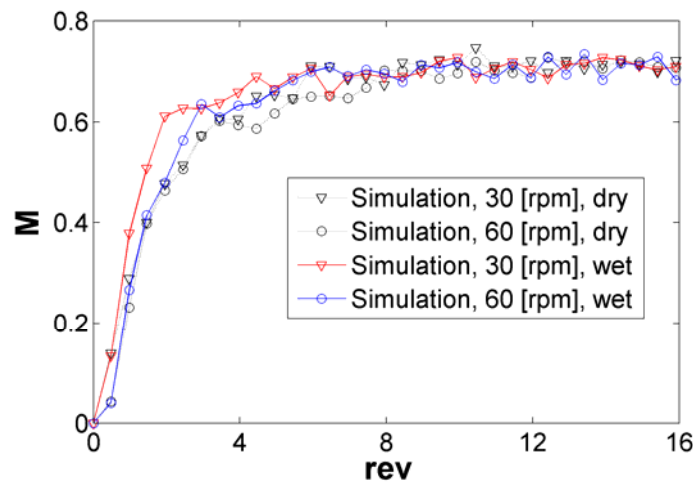
Figure 7.25: Time evolution of the mixing index M over the number of revolutions for different stirrer speeds and wet and dry particles.

Thus, it does not reflect mixing on a particle level in our work. Clearly, the mixing kinetics, as well as the final mixing quality, do not depend much on the stirrer speed or the moisture content of the granular matter. This can be explained by the fact, that for the mixing index M

the mixing near the impeller is considered, which is rather insensitive to both stirrer speed and moisture content.

This fact can be seen in Figure 7.12, where only small differences in the normalized mean velocity fluctuations are visible up to a radial distance of approximately 0.025 m. Clearly, even if mixing is much faster near the wall for wet particles, it has a relatively small effect on overall mixing performance for the analysis we have carried out. This may be due to the relatively small number of particles per sample and the coarse particles used in the simulation. However, as demonstrated in the previous chapter, significant differences in local mixing rates do exist.

7.4 Summary and Conclusions

In this work we studied the differences between wet and dry granular flow and mixing in a bladed mixer. Simulations of wet granular flow were performed using a granular Bond number of $Bo_g = 71$, i.e., under very cohesive conditions. The discrete element method (DEM) was used and our simulation parameters were chosen to mimic glass beads with a diameter of 3 mm and 1 mm in a mixer with a diameter of 100 mm. The simulation results are consistent with experimental data. Furthermore, the comparison of simulations with experiments showed that the qualitative behavior of a real dry powder bed can be captured with significantly larger particles in the simulation. However, the fast oscillating motions and small-scale fluctuations of small particles observed experimentally on the surface of the powder bed experiments could not be reproduced. Thus, we conclude that this study is restricted to macroscopic mixing only. For a wet powder bed, it is also necessary to use much smaller beads to simulate the physics of cohesive granular flow.

The flow of wet granular matter in a bladed mixer can be summarized as follows:

- Wet granular matter results in significantly increased blade relative velocities and a change in flow pattern behind the blade is observed.

- Heap formation is strongly increased in the case when particles are wet.

- The ratio between particle and impeller diameter plays a certain role for the fluctuating velocity fields. This is especially true for wet particles where it strongly impacts the variance of particle velocities. Specifically, the variance is suppressed by cohesive forces, if particles are sufficiently small and far away from the surrounding walls.

- Wet particles lead to an increased mean velocity fluctuation in a bladed mixer. However, the particle motion becomes more coherent, which is reflected by a lower variance in the particle velocities in a certain Eulerian grid cell. Heap formation is possibly one cause for this increased velocity fluctuation in wet granular matter. The observed coherent particle motion, i.e., the lower variance in the particles velocities in wet granular matter, is caused by liquid bridge forces.

- Mean velocity fluctuations are highly anisotropic in wet granular matter due to the damping action of capillary forces. However, the integral influence of capillary forces is complicated with respect to mixing. For example, the change in flow pattern behind the blade suggests that capillary forces transmit more shear forces into the powder bed. To some extent this will enhance velocity fluctuations in the radial and circumferential directions. However, a clear quantitative analysis of this contribution is yet to be performed and will be addressed in future work.

- The analysis of the mixing quality based on the distribution of marked particles reflects the differences in the fluctuation velocities between wet and dry particles. Hence, we can confirm the well known fact that higher velocity fluctuations lead to increased diffusive mixing. Our simulations show that this is also true for wet granular matter, i.e., mixing is improved in wet granular beds. However, the velocity variances on a particle level decrease if the particle size is chosen sufficiently small in the simulation. This means that mixing on a particle level may decrease when the powder bed is wet. Mixing on a particle level can be characterized by the granular temperature (see Figure 7.20), which supports this finding.

- Mixing for wet particles in bladed mixers is much more heterogeneous compared to dry particles. This is due to the fact that a certain threshold is necessary to break agglomerates of wet particles apart. For example, there exist regions near the impeller where localized forces are too low to break up agglomerates and particles essentially rotate with the impeller. Once the threshold is overcome, particles have significant higher kinetic energy. This effect results in stronger velocity fluctuations and a strongly nonlinear distribution of mean velocity fluctuations in the radial direction.

The results of our work provide insight into wet granular flows, which are of high relevance to the powder processing industry. Although some important conclusions can be drawn, this is

possibly only a small step towards the full understanding of agitated flows of wet granular matter. Future work will include the investigation of different bed heights on heap formation and mixing.

7.5 Abbreviations

COR   Coefficient of Restitution

DEM   Discrete Element Method

FFT   Fast Fourier Transformation

KTGF   Kinetic Theory of Granular Flow

PETP   Positron Emission Particle Tracking

PIV   Particle Image Velocimetry

TDM   Time-Driven Method

7.6 Nomenclature

A, B, C   fit function

Bo   Bond number

Ca   capillary number

c_n normal damping coefficient [kg/s]

c_t tangential damping coefficient [kg/s]

d_p particle diameter [m]

d_{capill} particle diameter for capillary forces [m]

$\vec{F}_{b,i}$ body force acting on particle i [N]

$\vec{F}_{c,ij}$ contact force between particle i and j [N]

$\vec{F}_{c,n,ij}$ normal contact force between particle i and j [N]

$\vec{F}_{c,t,ij}$ tangential contact force between particle i and j [N]

$\vec{F}_{coh,ij}$ cohesive force between particle i and j [N]

$f_1 - f_4$	fit function
g	gravitational acceleration [m/s²]
i, j	indices
k_n	normal stiffness coefficient [N/m]
M	mixing index
M_r	moment due to rolling friction [Nm]
$\vec{M}_{total,i}$	total moment acting on particle i [Nm]
N	total number of particles in the mixture
N_p	number of particles per sample
$N_{pm,ij}$	number of marked particles in region ij
$N_{s,j}$	number of samples taken at the radius with index j
N_s	total number of samples taken
p	proportion of component 1 in the mixture
$p_{i,j}$	list of particles in the grid cell ij
q	proportion of component 2 in the mixture
r_i	radius of particle i [m]
$r_{1,2}$	harmonic mean radius of particle 1 and 2 [m]
S	half distance between two particles or distance between particle and wall [m]
$S*$	dimensionless half distance between two particles or dimensionless distance between particle and wall
S_{rup}	rupture distance [m]
S^2	mean particle velocity fluctuation [m²/s²]
$\vec{s^2}$	particle velocity fluctuation [m²/s²]
t	time [s]

t_P	characteristic time for particle motion in the mixer [s]
T_{gran}	granular temperature [m²/s²]
U_c	characteristic velocity of the collision [m/s]
U^2	mean velocity fluctuation [m²/s²]
U^*, V^*	normalized mean velocities in x- and y-direction
$\vec{u}_{av}$	locally-averaged absolute velocity [m/s]
$\vec{u}_{av,rel}$	locally-averaged relative velocity [m/s]
$\overline{u^2}$	time-averaged velocity fluctuations [m²/s²]
u, v, w	fluctuating velocities in Cartesian coordinates [m/s]
u_{circ}, u_{rad}, u_z	fluctuating velocities in cylindrical coordinates [m/s]
V_L	liquid volume per capillary bridge [m³]
V^*	dimensionless liquid volume per capillary bridge [$V_L/(d_p/2)^3$]
V_{circ}	velocity component in circumferential direction [m/s]
V_r	velocity component in radial direction [m/s]
V_{tip}	blade tip velocity [m/s]
$\vec{v}_P$	velocity vector of a particle [m/s]
x_{ij}	content of marked particles in region ij
$\overline{x}_j$	mean content of marked particles at the radius with index j
$\overline{x}$	mean content of marked particles
x^*, y^*	normalized coordinates

Greek letters

$\delta_{n,ij}$	normal overlap between particle i and j [m]
$\delta_{t,ij}$	tangential overlap between particle i and j [m]
η	dynamic viscosity [Pa·s]

ϕ	contact angle
$\dot{\vec{\theta}}_i$	vector of the angular velocity for particle i [1/s]
$\dot{\gamma}^*$	normalized shear rate
γ_s	surface tension [N/m]
μ	sliding friction coefficient
μ_r	rolling friction coefficient
ρ_p	particle density [kg/m³]
σ^2	variance
σ_0^2	variance of the fully segregated state
σ_j^2	variance in circumferential direction at the radius with index j
σ_r^2	variance of the perfectly mixed state

7.7 References

(1) Shinbrot T, Alexander A, Muzzio FJ. Spontaneous chaotic granular mixing. Nature. 1999; 397:675-678.

(2) Seville JPK, Ingram A, Parker DJ. Probing processes using positrons. Chemical Engineering Research & Design. 2005; 83:788-793.

(3) Kuo HP, Knight PC, Parker DJ, Tsuji Y, Adams MJ, Seville JPK. The influence of DEM simulation parameters on the particle behaviour in a V-mixer. Chem Eng Sci. 2002; 57:3621-3638.

(4) Stewart RL, Bridgwater J, Zhou YC, Yu AB. Simulated and measured flow of granules in a bladed mixer - a detailed comparison. Chem Eng Sci. 2001; 56:5457-5471.

(5) Jain N, Ottino JM, Lueptow RM. Effect of interstitial fluid on a granular flowing layer. Journal of Fluid Mechanics. 2004; 508:23-44.

(6) Liu GQ, Li SQ, Zhao XL, Yao Q. Experimental studies of particle flow dynamics in a two-dimensional spouted bed. Chem Eng Sci. 2008; 63:1131-1141.

(7) Zeilstra C, Collignon JG, Van der Hoef MA, Deen NG, Kuipers JAM. Experimental and numerical study of wall-induced granular convection. Powder Technology. 2008; 184:166-176.

(8)   Conway SL, Lekhal A, Khinast JG, Glasser BJ. Granular flow and segregation in a four-bladed mixer. Chem Eng Sci. 2005; 60:7091-7107.

(9)   Lekhal A, Conway SL, Glasser BJ, Khinast JG. Characterization of granular flow of wet solids in a bladed mixer. AIChE Journal. 2006; 52:2757-2766.

(10)   Darelius A, Lennartsson E, Rasmuson A, Bjorn IN, Folestad S. Measurement of the velocity field and frictional properties of wet masses in a high shear mixer. Chem Eng Sci. 2007; 62:2366-2374.

(11)   Lacey PMC. Developments in the Theory of Particle Mixing. Journal of Applied Chemistry. 1954; 4:257-268.

(12)   Bridgwater J. Fundamental Powder Mixing Mechanisms. Powder Technology. 1976; 15:215-236.

(13)   Ansari MA, Stepanek F. Design of granule structure: Computational methods and experimental realization. AIChE Journal. 2006; 52:3762-3774.

(14)   Grof Z, Lawrence CJ, Stepanek F. Computer simulation of evolving capillary bridges in granular media. Granular Matter. 2008; 10:93-103.

(15)   Grof Z, Lawrence CJ, Stepanek F. The strength of liquid bridges in random granular materials. Journal of Colloid and Interface Science. 2008; 319:182-192.

(16)   Stepanek F, Rajniak P. Droplet morphologies on particles with macroscopic surface roughness. Langmuir. 2006; 22:917-923.

(17)   Zhou YC, Yu AB, Stewart RL, Bridgwater J. Microdynamic analysis of the particle flow in a cylindrical bladed mixer. Chemical Engineering Science. 2004; 59:1343-1364.

(18)   Zhou YC, Yu AB, Bridgwater J. Segregation of binary mixture of particles in a bladed mixer. Journal of Chemical Technology and Biotechnology. 2003; 78:187-193.

(19)   Remy B, Khinast JG, Glasser BJ. Discrete Element Simulation of Free Flowing Grains in a Four-Bladed Mixer. AIChE Journal. 2009; 55:2035-2048.

(20)   Zhu HP, Zhou ZY, Yang RY, Yu AB. Discrete particle simulation of particulate systems: Theoretical developments. Chem Eng Sci. 2007; 62:3378-3396.

(21)   Faqih AMN, Mehrotra A, Hammond SV, Muzzio FJ. Effect of moisture and magnesium stearate concentration on flow properties of cohesive granular materials. International Journal of Pharmaceutics. 2007; 336:338-345.

(22)   Chaudhuri B, Mehrotra A, Muzzio FJ, Tomassone MS. Cohesive effects in powder mixing in a tumbling blender. Powder Technology. 2006; 165:105-114.

(23)   Mehrotra A, Llusa M, Faqih A, Levin M, Muzzio FJ. Influence of shear intensity and total shear on properties of blends and tablets of lactose and cellulose lubricated with magnesium stearate. International Journal of Pharmaceutics. 2007; 336:284-291.

(24) Mehrotra A, Chaudhuri B, Faqih A, Tomassone MS, Muzzio FJ. A modeling approach for understanding effects of powder flow properties on tablet weight variability. Powder Technology. 2008; 188:295-300.

(25) Bertrand F, Leclaire LA, Levecque G. DEM-based models for the mixing of granular materials. Chem Eng Sci. 2005; 60:2517-2531.

(26) Remy B, Glasser BJ, Khinast JG. The Effect of Mixer Properties and Fill Level on Granular Flow in a Bladed Mixer. AIChE Journal. 2010; 56:336-353.

(27) Lemieux M, Bertrand F, Chaouki J, Gosselin P. Comparative study of the mixing of free-flowing particles in a V-blender and a bin-blender. Chem Eng Sci. 2007; 62:1783-1802.

(28) Arratia PE, Duong NH, Muzzio FJ, Godbole P, Reynolds S. A study of the mixing and segregation mechanisms in the Bohle Tote blender via DEM simulations. Powder Technology. 2006; 164:50-57.

(29) Goldschmidt MJV, Weijers GGC, Boerefijn R, Kuipers JAM. Discrete element modelling of fluidised bed spray granulation. Powder Technology. 2003; 138:39-45.

(30) Pandey P, Song YX, Kayihan F, Turton R. Simulation of particle movement in a pan coating device using discrete element modeling and its comparison with video-imaging experiments. Powder Technology. 2006; 161:79-88.

(31) Li HM, McCarthy JJ. Phase diagrams for cohesive particle mixing and segregation. Physical Review e. 2005; 71:021305.

(32) Di Renzo A, Di Maio FP. Comparison of contact-force models for the simulation of collisions in DEM-based granular flow codes. Chem Eng Sci. 2004; 59:525-541.

(33) Li X, Chu X, Sheng DC. A saturated discrete particle model and characteristic-based SPH method in granular materials. International Journal for Numerical Methods in Engineering. 2007; 72:858-882.

(34) McCarthy JJ. Micro-modeling of cohesive mixing processes. Powder Technology. 2003; 138:63-67.

(35) Lian GP, Thornton C, Adams MJ. A Theoretical-Study of the Liquid Bridge Forces Between 2 Rigid Spherical Bodies. Journal of Colloid and Interface Science. 1993; 161:138-147.

(36) Rognon PG, Roux JN, Naaim M, Chevoir F. Dense flows of cohesive granular materials. Journal of Fluid Mechanics. 2008; 596:21-47.

(37) Soulie F, El Youssoufi MS, Cherblanc F, Saix C. Capillary cohesion and mechanical strength of polydisperse granular materials. European Physical Journal e. 2006; 21:349-357.

(38)   Kohonen MM, Geromichalos D, Scheel M, Schier C, Herminghaus S. On capillary bridges in wet granular materials. Physica A-Statistical Mechanics and Its Applications. 2004; 339:7-15.

(39)   Fournier Z, Geromichalos D, Herminghaus S, Kohonen MM, Mugele F, Scheel M et al. Mechanical properties of wet granular materials. Journal of Physics-Condensed Matter. 2005; 17:S477-S502.

(40)   Herminghaus S. Dynamics of wet granular matter. Advances in Physics. 2005; 54:221-261.

(41)   Schulz M, Schulz BM, Herminghaus S. Shear-induced solid-fluid transition in a wet granular medium. Physical Review e. 2003; 67:052301.

(42)   Scheel M, Seemann R, Brinkmann M, Di Michiel M, Sheppard A, Breidenbach B et al. Morphological clues to wet granular pile stability. Nature Materials. 2008; 7:189-193.

(43)   Mikami T, Kamiya H, Horio M. Numerical simulation of cohesive powder behavior in a fluidized bed. Chem Eng Sci. 1998; 53:1927-1940.

(44)   Yang SC, Hsiau SS. The simulation of powders with liquid bridges in a 2D vibrated bed. Chem Eng Sci. 2001; 56:6837-6849.

(45)   Yang RY, Zou RP, Yu AB. Numerical study of the packing of wet coarse uniform spheres. AIChE Journal. 2003; 49:1656-1666.

(46)   Willett CD, Adams MJ, Johnson SA, Seville JPK. Capillary bridges between two spherical bodies. Langmuir. 2000; 16:9396-9405.

(47)   Soulie F, Cherblanc F, El Youssoufi MS, Saix C. Influence of liquid bridges on the mechanical behaviour of polydisperse granular materials. International Journal for Numerical and Analytical Methods in Geomechanics. 2006; 30:213-228.

(48)   Luding S. Cohesive, frictional powders: contact models for tension. Granular Matter. 2008; 10:235-246.

(49)   Gantt JA, Gatzke EP. High-shear granulation modeling using a discrete element simulation approach. Powder Technology. 2005; 156:195-212.

(50)   Liu LX, Litster JD, Iveson SM, Ennis BJ. Coalescence of deformable granules in wet granulation processes. AIChE Journal. 2000; 46:529-539.

(51)   Gantt JA, Cameron IT, Litster JD, Gatzke EP. Determination of coalescence kernels for high-shear granulation using DEM simulations. Powder Technology. 2006; 170:53-63.

(52)   Gantt JA, Gatzke EP. Kinetic theory of granular flow limitations for modeling high-shear mixing. Industrial & Engineering Chemistry Research. 2006; 45:6721-6727.

(53)   Talu I, Tardos GI, Khan MI. Computer simulation of wet granulation. Powder Technology. 2000; 110:59-75.

(54)   Khan MI, Tardos GI. Stability of wet agglomerates in granular shear flows. Journal of Fluid Mechanics. 1997; 347:347-368.

(55)   Richefeu V, El Youssoufi MS, Radjai F. Shear strength properties of wet granular materials. Physical Review e. 2006; 73:051304.

(56)   Richefeu V, Radjai F, El Youssoufi MS. Stress transmission in wet granular materials. European Physical Journal e. 2006; 21:359-369.

(57)   Dziugys A, Peters B. An approach to simulate the motion of spherical and non-spherical fuel particles in combustion chambers. Granular Matter. 2001; 3:231-265.

(58)   Cundall PA, Strack ODL. Discrete Numerical-Model for Granular Assemblies. Geotechnique. 1979; 29:47-65.

(59)   EDEM 1.3 User Guide. 2007.

(60)   Mitarai N, Nori F. Wet granular materials. Advances in Physics. 2006; 55:1-45.

(61)   Nase ST, Vargas WL, Abatan AA, McCarthy JJ. Discrete characterization tools for cohesive granular material. Powder Technology. 2001; 116:214-223.

(62)   Bird RB, Stewart WE, Lightfood EN. Transport Phenomena. New York: John Wiley & Sons, Inc., 2002.

(63)   Goldhirsch I. Introduction to granular temperature. Powder Technology. 2008; 182:130-136.

(64)   Rosato AD, Lan YD, Richman MW. On the calculation of self-diffusion in vertically agitated granular beds. Powder Technology. 2008; 182:228-231.

(65)   Ottino JM, Khakhar DV. Mixing and segregation of granular materials. Annual Review of Fluid Mechanics. 2000; 32:55-91.

(66)   Abreu CRA, Tavares FW, Castier M. Influence of particle shape on the packing and on the segregation of spherocylinders via Monte Carlo simulations. Powder Technology. 2003; 134:167-180.

(67)   Gyenis J. Assessment of mixing mechanism on the basis of concentration pattern. Chemical Engineering and Processing. 1999; 38:665-674.

(68)   Savage SB, Dai R. Studies of Granular Shear Flows - Wall Slip Velocities, Layering and Self-Diffusion. Mechanics of Materials. 1993; 16:225-238.

(69)   Hsiau SS, Yang SC. Numerical simulation of self-diffusion and mixing in a vibrated granular bed with the cohesive effect of liquid bridges. Chem Eng Sci. 2003; 58:339-351.

"Measure properties, don't perform rituals."

(Roland Clift, 1994)

8

Investigation of Granular Flow and Mixing due to a Blade[*]

The granular flow over a blade is of significant importance for mixing operations in various industries. However, there is no profound understanding of this flow and the effect of various process parameters (i.e., bed height, blade angle, etc.) on mixing performance is currently unknown. We performed well-defined experiments in a bladed mixer, as well as in a two-dimensional setup, to study the flow field and mixing performance of single and multiple blades. The goal was to provide validation data for particle flow simulations using spherical glass beads of various sizes. Also, the influence of process parameters (e.g., bed height, moisture content, blade angle) on the behavior of the particle bed was investigated.

We found that the bed height had the most pronounced effect on the velocity profile on top of the particle bed. When the particle size was increased in the bladed mixer, blocking effects, as well as large gaps between individual particles, lead to a change in the instantaneous flow field. The addition of moisture to the particles led to agglomerate formation and significant changes in the velocity distribution. This agglomerate formation is also of paramount importance for the mixing in the granular bed. Specifically, we observed an increased mixing rate when moisture is added to a particle bed.

8.1 Introduction

Granular flow and mixing is an important process in many industries including the pharmaceutical industry, food technology, biotechnology, etc. Due to the frequent application of so-called convective mixers with rotating internals (e.g., bladed mixers, ploughshare mixers, etc.), the dense particle flow over knives or blades is of great industrial interest. Often, the bulk solid is cohesive, i.e., significant particle-particle interaction forces exist, complicating the flow behavior.

The rate of mixing or de-mixing, i.e., segregation, connected to this flow is essential for the outcome of a mixing process involving this type of mixing. There is, however, no simple theory for these problems, since dense granular flows in general cannot be predicted by simple mathematical models. This is due to the complex rheological behavior of bulk solids that has been extensively analyzed using numerical,[1-8] as well as experimental[9-14] tools in the past. The recent review of Forterre and Pouliquen[15] reflects most of the theoretical work undertaken within the last 50 years. While large collections of data on steady granular flows are available,[16] a single model for the rheology of dense granular matter is definitely not available. It is even more demanding to predict mixing and segregation processes. Clearly, currently there is no quantitative mathematical model available to design mixing instruments based on a desired final mixing quality and the properties of the particles to be mixed.

The recent experimental studies[11,13] of our group on dense granular flows relied on high-speed imaging of the particle bed at the free surface or near transparent walls in agitated devices. This work was based on rather undefined, non-spherical particles and only a few key parameters have been studied. Still it is difficult to measure the flow within the particle bed, i.e., below the free surface or far away from the wall, due to limited optical access. Consequently, researchers started using positron emission particle tracking (PEPT) to investigate granular flows (see, e.g., Parker et al.[17] or Parker and Fan[18]). However, this is a very costly and time-intensive method, and the information gained is still limited (e.g., it is impossible to record the instantaneous flow field in a complete cross section of a granular bed using this method).

Lekhal et al.[13] investigated the granular flow in a cylindrical vessel stirred by a bladed mixer. They used non-spherical sand particles with a relatively narrow size distribution. The flow

field was measured at the free surface and the transparent side wall of the vessel using a PIV system. However, the work of Lekhal et al. leaves some open questions concerning

- the effect of the particle size and shape,

- the exact spatial distribution of the granular temperature in circumferential direction,

- the effect of the stirrer speed,

- the exact geometrical configuration of the system (e.g., stirrer position, blade angle, etc.)[a]

- the quantification of mixing, as well as

- the three-dimensional characterization of the flow field

in wet granular matter.
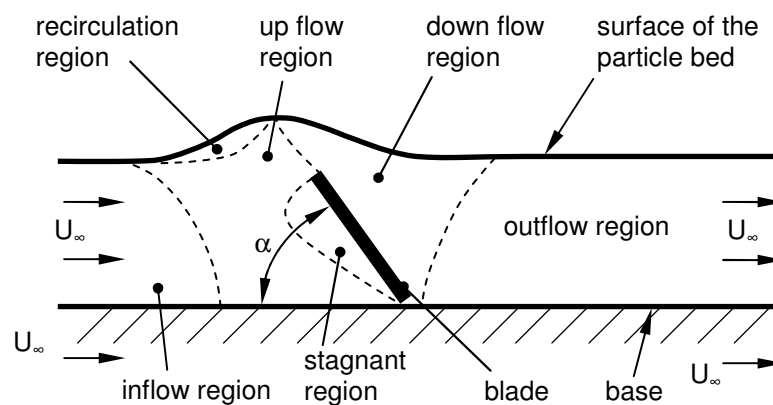
Figure 8.1: Schematic representation of the flow regions in the flow over a blade. The blade is stationary while the material is flowing over it (adapted from Bagster and Bridgewater[19]).

For the study of granular flows over obstacles, Bagster and Bridgwater[19] developed a specialized experimental setup. They used an open moving box apparatus, while the obstacle (blade) was standing still. The dimensions of the box were 600 x 300 x 100 [mm] and images were taken to analyze the flow. A blade was mounted on a long rod and placed inside the box. The front and the rear face were made of glass. For box movements they mounted a variable speed electric motor. Glass beads with a mean diameter of 2.13 +/- 0.09 [mm] were taken as material for their experiments. The effect of blade immersion, blade angle α (if $\alpha < 90$ the blade arrangement is called "obtuse", and when $\alpha > 90$ the blade arrangement is "acute"), box

---

[a] Recent work of Remy et al.[3,5] provides some computational results on the effect the blade geometry.

velocity and blade material were studied in this early work. This work also included investigations of the force that acts on the blade, a topic that was already investigated in their previous publication.[20,21] Although the work of Bagster and Bridgewater gave qualitative predictions of the flow field (e.g., see Figure 8.1 for some typical features of the flow over a single blade) and some integral parameters (e.g., the force acting on the blade or a transport rate), it could not quantify all details of the granular flow. This is especially true for the down flow region of the blade, i.e., the region where mixing is thought to occur primarily. Also, there was no effort by Bagster and Bridgewater to quantify mixing or segregation rates in this setup.

8.2 Goals

The primarily goal of this study is to supply detailed experimental data on granular mixing in a bladed mixer. These data should be suitable as validation data for numerical studies on granular flows in agitated mixers. Consequently, it is of great importance to (i) investigate the effect of particle size, as well as to (ii) use spherical particles with a narrow particle size distribution. Thus, the experimental setup was also driven by some numerical aspects. Specifically, we investigated the effect of

- the particle size,

- the moisture content,

- the filling height,

- the stirrer speed, as well as

- the stirrer position.

in a cylindrical, four-bladed mixer under a well-defined atmosphere. A granular PIV system was used to measure the velocity distribution of the particle bed. In order to assess the details of granular mixing occurring in this bladed mixer, an additional experimental setup was build. This setup consisted of a two-dimensional granular flow system for investigating the granular flow and mixing over a single blade. In this system the effect of

- the particle size,

- the filling height,

- the blade speed,

- the blade position, as well as the

- blade geometry (i.e., the blade angle)

on the granular flow was measured using a granular PIV system. Finally, the goal was to study the effect of particle size and moisture content on the mixing performance of a single blade submerged in a particle bed.

8.3 Experimental Method

8.3.1 Particle Characterization

For our experiments we used spherical glass beads. These beads were used due to their defined size and shape, their frequent use in granular flow experiments,[22,23] their inability to absorb liquids, as well as the possibility to measure their (true) static friction coefficient. Glass beads of various sizes were characterized with a focus on their mechanical properties. As we have used manually-colored glass beads in our mixing experiments (see Chapter 8.4.3), we have also investigated the effect of the applied coating (i.e., a thin polymer film).
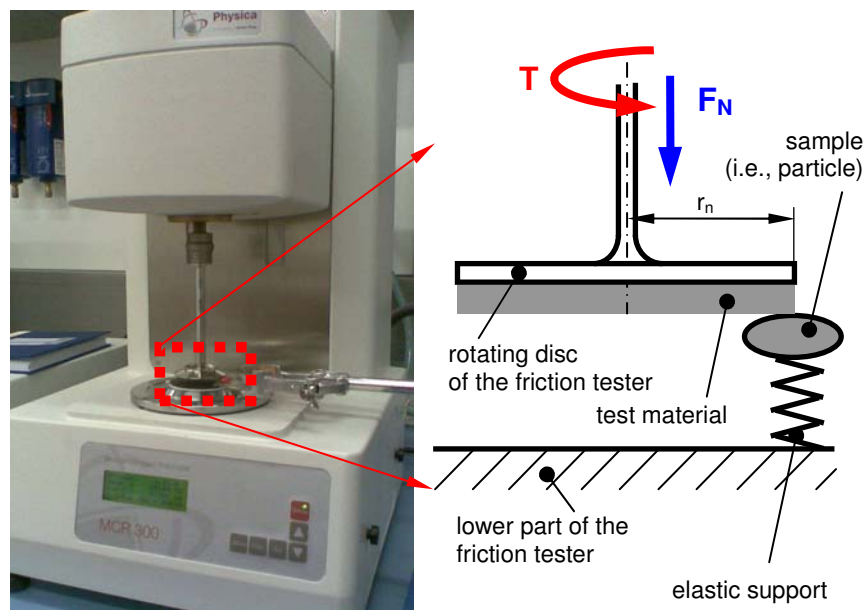
Figure 8.2: "Pin-on-Disc" setup for the measurement of the friction coefficient between a particle and a rotating disc.

i) Pin-on-Disc Friction Tester

A simple friction tester, similar to the standardized Pin-on-Disc apparatus,[24] has been set up. The principle of this tester is to measure the torque on a rotating disc that is in contact with a

sample under a predefined normal force F_N. From the torque T the friction force can be easily calculated (i.e., by division with the normal distance r_n) and hence the friction coefficient can be directly calculated from:

$$\mu = \frac{T/r_n}{F_N} \, .$$

(8.1)

An Anton Paar "MCR 300" rheometer has been modified (see Figure 8.2) to perform the friction experiments. The upper disc of the 50mm parallel disc assembly of this rheometer was used as the rotating disc of the friction tester. The material to be tested has been mounted on the rotating disc. An elastic support for the sample (i.e., a glass particle) has been constructed and fitted to the lower part of the rheometer. The sample has been placed on the elastic support and the rotating disc of the rheometer has been placed on the particle. The normal force F_N has been controlled by the rheometer by adjusting the vertical position of the rotating disc. The rotating disc has then set into motion. The torque, as well as the normal force was recorded with a sampling frequency of 10 Hz for 100 [s] (i.e., a total of 1000 measurements were recorded). The friction coefficient has then been calculated from the measured torque and normal force, as well as the normal distance r_n to the contact point. Typical results of the measured friction coefficient are shown in Figure 8.3 for two different (mean) normal forces F_N.
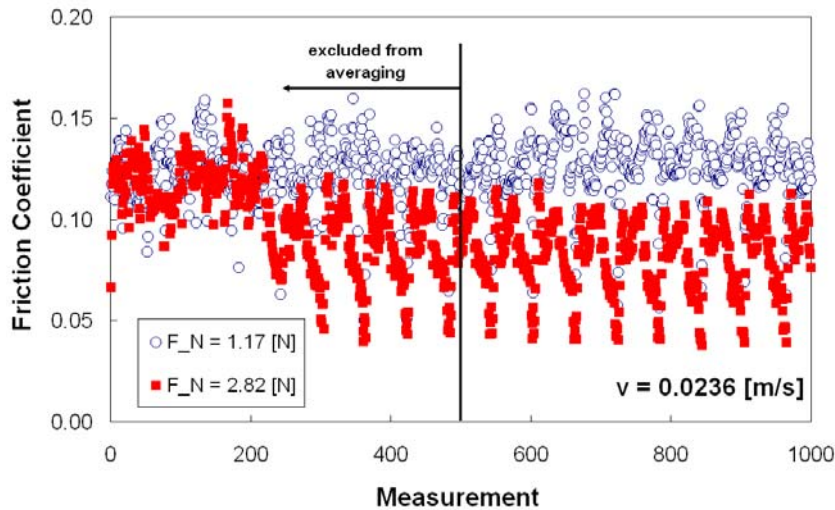
Figure 8.3: Typical results of a friction coefficient measurement for two different normal forces (4 mm glass bead vs. glass plate, blue circles: 1.17 [N] normal load, red rectangles: 2.82 [N] normal load).

As can be seen, the friction coefficient is fluctuating due to the stick-slip transition at the contact point. Also, it takes approximately 300 measurements (i.e., 30 s) until this fluctuation

becomes stable. It is speculated that this is due to the alignment of the two surfaces in contact with each other (the sample could not be fixed completely rigid on the elastic support leading to a small displacement of the sample when the disc started to rotate). Thus, averaging was done over the last 500 measurements (see Figure 8.3). Various material combinations have been tested in the Pin-on-Disc friction tester and the results are shown in Figure 8.4. "Glass" hereby refers to glass beads (whether 4 or 6 mm in diameter, there were only insignificant differences depending on the particle size) and a conventional glass plate. "PMMA" refers to the transparent polymer wall used in the single-blade system (refer to Chapter 8.3.3iii) for details on this system), and "Steel" refers to a turned sample of stainless steel (material grade 1.4301). "freshCoat" and "usedCoat" refer to glass coated with a thin polymeric film from a conventional paint before and after the use in the experiments, respectively.
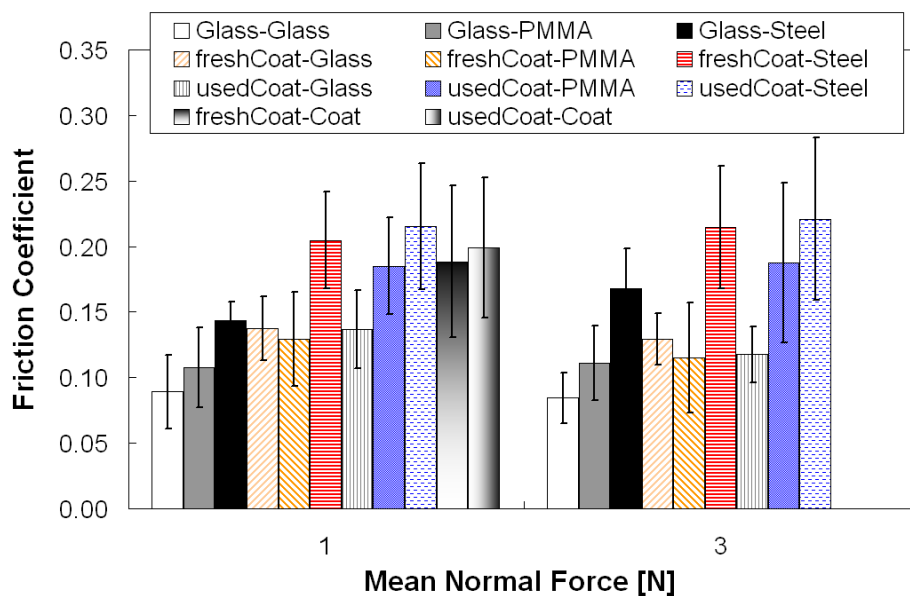
Figure 8.4: Results for the mean friction coefficient for different material partners (results are classified in a low, i.e., 1 [N], and a high, i.e., 3 [N], mean normal force, error bars indicate the total standard deviation, measurements were repeated at least five times).

As can be seen, the friction coefficient between two glass surfaces is significantly lower compared to a glass-steel contact. In case of a glass-PMMA contact, the friction coefficient is insignificantly higher compared to the glass-glass contact. Coating significantly increases the friction coefficient. There are only small differences between fresh and used coated glass beads, except for the coat-PMMA contact. For this contact, small differences in the coating have obviously a larger effect on the friction coefficient. Higher normal forces slightly increase the friction coefficient. The trends for the material partners are, however, exactly the same.

Consequently, we have used primarily untreated glass beads in the flow experiments. Coated beads were only used in our final mixing experiments. For these experiments, all beads have been coated to avoid differences in the friction coefficient between beads of different colors. As the differences between the friction coefficients of the glass-glass and glass-PMMA contact were small, PMMA was accepted as a transparent material for the single blade experiments described in Chapter 8.4.2 and 8.4.3.

ii)   Normal Coefficient of Restitution

The normal coefficient of restitution COR_n (or short COR) is defined as the ratio between the post- and pre-collisional velocities of an impact between two bodies:

$$COR_n = \frac{v_{post}}{v_{pre}} \ . \tag{8.2}$$
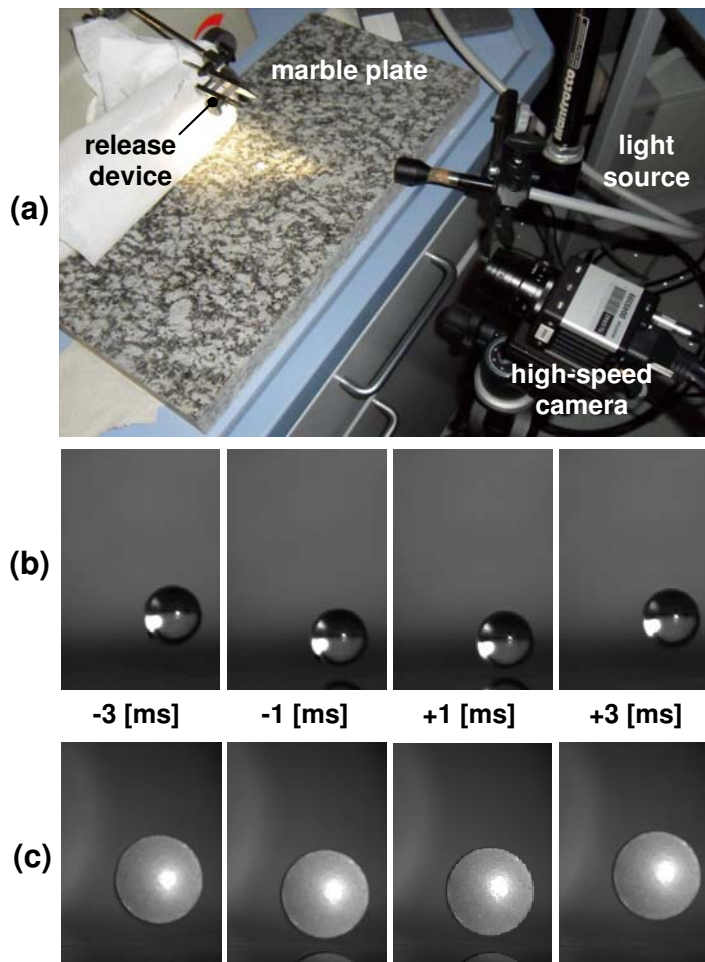
Figure 8.5: (a) Setup for the determination of the coefficient of restitution, (b) image sequence for different times relative to the impact for 6 mm glass particles (untreated, polished surface), as well as (c) for a spherical-cap tablet.

In can be measured in various ways (even *in situ*, as shown in Wu et al.[25]) and some simple techniques are reviewed by Farkas and Ramsier,[26] as well as by Cross.[27] For the method proposed by Farkas and Ramsier,[26] a massive horizontal surface with appropriate hardness, as well as a stop watch is needed. The principle is based on measuring the total time t_{total} it takes a spherical particle to stop bouncing. Hence, it has to be ensured that the particle has to be spherical, without spin at the release and does not collide with vertical walls during the experiments. Using this method, it has to be assumed that the COR_n is independent of the impact velocity. The method proposed by Cross[27] uses two horizontal laser beams to measure the pre- and post-collisional velocities on a ceramic disc mounted on a brass rod. A small correction has to be made to the velocity measurements to take the effect of gravitational acceleration into account.

Parameter	6 mm glass beads (untreated)	4 mm glass beads (untreated)	4 mm glass beads (coated)	500 mg tablet (coated)
Mean Value	0.96	0.92	0.90	0.74
Std. Deviation Run-Run	0.018	0.042	0.031	0.040
Std. Deviation Particle-Particle	0.011	0.023	0.031	0.028
Total Std. Deviation	0.021	0.048	0.044	0.049

Table 8.1: Results for the coefficient of restitution for different particle types.

To determine the coefficient of restitution, a simple experimental setup was built to measure the pre- and post-collisional velocities during a particle-wall impact (see Figure 8.5a). The collision partner (i.e., the wall) was made up of a very hard and smooth material (i.e., marble) in order to exclude wall damping from the experimental results. The particles were dropped from a release device located approximately 75 mm above the marble plate to give an impact velocity of approximately 1.2 m/s. The particle velocities were extracted directly from the image sequences (see Figure 8.5b and c) obtained via a "MotionScope M3" high-speed camera operating at 1 kHz acquisition rate (for the specifications of the camera refer to Chapter 8.3.3i)). To obtain statistically meaningful data, the experiments have been done in triplicate and at least three individual particles were used for each material. The mean values, as well as the standard deviations (split into a run-to-run, as well as into a particle-to-particle standard deviation) for the COR are displayed in Table 8.1. Various glass beads and coated spherical-

cap tablets (the latter has been included for comparison purposes; the 500 mg-tablets consisted of a placebo-mixture and were supplied by DRIAM Anlagenbau GmbH, Eriskirch, Germany) were investigated. Experimental difficulties arose due to the slightly non-spherical 4 mm glass beads, giving slightly lower values for the COR compared to the perfectly round, polished 6 mm glass beads. This resulted in larger run-to-run variations (see third line from the top in Table 8.1) for the 4 mm glass beads. However, the differences were small and within the total standard deviation observed during our experiments. Coating the 4 mm glass beads had only an insignificant effect on the COR (compare column three and four in Table 8.1). The experiments for the coated 500 mg tablet required a precisely controlled release of the particle to ensure that the particle hit the marble surface with the cylindrical part (see Figure 8.5c). These difficulties also lead to the highest total standard deviation of 0.049.

iii) Powder Rheology

Dynamic and static powder rheometers are increasingly used to characterize powder mixtures. Recent examples include the work of Patel et al.[28] for the characterization of dry and wet powders during granulation, the prediction of powder permeability using multivariate models including the unconfined yield strength,[29] or to correlate powder rheology to the ability to fill a die.[22]

Various quantities (e.g., the unconfined yield stress, internal and effective friction angle, cohesion, the basic flowability energy, permeability, consolidation indices, etc.) can be measured using advanced powder rheometers. However, this information typically has to be correlated to the final product quality (e.g., mixing uniformity, granule properties in case of wet granulation, tablet weight standard deviation) using black-box models. While there is the possibility to interpret these correlations, there is no mechanistic model that can take use of all the measured data.

We have measured the rheological behavior of dry and wet glass beads of various sizes (0.15-0.25, 1.5-1.85 and 4.0 mm glass beads). The wet glass beads were produced by mixing 0,993 mL water with 248.2 g of particles. Assuming a solid density of 2,500 kg/m³, the moisture content of the particle bed was 1.0 Vol% m^3_{liq}/m^3_{solid}. Tests of 0.15-0.25 mm dry and wet glass beads were performed and are summarized in Table 8.2. A "FT4" powder rheometer (consisting basically of a blade and a cylindrical glass vessel with a nominal diameter of 50 mm, provided by Freeman Technology, Worcestershire, UK) was used for that purpose.

Parameter	0.15-0.25 mm glass beads (dry)	0.15-0.25 mm glass beads (1.0 Vol.%)
Bulk density [kg/m³]	1,470	1,150
Specific energy [mJ/g]	2.96	6.13
Basic flowability energy [mJ]	1,225	1,442
Stability index	0.977	1.01

Table 8.2: Results of the stability testing of dry and wet glass beads.

The tested parameters were (i) the specific energy (SE, i.e., a measure for particle flow in a "loose" state under the action of shear), (ii) the basic flowability energy (BFE, i.e., a measure for particle flow in a relatively high-stress, compacting flow situation), as well as the stability index (SI, i.e., the ratio of the BFE of the last and the first test run in multiple, typically seven, consecutive experiments). The BFE is the amount of energy required to force a blade through a conditioned, precise amount of bulk solid. The blade motion as well as the volume of the bulk solid (i.e., 200 mL) is precisely controlled in order to guarantee reproducible measurements. The SE is similar to the BFE, however, the blade motion is different (i.e., the blade is moving through the bulk solid in a gentle lifting motion to induce unconfined powder flow). All of these parameters have been previously described in literature (see, e.g., Freeman[30]). The results displayed in Table 8.2 clearly indicate that dry and wet glass beads are perfectly stable (i.e., the SI is close to one). However, the bulk density decreases by almost 22% when liquid is added to the particles indicating significant cohesive effects. The most dramatic change is observed for the specific energy taken up by the particle bed: it increases by a factor of 2.07. The measured value of SE of over 6 mJ/g already indicates a moderately cohesive system.

The rheology of the particle bed has been furthermore assessed using variable speed tests. Different particle sizes, as well as coated 4 mm glass beads, have been used for this analysis and the results are shown in Figure 8.6. Note, that the tip speed is negative, since the tool of the powder rheometer moves in an anti-clockwise direction into the powder bed. Clearly, the difference between dry and wet 0.15-0.25 mm particles is clearly visible from the offset in this figure. However, the tip speed does not have any influence on the basic flowability energy.
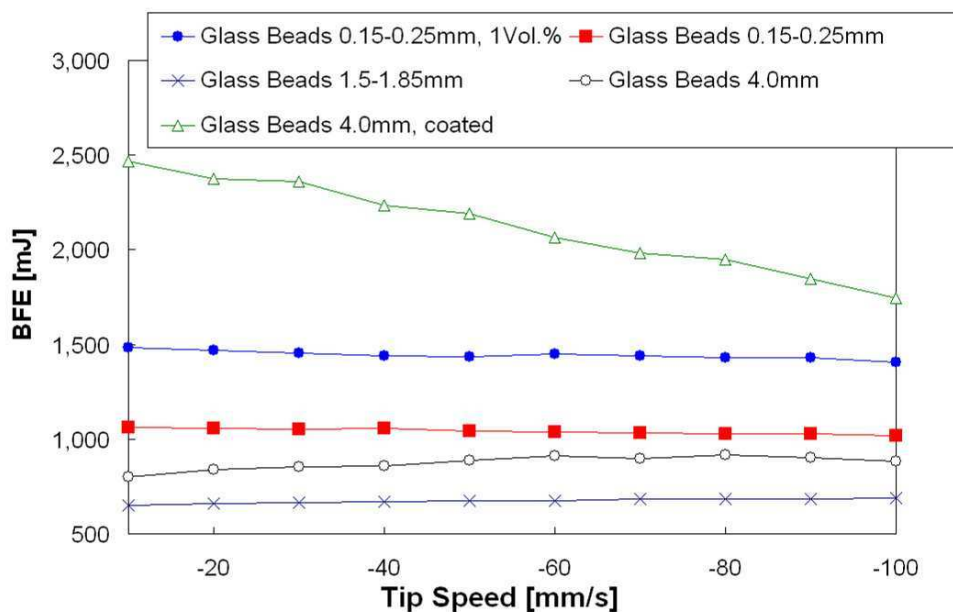
Figure 8.6: Basic flowability energy vs. tip speed for various coating and uncoated glass beads.

Interestingly, the 1.5-1.85 mm glass beads have the lowest BFE, while 0.15-0.25 mm and (uncoated) 4.0 mm beads show higher levels of BFE. This behavior is to some extent unexpected, since the previous study of Freeman and Fu[22] has shown that larger glass beads (in their study approximately 0.174 mm) have a larger BFE than smaller ones (in their study 0.068 mm). Our experiments for the 0.15-0.25 mm glass beads show a similar level compared to that measured by Freeman and Fu[22] for the 0.174 mm beads (i.e., 1017 and 1431 mJ for our and their measurements, respectively). These beads are smaller than the gap between the impeller and the cylindrical wall of the FT4 powder rheometer. Hence, beads will be squeezed into this gap and will absorb more energy. In case the particles are significantly larger than the gap (i.e., in case of the 1.5-1.85 mm glass beads we have used), there will be no particles in this gap and the energy uptake of the particle bed will be smaller. This explains our massive decrease for this particle size from 1017 to 688 mJ for 1.5-1.85 mm glass beads. If the particle size is further increased (i.e., when 4.0 mm glass beads are used), the BFE increases again. It is speculated that this higher energy uptake is due to a blockage of particles in the rheometer. Thus, the particle diameter is already in the order of the blade diameter in the cylindrical vessel (50 mm diameter).

Comparing the coated and uncoated 4.0 mm glass beads, we see a significant increase in the BFE for the case of coated particles. This change reflects the change in the friction coefficient when glass beads are coated (see the first section of this chapter) and is more pronounced at

lower tip speeds. It is speculated, that this is due to the longer particle-particle contacts at low tip speeds. This will leading to a more pronounced effect of the friction coefficient, and hence a higher energy uptake compared to the case of a larger tip speed. Also, in the experiments involving the coated glass beads, there was a pronounced heap formation near the cylindrical glass vessel of the FT4. This was due to the difference in the friction coefficient between the particles (i.e., between two coated surfaces) and the particles and the wall (i.e., between a coated and an uncoated surface).

8.3.2 Granular Particle Image Velocimetry

i)   Background

Granular particle image velocimetry (gPIV) is an optical measurement technique for the analysis of the velocity of a particle bed. With the arrival of relatively cheap digital cameras, it has become an important tool for experiments in the area of fluid and solid mechanics. However, conventional PIV is based on the analysis of (two-dimensional) images, and hence, can provide only the flow field in a certain cross section of the flow. For granular PIV, the illumination of the particle bed in a cross section is impossible. This means that only the projection of the granular bed can be observed, and hence, only the velocity field in this projection can be determined.

In the traditional use of PIV in the area of fluid mechanics, the scattering or the emission (e.g., due to fluorescence) of light by suspended particles is used. Thus, tracer particles are used in these applications to visualize the flow. In the case of granular flow, only an appropriate pattern in the particle bed has to be present. Thus, the particle making up the particle bed itself can act as a tracer. For granular flows, the amount of tracer particles should be about 25 Vol.% to avoid similarity effects, i.e., multiple strong correlation peaks in the interrogation area.[31]

Early PIV measurements for granular flows have been performed by Lueptow et al.[32] They used a TSI system using a 640×480 pixel CCD camera. A YAG-laser synchronized with the oscillator of their powder bed was used to illuminate the granular bed. To avoid effects of static electricity, the humidity in the room was controlled. The approach has been applied to wet granular flows by Jain et al.[33] They also used a TSI system with a CCD camera with a resolution of 1016×1000 pixels. A dual-YAG laser system was used to illuminate the particles. Glass beads were avoided in their experiments, because glass has a similar refractive

index as water. Zeilstra[31] used a LaVision Imager Pro high-speed camera for his studies on vibrated beds. He used a maximum acquisition frequency of up to 2,000 Hz. His standard setup included frequencies of approximately 50 Hz. To trigger the camera, a sinus generator was used. A similar system was used by Darmana[34] with a somewhat lower acquisition rate (up to 625 Hz at full resolution). Reynolds et al.[35] used the same setup as Pudasaini et al.[36] Both studies used a Photron DVR high-speed camera with an acquisition rate of 1125 Hz at a resolution of 1024×512 pixels and a total memory for 4000 images. This was sufficient to measure the granular temperature in a granulator with a rotor speed of 300 rpm and particles (i.e., granules) with a size between 0.71 and 2 mm. Also, Pouliquen[37] used movies with an acquisition frequency of 500 to 1,000 Hz for the determination of particle paths. The research group around Glasser at Rutgers University uses a MotionScope PCI camera to perform gPIV at 500 Hz.

In summary, a measurement system to analyze granular flows consists of the following components:

- an image acquisition system (i.e., a high-speed camera with a typical acquisition frequency of 10 to 2,000 Hz, as well as appropriate illumination),

- a triggering and image recording system (i.e., hard- and software to synchronize the camera, as well as to save the recorded images), and

- software for post-processing of the image data (i.e., for calculating the velocity fields).

While image acquisition and recording are standard nowadays, the software used for calculating the velocity fields is more complex.

ii)   Software for Post-Processing

During post-processing, each image is split-up into a grid of sub-images, i.e., so-called "interrogation areas" (IAs). For each of these IAs, a velocity is calculated using the images from two time instances of the same IA. For calculating the velocity in each IA, typically the cross-correlation method is used. The cross-correlation algorithm basically compares two instances of the same IA (i.e., IA^n and AI^{n+1}) by multiplication of IA^n and a shifted version of AI^{n+1}, as well as a subsequent summation operation of the multiplicated IAs. The displacement for which this sum is at a maximum corresponds to the correct displacement of the IA. More background on the numerical algorithm, as well as a calculation example is presented in Appendix F.

Zeilstra[31] used the PIV software "DaVis", which is based on FFT (Fast Fourier Transformation) augmented by zero padding to avoid bias of large displacements. A correction to avoid biases towards lower velocities is described in Dijkhuizen et al.[38] A multipoint Gaussian peak fit to the correlation peak was used by Zeilstra[31] to increase the accuracy in evaluating the displacement (similarly to the work of Dijkhuizen et al.[38]). Window shifting, i.e., a two-step method for evaluating the velocity vectors was used by him. Post-processing involved a median test to exclude outliers from the analysis of the experimental data. The interrogation area had a size of 64 × 64 pixels and an overlap of 75 % of the interrogation areas was allowed. Reynolds et al.[35] used the free software MPIV[39] for post-processing the high-speed images in a MATLAB environment. Interrogation areas of 8 × 8 to 64 × 64 pixels have been used. Other (free) software for post-processing of PIV-images is (i) MatPIV[40] and (ii) OpenPIV.[41]

For the calculation of the vector fields in this work we established an extension of MatPIV.[40] This was done by writing our own MATLAB routines that are based on the original version of MatPIV. In MatPIV, the cross-correlation method is used to determine the displacement between two time instances of an IA. The extension of MatPIV is detailed in Brandl.[42,43] After finding the displacement Δx for each IA, the velocity for this IA is calculated using:

$$v = \frac{\Delta x}{\Delta t}.$$ (8.3)

This raw information of the velocity field is then filtered to avoid unrealistic velocities in the IAs for which the cross-correlation algorithm did not work correctly. Typically, the following filters are used in our work.

- **"Signal to noise ratio" Filter (SNR Filter)**

The correlation matrix is used to calculate a "quality" attribute. Thus, the ratio of the dominant correlation peak and the surrounding "noise" (i.e., the height of local maxima in the correlation matrix) is calculated. If this ratio is below a certain threshold (the default value is 1.3), the calculated velocity is dismissed.

- **„Peak height" Filter**

The height of the dominant correlation peak is used for this filter. If the height is below a certain threshold (the default value is 0.8), the calculated velocity is dismissed.

- **Global Filter**

This filter will remove vectors from IAs that have a magnitude significantly larger or smaller than the majority of the magnitude of the vectors in all other IAs. The default value for the critical ratio has been set to 3.5.

- **Local Filter**

Vectors are removed that deviate from the median (this is the default setting) or the mean of the vectors in the surrounding IAs. Thus, a ratio of the vector in the IA to be filtered and the surrounding vectors is calculated and compared to a threshold (the default value is 2.5).

IAs for which the filters have eliminated the calculated velocity are filled with interpolated velocities from the surrounding IAs. The sensitivities to these filters are of major importance to produce correct results. The filter settings were adjusted for each individual run to guarantee filter-independent results for the velocity fields.

8.3.3 Experimental Setup

i)   Camera System

The camera system used is based on a "MotionScope M3" high-speed camera (Imaging Solutions GmbH, Eningen, Germany). This extremely compact, monochrome (i.e., 8-bit grayscale) camera has a native resolution of 1280 × 1024 (1.3 MPixel) and a film speed of 3000 ASA. The nominal acquisition rate is 520 Hz at full resolution, and goes up to 16,100 Hz at a reduced resolution (the latter is the maximal acquisition rate at resolution of 1280 × 32). The camera is connected to a frame-grabber card, such that the image data is directly transferred to the main memory (i.e., the random access memory, RAM) of the computer. Currently, this enables us to record up to 8 GB (equal to approximately 8,000 images at full resolution) during one shot. A software trigger, as well as manual triggers (e.g., manually activated or activated by a photo sensor) can be used to control the recording of images. A metal-halide cold light source (Imaging Solutions GmbH, Eningen, Germany) equipped with a liquid-based light guide provides extremely bright light.

ii)   Bladed Mixer

A similar experimental setup as the one used be Lekhal et al.[13] has been used (see Figure 8.7). It consists of a fully temperature- and pressure-controlled cylindrical mixing chamber (d_{inner} =

145 mm, H_{inner} = 250 mm, at the bottom there is a ca. 10 mm rounded corner), as well as a four-bladed stirrer.
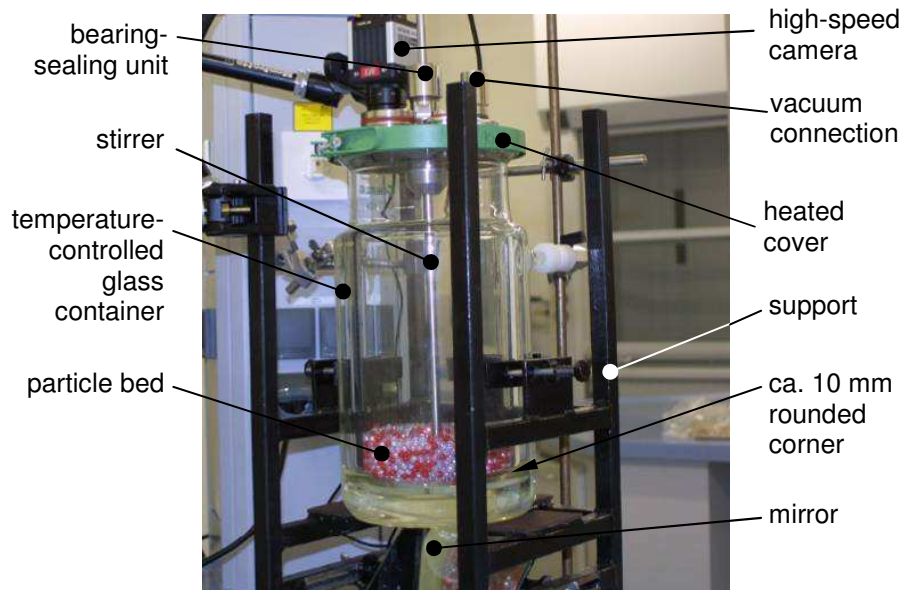
Figure 8.7: Vacuum dryer with PIV camera.
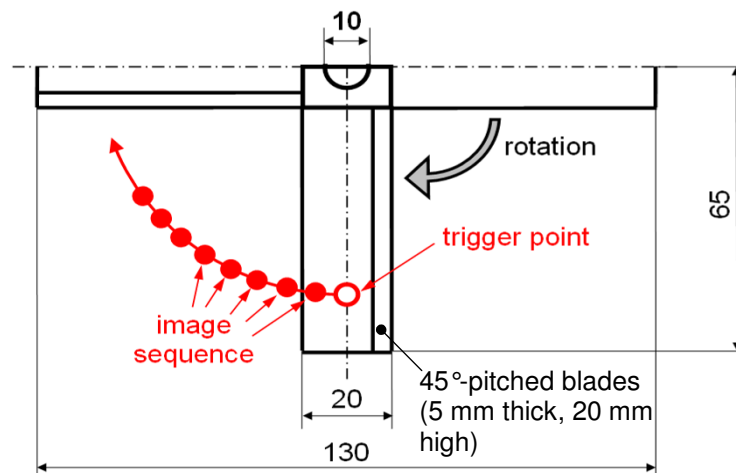
Figure 8.8: Top view of the stirrer and trigger positions.

A heating bath (T_{min} = 25°C, T_{max} = 95°C), as well as a vacuum pump ($p_{min,abs}$ = 7 mbar) can be connected to the mixing chamber. The stirrer (four 45°-pitched blades, see Figure 8.8) is connected to a gearbox to realize also low stirrer speeds (i.e., down to 1 rpm). The rotation was clockwise, i.e., a so-called "acute" blade arrangement was used in all experiments. The stirrer drive consisted of a standard variable-speed electric drive unit. Using our setup, the granular bed can be observed at the free surface, as well as at the bottom (via a mirror) and

the side wall of the glass vessel. The system has been constructed and built-up by Daniel Brandl.[42]

iii)   Two-Dimensional Single Blade System
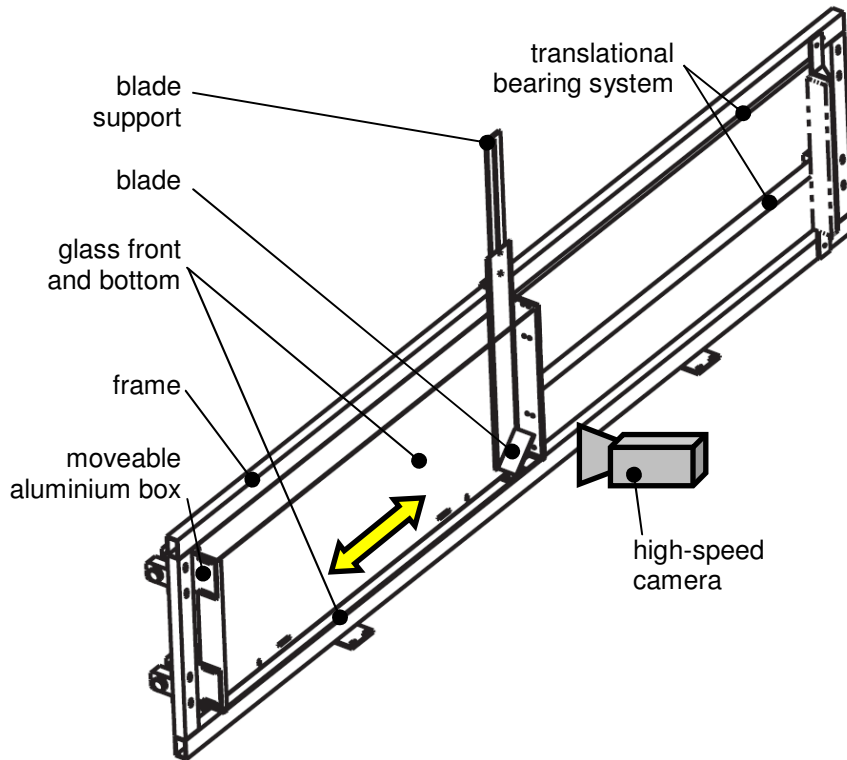
Figure 8.9: Isometrical view of the two-dimensional experimental setup with camera, blade and translational bearing system.

To investigate granular flow over a single blade, an experimental setup similar to that of Bagster and Bridgwater[19] was set up (see Figure 8.9). It consists of an aluminium box (395 mm high and 1200 mm long, 32 mm inside width, the front wall was transparent) filled with particles, a translational bearing system, as well as frame with a fixed blade (32 mm width, different angles and heights). The clearance between the blade and the bottom of the box was typically chosen to be 10 mm. The box is fixed on the bearing system, such that the particle bed in the box can be forced to flow over the blade. The front and bottom of the box are made of plexiglass to allow optical access to particle bed. A partially transparent ruler is mounted at the back of the box. This ruler together with a photo sensor is used to measure the position, as well as the velocity of the box. This position measurement is synchronized with the PIV system in order to correlate the position of the box and the flow field of the particle bed. A stopping device on each side of the frame is used to abruptly stop the box at the end position. The box is driven by an electric motor with a variable speed, direct current

(DC) drive. The voltage of the DC drive is kept constant in order to obtain a constant speed of the box. The system has been constructed and built-up during the diploma project of Daniel Brandl.[43]

8.4 Results

8.4.1 Particle Flow in a Bladed Mixer[b]

The calculated velocity fields from the top, side and bottom of the granular bed are shown in Figure 8.10. These images show instantaneous flow fields that are representative for the flow situation in the mixer.
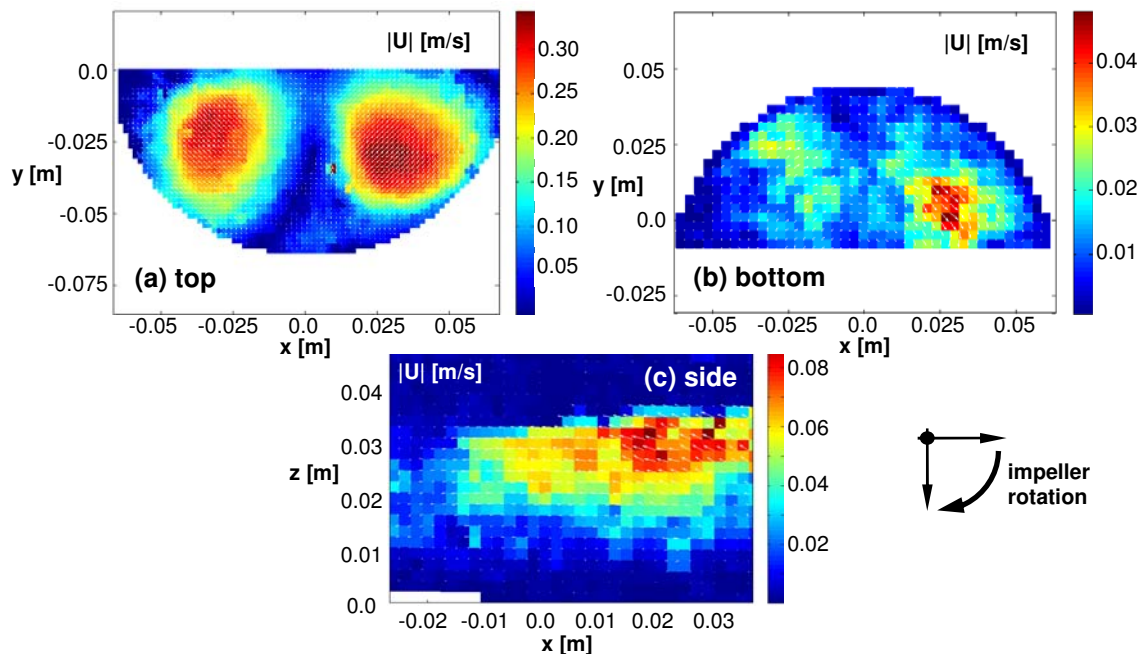
Figure 8.10: Instantaneous flow fields in a bladed mixer (d_p = 0.5 mm, 60 rpm, the tip speed is 0.41 m/s, glass beads).

Clearly, at the top of the particle bed the highest particle velocities are observed. The maximal velocity is approximately 0.8 times the tip speed. It can be seen that there exists a region, where the particles move faster than the blade (see Figure 8.10a, the blade speed linearly increases with the radial distance to the center of the mixer and the maximum velocity is observed half-way between the stirrer axis and the wall). Thus, there must be a region in front of the blade were particles cascade down the heaps formed by the blade. Such a zone was

---

[b] Experiments were performed by Hanna Heimburg and Daniel Brandl.[43]

already shown in the experiments of Bagster and Bridgewater.[19] Between the high-velocity regions on top of the particle bed, there exist regions with zero velocities in the x-y direction. This indicates that these regions are not effected by the stirrer or particles are vertically falling down (i.e., they move in the z-direction only). The instantaneous flow field from the bottom (see Figure 8.10b) shows significantly lower velocities. The high velocity regions near the blades are significantly less pronounced as those at the top of the bed. The absolute magnitude of the velocity field near the bottom will strongly depend on the details of the blade near the bottom and the exact blade-to-wall distance. For the results shown in Figure 8.10 (as well as in the subsequent recordings) the blade-to-wall distance was 10 mm in order to avoid abrasion of the cylindrical glass container. From the recordings of the side of the particle bed the velocity fields were extracted and are shown in Figure 8.10c. In this figure also higher velocities at the top of the particle bed can be observed. The maximum velocity is approximately 20% of the tip speed. This significantly lower velocity near the side wall is caused by the 7.5mm-gap between the impeller tip and the wall. However, the velocity vectors indicate a slight upward motion of the particles in front of the blade. This supports the existence of a recirculation region in front of the blade.

i)   **Particle Size Effects**
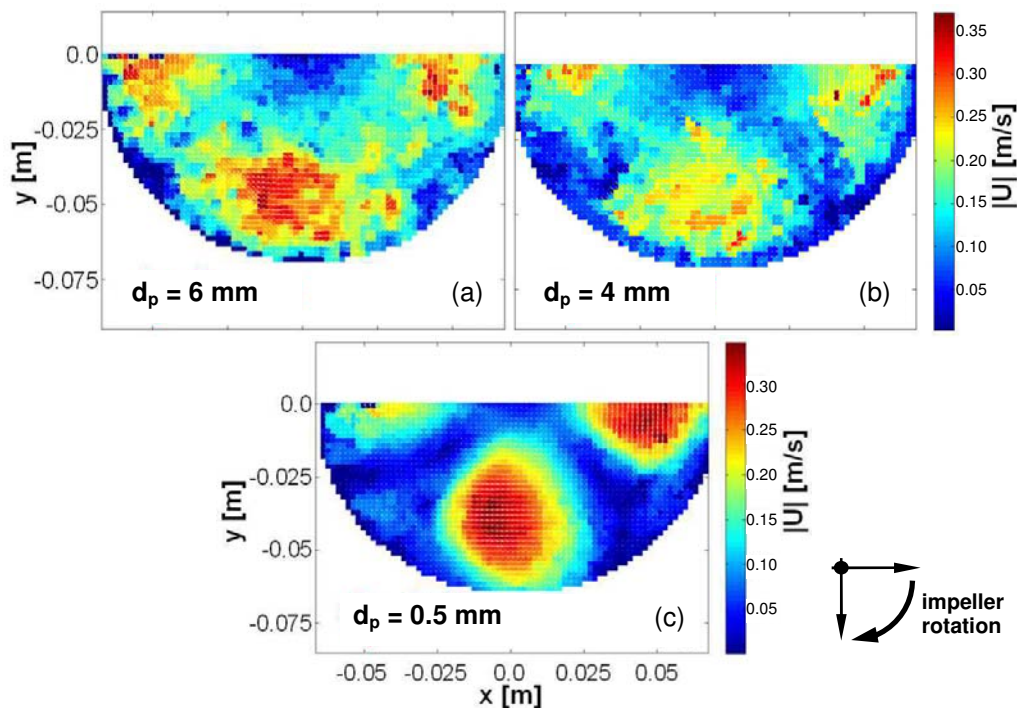
Figure 8.11: Flow field of stirred glass beads for different particle sizes (60 rpm, the tip speed is 0.41 m/s).

The results for different particle sizes at constant process parameters show a clear size dependency of the instantaneous velocity field (see Figure 8.11). Specifically, a transition from a smooth flow field in case of 0.5 mm glass beads (see Figure 8.11c, where a high-velocity region can be clearly distinguished from the regions with a lower velocity) to a more erratic behavior for the larger beads (i.e., 4 and 6 mm beads) is observed. The latter is expected to occur due to a "roll-and-lock" effect that is caused by the gaps between big particles. Thus, big particles fall in the gap between other particles, resulting in a measureable velocity fluctuation. Large particle also lead to a less pronounced high-velocity region near the impeller blades. Thus, the whole particle bed rotates to some extend with the impeller. In contrast, the particle bed consisting of smaller particles shows clearly regions having a very low (i.e., below 0.1 m/s) velocity in the x-y plane.

ii) The Effect of the Moisture Content
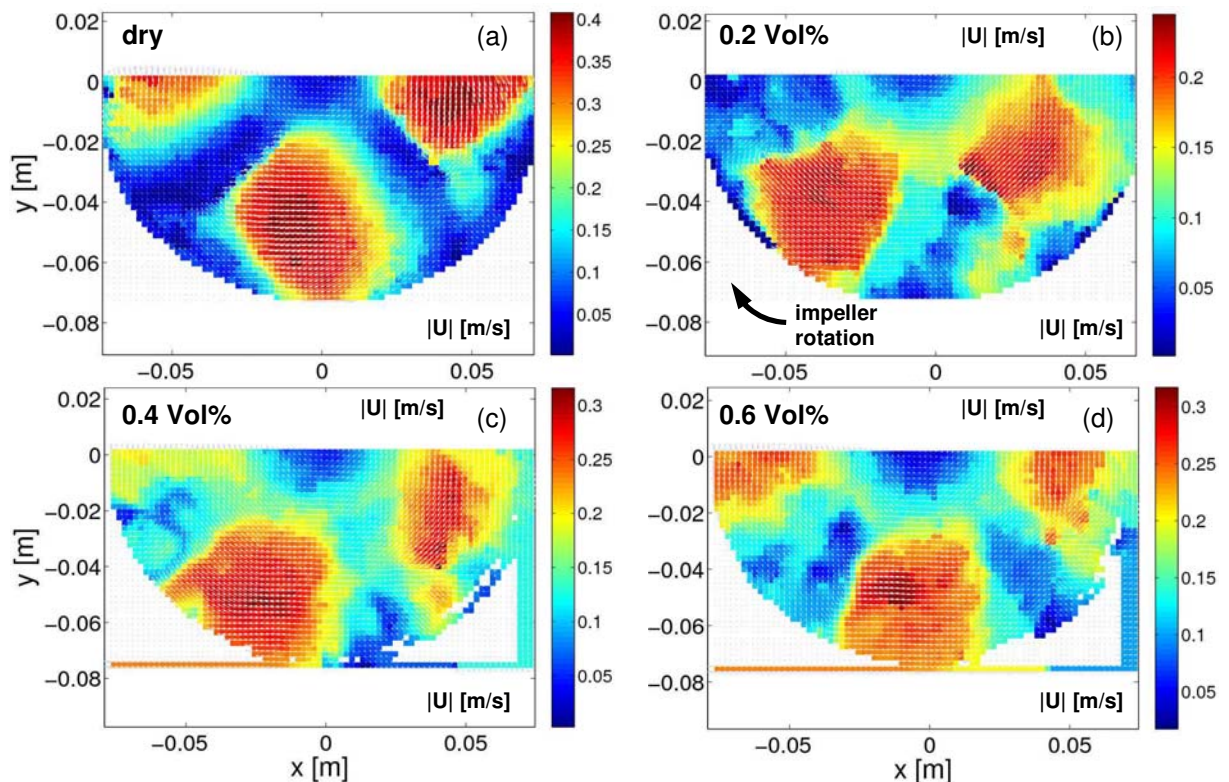
Figure 8.12: Flow field for 60 rpm and increasing moisture content (0.5 mm glass beads; (a) 0, (b) 0.2, (c) 0.4, (d) 0.6 Vol% moisture content).

In order to highlight the differences between dry and wet granular flows, selected results for two different stirrer speeds are presented in Figure 8.12 (for 60 rpm) and Figure 8.13 (for 10 rpm). In the case of a high stirrer speed (i.e., 60 rpm), the regions of a low flow velocity on

top of the granular bed vanish for the wet system. At a moisture content of 0.4 Vol%, these regions are almost completely gone. Only a small spot of low velocity near the impeller shaft remains. In general, also the maximum velocity at the top of the particle bed goes down with increasing moisture content (there are individually scaled color bars for each of the sub-images in Figure 8.12). However, the high-velocity regions near the impeller blades are clearly visible. For the case of a lower stirrer speed (i.e., 10 rpm), we also observe vanishing low-velocity regions with increasing moisture content. However, even in the case of a dry particle bed, the high velocity regions near the impeller blades are not as clearly visible as for the higher stirrer speed. Hence, the transition to a more uniformly distributed velocity in the circumferential direction is less obvious. Also, the velocity on top of the particle bed does not decrease as significantly as in the case of 60 rpm.
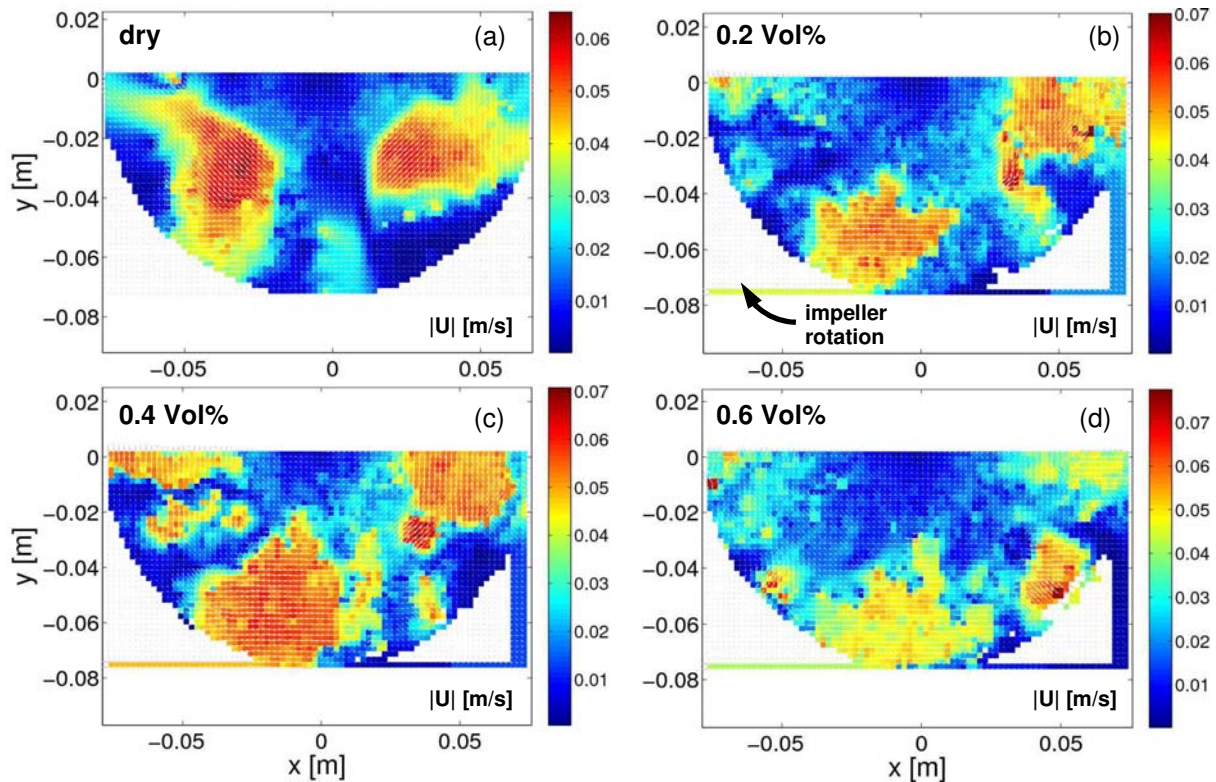
Figure 8.13: Flow field for 10 rpm and increasing moisture content (0.5 mm glass beads; (a) 0, (b) 0.2, (c) 0.4, (d) 0.6 Vol% moisture content).

The raw images showing ¼ of the particle bed from the top of the mixer are displayed in Figure 8.14. There are large agglomerates visible for both stirrer speeds and even the smallest liquid content of 0.2 Vol%. These agglomerates are separated from each other by deep "cracks" (visible via dark regions in the images) throughout the wet particle bed. The clumps also lead to a significant bed extension (therefore also some regions of the granular bed are

not perfectly focused) and a "rough" surface. Similar observations have been also made by Lekhal et al.[13] in experiments with non-spherical sand particles. However, they reported this bed extension at a significantly higher moisture content (i.e., at 2 w% water corresponding to approximately 4 Vol.%).
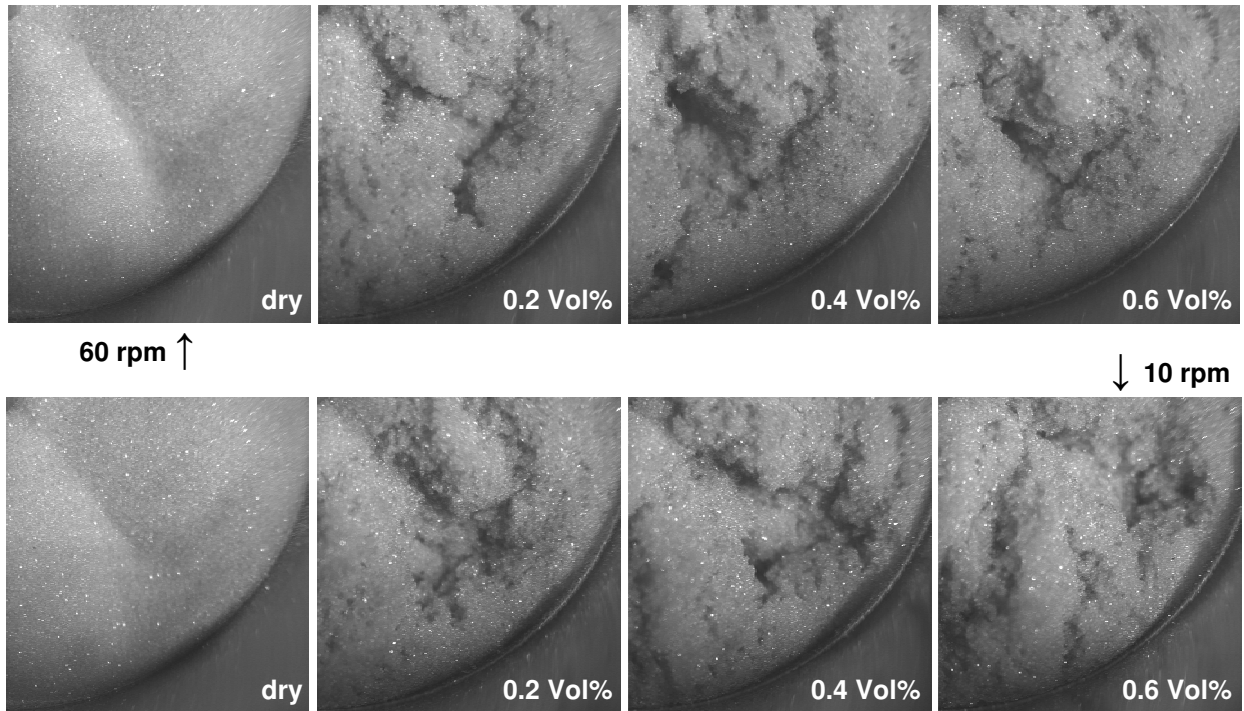
Figure 8.14: Raw images from the top of the mixer for dry and wet granular matter for two different stirrer speeds (top row: 60 rpm, bottom row: 10 rpm, 0.5 mm glass beads).

The surface roughness can be observed throughout the bed, with the exception of the region close to the wall. Here the particle bed has aligned with the glass wall and forms a relatively smooth surface that periodically breaks off the wall. Regions of a high porosity may be anticipated from our recordings and are visible even at the lowest moisture content of 0.2 Vol%. In summary, it is hard to quantitatively differentiate between the images for different moisture contents in Figure 8.14.

iii) The Effect of the Filling Height

The effect of filling height in the bladed mixer has been investigated at a constant impeller position relative to the bottom wall (i.e., the 10 mm distance to the bottom was kept constant). The results for the velocity field on top of the particle bed (see Figure 8.15) indicate a clear decrease of the surface motion for a fill level larger than 60 mm (note, the impeller height is 20 mm and the distance of the impeller to the bottom of the vessel is 10 mm). The

particle motion then gets also more diffused in circumferential direction. Thus, the high velocity region near the impeller is significantly less pronounced.
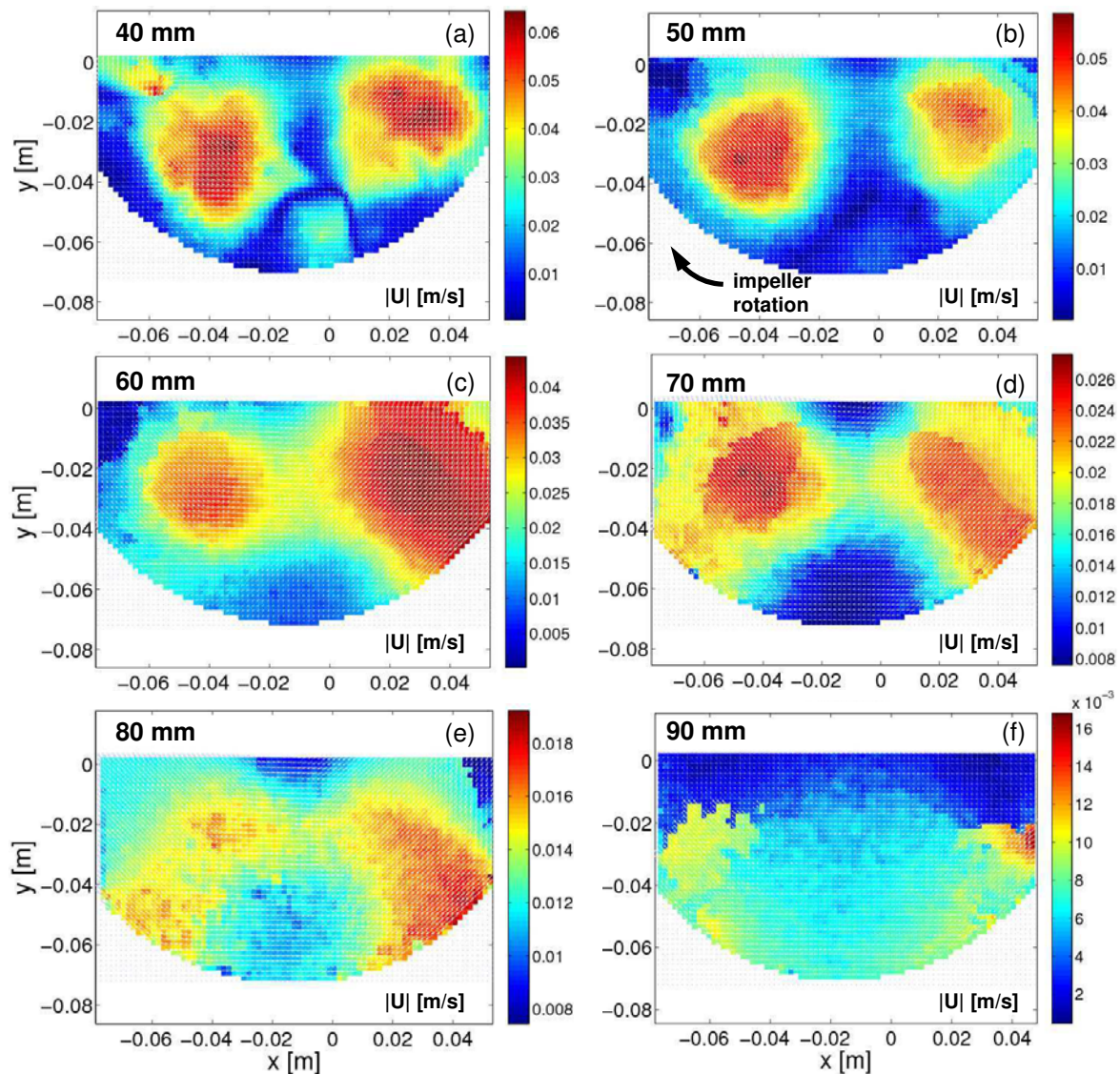
Figure 8.15: Flow field for 10 rpm and increasing filling height (0.5 mm glass beads; (a) 40 mm, (b) 50 mm, (c) 60 mm, (d) 70 mm, (e) 80 mm, (f) 90 mm).

To highlight this decrease with the filling height, time profiles of the radial and tangential velocity at a radial position of 30 mm are shown in Figure 8.16. While the oscillation of the surface velocity (due to the passing of the blades) at the filling height of 40 mm is clearly visibly, this oscillation has completely vanished for the filling height of 100 mm (note the different scale of the y-axis). Instead, the measured surface velocity behaves in an erratic manner. Time averaging has been also performed for these velocity-time profiles. This has been done by calculating the mean and the standard deviation of the radial and tangential, as well as the magnitude of the surface velocity at a radial position of 30 mm. The standard

deviation of the velocities has been interpreted as the (mean) velocity fluctuation and is shown together with the mean values in Figure 8.17. The clear decrease of both the mean and fluctuating velocities with the filling height is visible from these graphs. As expected, the decrease is significantly more pronounced for the tangential velocity compared to the radial velocity.
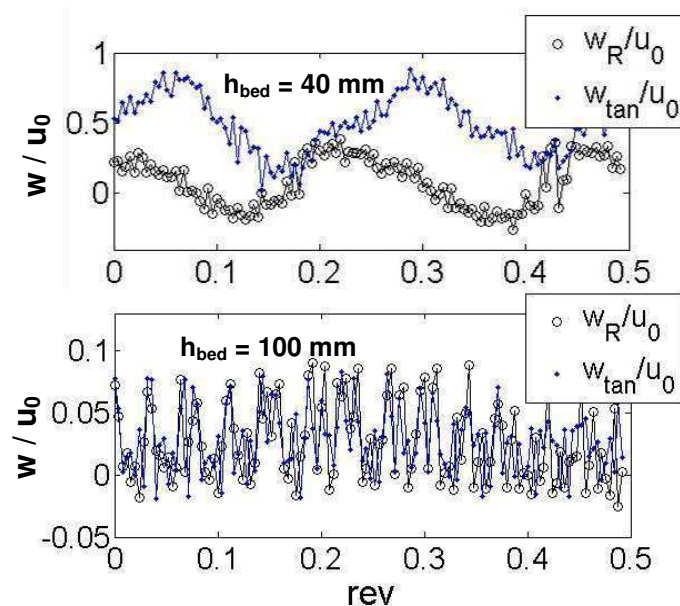
Figure 8.16: Time profile of the dimensionless velocity at r = 0.03 m (10 rpm, two different filling heights, w_R...radial velocity, w_{tan}...tangential velocity, u_0...tip speed).
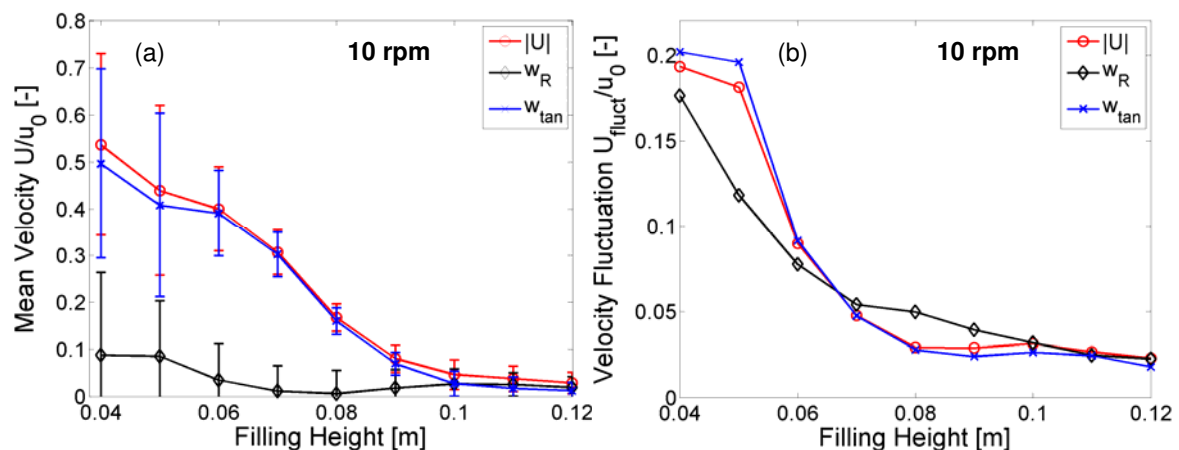
Figure 8.17: Velocity statistics at r = 0.03 m (10 rpm, various filling heights, (a) mean values and velocity fluctuations shown as error bars, (b) velocity fluctuations vs. the filling height).

iv) The Effect of the Stirrer Position

Two stirrer positions have been investigated (Figure 8.18). The default stirrer position was 10 mm from the bottom of the cylindrical vessel and the flow field for this situation is shown in

Figure 8.18a. At a constant fill level of 40 mm, the stirrer has then been raised by 10 mm, resulting in the flow field shown in Figure 8.18b. This resulted in (i) a higher peak surface velocity, in (ii) a less smooth flow field with sharp, V-shaped interface between high- and low-velocity regions, as well as (iii) the fact that the high-velocity region now extends to the cylindrical wall of the mixer. Thus, the lower amount of particles over the blade primarily leads to a higher average velocity in the granular bed.
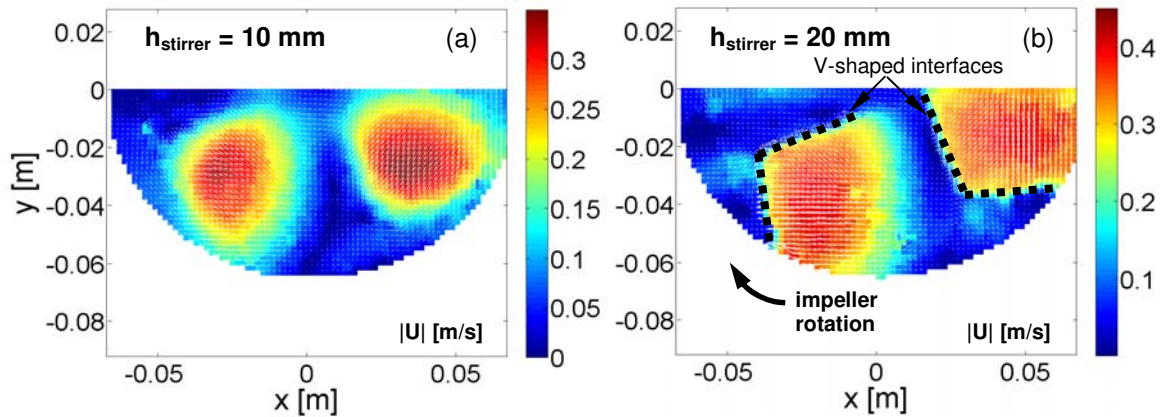
Figure 8.18: Velocity field of a 40 [mm] high particle bed, using a stirrer height h$_{stirrer}$ of (a) 10mm and (b) 20 mm (60 rpm).

A more rapid mixing in this case can be expected, because also the particles near the wall move faster and hence are expected to mix faster. The sharp interfaces between low- and high-velocity region is caused by the fact, that in the case of h$_{stirrer}$ = 20 mm the heaps are more pronounced and particles flow into the "valleys" of the particle bed. At this position the particles abruptly stop, forming the sharp interface. The V-shaped interface is due to the shape of the heaps in the particle bed. Thus, in the region from the shaft of the mixer to a radial position of approximately 40 mm, particles are falling from the rear edge of the blade and form a heap. This heap limits the extension of high-velocity region in that part of the mixer. Near the wall of the cylinder, particles also form a smaller heap limiting the extension of the high-velocity region at this location. This smaller heap is formed by particles that were initially pushed to the wall by the blade.

8.4.2 The Flow over a Single Blade[c]

The flow over a single blade was studied using the two-dimensional blade system described in Chapter 8.3.3iii). Because this system is based on a moving box with a finite length, a short acceleration and deceleration phase has to be taken into account. Thus, a time-averaged flow field during a (nearly) constant translational motion of the box was used for post-processing our results. For example, for the experiment shown in Figure 8.19 we used 200 images during a time span between 1.7 and 2.1 [s] after starting the experiment. Figure 8.19a shows a raw image of this image sequence and Figure 8.19b the corresponding box velocity profile. The box velocity during this image sequence was about 0.145 m/s. Thus, after a short acceleration distance (approximately 0.15 m), the velocity is nearly constant. A small increase is observed after 2.1 s (see Figure 8.19b), which is possibly due to the elastic deflection of the translational bearing system when the box moves towards the center of the experimental setup (see Figure 8.9). This deflection could not be avoided, and also limiting the electric current to the DC drive has not been done. However, the short image sequence of 200 images was enough to calculate a representative time-averaged flow field.
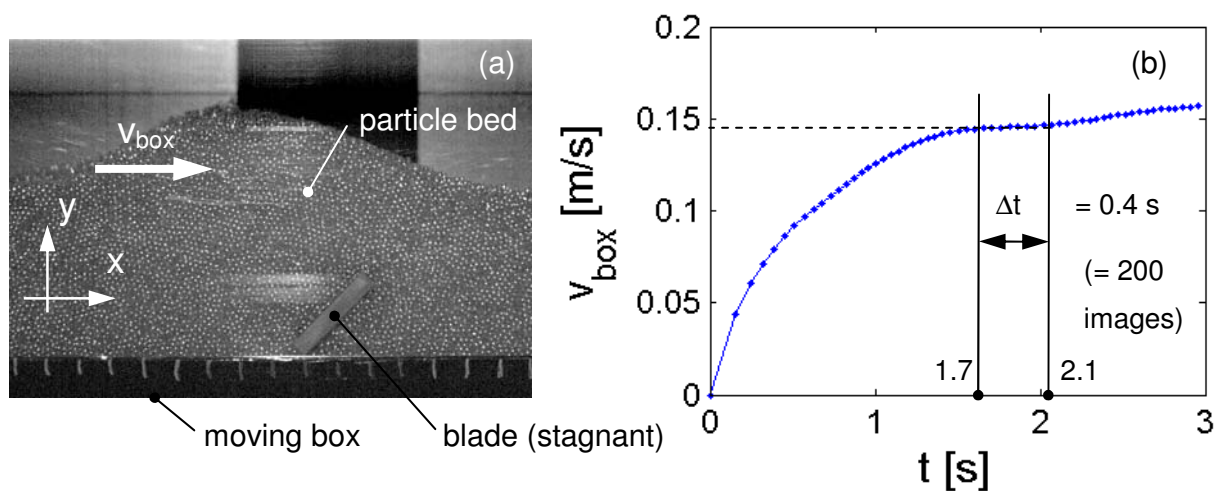
Figure 8.19: (a) Raw image and (b) measured box velocity for the single blade experiments.

i)   Flow Regime Determination

Experiments with different blade speeds have been performed. The dimensionless shear rate is known to be one of the most important parameters that determine the regime of a granular flow:[16]

---

[c] The experiments were performed and post-processed during the Diploma thesis of Daniel Brandl.[43]

$$I = \frac{\dot{\gamma} \cdot d_p}{\sqrt{P/\rho}} \, .$$

(8.4)

Here, $\dot{\gamma}$ is the shear rate, d_p is the particle diameter, P is a characteristic normal stress (or pressure) and ρ is the bulk density. The dimensionless parameter I describes the relative importance of inertia to the normal stress in the particle bed. For vertical free surface flows, the characteristic normal stress can be approximated by:[16]

$$P = \rho \cdot g \cdot h \, ,$$

(8.5)

and the shear rate can be approximated with:[16]

$$\dot{\gamma} = V/h \, .$$

(8.6)

Here, h and V are a characteristic bed height and bed velocity, respectively. Inserting these approximations into the definition of the dimensionless shear rate yields:

$$I = \frac{V \cdot d_p}{\sqrt{g \cdot h^3}} \, .$$

(8.7)
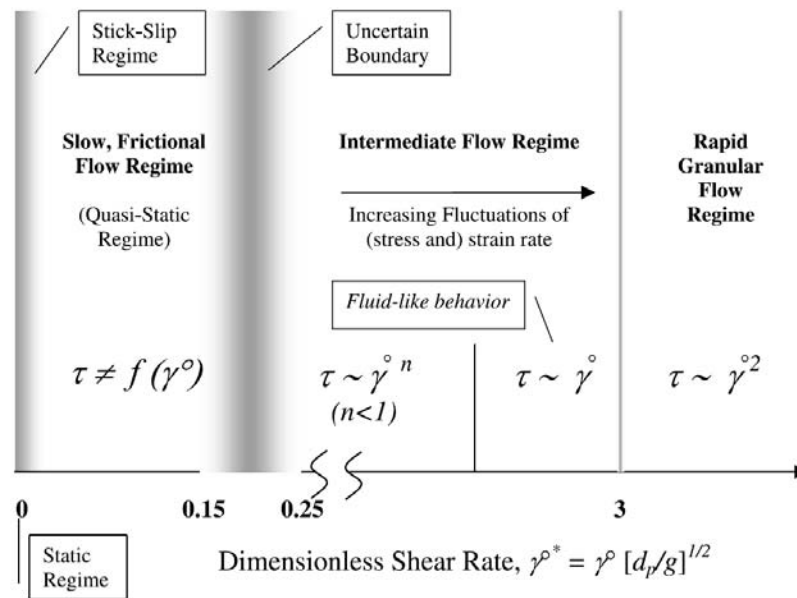
Figure 8.20: Regime map of granular flow (Tardos et al.[44]).

If the parameter I is above 10^{-2}, the quasi-static regime (where the effective friction coefficient is constant) is no longer valid, and the dense inertial regime has been reached.[16] In the dense inertial regime, the effective friction coefficient of the bulk solid depends on the dimensionless shear rate. A regime map for granular flows has been published by Tardos et

al.[44] In this regime map, a similar dimensionless parameter, i.e., $\dot{\gamma}^{0*} = \dot{\gamma} \cdot \sqrt{d_p / g}$, is used to separate the quasi-static regime from an "intermediate" flow regime (see Figure 8.20). The latter regime corresponds to the dense inertial regime mentioned by the GDR Midi group.[16] The boundaries between the flow regimes shown in Figure 8.20 and that mentioned by the GDR Midi group[16] are somewhat different due to slightly different definitions. Also, the regimes defined by Tardos et al.[44] have been developed for granular flows in the Couette geometry. The dimensionless shear rate calculated via Eqn. 8.7 is an average value for the particle bed and strongly depends on the bed height. For the flow over a blade, the characteristic bed height has been taken as the undisturbed bed height h_{bed} far away from the blade. The characteristic velocity is chosen as the box speed v_{box}.

ii)   The Effect of the Blade Speed

The effect of different box velocities, particle diameters and bed heights, i.e., dimensionless shear rates, has been investigated. Figure 8.21 shows the time-averaged velocity fields for these experiments. In these plots the velocity field is relative to the blade, i.e., the velocities are shown in a blade-fixed coordinate system. In all of these experiments a recirculation region at the top of the granular bed has been observed. This region is stagnant with respect to the blade and particles circulate inside the particle bed upwards and roll downwards at the surface of the particle bed.

As can be seen from Figure 8.21a and b, the box velocity has only a small effect on the qualitative features of the granular flow in the dense inertial regime (i.e., I > 10^{-2}). In these two figures, i.e., Figure 8.21a and b, the transition from a relatively fast moving inflow region (i.e., the region in the lower right corner of the image, see Figure 8.1) and the almost stagnant up flow region is clearly visible. Particles strongly accelerate in the down flow region near the blade tip. When the particles hit the particles in the outflow region of the granular flow, they may also move against the box direction, i.e., they have a positive x-velocity in a blade-fixed coordinate system as shown in Figure 8.21.

Similar flow features are observed in the quasi-static flow regime (see Figure 8.21c and d). Note, for these experiments we have used a smaller blade, as well as a slightly larger bed height to explore a wider range of the dimensionless shear rate I. The inflow and the up flow region are not clearly separated. However, the down flow region characterized by a high velocity is clearly visible. The recirculation region is present, however, only weakly developed

and heap formation is significantly smaller as that observed in Figure 8.21a and b. Also, the maximum velocity is significantly lower as in Figure 8.21a and b, despite the same box velocities have been used (note the differences in the color bars).
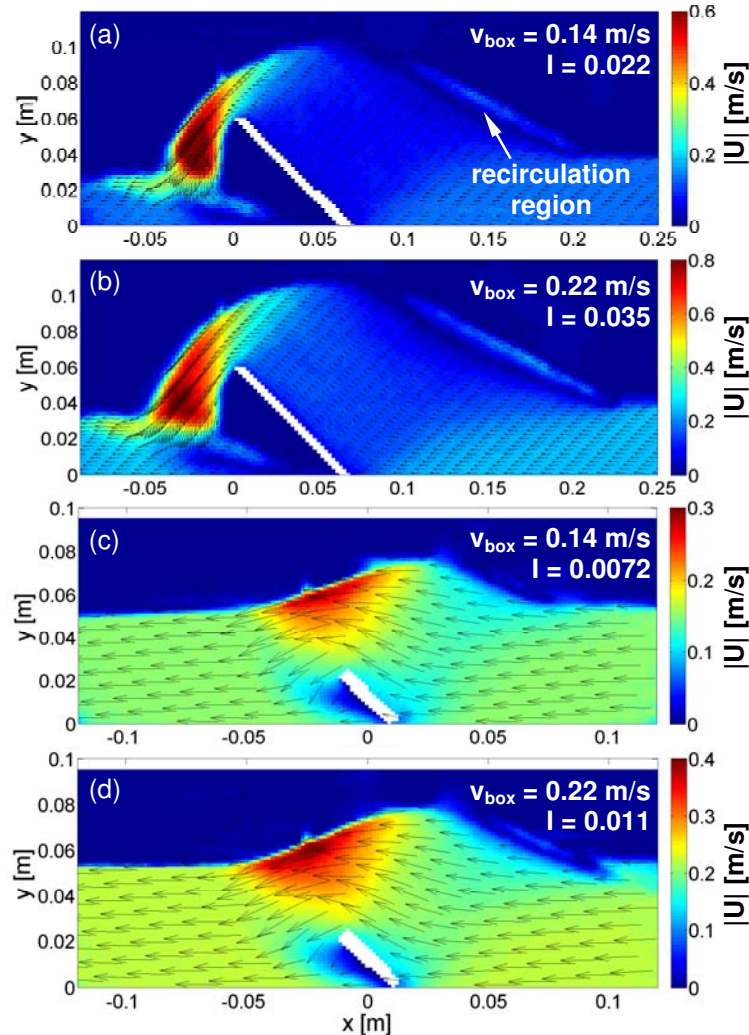
Figure 8.21: Velocities relative to the blade. (a) and (b) show velocity fields for 4 [mm] glass beads, blade number DA04_45° and a bed height of 40 mm. (c) and (d) show velocity fields for 1.675 mm glass beads, blade number DA04S_45° and a bed height of 50 mm.

iii) The Effect of the Bed Height

By changing the bed height at a constant blade geometry, we observe a significant change in the down flow region when the bed height exceeds 80 mm (Figure 8.22). At this point also the velocity at the top of the particle bed goes down. The velocity at the top of the particle bed is more uniform and the localized high-velocity region near the upper blade tip vanishes. The region behind the blade completely void of particles vanishes if the bed height goes above this critical bed height. Furthermore, the recirculation region is no longer present when $h_{bed} > 60$ mm.

Focusing on the dimensionless shear rate, it is clear that the transition in the down flow region (visible in Figure 8.22d) occurs at $I < 0.0062$. However, this parameter is definitely not enough to indicate the transition alone. Also, the ratio of the blade height and the bed height has an influence (compare Figure 8.21d and Figure 8.22b with identical values for I but different flow features).
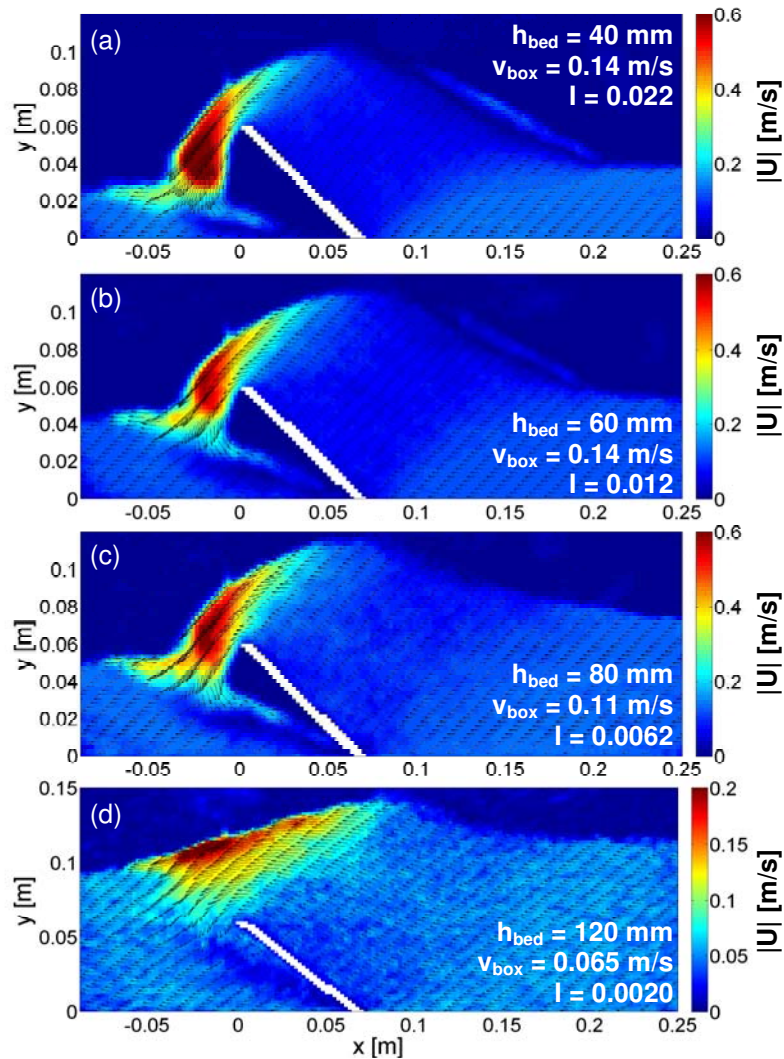
Figure 8.22: Comparison of the velocity fields for different bed heights h_{bed}: (a) 40 mm, (b) 60 mm, (c) 80 mm, (d) 120 mm (4 mm glass beads).

iv) The Effect of the Blade Position

While the bed height is kept constant, the blade position was varied in the y-direction. Our results clearly reveal that the particle bed below the lower blade tip is essentially undisturbed (see Figure 8.23b and c). Hence, the situations with $h_{blade} > 0$ correspond to situations with a bed height equal to $h_{bed} - h_{blade}$. This is supported by a comparison of Figure 8.23c and Figure 8.22c which have similar dimensionless shear rates and flow features (i.e., a recirculation zone

in front of the blade, a well pronounced down flow region, as well as a region completely void of particles below the upper blade tip). Thus, the blade position essentially does not play a role, but only the bed height relative to the blade.
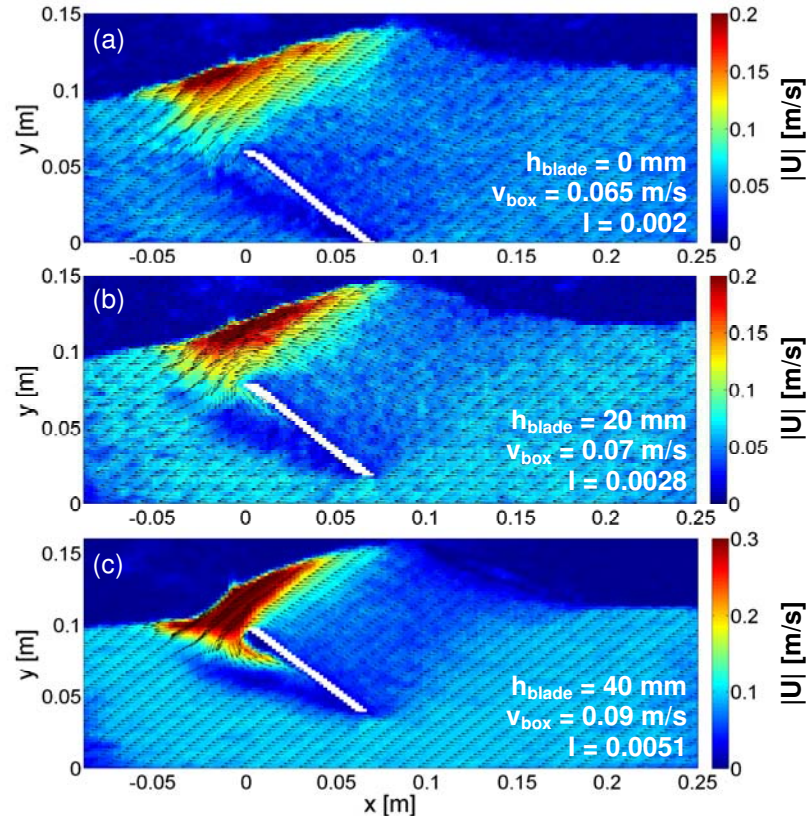
Figure 8.23: Comparison of velocity fields at three different blade positions (h_{blade}): (a) 0 mm, (b) 20 mm, (c) 40 mm (4 mm glass beads, h_{bed} = 120 mm).

v)   The Effect of the Blade Angle

Results for different blade angles are displayed in Figure 8.24. No significant changes of the flow features were observed. Most important, the recirculation region in front of the blade is not observed for a blade angle of 45° (see the thin layer on top of the particle bed that has a higher velocity). This recirculation region is well developed in the case of α = 90°, a case where also the highest velocity in the down flow region has been measured. Thus, at this angle more particle motion is induced in the bulk solid compared to the other blade angles.

The zone in the vicinity of the blade with extremely low particle velocities also depends on the blade angle. While this zone is in front of the blade for α = 45° and α = 90°, it is located at the down-stream region for the case of α = 135°.
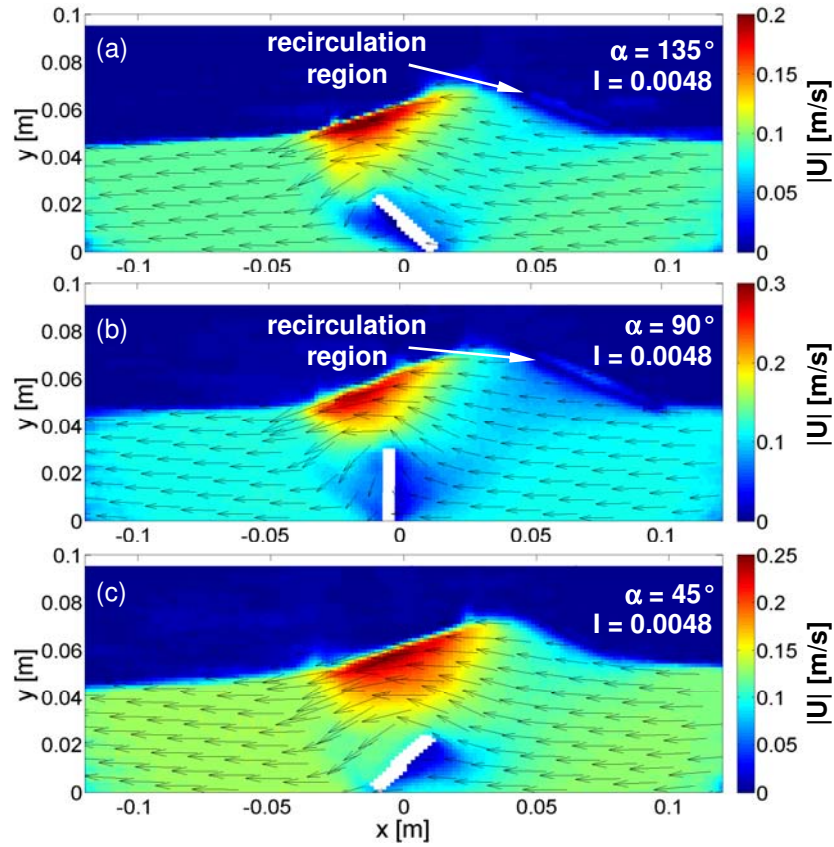
Figure 8.24: Comparison of velocity fields by using three different blade angles α: (a) 135°, (b) 90°, (c) 45° (v_box = 0.1 m/s, 1.675 mm glass beads, h_bed = 50 mm).

vi)   The Effect of the Particle Size
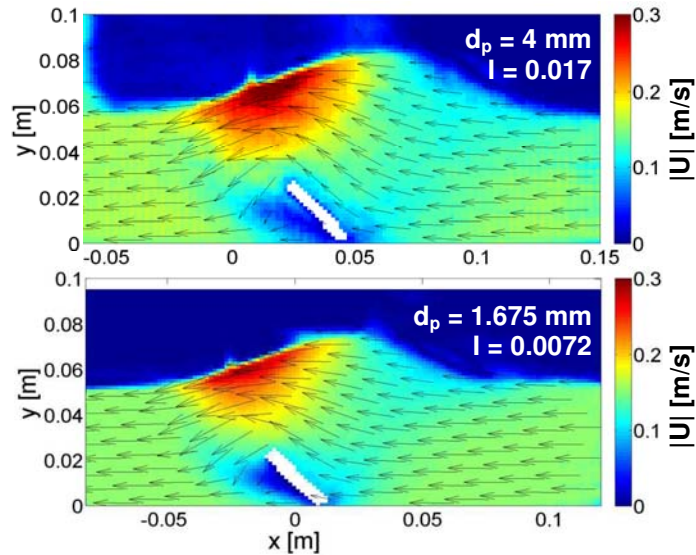
Figure 8.25: Velocity fields for different particle sizes d_p: (a) 4 mm, and (b) 1.675 mm (v_box = 0.15 m/s, h_bed = 50 mm).

Experiments with different particles sizes did not show significant differences in the time-averaged flow field (see Figure 8.25). The recirculation zone is not developed in both cases, and also the down flow region, as well as the region near the blade, show similar features. Thus, despite the particle size linearly impacts the dimensionless shear rate, an effect on the flow pattern cannot be observed. Experiments using 0.5 mm particles did not gave satisfactory velocity fields. This was because particles were sticking at the front wall during the experiments (due to electrostatic charging).

8.4.3 Single-Blade Mixing[d]

In the experiments presented in Chapter 8.4.2 the focus was on the flow pattern around a single blade. Of greater industrial significance is the mixing induced by this particle motion. Most important, the effect of the particle size, as well as of added moisture on the mixing rate is of interest. Consequently, we studied the dependency of the mixing process during multiple blade passages. Therefore, the two-dimensional experimental setup described in Chapter 8.3.3iii) was used. Due to the fact that a blade angle α of 90° was used, the blade was moved with a constant velocity of 0.15 m/s alternatively from left to right or vice versa to mix the particle bed. The bed height was equal to the blade height and was equal to 32 mm. The particle flow over the blade was captured with a camera at an acquisition rate of 210 Hz. The same camera was used to capture the particle distribution in the particle bed (the particles were colored red and white, the bed was filled as shown in Figure 8.26a).

i) Approach

In total, four experiments have been conducted using two differently-sized particles with and without added moisture. For the investigation of the influence of cohesive forces that arise due to liquid bridges, 1 Vol% distilled water was added to 0.75-1 mm particles in one experiment.

When the box was moved, the particles flow over the blade (the blade angle was 90°) that was held stationary. After each run the particle bed was recorded using a digital camera and the color intensity distribution was calculated. Care was taken to avoid an overlap of the images by using a scale at the bottom of the box. The distribution of the particles was averaged over the bed length (approximately 700 mm) to obtain the mean particle distribution C over the bed

---

[d] Experiments were performed and post-processed by Hanna Heimburg during her Bachelor thesis.[45]

height. For analyzing the data, a Matlab® program was used that detected the spatial distribution of the differently-colored particles.

After the particle distribution was determined, the information was used to fit a simple model for granular mixing. Therefore, a model treating the mixing in a granular flow as a purely diffusive process has been adopted (similar approaches were taken by Lu and Hsiau,[46] Zik and Stavans,[47] as well as Rosato et al.[48]). An especially attractive method is the one proposed by Lu and Hsiau,[46] which basically relies on the comparison of experimental data with an analytical solution for a diffusion process. This route is also taken in this work, and we model the diffusion process by:

$$\frac{\partial C}{\partial t'} = \frac{\partial}{\partial y'} \cdot \left(D \cdot \frac{\partial C}{\partial y'} \right). \tag{8.8}$$

Where t' is the number of blade passages (a discrete number that can be interpreted as a dimensionless time, i.e., the time divided by a characteristic time for the blade passage), y' is a dimensionless coordinate (i.e., the y-position made dimensionless with the bed height) and D is a dimensionless diffusion coefficient. In our experiments the bed height h_{bed} was rather small and we were interested in mixing the complete particle bed. Hence, we cannot assume fixed values for C at the bottom and top of the bed. Instead, we assumed a zero-gradient boundary condition, corresponding to the fact that particles cannot exit the bed at the bottom and top of the bed:

$$\left. \frac{\partial C}{\partial y'} \right|_{y'=0} = \left. \frac{\partial C}{\partial y'} \right|_{y'=1} = 0. \tag{8.9}$$

A numerical algorithm has to be used to calculate the colored-particle profiles C(y',t). This has been done by using the function `pdepe` in Matlab®.[49] In case one fixes the dimensionless time t', the diffusion coefficient D can be adjusted to match the experimental results for C with the model predictions.

ii)   Colored-Particle Profiles

The calculated colored-particle profiles are fitted to minimize the squared differences between them and the experimental results and are shown in Figure 8.26. Clearly, the complex shape of the experimentally observed colored-particle profiles (see Figure 8.26c and d) cannot be perfectly fitted for a larger number of blade passages. This is especially true for the regions

near the lower wall and the top of the particle bed (the cause are side-wall effects, i.e., particles from the bottom of the box were forced to the top when the blade was near the vertical side walls to the left and right of the box). This disturbing effect from the side-walls is most pronounced for the large (i.e., 4 mm) glass beads. For this experiment, the dimensionless shear rate of I = 0.034 indicates granular flow in the dense inertial regime. The diffusion model reasonably well predicts the colored-particle profile near the center of the bed (i.e., between approximately y' = 0.2 to y' = 0.8).
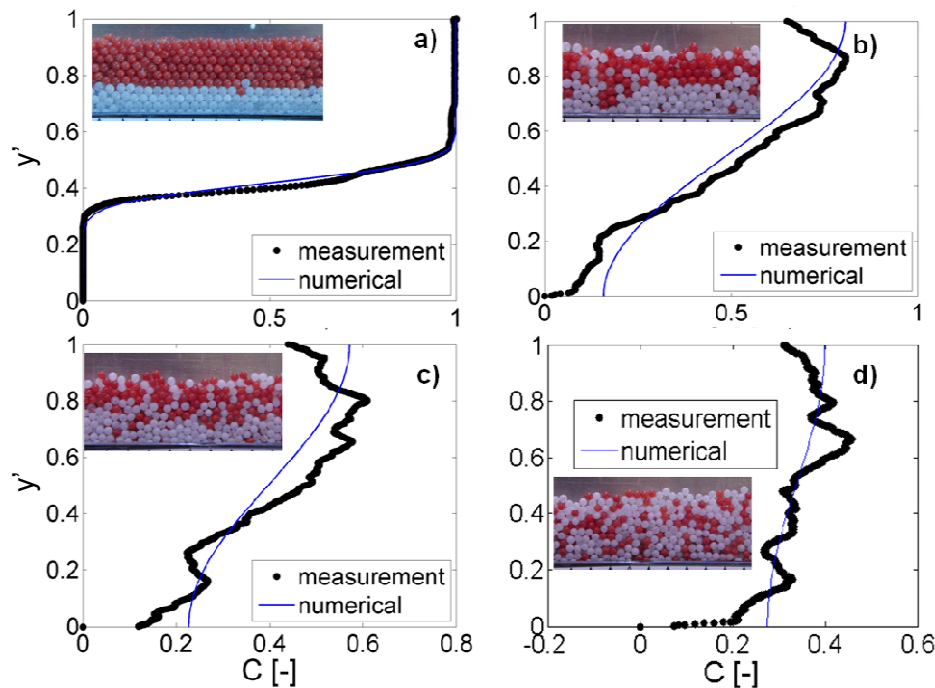
Figure 8.26: Fitted colored-particle profiles of experiment 2 (dry, 4 mm glass beads): initial state (a), after 8 b), 14 (c) and 20 (d) blade passages (I = 0.034).

The colored-particle profiles in Figure 8.27 and Figure 8.28 show significantly less side-wall effects. In these experiments the dimensionless shear rate suggests flow in the quasi-static regime. Especially in Figure 8.27 the fit of the model to the experimental results is excellent, even after 25 blade passages. In case of the wet particles (i.e., in Figure 8.28), it seems that the diffusion model does not very well predict the mixing of the particle bed and red particles are quickly transported downwards. Since the number of red and white particles in the bed is constant, also the area between the curves and the y-axis in Figure 8.28 should be constant. However, this does not seem to be the case for the wet particles, where a large fraction of red particles is observed. This fact may be explained by a preferential movement of red (i.e., top) particles to the front wall. The cause for this motion is unclear, it is speculated that this

motion is due to cohesive forces between the front wall and the particles that induce a secondary motion in the particle bed (i.e., a circulation roll from the top to the bottom).
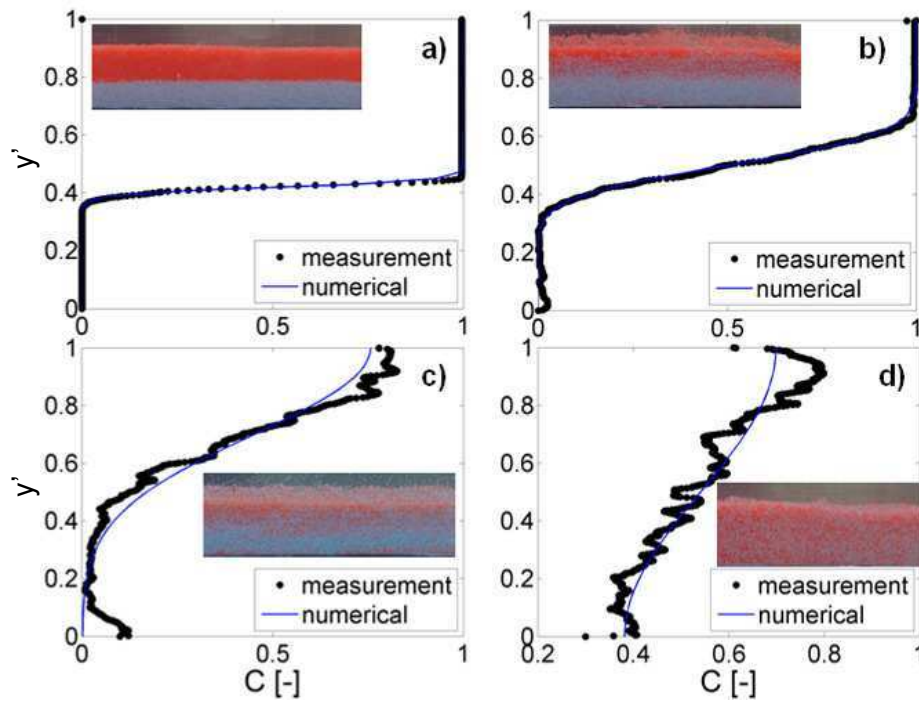
Figure 8.27: Fitted colored-particle profiles of experiment 3 (dry, 0.75-1 mm glass beads): initial state (a), after 8 (b), 14 (c) and 25 (d) blade passages (I = 0.0073).
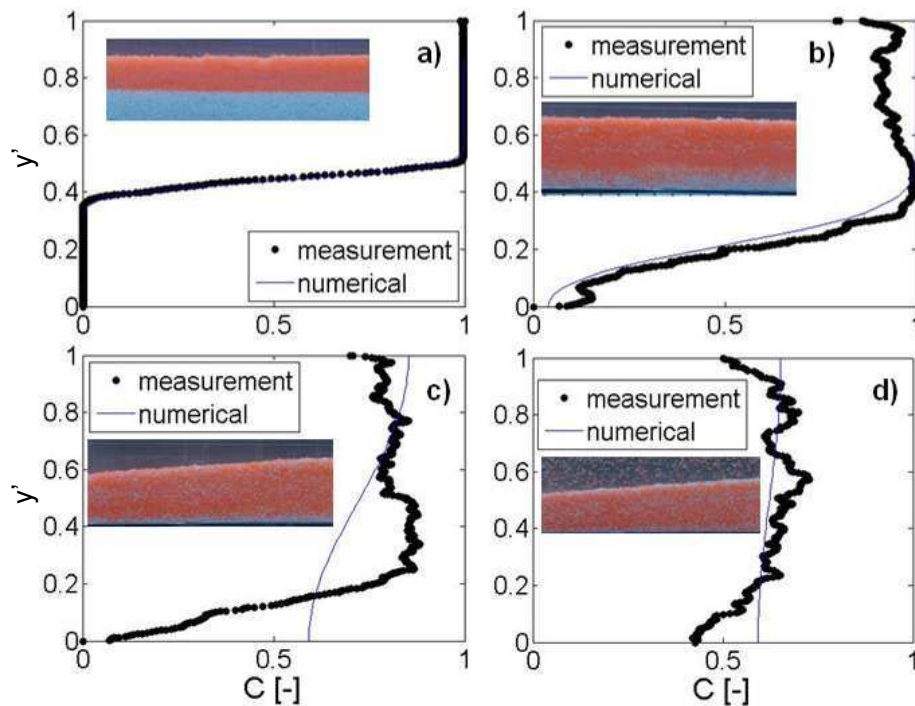
Figure 8.28: Fitted colored-particle profiles of experiment 4 (1 Vol% water, 0.75-1 mm glass beads): initial state (a), after 5 (b), 10 (c) and 15 (d) blade passages (I = 0.0073).

However, the generally faster mixing (compare Figure 8.27c and Figure 8.28d that were obtained for dry and wet particles after a similar number of blade passages) in case of wet particles is clearly visible. This may be explained by (i) a secondary motion in the particle bed that is not present in the dry case and (ii) the formation of agglomerates that are more effectively transported over the height of the particle bed.

iii)   Diffusion Coefficient for Multiple Blade Passages

In Figure 8.29 the values for the measured diffusion coefficient D of experiment 2 and 3 are plotted against the number of runs. The measured data of each experiment is approximated by a trend line based on an exponential equation. It is obvious that the diffusion coefficient D is higher for larger particles, but the slope of the trend line is smaller than the slope of the smaller particle's trend line. The diffusion coefficient for the small (i.e., 1 mm) particles can be described well with an exponential function (resulting in a R^2 value larger than 0.83), whereas the values for the larger particles have a higher deviation around the trend line (i.e., approximately 0.33). The range of the value for the diffusion coefficient for 4 mm particles is from $13 \cdot 10^{-4}$ to $94 \cdot 10^{-4}$, whereas it ranges between $1.25 \cdot 10^{-4}$ and $54 \cdot 10^{-4}$ for the small glass beads. The lowest measured value for the diffusion coefficient of the large particles is therefore about one order of magnitude higher than the minimum value of the smaller particles.
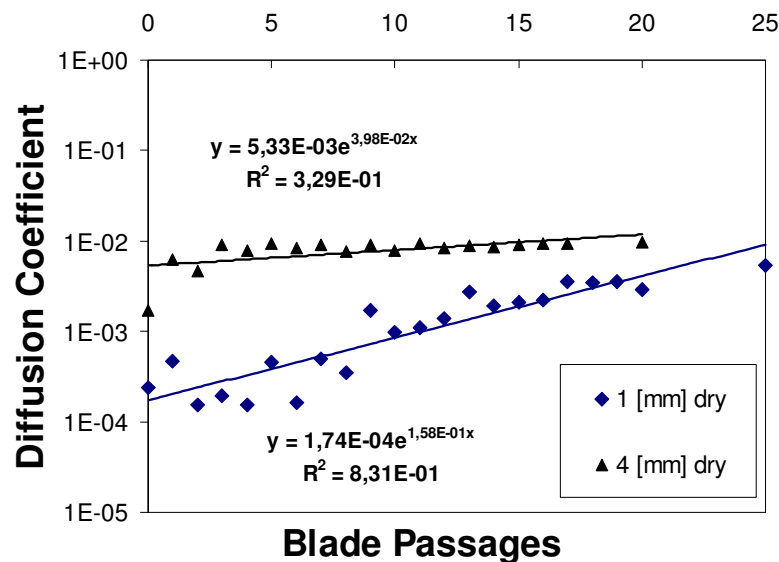
Figure 8.29: Diffusion coefficient D of experiment 2 (dry 4 mm glass beads) and 3 (dry 0.75-1 mm glass beads) plotted against the number of runs.

In Figure 8.30 the diffusion coefficient of dry particles (i.e., experiment 3) is compared with the diffusion coefficient of wet particles with the same diameter (i.e., experiment 4). The

minimum value of the diffusion coefficient D of experiment 4 is $5.4 \cdot 10^{-4}$, the maximum value is $367 \cdot 10^{-4}$. The slope of the trend line of the 4th experiment is much higher which means that self diffusion of wet particles strongly increases during the mixing process. Thus, mixing seems to be strongly accelerated for wet particles. In contrast, the diffusion coefficient of dry particles increases only moderately. This is because in wet particle beds, the particle flow is not dominated by the motion of individual grains, but by the motion of small clumps that form as a result of the cohesive forces. This effect has been observed by various researchers,[13] who studied wet granular flow. Thus, we speculate that the agglomerates behave similar as larger particles that diffuse more easily, a fact that can be also seen in Figure 8.29.
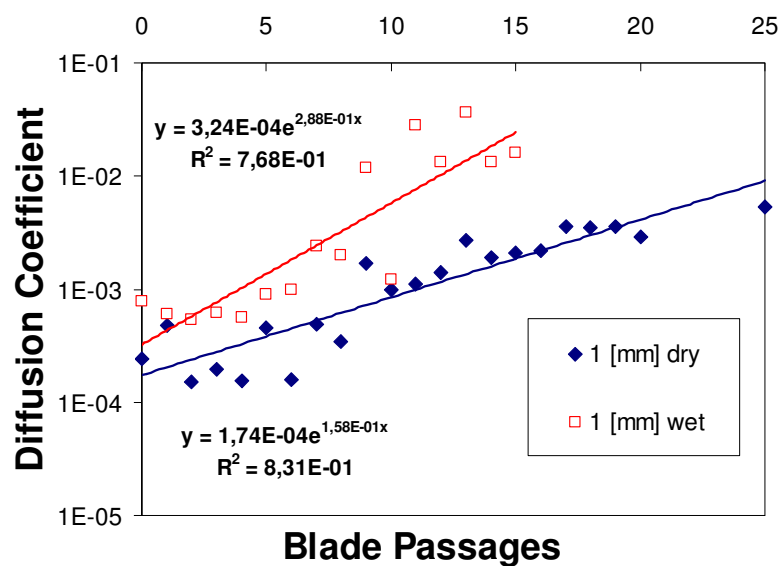
Figure 8.30: Diffusion coefficient _D_ of experiment 3 (dry 0.75-1 mm glass beads) and 4 (wet 0.75-1 mm glass beads) plotted against the number of runs.

8.5 Summary and Conclusions

We have performed well defined experiments on granular flow and mixing using spherical glass beads. The goal was to provide validation data for simulations of granular flow, the latter are typically based on mono-disperse spherical particles with defined mechanical properties (i.e., the friction coefficient and the coefficient of restitution). Hence, the particles were characterized with respect to their mechanical properties. This characterization was also performed for wet glass beads (i.e., a cohesive granular bed of particles) using a powder rheometer. The wet glass beads were stable, i.e., the rheology did not change over time. The powder rheometer also detected differences in the particle size. This was obviously due to the blockage of particles between the impeller of the powder rheometer and the vessel causing an

excessive energy uptake by the particle bed. Coating the particles also led to a detectable change in the rheology of the particle bed. For the coated particles, an increasing energy uptake with decreasing tip speed of the rheometer tool was observed.

Granular particle image velocimetry (gPIV) was used to measure the instantaneous flow field in a bladed mixer, as well as in a two-dimensional single blade system. The following effects were observed:

- The particle size showed a significant effect on the measured instantaneous flow field in the bladed mixer. It is speculated that this is due to (i) the relatively large gaps in case of large particles leading to erratic motion of individual particles at the surface of the particle bed, and (ii) a blockage effect. The latter effect leads to a clearly detectable change in the circumferential velocity distribution that is more homogeneous for larger particles.

- When moisture is added to the glass beads, agglomerates form. This leads to a significant change in the flow field at the top of the particle bed. Thus, the velocity at the top surface decreases and the velocity distribution in circumferential direction gets more homogeneous.

- Changing the fill level has a similar, but much stronger effect. A 100% overfilling of the mixer (i.e., a doubled bed height) leads to a more than 60% reduced mean tangential velocity and a more than 80% reduced velocity fluctuation in tangential direction. This is expected to cause a dramatic reduction in the mixing rate of the mixer which has, however, not been directly measured in our work.

- In contrast, lifting the stirrer (i.e., a decreased coverage of the impeller blades by the particle bed) leads to higher surface velocities, and a characteristic V-shaped, well defined interface between high- and low-velocity regions. It can be expected, that this situation leads to an improved mixing performance.

The single blade experiments were performed in the quasi-static and in the dense inertial regime of granular flow. Time-averaged data of the velocity fields were analyzed and differences between these flow fields were qualitatively interpreted. We conclude that:

- Beside the dimensionless shear rate I, also the relative blade height has a significant impact on the flow pattern.

- Increasing the bed height (i.e., overfilling the mixer) by more than two times the blade height, leads to a significant change in the flow profile and the absolute magnitude of the velocities on top of the particle bed. The recirculation zone then vanishes, and the velocity distribution is less localized compared to the case with a lower filling height.

- The distance between the blade and the bottom of the container did not significantly influence granular flow. This is because the particle bed under the blade was nearly unaffected by the blade motion.

- A change in the blade angle did not significantly affect the flow. However, at a 90° blade angle the particle velocities on top of the particle bed were slightly higher and a recirculation zone in front of the blade was clearly visible. This might improve mixing, i.e., a blade angle of 90° seems to be optimal for efficient mixing.

- The particle size also did not have a significant impact on the time-averaged flow field at an identical bed height, blade angle and blade velocity. Despite the dimensionless shear rate I linearly depends on the particle size, the experiments with different particle sizes (i.e., different values for I) gave nearly identical results. Hence, we conclude that beside I and the relative blade height, also a dimensionless parameter involving the particle size determines the flow of particles over a single blade.

Finally, we performed mixing experiments in the single blade system to show the effect of the particle size and cohesion on the rate of mixing. This rate was quantified using a simple diffusion model, i.e., a self diffusion coefficient has been extracted from the experimental data. We found that:

- The diffusion model fits our experimental data for the particle distribution near the center of the particle bed reasonably well. However, the diffusion coefficient is not constant over time (i.e., the number of blade passages) and shows an exponential increase. This may indicate that the diffusion coefficient is not constant over the bed height (as was assumed in our work) and hence may accelerate the mixing process when particles come into these regions.

- The particle distribution profile for more than approximately ten blade passages shows pronounced oscillations that are not predicted by the diffusion model. This was true for all experiments and may suggest that mixing down to the particle scale could not be achieved with our experiments.

- Small, dry glass beads were most difficult to mix. This may be explained by the different flow regimes that were present due to the different particle sizes (i.e., dense inertial and quasi-static for the large and small glass beads).

- A wet particle bed mixes faster due the formation of large clumps. This larger clumps mix easier in the bed, as they behave like larger particles. Thus, the wet particle flow is not dominated by the motion of single particles but by the motion of agglomerates and the mixing behavior differs significantly from the behavior of dry particles.

While we have attempted to interpret our experimental data with dimensionless parameters, there is still a significant lack of understanding on which parameters influence the particle flow in bladed mixers. This flow seems considerably more complex than other granular flows (i.e., that reported by the GDR Midi group[16]) for which a sound theoretical understanding has been already achieved. Clearly, significantly more experiments must be performed, especially in a single blade system to fully characterize the interdependencies between the dimensionless shear rate, the relative blade height and the particle diameter. To understand industrial-scale mixers, it will be necessary to include multiple blades in the two-dimensional experiments. This is because the blade-to-blade distance in industrial applications is often too small to assume that there is no interaction between the individual blades.

Similarities between the experiments in the bladed mixer and the two-dimensional system could be shown. Thus, in both experiments the bed height had the most pronounced effect and led to a dramatic decrease of the velocity at the top of the particle bed. However, the blocking effect of large particles is not present in the two-dimensional system, and hence, we could not detect significant differences for large and small particles there. However, these differences were clearly visible in the instantaneous flow fields recorded in the bladed mixer. Also, we did not perform two-dimensional granular flow experiments involving the same wet particles as in the bladed mixer. This was because these particles were too sticky and attached to the front wall of the single blade system. Future investigations are necessary to resolve this problem and to observe agglomerate formation induced by single and multiple blades.

8.6 Abbreviations

BFE   Basic Flowability Energy

CCD   Charge Coupled Device

COR	Coefficient of Restitution
DC	Direct Current
FFT	Fast Fourier Transformation
gPIV	Granular Particle Image Velocimetry
IA	Interrogation Area
PETP	Positron Emission Particle Tracking
PIV	Particle Image Velocimetry
PMMA	Poly(methyl-methacrylate)
RAM	Random Access Memory
SE	Specific Energy
SI	Stability Index
SNR	Signal to Noise Ratio
YAG	Yttrium Aluminium Garnet

8.7 Nomenclature

C	fraction of colored particles
D	dimensionless diffusion coefficient
d_{inner}	inner diameter of the cylindrical vessel [m]
d_p	particle diameter [m]
F_N	normal force [N]
g	gravitational acceleration [m/s²]
H_{inner}	inner height of the cylindrical vessel [m]
h	characteristic height [m]
h_{bed}	bed height [m]
h_{blade}	blade height [m]
$h_{stirrer}$	stirrer position [m]

I	dimensionless shear rate
P	normal stress [Pa]
$p_{min,abs}$	minimal absolute pressure [mbar]
r_n	normal distance [m]
Δt	time difference [s]
t'	dimensionless time
T	torque [Nm]
T_{max}	maximal temperature [°C]
T_{min}	minimal temperature [°C]
x, y, z	position [m]
Δx	displacement [m]
y'	dimensionless bed height coordinate
U	velocity vector [m/s]
u_0	tip speed [m/s]
V	characteristic velocity [m/s]
v	velocity [m/s]
v_{box}	box velocity [m/s]
v_{post}	post-collisional velocity [m/s]
v_{pre}	pre-collisional velocity [m/s]
w_R	velocity in radial direction [m/s]
w_{tan}	velocity in tangential direction [m/s]

Greek letters

α	blade angle [°]
$\dot{\gamma}$	shear rate [1/s]

μ   friction coefficient

ρ   bulk density [kg/m³]

8.8 References

(1)   Radl S, Brandl D, Heimburg H, Khinast JG. Granular Flows - How Size Matters. 5th
        Minisymposium Verfahrenstechnik. Vienna, Austria: TU Wien, 2009.

(2)   Radl S, Kalvoda E, Glasser BJ, Khinast JG. Mixing Characteristics of Wet Granular
        Matter in a Bladed Mixer. Powder Technology. 2010; 200:171-189.

(3)   Remy B, Khinast JG, Glasser BJ. Discrete Element Simulation of Free Flowing Grains
        in a Four-Bladed Mixer. AIChE Journal. 2009; 55:2035-2048.

(4)   Remy B, Canty TM, Khinast JG, Glasser BJ. Kinematics of Cohesionless Particulate
        Flows in a Bladed Mixer. Chem Eng Sci. 2009; (submitted).

(5)   Remy B, Glasser BJ, Khinast JG. The Effect of Mixer Properties and Fill Level on
        Granular Flow in a Bladed Mixer. AIChE Journal. 2010; 56:336-353.

(6)   Rognon PG, Roux JN, Naaim M, Chevoir F. Dense flows of cohesive granular
        materials. Journal of Fluid Mechanics. 2008; 596:21-47.

(7)   Zhu HP, Zhou ZY, Yang RY, Yu AB. Discrete particle simulation of particulate
        systems: Theoretical developments. Chem Eng Sci. 2007; 62:3378-3396.

(8)   Zhu HP, Zhou ZY, Yang RY, Yu AB. Discrete particle simulation of particulate
        systems: A review of major applications and findings. Chem Eng Sci. 2008; 63:5728-
        5770.

(9)   Alexander AW, Chaudhuri B, Faqih A, Muzzio FJ, Davies C, Tomassone MS.
        Avalanching flow of cohesive powders. Powder Technology. 2006; 164:13-21.

(10)   Carr RL. Evaluating flow properties of solids. Chemical Engineering. 1965; 72:163-168.

(11)   Conway SL, Lekhal A, Khinast JG, Glasser BJ. Granular flow and segregation in a four-
        bladed mixer. Chem Eng Sci. 2005; 60:7091-7107.

(12)   Faqih AMN, Mehrotra A, Hammond SV, Muzzio FJ. Effect of moisture and magnesium
        stearate concentration on flow properties of cohesive granular materials. International
        Journal of Pharmaceutics. 2007; 336:338-345.

(13)   Lekhal A, Conway SL, Glasser BJ, Khinast JG. Characterization of granular flow of wet
        solids in a bladed mixer. AIChE Journal. 2006; 52:2757-2766.

(14)   Shinbrot T, Alexander A, Muzzio FJ. Spontaneous chaotic granular mixing. Nature.
        1999; 397:675-678.

(15)   Forterre Y, Pouliquen O. Flows of dense granular media. Annual Review of Fluid Mechanics. 2008; 40:1-24.

(16)   GDR Midi. On dense granular flows. European Physical Journal e. 2004; 14:341-365.

(17)   Parker DJ, Leadbeater TW, Fan X, Hausard MN, Ingram A, Yang Z. Positron imaging techniques for process engineering: recent developments at Birmingham. Measurement Science & Technology. 2008; 19.

(18)   Parker DJ, Fan XF. Positron emission particle tracking - Application and labelling techniques. Particuology. 2008; 6:16-23.

(19)   Bagster DF, Bridgwater J. The Flow of Granular Material Over A Moving Blade. Powder Technology. 1970; 3:323-338.

(20)   Bagster DF, Bridgwater J. The measurement of the force needed to move blades through a bed of cohesionless granules. Powder Technology. 1967; 1:189-198.

(21)   Bagster DF. The prediction of the force needed to move blades through a bed of cohesionless granules. Powder Technology. 1970; 3:153-162.

(22)   Freeman R, Fu XW. Characterisation of powder bulk, dynamic flow and shear properties in relation to die filling. Powder Metallurgy. 2008; 51:196-201.

(23)   Herminghaus S. Dynamics of wet granular matter. Advances in Physics. 2005; 54:221-261.

(24)   ASTM. ASTM G99-05(2010) - Standard Test Method for Wear Testing with a Pin-on-Disk Apparatus. West Conshohocken, Pennsylvania, U.S.: American Society for Testing and Materials, 2010.

(25)   Wu XC, Wang QH, Luo ZY, Fang MX, Cen KF. Experimental investigation of interparticle collision in the upper dilute zone of a cold CFB riser. International Journal of Multiphase Flow. 2008; 34:924-930.

(26)   Farkas N, Ramsier RD. Measurement of Coefficient of Restitution Made Easy. Physics Education. 2006; 41:73-75.

(27)   Cross R. The bounce of a ball. American Journal of Physics. 1999; 67:222-227.

(28)   Patel HH, Wu S, Pugh R, Freeman T, Armstrong B, Dave RH. Determining Endpoint for Wet Granulation Using Rheological and Effusivity Measurement. AAPS Annual Meeting.: AAPS, 2009.

(29)   Carlson G, Hancock B. Development of a Material Sparing Method to Determine Powder Permeability to Air. AAPS Annual Meeting.: AAPS, 2008.

(30)   Freeman R. Measuring the flow properties of consolidated, conditioned and aerated powders - A comparative study using a powder rheometer and a rotational shear cell. Powder Technology. 2007; 174:25-33.

(31) Zeilstra C. Granular Dynamics in Vibrated Beds. Enschede, NL: University of Twente, 2007.

(32) Lueptow RM, Akonur A, Shinbrot T. PIV for granular flows. Experiments in Fluids. 2000; 28:183-186.

(33) Jain N, Ottino JM, Lueptow RM. Effect of interstitial fluid on a granular flowing layer. Journal of Fluid Mechanics. 2004; 508:23-44.

(34) Darmana D. On the multiscale modelling of hydrodynamics, mass transfer and chemical reactions in bubble columns. Twente, Netherlands: University of Twente, 2006.

(35) Reynolds GK, Nilpawar AM, Salman AD, Hounslow MJ. Direct measurement of surface granular temperature in a high shear granulator. Powder Technology. 2008; 182:211-217.

(36) Pudasaini SP, Hutter K, Hsiau SS, Tai SC, Wang Y, Katzenbach R. Rapid flow of dry granular materials down inclined chutes impinging on rigid walls. Physics of Fluids. 2007; 19.

(37) Pouliquen O. Velocity correlations in dense granular flows. Physical Review Letters. 2004; 93.

(38) Dijkhuizen W, Bokkers GA, Deen NG, Annaland MV, Kuipers JAM. Extension of PIV for measuring granular temperature field in dense fluidized beds. AIChE Journal. 2007; 53:108-118.

(39) Mori N, Chang K-A. Introduction to MPIV. http://www.oceanwave.jp/softwares/mpiv. 2003.

(40) Sveen JK. An introduction to MatPIV v.1.6.1. http://folk.uio.no/jks/matpiv/. 2004. Oslo, Norway, Dept. of Mathematics, University of Oslo.

(41) Shavit U, Gurka R, Liberzon A. OpenPIV. www.openpiv.net. 2010.

(42) Brandl D. Granulare Particle Image Velocimetry für einen Vakuumtrockner. Graz University of Technology, 2009.

(43) Brandl D. Experimental Investigation of Granular Flow and Mixing. Graz University of Technology, 2010.

(44) Tardos GI, McNamara S, Talu I. Slow and intermediate flow of a frictional bulk powder in the Couette geometry. Powder Technology. 2003; 131:23-39.

(45) Heimburg H. Granular Mixing in a 2D Blade System. Graz University of Technology, 2010.

(46) Lu LS, Hsiau SS. DEM simulation of particle mixing in a sheared granular flow. Particuology. 2008; 6:445-454.

(47) Zik O, Stavans J. Self-Diffusion in Granular Flows. Europhysics Letters. 1991; 16:255-258.

(48) Rosato AD, Lan YD, Richman MW. On the calculation of self-diffusion in vertically agitated granular beds. Powder Technology. 2008; 182:228-231.

(49) Matlab 7.3.0 (R2008a). The Mathworks, Inc., 2008.

"In the book of life, the answers aren't in the back."

(Charlie Brown)

9

Conclusions and Outlook

9.1 Conclusions

Several multiphase systems have been analyzed with respect to their mechanistic modeling. For some applications, there was essentially no previous published work that used a sophisticated mathematical model to predict the outcome of a pharmaceutical production process. This is true, e.g., for spray coating processes, where the coating-tablet interaction has not been studied using state-of-the-art computational tools in the past.

In other areas, simple models are already in use that focus on predicting the outcome of a process based on experimentally determined correlations. For example, the use of the population balance equation (PBE) to model granulation processes (e.g., to predict the distribution of the granules size) is widespread in the pharmaceutical industry. Despite these models are extremely useful, there is always some empiricism involved. Granular flow is typically completely neglected when using the PBE - thus these models are not, and can never be, "fully" predictive on their own. Predictive models for granular flow processes have the major benefit to deliver information on the mean and fluctuating particle velocities depending on the system (e.g., particle size, moisture content) and process (e.g., stirrer speed) parameters. These data themselves can be useful for various purposes (e.g., to improve design and operation of equipment) as has been shown in Chapter 7 of this thesis. Furthermore, the information from granular flow models can be supplied to the above mentioned "simpler" models (e.g., the PBE) for improved modeling on a larger scale. This so-called multiscale approach is well-known in many branches of chemical engineering nowadays. In this thesis there has been no attempt to follow such an approach for granular flows. Instead, the focus was to provide granular flow simulations, as well as experimental evidence on some cause-and-effect relationships. Already these investigations required huge amounts of time, and the detailed prediction of dense granular flows with computer models turned out to be relatively imprecise. This is clearly due to the large number of variables involved (e.g., the number of particles having an individual size, shape, etc., already does not allow a "direct" description of bulk solids) and the inability to simulate the real system directly (a larger particle size had to be used in the simulation). Clearly, current particle-based simulation tools for dense granular flows have severe limitations in the total numbers of particles to be simulated. Experimental evidence is necessary to justify simulations using a significantly lower amount of particles (i.e., several orders of magnitude) as in reality.

The experimental technique used for granular flows, i.e., granular particle image velocimetry, could reveal some of these particle-size effects. Also, it was demonstrated that gPIV is able to measure velocity fields of transparent and colored glass beads under dry and wet conditions. However, there are clear limitations to the image-based experimental technique used in this work. For example, gPIV cannot distinguish between the translational and rotational motion of particles. This is due to the fact, that in the gPIV method no individual particles are tracked, but a certain pattern on the surface of the granular bed is observed. For large particles with a non-uniform color on their surface, the measured "surface" velocity may not be exactly the translational motion of the particles but may also contain some contribution of particle rotation. Also, there is no possibility to measure velocities inside of the particle bed. Furthermore, to record three-dimensional velocity fields would require a second set of image data, as well as more sophisticated software - both was not available.

Chapters 4 to 6 of this thesis were dedicated to provide the basis for a rigorous multiscale model for chemical reactions in bubbly flows. Such a model should be based on a particle-based (i.e., Lagrangian) description of the bubbles in order to generate detailed information of the local flow situation. The best strategy to bridge the scale gap seems to be to adopt simple models (e.g., the film model) and calibrate them with more detailed information (e.g., from Direct Numerical Simulations). Such a calibrated model alone can be already very useful for parameter studies of complex reactive systems. The coupling of these linking models to particle-based simulations yields an extremely powerful tool to study reactions in multiphase reactors. It was demonstrated, that lab- to pilot-scale equipment (i.e., a bubble column with 60 L volume) can be studied with this approach. However, similar restrictions on the total number of particles (compared to those for granular flows) apply to bubbly flows. The study of industrial-scale problems is currently not possible, and bubble-swarm approaches and statistical collision models have to be used in future.

9.2 Outlook

9.2.1 Simulation Tools

It can be expected that particle-based simulation methods will gain significant more attention compared to a continuum description of the dispersed phase in multiphase systems. Particle-based methods provide a good compromise between accuracy and the feasibility to be applied to industrial-scale problems. The major challenge will be to extend the current models to

industrial-scale processes, in which billions and more particles have to be described. This will require the modeling of a particle (or a bubble) swarm as a single Lagrangian object to be followed. This approach is already in use for, e.g., spray modeling. However, the extension to dense coalescing systems seems to be challenging. Besides describing more particles in a system, it will be necessary to improve the calculation of particle-particle interactions (i.e., primarily the collision frequency and the associated contact forces). Statistical approaches will have to be adopted, extended to systems with coalescence and breakage and finally incorporated into an appropriate software code.

The coupling of a sophisticated particle-based simulation tool with a module for chemical reactions will require the use of a flexible software platform. The library "OpenFOAM" has already been used for this thesis and Universities (e.g., the TU München, Germany), as well as major companies (BASF AG, Germany) started in investing into this open-source platform. Mid- and long-term cooperations with these partners should guarantee a sustainable development of simulation tools that are useful for the prediction of processes in complex multiphase systems.

Direct numerical simulations (DNS) of flow and mass transfer will remain a tool for Universities and research institutions. The future challenge will be to filter out relevant data from the enormous data streams generated by these simulations. More effort should be devoted to deriving closure models, e.g., for LES, based on DNS results for reactive systems. Otherwise, the understanding gained from these costly simulations cannot be directly applied to engineering problems.

9.2.2 Experimental Methods for Granular Flows

Experimental methods to investigate the flow of bulk solids should be further developed into two major directions. First, experiments should be designed with the goal to validate simulation results. Especially in the area of wet granular flows, e.g., it is still necessary to assume the distribution of the liquid in a moving granular bed. Experiments, e.g., based on fast x-ray tomography, are necessary to obtain more information about the liquid distribution in agitated granular beds. Also the forces associated with different shapes of capillary bridges (especially in the funicular state where liquid bridges between more than two particles exist), as well as their effect on the rheology of the particle bed need more investigation. Specifically, such investigations could be done using an advanced capillary force measurement device that can handle single particles, as well as particle assemblies on a suitable microbalance. Also,

powder rheometers and shear cells may be useful to provide validation data for simulations. Last but not least, high-speed imaging and appropriate post-processing is a relatively cheap method to obtain large amounts of data for granular flows. To improve the quality of this data and to check their reproducibility are also necessary future goals.

Second, future work should focus on tools to characterize the state of a granular flow process. The knowledge gained during this thesis could be useful to setup an image-based system to monitor, e.g., granulation processes. This will require robust image acquisition and illumination hardware, as well as smart software to interpret the raw image data, the calculated velocity distribution or even the properties of single particles (e.g., the color distribution on the surface of a tablet). Also, it would be interesting to measure the rotation rate of particles in industrial equipment. Measuring the rate of rotation of particles in process equipment is expected to be useful for, e.g., tablet coaters, where the homogeneity of the film on a single tablet or tablet attrition is of interest.

Acknowledgement

A   Mass Transfer Enhancement and Selectivity using Film Theory

A.1 Governing Equations

In this appendix the mathematical framework for a simplified analysis of an irreversible consecutive reaction network near a gas liquid interface is provided. For this purpose the film theory is used to model the mass transfer in the liquid-phase boundary layer.

There exists a broad basis of literature in the field of mass transfer involving chemical reactions, e.g., the book of Westerterp et al.[1] For example, Bhat et al.[2] analyzed mass transfer and complex chemical reaction using film and penetration theory. Their results show that film theory can provide a reasonable prediction of the mass transfer enhancement factors. Later Bhat et al.[3] applied their model to unequal diffusivities and compared their results to literature data for the chlorination of p-cresol. The strong influence of mass transfer on the selectivity of the reaction was illustrated by them. However, their results did not provide an analytical (or semi-analytical) solution for determining the selectivity of the reaction. Onda et al.[4] performed an analysis of arbitrary irreversible consecutive chemical reactions with mass transfer. The mass transfer enhancement factor was calculated using a semi-analytic solution procedure requiring the simultaneous solution of three algebraic equations. Their technique is used as a starting point to predict the selectivity of two consecutive reactions near a gas-liquid interface. In contrast to Onda et al.,[4] we allow the bulk concentration of the intermediate product R to be non-zero. This is important as accumulated intermediate product in the bulk changes the concentration profiles and the selectivity of the reaction network in the liquid-phase boundary layer. We also consider different diffusion coefficients for each species i.

The reaction network considered consists of two consecutive hydrogenations:

$$\nu_{H_2} \cdot H_2(g) + \nu_A \cdot A(l) \overset{r_1}{\rightarrow} \nu_R \cdot R(l) \tag{A.1}$$

$$\nu_{H_2} \cdot H_2(g) + \nu_R' \cdot R(l) \overset{r_2}{\rightarrow} \nu_S \cdot S(l) \tag{A.2}$$

The general rate laws for reaction 1 and 2 are:

$$r_1 = k_1 \cdot c_{H_2}^m \cdot c_A^n \tag{A.3}$$

$$r_2 = k_2 \cdot c_{H_2}^p \cdot c_R^q \tag{A.4}$$

Note that the reaction network considered in Chapter 4 is a special case of Eqs. A.1-A.2. The differential material balances in dimensionless form can be written as

$$0 = \frac{\partial^2 \bar{c}_{H_2}}{\partial \bar{x}^2} - \nu_{H_2} \cdot Ha^2 \left(\bar{c}_{H_2}{}^m \cdot \bar{c}_A{}^n + K_2 \cdot \bar{c}_{H_2}{}^p \cdot \bar{c}_R{}^q \right) \tag{A.5}$$

$$0 = \frac{\partial^2 \bar{c}_A}{\partial \bar{x}^2} - \nu_A \cdot Ha^2 \cdot \frac{D_{H_2}}{D_A} \cdot \bar{c}_{H_2}{}^m \cdot \bar{c}_A{}^n \tag{A.6}$$

$$0 = \frac{\partial^2 \bar{c}_R}{\partial \bar{x}^2} + \nu_R \cdot Ha^2 \cdot \frac{D_{H_2}}{D_R} \cdot \left(\bar{c}_{H_2}{}^m \cdot \bar{c}_A{}^n - \frac{\nu_R'}{\nu_R} \cdot K_2 \cdot \bar{c}_{H_2}{}^p \cdot \bar{c}_R{}^q \right). \tag{A.7}$$

All concentrations have been made dimensionless with the concentration of the liquid phase reactant in the bulk $c_{A,0}$. The Hatta number has been defined as

$$Ha^2 = \frac{k_1 \cdot c_{A,0}{}^{m+n-1} \cdot D_{H_2}}{k_l{}^2} = \frac{k_1 \cdot c_{A,0}{}^{m+n-1} \cdot \delta^2}{D_{H_2}} \tag{A.8}$$

The boundary layer thickness δ is defined as $\delta = D_{H_2} / k_l$ and has been used to make the film thickness coordinate dimensionless, i.e., $\bar{x} = x / \delta$. The parameter K_2 characterizes the relative rate of the second reaction:

$$K_2 = \frac{k_2}{k_1} \cdot c_{A,0}{}^{p+q-m-n} \tag{A.9}$$

The boundary conditions are the constant concentrations in the bulk (subscript 0) and the dimensionless interface concentration of hydrogen $\bar{c}_{H_2,i}$. Furthermore, we assume that A, R and S cannot evaporate, and therefore, have a zero gradient at the gas-liquid interface. Using this boundary conditions, the set of ordinary differential equations (Eqs. A.5 – A.7) can be solved numerically for the unknown dimensionless concentration profiles $\bar{c}_{H_2}, \bar{c}_A, \bar{c}_R$. However, also a semi-analytical solution procedure can be used instead to solve this reaction-diffusion problem.

A.2 Semi-Analytical Solution Strategy

The main influence factors for the selectivity in the film are the dimensionless concentrations of reactant A, i.e., $\bar{c}_{A,i}$, and intermediate Product R, i.e., $\bar{c}_{R,i}$, at the interface. Hence, to predict the selectivity, the characteristic values for these concentrations at the boundaries are

of major importance. The mass transfer enhancement factor E_a describes the influence of the reaction on mass transfer. This factor is proportional to the negative gradient of the hydrogen concentration profile at the interface. The details of the semi-analytical solution procedure are described in Onda et al.[4] Basically, three equations have to be solved simultaneously:

$$E_a = 1 - \frac{\overline{c}_{H_2,0}}{\overline{c}_{H_2,i}} - \frac{\nu_{H_2}}{\overline{c}_{H_2,i} \cdot D_{H_2}} \cdot \left[\left(1 + \frac{\nu_R}{\nu_R'} \right) \cdot \frac{D_A}{\nu_A} \cdot \left(\overline{c}_{A,i} - 1 \right) + \frac{D_R}{\nu_R'} \cdot \left(\overline{c}_{R,i} - \overline{c}_{R,0} \right) \right] \tag{A.10}$$

$$E_a = \frac{\sqrt{M_3\left(\overline{c}_{A,i}, \overline{c}_{R,i}\right)} \cdot \left[1 - \frac{\overline{c}_{H_2,0}}{\overline{c}_{H_2,i}} \cdot \sec h\left(\sqrt{M_3\left(\overline{c}_{A,i}, \overline{c}_{R,i}\right)} \right) \right]}{\tanh\left(\sqrt{M_3\left(\overline{c}_{A,i}, \overline{c}_{R,i}\right)} \right)} \tag{A.11}$$

$$\overline{c}_{R,i} = \frac{\overline{c}_{R,0} + \frac{D_A}{D_R} \cdot \frac{\nu_R}{\nu_A} \cdot \left(1 - \overline{c}_{A,i}\right)}{1 + \frac{D_A}{D_R} \cdot \frac{\nu_R'}{\nu_A} \cdot T\left(\overline{c}_{A,i}, \overline{c}_{R,i}\right) \cdot \frac{T\left(\overline{c}_{A,i}, \overline{c}_{R,i}\right) + \frac{5}{6}}{T\left(\overline{c}_{A,i}, \overline{c}_{R,i}\right) + 1} \cdot \frac{1 - \overline{c}_{A,i}}{\overline{c}_{A,i}}} . \tag{A.12}$$

The functions M_3 and T are defined as:

$$M_3\left(\overline{c}_{A,i}, \overline{c}_{R,i}\right) = \frac{2}{m+1} \cdot \frac{\nu_{H_2} \cdot k_1 \cdot c_{A,0}^{m+n-1} \cdot \delta^2 \cdot \overline{c}_{H_2,i}^{m-1}}{D_{H_2}} \cdot \left[\overline{c}_{A,i}^n + \frac{m+1}{p+1} \cdot K_2 \cdot \left(\frac{1}{\overline{c}_{H_2,i}} \right)^{q-n} \cdot \overline{c}_{R,i}^q \right] \tag{A.13}$$

$$T\left(\overline{c}_{A,i}, \overline{c}_{R,i}\right) = K_2 \cdot \left(\frac{1}{\overline{c}_{H_2,i}} \right)^{q-n} \cdot \frac{\overline{c}_{R,i}^{q-1}}{\overline{c}_{A,i}^{n-1}} . \tag{A.14}$$

Eq. A.10 can be found from an integral material balance over the film width. Eq. A.11 is obtained from an approximation for the enhancement factor taking into account a modified Hatta number $\sqrt{M_3}$. Eqn. A.12 is derived from a given concentration profile (see Onda et al.[4]) using the differential balances for the liquid phase reactant A and the intermediate product R. M_3 and T are weak functions of the interfacial concentrations of species A and R. The nonlinear system of equations (Eqs A.10 - A.12) can be solved only numerically, e.g., using a Newton algorithm.

A.3 Results

The semi-analytical solution was compared with the exact solution that is obtained by numerical solution of the boundary value problem Eq. A.5 – A.7. A plot of the computed

mass transfer enhancement factor E_a is given in Figure A.1. The mass transfer enhancement factor E_a is defined as

$$E_a = \frac{-D_{H_2} \cdot \frac{\partial c_{H_2}}{\partial x}\bigg|_{x=0}}{k_l \cdot c_{H_2,i}} = \frac{\partial \bar{c}_{H_2}}{\partial \bar{x}}\bigg|_{\bar{x}=0} \cdot \frac{-1}{\bar{c}_{H_2,i}},$$ (A.15)

and thus, can be calculated using the gradient of the dimensionless hydrogen concentration profile at the gas-liquid interface. As can be seen from the results, the agreement between semi-analytical and exact solution is very good. The curve for $\bar{c}_{R,0} = 0$ coincides with results reported by Onda et al.[4]
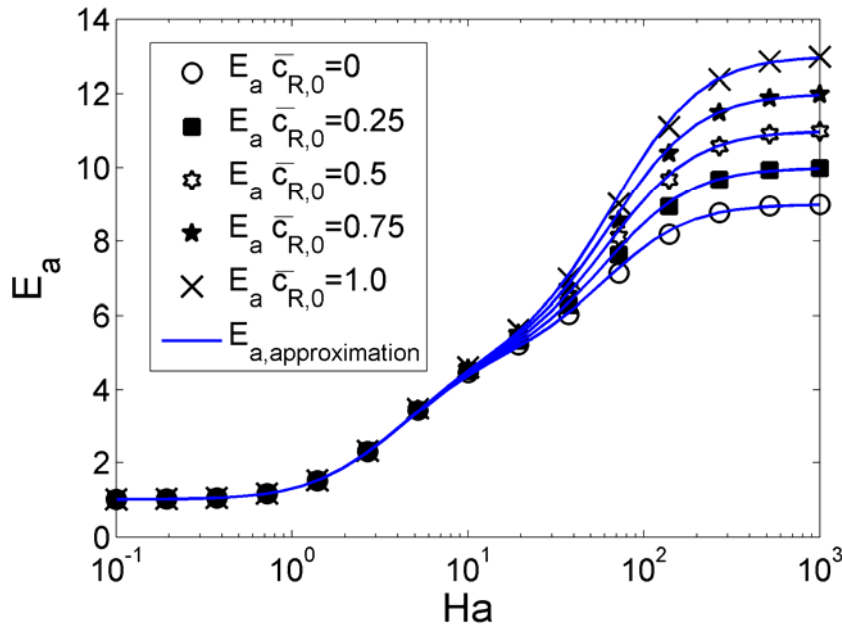
Figure A.1: Mass transfer enhancement factors as a function of the Hatta number for different intermediate product concentrations in the liquid bulk.

In addition to the mass transfer enhancement, the selectivity towards the final product S can be evaluated. We have defined the differential selectivity towards final product S as

$$\sigma' = \frac{\dot{N}_S}{\dot{N}_R + \dot{N}_S}.$$ (A.16)

$\dot{N}_R$ and $\dot{N}_S$ denote the net formation rate of intermediate product R and final product S in the film, respectively. The net formation rate has the units [kmol/m².s], i.e., is defined per unit interfacial area. The net formation rate of S can be calculated from

$$\dot{N}_S = \nu_S \cdot \delta \cdot \int_0^1 r_2(\overline{x}) \cdot d\overline{x} , \qquad (\text{A.17})$$

whereas the net formation rate of intermediate product R is:

$$\dot{N}_R = \nu_R \cdot \delta \cdot \int_0^1 r_1(\overline{x}) \cdot d\overline{x} - \nu_R' \cdot \delta \cdot \int_0^1 r_2(\overline{x}) \cdot d\overline{x} . \qquad (\text{A.18})$$

Thus, the selectivity can be evaluated as

$$\sigma' = \frac{\nu_S \cdot \displaystyle\int_0^1 r_2(\overline{x}) \cdot d\overline{x}}{\nu_R \cdot \displaystyle\int_0^1 r_1(\overline{x}) \cdot d\overline{x} + (\nu_S - \nu_R') \cdot \displaystyle\int_0^1 r_2(\overline{x}) \cdot d\overline{x}} . \qquad (\text{A.19})$$

The shape of the concentration profiles in the film has to be assumed to calculate the integral reaction rates and hence the selectivity. In this work the concentration profiles are approximated with straight lines in two separate zones, i.e., (i) a zone close to the gas-liquid interface (referred to as reaction zone) and (ii) a zone next to the liquid bulk phase. The thickness δ_r of the reaction zone is defined by:

$$\overline{x}_r = \frac{\delta_r}{\delta} = \frac{-c_{H_2,i}}{\left. \dfrac{\partial c_{H_2}}{\partial x} \right|_{x=0}} \cdot \frac{1}{\delta} = \frac{1}{E_a} \qquad (\text{A.20})$$

This definition is based on the linearization of the concentration profile at the gas-liquid interface. Under this assumption the integral reaction rates can be computed analytically, yielding

$$\int_0^1 r_1(\overline{x}) \cdot d\overline{x} = k_1 \cdot c_{A,0}{}^{m+n} \cdot \overline{c}_{H_2,i}{}^{m} \cdot \overline{c}_{A,i}{}^{n} \cdot \left[\frac{\overline{x}_r}{m+1} \cdot \frac{\left(\overline{c}_{H_2,0} \middle/ \overline{c}_{H_2,i} \right)^{m+1} - 1}{\overline{c}_{H_2,0} \middle/ \overline{c}_{H_2,i} - 1} + \frac{1-\overline{x}_r}{n+1} \cdot \left(\overline{c}_{H_2,0} \middle/ \overline{c}_{H_2,i} \right)^{m} \cdot \frac{\left(\overline{c}_{A,0} \middle/ \overline{c}_{A,i} \right)^{n+1} - 1}{\overline{c}_{A,0} \middle/ \overline{c}_{A,i} - 1} \right]$$

$$(\text{A.21})$$

and

$$\int_0^1 r_2(\overline{x}) \cdot d\overline{x} = k_2 \cdot c_{A,0}{}^{p+q} \cdot \overline{c}_{H_2,i}{}^{p} \cdot \overline{c}_{R,i}{}^{q} \cdot \left[\frac{\overline{x}_r}{p+1} \cdot \frac{\left(\overline{c}_{H_2,0} \middle/ \overline{c}_{H_2,i} \right)^{p+1} - 1}{\overline{c}_{H_2,0} \middle/ \overline{c}_{H_2,i} - 1} + \frac{1-\overline{x}_r}{q+1} \cdot \left(\overline{c}_{H_2,0} \middle/ \overline{c}_{H_2,i} \right)^{p} \cdot \frac{\left(\overline{c}_{R,0} \middle/ \overline{c}_{R,i} \right)^{q+1} - 1}{\overline{c}_{R,0} \middle/ \overline{c}_{R,i} - 1} \right]$$

$$(\text{A.22})$$

In Figure A.2 we compare this approximate semi-analytical solution (σ'_{approx}) for the selectivity with an exact numerical calculation (σ'_{num}). Clearly, the agreement is less accurate but seems to be still acceptable for estimating the selectivity (Figure A.2). The relative error between the two solutions is less than 25% for Hatta number smaller than two. For Hatta numbers higher than 2, the relative error can be up to 50%. Due to the fact, that the semi-analytical solution is based on simplified concentration profiles, the interfacial concentrations in this case are not accurate for high Hatta numbers. The situation gets worse if the Hatta number is very high, e.g. above 100.
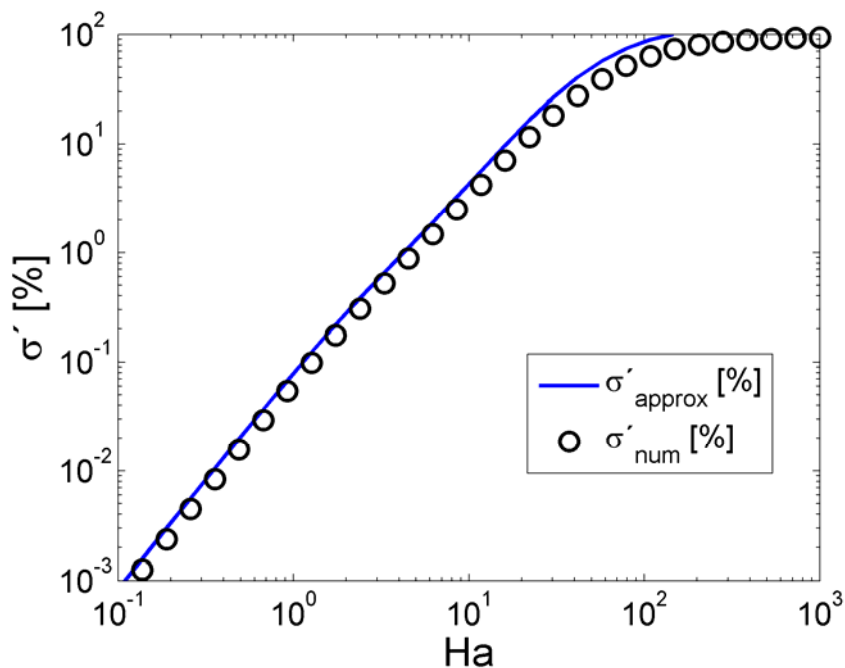
Figure A.2: Comparison of the approximate semi-analytical solution and the numerical calculation for the selectivity in the film.

A.4 References

(1) Westerterp KR, van Swaaij WPM, Beenackers AACM. Chemical Reactor Design and Operation (2nd edition). Norwich, GB: John Wiley & Sons, 1984.

(2) Bhat RDV, van Swaaij WPM, Kuipers JAM, Versteeg GF. Mass transfer with complex chemical reaction in gas-liquid systems - I. Consecutive reversible reactions with equal diffusivities. Chem Eng Sci. 1999; 54:121-136.

(3) Bhat RDV, van Swaaij WPM, Kuipers JAM, Versteeg GF. Mass transfer with complex chemical reaction in gas-liquid systems - II: Effect of unequal diffusivities on consecutive reactions. Chem Eng Sci. 1999; 54:137-147.

(4) Onda K, Sada E, Kobayash T, Fujine M. Gas Absorption Accompanied by Complex Chemical Reactions: 2. Consecutive Chemical Reactions. Chem Eng Sci. 1970; 25:761-768.

B   Verification of the Particle Tracking Algorithm

B.1 Lift Force Verification

The lift force model used mimics the action of Saffman forces on the particle due to a velocity gradient in the liquid phase. Higher velocity differences between particle and liquid give rise to a low pressure whereas low velocity differences lead to a high pressure in the vicinity of a bubble. Hence, a bubble located at y = 0 moving with $\boldsymbol{U}_{rel} = \boldsymbol{U}_T = (0,0,U_T)$ in a flow field with $U_{Liq} = (0,0,-y \cdot \omega_x)$ will migrate in positive y-direction. This liquid-phase flow field is represented by a vorticity vector equal to $\boldsymbol{\omega} = (-\omega_x,0,0)$ and is illustrated in Figure B.1.
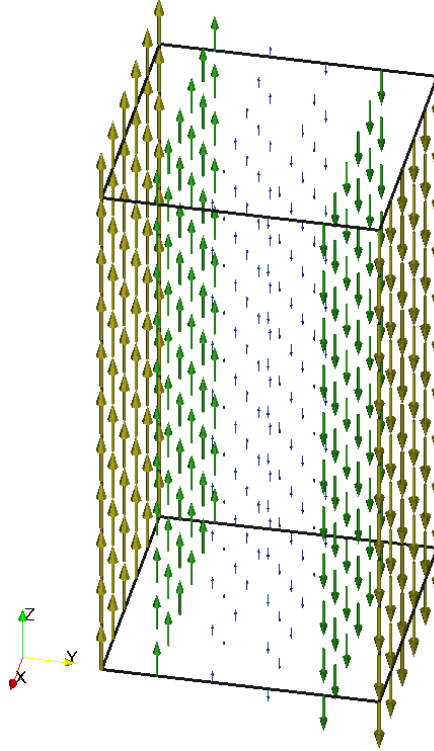
Figure B.1: Schematic representation of the liquid-phase flow field used for the verification of the lift force model implementation.

The lift force for this case is

$$\mathbf{F}_L = -C_L \cdot \rho_L \cdot V_p \cdot \mathbf{U_{rel}} \times \boldsymbol{\omega} = C_L \cdot \rho_L \cdot V_p \cdot U_T \cdot \omega_x \cdot \begin{pmatrix} 0 \\ 1 \\ 0 \end{pmatrix}. \qquad (\text{ B.1 })$$

At steady-state this force will be in equilibrium with the drag force in the y-direction, resulting in a constant migration velocity $U_{migr,y}$.

In Eqn. B.1, V_P and ρ_L is the volume of the particle and the density of the continuous phase, respectively.

$$\boldsymbol{F}_{L,y} + \boldsymbol{F}_{D,y} = 0 \tag{B.2}$$

$$U_{migr,y} = \frac{C_L \cdot \rho_L \cdot V_p \cdot U_T \cdot \omega_x}{C_D \cdot 0.5 \cdot \rho_L \cdot |\boldsymbol{U_{rel}}| \cdot A_{cross}} \tag{B.3}$$

Here, A_{cross} is the cross-sectional area of the particle. For a spherical particle the migration velocity is:

$$U_{migr,y} = \frac{4 \cdot C_L}{3 \cdot C_D} \cdot d_p \cdot \omega_x \tag{B.4}$$

This is true under the assumption that the terminal rise velocity is much bigger than the migration velocity such that U_{rel} can be set equal to U_T. The parameters of the test case are summarized in Table B.1 and the results are shown in Figure B.2.

Parameter	Value
d_p	0.01 m
U_T	0.543 m/s
Re_p	5450
ω_x	1 1/s
C_D	0.44
C_L	0.53
$U_{migr,y}$	0.0161 m/s

Table B.1: Parameters for the verification of the lift force model implementation.
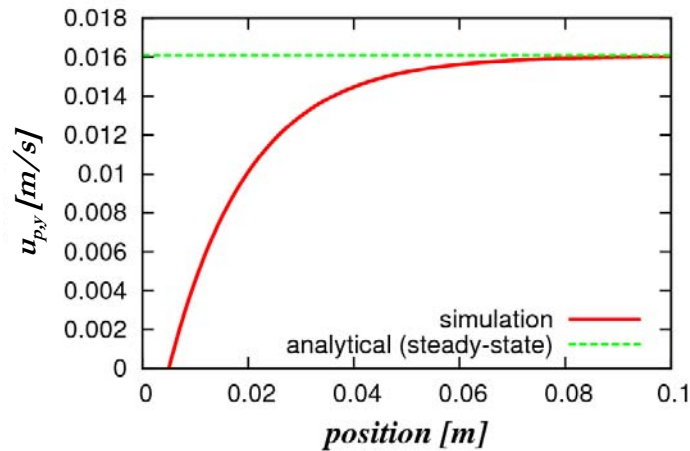
Figure B.2: Particle velocity in y-direction vs. the particle position for the lift force test case.

B.2 Gravitational Settling

The settling of a spherical particle in a quiescent fluid at small Reynolds numbers has been used to verify the drag force implementation. The analytical solution is (from Hu[1]):

$$u_p(t) = (u_{p,0} - g \cdot \tau_p) \cdot \exp[-t/\tau_p] + g \cdot \tau_p, \quad \text{and} \tag{B.5}$$

$$x_p(t) = (u_{p,0} - g \cdot \tau_p) \cdot \tau_p \cdot (1 - \exp[-t/\tau_p]) + g \cdot \tau_p \cdot t + x_{p,0}, \tag{B.6}$$

with

$$\tau_p = \frac{\rho_p \cdot d_p^2}{18 \cdot \mu}. \tag{B.7}$$

Here, u_p and x_p are the particle settling velocity and the particle position, respectively. The test case parameters are defined in Table B.2 and the results are shown in Figure B.3.

Parameter	Value
d_p	$50 \cdot 10^{-6}$ m
ρ_p	1,000 kg/m³
ρ_{amb}	1.0 kg/m³
μ	$1.0 \cdot 10^{-5}$ Pa·s
g	9.81 m/s²
C_D	$24/Re_p$

Table B.2: Parameters for the gravitational settling test case.
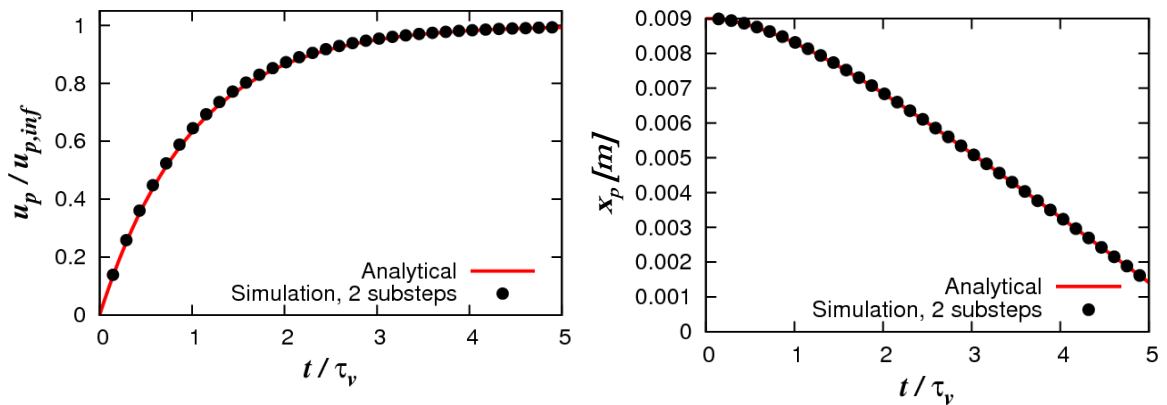
Figure B.3: Particle velocity (left) and position (right) for the gravitational settling test case (a time step of 0.5 ms for particle tracking was used resulting in a maximum relative error of the velocity prediction of 1.06%, the particle velocity has been made dimensionless with the steady-state settling velocity $u_{p,inf}$ = g·τ_p).

B.3 Particle Injection into a Uniform Cross Flow

The injection of a water droplet into air at small Reynolds numbers was analyzed (the setup is illustrated in Figure B.4). The analytical solution for the velocities and positions in x- and y-direction are (from Hu[1]):

$$u_p(t) = (u_{p,0} - U) \cdot \exp[-t/\tau_p] + U \qquad\qquad (\text{B.8})$$

$$v_p(t) = v_{p,0} \cdot \exp[-t/\tau_p] \qquad\qquad (\text{B.9})$$

$$x_p(t) = \tau_p \cdot (u_{p,0} - U) \cdot (1 - \exp[-t/\tau_p]) + U \cdot t + x_{p,0} \qquad\qquad (\text{B.10})$$

$$y_p(t) = \tau_p \cdot v_{p,0} \cdot (1 - \exp[-t/\tau_p]) + y_{p,0} \qquad\qquad (\text{B.11})$$

The particle relaxation time τ_p has been already defined in Eqn. B.7.
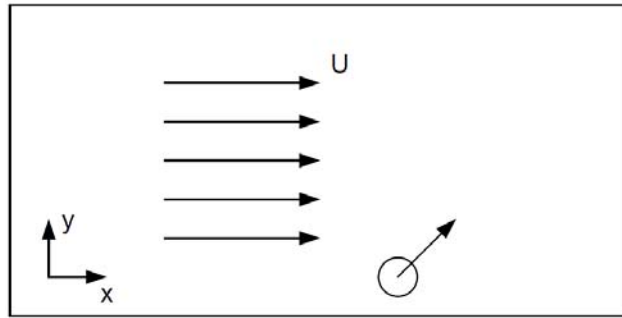
Figure B.4: Schematic representation of the test case for particle injection into a cross flow.[1]

Test case parameters are defined in Table B.3 and the results are shown in Figure B.5.

Parameter	Value
d_p	$100 \cdot 10^{-6}$ m
$(u_{p,0}, v_{p,0})$	(0, 0.05) m/s
U	0.01 m/s]
ρ_p	1,000 kg/m³
ρ_{amb}	1.0 kg/m³
μ	$1.0 \cdot 10^{-5}$ Pa$\cdot$s
x (domain size)	1.0 m
y, z (domain size)	0.3 m
C_D	$24/Re_p$

Table B.3: Parameters for the particle injection test case.
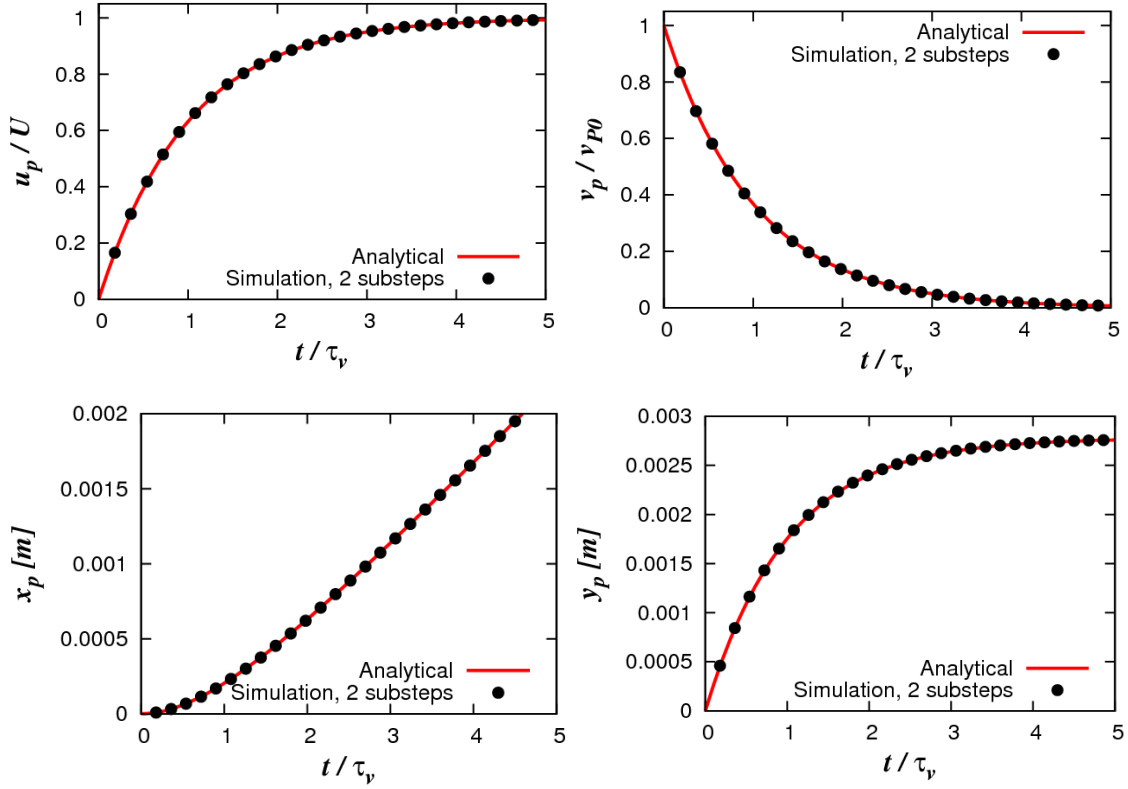
Figure B.5: Particle velocity (top row) and position (bottom row) for the particle injection test case (a time step of 0.25 ms for particle tracking was used resulting in a relative error of the velocity prediction below 0.15%).

B.4 Particle Motion in an Oscillating Flow

The motion of an inertial particle in a spatially homogeneous, but unsteady flow field described by

$$u(t) = U_0 \cdot \sin(\omega \cdot t) \tag{B.12}$$

at small Reynolds numbers has been studied. This enables the verification of the particle tracking algorithm in an unsteady continuous-flow situation. The analytical solution for the velocity in x-direction and the particle position for $t \gg \tau_p$ is (adapted from Hu[1]):

$$u_p(t) = \frac{U_0}{\left[1 + (\omega \cdot \tau_p)^2\right]^{1/2}} \cdot \sin(\omega \cdot t + \phi) + \left(u_{P,0} + \frac{U_0 \cdot \omega \cdot \tau_p}{1 + (\omega \cdot \tau_p)^2}\right) \cdot \exp\left[-t/\tau_p\right], \tag{B.13}$$

with

$$\phi = \arctan(-\omega \cdot \tau_p), \text{ and} \tag{B.14}$$

$$x_p(t) = \bar{x} - \frac{U_0}{\omega \cdot \left[1 + (\omega \cdot \tau_p)^2\right]^{1/2}} \cdot \cos(\omega \cdot t + \phi), \tag{B.15}$$

with

$$\overline{x} = \tau_p \cdot \left[u_{P,0} + \frac{U_0}{1+\left(\omega \cdot \tau_p\right)^2} \cdot \left(\omega \cdot \tau_p\right) \right].$$

(B.16)

Test case parameters are defined in Table B.4 and the results are shown in Figure B.6.

Parameter	Value
d_p	$1.0 \cdot 10^{-3}$ m
$u_{p,0}$	1.0 m/s
U_0	1.0 m/s
t_{osc}	4 s
ω	$\pi/2$ rad/s
ρ_p	1,000 kg/m³
ρ_{amb}	1.0 kg/m³
μ	$1.0 \cdot 10^{-5}$ Pa·s
x (domain size)	8.0 m
y, z (domain size)	0.1 m
C_D	$24/Re_p$

Table B.4: Parameters for the oscillating flow test case.

These parameters result in a Reynolds number of 100, for which the used drag coefficient is strictly not applicable. However, for this drag law an analytical solution exists.
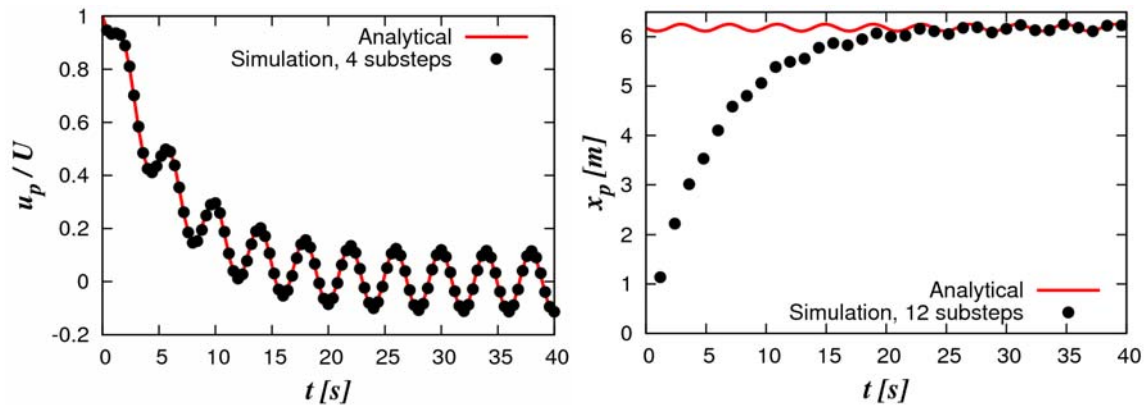
Figure B.6: Particle velocity (left) and position (right) for the oscillating flow test case (a time step of 100 ms for particle tracking was used resulting in a relative error of the velocity prediction below 1.0%, the analytical solution for $x_P(t)$ is only valid for long times $t \gg \tau_p$).

B.5 Bubble Motion in a Swirling Flow

The bubble motion at small Reynolds numbers in a flow that rotates with a constant angular velocity ω superimposed to a uniform axial velocity was studied (the setup is shown in Figure B.7).
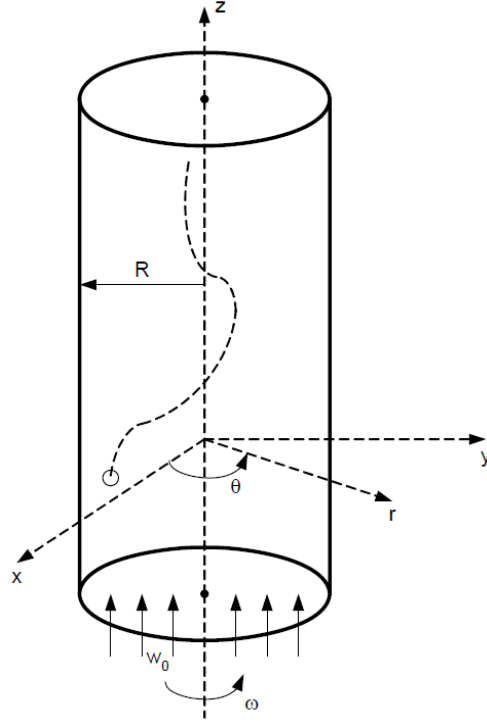
Figure B.7: Setup for the study of particle flow in a swirling flow.[1]

This flow has been experimentally and theoretically investigated by Magaud et al.[2] This flow can be effectively used to verify three-dimensional particle tracking routines because drag, lift, added-mass, and buoyancy forces, as well as forces due to the fluid stress (i.e., the force due to a pressure gradient in the continuous phase) have to be taken into account. The analytical solution for the radial position of the bubble is (from Hu[1]):

$$r^*\left(t^*\right)=r_0^* \cdot \exp\left[-f \cdot t^*/2\right]\cdot\left(\cosh\left(\frac{\sqrt{\Delta}}{2}\cdot t^*\right)+\frac{f}{\sqrt{\Delta}}\cdot\sinh\left(\frac{\sqrt{\Delta}}{2}\cdot t^*\right)\right) \; for \; \omega \le \omega_{crit}, \qquad (\text{B.17})$$

and

$$r^*\left(t^*\right)=r_0^* \cdot \exp\left[-f \cdot t^*/2\right]\cdot\left(\cos\left(\frac{\sqrt{\Delta}}{2}\cdot t^*\right)+\frac{f}{\sqrt{\Delta}}\cdot\sin\left(\frac{\sqrt{\Delta}}{2}\cdot t^*\right)\right) \; for \; \omega \ge \omega_{crit}, \qquad (\text{B.18})$$

with

$$r^* = \frac{r}{R}, t^* = \omega \cdot t, \qquad (\text{B.19})$$

$$f = \frac{3 \cdot k}{8} \cdot \frac{\mu/\rho_{amb}}{\omega \cdot (d_p/2)^2} \, , \text{ and} \qquad\qquad (\text{B.20})$$

$$\Delta = \left| f^2 - 8 \right| \, . \qquad\qquad (\text{B.21})$$

The constant k is equal to 24 for Stokes' drag law, which has been also assumed in this work. Here, ω_{crit} is the critical rotational speed that is given by (adapted from Hu[1]):

$$\omega_{crit} = \frac{3 \cdot k}{16 \cdot \sqrt{2}} \cdot \frac{\mu / \rho_{amb}}{(d_p / 2)^2} \qquad\qquad (\text{B.22})$$

This solution is valid for a lift and added mass coefficient equal to 0.5. We did not use the same implementation as described in the work of Hu,[1] but have also interpolated the pressure gradient from the grid. The parameters studied for this flow situation are detailed in Table B.5. For these parameters Stoke's drag law is strictly not valid. However, for this drag law an analytical solution exists.

Parameter	Value
d_p	$1.0 \cdot 10^{-3}$ m
$v_{p,0}$	$0.2614 - 1.312$ m/s
w_0	1.0 m/s
n	$104 - 522$ rpm
ω	$10.89 - 54.66$ rad/s
ω_{crit}	12.73 rad/s
ρ_p	1.0 kg/m³
$x_{P,0}$	$(0.024, 0, 0)$ m
ρ_{amb}	$1,000$ kg/m³
μ	$1.0 \cdot 10^{-3}$ Pa·s
R	0.030 m
x, y, z	$0.06 \times 0.06 \times 1.2$ m
C_D	$24/Re_p$

Table B.5: Parameters for the swirling flow test case.

The results for the bubble's dimensionless radial position r/R, as well as the projection of the bubble's trajectory in the x-y plane are shown in Figure B.8.
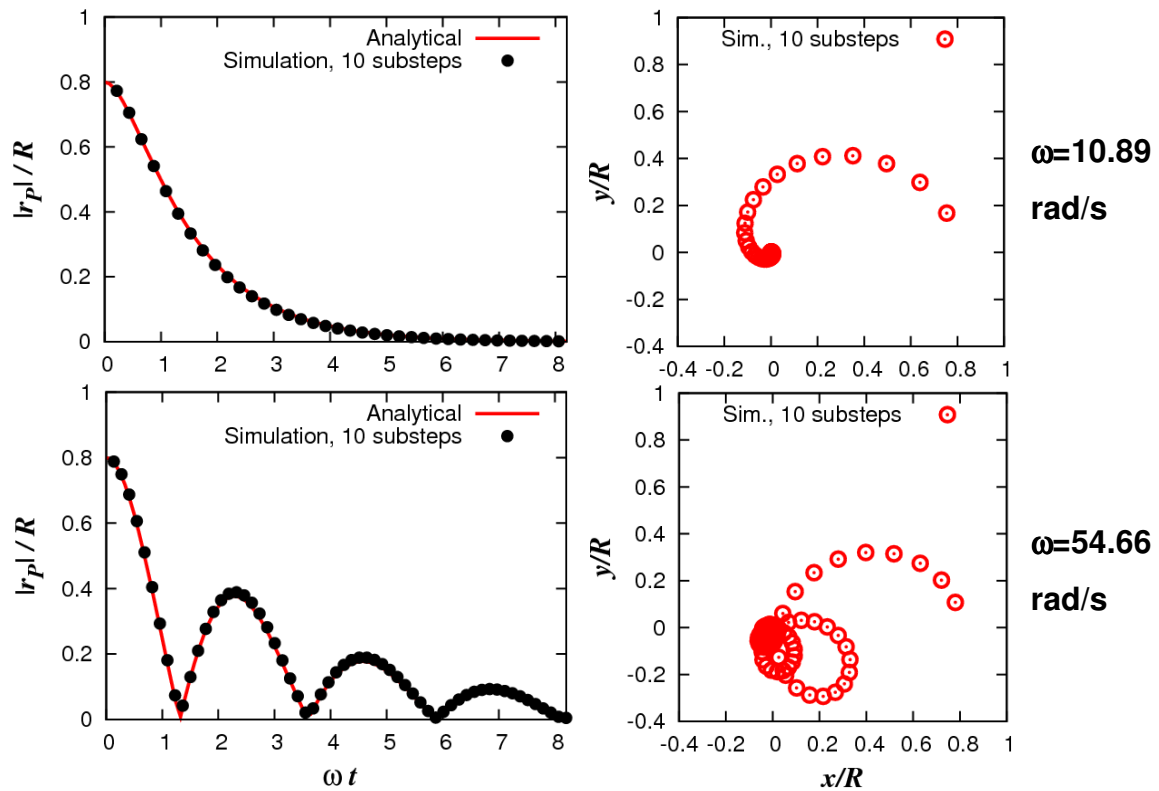
Figure B.8: Radial position (left) and trajectory (right) of a bubble in a swirling flow with two different rotation rates (top row: $\omega < \omega_{crit}$, bottom row: $\omega > \omega_{crit}$; a time step of 10 ms for particle tracking was used resulting in a relative error of the particle radial position below 1.4%, a 10 x 10 x 100 uniform grid was used to save the imposed flow field from which a linear interpolation to the particle position was performed).

B.6 References

(1) Hu GS. Towards Large Eddy Simulation of Dispersed Gas-Liquid Two-Phase Turbulent Flows. West Virginia University, Morgantown, U.S., 2005.

(2) Magaud F, Najafi AF, Angilella JR, Souhar M. Modeling and qualitative experiments on swirling bubbly flows: Single bubble with Rossby number of order 1. Journal of Fluids Engineering-Transactions of the ASME. 2003; 125:239-246.

C   Validation of the Reactive Micro Mixing Model

C.1 Setup

In order to validate the calculation strategy for the reaction term presented in chapter 6, a well-known test case for fast reactions has been selected, i.e., a confined impinging jet reactor (CIJR), that can be used to produce nano-particles via precipitation. For different designs of this reactor, Johnson and Prud'homme[1] performed a rigorous experimental study, while CFD predictions were made by Liu and Fox,[2] Gavi et al.[3], as well as Marchisio.[4]
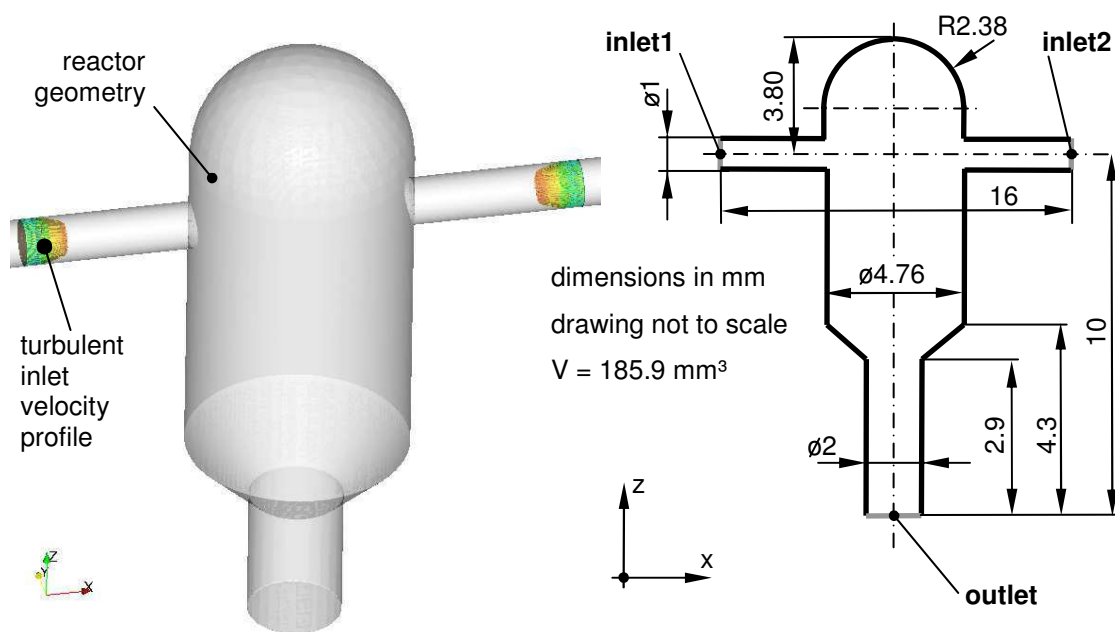
Figure C.1: Isometric view (left) and dimensioned drawing (right) of the 1000A-Y2X micro reactor.

In this work the focus is on the reactor labeled 1000A-Y2X in previous work,[1] which consists of a cylindrical main body with a half-spherical top, as well as a conical outlet. The main body has a diameter of 4.76 mm and a total length (including the spherical top and the conical outlet) of 10.9 mm. A 2.9 mm long outlet pipe with a diameter of 2 mm is connected to the conical part. The two inlets are formed by two straight pipes with a diameter of 1 mm with a total length of 16 mm. The resulting computational domain has a volume of 185.9 mm³. The Reynolds numbers studied (calculated from the inlet diameter and velocity) ranged from 700 to 2,700. All other process parameters are summarized in Table C.1. The computational mesh consisted of approx. 1.1 Mio. cells, to give an average mesh spacing of 55 μm. The volume where the collision of the jets occurred and the near-wall regions were refined.

Parameter	Value
T	298 K
ρ	962.5 kg/m³
μ	0.001995 Pa·s
D	$2.0 \cdot 10^{-9}$ m²/s
$\phi_{A,0} = \phi_{C,0} = \phi_S$	202 mol/m³
$\phi_{B,0}$	212 mol/m³
k_2	0.6855 m³/mol/s
t_{ref}	$14.10 \cdot 10^{-3}$ s
Re	700; 1,900; 2,700

Table C.1: Reaction conditions for the hydrolysis of DMP used for the analysis of the micro reactor.

C.2 Results

In Figure C.2, we have displayed the instantaneous and the time-averaged (mean) velocity together with the sub-grid-scale viscosity. Scaling of these quantities is different for each Reynolds number studied and is displayed in the caption of Figure C.2. Starting with the lowest Reynolds number studied, i.e., Re = 700, we observe that the flow is already unstable. However, from the mean flow field we conclude that velocity fluctuations are quickly damped by the action of viscous forces. The maximum sub-grid-scale viscosity ν_{sgs} (Figure C.2, right) for Re = 700 is significantly smaller than the molecular viscosity, i.e., $\nu_{sgs,max}$ = approx. 0.5ν. This indicates that the sub-grid-scale model has only a small effect on the flow and the simulation is close to a direct numerical simulation (DNS). Increasing the jet velocity, and hence the Reynolds number, sub-grid-scale motion becomes more and more important. At Re = 1,900, ν_{sgs} is already in the order of the molecular viscosity ν, and at Re = 2,700, the maximum ν_{sgs} is approximately twice ν. Similar findings were reported by Marchisio[4] in his LES study (he observed a scaling of 0.6, 1.67, as well as 2.32 for the maximum ν_{sgs} for Re = 704; 1,892 and 2696 respectively). However, Marchisio used a slightly coarser mesh, explaining his 20 to 65 % higher values for ν_{sgs}. This is especially true for the refined area near the impingement surface, where we can see from our simulation that the level of sub-grid-scale viscosity is significantly smaller than in the rest of the reactor (see Figure C.2, right).
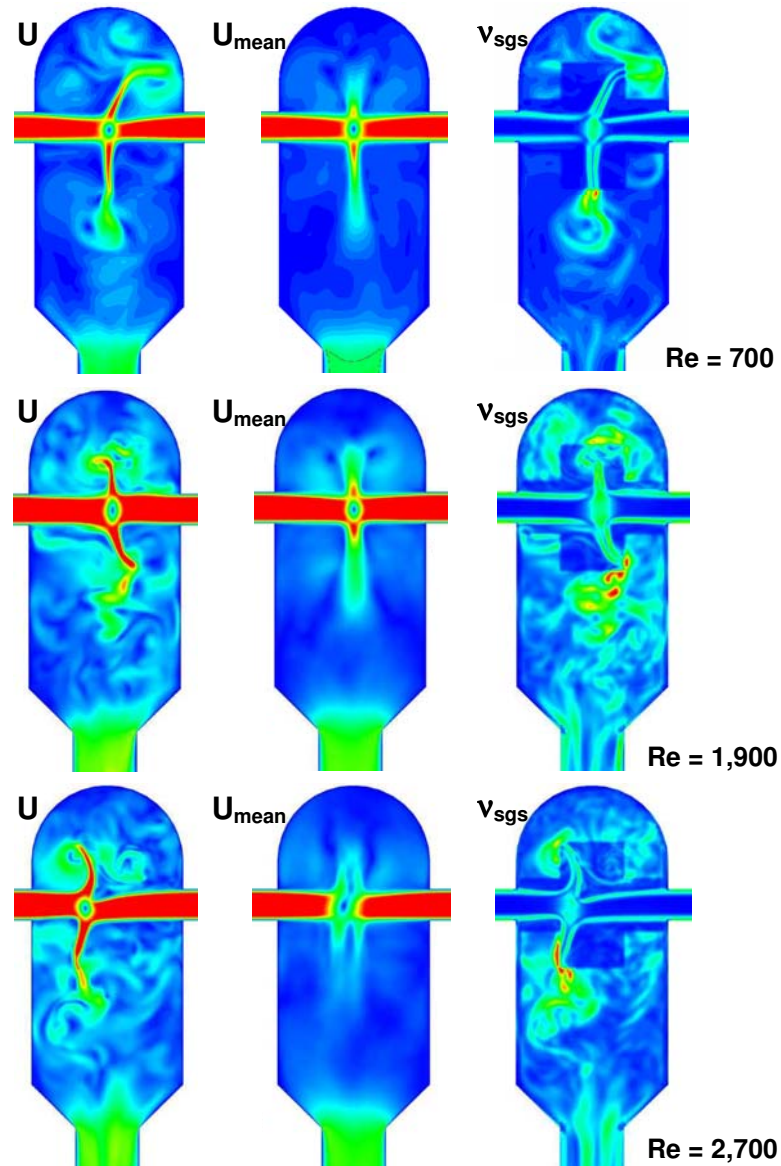
Figure C.2: Instantaneous velocity U, mean velocity U$_{mean}$, as well as sub-grid-scale viscosity ν$_{sgs}$ for three different Reynolds numbers in a CIJR (scaling of the velocities: 0 to 2 m/s for Re = 700; 0 to 4 m/s for Re = 1,900; 0 to 6 m/s for Re = 2,700; scaling of the sub-grid-scale viscosity: 0 to 1·10^{-6} m²/s for Re = 700; 0 to 2·10^{-6} m²/s for Re = 1,900; 0 to 4·10^{-6} m²/s for Re = 2,700).

From the instantaneous flow fields (Figure C.2, left) it is also clear that the flow structure is increasingly finely developed with increasing Reynolds number. Time-averaged mean velocity contour plots (Figure C.2, center) indicate that the turbulent transport increases the magnitude of fluid motion in the reactor, i.e., the fluid agitation is improved. In addition, it can be observed that for the highest Reynolds number the mean flow field does not have a pronounced peak in the impingement plane normal to the jet axis. This is due to the fact, that at high Reynolds number the flow is unsteady (as can be seen from the instantaneous velocity field, the actual impingement plane moves to left and right in an erratic motion). This leads to

a smeared-out mean velocity field. Similar findings were reported by Marchisio,[4] who observed an increase in this velocity peak from Re = 700 to Re = 1,900 and a decrease from Re = 1,900 to Re = 2,700. This trend is fully confirmed by our simulations.
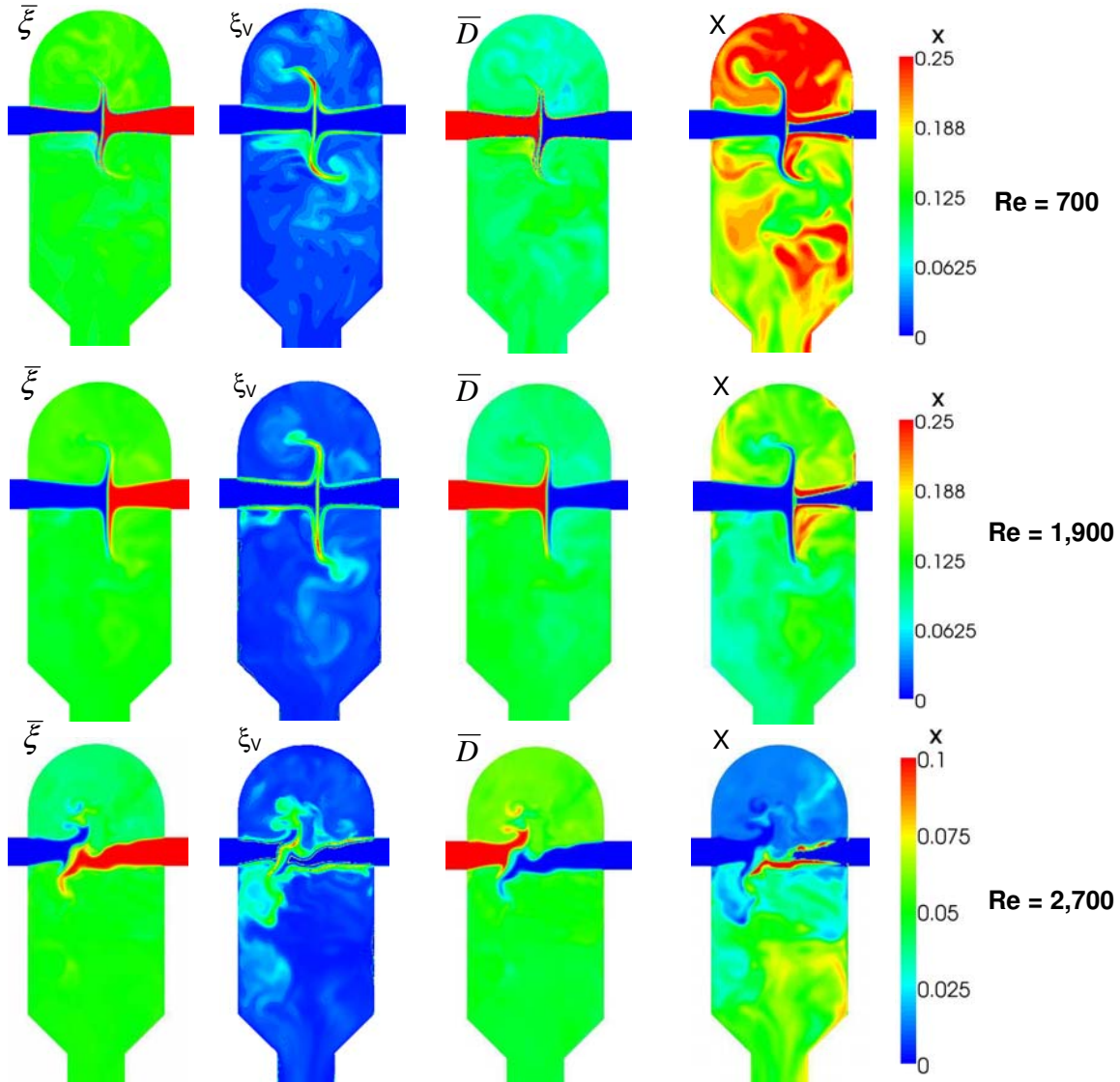
Figure C.3: Instantaneous filtered mixture fraction, variance of the mixture fraction, concentration of DMP, as well as conversion of DMP (scaling of the mixture fraction and species concentration of DMP: 0 to 1; variance of the mixture fraction 0 to 0.02; scaling of the conversion of DMP is shown in the figure for each Reynolds number, the time instant plotted is at t = 3·$t_{r,mean}$).

As there are currently no experimental data for the fluid flow available, neither by our own experiments nor in the literature, we can only conclude that the flow field agrees well with already published simulations. A rigorous validation of the used sub-grid-scale turbulence model, i.e., the Smagorinsky model, is hence not possible in this work and will be investigated in the future.

In order to validate the reaction solver, there are, however, excellent data available. First, we show some contour plots of the four main variables of the reactive flow in Figure C.3: (i) the filtered mixture fraction $\bar{\xi}$, (ii) the variance of the mixture fraction ξ_V, (iii) the filtered concentration of DMP, and (iv) the local conversion of DMP X. The latter can be calculated from the mixture fraction, as well as from the concentration of DMP via

$$X = \frac{1 - \bar{\xi} - \overline{Y_D}}{1 - \bar{\xi}}. \qquad (\text{C.1})$$

The plots in Figure C.3 are snapshotted after three times the mean residence time $t_{r,mean}$, the latter is 0.0821, 0.0302 and 0.0213 s for Re = 700; Re = 1,900 and Re = 2,700, respectively. As can be seen from this figure, the filtered mixture fraction and the species concentration of D are almost homogeneously distributed in the reactor. Only in the case of Re = 700, spatial gradients are visible in these two fields. The variance of the mixture fraction is significant only near the impingement region and vanishes rapidly. The production of mixture fraction variance can be anticipated and occurs in an annular region around the two jets, as well as directly at the impingement plane. Comparing the level of mixture fraction variance with that reported by Marchisio,[4] we find significant differences, i.e., 0.02 in our work vs. 0.12 in that of Marchisio. This is due to the finer grid in our simulation, especially near the impingement plane. Thus, we resolve significantly more of the mixture fraction variance as in the work of Marchisio.[4] A finer mesh causes a dramatically shorter timescale for dissipation (see Eqn. 6.25), that substantially increases the dissipation rate of mixture fraction variance. Finally, focusing on the local distribution of conversion X, we find that at the right side of the impingement plane, i.e., the side where the acid enters the reactor, the conversion is locally extremely high. Clearly, this is due to the local excess of acid, leading to high reaction rates and consequently to a fast consumption of the available DMP. In the case of Re = 2,700, we find good agreement for the conversion X at the outlet between the simulation results of Marchisio[4] and Gavi et al.,[3] our simulations and the experimental results of Johnson and Prud'homme.[1] Our simulations for the time-averaged conversion at the outlet of the reactor give values of 15.6%, 11.7%, and 5.0 % for Re = 700, Re = 1,900, and Re = 2,700, respectively. The results of Johnson and Prud'homme[1] indicate 30%, 13% and 7.1% conversion for the above mentioned Reynolds numbers, while Marchisio[4] obtains values close to that of our simulations (see Figure C.4). The results at lower Reynolds numbers confirm the trend in DMP conversion, i.e., higher conversion with lower Reynolds number. This is due to

the less intensive mixing, which results in a local excess of acid and hence a fast hydrolysis of DMP. However, our predictions for the conversion, as well as that of Marchisio, are significantly lower than the experimental data for low values of the Reynolds number. As already mentioned in the work of Marchisio, this is due to sensitivity of the simulation results with respect to the constant C_ϕ. Simulations using lower values of C_ϕ would yield higher conversion rates for lower Reynolds numbers.
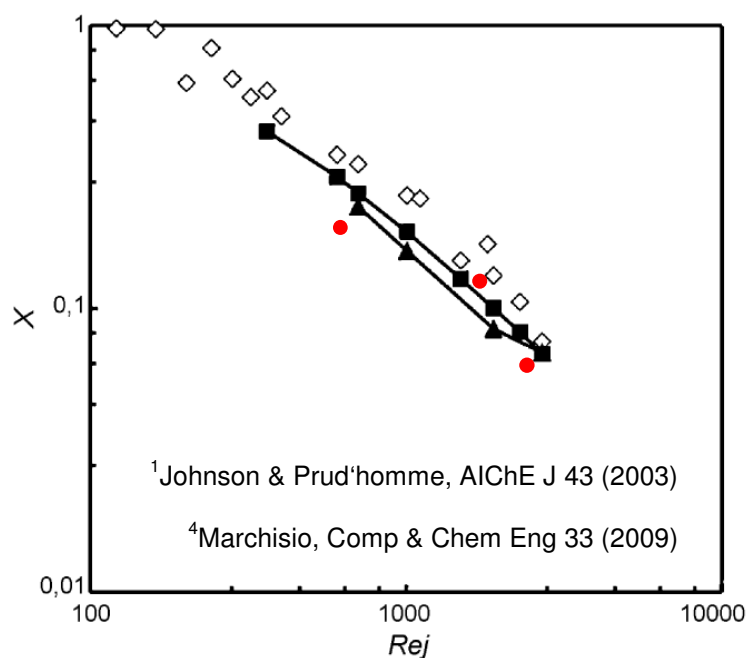
Figure C.4: DMP conversion vs. Reynolds number (diamonds: experiments by Johnson & Prud'homme,[1] filled symbols: reference simulations by Marchisio,[4] red circles: this work).

C.3 References

(1)   Johnson BK, Prud'homme RK. Chemical processing and micromixing in confined impinging jets. AIChE J. 2003; 49:2264-2282.

(2)   Liu Y, Fox RO. CFD predictions for chemical processing in a confined impinging-jets reactor. AIChE J. 2006; 52:731-744.

(3)   Gavi E, Marchisio DL, Barresi AA. CFD modelling and scale-up of Confined Impinging Jet Reactors. Chem Eng Sci. 2007; 62:2228-2241.

(4)   Marchisio DL. Large Eddy Simulation of mixing and reaction in a Confined Impinging jets Reactor. Computers & Chemical Engineering. 2009; 33:408-420.

D   Liquid Bridge Model Testing

D.1 Implementation Strategy

The liquid bridge model was implemented via a user-defined contact force model in the commercial software EDEM.[1] Specifically, the implementation is done via the function CALCULATEFORCE, to which all relevant contact information (e.g., collision velocities, time step information, particle properties, etc.) are passed by EDEM. Relevant parameters for the liquid bridge model (i.e., the characteristic collision velocity for the determination of the spring constant, the dimensionless liquid volume, the surface tension, as well as the contact angle) are read-in via the text file "lin_spring_prefs.txt". All other parameters (e.g., particle density or coefficient of restitution) are taken from the graphical user interface of EDEM.

The function CALCULATEFORCE is called when particles are in contact with their so-called "contact radius". This radius can be chosen independently of the physical radius of the particles to allow force calculations even when there is no physical contact. All quantities are calculated at the contact point, i.e., the point where the contact radii overlap. This has to be considered in the calculation of the overlap (i.e., the difference between contact and physical radius has to be subtracted to calculate the physical overlap) and in the tangential contact velocity calculation (i.e., the relative tangential velocity at the physical contact point is different from that at the contact point). The collision process of two particles with a contact radius larger than the physical radius is illustrated in Figure D.1.
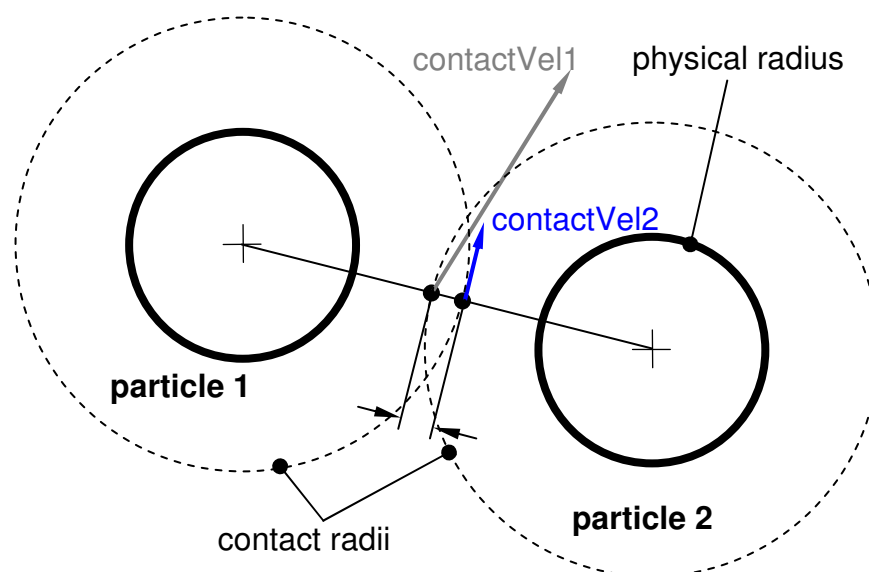
Figure D.1: Schematic representation of two colliding particles.

D.2 Force Calculation Implementation

The contact force model used is based on a Linear-Spring-Dashpot including rolling friction. The model is described in Appendix A of the EDEM User Guide.[1] The implementation is such that the normal (k_n) and tangential (k_t) stiffness are equal and calculated via:

$$k_n = k_t = \frac{16}{15} \cdot \sqrt{R_{1,2}} \cdot E_{1,2} \cdot \left(\frac{15 \cdot m_{1,2} \cdot V^2}{16 \cdot \sqrt{R_{1,2}} \cdot E_{1,2}} \right)^{1/5} . \qquad (\text{D.1})$$

Here, $R_{1,2}$, $E_{1,2}$ and $m_{1,2}$ are the effective radius, Young's modulus and mass, respectively. These quantities are calculated from the collision partners' properties. V is the characteristic impact velocity. V can be used to make the spring stiffer or softer (besides tweaking Young's modulus of the collision partners). The damping coefficients in normal and tangential direction are then evaluated from this calculated stiffness using:

$$c_n = \sqrt{\frac{4 \cdot m_{1,2} \cdot k_n}{1 + \beta^2}} , \qquad (\text{D.2})$$

$$c_t = \sqrt{\frac{4 \cdot m_{1,2} \cdot k_t}{1 + \beta^2}} , \qquad (\text{D.3})$$

where the constant β is a function of the coefficient of restitution (COR):

$$\beta = \frac{\pi}{\ln(COR)}, \qquad (\text{D.4})$$

The capillary force is directly added to the force from the Linear-Spring-Dashpot and the moment stemming from the rolling friction model.

D.3 Setup

The setup for testing the capillary force model consisted of (i) a particle-wall and (ii) a particle-particle collision scenario. The collisions were primarily performed in the z-direction, i.e., the particle(s) had only non-zero z-velocities. Gravity was set to zero. To test the implementation in the tangential direction, also particle-wall collisions under an angle of 45° were performed. The parameters used in the simulation are provided in Table D.1. The following results show logged simulation data to test the correct calculation of forces during the simulation.

D.4 Results

D.4.1 Impact Normal to Wall

Simulations of particles-wall collisions were performed, in which the particle had only a wall-normal velocity. The simulated normal overlap, i.e., the overlap of the particle's contact radius with the wall, is plotted in Figure D.2. As the contact radius is 0.3 mm larger than the physical radius, the physical (normal) overlap is the contact-radius overlap minus $3 \cdot 10^{-4}$ [m]. As can be seen from this graph, the particle impacts the wall, causing a physical overlap of the particle with the wall (i.e., the overlap is greater than $3 \cdot 10^{-4}$ [m]). Then, the particle is repelled from the wall and detaches from the wall. The particle is attracted again by the liquid-bridge force and is in continuous physical contact after $4 \cdot 10^{-4}$ [s].

Parameter	*Symbol*	*Value*
Particle radius	r_P	1 mm
Contact radius	r_c	1.3 mm
Particle density	ρ_P	2,700 kg/m³
Normal stiffness	k_n	$1.47 \cdot 10^5$ N/m
Tangential stiffness	k_t	$1.47 \cdot 10^5$ N/m
Coefficient of restitution	COR	0.7
Sliding friction coefficient	μ	0.1
Rolling friction coefficient	μ_r	0.01
Dimensionless liquid volume	V*	0.01
Contact angle	ϕ	0 °
Surface tension[a]	γ_s	1 N/m
Bond number	Bo	0.106
Wall-normal velocity	u_z	-0.05 m/s

Table D.1: Simulation input parameters for the test cases.

---

[a] The value for the surface tension has been adjusted to obtain a Bond number in the order of $O(10^{-1})$.
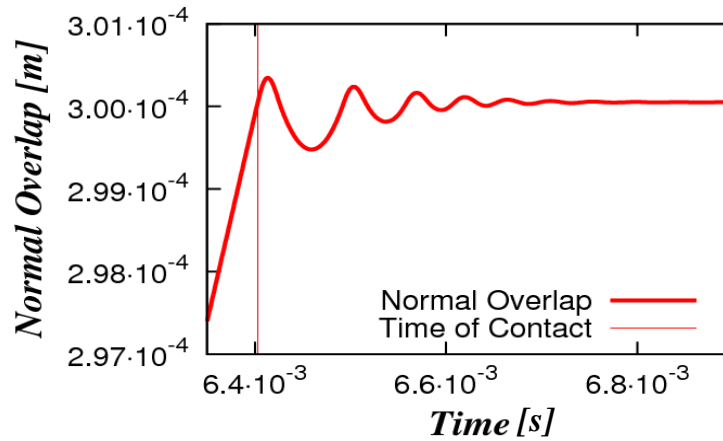
Figure D.2: Normal overlap vs. time for a particle-wall impact including liquid-bridge forces.

The total force on the particle (i.e., the sum of the liquid-bridge force and the contact force) is shown in Figure D.3. It is equal to zero before the impact (i.e., before a physical overlap occurs, this happens at a time of 6.4 ms after starting the simulation) and when the capillary force and the elastic force of the contact force model are in equilibrium (i.e., at t > $7 \cdot 10^{-3}$ [s]). After the initial impact (characterized by the first positive peak of the normal force), the particle lifts off the wall and experiences only the liquid bridge force equal to -0.0114 [N].[b] This is in agreement with the liquid bridge force at zero physical overlap using the parameters in Table D.1.
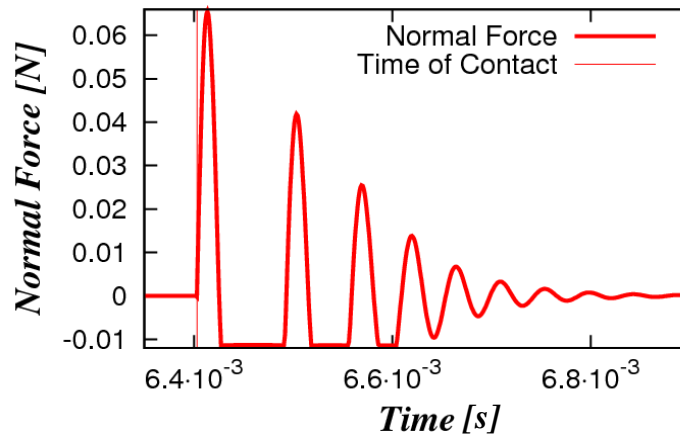
Figure D.3: Wall-normal component of the total force acting on the particle vs. time for a particle-wall impact including liquid-bridge forces.

The velocity-time profile for the wall-normal impact is shown in Figure D.4. Clearly, the capillary force model does not have an impact on the rebound velocity of the particle (it is

---

[b] The liquid bridge force changes slightly (i.e., from -0.01140 to -0.01129) during the lift-off of the particle due to the change in the wall-normal direction.

equal to 0.035 [m/s], see the global maximum of the velocity in Figure D.4; the value without capillary force would be equal to COR·u$_z$, i.e., 0.035 [m/s]). This is because we do not take into account any viscous dissipation, or other hydrodynamic forces, in our capillary bridge model. During the (relatively short) compression phase of the particle, i.e., when the physical overlap increases, there is a net energy input by the capillary force, because the liquid bridge force acts in the same direction as the particle velocity (i.e., both quantities are directed towards the wall). During the unloading phase, exactly the same amount of energy is taken up by the liquid bridge. Thus, there is no net energy input or dissipation due to the capillary bridge model during the wall impact.
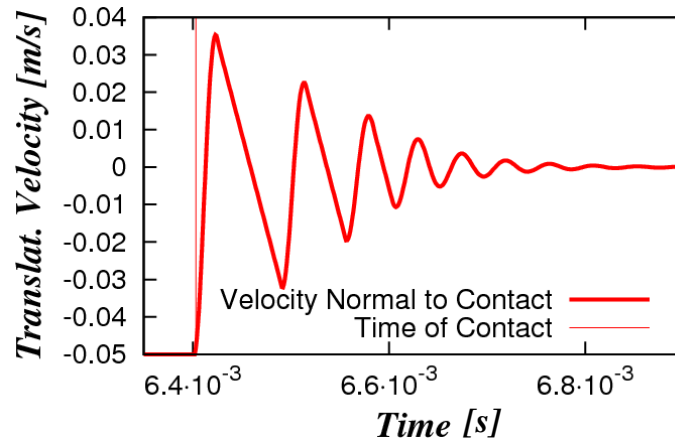
Figure D.4: Velocity of the particle vs. time for a particle-wall impact including liquid-bridge forces.

However, if the particle lifts off the wall and the liquid bridge is stretched, a certain amount of energy is dissipated by the liquid bridge. Thus, the particle has to be pulled a certain distance (i.e., the rupture distance) away from the surface against the capillary force. The energy needed for this is equal to

$$E_{rup} = \int_0^{S_{rup}} F_{cap} \cdot ds .$$
(D.5)

Thus, for a fully elastic particle with a kinetic energy lower than this rupture energy, the particle will stay in contact with the wall (or the particle). For particle-wall collisions and the used capillary force model, the rupture energy E_{rup} is

$$E_{rup,pw} = \pi \cdot r_{1,2}{}^2 \cdot \gamma_s \int_0^{S_{rup}^*} \left(\exp\left[A \cdot S^* + B\right] + C \right) \cdot dS^* .$$
(D.6)

This yields

$$E_{rup,pw} = \pi \cdot r_{1,2}{}^2 \cdot \gamma_s \cdot \left(\frac{\exp[A \cdot S_{rup}^* + B] - \exp[B]}{A} + C \cdot S_{rup}^* \right),$$ (D.7)

with

$$S_{rup}^* = \frac{1 + \phi/2}{2} \cdot \sqrt[3]{V^*}.$$ (D.8)

The critical velocity for a particle impacting on a wall resulting in a liquid bridge rupture is

$$v_{rup,pw} = \sqrt{\frac{3 \cdot r_{1,2}{}^2 \cdot \gamma_s}{2 \cdot r_1{}^3 \cdot \rho_p} \cdot \left(\frac{\exp[A \cdot S_{rup}^* + B] - \exp[B]}{A} + C \cdot S_{rup}^* \right)}.$$ (D.9)

For the parameters shown in Table D.1 (but for a fully elastic particle, i.e., COR = 1), this yields the results as shown in Table D.2.

Parameter	Symbol	Value
Rupture distance	$S_{rup}*$	0.215
Max liq. bridge force	$F_{cap,pw,max}$	0.0114 N
Min liq. bridge force	$F_{cap,pw,min}$	0.000529 N
Rupture energy	$E_{rup,pw}$	$6.28 \cdot 10^{-7}$ Nm
Critical rupture velocity	$v_{rup,pw}$	0.333 m/s

Table D.2: Critical values for liquid-film rupture for particle-wall collisions.

In Figure D.5 we show the overlap for a particle impacting the wall with a velocity 2% below (solid line) and 2% above (dashed line) the critical rupture velocity. Clearly, in case of the lower velocity, the particle overlap decreases after the impact (i.e., at the point with the highest overlap of $3 \cdot 10^{-4}$ [m]) and then increases again. Thus, the particle bounces from the wall, but the liquid bridge force cannot be overcome and the particle moves again towards the wall. However, if the particle's impact velocity is slightly higher than the critical velocity, the overlap steadily increases until the liquid bridge ruptures (this occurs after 2.7 [ms]). The total force on the particle is then zero and the particle moves away from the wall with a constant velocity. This is also visible from Figure D.6, where the particle velocity normal to the wall is plotted.
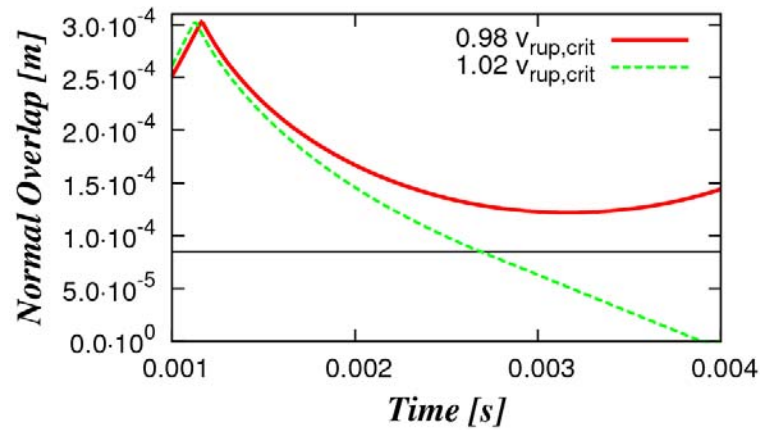
Figure D.5: Normal overlap vs. time for a sub- and supercritical particle-wall impact including liquid-bridge forces (the horizontal black line indicates the overlap at which the liquid bridge ruptures).
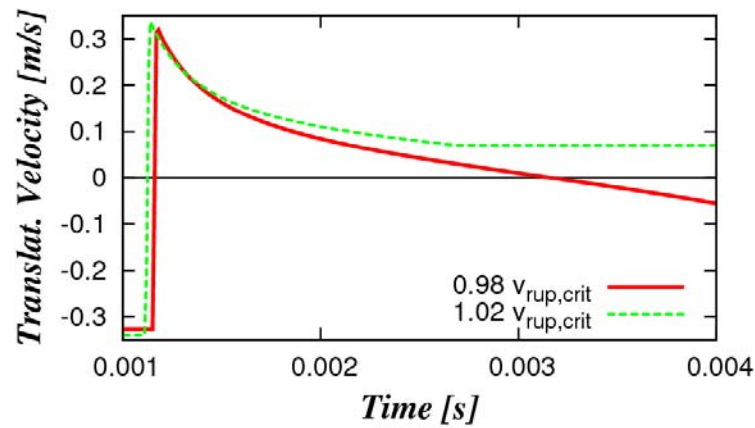
Figure D.6: Velocity of the particle vs. time for a sub- and supercritical particle-wall impact including liquid-bridge forces.

D.4.2 Impact at 45° to Wall

To test the implementation of the tangential force calculation, a particle impact with a wall-normal velocity of $u_z = -0.05$ [m/s] and a wall-tangential velocity of $u_x = 0.05$ [m/s], i.e., a collision under an impact angle of 45°, was studied. For this situation, the forces, the particle velocities and the overlap in the direction normal to the wall are identical to the situation described in Chapter D.4.1. This can be seen from the bold solid lines in Figure D.7 to Figure D.9. These curves are identical to the curves shown in Figure D.2 to Figure D.4. However, in the case of a 45° impact, there is also a tangential force that promotes a rotation of the particle. Clearly, there exists a tangential force during physical contact of the particle and the wall (see the dashed line in Figure D.7) that rapidly increases or decreases the angular velocity (see the dashed line in Figure D.8). When the particle lifts off the wall (i.e., when there is no physical contact between particle and wall), the angular velocity decreases slightly due to the

action of the liquid bridge force. After approximately $4{\cdot}10^{-4}$ [s] the particle angular velocity is constant, i.e., the particle rolls on the surface and is slowly decelerated by rolling friction.
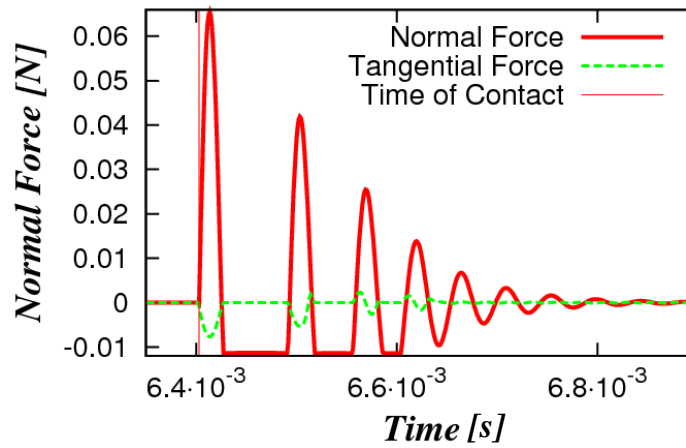
Figure D.7: Wall-normal and tangential component of the total force acting on the particle vs. time for a particle-wall impact at 45° including liquid-bridge forces.
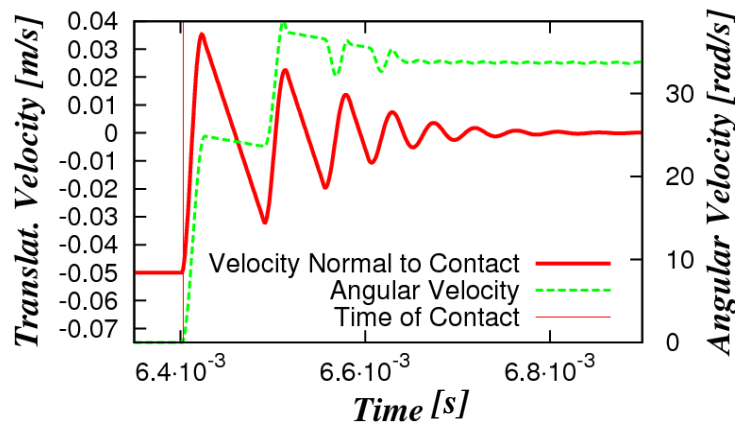
Figure D.8: Velocity normal to the wall and angular velocity of the particle vs. time for a particle-wall impact at 45° including liquid-bridge forces.

Normal and tangential overlaps are shown in Figure D.9. As can be clearly seen, the normal overlap is identical to that reported in the case of a normal-to-wall impact as it should be. The tangential overlap (of the contact radius with the wall) is large when the first physical contact occurs (i.e., it is approximately $2.5{\cdot}10^{-5}$ [m], data not shown) and very small for the following impacts. It increases only when the particle bounces back, i.e., in case of no physical contact, and quickly approaches zero when the particle is in contact with the wall.
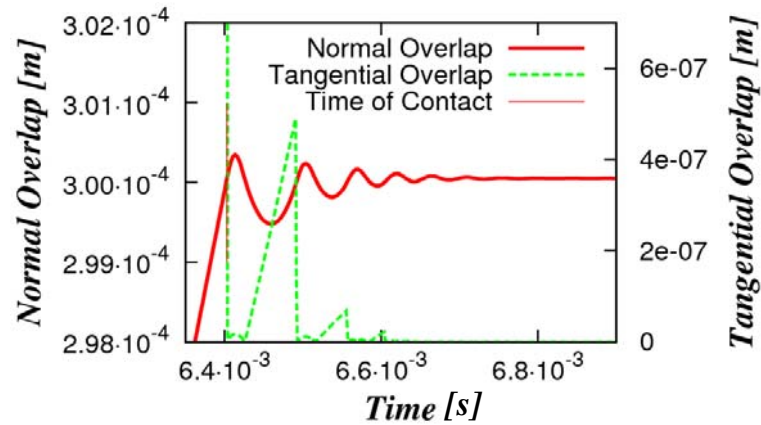
Figure D.9: Normal and tangential overlap vs. time for a particle-wall impact at 45° including liquid-bridge forces.

D.4.3 Particle-Particle Collision

Similar tests to those performed in Chapter D.4.1 were done for the collision of two equally-sized particles (the parameters were the same as in Table D.1). Plots for the normal overlap and the total (normal) force acting on a particle during a head-on collision are shown in Figure D.10 and Figure D.11. The maximum force that is computed within the simulation and shown in Figure D.11 (i.e., 0.005476 [N]) is identical to the value obtained from Eqn. 7.4 and the parameters in Table D.1.
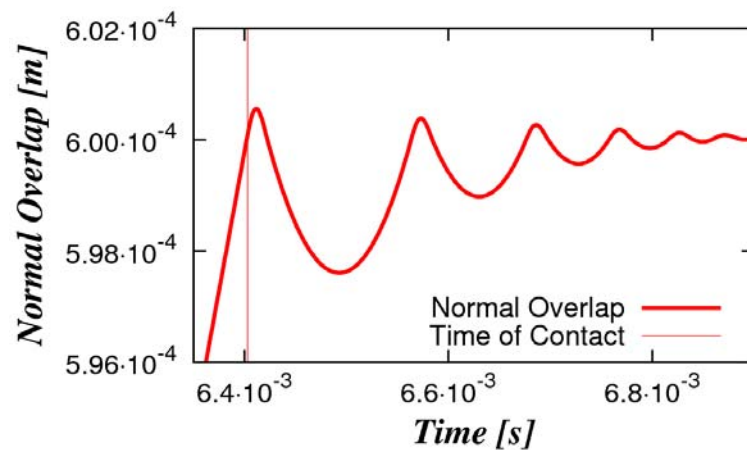
Figure D.10: Normal overlap vs. time for a particle-particle collision including liquid-bridge forces.
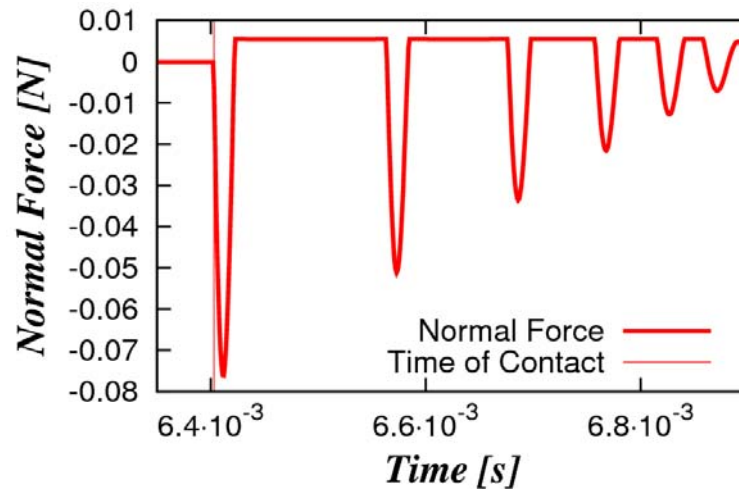
Figure D.11: Total force acting on a particle vs. time for a particle-particle collision including liquid-bridge forces.

D.5 References

(1) EDEM 2.1 User Guide. 2009.

E   Calculation of Blade-relative Velocities

In order to calculate a meaningful time-averaged blade-relative velocity of particles, we calculated the particle velocity in a coordinate system that rotates with the impeller. Thus, we performed a coordinate transformation, i.e., a rotation, by using the rotary matrix $\mathbf{R}$:

$$\mathbf{R} = \begin{pmatrix} \cos(\alpha_{Blade}) & \sin(\alpha_{Blade}) \\ -\sin(\alpha_{Blade}) & \cos(\alpha_{Blade}) \end{pmatrix} \qquad (\text{E.1})$$

Multiplication of this matrix with the particle coordinates or the particle's blade-relative velocity gives the quantities in the rotating coordinate system K':

$$\begin{aligned} \vec{r}' &= \mathbf{R} \cdot \vec{r} \\ \vec{v}_{P,\mathrm{Re}l}{}' &= \mathbf{R} \cdot \vec{v}_{P,\mathrm{Re}l} \end{aligned} \qquad (\text{E.2})$$

By performing this transformation, we obtain the blade-relative velocity field in a blade-fixed coordinate system K'. We are now able to calculate a time-averaged blade-relative velocity field that is phase resolved, i.e., also depends on the circumferential coordinate. Such a phase-resolved time-averaged velocity would not be obtained when taking the blade-relative velocity in an absolute coordinate system K. This is because the dependency on the circumferential coordinate would be lost due to the rotational motion of the impeller.

F   Basics of the Cross-Correlation Method for PIV

F.1 Introduction

The algorithm described here is that used in the `singlepass` routine of MatPIV[1] 1.6.1. This appendix is an introduction to the cross-correlation method for particle image velocimetry (PIV), where the displacement between two images has to be calculated. Thus, the goal is to find the position an image has to be displaced in order to match a second image. A more elaborate introduction to PIV algorithms as well as their accuracy is provided by Scarano.[2]

MatPIV uses the function `xcorr` to perform the cross correlation operation in MATLAB. The function `R=xcorr(A,B)` returns the cross-correlation of two matrices A(Ma, Na) and B(Mb, Nb). The result is a matrix of dimension R(Ma+Mb-1, Na+Nb-1) which is calculated by:

$$R(i, j) = \sum_{m=0}^{(M_a-1)} \sum_{n=0}^{(N_a-1)} A(m,n) \cdot conj\left[B(m+i, n+j)\right] \qquad (\,\text{F.1}\,)$$
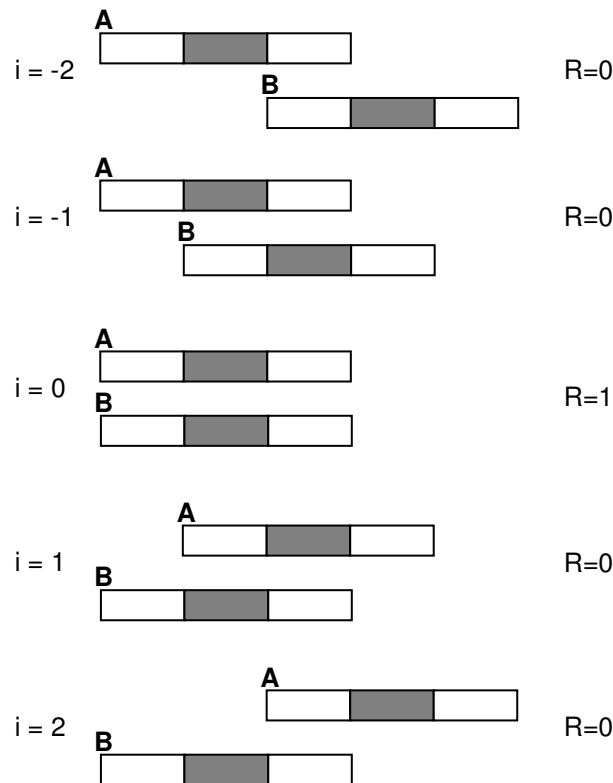
Figure F.1: Graphical representation of a one-dimensional cross correlation.

This matrix is defined for $1 \leq i \leq M_a + M_b - 1$ and $1 \leq j \leq N_a + N_b - 1$. For a simple 1D-system, i.e., $N_a = N_b = 1$, we get the following graphical representation of this operation (see Figure F.1, bright = 0, dark = 1). For i = 0 the two matrices correlate and R is unity.

F.2 Application to Image Processing

Two matrices are used to represent the intensity distribution in an interrogation area (IA), i.e., a sub-image of an image. To limit the number of calculations, Eqn. F.1 is evaluated using a fast Fourier transformation (FFT). The correlation matrix R(i,j) is obtained and the position (i.e., the values for i and j) where R has a global maximum is detected. This position is equal to the displacement of the two IAs. This information can be used to calculate the velocity by division with the time difference between the two images.

In the following, these sub steps of such an image processing algorithm are described using two simple (synthetic) images shown in Figure F.2. These two images represent IAs at two different time instances.
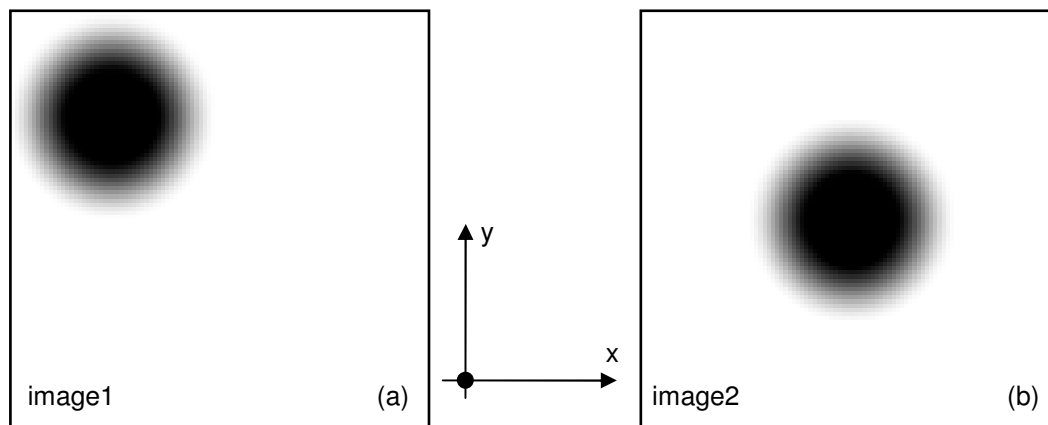
Figure F.2: Raw images for cross-correlation analysis (a: image1, b: image2).

F.2.1 Reading the Image

The images (e.g., in TIF format) are read in into MATLAB via the `imread` command. The image is then converted to a matrix in double-precision number format and normalized. The mean is subtracted to avoid correlation of the mean background intensities. These data is shown in Figure F.3. Note, that due to the numbering convention in MATLAB the y-axis is inverted during the reading process.
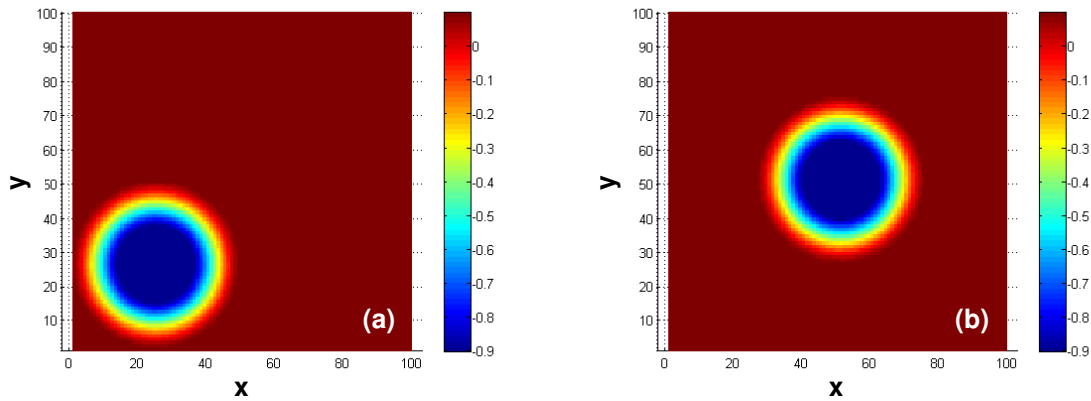
Figure F.3: Normalized data as in MATLAB (a: image1, b: image2).

F.2.2 Weighting the Image Data

Each IA (in this example the image "image1" and "image2") is weighted with a two-dimensional function w. This has to be done because in the subsequent FFT calculation it is assumed that the input is of a periodic nature. The obtained correlation field would be biased for large displacements if no weighting is performed.

Weighting adds values of zeros around the original interrogation areas by multiplication with a two-dimensional function. The choices for this function are:

- Gaussian
- Hanning
- Hann
- Hamming
- Blackman
- Cosn

Typically, the function `Cosn` is used with a value for d of 20 (see Figure F.4). The function `Cosn` is defined as:

$$w(m,n) = \left(1 - \cos^d\left(\pi \cdot \frac{m}{M}\right)\right) \cdot \left(1 - \cos^d\left(\pi \cdot \frac{n}{N}\right)\right). \qquad (\text{F.2})$$

Here M and N are the size of the IA to be processed in x and y-direction, respectively.
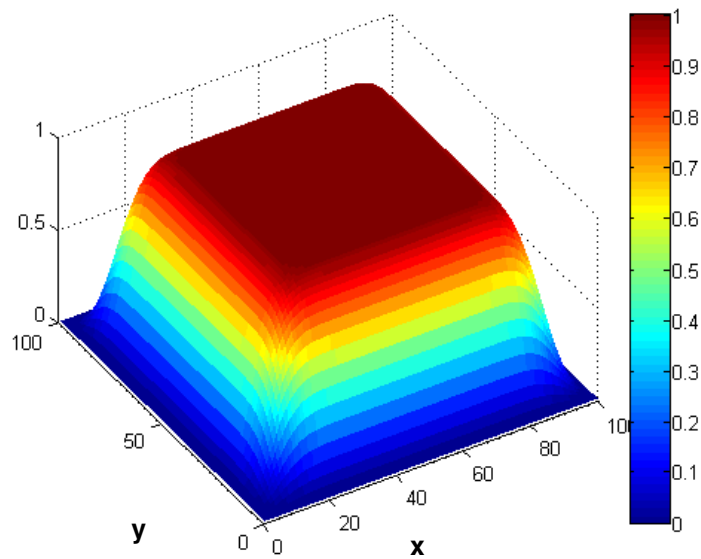
Figure F.4: Function `Cosn` as used for the weighting of the images (n = 20).

The weighted "image1" is shown in Figure F.5.
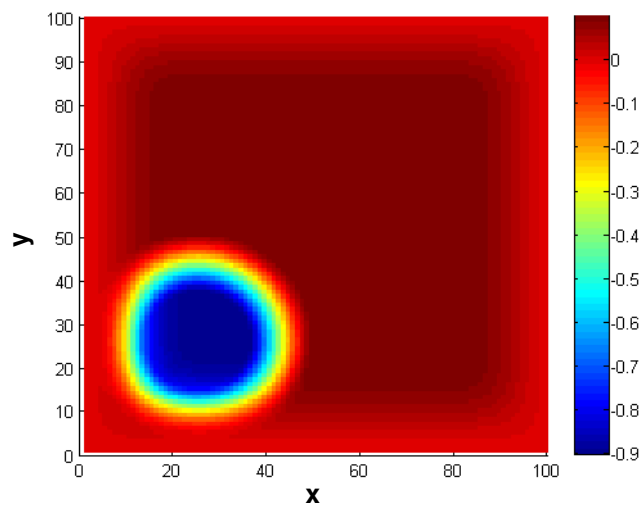
Figure F.5: 'image1' weighted with function `Cosn` (n=20).

F.2.3 Performing the Cross-Correlation

After weighting the image, the (FFT) cross-correlation is performed using the `xcorrf2` of MatPIV. The result is again normalized, and a matrix containing the cross-correlation information with a size (Ma+Mb-1, Na+Nb-1) is obtained. To correctly visualize the displacement between the two images, the matrix has to be displayed on a grid that starts at

(-Ma+1, Na+1) and ends at (Mb-1, Nb-1). The resulting correlation matrix is shown in Figure F.6.
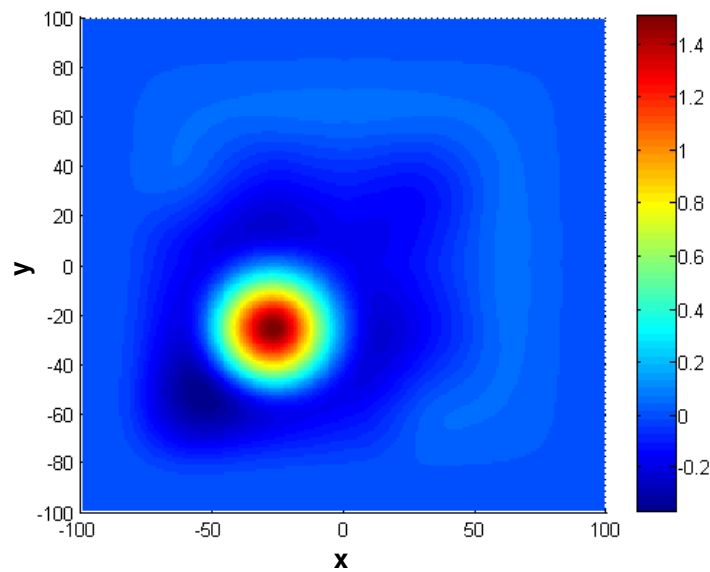
Figure F.6: Correlation matrix of 'image1' and 'image2'.

F.2.4 Locating the Global Maximum

The function find of MATLAB is used to locate the highest value (i.e., the global maximum) in the correlation matrix at a discrete displacement level. To increase the precision, a fitting of the correlation matrix near the highest peak can be performed. This is done using different fitting functions (e.g., a centroid, Gaussian or parabolic fit) in MatPIV. This sub-pixel fitting is done in the function intpeak that returns the values of the correlation matrix in a significantly finer resolution than the native IA resolution. The peak position then can be found again using the function find of MATLAB. This yields the coordinates of the displacement in the correlation diagram of (-27.1450, -25.8155).

Finally, the displacement in x-direction has to be multiplied with -1 again to give the true displacement of the data (this is because of the numbering convention in MATLAB). Thus, the true displacement is (+27.1450, -25.8155) [pixel].

F.3 References

(1) Sveen JK. An introduction to MatPIV v.1.6.1. http://folk.uio.no/jks/matpiv/. 2004. Oslo, Norway, Dept. of Mathematics, University of Oslo.

(2) Scarano F. Iterative image deformation methods in PIV. Measurement Science & Technology. 2002; 13:R1-R19.